Springer Series in Surface Sciences 48

Sascha Sadewasser
Thilo Glatzel *Editors*

Kelvin Probe Force Microscopy

Measuring and Compensating Electrostatic Forces

Springer

SPRINGER SERIES IN SURFACE SCIENCES

Series Editors: G. Ertl, H. Lüth and D.L. Mills

This series covers the whole spectrum of surface sciences, including structure and dynamics of clean and adsorbate-covered surfaces, thin films, basic surface effects, analytical methods and also the physics and chemistry of interfaces. Written by leading researchers in the field, the books are intended primarily for researchers in academia and industry and for graduate students.

Please view available titles in *Springer Series in Surface Sciences*
on series homepage http://www.springer.com/series/409

Sascha Sadewasser
Thilo Glatzel
Editors

Kelvin Probe Force Microscopy

Measuring and Compensating Electrostatic Forces

With 189 Figures

Springer

Volume Editors

Dr. Sascha Sadewasser

INL - International Iberian Nanotechnology Laboratory
Avda. Mestre José Veiga s/n, 4715-330 Braga, Portugal
E-mail: sascha.sadewasser@inl.int

Dr. Thilo Glatzel

Universität Basel, Institut für Physik
Klingelbergstr. 82, 4056 Basel, Switzerland
E-mail: thilo.glatzel@unibas.ch

Series Editors:

Professor Dr. Gerhard Ertl

Fritz-Haber-Institute der Max-Planck-Gesellschaft, Faradayweg 4–6,
14195 Berlin, Germany

Professor Dr. Hans Lüth

Institut für Schicht- und Ionentechnik
Forschungszentrum Jülich GmbH,
52425 Jülich, Germany

Professor Douglas L. Mills, Ph.D.

Department of Physics, University of California,
Irvine, CA 92717, USA

Springer Series in Surface Sciences ISSN 0931-5195
ISBN 978-3-642-22565-9 e-ISBN 978-3-642-22566-6
DOI 10.1007/978-3-642-22566-6
Springer Heidelberg Dordrecht London New York

Library of Congress Control Number: 2011939753

Preface

When we started to apply Kelvin probe force microscopy (KPFM) for the characterization of thin film solar cell materials in 1998 at the Hahn Meitner Institute in Berlin, KPFM was still a very specialized technique, little known and only available in a few laboratories world wide. Nevertheless, at this time already 7 years had passed since the first report of KPFM in 1991.

Eight years later, KPFM had become a quite well spread technique being applied in many laboratories for a whole variety of sample characterization and for the investigation of different questions in many material systems. At this time, we decided to organize a KPFM workshop as a satellite meeting to the Non-Contact Atomic Force Microscopy conference in the fall 2008 in Madrid, Spain. We expected the number of participants to be on the order of 20–40, since this was the number of experts that were more or less working in this field. However, to our surprise, the workshop found many more interested participants reaching an attendance of more than 100 participants. Being a half day workshop, the program was rather limited and consisted in only five oral presentations and one discussion session. The talks were given by KPFM experts, namely Christian Loppacher on "Kelvin Probe Force Microscopy: A comparison of different methods and their resolution in experiment and simulation," Yossi Rosenwaks on "Quantitative KPFM: Semiconductors and self-assembled monolayers," Lev Kantorovich on "Atomistic simulations of AFM junctions using SciFi code with possible applications for KPFM," Laurent Nony on "Some aspects of high-resolution imaging in KPFM," and Hiroshi Onishi on "Charge transfer induced by adatoms and admolecules."

After this event the idea came up to ask the speakers to write down their notes and assemble some kind of a compendium for future use and reference. This initial idea finally developed into the present book, extending the workshop contributions by 8 additional chapters on further topics of interest. After 2 years we finally finished assembling the first book on KPFM, hoping to give many readers, newcomers to the field as well as experts, a way to learn a new technique, expand their knowledge about KPFM and as a reference for the daily use.

We would like to thank the patient contributing authors and our many collaborators we had in our respective institutions throughout the last 12 years working in the field of KPFM and NC-AFM.

Berlin and Basel,
August 2011

Sascha Sadewasser
Thilo Glatzel

Contents

Contributors

Amir Boag School of Electrical Engineering, Faculty of Engineering, Tel Aviv University, Ramat-Aviv 69978, Israel, boag@eng.tau.ac.il

Franck Bocquet Aix-Marseille Université, IM2NP, Centre scientifique de Saint-Jérôme Avenue Escadrille Normandie-Niemen, Case 151 F-13397 Marseille CEDEX 20, France, franck.bocquet@univ-cezanne.fr

Lynda Cockins McGill University, Department of Physics, 3600 rue University, Montreal H3A 2T8, Canada, cockinsl@physics.mcgill.ca

Dominique Deresmes IEMN Dept. ISEN, CNRS UMR 8520, Centre National de Recherche Scientifique (CNRS), Av. Henri Poincaré, B.P. 60069, 59652 Villeneuve d'Ascq, France, dominique.deresmes@isen.iemn.univ-lile1.fr

Heinrich Diesinger IEMN Dept. ISEN, CNRS UMR 8520, Centre National de Recherche Scientifique (CNRS), Av. Henri Poincaré, B.P. 60069, 59652 Villeneuve d'Ascq, France, hpdiesinger@ntu.edu.sg

George Elias School of Electrical Engineering, Faculty of Engineering, Tel Aviv University, Ramat-Aviv 69978, Israel, egeorge.email@gmail.com

Adam S. Foster Department of Physics, Tampere University of Technology, P.O. Box 692, FIN-33101 Tampere, Finland

Department of Applied Physics, Aalto School of Science, P.O. Box 1100, 02015 Helsinki, Finland, adam.foster@tut.fi

Thilo Glatzel University of Basel, Department of Physics, Klingelbergstr. 82, 4056 Basel, Switzerland, thilo.glatzel@unibas.ch

Peter Grütter McGill University, Department of Physics, 3600 rue University, Montreal H3A 2T8, Canada, grutter@physics.mcgill.ca

Sergei V. Kalinin Materials Science and Technology Division and Center for Nanophase Materials Science, Oak Ridge National Laboratory, Oak Ridge, Tennessee 37831, USA, sergei2@ornl.gov

Jerzy Konior Institute of Physics, Jagiellonian University, ul. Reymonta 4, 30-059 Krakow, Poland, jerzy.konior@uj.edu.pl

Franciszek Krok Institute of Physics, Jagiellonian University, ul. Reymonta 4, 30-059 Krakow, Poland, franciszek.krok@uj.edu.pl

Christian Loppacher Aix-Marseille Université, IM2NP, Centre scientifique de Saint-Jérôme Avenue Escadrille Normandie-Niemen, Case 151 F-13397 Marseille CEDEX 20, France, christian.loppacher@im2np.fr

Thierry Mélin IEMN Dept. ISEN, CNRS UMR 8520, Centre National de Recherche Scientifique (CNRS), Av. Henri Poincaré, B.P. 60069, 59652 Villeneuve d'Ascq, France, thierry.melin@isen.iemn.univ-lille1.fr

Yoichi Miyahara McGill University, Department of Physics, 3600 rue University, Montreal H3A 2T8, Canada, miyahara@physics.mcgill.ca

Laurent Nony Aix-Marseille Université, IM2NP, Centre scientifique de Saint-Jérôme Avenue Escadrille Normandie-Niemen, Case 151 F-13397 Marseille CEDEX 20, France, laurent.nony@im2np.fr

Hiroshi Onishi Department of Chemistry, Kobe University, Rokko-dai, Nada, Kobe 657-8501, Japan, oni@kobe-u.ac.jp

Brian J. Rodriguez Conway Institute of Biomolecular and Biomedical Research, University College Dublin, Belfield, Dublin 4, Ireland, brian.rodriguez@ucd.ie

Yossi Rosenwaks School of Electrical Engineering, Faculty of Engineering, Tel Aviv University, Ramat-Aviv 69978, Israel, yossir@eng.tau.ac.il

Sascha Sadewasser International Iberian Nanotechnology Laboratory - INL, Avda. Mestre José Veiga s/n, 4715-330 Braga, Portugal, sascha.sadewasser@inl.int

Akira Sasahara School of Materials Science, Japan Advanced Institute of Science and Technology, Ishikawa 923-1292, Japan, sasahara@jaist.ac.jp

Alexander Schwarzman School of Electrical Engineering, Faculty of Engineering, Tel Aviv University, Ramat-Aviv 69978, Israel, alexsch@eng.tau.ac.il

Rafi Shikler Department of Electrical and Computer Engineering, Ben-Gurion University of the Negev, P.O. Box 653, Beer-Sheva 84105, Israel, rshikler@ee.bgu.ac.il

Eran Strassbourg School of Electrical Engineering, Faculty of Engineering, Tel Aviv University, Ramat-Aviv 69978, Israel, eran_str@yahoo.com

Marek Szymonski Institute of Physics, Jagiellonian University, ul. Reymonta 4, 30-059 Krakow, Poland, ufszymon@cyf-kr.edu.pl

Chapter 1
Introduction

S. Sadewasser and Th. Glatzel

Abstract The Kelvin probe force microscope allows to image surface electronic properties, namely the contact potential difference (CPD) with nanometer scale resolution. With the steadily increasing variety of applications and materials investigated, the increasing trend of research performed applying this techniques is foreseen to continue.

Surface science was revolutionized in 1982 by the invention of the scanning tunneling microscope (STM) by Binnig and Rohrer who received the Nobel prize only 4 years later in 1986 [1]. Shortly after the invention, the first images showing atomic resolution on a Si(111) 7×7 surface were obtained. As this allowed real space imaging of atomic structure, it gave a new turn on nanotechnology research. By means of its working principle, namely the quantum mechanical tunneling current, the STM is inherently limited to the study of conducting surfaces. In 1986, the invention of the atomic force microscope (AFM) solved this limitation by using a tip supported by a cantilever beam [2]. The tip can be scanned across a surface in contact and the deflection of the beam can be measured, for example by employing optical detection on the back side of the cantilever. Using the AFM also insulators were now accessible on nanometer and even atomic scale. Further development led to the non-contact (or dynamical) mode of the AFM [3], where the cantilever is vibrated close to its resonance frequency and changes in the vibration due to tip–sample interaction are employed to maintain a constant distance to the sample

S. Sadewasser (✉)
International Iberian Nanotechnology Laboratory - INL, Avda. Mestre José Veiga s/n, 4715-330 Braga, Portugal
e-mail: sascha.sadewasser@inl.int

Th. Glatzel
Department of Physics, University of Basel, Klingelbergstr. 82, 4056 Basel, Switzerland
e-mail: thilo.glatzel@unibas.ch

S. Sadewasser and T. Glatzel (eds.), *Kelvin Probe Force Microscopy*, Springer Series in Surface Sciences 48, DOI 10.1007/978-3-642-22566-6_1,

surface while scanning across the sample. Forces exerted by the tip on the sample are minimal in non-contact mode; therefore, it is the method of choice for soft samples, as, for example, biological or polymer samples.

A wide field of applications was opened by the combination of the AFM with other measurement methods, which provides access to additional sample properties on a lateral scale in the nanometer range. One representative, the Kelvin probe force microscope (KPFM), was first developed by Nonnenmacher et al. [4] and Weaver et al. [5] and it allows to image surface electronic properties, namely the contact potential difference (CPD). The name "Kelvin probe force microscope" originates from the macroscopic method developed by Lord Kelvin in 1898 using a vibrating parallel plate capacitor arrangement, where a voltage applied to one vibrating plate is controlled such that no current is induced by the vibration [6]. The reduction of this exact principle to the microscopic scale, however, results in poor sensitivity, since the size of the plates is too small to generate a sufficient current. Therefore, in KPFM the electrostatic force is used. The cantilever in AFM is a very sensitive force sensor; thus, the contact potential difference can be measured with high sensitivity. A dc-bias applied to the sample (or the tip) is controlled such that the electrostatic forces between tip and sample are minimized.

Invented in 1991, it took almost 10 years before there was a sizeable number of publications per year involving the KPFM technique (Fig. 1.1). Nevertheless, starting with the new millennium, the KPFM found more and more applications and interest, visible in a considerably increased publication activity. This went hand in hand with the more wide-spread availability of AFM equipment in many laboratories world wide. In the recent years, the publication number is nearly 10 times as high as in the early years after invention. With the steadily increasing variety of applications and materials investigated, the increasing trend of research performed applying KPFM techniques is foreseen to continue. A similar trend can be observed for the number of citations per year (Fig. 1.1).

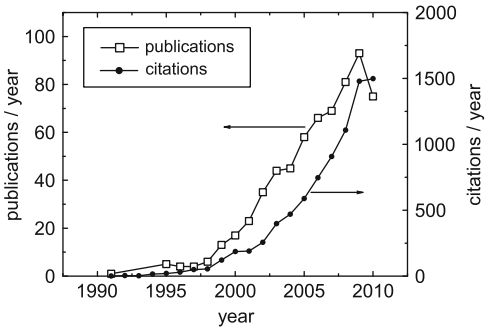

Fig. 1.1 Publications and citations per year since the invention of the KPFM (The search was performed on December 2nd 2010 using the search term "KPFM OR SKPM OR Kelvin force microscopy" in Inspec)

In the recent years, many books and review articles have been published on the topic of scanning probe microscopy, AFM or even nc-AFM [7–9]. Sometimes these books comprise a small description or a chapter on KPFM; however, a major monograph on KPFM has not been published so far. Therefore, interested researchers have to compile their information from a variety of sources. At a time where 20 years have passed since the invention of the KPFM and a steadily increasing number of publications every year, we feel that it is an excellent point in time to provide such a compilation on KPFM. We hope to give an overview about the details of the technique and many examples of their applications in a variety of fields.

The book is divided into two parts. The first part is dedicated to the technique of KPFM itself, providing in Chap. 2 a detailed description of the working principles, the various different techniques that can be employed and advantages as well as drawbacks of the various realizations of KPFM. Chapter 3 will discuss in detail the capacitive cross talk and its effect on KPFM measurements. The effect of the long range electrostatic force on the spatial resolution in KPFM is discussed in Chap. 4, mainly based on analytical and simulation work. Chapter 5 then presents a theoretical discussion about the involved effects in atomic-resolution KPFM, based on a KPFM simulator.

The second part of the book is focused on the application of KPFM to a variety of sample systems and goals. Chapters 6–9 are devoted to semiconductor samples, where in Chap. 6 a general treatment of semiconductor studies is given. Chapter 7 discusses the implications of nanostructures supported on semiconductor substrates, and Chap. 8 is dedicated to the studies of solar cell related semiconductor materials. Chapter 9 deals with the investigation of electrostatic forces for the study of low-dimensional semiconductor structures.

In Chap. 10, the additional insight into catalysts gained by KPFM will be reviewed. Chapter 11 deals with studies of organic molecules on metal substrates and the lessons that can be learned on their electronic properties. Chapter 12 is devoted to the study of biologically relevant materials. Finally, Chap. 13 will review the very recent advances that have been made in the experimental investigations of atomic resolution KPFM.

References

1. G. Binnig, H. Rohrer, Ch. Gerber, E. Weibel, Phys. Rev. Lett. **49**, 57 (1982)
2. G. Binnig, C.F. Quate, Ch. Gerber, Phys. Rev. Lett. **56**, 930 (1986)
3. Y. Martin, C.C. Williams, H.K. Wickramasinghe, J. Appl. Phys. **61**, 4723 (1987)
4. M. Nonnenmacher, M.P. O'Boyle, H.K. Wickramasinghe, Appl. Phys. Lett. **58**, 2921 (1991)
5. J.M.R. Weaver, D.W. Abraham, J. Vac. Sci. Technol. B **9**, 1559 (1991)
6. L. Kelvin, Phil. Mag. **46**, 82 (1898)
7. R. Wiesendanger, *Scanning Probe Microscopy* (Springer, Berlin, 1998)
8. S. Morita, R. Wiesendanger, E. Meyer (eds.), *Noncontact Atomic Force Microscopy* (Springer, Berlin, 2002)
9. E. Meyer, H.J. Hug, R. Bennewitz, *Scanning Probe Microscopy* (Springer, Berlin, 2004)

Part I
Technical Aspects

Chapter 2
Experimental Technique and Working Modes

S. Sadewasser

Abstract Kelvin probe force microscopy is a scanning probe microscopy technique providing the capability to image the local surface potential of a sample with high spatial resolution. It is based on the non-contact atomic force microscope and minimizes the electrostatic interaction between the scanning tip and the surface. The two main working modes are the amplitude modulation and the frequency modulation mode, in which the electrostatic force or the electrostatic force gradient are minimized by the application of a dc bias voltage, respectively. For metals and semiconductors, the contact potential difference is determined, which is related to the sample's work function, while for insulators information about local charges is obtained. This chapter provides a brief introduction to non-contact atomic force microscopy and describes the details of the various Kelvin probe force microscopy techniques.

2.1 Introduction

Surface science was revolutionized in 1982 by the invention of the scanning tunneling microscope (STM) by Binnig and Rohrer [3]. In 1986 the invention of the atomic force microscope (AFM) widened the range of samples from conductive to non-conductive ones [4]. Further development led to the non-contact (or dynamical) mode of the AFM [20], where a cantilever supporting a sharp tip at its end is vibrated close to its resonance frequency and changes in the vibration due to tip-sample interaction are employed to maintain a constant distance to the sample surface while scanning across the sample. Forces exerted by the tip on the sample are minimal in non-contact mode.

S. Sadewasser (✉)
International Iberian Nanotechnology Laboratory - INL, Avda. Mestre José Veiga s/n, 4715-330 Braga, Portugal
e-mail: sascha.sadewasser@inl.int

S. Sadewasser and T. Glatzel (eds.), *Kelvin Probe Force Microscopy*, Springer Series in Surface Sciences 48, DOI 10.1007/978-3-642-22566-6_2,

A wide field of applications has been opened by the combination of the AFM with other measurement methods, thus providing additional sample properties on a lateral scale in the nanometer range. One representative, the Kelvin probe force microscope (KPFM) was first developed by Nonnenmacher et al. [23] and it allows to image surface electronic properties, namely the contact potential difference (CPD). The name "Kelvin probe force microscope" originates from the macroscopic method developed by Lord Kelvin in 1898 using a vibrating parallel plate capacitor arrangement, where a voltage applied to one vibrating plate is controlled such that no current is induced by the vibration [17]. The reduction of this exact principle to the microscopic scale however results in a poor sensitivity, since the size of the plates is too small to generate a sufficient current. Therefore, in KPFM the electrostatic force is used. The cantilever in an AFM is a very sensitive force sensor, thus the CPD can be measured with high sensitivity. A dc-bias applied to the sample (or the tip) is controlled in such a way that the electrostatic forces between tip and sample are minimized.

This chapter will initially describe the working principle of non-contact atomic force microscopy (nc-AFM) and then explain the KPFM technique. Two working modes will be described which are both widely applied in research laboratories. At the end of the chapter some notes on other working modes are given.

2.2 Non-Contact Atomic Force Microscopy

An AFM consists of a sharp tip supported at the end of a cantilever serving as a force sensor [4]. The sample's topography is imaged by scanning the tip across a sample surface while maintaining a constant force or force gradient by a feedback loop. Different modes for AFM operation can be used. In contact mode the tip is brought into contact with the sample, and repulsive tip-sample interaction is measured. In non-contact mode (also called dynamic mode) the tip is oscillated at or near its fundamental resonance frequency [20]. The oscillation is mechanically excited using a piezoelectric element on which the cantilever-chip is mounted. Interaction forces between tip and sample cause a shift in the resonance frequency. A third mode uses an oscillating cantilever, however, the regime of repulsive tip-sample interaction is reached in the lower turn-around point of the oscillation cycle, while in the rest of the oscillation cycle attractive forces act. In this tapping mode and in the non-contact mode the forces exerted by the scanning tip on the sample are considerably reduced with respect to the contact mode.

In nc-AFM the cantilever is oscillated at or near its resonance frequency and the change in the oscillation is monitored in dependence of the tip-sample interaction. Figure 2.1 shows the basic AFM experimental setup consisting of the cantilever and tip, the sample on a xyz-stage with piezo control, and the detection system with a laser and a position sensitive photo diode. Alternatively to the displayed beam-deflection detection an interferometric technique or a piezoelectric and piezoresistive detection can be used.

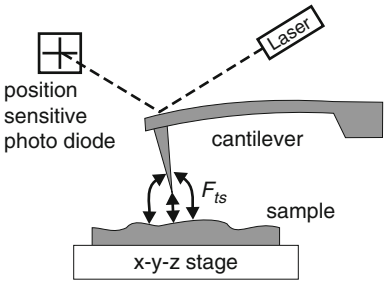

Fig. 2.1 Working principle of an AFM consisting of the beam deflection detection system with laser and position sensitive photo diode and the sample on a piezo-driven xyz-stage

The oscillation of the cantilever can be described by its equation of motion, which in general is a three dimensional problem. By considering the tip as a point-mass spring the equation of motion for the tip can be represented as [10]:

$$m\ddot{z} + \frac{m\omega_0}{Q}\dot{z} + kz = F_{\mathrm{ts}} + F_0 \cos(\omega_{\mathrm{d}} t), \tag{2.1}$$

where k denotes the spring constant, Q the quality factor, F_{ts} the tip-surface interaction, F_0 and ω_{d} the amplitude and angular frequency of the driving force, respectively. The free resonance frequency f_0 (without tip-surface interaction, $F_{\mathrm{ts}} = 0$) is a function of the spring constant k and the effective mass m^*, which also accounts for the specific geometry of the cantilever:

$$\omega_0 = 2\pi f_0 = \sqrt{\frac{k}{m^*}}. \tag{2.2}$$

When the tip is approached to the surface, forces act between tip and sample. This tip-surface interaction may consist of various contributions, short range repulsive and chemical binding forces, the van der Waals force F_{vdW}, and the long-range electrostatic and magnetic forces, F_{el} and F_{mag}, respectively. The short-range interaction is usually described by the empirical Lennard-Jones type interaction potential, which is illustrated in Fig. 2.2 [15]. The repulsive force can be described by a power law interaction potential:

$$U_{\mathrm{rep}} = \left(\frac{\sigma_0}{r}\right)^n, \tag{2.3}$$

where the exponent is usually set to $n = 12$. Frequently, this repulsive part is also described by an exponential dependence:

$$U_{\mathrm{rep}} = c \cdot \mathrm{e}^{-r/\sigma'}. \tag{2.4}$$

Here σ_0 and σ' are characteristic lengths, where σ' is on the order of 0.02 nm.

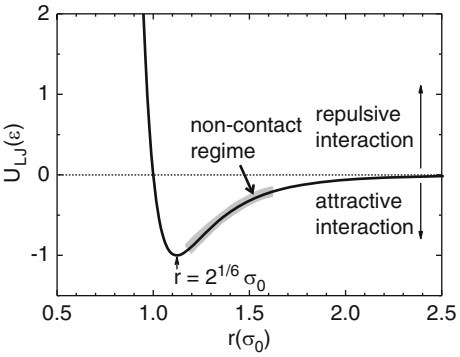

Fig. 2.2 Lennard-Jones type interaction potential describing the typical interaction of an AFM tip and the sample surface at small tip-sample distances

At larger distance, the interaction potential becomes attractive, goes through a minimum and then becomes smaller toward large tip-sample distances. The total short-range interatomic interaction potential comprising the repulsive and attractive part is thus described by a Lennard-Jones potential [15]:

$$U_{\mathrm{LJ}} = 4\epsilon \left[\left(\frac{\sigma_0}{r} \right)^{12} - \left(\frac{\sigma_0}{r} \right)^{6} \right], \tag{2.5}$$

as illustrated in Fig. 2.2.

The repulsive force at very small tip-sample distances results from the Pauli exclusion principle for the overlapping electron clouds of the tip and sample atoms. The chemical forces are due to the bonding state of a quantum mechanical overlap of the electron wave functions of tip and sample. These chemical interactions obey an exponential distance dependence and are only relevant at distances below ∼5 Å[24].

An additional contribution to the attractive part of the short-range interaction force is the van der Waals force. It is an always present interaction between atoms and molecules due to the interaction between induced electrostatic dipoles, i.e., as a result of electromagnetic field fluctuations. For the case of AFM, it can be approximated by considering a sphere of radius R in front of an infinite plane, representing the sample surface, and is usually expressed as [10, 15]:

$$F_{\mathrm{vdW}} = -\frac{HR}{6d^2}, \tag{2.6}$$

where H is the Hamaker constant, and d the closest distance between the sphere and the plane (the tip and the sample). For tip-sample distances smaller than an intermolecular distance a_0, F_{vdW} is replaced by the adhesion force F_{adh}. For the case of a stiff contact and a small tip radius the adhesion force can be described by $F_{\mathrm{adh}} = -4\pi R\gamma$, where γ is the surface energy [7, 10, 38]. As indicated by the

gray area of the interaction potential in Fig. 2.2, nc-AFM is operated in the attractive region of the interaction.

The relevant force for KPFM is the electrostatic force F_{el}. It can be expressed by considering the tip-sample system as a capacitor. Thus, with the energy of a capacitor, $U_{\mathrm{el}} = 1/2C\,V^2$, the force can be written as:

$$F_{\mathrm{el}} = -\nabla U_{\mathrm{el}} = -\frac{1}{2}\frac{\partial C}{\partial r}V^2 - C\,V\frac{\partial V}{\partial r}, \tag{2.7}$$

where C is the capacitance and V the total voltage. For simplicity, a metallic tip and sample can be considered. In the case of AFM, the most significant contribution is due to the forces perpendicular to the sample surface (denominated z-direction), therefore (2.7) simplifies to:

$$F_{\mathrm{el}} = -\frac{1}{2}\frac{\partial C}{\partial z}V^2. \tag{2.8}$$

A detailed discussion of the electrostatic force will follow in the next section. The magnetic forces are only relevant if tip and/or sample material are magnetic. Generally, for KPFM this is not the case and therefore these forces will not be considered here.

When approaching the tip to the sample, the interaction forces will cause a shift of the resonance curve of the cantilever. For small oscillation amplitudes the system can be regarded as a weakly perturbed harmonic oscillator. In this case the shift of the resonance curve can be approximated by introducing an effective spring constant k_{eff} [10]:

$$k_{\mathrm{eff}} = k - \frac{\partial F_{\mathrm{ts}}}{\partial z}. \tag{2.9}$$

The spring constant is lowered by the force gradient. For small force gradients this shifts the resonance curve, in the case of attractive forces to lower frequencies and vice versa. The frequency shift can be approximated by [2, 10]:

$$\Delta f_0 = -\frac{f_0}{2k}\frac{\partial F_{\mathrm{ts}}}{\partial z}. \tag{2.10}$$

Equation (2.9) and (2.10) are approximations to the solution of the equation of motion (2.1) for small oscillation amplitude and small force gradients. In many situations they provide a quick and easy way to interpret the experiments. However, in many practical cases of KPFM, large oscillation amplitudes are used, and thus throughout the oscillation cycle the tip-sample interaction continuously varies. The above approximations are no longer valid in this case and more elaborate methods have to be used. In classical first-order pertubation theory the solution to the equation of motion gives the frequency shift Δf_0 as a function of the tip-sample distance d, the oscillation amplitude A_0, the spring constant k and the free resonance frequency f_0 as [10, 11]:

$$\Delta f_0 = -\frac{f_0}{kA_0^2}\frac{1}{T_0}\int_0^{T_0} F_{\mathrm{ts}}\left(d + A_0 + A_0\cos(2\pi f_0 t)\right) A_0\cos(2\pi f_0 t)\,\mathrm{d}t. \quad (2.11)$$

Two different detection modes can be applied in nc-AFM. For the amplitude modulation technique (AM-mode) [20] the cantilever is excited at a constant frequency slightly off resonance. A change in the tip-sample distance leads to a change of the force gradient, which results in a shift of the resonance peak; thus, the oscillation amplitude at the fixed driving frequency changes. A feedback loop adjusts the tip-sample distance to maintain a constant amplitude. This detection method is usually applied in air, where the quality factor Q of the cantilever is on the order of 1–10^2. When operating a nc-AFM in vacuum, the quality factor increases by several orders of magnitude (typically above 10^5) due to the reduced damping. This results in a reduced band width for the detection and a very slow response time of the system is the consequence [2]. Albrecht et al. [2] have introduced the frequency modulation technique (FM-mode) for application in vacuum. In this mode, the change of the resonance curve is detected by directly measuring the frequency shift of the resonance curve. The cantilever serves as the frequency determining element and is excited at its resonance frequency using a positive feedback. Through an automatic gain control (AGC) the oscillation amplitude is kept constant. The resonance frequency is measured using a frequency demodulator, or a phase locked loop (PLL), for example. For a change of the tip-sample distance during the scan the resonance frequency changes and the z-controller adjusts the tip-sample distance to maintain a constant frequency shift Δf_0 with respect to the free resonance of the cantilever. The experimental set-up of this FM-mode is illustrated in Fig. 2.7 in Sect. 2.7 below. For both modes, according to (2.10), the measured surface topography approximately corresponds to a surface of constant force gradient.

2.3 Kelvin Probe Force Microscopy

The KPFM combines the nc-AFM with the Kelvin probe technique. The macroscopic Kelvin probe technique was developed in 1898 by Lord Kelvin [17] for the measurement of surface potentials: the sample constitutes one plate of a parallel plate capacitor, with a known metal forming the other plate, which is vibrated at frequency ω. Due to the changing distance between the plates, the capacitance changes, resulting in an alternating current in the circuit connecting the plates. This current is reduced to zero by applying a dc-voltage to one of the plates. This voltage corresponds to the CPD of the two materials.

The KPFM employs the same principle, applying a dc-voltage to compensate the CPD between the AFM tip and the sample [34]. However, instead of the current as the controlling parameter, the electrostatic force is used. As the cantilever of an AFM is a very sensitive force probe, this technique results in a high sensitivity of

the CPD measurement, even for the very reduced size of the capacitor formed by the tip and the sample.

In addition to the compensation dc-voltage (V_{dc}) between tip and sample, an ac-voltage $V_{ac}\sin(\omega_{ac}t)$ at the frequency ω_{ac} is applied. The resulting oscillating electrostatic force induces an oscillation of the cantilever at the frequency ω_{ac}. Considering the tip-sample system as a capacitor, the electrostatic force in (2.8) can now be expressed as:

$$F_{el} = -\frac{1}{2}\frac{\partial C}{\partial z}[V_{dc} - V_{CPD} + V_{ac}\sin(\omega_{ac}t)]^2, \tag{2.12}$$

where $\partial C/\partial z$ is the capacitance gradient of the tip-sample system and the CPD is the difference in work function Φ between sample and tip:

$$V_{CPD} = \frac{\Delta\Phi}{e} = \frac{(\Phi_{sample} - \Phi_{tip})}{e}, \tag{2.13}$$

where e is the elementary charge.[1]

Equation (2.12) can be written as $F_{el} = F_{dc} + F_{\omega_{ac}} + F_{2\omega_{ac}}$, where the spectral components are:

$$F_{dc} = -\frac{\partial C}{\partial z}\left[\frac{1}{2}(V_{dc} - V_{CPD})^2 + \frac{V_{ac}^2}{4}\right], \tag{2.14}$$

$$F_{\omega_{ac}} = -\frac{\partial C}{\partial z}(V_{dc} - V_{CPD})V_{ac}\sin(\omega_{ac}t), \tag{2.15}$$

$$F_{2\omega_{ac}} = \frac{\partial C}{\partial z}\frac{V_{ac}^2}{4}\cos(2\omega_{ac}t). \tag{2.16}$$

Here, F_{dc} contributes to the topography signal, $F_{\omega_{ac}}$ at the ac-frequency is used to measure the CPD and $F_{2\omega_{ac}}$ can be used for capacitance microscopy (see Sect. 2.8) [14].

While the KPFM measurement results in the determination of the CPD, which is the work function of the sample relative to that of the tip, (2.13) can be used to deduce the sample's work function on an absolute scale. Using a calibrated tip with a known work function, the work function of the sample can be calculated from the CPD measurement according to (2.13). However, for absolute work function

[1] In principle, the definition of the CPD could also be selected as $V_{CPD} = (\Phi_{tip} - \Phi_{sample})/e$, which corresponds to $-V_{CPD}$ of (2.13). We selected the definition of (2.13) such that the changes in V_{CPD} directly correspond to changes in the work function. Thus, images of V_{CPD} represent the same contrast as images of the sample's work function Φ_{sample}, just with a constant absolute offset, which is equal to the work function of the tip. In the experimental realization this would correspond to a situation, where the voltage is applied to the sample and the tip is grounded (see Sect. 2.7).

measurements, operation under ultrahigh vacuum (UHV) conditions is mandatory [18], as it is well known that the work function is highly sensitive to the surface cleanness [23].

As in the case of the topography measurement, also for the CPD measurement two different modes can be distinguished. The amplitude modulation technique (AM-mode) controls the applied dc-bias by reducing the amplitude of the induced oscillation at the ac-frequency to zero, and the frequency modulation technique (FM-mode) minimizes the variation in the frequency shift Δf_0 at the ac-frequency.

2.4 AM-KPFM

In the AM-mode, the amplitude of the cantilever oscillation at the ac-frequency ω_{ac} is measured; it is induced by the electrostatic force and is proportional to this. The amplitude is detected using the beam deflection signal and a lock-in amplifier tuned to the frequency of the ac-bias (see also Sect. 2.7). As can be seen from (2.15), this signal is minimized by controlling V_{dc} to match the CPD V_{CPD}. Recording V_{dc} while scanning the topography, an image of the CPD is obtained. Many KPFM systems use this technique with ac-frequencies of several kHz to several tens of kHz. To get sufficient sensitivity, ac-voltages of 1–3 V are typically used [29, 30].

An improvement to this technique is obtained by tuning the ac-frequency to a resonance frequency of the cantilever. In this way a resonance-enhanced detection is achieved, providing the possibility to lower the ac-voltage maintaining a high sensitivity to the electrostatic force. Frequently, this is realized in the two-pass mode, where in the first scan-line the topography is determined, which is then retraced with the tip lifted up by several tens of nm, while an ac-voltage at the fundamental resonance frequency is applied for KPFM detection of V_{CPD}. This mode is described in more detail in Sect. 2.8 below. A more elegant way to use resonance-enhanced KPFM is to tune the ac-frequency to the second oscillation mode of the cantilever [19, 31]. While the fundamental resonance is mechanically excited and used for topography detection, the ac-voltage simultaneously excites electrostatically a cantilever oscillation, for example of the second oscillation mode, which is used for the CPD detection. Then the oscillation at ω_{ac} is amplified by the quality factor Q. This enhances the sensitivity and permits to use lower ac-voltages, down to the order of 100 mV. Working with the resonance-enhanced detection, also the response time of the system is determined by the quality factor. This can be quantitatively expressed in a similar way as for the fundamental resonance used for the topography detection [2]. The system reacts to a change (for example a change in the CPD upon scanning the tip) with a response time τ until a new stable state is reached, where [2, 16]:

$$\tau = \frac{Q}{\pi f_2}. \tag{2.17}$$

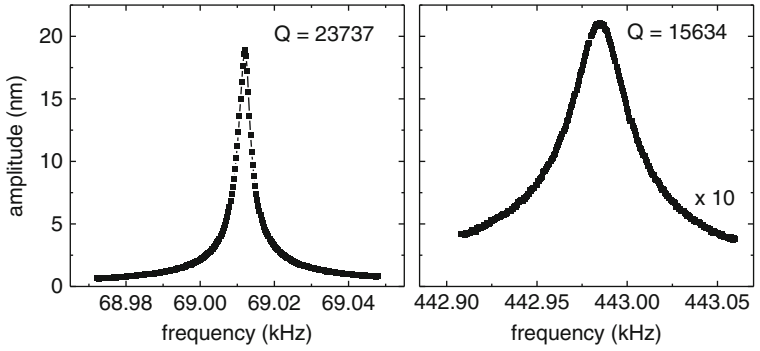

Fig. 2.3 Resonance peaks of the fundamental and second oscillation mode of a typical cantilever for force modulation AFM (Nanosensors PPP-EFM). The Q-factors for the two resonances are also given

Using typical values of $Q = 15,000$ and $f_2 = 450\,\text{kHz}$ the response time results to $\tau \approx 11\,\text{ms}$. This means that scanning is easily possible with scan speeds on the order of 1 s/line.

The limiting factor in this mode is the bandwidth of the photodiode used for the detection of the cantilever oscillation. This depends on the specific type and manufacturer of the AFM system. In many commercial systems a photodiode with a bandwidth of $\sim$500 kHz is used; therefore, the stiffest cantilevers used for detection on the second oscillation mode have the fundamental resonance frequency in the range of 70–80 kHz, and the second resonance around 400–470 kHz ($f_2 \sim 6.3 f_0$, due to the geometry of the cantilever [5]). Typical resonance curves for the fundamental and second oscillation mode are shown in Fig. 2.3. The amplitude of the second resonance mode is smaller by about a factor of 10 when the same excitation amplitude is used for the mechanical excitation of the dither-piezo.

Thus, the resonance-enhanced AM-mode KPFM has two advantages: (1) a simultaneous measurement of topography and CPD is possible due to the use of two independent resonance modes and (2) the resonance enhancement provides a higher sensitivity to the electrostatic force and therefore allows to use smaller ac-voltages. This in turn has two additional advantages. First, the ac-amplitude affects the topography image by inducing a constant electrostatic background, as can be seen by the $V_{\text{ac}}^2/4$-term in (2.14). Second, large ac-voltages possibly induce band bending at the surface of semiconductors [33], which would cause an incorrect determination of the work function.

2.5 FM-KPFM

In the frequency modulation mode, the applied ac-bias voltage induces a modulation of the electrostatic force, which results in an oscillation of the frequency shift Δf_0 at the frequency ω_{ac} of the ac-bias. This oscillation is detected by a lock-in amplifier

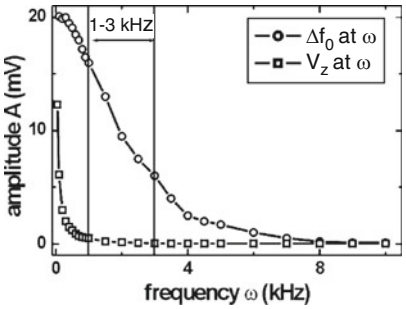

Fig. 2.4 Dependence of the frequency shift Δf_0 and the height control signal of the topography V_z at the frequency ω of the ac-voltage. The measurements were obtained on a HOPG sample with a bias slightly above the CPD using a room temperature UHV-AFM system by Omicron nanotechnology [12]

tuned to the frequency of the ac-bias. The measured signal is approximately proportional to the force gradient, as can be concluded from (2.10) and (2.15):

$$\Delta f_0(\omega_{\mathrm{ac}}) \propto \frac{\partial F_{\omega_{\mathrm{ac}}}}{\partial z} = \frac{\partial^2 C}{\partial z^2}(V_{\mathrm{dc}} - V_{\mathrm{CPD}})V_{\mathrm{ac}}\sin(\omega_{\mathrm{ac}}t). \tag{2.18}$$

As was shown in [12], the frequency ω_{ac} has to be chosen in an appropriate range. The lower limit is dictated by an increasing cross talk to the topography signal: if the frequency is too low, the tip-sample distance control follows the additional electrostatic force and the tip-sample distance starts to oscillate at the frequency ω_{ac}. The higher the frequency the lower the coupling to the topography. On the other hand, the bandwidth of the frequency demodulator or the PLL determines the upper limit of the frequency range. Figure 2.4 shows the amplitudes at ω_{ac} of the oscillation of Δf_0 and of the oscillation of the piezo-voltage V_z, which controls the tip-sample distance. With increasing frequency ω_{ac} the cross talk to the topography signal decreases but also the signal intensity of the electrostatic force decreases due to the restricted bandwidth of the frequency demodulator. Also in this mode, higher V_{ac} results in higher sensitivity at the cost of an influence on the topography and a possibly induced band bending on semiconductor samples (see above). Typical values for $f_{\mathrm{ac}} = \omega_{\mathrm{ac}}/2\pi$ and V_{ac} are in the range of 1–3 kHz and 1–3 V, respectively.

2.6 Comparison of AM- and FM-KPFM

As was shown in the previous two chapters, the AM-mode KPFM is sensitive to the electrostatic force, whereas the FM-mode is sensitive to the electrostatic force gradient. As a result of this difference, also different properties of the two modes can

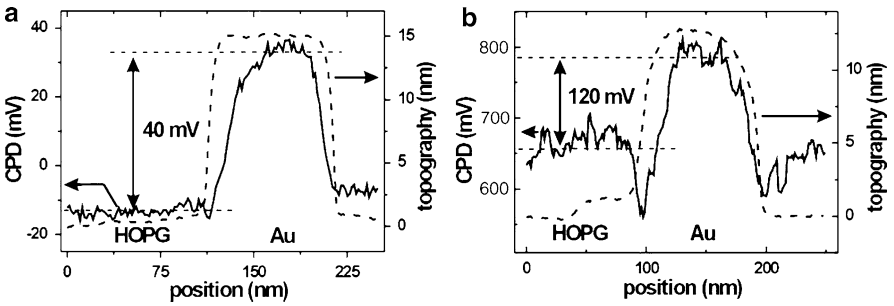

Fig. 2.5 AM- and FM-mode measurements on a HOPG sample with Au islands. Single line profiles are shown for the topography (*dashed lines*) and CPD (*solid lines*) in (**a**) AM-mode and (**b**) FM-mode KPFM. The AM-mode was conducted with a cantilever with force constant $\sim 3\,\mathrm{N\,m^{-1}}$ and the FM-mode with a stiffer cantilever of $\sim 42\,\mathrm{N\,m^{-1}}$ [12]

be expected in KPFM measurements. Especially the spatial and energy resolution can be different, as will be shown in this section.

The first concise study for the comparison of AM- and FM-KPFM was presented by Glatzel et al. [12]. In this experimental study, the authors used dendritic gold islands on highly oriented pyrolytic graphite (HOPG) as a model system so study the spatial and energy resolution in both operation modes. As can be seen in Fig. 2.5, the difference in CPD between graphite and gold amounts to about 40 meV in the AM-mode and about 120 meV in the FM-mode. As the gold island size is on the order of $\sim$100 nm, the large difference is explained by the fact that in the AM-mode, the tip averages over a larger area on the sample, where more of the surrounding gold islands and graphit substrate are "seen" by the tip due to the longe-range nature of the electrostatic force; this leads to a measurement of an averaged CPD value for Au and graphite. In contrast, the difference in CPD between gold and graphite is about 3 times larger in the FM-mode. The relevant force gradient in this mode is much more short-ranged and therefore averaging takes place over a much smaller area below the tip. Thus, the tip mainly "sees" only the confined area right below the tip. This also affects the spatial resolution [12], as is also visible in Fig. 2.5.

A subsequent study by Zerweck et al. [37] presented a comparison between AM- and FM-KPFM by experiments on KCl islands deposited on a Au(111) substrate. In addition, the authors also performed three dimensional (3D) finite element simulations describing the electrostatic field between the metallic tip and the sample surface. Thereby, a comparison between experimental and simulation result became possible. In the simulations the tip is modeled as a truncated cone merging into a half sphere with radius R opposed to a circular surface representing the sample. The cantilever is described as a disk at the base of the cone. For the simulation of the spatial resolution, the sample consists of two halves, one at negative and the other at positive potential. For this model, the electric field distribution was calculated for different potential differences V between tip and sample. The electric field energy

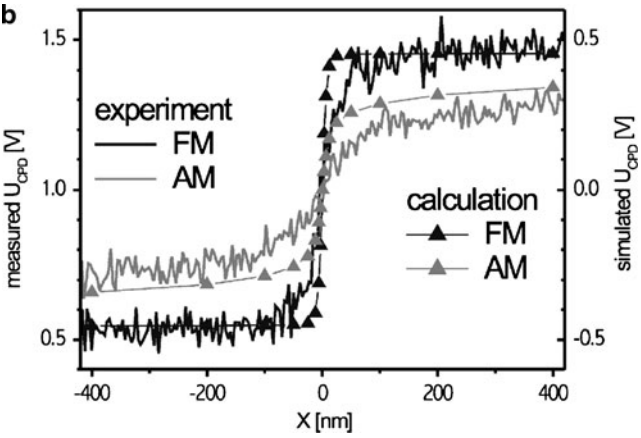

Fig. 2.6 Experimental line profiles (*solid lines*) extracted from KPFM images of a KCl island (*left half*) on a Au substrate (*right half*) recorded in AM- (*gray*) and FM-mode (*black*). The simulation of the two modes is shown as the *triangular* symbols and provides a good description of the experimental data. For the simulation, a potential difference of 0.9 V between the two regions was assumed [37]

was then obtained by integration of the square of the electric field. Differentiation of the electric field energy with respect to the vertical direction then gives the electrostatic force $F_{\mathrm{el}}(z, V)$ acting normal to the surface and further differentiation results in the electrostatic force gradient $\partial F_{\mathrm{el}}(z, V)/\partial z$ [37]. For a fixed separation and lateral position, both F_{el} and $\partial F_{\mathrm{el}}/\partial z$ depend on V. Consequently, the CPD for the AM-KPFM corresponds to the minimum of $F_{\mathrm{el}}(z, V)$, and the CPD for FM-KPFM to that of $\partial F_{\mathrm{el}}(z, V)/\partial z$.

Figure 2.6 shows a comparison of experimental data obtained in AM- and FM-mode on a sample consisting of KCl islands on a Au(111) substrate and a simulation of both modes [37]. As can be seen, the energy resolution is considerably better in the FM-mode, which reaches the expected CPD difference between KCl and Au within about 50 nm of the transition. For the AM-mode, the full CPD difference is not even reached within 400 nm of the transition, showing clearly that the spatial resolution of the transition is much better in the FM-mode. Additionally, the authors evaluated the dependence of the energy resolution on the tip-sample separation, finding that for separations up to about 30 nm the FM-mode gives an excellent agreement between experiment and simulation. For larger tip-sample distances the force gradient becomes too small and the controller becomes unstable. For the AM-mode a large deviation from the expected CPD values is found for all distances considered in the study [37]. Therefore, it is recommended to maintain a tip-sample distance as small as possible. It has to be mentioned that in the experiments and simulations of [37] the regular AM-mode was considered. Thus the results are not directly comparable to the resonance-enhanced AM-mode KPFM, where the ac-frequency is applied at the second oscillation mode, as used in the experimental study of [12].

2.7 Technical Realization

Figure 2.7 shows a typical setup of the electronic system of a KPFM. The cantilever oscillation is detected by a beam deflection method using a laser, reflected from the backside of the cantilever onto a position sensitive photo diode. The signal is fed into a frequency detector, as for example a PLL or a frequency demodulator, which mechanically excites the cantilever oscillation on the fundamental resonance frequency. A frequency generator feeds the desired ac-voltage into an adder element, and at the same time provides the reference frequency for the lock-in amplifier. Depending on the used lock-in amplifier, also the reference output voltage can be used directly as the ac-bias for the sample. In FM-mode KPFM, the signal from the frequency detector is directly fed into the Lock-In amplifier (see dashed arrow in Fig. 2.7), which then detects the magnitude of the frequency shift at the ac-frequency, induced by the resulting additional electrostatic forces. The lock-in output serves as input to the Kelvin-controller, which adjusts a dc-voltage such that the input signal (S) goes toward zero. This dc-voltage is the second input to the adder, which provides then the complete voltage to the sample, consisting of the sum of ac- and dc-bias. On the other hand, as was shown above, the dc-bias matches the CPD and thus the dc-bias is recorded with the scan, to provide the spatially resolved CPD image.

Figure 2.7 shows also the setup for the AM-mode KPFM. In this case, the output signal from the position sensitive photodiode is passed not only to the FM-demodulator, but additionally to the input of the lock-in amplifier, as shown

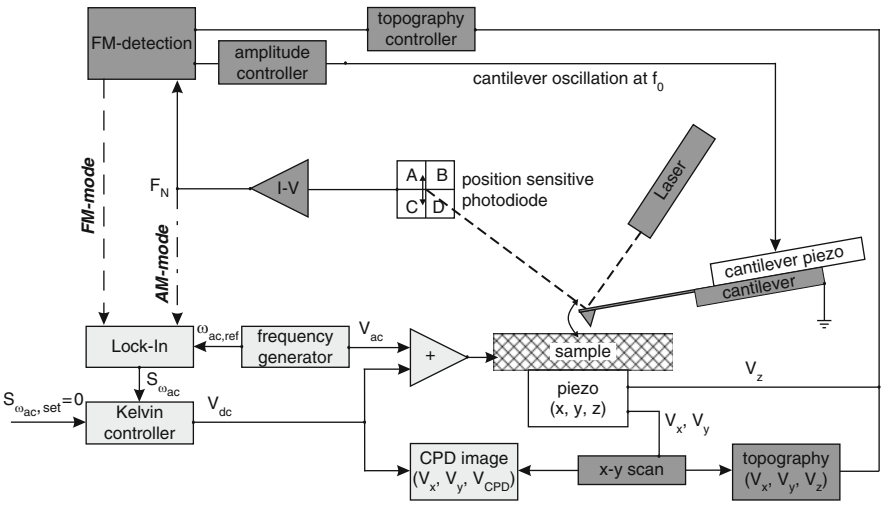

Fig. 2.7 Block diagram of the electronic realization of a KPFM. The *dashed line* indicates the FM-mode and the *dashed-dotted line* the AM-mode setup. *Dark grey boxes* are the regular non-contact AFM topography part and the *light gray boxes* are the KPFM part of the setup. See text for details

by the dashed-dotted arrow in Fig. 2.7. The rest of the setup is identical to the FM-mode setup. Thus, in the AM-mode, the amplitude of the induced oscillation of the cantilever is measured directly, as described above in Sect. 2.4. For a better separation of the fundamental resonance frequency from the ac-frequency signal from the photo diode a high and/or low-pass filter might optionally by used.

2.8 Other Modes and Additional Experimental Options

As described above, the KPFM uses a controller to compensate the electrostatic forces between the AFM-tip and the sample by applying a dc-bias which matches the CPD. The signal which is fed into the controller is the output of a lock-in amplifier (see Fig. 2.7). This lock-in measures the magnitude of the electrostatic forces induced by the applied ac-voltage. Instead of compensating the electrostatic forces through application of the dc-bias by the controller, one can also directly image the electrostatic forces by recording the magnitude of the lock-in signal. This measurement mode is called electrostatic force microscopy (EFM) and provides the advantage of a possibly higher imaging speed, as the additional Kelvin-controller is avoided. For getting reasonable signal-to-noise ratios, the Kelvin controller time constant is usually kept on the order of several ms up to several tens of ms, reducing the scan speed to the order of a few seconds per scan line. On the other hand, a clear disadvantage of the EFM is the lack of a quantitative measurement of the CPD. The EFM signal gives only access to relative changes in the CPD, however, the KPFM provides a quantitative measure of the CPD. Nevertheless, the literature reports many EFM studies, likely motivated by the fact, that experimentally the EFM technique is simpler to handle and requires less equipment, namely it does not require a Kelvin controller.

The capability of KPFM to acquire images of the CPD relies on (2.15), as discussed above. A closer examination of (2.15) shows that the electrostatic force component at the ac-frequency ω_{ac} not only exhibits the dependence on the voltage difference $(V_{dc} - V_{CPD})$, but also a possible contribution from the capacitance gradient $\partial C/\partial z$ has to be considered. Local variations of this contribution possibly affect measurements. This effect should be severe for EFM imaging, where the CPD is not compensated and therefore variations in the EFM signal obtained from the lock-in amplifier might erroneously be attributed to CPD variations. However, the effect on KPFM images should be much smaller or even negligible, as the Kelvin-controller reduces the $(V_{dc} - V_{CPD})$ part of (2.15) to zero. Therefore the $\partial C/\partial z$ contribution should not affect KPFM imaging. Moreover, considering (2.16), it is seen that by monitoring the induced oscillation of the cantilever at the frequency $2\omega_{ac}$ it becomes possible to acquire an image of $\partial C/\partial z$ [1, 21]. In the case of applying the FM-mode imaging, the corresponding second derivative would be imaged: $\partial C^2/\partial^2 z$. As (2.16) is independent of the applied dc-bias V_{dc} and V_{CPD}, the only dependence of this force component stems from variations in the capacitance

gradient. In the experimental set-up, such a measurement can be realized by using an additional lock-in amplifier with the reference tuned to $2\omega_{ac}$, which then as an output signal provides the capacitance gradient [14].

Hochwitz et al. [14] have used this capacitance imaging to study complementary metal-oxide-semiconductor (CMOS) gates. Comparing individual devices in a CMOS chip, the monitored CPD did not show a clear distinction between properly functioning gates and gates that failed in operation. However, the capacitance gradient provided a clear signal difference between functional and non-functional CMOS gates. The authors concluded therefore, that the mechanism for the failure is beneath the surface. While the KPFM imaging is highly surface sensitive, the capacitance gradient provides also information from a region below the surface.

The subsurface sensitivity of the capacitance imaging is explained by the fact that for semiconductors the application of the ac-bias V_{ac} affects the charge distribution at the surface and subsurface region below the tip. Depending on the doping type of the sample and whether the ac-bias is in the positive or negative half of the oscillation cycle, the surface will undergo accumulation or depletion, respectively. The magnitude of the resulting change in the capacitance gradient depends on the charge carrier concentration [22, 25], similar to the way scanning capacitance microscopy works [35].

It was described above, that the sensitivity of KPFM can be enhanced by tuning the ac-frequency to a resonance of the cantilever and therefore obtain a resonance enhanced detection of the CPD. When using the second resonance mode for the ac-frequency, the simultaneous measurement of topography and CPD becomes possible (see above). However, frequently a two-pass method of KPFM is used. In this operation mode, the sample topography is scanned in either non-contact or in TappingMode™ and then in a second scan across the same line, this topography is retraced with the tip being retracted from the surface and the mechanical cantilever oscillation switched off. For the retrace the tip is usually lifted a few tens of nm away from the surface. The ac-bias for the KPFM measurement can now be applied at the fundamental resonance frequency and thus allow a resonance enhanced detection of the electrostatic forces and their compensation by the Kelvin-controller [25]. While the resonance-enhanced detection presents advantages for the sensitivity of the KPFM measurement, several problems with this technique have to be considered. (1) In the case of piezo creep or thermal drift, the retraced topography profile might not exactly match the topography right beneath the tip and therefore the exact tip-sample distance is not known during the Kelvin scan. (2) The larger tip-sample distance due to the lifted tip results in a lower resolution of the KPFM image, due to the resulting larger averaging effect. (3) The measurement of the topography is subject to electrostatic forces due to local CPD differences, which results in an incorrect determination of the sample topography during the first scan [27, 36]. When using the two-pass method for KPFM, all these effects will influence the CPD image. Therefore, care has to be taken when data are analyzed, especially when small details are considered, or when CPD contrast is related to changes in the sample topography.

2.9 Additional Remarks

Due to the extremely short-range nature of the tunneling current, an STM provides a high sensitivity to the sample topography; the tunneling current passes almost exclusively through the outer-most tip atom. In contrast to this, in KPFM the electrostatic forces are relevant for the imaging process. Since those have a long-range character, it is not anymore the outer-most tip atom, but the whole tip, which determines the interaction between tip and sample, possibly also the cantilever itself. Therefore, the tip shape plays a role in KPFM imaging and several authors have studied the influences. Colchero et al. [6] have analytically investigated the influence of the tip and the cantilever in EFM. Based on their analysis, the cantilever plays an important role in EFM and AM-KPFM imaging, despite the fact that the distance between cantilever and sample is $\sim 10^4$ times larger than the distance between the tip apex and the sample. However, due to the much larger surface area of the cantilever with respect to the tip apex, its role remains important. Their suggestion to avoid a reduction in spatial resolution due to interaction with the cantilever is to use the FM-KPFM. Due to the shorter interaction range of the force gradient, the influence of the cantilever is considerably reduced, providing for a good spatial resolution. This was later confirmed quantitatively by Zerweck et al. [37], who performed finite element simulations to describe the electrostatic interaction between the tip and a sample and extract the spatial resolution from scan lines of model structures (see Sect. 2.5). Basically, the resolution in FM-mode imaging is limited by the tip radius [28]. However, both studies did not consider the resonance-enhanced AM-mode KPFM, which in many experimental studies has also provided very high resolution on the order of the tip radius [26, 32], even down to the atomic scale [9].

The influence of the cantilever on EFM and KPFM imaging was also studied by investigating the dependence of the relative contribution of the capacitance derivative for the tip and the cantilever. Hochwitz et al. [13] numerically simulated the influence of the tip-to-cantilever area and the relative tip-to-cantilever distance to the sample on the ratio $\left(\partial C_{\mathrm{tip}}/\partial z\right) / \left(\partial C_{\mathrm{cantilever}}/\partial z\right)$. The relative area of the cantilever to the tip was varied between 10^1 and 10^9 and the ratio between the tip-sample distance and the cantilever-sample distance was varied between 10^{-1} and 10^{-4}. As is shown in Fig. 2.8, the ratio of tip to cantilever capacitance gradient varies in form of a relatively sharp step function. The authors find an optimal working region for KPFM or EFM with the cantilever to tip area in the range between 10^3 and 10^6 and the tip-sample distance to cantilever-sample distance to be less than 10^{-3}. This last criterium means that for a typical tip height of $\sim 10\,\mu\mathrm{m}$ a tip-sample distance of 10 nm or less should be maintained. On the other hand, the first criterium leads to the conclusion, that the intuitive guess that a finer tip results in a finer resolution only applies to a certain limit. If the tip gets too sharp, a decrease in resolution results, since the ratio of cantilever area to tip area increases. Thus, long, slender and slightly blunt tips should provide better resolution [13].

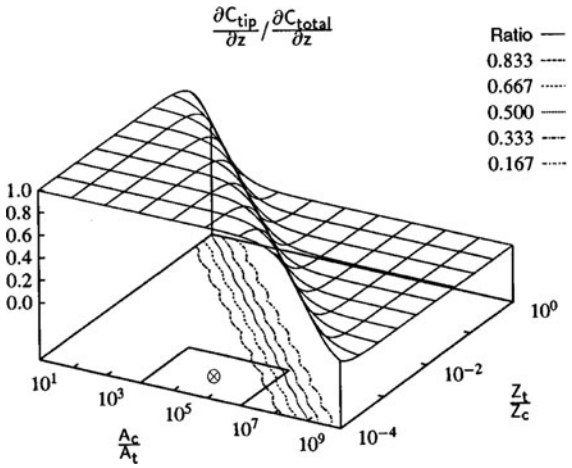

Fig. 2.8 Surface plot showing the relative contribution of the tip/sample capacitance compared to the total probe/sample capacitance as functions of the area and sample spacing over a topographically flat surface. A_c/A_t is the ratio of the cantilever area to the tip area and Z_t/Z_c is the ratio of the tip/sample distance to the cantilever/sample distance [13]

An experimental study confirming the simulations of Hochwitz et al. [13] was presented by Glatzel et al. [12]. Different cantilever types were comparatively used for the imaging of gold islands on a HOPG substrate. For the nominally same tip radius, short tips provide less potential contrast between Au and HOPG as compared to measurements with tips with a 3–5 times larger tip height. For the latter tips, the cantilever is further away from the sample and therefore the averaging due to the long-range electrostatic force is reduced. Experimentally, the CPD contrast between gold and graphite was about twice as large for the longer tips.

Sadewasser and Lux-Steiner [27] showed the impact of the electrostatic forces on the topography imaging with regular nc-AFM imaging at fixed sample bias. For a fixed sample bias the electrostatic force acting on the tip is different depending on the local CPD under the present tip position, as can be seen from (2.12). Thus, these uncompensated electrostatic forces contribute to the topography contrast, in addition to the van-der-Waals forces. For a sample consisting of only two materials with different CPD, correct topography imaging is possible, when the sample bias is selected to correspond to the average CPD of the two materials. However, for more than two materials, it is not possible to apply a fixed bias and maintain a correct imaging of the topographic structure in nc-AFM [27]. In such a case, KPFM has to be used to provide a local compensation of the electrostatic forces and allow imaging of the topography based on purely van der Waals forces. These conclusions apply to KPFM imaging in the AM- as well as in the FM-mode. Thus, KPFM not only allows imaging the CPD structure of a sample, but also provides for a topography imaging free from the influence of electrostatic forces. The relevance of electrostatic forces for topography imaging in nc-AFM was also addressed by Dianoux et al. [8].

References

1. D.W. Abraham, C. Williams, J. Slinkman, H.K. Wickramasinghe, J. Vac. Sci. Technol. B **9**, 703 (1991)
2. T.R. Albrecht, P. Grütter, D. Horne, D. Rugar, J. Appl. Phys. **69**, 668 (1991)
3. G. Binnig, H. Rohrer, Ch. Gerber, E. Weibel, Phys. Rev. Lett. **49**, 57 (1982)
4. G. Binnig, C.F. Quate, Ch. Gerber, Phys. Rev. Lett. **56**, 930 (1986)
5. H.-J. Butt, M. Jaschke, Nanotechnology **6**, 1 (1995)
6. J. Colchero, A. Gil, A.M. Baró, Phys. Rev. B **64**, 245403 (2001)
7. B.V. Derjaguin, V.M. Muller, Y.P. Toporov, J. Colloid. Interf. Sci. **53**, 314 (1975)
8. R. Dianoux, F. Martins, F. Marchi, C. Alandi, F. Comin, J. Chevrier, Phys. Rev. B **68**, 045403 (2003)
9. G.H. Enevoldsen, Th. Glatzel, M.C. Christensen, J.V. Lauritsen, F. Besenbacher, Phys. Rev. Lett. **100**, 236104 (2008)
10. R. García, R. Pérez, Surf. Sci. Rep. **47**, 197 (2002)
11. F.J. Giessibl, Phys. Rev. B **56**, 16010 (1997)
12. Th. Glatzel, S. Sadewasser, M.Ch. Lux-Steiner, Appl. Sur. Sci. **210**, 84 (2003)
13. T. Hochwitz, A.K. Henning, C. Levey, C. Daghlian, J. Slinkman, J. Vac. Sci. Technol. B **14**, 457 (1996)
14. T. Hochwitz, A.K. Henning, C. Levey, C. Daghlian, J. Slinkman, J. Never, P. Kaszuba, R. Gluck, R. Wells, J. Pekarik, R. Finch, J. Vac. Sci. Technol. B **14**, 440 (1996)
15. J.N. Israelachvili, *Intermolecular and Surface Forces* (Academic, London, 1992)
16. S. Kawai, H. Kawakatsu, Appl. Phys. Lett **89**, 013108 (2006)
17. L. Kelvin, Phil. Mag. **46**, 82 (1898)
18. A. Kikukawa, S. Hosaka, R. Imura, Appl. Phys. Lett. **66**, 3510 (1995)
19. A. Kikukawa, S. Hosaka, R. Imura, Rev. Sci. Instrum. **67**, 1463 (1996)
20. Y. Martin, C.C. Williams, H.K. Wickramasinghe, J. Appl. Phys. **61**, 4723 (1987)
21. Y. Martin, D.W. Abraham, H.K. Wickramasinghe, Appl. Phys. Lett. **52**, 1103 (1988)
22. F. Müller, A.-D. Müller, M. Hietschold, S. Kämmer, Meas. Sci. Technol. **9**, 734 (1998)
23. M. Nonnenmacher, M.P. O'Boyle, H.K. Wickramasinghe, Appl. Phys. Lett. **58**, 2921 (1991)
24. R. Pérez, M.C. Payne, I. Stich, K. Terukura, Phys. Rev. Lett. **78**, 678 (1997)
25. P.A. Rosenthal, E.T. Yu, R.L. Pierson, P.J. Zampardi, J. Appl. Phys. **87**, 1937 (1999)
26. Y. Rosenwaks, R. Shikler, Th. Glatzel, S. Sadewasser, Phys. Rev. B **70**, 085320 (2004)
27. S. Sadewasser, M.Ch. Lux-Steiner, Phys. Rev. Lett. **91**, 266101 (2003)
28. K. Sajewicz, F. Krok, J. Konior, Jpn. J. Appl. Phys. **49**, 025201 (2010)
29. R. Shikler, T. Meoded, N. Fried, Y. Rosenwaks, Appl. Phys. Lett. **74**, 2972 (1999)
30. R. Shikler, T. Meoded, N. Fried, B. Mishori, Y. Rosenwaks, J. Appl. Phys. **86**, 107 (1999)
31. Ch. Sommerhalter, Dissertation, Freie Universität Berlin (1999)
32. Ch. Sommerhalter, Th.W. Matthes, Th. Glatzel, A. Jäger-Waldau, M.Ch. Lux-Steiner, Appl. Phys. Lett. **75**, 286 (1999)
33. Ch. Sommerhalter, Th. Glatzel, Th.W. Matthes, A. Jäger-Waldau, M.Ch. Lux-Steiner, Appl. Surf. Sci. **157**, 263 (2000)
34. J.M.R. Weaver, D.W. Abraham, J. Vac. Sci. Technol. B **9**, 1559 (1991)
35. C.C. Williams, Annu. Rev. Mater. Sci. **29**, 471 (1999)
36. M. Yan, G.H. Bernstein, Ultramicroscopy **106**, 582 (2006)
37. U. Zerweck, Ch. Loppacher, T. Otto, S. Grafström, L.M. Eng, Phys. Rev. B **71**, 125424 (2005)
38. L. Zitzler, S. Herminghaus, F. Mugele, Phys. Rev. B **66**, 155436 (2002)

Chapter 3
Capacitive Crosstalk in AM-Mode KPFM

H. Diesinger, D. Deresmes, and T. Mélin

Abstract In Kelvin probe force microscopes based on electrostatic tip excitation, a nonnegligible capacitive crosstalk occurs between the electrostatic probe excitation signal and the probe deflection output signal. In atomic force microscopy setups where a self-oscillation force feedback loop is used, the parasitic coupling may also superpose onto the piezomechanical tip excitation signal which provides the oscillation for topography imaging. As a result, the crosstalk cannot be described as a constant coupling to the deflection signal output, but rather has the effect of a spurious excitation signal, which makes it more difficult to quantify and compensate the effect. In this chapter, the phenomenon of capacitive crosstalk is studied in two frequently used AM-KPFM setups, operating in ultrahigh vacuum and in air. Different methods of reducing or eliminating the effect on the measured surface potential are described and compared.

3.1 Introduction

KPFM setups often suffer from capacitive crosstalk between the ac voltage used to electrostatically excite cantilever oscillation and the cantilever deflection signal. Therefore, in addition to the electrostatically induced tip oscillation that is to be measured by the KPFM electronics, an apparent or parasitic tip oscillation is measured in the deflection signal that can cause faulty surface potential values if no precautions are undertaken to prevent or compensate this effect. Frequently, KPFM is based on atomic force microscopy (AFM) setups that were not particularly optimized for KPFM use. The KPFM mode based on frequency detection (FM-KPFM)

H. Diesinger · D. Deresmes · T. Mélin (✉)
IEMN Dept. ISEN, CNRS UMR 8520, Centre National de Recherche Scientifique (CNRS),
Av. Henri Poincaré, B.P. 60069, 59652 Villeneuve d'Ascq, France
e-mail: hpdiesinger@ntu.edu.sg; dominique.deresmes@isen.iemn.univ-lile1.fr;
thierry.melin@isen.iemn.univ-lille1.fr

S. Sadewasser and T. Glatzel (eds.), *Kelvin Probe Force Microscopy*, Springer Series in Surface Sciences 48, DOI 10.1007/978-3-642-22566-6_3,

[1] does not suffer from this crosstalk because the ac component of the tip bias, meant to electrostatically detune the resonance frequency, has no effect if it adds to the deflection signal by capacitive coupling. The focus of this chapter is the compensation of the capacitive crosstalk in amplitude modulation (AM) mode in two commonly used setups, AM-KPFM in ultrahigh vacuum with simultaneous nc-AFM for distance control (Sect. 3.2), and in AM-KPFM in air without simultaneous distance control (Sect. 3.3). In the UHV setup using two probe oscillation frequencies simultaneously, the main effort is made on isolating the probe excitation of the distance control and the Kelvin control loops. Different methods, including active compensation, filtering and the use of a phase locked loop (PLL), are presented and compared. For the KPFM implementation operating in air, the crosstalk compensation is rather straightforward but the procedure of quantitatively determining the effect needs more attention and is described in detail. Section 3.4 shows how the capacitive crosstalk influences complementary measurements that are frequently performed during the setup of the KPFM loop.

3.2 AM-KPFM in Ultrahigh Vacuum

AM-KPFM is implemented in ultrahigh vacuum simultaneously to noncontact AFM (nc-AFM) imaging. Distance control is based on frequency detection of the mechanically excited first cantilever resonance [2] under the effect of Van-der-Waals forces, while amplitude detection of the electrostatically excited second cantilever resonance is used for surface potential imaging. Two setups are presented here: in the first, the AFM imaging is based on a self-oscillation loop used to excite the first cantilever resonance, while in the second one a PLL is used.

3.2.1 Self-Oscillating AFM Configuration

The first setup is shown in Fig. 3.1. The left block is the self-oscillating loop for mechanical tip oscillation. The cantilever is a part of this force feedback circuit that comprises the photodiode, amplifier, phase shifter, and piezo dither. The parameters of this loop are chosen to bring it deliberately into oscillation at the first resonance frequency of the cantilever. The amplifier of this loop has a variable gain that is part of an amplitude control circuit and maintains the oscillation amplitude stable. The amplitude control feature is not shown here for simplicity. The AFM tip is a Pt/Ir-coated Nanosensors PPP with its first resonance frequency at 62.3 kHz. The distance control loop (right block) detects the oscillation frequency by a demodulator and compares it to a setpoint with a comparator of variable gain. It maintains the frequency constant by adjusting the tip–sample distance. The KPFM part is the middle loop consisting of a lock-in amplifier, low-pass filter and error amplifier. The oscillator of the lock-in amplifier applies an ac signal to the cantilever at its

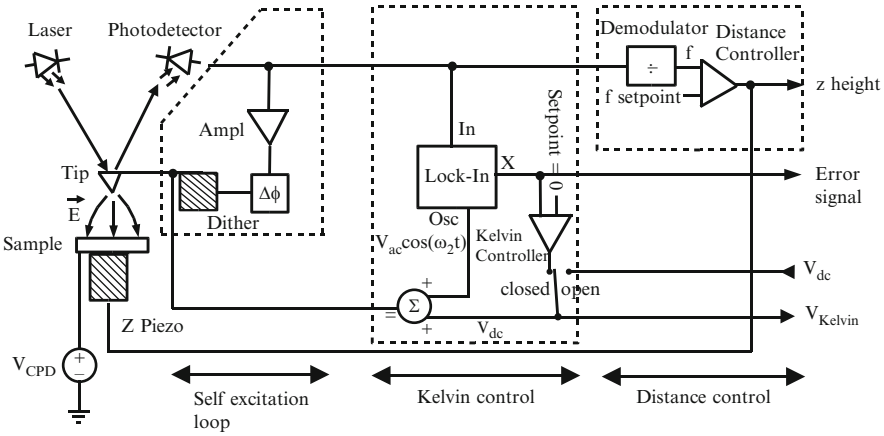

Fig. 3.1 AM-KPFM with simultaneous noncontact topography imaging. The cantilever is mechanically oscillated at its first resonance by a self-oscillating loop (*left block*), and the distance control loop (*right block*) regulates the distance by maintaining a constant resonance frequency. The Kelvin loop (*middle block*) applies an ac signal to the tip at its second resonance frequency, detects the electrostatically excited oscillation, and minimizes it by adjusting the dc voltage component applied to the tip. The Kelvin loop can be opened to apply a constant dc component to the cantilever voltage

second resonance frequency of 393.85 kHz, which corresponds to a higher flexural mode at 6.25 times the frequency of the fundamental mode. The lock-in amplifier then detects the electrostatically excited oscillation at this frequency and minimizes it by adjusting a dc voltage component applied to the tip through a feedback circuit.

The electrostatic force on the tip, polarized with respect to the sample at $V_{\mathrm{dc}} + V_{\mathrm{ac}} \cos(\omega t)$ is proportional to the square of the voltage

$$F \propto (V_{\mathrm{dc}} + V_{\mathrm{ac}} \cos(\omega t) - V_{\mathrm{CPD}})^2. \tag{3.1}$$

V_{CPD} is the contact potential difference (CPD) due to different material work functions, band bending in response to charged interface states, or voltage drops within the sample if it is a biased circuit. The 1ω component of the electrostatic force is

$$F_{\omega} \propto V_{\mathrm{ac}}(V_{\mathrm{dc}} - V_{\mathrm{CPD}}). \tag{3.2}$$

By detecting the electrostatically excited oscillation at this frequency and adjusting the dc component to minimize it, V_{dc} is matched to the CPD and can be plotted as function of the coordinates.

The objective of this section is to reveal and to compensate the effect of apparent tip oscillation or oscillation caused by spurious mechanical excitation rather than by the electrostatic force.

3.2.2 Electrostatic Excitation Dependence on dc Bias

Therefore, electrostatically excited spectra of the second resonance are acquired with disabled Kelvin loop (switch of Fig. 3.1 open) and at different externally applied dc bias V_{dc}. Since distance control is enabled during these measurements, the cantilever is simultaneously excited at its first resonance frequency by the self-oscillating loop with 10 nm amplitude and the setpoint of the z feedback is set to $\Delta f = -50$ Hz. The ac drive signal is $V_{ac} = 0.25$ V. The projection signal rather than the oscillation amplitude is used for KPFM since it contains polarity information on $V_{dc} - V_{CPD}$. Any one of the projection outputs (real X or imaginary Y) can be used as error signal. The frequency should be set to maximize the chosen projection signal, and the polarity might need to be inverted by setting a negative gain in the error amplifier, depending on the reference phase. Some X projection resonance curves are recorded at different V_{dc} and plotted in Fig. 3.2. Sharp resonance curves are obtained due to the high Q-factor of about 10,000 in vacuum. According to (3.2), the tip excitation force scales with $V_{dc} - V_{CPD}$ and so should the resonance curves, meaning that they should be identical up to a factor. In contrast to (3.2), the curves have different shapes. Furthermore, the X projection should be an asymmetric function and the Y projection a symmetric one. A deviation of all curves from this predicted shape can be explained by the working frequency of 394 kHz, which is above the cutoff frequency of the photodetector of 250 kHz. However, this cannot explain why the spectra at different dc bias have apparent phase differences between each other.

To verify if the self-oscillating loop has any effect on the shape of the curves, a spectrum with disabled self-oscillating loop and disabled distance control is recorded at $V_{dc} = 1$ V. It is shown in Fig. 3.3. It is observed that with open self-oscillating loop, the phase and the Q-factor change with respect to the

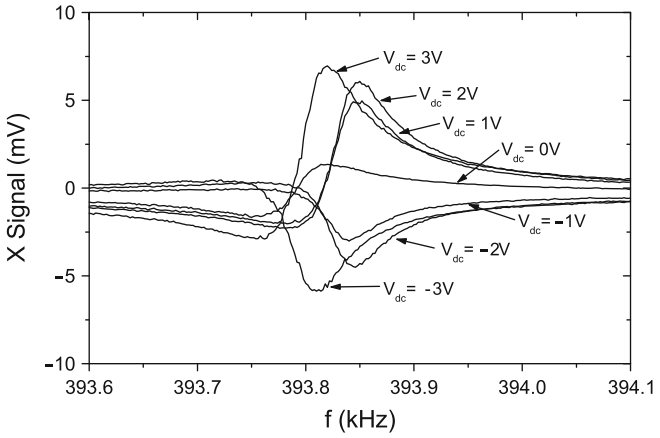

Fig. 3.2 Electrostatic excitation spectra of the second resonance for different V_{dc} values and with enabled self-oscillating loop (X-axis projection only)

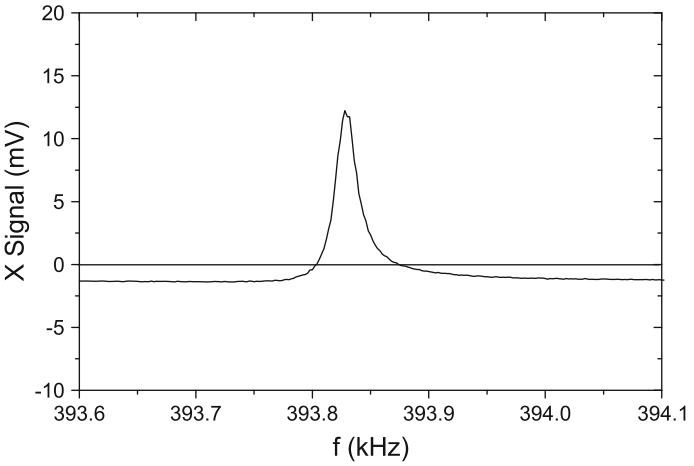

Fig. 3.3 Electrostatic excitation spectrum of the second resonance with $V_{dc} = 1\,V$ and with disabled self-oscillating loop (X-axis projection only)

corresponding curve of Fig. 3.2, and if V_{dc} is varied, the spectra scale perfectly (not shown).

Since on the curves with activated force feedback loop, the phase of the cantilever oscillation seems to vary for different dc bias, the effect of this loop must be studied. The electrostatic excitation force according to (3.2) is always in phase with the ac voltage. If the phase of the probe oscillation varies depending on V_{dc}, a second excitation mechanism is likely to be involved. Furthermore, the difference between the open and closed loop spectra also suggest that closing the force feedback loop modifies the excitation at the second resonance.

3.2.3 Measurement of the Crosstalk

On the spectrum with disabled force feedback loop (Fig. 3.3), a background is found which is independent of the output time constant of the lock-in amplifier, meaning that it is not noise related. It is not quasistatic deflection either since it is found on both sides of the resonance. It can be attributed to capacitive crosstalk from the ac excitation signal to the photodetector output and has been observed by other users before [3, 4]. As long as the force feedback loop is open, this background can be subtracted easily from the demodulated lock-in output signal since it is largely frequency independent on a range much wider than the resonance peak width. If, however, the force feedback loop is closed, the photodiode output signal is transmitted to the piezo dither via the feedback and contributes to the excitation of the tip. Therefore, the crosstalk between the ac excitation signal and the photodetector output results in a superposition of the electrostatic excitation plus

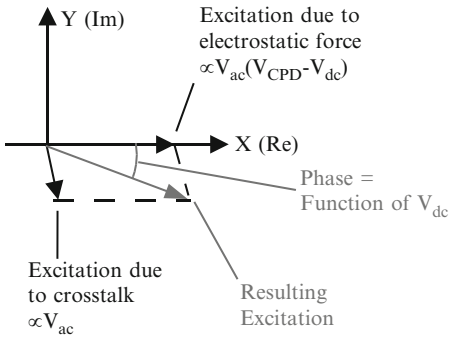

Fig. 3.4 Vector sum of the total excitation force on the cantilever in the complex plane. The electrostatic excitation force is proportional to $V_{ac}(V_{dc} - V_{CPD})$ and in phase with $V_{ac} \cos(\omega_2 t)$; the capacitive crosstalk causes a force at a different phase via the self-oscillating loop

a spurious mechanical excitation via the force feedback. The excitation due to the crosstalk is proportional to V_{ac} only and is subject to phase shift by the feedback amplifier, phase shifter, and the piezo response. The electrostatic excitation force is proportional to $V_{ac}(V_{dc} - V_{CPD})$ and in phase with $V_{ac} \cos(\omega_2 t)$.

Figure 3.4 shows the resulting overall excitation in the imaginary plane. The direct electrostatic force is on the X axis with sign and amplitude depending on V_{dc}. The crosstalk term, lagging behind in phase, is independent of V_{dc}. Therefore, the phase of the sum of both excitation forces depends on V_{dc}. In KPFM, where the CPD is found by applying a V_{dc} that cancels the electrostatic oscillation, the projection of the crosstalk vector on the X axis would correspond to a modification of the value of V_{dc} applied by the Kelvin control loop to cancel the excitation, introducing an error in the measured surface potential.

In open force feedback loop configuration (Fig. 3.3), the crosstalk causes a background that can be considered constant on the frequency range of the spectrum around the resonance and that could be easily subtracted in the demodulated signal of the lock-in projection output. However, as soon as the force feedback loop is closed, the entire force feedback loop responds to the crosstalk, including the cantilever with its resonance. The closed loop response has a strong resonance peak at the second cantilever resonance in contrast to the initial crosstalk to the photodiode in open loop that is constant on a wide range around the resonance peak. It would still be possible to subtract the closed loop response to the crosstalk only at the output of the lock-in amplifier, but the problem is to quantify it separately: if measured directly at the resonance frequency, both excitation mechanisms, spurious mechanical excitation due to the crosstalk and electrostatic excitation, are active. The electrostatic excitation could be cancelled by setting $V_{dc} = V_{CPD}$ but both the crosstalk and the CPD are a priori unknown. Therefore, the following approaches of compensation consist in suppressing the initial crosstalk before the force feedback loop is closed. The use of shielded UHV cabling as a means of reducing the effect has been proposed in references [3, 4] and is not resumed here. The following

sections concentrate on methods that do not require in-situ changes within the vacuum chamber.

3.2.4 Active Compensation at the Cantilever Frequency

An experimentally feasible method is the active compensation of the crosstalk in the high frequency signal before demodulation. Therefore, the initial crosstalk to the photodiode is first measured in open force feedback loop by determining the background at a frequency off the resonance peak. A high frequency signal is then subtracted from the photodiode signal to cancel this background. The necessary signal is obtained from the ac excitation signal through a variable phase shifter and a variable gain amplifier. The settings are determined empirically until the background disappears.

The setup with crosstalk correction is shown in Fig. 3.5. The compensation circuit consists of a phase shifter, a variable gain amplifier and a signal adder, allowing to shift the phase by up to $\pm 180°$ and to set the amplitude in a wide range before adding it to the photodiode signal.

Once the background signal is cancelled in open loop, the force feedback loop is closed, and a series of electrostatic excitation spectra at different V_{dc} is acquired, shown in Fig. 3.6. In contrast to Fig. 3.2, the spectra now scale perfectly, proving that the crosstalk is compensated.

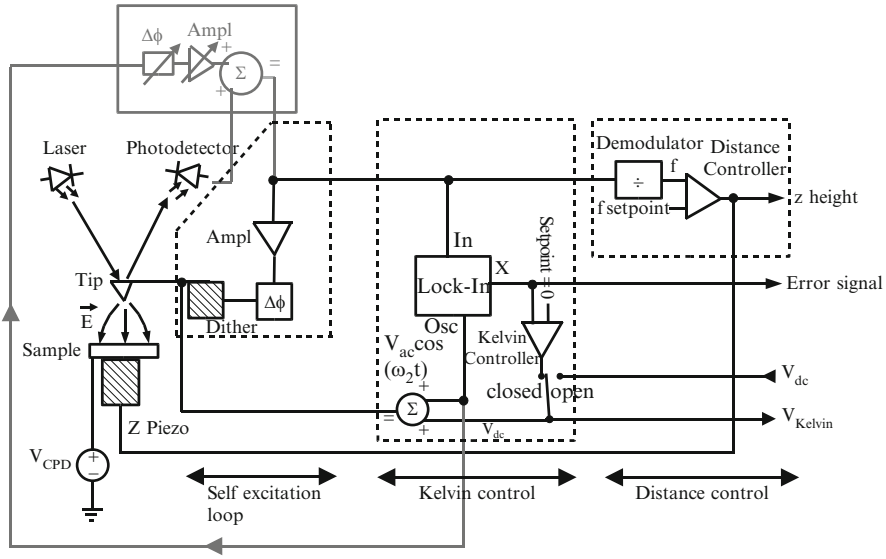

Fig. 3.5 Active compensation of the capacitive crosstalk by an external circuit consisting of a phase shift chain, amplifier and signal adder

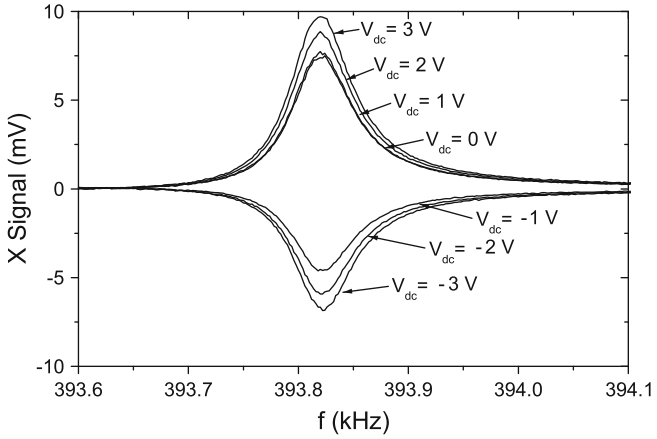

Fig. 3.6 Electrostatic excitation spectra as in Fig. 3.2 but with the crosstalk compensation of Fig. 3.5

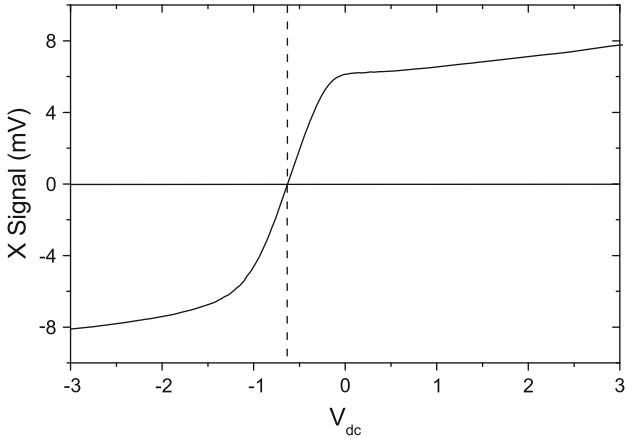

Fig. 3.7 X projection of the cantilever oscillation as function of V_{dc}; acquired at resonance frequency, with $V_{\mathrm{ac}} = 0.1$ V and using the crosstalk compensation circuit of Fig. 3.5

If V_{dc} is swept while the frequency is fixed at the resonance frequency, the lock-in output as function of voltage $X(V_{\mathrm{dc}})$ characteristics of Fig. 3.7 is obtained. For V_{dc} values near the CPD, the signal dependence is quite linear but a sudden slope change appears if the mismatch is more than 500 mV. This can be attributed to tip retraction beyond certain critical values of V_{dc} and can be verified by acquiring $z(V_{\mathrm{dc}})$ spectra. To make sure that $V_{\mathrm{dc}} - V_{\mathrm{CPD}}$ always remains within the tip retraction limits, the dynamic response of the Kelvin controller should be studied and optimized. This is beyond the scope of this chapter and described elsewhere [5]. In short, it is important that the quasistatic gain of the Kelvin loop is near unity, that the cutoff

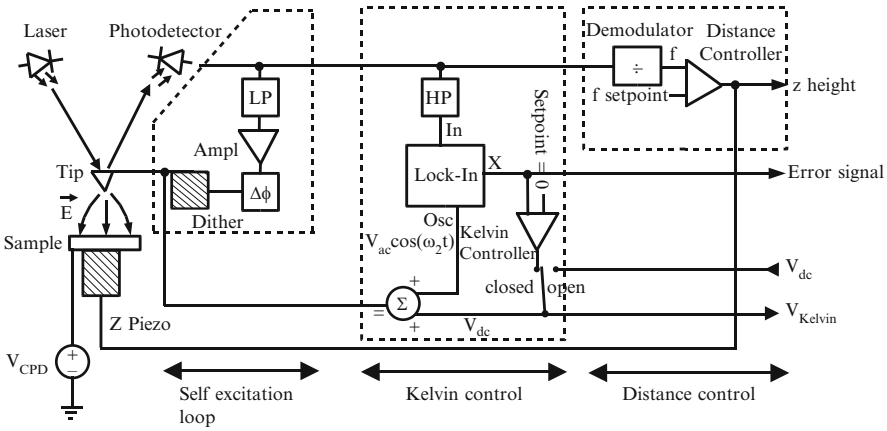

Fig. 3.8 Setup using high-pass and low-pass filters to separate the oscillation signals of the first and second resonance, thereby contributing to reduce the crosstalk problem

frequency of its response is as high as possible (more than 100 Hz was achievable in reference [6]), and that the loop is stable without harmonic overshoot.

3.2.5 Crosstalk Reduction by Filtering

Another approach to reduce the effect of the crosstalk is the use of high-pass and low-pass filters to split the signals of the first and second resonance at the photodiode output, as shown in Fig. 3.8. It has been proposed for the first time by Kikukawa [7], although it was not explicitly intended for reducing the effect of the crosstalk. The low-pass filter in the self-oscillating loop prevents the second resonance frequency from being fed back to the dither. This helps the force feedback to oscillate favorably at the first resonance and prevents it from spontaneously oscillating at the second resonance or even jumping between both frequencies. It does not avoid the crosstalk between the electrostatic excitation signal and the photodiode, but by considering that the signal at the second resonance frequency is not fed back to the dither, the crosstalk correction is facilitated: the capacitive coupling itself can be expected to be constant in a range around the peak of the second resonance frequency and therefore subtracted after demodulating by the lock-in amplifier. Without the low-pass filter, the crosstalk is transferred to the dither. It is unlikely to make the self-oscillating loop oscillate spontaneously at the second resonance since the loop should be adjusted to meet the criterion of spontaneous oscillation only for the first resonance, but nevertheless it alters the electrostatically excited second resonance peak due to spurious mechanical excitation. The highpass for the Kelvin loop is not absolutely necessary but has the advantage of reducing the contribution of the first resonance in the input signal of the Kelvin lock-in (which usually has a much higher amplitude

than the second resonance frequency signal), therefore allowing the use of a higher input sensitivity. If the cutoff frequency of both filters is set to the geometric mean value between first and second resonance, which are a factor 6.25 apart, and if second- order filters are used, the signals of each resonance frequency seen by the other part of the circuit are reduced by a factor of exactly 6.25. This reduces the effect of the crosstalk on the KPFM reading by almost an order of magnitude but does not completely eliminate the problem. Of course it is also possible to use a combination of filtering and active crosstalk suppression.

3.2.6 PLL Controlled AFM Setup

Yet another approach is the use of a PLL to excite the first resonance frequency, as shown in Fig. 3.9. As the previous solution, it does not avoid the crosstalk between electrostatic excitation and photodiode output, but efficiently prevents the second resonance frequency from being fed back to the dither and giving rise to a resonance. Then, the crosstalk can be corrected by subtracting a background after demodulation by the Kelvin lock-in amplifier. It can be shown that a PLL, based on a lock-in amplifier as phase detector, is most efficient in suppressing the parasitic second resonance frequency signal from mechanically exciting the tip. If the PLL is phase locked to the tip oscillation at the first resonance frequency f_1 and with an amplitude A_1, and if simultaneously a parasitic signal at the second resonance frequency f_2 with amplitude $A_2 \ll A_1$ is present at the photodetector output, the phase detector of the PLL yields a phase signal with a phase excursion of A_2/A_1 oscillating at a frequency $f_2 - f_1$, in our particular case $394\,\text{kHz} - 62\,\text{kHz} = 323\,\text{kHz}$. Since the output bandwidth of the PLL phase detector is typically set to some hundreds

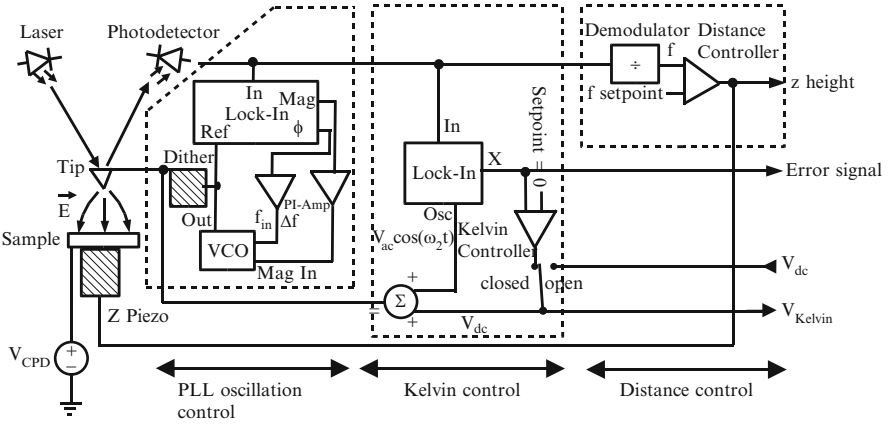

Fig. 3.9 Setup for simultaneous AM-KPFM and FM-AFM as in Fig. 3.1 but using a PLL to provide cantilever oscillation at the first resonance

of hertz, the effect of the parasitic signal on the phase detector output would be negligible. In contrast to the simple low-pass filter of Fig. 3.8, the PLL setup using a lock-in amplifier as phase detector has the advantage of superheterodyne filtering versus conventional filtering. For AFM operation, the PLL should have a capture and a tracking range as large as the expected shift of the first resonance frequency, which is three to four orders of magnitude below the frequency difference of the two resonance frequencies. This assures that the PLL can neither get locked to the second resonance frequency nor can it loose phase lock to the first resonance frequency by the superposition of a signal at the second frequency at equal or lower amplitude. For a detailed study of PLLs, see for example [8].

3.2.7 Comparison of the Countermeasures in UHV KPFM

Comparing the different approaches, it can be concluded that in the setup using a self-oscillating loop, the active crosstalk compensation gives good results since it allows to compensate the crosstalk completely. The drawbacks are that care has to be taken not to add noise to the deflection signal. The use of filters to split the signals of the first and second resonance frequency is easier to implement but can only reduce the effect by a factor of 6.25. The setup using the PLL eliminates the crosstalk completely and offers many advantages over the self-oscillating loop other than the crosstalk suppression that are very well described by Kim [9]. Even for plain NC-AFM operation, it has been found delicate by many users to find the appropriate settings of the self-oscillation loop to generate a proper oscillation at the first resonance. The signal risks to suffer from distortion due to nonlinear behavior if the gain is too high and is likely to jump spontaneously between different resonance frequencies of the cantilever.

3.3 AM-KPFM in Air

Here, the capacitive crosstalk and error terms in an AM-KPFM working in air are treated. Interaction with the distance control loop as in Sect. 3.2.1 can be excluded when the KPFM image is acquired in line alternation with the topographic image. Therefore, since real time distance control is not needed, KPFM operation is performed on the first cantilever resonance f_1.

3.3.1 Crosstalk Determination by Resonance Curve Fitting

In the absence of mechanical tip excitation during the KPFM operation, the measurement of the crosstalk is straightforward since only the background in the signal of the electrostatically excited tip oscillation has to be determined. However,

since the microscope is operating in air, the Q-factor is low and it is not possible to measure the background signal at a frequency close to the resonance. However, far from the resonance (3–10% above or below), it cannot be measured either since the crosstalk is itself frequency dependent and does not have the same value far from the resonance as it does have *on* the resonance. Therefore, it is necessary to measure it on both sides of the resonance peak and interpolate its value for the resonance frequency itself.

In the following, it will be described how to obtain the crosstalk term by fitting a Lorentzian plus a baseline to the tip resonance curve rather than finding a background approximately. By doing so, we assume that the crosstalk term can be approached as a simple baseline on the concerned frequency range.

An ideal Lorentz curve in X, Y projection representation can be expressed as function of prefactor A, resonance frequency f_0 and Q-factor:

$$\mathrm{Re[Osc]} = \frac{A\,(f_1^4 - f^2 f_1^2)}{f_1^4 + (1/Q^2 - 2) * f_1^2 f^2 + f^4} \tag{3.3}$$

$$\mathrm{Im[Osc]} = -\frac{A f_1^3 f}{Q(f_1^4 + (1/Q^2 - 2) f_1^2 f^2 + f^4)}. \tag{3.4}$$

For both components, the parameters A, f_1 and Q have to be the same when making a curve fit.

Next, since a drive phase (phase offset between ac drive signal and the X detection axis of the reference system) and other phase offset might be involved, we have to provide for this in both projections. On the X and Y axes, one does not have the purely real and imaginary component of an ideal resonance curve any more, but a mixing up of what would ideally be on the real and imaginary axes. This is illustrated in Fig. 3.10 that shows the frequency evolution of the oscillation vector and the rotated detection axes.

If a phase offset φ_{offs} between excitation and reference system is introduced (e.g., by setting a nonzero "drive phase"), then the excitation continues to be on the former X axis and the output signals are the projections of the complex signal onto the X' and Y' axes. Additionally, a crosstalk contribution is provided in the form of baselines added to the projections on both axes:

$$X'[\mathrm{Osc} + \mathrm{Ct}] = A\frac{(f_1^4 - f^2 f_1^2)\cos(-\varphi_{\mathrm{offs}}) - (f_1^3 f/Q)\sin(-\varphi_{\mathrm{offs}})}{f_1^4 + (1/Q^2 - 2) f_1^2 f^2 + f^4} + Bf + C \tag{3.5}$$

$$Y'[\mathrm{Osc} + \mathrm{Ct}] = -A\frac{(f_1^4 - f^2 f_1^2)\sin(-\varphi_{\mathrm{offs}}) + (f_1^3 f/Q)\cos(-\varphi_{\mathrm{offs}})}{f_1^4 + (1/Q^2 - 2) f_1^2 f^2 + f^4} + Df + F. \tag{3.6}$$

The two projections of such an oscillation signal suffering from crosstalk on the axes of a reference system with phase offset φ_{offs} are shown schematically in Fig. 3.11. The (exaggerated) crosstalk is represented as baselines to both curves.

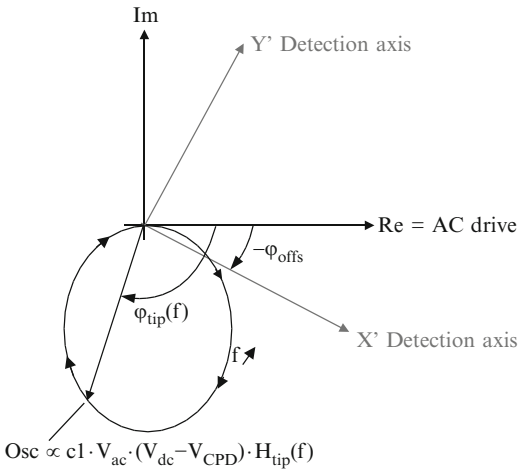

Fig. 3.10 Introduction of a phase offset: after setting a phase offset between the excitation signal and the reference system, the output signals will be the projection onto the X' and Y' axes. The *elliptical curve* indicates the oscillation of the AFM tip as the frequency of the excitation signal is swept across the resonance frequency

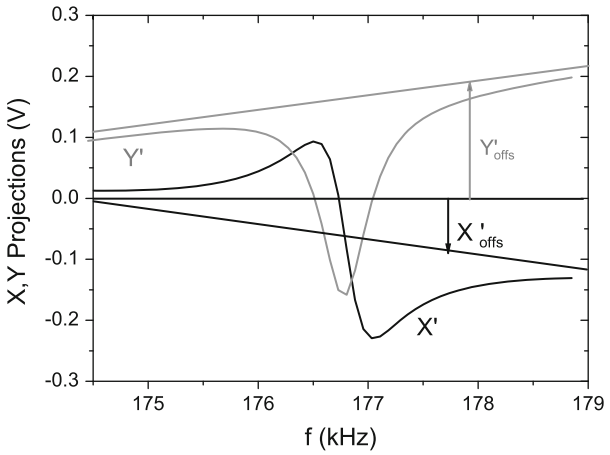

Fig. 3.11 Projections of a Lorentzian plus a capacitive crosstalk onto the real and imaginary axes of a phase shifted reference system. The capacitive crosstalk contributes a baseline (exaggerated) to each projection

Figure 3.12 is an example of a curve fit made to a measured electrostatically excited resonance curve. The common parameters of both projections are $A = 3.37\,\text{mV}$, $f_1 = 63.515\,\text{kHz}$, $Q = 196.8$ and $\varphi_{\text{offs}} = 1.393\,\text{rad}$. As baseline parameters for X', we find $B = 0.16\,\text{mV}\,\text{kHz}^{-1}$ and $C = 3.55\,\text{mV}$, and for Y' $D = 1.4\,\text{mV}\,\text{kHz}^{-1}$ and $F = -94.03\,\text{mV}$. At a frequency of $\approx$63.5 kHz, we find a

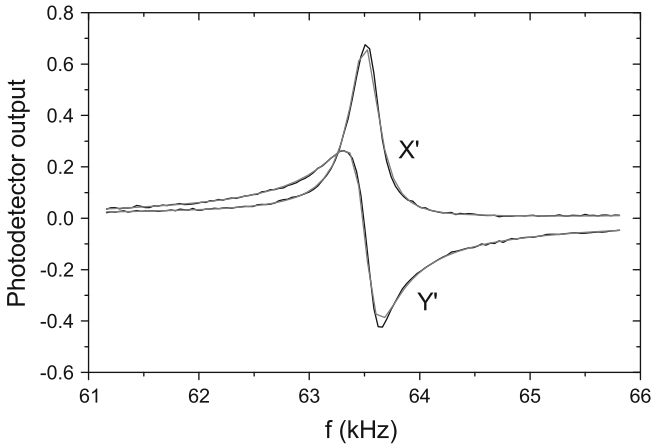

Fig. 3.12 Curve fit with (3.5) and (3.6) to an electrostatically excited resonance curve

crosstalk projection onto the offset detection axes:

$$X'[\mathrm{Ct}] = B \cdot 63.5\,\mathrm{kHz} + C = 13.71\,\mathrm{mV} \tag{3.7}$$

$$Y'[\mathrm{Ct}] = D \cdot 63.5\,\mathrm{kHz} + F = -5.13\,\mathrm{mV}. \tag{3.8}$$

3.3.2 Crosstalk Compensation

If the demodulated projection signals are accessible, the offset can be corrected by subtracting these values as dc offsets. If not, a compensation signal at the cantilever frequency must be generated. Therefore, the crosstalk is calculated in terms of real and imaginary components on the nonrotated system (in which the ac drive signal is purely real).

$$X[\mathrm{Ct}] = (X'[\mathrm{Ct}]\cos(\varphi_{\mathrm{offs}}) + Y'[\mathrm{Ct}]\sin(\varphi_{\mathrm{offs}})) \tag{3.9}$$

$$Y[\mathrm{Ct}] = (-X'[\mathrm{Ct}]\sin(\varphi_{\mathrm{offs}}) + Y'[\mathrm{Ct}]\cos(\varphi_{\mathrm{offs}})), \tag{3.10}$$

or in amplitude R and phase φ_{Ct} information, this would be $R = 14.6\,\mathrm{mV}$, $\varphi_{Ct} = -100.14°$. The compensation signal is then generated at the complementary phase and added to the photodetector output signal.

3.4 Crosstalk Effect on Complementary Measurements

This part describes the effect of the crosstalk on two measurements that are frequently performed when setting up the KPFM loop: the first method is a sweep of the dc bias while the ac excitation bias is applied to the probe to check whether

the probe can be electrostatically excited to oscillate; the second is a sweep of the reference phase to find a reference phase setting where the KPFM is operating reliably. The measurements shown here were obtained in a setup in ambient air but the reasoning would be valid for vacuum operation, too.

3.4.1 V_{dc} Sweep of the Oscillation Amplitude

A very common experiment in setting up the KPFM mode is the acquisition of a tip voltage sweep of the electrostatically excited oscillation *amplitude*. Although the amplitude is not used as error signal in the KPFM feedback loop because it does not contain polarity information, this experiment allows to verify that the oscillation is electrostatically excited (e.g., to verify that the tip does have electrical contact with the tip holder) and to estimate the surface potential from the minimum of the resulting curve. The advantage of this experiment is that no care has to be taken about the reference phase of the lock-in amplifier for a first check if an oscillation can be obtained. Later, during KPFM operation, the internally used error signal of the KPFM control loop is the projection of the tip oscillation onto an axis in the complex plane. Unfortunately, the amplitude signal is computed from the projection signals that are measured first, and more error sources in the processing path are likely to deviate the amplitude signal from the expected value. If the oscillation amplitude is plotted over the bias voltage while applying an ac signal at the resonance frequency, a "V"-shaped spectrum with an apex at the CPD and at zero amplitude is expected. For the V_{dc} sweep, the difference between this ideal curve and the experimentally obtained one is shown in Fig. 3.13.

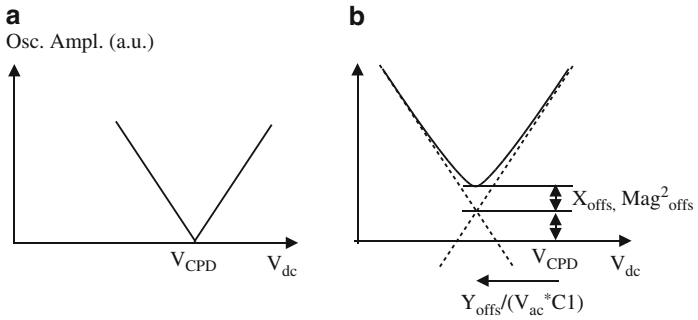

Fig. 3.13 Electrostatically excited cantilever oscillation amplitude as function of the applied dc bias: (**a**) ideal behavior, i.e., zero oscillation when the dc bias corresponds to the CPD; (**b**) real behavior including all possible error terms: horizontal shift due to an offset of the complex projection used as error signal, apex rounded off due to an offset of the perpendicular projection signal or an offset of the square sum of the projections, and vertical shift due to an offset of the RMS amplitude

The experimental curve can be a "V" shifted in voltage (laterally) and in amplitude (vertically, meaning the tangents do not cross at zero amplitude) and have a round apex rather than the ideal shape. In the following, a general expression of the oscillation amplitude with all possible error terms is given. Then, the error terms are attributed to the deviations between ideal and experimental shape of the amplitude(bias) curve. Therefore, it shall be reminded that the amplitude is obtained with a lock-in amplifier. The amplitude is calculated from the real and imaginary projections X and Y that are obtained first and one of which is internally used as KPFM error signal but not accessible for plotting or output.

The most general expressions of the amplitude as function of the real and imaginary projections, with error sources in all intermediate stages of the signal path, is

$$\mathrm{Mag} = \sqrt{(X + X_{\mathrm{offs}})^2 + \langle(\Delta X)^2\rangle + (Y + Y_{\mathrm{offs}})^2 + \langle(\Delta Y)^2\rangle + \mathrm{Mag}_{\mathrm{offs}}^2} + \mathrm{RMS}_{\mathrm{offs}}. \tag{3.11}$$

The projections of the oscillation amplitude are if the ac bias is at resonance frequency and the phase origin is zero: $X = 0$ and $Y = \mathrm{C1} \times (V_{\mathrm{dc}} - V_{\mathrm{CPD}}) \times V_{\mathrm{ac}}$. The offsets X_{offs} and Y_{offs} may be caused by capacitive crosstalk (effect $\propto V_{\mathrm{ac}}$), or by erroneous offsets that apply to the projection outputs of the lock-in amplifier (independent of V_{ac}), yielding $X_{\mathrm{offs}} + iY_{\mathrm{offs}} = \mathrm{Ct} \times V_{\mathrm{ac}} + \mathrm{C2}$. In contrast to these terms that are static in the reference system of the lock-in amplifier, ΔX and ΔY is random noise. It is uncorrelated with the other terms and is added geometrically (squared), where $\langle(\Delta X)^2\rangle$ and $\langle(\Delta Y)^2\rangle$ are proportional to the bandwidth of the projection output low-pass filters. $\mathrm{Mag}_{\mathrm{offs}}^2$ is an offset of the sum of the squares, and $\mathrm{RMS}_{\mathrm{offs}}$ an offset of the RMS amplitude output.

The offset terms X_{offs} and Y_{offs} interact constructively or destructively with the projection signal X and Y. If, for simplicity, the cantilever deflection is assumed to be parallel to the Y axis ($X = 0$), and the Y projection is consequently used as error signal, then Y_{offs} adds to the cantilever deflection Y and changes the dc bias V_{dc} for which the oscillation amplitude is minimized. This shifts the "V" spectrum of Fig. 3.13 horizontally. All other terms inside the root round the apex of the "V" but the tangents would still cross at zero amplitude. Only the offset that applies to the output of the RMS calculation, $\mathrm{RMS}_{\mathrm{offs}}$, can shift the "V" as a whole in vertical direction. This is shown by a series development of the root of (3.11):

$$\mathrm{Mag} - \mathrm{RMS}_{\mathrm{offs}} = |Y + Y_{\mathrm{offs}}| \sqrt{1 + \frac{X_{\mathrm{offs}}^2 + \langle(\Delta X)^2\rangle + \langle(\Delta Y)^2\rangle + \mathrm{Mag}_{\mathrm{offs}}^2}{(Y + Y_{\mathrm{offs}})^2}} \tag{3.12}$$

If the Y term in the denominator becomes much bigger than the numerator, the square root can be approximated by its series development $\sqrt{1 + x} \approx 1 + x/2$, showing that for large oscillation amplitudes, the behavior without the error terms

in the square root is asymptotically approached and therefore, the error terms X_{offs}^2 and $\text{Mag}_{\text{offs}}^2$ in the root only round off the apex but do not change the crossing point of the asymptotes. The noise terms $\langle(\Delta X)^2\rangle$ and $\langle(\Delta Y)^2\rangle$ translate into noise in the 'V' curve (not shown in Fig. 3.13).

A quantitative determination of Y_{offs} cannot be deduced from these measurements if the surface potential is unknown.

3.4.2 Phase Dependent KPFM Reading

In the general case, it can be expected that the electrostatic tip excitation and the electrostatic coupling between excitation signal and photodetector lead to photodetector output signals of different phase. The phase reference for the detection of the error signal can be chosen. The KPFM control loop then tries to adjust V_{bias} to cancel the projection of both output signals onto the reference axis. Depending on the reference phase angle, a different V_{bias} value is then needed for the projection of the electrostatically excited oscillation to cancel the projection of the crosstalk. This phase dependence of the KPFM reading is experimentally observed by performing a drive phase sweep of the Kelvin voltage, and is shown in Fig. 3.14.

Figure 3.15 shows the different components of the photodetector output and the reference axis in the complex plane. The oscillation of the tip has a phase φ_{osc}, the crosstalk has the phase φ_{Ct}. The excitation is at zero phase (X-axis) and the detection is at minus drive phase, $-\varphi_{\text{offs}}$. The Kelvin regulation loop sets V_{dc} such that the projection of the electrostatically excited oscillation vector on the detection axis compensates the projection of the crosstalk on the detection axis. When the electrostatically excited oscillation is perpendicular to the detection axis,

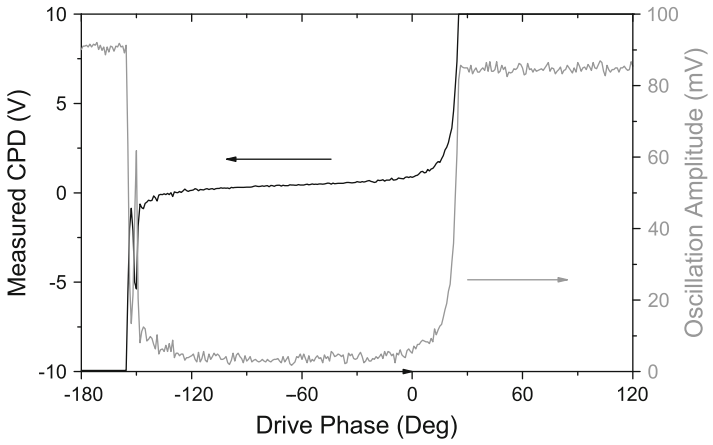

Fig. 3.14 Drive phase sweep of the apparent CPD in presence of a capacitive crosstalk

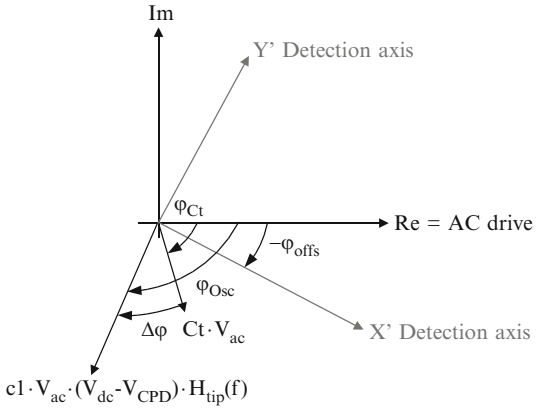

Fig. 3.15 Vector diagram showing the tip oscillation with its amplitude and phase depending on the frequency, the amplitude depending furthermore on $V_{dc} - V_{CPD}$ and on V_{ac}; the crosstalk term $Ct \cdot V_{ac}$ only depends on V_{ac}; the detection axis has an angle $-\varphi_{offs}$. The phase difference between the crosstalk vector and the tip oscillation vector is $\Delta\varphi$

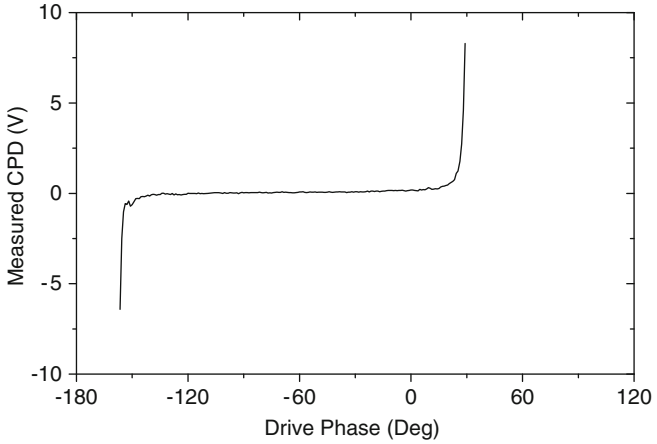

Fig. 3.16 Measured CPD as in Fig. 3.14 but with crosstalk compensation. The CPD is now nearly independent of the phase in a range of 180°, i.e., as long as the phase of the electrostatically excited oscillation is not perpendicular to the detection axis

this becomes impossible and the applied tip bias tends toward infinity, as observed by the two poles in Fig. 3.14.

If the drive phase sweep of Fig. 3.14 is repeated with crosstalk compensation, the resulting drive phase sweep shows a measured CPD, which is nearly independent of the drive phase over a wide phase range, shown in Fig. 3.16. The compensation of crosstalk in an AM-KPFM setup working in ambient air plays an important role in obtaining quantitative surface potential measurements [10].

3.5 Comparison of Crosstalk Compensation in Vacuum and in Air

In ultrahigh vacuum, the contribution from capacitive crosstalk to the electrostatically excited cantilever oscillation can be estimated by measuring the background signal because of the very sharp resonance peak due to the high Q-factor: it is accurate enough to determine the background at a frequency off but near to the resonance peak, after disabling the self-oscillating loop. However, the knowledge of the crosstalk alone is not necessarily the key to convenient and efficient compensation: when using a setup based on a self-excitation loop for the AM-KPFM distance control, it has to be kept in mind that the parasite signal propagates through this force feedback loop and causes spurious mechanical excitation causing the tip to resonate, making it impossible to correct the crosstalk by purely subtracting the background signal that was initially coupled to the photodetector. Solutions are either the compensation of the crosstalk directly in the high frequency photodetector signal and hence before it is transferred to the piezo dither, or the replacement of the force feedback loop by a PLL.

In setups working in ambient air, often no real-time distance control is used during KPFM acquisition since the real noncontact AFM mode is difficult to implement in ambient conditions. The KPFM image is then acquired in line alternation with the topography, and KPFM operation is based on electrostatically exciting the first resonance. The crosstalk could be corrected easily by subtracting it after demodulation, since it cannot cause a resonance by spurious mechanical excitation. Two difficulties may appear: first, the oscillation projection signal is not accessible in some AFM controllers, making it necessary to generate a compensation signal at the cantilever resonance frequency and to add it to the photodiode output; second, the crosstalk is difficult to quantify since the Q-factor of the probe is low in air and a wider spectrum has to be acquired to see the background. It has been found experimentally that the background cannot be considered constant over the width of the resonance peak and curve fitting has to be performed to obtain an accurate value by interpolation.

References

1. S. Kitamura, M. Iwatsuki, Appl. Phys. Lett. **72**(24), 3154 (1998)
2. T.R. Albrecht, P. Grütter, D. Horne, D. Rugar, J. Appl. Phys. **69**(2), 668 (1991)
3. C. Sommerhalter, T.W. Matthes, T. Glatzel, A. Jäger-Waldau, M.C. Lux-Steiner, Appl. Phys. Lett. **75**(2), 286 (1999)
4. C. Sommerhalter, T. Glatzel, T. Matthes, A. Jäger-Waldau, M. Lux-Steiner, Appl. Surf. Sci. **157**, 263 (2000)
5. H. Diesinger, D. Deresmes, J.P. Nys, T. Melin, Ultramicroscopy **110**, 162 (2010)
6. H. Diesinger, D. Deresmes, J.P. Nys, T. Melin, Ultramicroscopy **108**(8), 773 (2008)
7. A. Kikukawa, S. Hosaka, R. Imura, Appl. Phys. Lett. **66**(25), 3510 (1995)

8. H.M. Berlin, *Design of Phase-Locked-Loop Circuits, with Experiments* (Howard W. Sams and Co. Inc., IN, 1978)
9. B.I. Kim, Rev. Sci. Instrum. **75**(11), 5035 (2004)
10. T. Melin, S. Barbet, H. Diesinger, D. Theron, and D. Deresmes. Quantitative (artifact-free) surface potential measurements using Kelvin force microscopy. Rev. Sci. Instrum., **82**(3):36101, 2011.

Chapter 4
The Effect of the Measuring Tip and Image Reconstruction

Y. Rosenwaks, G. Elias, E. Strassbourg, A. Schwarzman, and A. Boag

Abstract In all electrostatic force-based microscopy types, the tip has a profound effect on the measured image because the measured forces are long range. In this chapter, we review most of the important literature devoted to this subject in the last two decades. It is shown that the combined effect of the cantilever, the tip cone and the tip apex is well understood for both conducting and semiconducting surfaces. In KPFM measurements conducted in air, the lateral resolution is in the range of 20–50 nm, but the measured potential is reduced by almost an order of magnitude relative to the theoretical value. In measurements conducted under UHV conditions the resolution is improved to around 10 nm, but the value of the measured potential is still significantly affected by the cantilever. In the second part, it is shown that today KPFM images can be reconstructed, using convolution to overcome the effect of the measuring tip and to give the actual sample surface potential. In addition, it is found that the exact tip apex shape is not an important factor in KPFM measurements conducted at tip–sample distances larger than 1.5 nm.

4.1 Introduction

It is well known that the finite tip size in scanning probe microscopes has a profound effect on the measured image. In electrostatic force-based microscopies, the effect of the measuring tip is enhanced because the measured forces have an infinite range. This effect is best demonstrated with the help of Fig. 4.1, showing to scale an AFM tip scanning a *p–n* junction, which is a good structure for KPFM measurements because under certain conditions the potential is accurately defined. The figure clearly demonstrates that the size of the tip apex alone (right) is huge compared

Y. Rosenwaks (✉) · G. Elias · E. Strassbourg · A. Schwarzman · A. Boag
School of Electrical Engineering, Faculty of Engineering, Tel Aviv University, Ramat-Aviv, 69978, Israel
e-mail: yossir@eng.tau.ac.il

S. Sadewasser and T. Glatzel (eds.), *Kelvin Probe Force Microscopy*, Springer Series in Surface Sciences 48, DOI 10.1007/978-3-642-22566-6_4,

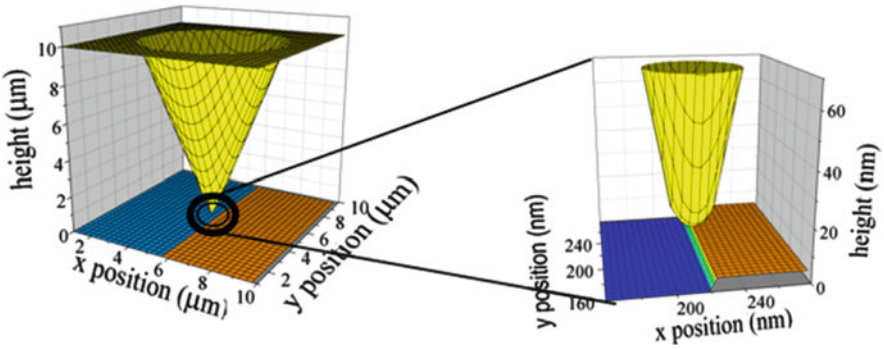

Fig. 4.1 Schematics of a typical KPFM tip scanning a *p–n* junction: it is clear that the tip apex alone is huge in size compared with the measured junction underneath [1]

with the typical junction dimensions, a fact that emphasizes further the significant averaging effect in KPFM. In the first part of this chapter, we review most of the important literature devoted to this subject in the last 20 years. It is shown that the combined effect of the cantilever, the tip cone and the tip apex is well understood for both conducting and semiconducting surfaces. In the second part, it is shown that today KPFM images can be reconstructed, using convolution to give the actual sample surface potential.

Since the KPFM method is based on electrostatic force microscopy (EFM), the distinction between them should be pointed out clearly right at the beginning. While the EFM measures the electrostatic force, F_ω, the KPFM as described in Chap. 2, measures the contact potential difference (CPD) by nullifying this force component. Therefore, the big advantage of the KPFM method relative to the EFM is the fact that a quantitative and a very well-defined physical parameter, the CPD, is directly measured. On the other hand, F_ω is proportional to the derivative of the tip–sample capacitance $(-\partial C/\partial z)$ and therefore strongly depends on the tip and cantilever geometry, and the measuring distance. Nevertheless, Brus et al. [2] and others have used this method extensively for measuring the electronic polarizability (via the tip-sample capacitance) of nanoparticles and quantum dots.

4.2 Tip–Sample Electrostatic Interaction: A Review

4.2.1 Conducting Surfaces

The significance of the long-range tip–sample electrostatic interaction was realized shortly following the first KPFM publication by Nonnenmacher et al. [3]. One of the first and simplest models was suggested by Hochwitz et al. [4] who modeled the tip by a series of (staircase) parallel plate capacitors as shown schematically in Fig. 4.2.

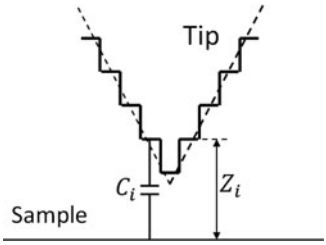

Fig. 4.2 Staircase model in which the AFM tip is modeled by a series of parallel plate capacitors C_i at distances z_i from the sample surface

The tip–sample electrostatic interaction is then calculated by representing the tip as a series of small capacitors connected in parallel, and V_{dc}, the voltage applied in order to nullify the electrostatic force at a frequency f is given by:

$$V_{\mathrm{dc}} = \frac{\sum_i \frac{\partial C_i}{\partial z} \cdot V_{\mathrm{CPD}_i}}{\sum_i \frac{\partial C_i}{\partial z}}, \tag{4.1}$$

where V_{CPD} is the actual tip–sample CPD, and $\partial C_i / \partial z$ is the derivative of the capacitance of capacitor i with respect to its distance from the surface, z. The staircase model has two approximations: (a) The area under the tip is underestimated, and (b) the parallel plate capacitor assumption is valid only when the distance between the capacitor plates is much smaller than their area; this is not valid for the KPFM setup. However, this model was used by several groups and found to be in a fair agreement with rigorous 3D electrostatic simulations that will be discussed in detail below.

Sadewasser et al. [5] have modified the staircase model to include the cantilever, which was modeled as a square neglecting most of its length. Since the cantilever is inclined at a certain angle to the reference plain, the outermost part of the cantilever will have the dominant contribution. They have used this model to estimate the KPFM resolution and sensitivity. Although, as will be shown below, these two parameters were analyzed more accurately by other methods, this simple model gave reasonable results. For example, it was estimated that the KPFM lateral resolution is a strong function of the tip-sample distance, d, and is around 20–30 nm for d below 10 nm. On the other hand, the magnitude of the measured CPD has a much stronger dependence on d, and for $d > 30$ nm the magnitude was calculated to be around 0.02 of the theoretical value. As will be shown in Sect. 4.3.1, this is supported by a more rigorous analysis, and implies that KPFM measurements conducted in air (where the tip–sample distance is typically around 30 nm due to water film and much lower Q factor of the cantilever) are at least one order of magnitude less sensitive relative to UHV measurements.

Belaidi et al. [6] were one of the first groups to develop and use a precise model (equivalent charge model) to calculate the electrostatic force acting on the tip and the cantilever. They have modeled the tip by a cone ending in a semi-spherical

Table 4.1 The three main regimes of electrostatic forces between a metalic tip and surface; d is the tip sample distance, R is the tip apex radius, and L the total tip length [6]

	Small tip-sample distance, $d < R$	Intermediate distance, $R < d < L$	Large distance, $R < d < L$
Electrostatic force, F	$1/d$	$\ln(1/d)$	$1/d^2$
Force gradient	$1/d^2$	$1/d$	$1/d^3$
Force contribution	Tip apex	Tip cone	Not localized

apex, and a V-shaped cantilever inclined at an angle to the sample surface. Their results showed that there are three main force regimes as a function of the tip–sample distance. For $d < 10$ nm, the electrostatic force is proportional to $1/d$, at very large distances, $d > 1$ μm, it is proportional to $1/d^2$ as expected for a parallel plate capacitor, and in between the slope is lower. These results are summarized in Table 4.1.

Belaidi et al. [7] have then used their calculations to estimate the EFM resolution. By defining the resolution as the distance over which 25–75% of a 1 V potential step is measured (for a tip–sample potential difference of 1 V), they have calculated a resolution, which is roughly linear with the tip–sample distance. A resolution of around 10 and 200 nm was obtained for tip-sample distances of 5 nm (UHV) and 30 nm (air), respectively; these values were obtained for a tip apex radius $R = 10$ nm and a cone half angle of 10°. By comparing their numerical calculations to analytical expressions (which was found to be a reasonable approximation up to a tip–sample distance of $d/R < 0.5$), they have estimated the resolution as $R_e = 1.63\sqrt{Rd}$.

This work was extended by Leveque et al. [8] who analyzed the amplitude and the phase of the cantilever under an applied bias of 1 V and a constant frequency. They have found that in the linear regime (cantilever flexion $\ll d$) the lateral resolution is $R_e = 1.047\sqrt{Rd}$, not very different from the expression obtained by Belaidi et al. [7].

Hudlet et al. [9, 10] have derived analytical expressions of the electrostatic force between a conductive tip and a metallic surface and compared it to the van der Waals forces. The most important conclusion from their work is that at tip–sample distances larger than 10 nm, the dominant measured force is electrostatic. This implies that in almost all ambient noncontact AFM measurements the "topography" image is a measure of the electrostatic forces. However, as was shown by several authors recently [11], this image will not be very different from the van der Waals forces image as long as the sample surface potential variations are not very large.

As discussed in Chap. 2, the KPFM is performed either using amplitude-modulation (AM) or the frequency-modulation (FM) method, which are sensitive to the electrostatic force and its gradient, respectively [12]. Zerweck et al. [13] have described in detail the accuracy and resolution provided by the two methods. They concluded that: (1) the FM method deduces an accurate CPD, which was in excellent agreement with macroscopic UPS measurements; (2) the FM method is best used with the sharpest tips and might even achieve atomic contrast with accurate values; (3) in the AM method, reasonable accuracy can only be expected for tips with a front end having a similar size as the measured object.

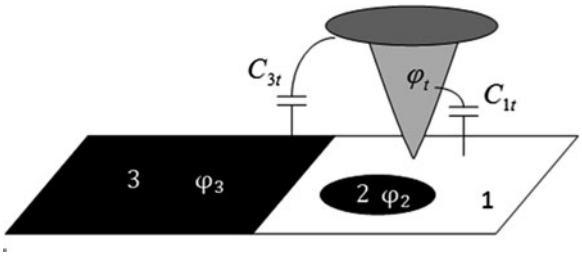

Fig. 4.3 Schematic description of the tip–sample system used by Jacobs et al. [14] for their KPFM calculations of semiconducting samples. The sample is divided into a system of ideal conductors with electrostatic interactions represented by mutual capacitances C_{ij}

4.2.2 Semiconducting Surfaces

The basic difference between a semiconducting surface and conducting samples discussed in the previous section is that on a semiconductor the surface potential is not constant. This important difference was first analyzed by Jacobs et al. [14], who have conducted extensive calculations of the tip–sample interaction in KPFM measurements of conductors and semiconductors. They have replaced the semiconductor sample by a set of ideal conductors of constant potentials φ_i with mutual capacitances between them, and a tip with a constant potential φ_t as shown schematically in Fig. 4.3.

Their analysis expressed the KPFM signal, V_{dc}, as:

$$V_{\mathrm{dc}} = \frac{\sum_{i=1}^{n} C_{\mathrm{it}}' \cdot \varphi_i}{\sum_{i=1}^{n} C_{\mathrm{it}}'}, \tag{4.2}$$

where $C_{\mathrm{it}}{}' = \partial C_{\mathrm{it}}/\partial z$ are the capacitance derivatives between a sample element i and the tip. The above equation demonstrates (like the naive staircase model) that the KPFM signal is determined by the electrostatic interaction between the tip and the different sample regions. The measured CPD does not exactly match the surface potential below the tip, rather it is a weighted average over all surface potential φ_i, with the derivatives of the capacitances, $C_{\mathrm{it}}{}'$, being the weighing factors. Consequently, they have concluded that the KPFM images of infinitely large conducting surfaces are two-dimensional (2D) convolutions of the actual surface potential distribution with a tip transfer function, $h(x, y)$ defined by the tip geometry [15].

$$V_{\mathrm{dc}}(x_t, y_t) = \int_{-\infty}^{\infty}\int_{-\infty}^{\infty} h(x - x_t, y - y_t)\varphi(x, y)\mathrm{d}x\mathrm{d}y \tag{4.3}$$

$$h(x - x_t, y - y_t) \equiv \lim_{\Delta x, \Delta y \to 0}\left[\left(\frac{C'(x - x_t, y - y_t)}{C_{\mathrm{tot}}{}'\Delta x \Delta y}\right)\right] \tag{4.4}$$

Jacobs et al. [15] have then used this formalism to calculate the KPFM system response, defined here as a point spread function (PSF), for various tip and cantilever geometries. They have drawn the following important conclusions:

(a) The cantilever affects the PSF amplitude despite being 15 μm above the sample surface;
(b) A minimal cantilever width and surface area will improve the KPFM resolution and sensitivity;
(c) The PSF is determined by the relative tip and cantilever geometries for a given tip–sample distance. When the tip apex radius of curvature is small (10 nm), the cantilever will have a larger effect on the PSF. For a given tip opening angle, a larger tip apex (blunter tip) will sharpen the PSF (improve lateral resolution). A good agreement between the above model and test structures measurements was also demonstrated.

Almost all of the works that analyze semiconductor KPFM measurements replace the semiconductor sample by a surface with a fixed or variable surface potential that is not affected by the measuring tip. This is only valid for the case of a weakly interacting tip–sample system, i.e., when there is no tip-induced band-bending phenomenon as frequently is unavoidable in STM and EFM measurements.

We have analyzed in detail the effect of the measuring KPFM tip on the semiconductor surface potential; i.e., we have calculated if there is a significant tip-induced band bending at the semiconductor surface when the electrostatic force at the ac-frequency is nullified. As described in detail in Chap. 2, a calculation of the KPFM signal amounts to finding the voltage applied to the tip or to the sample, V_{dc}, that minimizes the total electrostatic force at the frequency. Our calculation [16] takes into account the electrostatic energy when the semiconductor energy bands are not flat due to the presence of surface states and/or due to tip-induced band bending. As an example, we show below a typical calculated surface-induced band bending for a KPFM tip, having a potential of 0.1 V higher than a GaP (S-doped $n = 5 \times 10^{17}\,\mathrm{cm}^3$) surface with no charged surface states, or zero band bending) and located 5 nm above it; the result is shown in Fig. 4.4 [17]. The figure shows that the surface band bending, expressed as $(E_F - E_{is})$ where E_{is} is the surface Fermi level position, due to the presence of the biased tip, is zero everywhere except for a small region in the middle where the band-bending is less than 6 mV. A similar calculation conducted for a tip–sample surface potential difference of 0.6 V resulted in an induced surface band bending of around 38 mV [16, 17].

The small-induced band bending effect can be explained in the following way. The tip-vacuum-semiconductor system can be modeled as two capacitors, tip-vacuum-semiconductor surface and the semiconductor space charge region (SCR) connected in series. Thus, an external voltage (in the present case, it

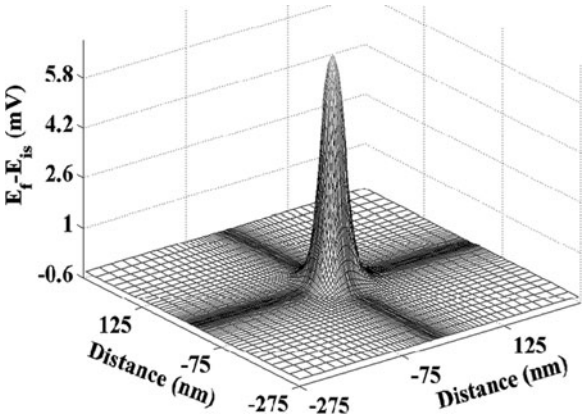

Fig. 4.4 Calculated local band bending, expressed as ($E_F - E_{is}$) for a GaP with no surface states, tip–sample distance of 5 nm and an applied bias of V_{tip}=0.1 V between tip and sample. The protrusion in the center is the tip-induced band bending at the GaP surface [17]

is the semiconductor-tip V_{CPD}) will "drop" mainly on the smaller of the two capacitors. The SCR capacitance is typically much larger (except for very low-doped semiconductors), thus causing the voltage to drop mainly between the tip and the sample surface, and hence inducing a negligible band bending in the SCR. It must be reemphasized that in KPFM measurements the CPD between the tip and the sample is nullified, so typically the potential difference between any point on the tip, and on the sample surface in a close distance to it, will be even lower than the 0.1 V used in calculating the potential in Fig. 4.4. It must be noted that we calculate the static (dc) electrostatic force; i.e., it is assumed that the ac voltage has a negligible effect on the tip–sample forces. This is a very good approximation for AM-KPFM measurements where the ac-voltage frequency used in the measurements (>300 kHz) is high and in addition the ac modulation amplitude applied to the tip is very low (100 mV). However in FM-KPFM, the applied ac bias is typically 1–2 V, and the modulation frequency is not larger than 5 kHz. In such cases, tip-induced band bending might occur due to charging or discharging of surface states at such frequencies.

The conclusion, which under typical KPFM measurement conditions a semiconductor surface potential changes very little, simplifies tremendously the simulation of semiconductors KPFM measurements. This is because it enables to replace the whole semiconductor sample by a single surface with a varying potential. The three-dimensional tip-sample system can now be accurately represented only by its boundaries, instead of the potential in the entire volume. The potential in this system is now solved using an integral equation-based boundary element method (BEM), which is a much faster numerical process as shown in the next section.

4.3 Deconvolution and Image Restoration

4.3.1 Accurate Algorithm for Image Restoration

In this section, we present an algorithm for restoring the V_{CPD} out of KPFM measurements conducted on flat surfaces following the methodology developed by us recently [18].

Based on the conclusion derived in the previous section, that in most practical cases the semiconductor surface potential does not change due to the presence of the KPFM tip, the system is analyzed using the BEM. The solution of the Poisson equation is determined by three boundary conditions for the tip–sample system: (a) the constant tip potential; (b) the surface potential; and (c) the potential far from the measured system, which is assumed to be zero. The tip potential can be viewed as:

$$\varphi_{\text{tip}}(\underline{r}) = \varphi^{\text{h}}_{\text{tip}}(\underline{r}) + \varphi^{\text{inh}}_{\text{tip}}(\underline{r}). \tag{4.5}$$

We divide the potential into two parts: (a) $\varphi^{\text{h}}_{\text{tip}}(\underline{r})$ which is the contribution of the charges on the tip surface in the homogeneous system of the tip above a grounded planar surface, and (b) inhomogeneous part, $\varphi^{\text{inh}}_{\text{tip}}(\underline{r})$, stemming directly from the surface potential on the sample. The homogeneous system is modeled by placing image charges, such that the boundary condition on the grounded plane is satisfied (Fig. 4.5a). The homogeneous potential on the tip is represented as:

$$\phi^{\text{h}}_{\text{tip}}(\underline{r}) = \int_{S_{\text{tip}}} [G(\underline{r}, \underline{r}') - \tilde{G}(\underline{r}, \underline{r}')]\sigma(\underline{r}')\text{d}s', \tag{4.6}$$

where $\sigma(\underline{r})$ is the unknown surface charge density on the tip surface. The function $G(\underline{r}, \underline{r}')$ is known as the three- dimensional electrostatic Green's function $G(\underline{r}, \underline{r}') = 1/(4\pi\varepsilon_0|\underline{r} - \underline{r}'|)$ and represents the potential of a unit charge at a point $\underline{r}'$ observed at point $\underline{r}$. Also in (4.6), $\tilde{G}(\underline{r}, \underline{r}')$ represents the image charge contribution: $\tilde{G}(\underline{r}, \underline{r}') = G(\underline{r}, \tilde{\underline{r}}'), \underline{r}' = (x', y', z'), \tilde{\underline{r}}' = (x', y', -z')$.

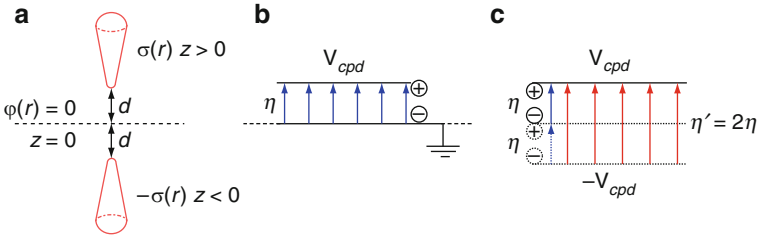

Fig. 4.5 (**a**) Homogeneous system represented by equivalent charge model. (**b**) Dipole layer on top of an infinite grounded plane. (**c**) The equivalent charge model creates an image dipole so that the image and original dipole layers are now represented as one dipole layer with double density

In order to evaluate the inhomogeneous contribution, due to the variations in the surface potential, we represent the sample by a dipole layer on top of a grounded plane. The dipole density, $\eta(\underline{r})$, is used to describe the variations in the sample surface potential. Since the dipole layer forms a potential discontinuity, we obtain: $\eta(\underline{r}) = V_{\mathrm{CPD}}(\underline{r})\varepsilon_0$. In order not to calculate the surface charge density on the ground plane, we use again the method of images (see Fig. 4.5b, c), which leads to a new dipole layer with twice the density $\eta'(\underline{r}) = 2\eta(\underline{r}) = 2V_{\mathrm{CPD}}(\underline{r})\varepsilon_0$ located in the free space.

The potential at a point $\underline{r}$ produced by the entire dipole layer is a result of the integration of dipole contributions over the entire surface S_{sample}

$$\varphi_{\mathrm{tip}}^{\mathrm{inh}}(\underline{r}) = \frac{1}{4\pi\varepsilon_0}\int_{S_{\mathrm{sample}}} \frac{(\underline{r}-\underline{r}')\cdot\hat{\underline{n}}(\underline{r}')}{|\underline{r}-\underline{r}'|^3}\eta'(\underline{r}')\mathrm{d}s' \tag{4.7}$$

$$= \frac{1}{2\pi}\int_{S_{\mathrm{sample}}} \frac{(\underline{r}-\underline{r}')\cdot\hat{\underline{n}}(\underline{r}')}{|\underline{r}-\underline{r}'|^3}V_{\mathrm{CPD}}(\underline{r}')\mathrm{d}s',$$

where $\hat{\underline{n}}(\underline{r}')$ is a unit vector normal to the surface. Obviously, for a planar sample $\hat{\underline{n}}(\underline{r}') = \hat{\underline{z}}$.

Equations (4.6) and (4.7) can be transformed into a discrete form by the BEM. To that end, we divide the tip and sample surfaces into boundary elements and by sampling the potential on those surfaces we can define matrices $\underline{\underline{G}}$ and $\underline{\underline{D}}$,which are the discrete representations of the integral operators in (4.6) and (4.7), respectively. For the sake of simplicity of the BEM formulation, we assume zero-order elements with constant charge density over each element. Thus, a continuous charge density distribution is represented in the discrete form by vector $\underline{\sigma}$. Note that underbars denote vectors and double underbars matrices. Finally, we can substitute the discrete forms of (4.6) and (4.7) into (4.5) to obtain

$$\varphi_{\mathrm{tip}}\underline{I} = \underbrace{\underline{\underline{G}}\,\underline{\sigma}}_{\substack{\texttt{tip surface charge}\\ \texttt{density contribution}\\ \texttt{to the tip potential}}} + \underbrace{\underline{\underline{D}}\,\underline{V}_{\mathrm{CPD}}}_{\substack{\texttt{sample surface potential}\\ \texttt{contribution to}\\ \texttt{the tip potential}}}, \tag{4.8}$$

where $\underline{I}$ is a vector whose elements are all ones and $\underline{V}_{\mathrm{CPD}}$ is a vector of samples of V_{CPD} on the surface.

Equation (4.8) can be formally solved for the charge density over the tip

$$\underline{\sigma} = \underline{\underline{G}}^{-1}(\varphi_{\mathrm{tip}}\,\underline{I} - \underline{\underline{D}}\,\underline{V}_{\mathrm{CPD}}) = \underbrace{\varphi_{\mathrm{tip}}\underline{\underline{G}}^{-1}\underline{I}}_{\substack{\texttt{homogeneous}\\ \texttt{charge}}} - \underbrace{\underline{\underline{G}}^{-1}\underline{\underline{D}}\,\underline{V}_{\mathrm{CPD}}}_{\substack{\texttt{inhomogeneous}\\ \texttt{charge}}}, \tag{4.9}$$

where $\underline{\underline{G}}^{-1}$ denotes the inverse matrix of $\underline{\underline{G}}$. The charge density over the tip can be viewed as a difference between the homogeneous and inhomogeneous charge

distributions. While the homogeneous charge generates a constant potential over the tip, the inhomogeneous charge produces an additional local potential, which cancels out the uneven influence on the different areas of the tip coming from the sample surface.

The z-component of the electrostatic force acting on the tip is calculated by integrating the Maxwell stress over the tip surface

$$F_z = \int_{s_{\text{tip}}} \frac{\sigma^2(\underline{r})}{2\varepsilon_0}(\hat{\underline{n}} \cdot \hat{\underline{z}})\mathrm{d}s, \tag{4.10}$$

where $\hat{\underline{n}}$ is the outward normal unit vector to the tip surface. Using the same BEM discretization of the tip surface, the force can be approximated by a quadratic form as:

$$F_z = \underline{\sigma}^t \underline{\underline{\Delta}}\, \underline{\sigma}, \tag{4.11}$$

where $\underline{\underline{\Delta}}$ is a diagonal matrix whose jjth element is given by $\int_{\Delta S_{\text{tip}}^j} (\hat{\underline{n}} \cdot \hat{\underline{z}})/2\varepsilon_0 \mathrm{d}s$, i.e., an integral of type (4.10) for a unit charge density over the jth boundary element ΔS_{tip}^j. Inserting (4.9) into (4.10), replacing the tip potential with $\varphi_{\text{tip}} = V_{\text{dc}} + V_{\text{ac}}\sin(\omega t)$, and extracting only the force amplitude at frequency ω, we obtain:

$$F_{z,\omega} = 2V_{\text{ac}} \left(\underbrace{V_{\text{dc}} \underline{\alpha}^t \underline{\underline{\Delta}}\, \underline{\alpha}}_{\substack{\texttt{homogeneous} \\ \texttt{force}}} \quad \underbrace{-\underline{\alpha}^t \underline{\underline{\Delta}}\, \underline{\underline{G}}^{-1} \underline{\underline{D}}\, \underline{V}_{\text{CPD}}}_{\substack{\texttt{inhomogeneous} \\ \texttt{force}}} \right), \tag{4.12}$$

where we define $\underline{\alpha}$ as $\underline{\underline{G}}^{-1}\underline{I}$.

The PSF, which is the measured V_{dc} in the presence of a Kronecker delta function surface potential shape, is determined by the force acting on the tip. This force has a homogeneous part: $F_{z,\omega}^{\text{h}} = 2V_{\text{ac}}(V_{\text{dc}}\underline{\alpha}^t \underline{\underline{\Delta}}\, \underline{\alpha})$ and an inhomogeneous part $F_{z,\omega}^{\text{inh}} = 2V_{\text{ac}}(\underline{\alpha}^t \underline{\underline{\Delta}}\, \underline{\underline{G}}^{-1} \underline{\underline{D}}\, \underline{V}_{\text{CPD}})$. The homogeneous part is independent of the sample surface potential and the tip position; therefore, it will not affect the KPFM resolution, but will change the value of the measured CPD. The inhomogeneous force will determine the measurement resolution. The distinction between the homogeneous and inhomogeneous force is important in order to quantify the KPFM resolution. Evaluating the resolution by using only the total force may lead to inaccurate results as presented by Colchero et al. [19].

Figure 4.6 shows a typical two-dimensional PSF calculated using the above formalism and the following tip parameters: $l = 4\,\mu\text{m}$ (tip length), $d = 10\,\text{nm}$ (tip–sample distance), $\theta = 10°$ (half opening angle), and $R = 10\,\text{nm}$ (tip apex radius).

One-dimensional PSFs derived from the 2D PSF and calculated for various tip parameters are presented in Fig. 4.7. The results show that the tip–sample distance,

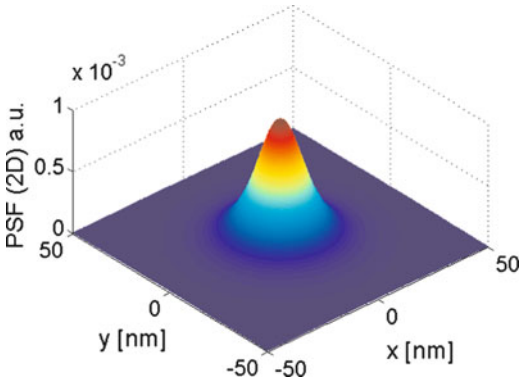

Fig. 4.6 A typical two-dimensional tip point spread function (PSF) calculated for a tip with $l = 4\,\mu\text{m}$, $\theta = 10°$, and $R = 10\,\text{nm}$ located at a height $d = 10\,\text{nm}$ above a sample

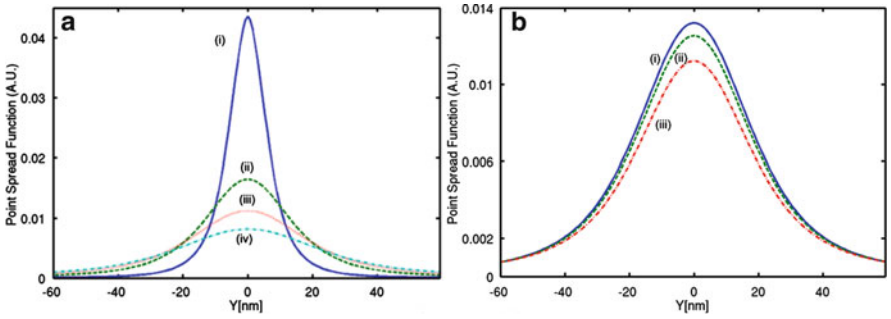

Fig. 4.7 One-dimensional point spread functions calculated as a function of: (**a**) tip–sample distances d of : (i) 1.2, (ii) 6.8, (iii) 11.9 (iv) 17.8 nm; and (**b**) tip half aperture angles θ_0 of : (i) 10, (ii) 12.5, and (iii) 17.5°, calculated with $d = 11\,\text{nm}$. The tip apex radius is 30 nm for all graphs

d has a very large effect on the PSF magnitude, and thus on the sensitivity in KPFM measurements. For example, Fig. 4.7a shows that increasing the tip–sample distance from 1.2 to 11.9 nm decreases the KPFM signal amplitude by a factor >4.

This implies that ultrahigh vacuum (UHV) KPFM measurements, typically carried out at distances around $d = 3\,\text{nm}$, are roughly one order of magnitude more sensitive than air KPFM measurements conducted at d>10 nm. The effect of the tip half opening angle, θ_0, on the PSF shown in Fig. 4.7b is weak; this is due to the fact that at small tip–sample separation (1.2 nm), the electrostatic force is mostly due to the tip apex as was also found and reported by several groups [9, 10] and described in the previous sections. The tip apex radius, R, was found to affect mainly the width of the PSF in agreement with previous works [14].

Figure 4.8 shows measured (dots), and noise-filtered and restored (solid line) surface potential line scans of an atomic step on a GaP (110) surface measured by

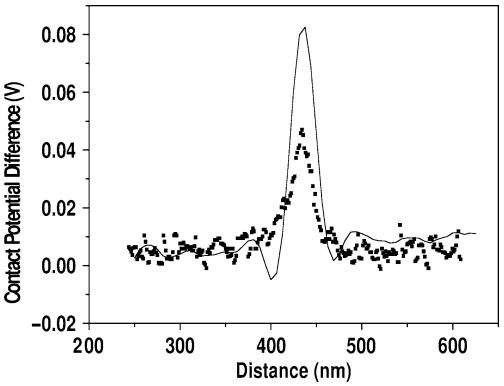

Fig. 4.8 Measured (*dots*) and reconstructed (*solid*) surface potential of an atomic step on a GaP (110) surface. The KPFM measurement [16] was conducted under UHV conditions where the tip–sample distance, d, was estimated as 5 nm. The sharp work function change at the step is due to localized surface charge

UHV-KPFM [16], at a tip-sample distance $d = 5$ nm. The sharp work function change at the step is due to localized surface charge as discussed in detail in [5, 16]. The potential reconstruction, based on deconvolution using the appropriate PSF, shows that the reconstructed CPD increases by more than a factor of 2 (relative to the measured one) even at the small tip–sample separation used in UHV measurements. This result demonstrates the importance of the reconstruction in KPFM measurements of small features; in ambient KPFM measurements, the effect is much larger as discussed above.

4.3.2 Tip Oscillation and the Effect of the Cantilever

The V_{CPD} measurement is achieved by minimizing the oscillatory electrostatic force on the tip. Therefore, we have derived an expression for the charge density that will fulfill the minimum force condition. In order to do so, we should recall that in single-pass KPFM measurements, the cantilever oscillates at its fundamental resonance frequency f_0 that is used to measure the sample topography. This frequency should not be confused with the ac modulation of the tip potential, f_{ac}, which produces an additional vibration of the tip at the same frequency, due to the electrostatic force. For tip–sample distances as small as 10 nm there is a very large effect of the tip movement because of the strong distance dependence of the inhomogeneous electrostatic force (Fig. 4.9). Therefore, the tip charge distribution becomes time dependent and so are the tip elements interaction matrix $\underline{G}$ and the sample–tip interaction matrix $\underline{\underline{D}}$. The contribution of this effect depends on the KPFM feedback circuit time constant relative to the cantilever resonance frequency.

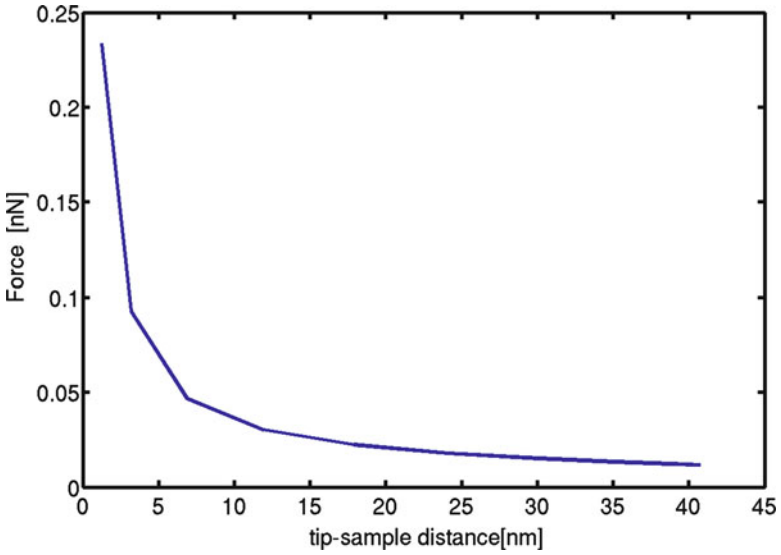

Fig. 4.9 Vertical inhomogeneous force contribution as a function of the tip–sample distance calculated for a tip-sample potential difference of 1 V. Tip geometry parameters: half-opening angle of 10°, bottom tip radius 10 nm

Typically, the cantilever oscillation amplitude at f_{ac} is much smaller than that at f_0. Thus, we assume that during the minimization process, the cantilever oscillations at frequency f_0 are perfectly sinusoidal and hardly affected by the electrostatic forces related to the tip–sample interaction at the higher frequencies. We consider the effect of the sinusoidal oscillations in two limiting cases:

(a) High-frequency KPFM controller – here the minimum force, $F_{z,\omega}(\omega = 2\pi f_{ac})$, condition is then applied for every tip–sample distance, and only then, the potential output is averaged. In this case, the measured potential can be written as:

$$V^{(a)}_{\text{measured}} = \lim_{T\to\infty} \frac{1}{T} \int_0^T \varphi_{\text{tip}}(t)|_{\min\{F_{z,\omega}(t)\}} \mathrm{d}t, \tag{4.13}$$

where $\varphi_{\text{tip}}(t)|_{\min\{F_{z,\omega}(t)\}}$ is the tip potential after minimizing the force at t.

(b) Low-frequency KPFM controller – in this case, the KPFM controller output minimizes the average force. Thus, the measured potential becomes:

$$V^{(b)}_{\text{measured}} = \varphi_{\text{tip}}|_{\min\{\lim_{T\to\infty} \frac{1}{T} \int_0^T F_{z,\omega}(t)\mathrm{d}t\}}. \tag{4.14}$$

In case (a), each tip–sample distance has the same weight to the measured potential. Finding the minimum for this case, using (4.12), is straightforward and leads to the conclusion that the PSF is a weighted average of the PSFs of each tip sample distance.

In case (b), smaller tip–sample distances will have a much larger effect on the average force. Since in most KPFM setups the controller time constant is not much less than 1 ms and a typical f_0 frequency at a noncontact setup is greater than 70 KHz, method (b) should be used in most cases. Therefore, we calculate the dc tip potential that will minimize the average force as:

$$\min\{\overline{F}_{z,\omega}\} = \min\left\{\lim_{T\to\infty}\frac{1}{T}\int_0^T F_{z,\omega}(t)\mathrm{d}t\right\}. \tag{4.15}$$

By replacing the integrand $F_{z,\omega}$ with (4.12) and setting the integration result to zero, we obtain an explicit expression for the measured tip potential in terms of the sample CPD and the tip geometry:

$$V_{\text{measured}}^{(b)} = \frac{\lim_{T\to\infty}\frac{1}{T}\int_0^T \left(\underline{\alpha}^t(t)\underline{\underline{\Delta}}\,\underline{\underline{G}}(t)^{-1}\,\underline{\underline{D}}(t)\right)\mathrm{d}t}{\lim_{T\to\infty}\frac{1}{T}\int_0^T \left(\underline{\alpha}^t(t)\underline{\underline{\Delta}}\,\underline{\alpha}(t)\right)\mathrm{d}t}\underline{V}_{\text{CPD}}. \tag{4.16}$$

Equation (4.16) provides an insight on how the averaging affects the PSF shape. The PSF shape is governed by the numerator, while the denominator is a scalar that can be treated as a normalization factor. Using method (b) both the numerator and denominator are averaged independently; therefore, each instantaneous time has the same contribution to the PSF shape; this is opposed to method (a) in which each time contribution is divided by a different normalization factor. Comparing the two methods, it can be shown that short tip–sample distances will have a much larger effect on the PSF shape, using method (b).

It is important to note that the same conclusion regarding the two averaging regimes can also be obtained using the staircase capacitor model presented in Sect. 4.2.1.

In order to reduce computation complexity, it is a common practice to ignore the cantilever contribution to the electrostatic force. Since the cantilever is very far from the sample (above 15 μm), it experiences a constant force which is independent of the tip position. Therefore, it does not affect the measurement resolution, but it does have a large effect on the measured potential value, as previously demonstrated by Jacobs et al. [14] and Colchero et al. [19]. Without the cantilever, using a model containing only the tip, we can express the expected measured potential as $V_{\text{measured}}^{\text{tip}}$; the average force can then be expressed using (4.16) and $V_{\text{measured}}^{\text{tip}}$ as:

$$F_{z,\omega}^{\text{tip}} = 2V_{\text{ac}}\overline{a}(V_{\text{dc}} - V_{\text{measured}}^{\text{tip}}), \tag{4.17}$$

where $\overline{a}$ is defined as $\lim_{T\to\infty}\frac{1}{T}\int_0^T \underline{\alpha}^t(t)\underline{\underline{\Delta}}\,\underline{\alpha}(t)\mathrm{d}t$, which can be viewed as a normalization factor of the PSF.

The cantilever-sample system may be approximated as a parallel plate capacitor. Due to the large distance between them, the potential affecting the cantilever is assumed to be an average of the V_{CPD} over of the whole sample, with no dependence

on the tip position. The ω component force in the z direction acting on the cantilever is equal to

$$F_{z,\omega}^{\text{cantilever}} = C'_{\text{cantilever}} V_{\text{ac}} (V_{\text{dc}} - \text{mean}\{V_{\text{CPD}}(\underline{r})\}), \tag{4.18}$$

where $C_{\text{cantilever}}$ is the cantilever-sample capacitance and $C'_{\text{cantilever}} = \frac{\partial C_{\text{cantilever}}}{\partial z}$.

The total force on the cantilever $F_{z,\omega}^{\text{tip}} + F_{z,\omega}^{\text{cantilever}}$ is then nullified at

$$\begin{aligned} V_{\text{measured}}^{\text{tip+cantilever}} &= \frac{2\overline{a} V_{\text{measured}}^{\text{tip}} + C'_{\text{cantilever}} \text{mean}\{V_{\text{CPD}}\}}{(2\overline{a} + C'_{\text{cantilever}})} \\ &= \frac{2\overline{a} V_{\text{measured}}^{\text{tip}}}{(2\overline{a} + C'_{\text{cantilever}})} + \text{const}, \end{aligned} \tag{4.19}$$

which means that the constant force on the cantilever introduces a factor of $2\overline{a}/(2\overline{a} + C'_{\text{cantilever}})$ into the measurement relative to a model neglecting the cantilever. In addition, this result implies that the cantilever force does not affect the lateral resolution, since it only changes the vertical scaling. However, it will have a very large effect on the absolute V_{CPD} within a measured image even at very small tip–sample distances in UHV measurements.

4.3.3 The Effect of Nano Scale Tip Protrusions

It is well known that actual AFM tips are nonideal and contain protrusions. To the best of our knowledge, all models to date consider a spherical tip with a cone above it (see Fig. 4.10), having a smooth surface [9,14,18,20]. In this section, we calculate the influence of an actual (non smooth) tip surface on the KPFM potential. In order to solve the charge distribution in such a system by the BEM method, the tip should be divided into surface elements.

Unlike our previous work [18], where the tip was divided to conical and spherical elements we use here a commercial finite elements software (Patran®) in order to divide the surface into triangular elements. Conical and spherical elements have some advantage since they cover exactly the whole tip surface. However, it is much more complicated to mesh complex shapes using these elements, especially in the case of nonsmooth surfaces. In addition, Patran® includes algorithms to scale the element sizes according to local surface shape or pre-defined mesh seed. In this way, it is simple to create an element area differentiation between the lower part of the tip, which is most affected from the sample, to the upper part of the tip, thus reducing the overall number of elements, and computing time, without affecting the calculation accuracy.

Figure 4.11 shows some typical mesh representations of the tip used in our calculations.

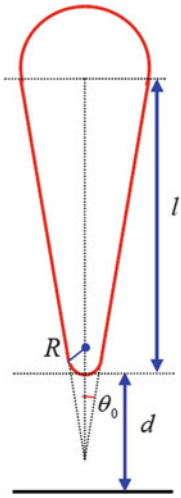

Fig. 4.10 Geometrical cross-section of a tip, with a finite length l, half aperture angle θ_0, tip-plane distance d and spherical apex radius R

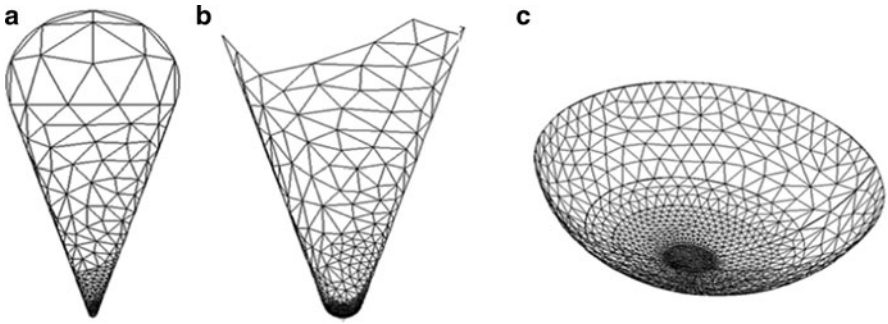

Fig. 4.11 Tip mesh (qualitative image). From *left* to *right*: (**a**) full tip mesh, (**b**) bottom tip mesh, and (**c**) bottom tip sphere. The mesh is designed so that smaller elements are used on the lower part of the tip, especially on the bottom part of the sphere, which is the most influenced by the local electrostatic forces

In order to discretize (4.6) and (4.7), it is necessary to calculate the integral of the two-dimensional Green's function over each tip element, and the dipole contribution integral over each sample surface element. Since there are no analytic expressions for such integrals, the calculations are performed using Gaussian numerical quadrature. This method transforms the integral into a sum of weighted values of the integrand at a predefined set of points.

We model the tip as a large cone of finite length l and a half- aperture angle θ_0, where the upper and lower ends of the tip are closed by spherical caps to ensure smooth boundaries. The bottom tip apex is modeled as a small spherical protrusion

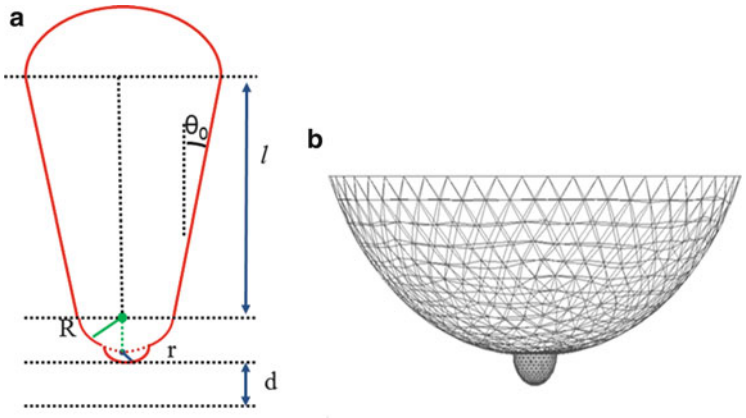

Fig. 4.12 (**a**) Geometrical cross-section of a tip with a spherical apex of radius R above an additional small sphere with radius r, cone half-aperture angle θ, and length of l, with tip-surface distance d. (**b**) Qualitative view of the meshing – in order to obtain the effect of the nano apex sphere, the mesh over it is much finer than the mesh over the bigger sphere

of radius r located on a larger sphere of radius R, where $r \ll R$. The center of the smaller sphere is positioned at distance R below the center point of the bigger sphere, as shown in Fig. 4.12a. The resulting BEM mesh is shown in Fig. 4.12b.

Figure 4.13 shows the calculated PSFs for several cases. Curve (d) and (c) represent a regular tip (without a nano spherical apex) with a radius of $R = 1$ nm and $R = 10$ nm, respectively, at a tip–sample distance of 1.24 nm. Curve (b) represents a tip with a radius of $R = 10$ nm but at a tip–sample distance of 2.24 nm. These graphs are compared to curve (a), which represents a tip of $R = 10$ nm, and an additional nano-spherical apex with $r = 1$ nm.

Based on the numerical experiment, it can be observed that the one-dimensional PSF of the tip with the additional spherical protrusion is very similar to that of a smooth bottom sphere with a radius of $R = 10$ nm that is 1 nm further away from the surface. This implies that the influence of the nano apex is small, since apparently most of the difference stems from the additional 1 nm distance of the tip from the surface.

The low influence of the nano tip is best understood by considering the inhomogeneous force contribution, previously defined in Sect. 4.3. Figure 4.14 (bars) shows the surface dependent force contribution for different regions of the tip. It is observed that the nano spherical apex contributes only around 10% of the overall inhomogeneous tip force. Most of the force (∼77%) stems from the bottom sphere and the rest is a contribution of the cone lower area. The rest of the tip cone does not contribute measurably to the inhomogeneous force. The right y-axis represents the force density of each slice; even though the force density over the nano apex is very large, it has only a limited contribution to the overall force due to its small area.

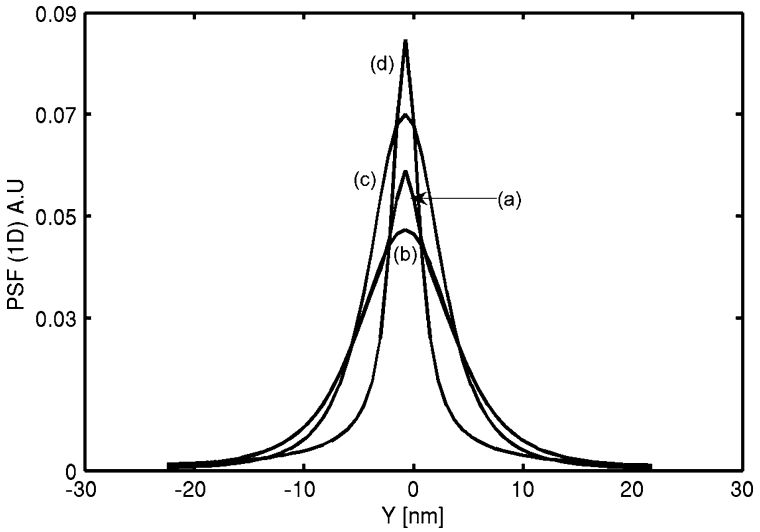

Fig. 4.13 One-dimensional PSFs of (**a**) nano tip with $R = 10\,\text{nm}$, $r = 1\,\text{nm}$, $d = 1.24\,\text{nm}$ (**b**) smooth regular sphere apex with $R = 10\,\text{nm}$, $d = 2.24\,\text{nm}$, (**c**) smooth regular sphere apex with $R = 10\,\text{nm}$, $d = 1.24\,\text{nm}$ and (**d**) regular spherical apex with $R = 1\,\text{nm}$, $d = 1.24\,\text{nm}$. All tips have half-opening angle of 17.5° and cone length of $l = 4\,\mu\text{m}$

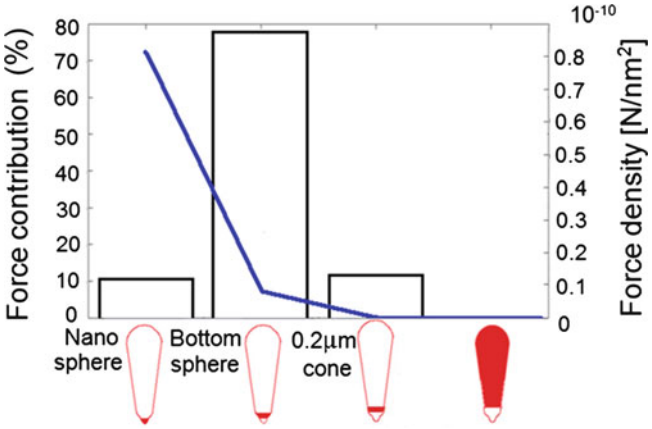

Fig. 4.14 Inhomogeneous force over the tip. Contributions are presented according to vertical tip slices. The *left vertical axis* (*bars*) represents the percentage of the slice to the overall force. The *right vertical axis* represents the force density for each slice. Tip– sample distance is $d = 1.24\,\text{nm}$. Tip geometry parameters: $r = 1\,\text{nm}$, $R = 10\,\text{nm}$, $\theta = 17.5°$, $L = 4\,\mu\text{m}$. Tip potential is set to 1 V. Sample potential is uniform and equal to 1 V

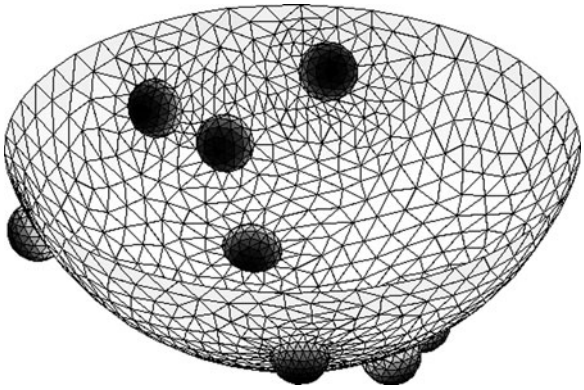

Fig. 4.15 Qualitative view of the bottom sphere ($R = 10$ nm) with eight nano spheres ($r = 1$ nm) placed at random locations

Additional calculations show that the influence of the nano sphere apex decreases as the tip–sample distance increases.

Since AFM tips may have several protrusions, we have calculated the effect of randomly located nano spherical protrusions at the bottom of the tip apex. All nano spheres have a radius of 1 nm and are placed on a sphere with radius 10 nm (see Fig. 4.15). The nano spheres were not placed near the big sphere apex in order to keep the tip–sample distance unaltered.

Figure 4.16 shows the two-dimensional PSF of the tip with additional nano spheres, and Fig. 4.17 presents a comparison between the one-dimensional PSFs of the tip with and without the additional nano spheres. It may be noted that since the nano spheres are not symmetrically distributed, the PSF of the tip with random protrusions is not symmetric either.

We use L_1-norm to evaluate the distance between the two-dimensional PSF of the tip with a smooth apex, $\underline{x}^T$, and that of the tip with an additional nano-sphere below its bottom sphere, $\underline{\tilde{x}}^T$. This distance defines the maximal difference in a measurement, for a normalized surface potential. In the comparison presented in Fig. 4.17, we obtain that $||\underline{x}^T - \underline{\tilde{x}}^T||_1 = 0.927$. This means that the small tip protrusions will have a minor effect on measured KPFM images and in most cases can be neglected in the reconstruction process. Consequently, the exact tip shape is not a necessary input for the KPFM image reconstruction.

4.3.4 Comparison with Experimental Results

In order to compare the reconstruction method described above with very high-resolution UHV-KPFM measurements, we apply it to the work of Glatzel et al. [21], who conducted KPFM measurements of NaCl thin films grown on Cu(111).

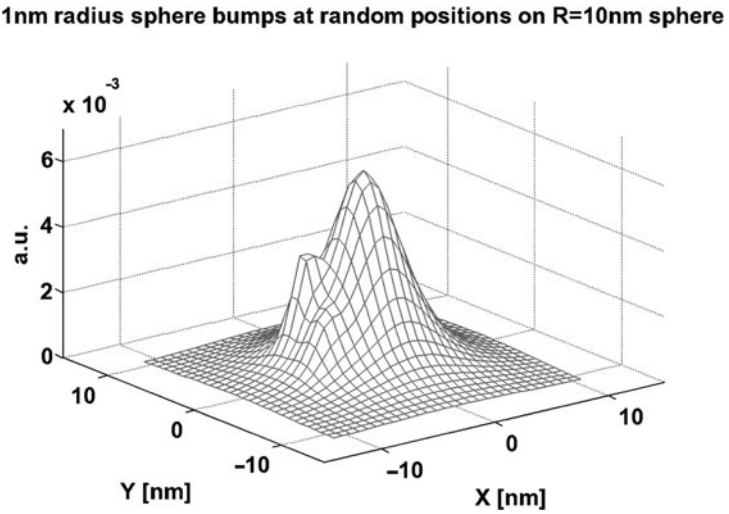

Fig. 4.16 Two-dimensional PSF for a tip with $R = 10\,\text{nm}$, $l = 4\,\mu\text{m}$, $\theta = 17.5°$, $d = 1.24\,\text{nm}$. On the bottom sphere, we added eight randomly located spheres each with radius $r = 1\,\text{nm}$

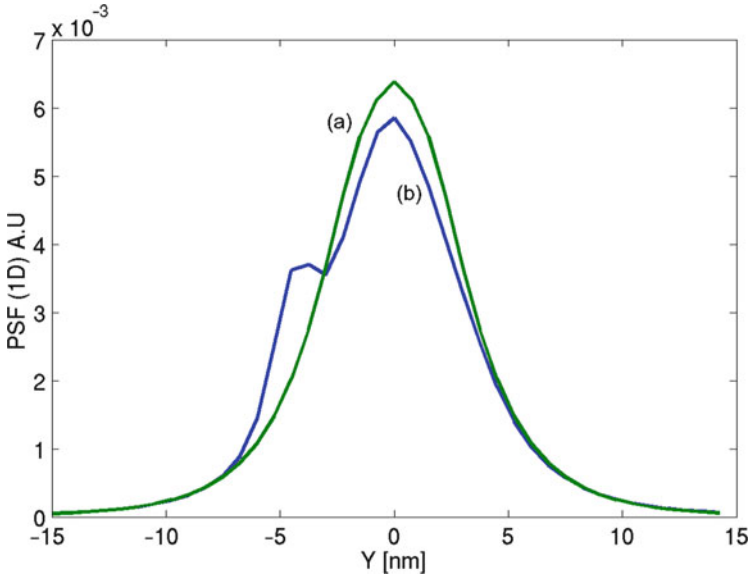

Fig. 4.17 One-dimensional PSF of the tip derived from the two-dimensional PSF for a tip with $R = 10\,\text{nm}$, $l = 4\,\mu\text{m}$, $\theta = 17.5°$, $d = 1.24\,\text{nm}$. Curve (**b**) represents the tip geometry including eight nano sphere, each with $r = 1\,\text{nm}$, on the spherical apex of $R = 10\,\text{nm}$. Curve (**a**) represents the regular smooth geometry with $R = 10\,\text{nm}$

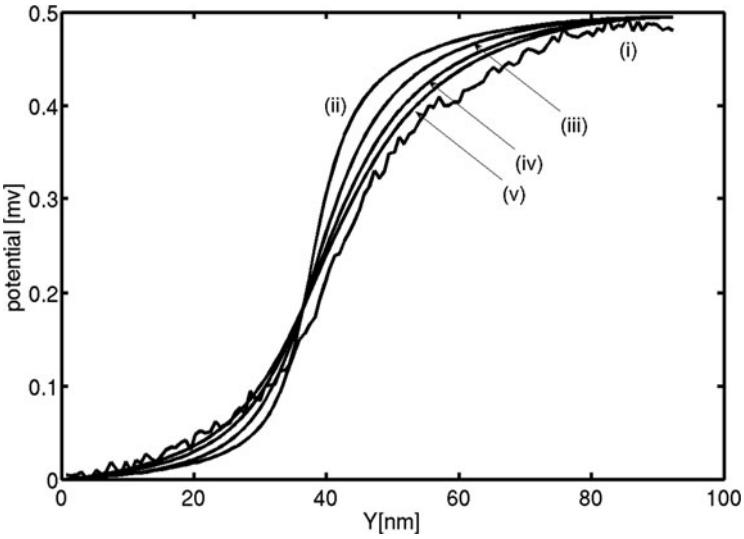

Fig. 4.18 Line section (*dashed line* in Fig. 4.19) comparison for different tip radii. Cone half-opening angle ($\theta = 17.5°$). (i) measurement, (ii) $R = 10\,\text{nm}$, (iii) $R = 30\,\text{nm}$, (iv) $R = 50\,\text{nm}$, and (v) $R = 70\,\text{nm}$

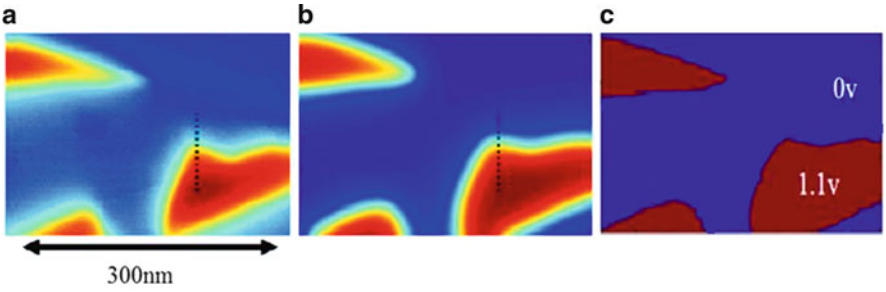

Fig. 4.19 (**a**) Measurements of NaCl thin films grown on Cu(111) [21]. (**b**) Simulated KPFM image using a tip geometry of $R = 50\,\text{nm}$, and $\theta = 17.5°$; the *dashed lines* correspond to the potential profiles shown in Fig. 4.18. The simulation is a a convolution of the two-dimensional PSF with the theoretical surface potential distribution imposed on the topography image shown in (**c**)

The measurements were carried out using a cantilever amplitude of 20 nm and a rest position of 21 nm above the sample.

Figure 4.18 shows calculated surface potential lines (for several tip apex radii) along the dashed line shown in Fig. 4.19b, in comparison with the measured profile along the dashed line in (a). The calculation shows a good agreement between the restoration and the measured KPFM image, but a very weak dependence on the tip apex radius. Although the best fit is obtained for tip radii ranging between 50 and

70 nm, we think that a more accurate cantilever modeling is required to rigorously support this conclusion.

4.4 Summary and Conclusions

In this chapter, we have reviewed most of the important literature devoted to the effect of the measuring tip in KPFM. It was shown that the combined effect of the cantilever, the tip cone, and the tip apex is well understood for both conducting and semiconducting surfaces. In KPFM measurements conducted in air, the lateral resolution is in the range of 20–50 nm, but the measured potential is reduced by almost an order of magnitude relative to the theoretical value. In measurements conducted under UHV conditions, the resolution is improved to around 10 nm, but the value of the measured potential is still significantly affected by the cantilever. In the second part, we have shown that today KPFM images can be accurately reconstructed, using convolution to overcome the effect of the measuring tip and to give the actual sample surface potential. In addition, it was shown that the exact tip apex shape is not an important factor in KPFM measurements conducted at tip–sample distances larger than 1.5 nm. This is an important advantage relative to both topography and atomic scale (LCPD) KPFM image analysis and reconstruction.

It must be emphasized that the image reconstruction presented in details above is rigorously correct only for flat surfaces. However, KPFM image reconstruction while ignoring the samples topography can lead to a large underestimation of the actual surface potential in general and in nanostructures in particular. Further work is definitely required in order to develop and implement methods for reconstructing KPFM images measured on real (rough) surfaces. This will allow to extract the actual surface potential from any KPFM measurement in general, and of nanostructures in particular.

When the measured surface is assumed flat, the operator relating the actual to the measured potential is in the form of a convolution (as described in details in this chapter), thus its inverse is easily and quickly performed by a deconvolution combined with noise filtering. However, when the sample topography is taken into account the operator *is not space invariant*, which means that it can no longer be represented as a convolution, and the KPFM image reconstruction by existing methods is practically impossible. Sadewasser et al. [22] have recently presented the first simulations considering the effects of specific surface topography features on the KPFM measurement of potential distributions. They have found that in most cases, the observed influence of the topography is quite small, probably in the range of the spatial resolution of many published KPFM measurements.

Definitely, more work is required to develop new methods for KPFM image reconstruction of rough surfaces. Work is in progress in our group based on: (1) Treating the effect of the sample topography as a perturbation, (2) iterative techniques, (3) nonuniform grid approach, and (4) fast direct solution based on the nonuniform grid approach. Such methods will allow extracting the actual surface

potential of many important systems such as: nanowires, quantum dots, and grain boundaries in polycrystalline materials. We therefore expect that KPFM image reconstruction of rough surfaces will be extremely valuable for the field of surface science in general, and of scanning probe microscopy in particular.

Acknowledgements We greatly acknowledge generous support to this work by Grant No. 2008140 from United States-Israel Binational Science Foundation, grant No. 32/08 from the Israel science foundation, and we acknowledge funding from the German Ministry for the Environment, Nature Conservation and Nuclear safety under contract # 0327559H.

References

1. S. Sadewasser, 5th International Conference on Non-Contact Atomic Force Microscopy, Montreal, 2002
2. O. Cherniavskaya, L. Chen, V. Weng, L. Yuditsky, L.E. Brus, J. Phys. Chem. B **107**, 1525 (2003)
3. M. Nonnenmacher, M.P. O'Boyle, H.K. Wickramasinghe, Appl. Phys. Lett. **58**, 2921 (1991)
4. T. Hochwitz, A.K. Henning, C. Levey, C. Daghlian, J. Slinkman, J. Vac. Sci. Technol. B **14**, 457 (1996)
5. S. Sadewasser, Th. Glatzel, R. Shikler, Y. Rosenwaks, M.Ch. Lux-Steiner, Appl. Surf. Sci. **210**, 32 (2003)
6. S. Belaidi, P. Girard, G. Leveque, J. Appl. Phys. **81**, 1023 (1998)
7. S. Belaidi, F. Lebon, P. Girard, G. Leveque, S. Pagano, Appl. Phys. A **66**, S239 (1998)
8. G. Leveque, P. Cadet, R. Arinero, Phys. Rev. B **71**, 205419 (2005)
9. S. Hudlet, M. Saint Jean, C. Guthmann, J. Berger, Eur. Phys. J. B **2**, 5 (1998)
10. M. Saint Jean, S. Hudlet, C. Guthmann, J. Berger, J. Appl. Phys. **86**, 2545 (1999)
11. D. Ziegler, N. Naujoks, A. Stemmer, Rev. Sci. Instrum. **79**, 063704 (2008)
12. Th. Glatzel, S. Sadewasser, M.Ch. Lux-Steiner, Appl. Sur. Sci. **210**, 84 (2003)
13. U. Zerweck, Ch. Loppacher, T. Otto, S. Grafström, L.M. Eng, Phys. Rev. B **71**, 125424 (2005)
14. H.O. Jacobs, P. Leuchtmann, O.J. Homan, A. Stemmer, J. Appl. Phys. **84**, 1168 (1998)
15. H.O. Jacobs, A. Stemmer, Surf. Interface Anal. **27**, 361 (1999)
16. Y. Rosenwaks, R. Shikler, Th. Glatzel, S. Sadewasser, Phys. Rev. B **70**, 085320 (2004)
17. R. Shikler, PhD Thesis, Tel-Aviv University (2003)
18. E. Strassburg, A. Boag, Y. Rosenwaks, Rev. Sci. Instrum. **76**, 083705 (2005)
19. J. Colchero, A. Gil, A.M. Baró, Phys. Rev. B **64**, 245403 (2001)
20. T. Machleidt, E. Sparrer, D. Kapusi, K.-H. Franke, Meas. Sci. Technol. **20**, 084017 (2009)
21. Th. Glatzel, L. Zimmerli, S. Koch, B. Such, S. Kawai, E. Meyer, Nanotechnology **20**, 264016 (2009)
22. S. Sadewasser, C. Leendertz, F. Streicher, M.Ch. Lux-Steiner, Nanotechnology **20**, 505503 (2009)

Chapter 5
Contribution of the Numerical Approach to Kelvin Probe Force Microscopy on the Atomic-Scale

Laurent Nony, Franck Bocquet, Adam S. Foster, and Christian Loppacher

Abstract The goal of this chapter is to gather and detail recent numerical developments addressing the issue of atomic-scale measurements in Kelvin Probe Force Microscopy (KPFM). It is argued why the problem requires the combination between the atomistic description of the distance- and bias voltage-dependent force field occurring between the tip and the surface, as well as an accurate numerical implementation of the complex noncontact atomic force microscopy and KPFM setup. When combining these tools, it is possible to draw conclusions regarding the origin of the atomic-scale KPFM contrast and its connections with usual physical observables such as the surface potential and the local work function. These aspects are discussed with respect to the surface of a bulk ionic crystal.

5.1 Atomic-Scale Contrast in KPFM: Relevance of the Numerical Approach

Over the past decade, the combination between *non-contact Atomic Force Microscopy* (nc-AFM) and *Kelvin Probe Force Microscopy* (KPFM) [1, 2] has attracted much interest owing to the unique capability of the latter method to map the

L. Nony (✉) · F. Bocquet · C. Loppacher
Aix-Marseille Université, IM2NP, Centre scientifique de Saint-Jérôme, Avenue Escadrille Normandie-Niemen, Case 151, 13397 Marseille, CEDEX 20, France

CNRS, IM2NP (UMR 6242), Marseille-Toulon, France
e-mail: laurent.nony@im2np.fr

A.S. Foster
Department of Physics, Tampere University of Technology, P.O. Box 692, 33101 Tampere, Finland

Department of Applied Physics, Aalto School of Science, P.O. Box 1100, 02015 Helsinki, Finland
e-mail: adam.foster@tut.fi

S. Sadewasser and T. Glatzel (eds.), *Kelvin Probe Force Microscopy*, Springer Series in Surface Sciences 48, DOI 10.1007/978-3-642-22566-6_5,

spatial distribution of electrostatic forces down to the nanometer scale. Electrostatic forces occur between the nanoscopic tip of the AFM and the sample, henceforth referred to as the electrodes, as soon as they are electrically connected. They stem from intrinsic work function differences between the electrodes when they do not consist of similar materials and/or when they carry charges. They are usually interpreted on the macroscopic level as capacitive forces and are known to influence the nc-AFM operating mode [3–6]. The KPFM controller supplies the proper DC voltage that aligns the Fermi levels of both electrodes, thereby compensating the electrostatic force. Thus, the KPFM provides the *Contact Potential Difference* (CPD) between the electrodes. Hence, beyond the regular nc-AFM channels, i.e., topography and dissipation, the combined nc-AFM/KPFM setup allows also for the simultaneous acquisition of a CPD image.

In the early stages of its development, KPFM proved its ability to map the spatial variations of the CPD on the nanometer scale with a resolution of few millivolts [7–9]. With the goal in mind to understand better the connection between the structural and the electrical properties of the investigated samples on the atomic-scale, some research groups reported outstanding results with atomically resolved CPD images [2, 10–19]. KPFM has also been used as a way to map the chemical identity of surface atoms [13]. Surprisingly, the latter work is the earliest experimental attempt dealing with atomic-scale chemical identification by KPFM, though the topic has been intensively addressed by other experimental strategies based on site-specific force vs. distance measurements [20–25]. So far, atomic-scale KPFM contrast was reported on semiconducting surfaces: Si(111)7×7 [10, 12, 15], Si(111)$5\sqrt{3}\times5\sqrt{3}$-Sb [13], GaAs(110) [11] and InSb(001) [16], and on two bulk dielectric surfaces: TiO_2(110) [17, 18] and KBr(001) [19]. In Figs. 5.1a, b and 5.1c, d are shown two examples of experimental results showing the simultaneous topographical-CPD atomic-scale contrast on the 7×7 Si(111) reconstruction [12] and on the KBr(001) surface [19], respectively.

Among the former references however, despite the consistency between the lateral periodicity of the CPD and topographical images, the CPD values neither fit the values reported by macroscopic methods, notably UV photoemission spectroscopy, nor the theoretical predictions [2, 10, 12]. Besides, it is now well stated that, when measured in the range of few angstroms up to 1–2 nm above the surface, the CPD varies with the tip-surface separation [14, 16, 26, 27]. These results are all the more surprising in that, when not used on the atomic-scale, i.e., down to a regime where the features at the surface have a size larger or similar to the size of the tip, KPFM provides CPD values that are compliant with the expected work function of the material [4, 8, 26, 28–34], the latter being not supposed to depend on the distance between the electrodes.

The experimental aspects of atomically resolved CPD images are not the scope of this chapter as these are presented in Chap. 13. However, it is interesting to point out some of their main findings. For instance, on the complex Si(111)$5\sqrt{3}\times5\sqrt{3}$-Sb surface, Okamoto et al. concluded that the CPD images mainly reflect the electrostatic force distribution rather than the work function distribution [13, 14].

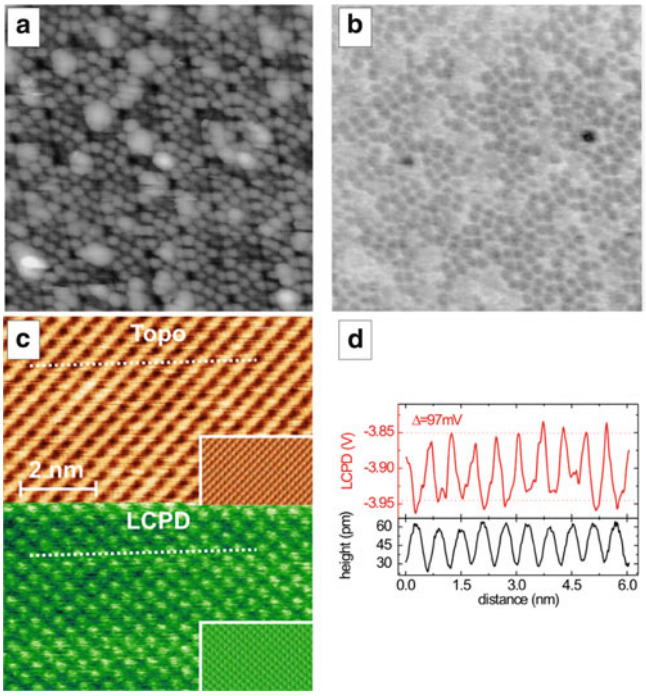

Fig. 5.1 Simultaneously acquired (**a**) topographical and (**b**) CPD nc-AFM images of a *p*-type Si(111)7 × 7 surface with deposited Au clusters. The atomic-scale contrast is well visible in both channels. The scan size is 20×20 nm^2. The vertical contrast of the CPD image ranges from −40 mV down to −180 mV and is brighter (larger CPD) on the Au clusters than on the adatoms of the 7 × 7 structure. Courtesy from [12]. (**c**) Simultaneously acquired topographical (*top*) and local CPD (LCPD, *bottom*) nc-AFM images of the KBr(001) surface. The insets show the corresponding error signals of the distance and KPFM controllers. The LCPD vertical contrast ranges from −3.95 to −3.85 V, corresponding to a contrast magnitude of 0.1 V. The magnitude of the topographical contrast is 30 pm only. Courtesy from [19]. (**d**) LCPD and topographical cross sections corresponding to the *dotted lines* shown in (**c**) showing the consistency between the atomic-scale topography and Kelvin contrast

On the Au/Si(111)7 × 7 surface, Kitamura et al. came also to the conclusion that the CPD does not reflect the work function of the observed atomic structures (see Fig. 5.1a, b), but rather the local electron density [12].

The discrepancy between the CPD values on the atomic-scale and the expected ones, as well as its unexpected distance dependence ultimately made KPFM measurements controversial and evoked questions of the origin and the relevance of the atomic-scale resolution in KPFM. What is the observable the technique provides access to: local work function, local surface potential, local surface charge density? Is the measurement quantitative? Why is the CPD distance dependent? Then, is it influenced by the distance regulator of the nc-AFM setup? The above elements can be rationalized as follows:

- When measured close to the surface, the CPD acquires a local character. Hence, the so-called *local CPD* (LCPD) must differ from its long-range value because the work function, well defined on the macroscopic scale, differs from the *local work function* on the atomic scale. The latter concept was introduced by Wandelt [35] to account for the fluctuations of the surface potential of real surfaces owing to fluctuations of the local density of states, presence of chemical and/or structural defects, steps, trapped charges, etc. Therefore, the discrepancy between CPD and LCPD was, to some extent, predictable.
- Since the KPFM technique is primarily sensitive to electrostatic forces, the atomic-scale CPD contrast relies on *Short-Range and bias dependent electrostatic forces* (SRE forces).

Two groups have initiated studies on the contribution of SRE forces in KPFM at this point [16, 19]. In a recent series of papers [19, 36], Bocquet et al. have described a self-consistent analytical approach to the LCPD probed by KPFM on the (001) facet of a bulk alkali halide single crystal. The approach, based on classical electrodynamics, relies on the estimate of the SRE force between a biased metallic tip and a semi-infinite dielectric slab. The analytic expression of the force allowed them to derive an expression of the LCPD. Although useful to understand the most important concepts of the problem, the analytical approach has two major drawbacks: (1) the tip must be restricted to a simple geometry and (2) deriving an expression of the LCPD requires an analytical description of the KPFM setup. This is only feasible with strong approximations. Therefore, the predicted values of the LCPD are hardly comparable to the experimental data, which ultimately restricts the relevance, as well as the accuracy of the analysis.

Following the experimental development of the nc-AFM technique, numerical methods such as ab initio and classical atomistic calculations have been developed by several groups to compute the distance dependence of short-range chemical forces for a wide set of realistic tips and surfaces [20–22, 37–44]. These methods brought a valuable gain to the nc-AFM technique as it is now possible to quantify the experimental images in terms of force and thus identify the interaction processes driving the atomic-scale topography contrast formation. Beyond the accurate description of the tip–surface interaction, numerical approaches tend to open new routes to the experimentalists such as chemical identification [20–22, 24, 25], dissipation processes [45–48], electron transfer processes [49], atomic or molecular manipulation [50–54], atomic or molecular diffusion barriers [51, 55, 56].

Following the works by Nony et al., atomistic calculations have been used to address the issue of SRE forces in the particular case of a bulk ionic sample [57]. However, when dealing with the nc-AFM/KPFM technique, the force field between the tip and the surface cannot be connected to the topography or LCPD contrast directly. It is also required to understand how the dynamics of the cantilever is changed when vibrating close to the surface under the dual influence of bias-dependent and non- bias-dependent interaction forces, that is actually the whole acquisition chain of the experimental setup. As said before, this is hardly feasible on the analytical level. Therefore, owing to the overall complexity of the tip–surface

interaction and the one of the nc-AFM/KPFM technique, a thorough analysis requires a combined numerical approach of the force field between the tip and the surface and of the experimental setup. This is the unique way to interpret the experimental results with the best accuracy. Thus, issues such as the origin and the quantitative character of the KPFM contrast on the atomic-scale can be addressed in details, while preventing imaging artifacts from occurring.

This chapter deals with recent developments of the numerical implementation of the two well-established KPFM setups, namely *Frequency Modulation-* and *Amplitude Modulation-KPFM* (FM- and AM-KPFM, respectively), coupled to atomistic simulations of the distance- and bias-dependent interaction force between a realistic tip and the (001) facet of a bulk single crystal of NaCl. The elements detailed hereafter are gathered in a set of three recent articles [19, 36, 57]. The implementation of the KPFM setups is performed within the core of an accurate numerical implementation of an existing nc-AFM setup, the so-called *nc-AFM simulator* [58], briefly described in Sect. 5.2. The connection between the simulator and FM- or AM-KPFM methods is described in Sect. 5.3. In Sect. 5.4, the atomistic simulations of the interaction force field between the NaCl crystal and a metallic tip including an ionic cluster in the topmost position will be presented. The use of the numerical force field as an input parameter of the nc-AFM/KPFM simulator allows for the simulation of spectroscopic measurements and topography and CPD images. The results will be discussed in Sect. 5.5. In Sect. 5.6, we will conclude by stressing the influence of the dynamic polarization of the ions at the tip–surface interface, which will allow us to draw conclusions concerning the relevance of the local CPD and its connection with physical observables such as the Madelung surface potential of the ionic crystal.

5.2 Prerequisite: The nc-AFM Simulator

To date, five groups have reported the implementation and/or performance of "virtual force microscopes" [58–63]. These simulation codes are almost analogous to ours, but differ in detail. Historically, our virtual instrument has been referred to as the nc-AFM simulator. It is a numerical implementation of an existing nc-AFM setup based on a *Phase-Locked-Loop-* (PLL-) excitation scheme [64]. Its original implementation is reported in Fig. 5.2. A simplified version is sketched in Fig. 5.3a, b. The PLL-excitation scheme consists in using the PLL to generate the time-dependent phase of the excitation signal of the cantilever. The PLL output is driven by the AC deflection signal of the cantilever and phase-locked to it, provided that the PLL settings are properly adjusted. Then the PLL continuously tracks the interaction-shifted resonance frequency of the cantilever $\widetilde{f}_0$ with high precision, whatever the tip-surface separation. One of the primary goals of the nc-AFM simulator was to address the issue of apparent dissipation (or apparent damping), that is of spurious variations in the driving amplitude caused by the nonlinear interaction occurring between the tip and the surface and by the finite response times of the various controllers (cf. section IV in [58]).

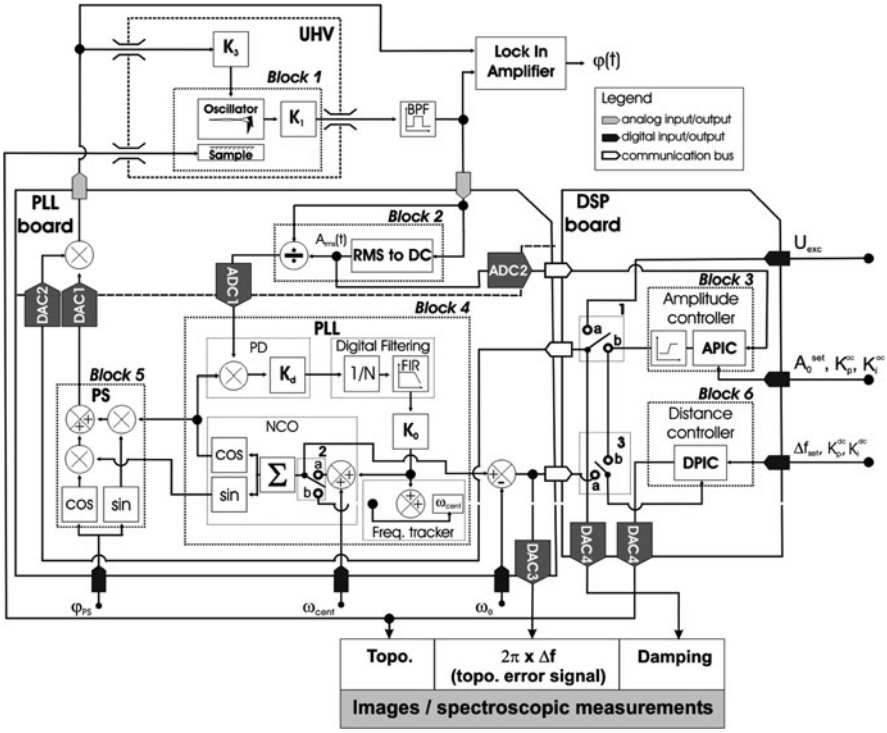

Fig. 5.2 Scheme of the numerical implementation of the nc-AFM simulator based on a real nc-AFM setup

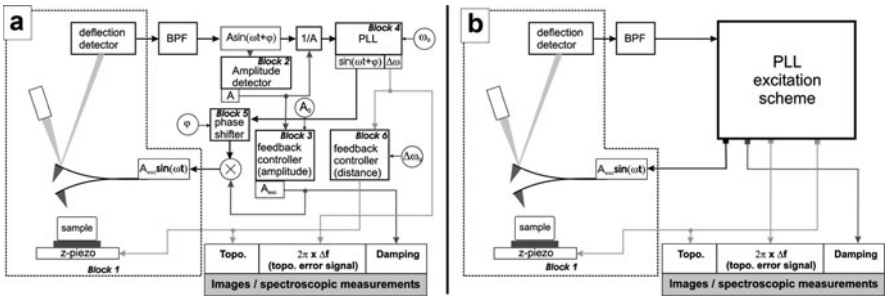

Fig. 5.3 (**a**) Simplified scheme of the nc-AFM simulator. The main features of the implementation are drawn. The PLL-excitation scheme ensures the continuous on-resonance driving of the cantilever while optimizing the quality of the driving signal. (**b**) Simplified scheme of the PLL-excitation scheme that is used for the KPFM implementation as discussed in Sect. 5.3

This section is built as follows: in Sects. 5.2.1 and 5.2.2, the numerical schemes of the blocks describing the dynamics of the cantilever and the *Lock-In Amplifier* (LIA) used to monitor the phase lag of the cantilever with respect to its excitation are detailed. They are indeed useful to understand the implementation of the KPFM setups. The numerical implementation of the PLL and the *proportional/integral controllers* (PIC) is not described here, but the equations ruling out their behavior are given in [58]. In Sect. 5.2.3, a brief summary of the main results obtained with the nc-AFM simulator is given.

5.2.1 Overview of the Numerical Implementation

The electronics of the simulated nc-AFM setup consists of analog and digital circuits described by six interconnected main blocks operating at various sampling frequencies (f_s), as sketched in Fig. 5.2. The highest sampling frequency among the digital blocks is the PLL one, $f_{s_1} = 20\,\text{MHz}$. The PLL electronics has initially been developed by Loppacher et al. [64]. Details regarding the operating mode of analog and digital PLLs can be found in the book by Best [65] for instance.

Block 1 in Fig. 5.2 mimics the detection of the vibration of the tip when interacting with the surface. In the simulation, the block is described by an equivalent analog circuit. More generally, all the analog parts of the electronics are described in the simulation using a larger sampling frequency compared to f_{s_1}, namely $f_{s_2} = 400\,\text{MHz}$. This is motivated by the ultrahigh vacuum environment within which the microscope is placed, thus resulting in a high quality factor of the cantilever, typically $Q = 30{,}000$ at room temperature. Besides, nc-AFM cantilevers have typical fundamental eigenfrequencies $f_0 \simeq 150\,\text{kHz}$. The chosen sampling frequency insures a proper integration of the differential equations minimizing the error. The signal of the oscillating cantilever then goes into a bandpass filter which cuts off its low and high frequency components. The bandwidth of the filter is typically 60 kHz, centered on the resonance frequency of the cantilever. Despite the implementation of a filter in the simulation, no noise has been introduced. The signal is then sent to other blocks depicting the interconnected parts of two boards, namely an analog/digital one, the "PLL board," and a fully digital one integrating a Digital Signal Processor (DSP), the "DSP board." The boards share data *via* a "communication bus" operating at $f_{s_3} = 10\,\text{kHz}$, the lowest frequency of the digital electronics.

Block 2 stands for the mere analog part of the PLL board ($f_s = f_{s_2}$). It is an RMS-to-DC converter, the output of which is the root mean square (RMS) value of the oscillation amplitude of the cantilever, $A_{\text{RMS}}(t)$. $A_{\text{RMS}}(t)$ is provided to block 3, one of the two PIC implemented on the DSP ($f_s = f_{s_3}$). When operating in the nc-AFM mode, the block output is the DC value of the driving amplitude that maintains constant the reference value of the oscillation amplitude, A_0^{set}. This is why it is referred to as the amplitude controller, APIC.

The dashed line in Fig. 5.2 depicts the border between analog and digital circuits in the PLL board. The digital PLL, block 4 ($f_s = f_{s1}$), consists of three sub-blocks: a Phase Detector (PD), a Numerical Controlled Oscillator (NCO) and a filtering stage consisting of a decimation filter and a finite impulse response (FIR) low-pass filter in series. The PLL receives the signal of the oscillation divided by $A_{\mathrm{RMS}}(t)$ plus an external parameter: the "center frequency," $f_{\mathrm{cent}} = \omega_{\mathrm{cent}}/2\pi$. f_{cent} specifies the frequency to which the input signal has to be compared for the demodulation frequency stage. The NCO generates the digital sin and cos waveforms of the time-dependent phase, ideally identical to the one of the input signal. The latter waveforms are then sent to a digital *phase shifter* (PS, block 5, $f_s = f_{s1}$) that shifts the incoming phase by a constant amount, set by the user to maximize the oscillation amplitude of the cantilever, i.e., actually to ensure its on-resonance excitation. The block output is converted into an analog signal and then multiplied by the APIC output, thus generating the full AC excitation applied to the piezoelectric actuator to drive the cantilever on resonance.

Block 6 is the second PIC of the DSP ($f_s = f_{s3}$). It controls the tip-surface separation to maintain constant either a given value of the frequency shift, or a given value of the driving amplitude (switch 3 set to location "a" or "b" in Fig. 5.2), respectively. The output is the so-called "topography" signal. The block is referred to as the distance controller, DPIC. In this work, the topography images have been calculated in the constant frequency shift mode (switch 3 set to location "a").

Finally, a digital LIA detects the phase lag, φ, between the excitation signal provided to the oscillator and the oscillating cantilever motion.

All the processed signals are properly converted by means of Analog-to-Digital or Digital-to-Analog Converters (ADC or DAC, respectively), the nominal bandwidths of which are much larger than the communication bus one. Therefore, although sketched in the figure, they are not implemented in the code of the simulator.

5.2.2 Numerical Schemes

5.2.2.1 Block 1: Cantilever and Optical Detection

The block mimics the photosensitive detector (PSD) acquiring the signal of the vibration of the cantilever. The equation describing its behavior is given by the differential equation of the harmonic oscillator:

$$\ddot{z}_0(t) + \frac{\omega_0}{Q_0}\dot{z}_0(t) + \omega_0^2 z_0(t) = \omega_0^2 \Xi_{\mathrm{exc}}(t) + \frac{\omega_0^2}{k_0}\left[F_{\mathrm{int}}(z) + F_{\mathrm{es}}(V_{\mathrm{b}}, z)\right] \qquad (5.1)$$

$\omega_0 = 2\pi f_0$, Q, k_0 stand for the angular resonance frequency, quality factor and stiffness of the fundamental bending eigenmode of the free cantilever, respectively. $z_0(t)$ and $\Xi_{\mathrm{exc}}(t)$ are the instantaneous location of the tip with respect to the rest position of the cantilever (cf. Fig. 5.4a) and the excitation signal driving the

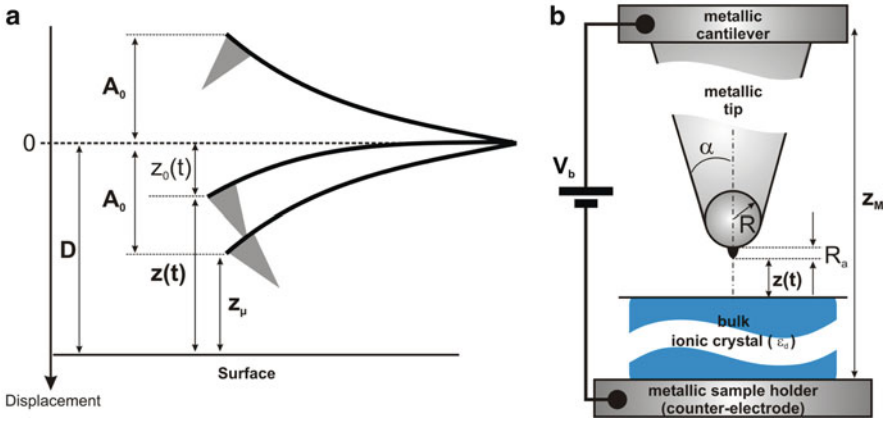

Fig. 5.4 (**a**) Geometrical parameters used for the description of the instantaneous position of the tip with respect to the surface. The tip is sketched for pedagogical purpose. (**b**) Actual geometry of the tip used in the simulations. The body of the tip is a cone with an open half-angle α. Its apex consists in a sphere with a radius R and a small cluster in topmost position protruding with a height R_a from the sphere. The dielectric ionic crystal below the tip is several millimeters thick

cantilever, respectively. $F_{\text{int}}(z)$ and $F_{\text{es}}(V_{\text{b}}, z)$ are the non-bias- dependent and bias-dependent (V_{b}) interaction forces acting between the tip and the surface, respectively. They primarily depend on the instantaneous tip-surface separation $z(t)$, connected to $z_0(t)$ and to the separation between the surface and the cantilever at rest, D (cf. Fig. 5.4a):

$$z(t) = D - z_0(t). \tag{5.2}$$

$z(t)$ is to be distinguished from the minimum tip-surface separation, referred to as z_μ in the following. z_μ stands for the position of the lower turning point of the oscillation of the cantilever with respect to the surface:

$$z_\mu = D - A_0, \tag{5.3}$$

where A_0 is the oscillation amplitude of the cantilever (cf. Fig. 5.4a).

$F_{\text{int}}(z)$ gathers long-range Van der Waals interactions and chemical short-range ones, and $F_{\text{es}}(V_{\text{b}}, z)$ gathers long-range and short-range electrostatic interactions. In the simulations, we have considered a long-range electrostatic force as a phenomenological force that consists of capacitive effects between the cantilever and the sample holder when mounted in the microscope. Van der Waals and long-range electrostatic interactions are implemented via common analytical forms (cf. equ. (2.4) in [66] and equ. (14) in [36], respectively):

$$F_{\text{int}}^{\text{vdW}}(z) = -\frac{H}{6}\left[\frac{R}{(z+R_a)^2} + \frac{\tan(\alpha)^2}{z+R_a+R'} - \frac{R'}{(z+R_a)^2+z+R_a+R'}\right] \tag{5.4}$$

and:

$$F_{\mathrm{es}}^{\mathrm{lr}}(V_{\mathrm{b}}, z) = -\frac{\epsilon_0 \epsilon_d^2 \mathcal{S} V_{\mathrm{b}}^2}{2(z + R_a + z_{\mathrm{M}})^2} \tag{5.5}$$

R, R_a, α and $R' = R(1 - \sin\alpha)$ are the geometrical parameters for the tip, as sketched in Fig. 5.4b. H, ϵ_0 and ϵ_d are the Hamaker constant of the tip-surface interface, vacuum and sample dielectric permittivities, respectively. S and z_M are the effective area involved in the capacitive coupling between the cantilever and the counter-electrode and the corresponding distance between the electrodes, respectively. In the problem addressed here, the sample is a bulk dielectric that is several millimeters high. A quick estimate for $\mathcal{S} = 1\,\mathrm{mm}^2$, $z_{\mathrm{M}} = 5\,\mathrm{mm}$ and $V_{\mathrm{b}} = 1\,\mathrm{V}$ yields $F_{\mathrm{es}}^{\mathrm{lr}} \simeq -3\,\mathrm{pN}$.

When using the nc-AFM simulator with atomistic force fields, a lookup table of the force values is built as a function of the tip-surface separation and the applied bias voltage, the size of which depends on the sampling rates of the tip-surface separation and of the bias voltage. By definition, it consists of the chemical and electrostatic short-range interactions. The total interaction force used to perform the simulations is then built for each value of the tip-surface separation and each value of the bias voltage as the sum between the latter short-range contributions and both long-range contributions derived from the former analytical expressions.

The differential equation is solved with a modified Verlet algorithm, so-called leapfrog algorithm [67], using a time step $\Delta t_{\mathrm{s}_2} = 1/f_{\mathrm{s}_2} = 5\,\mathrm{ns}$. The instantaneous value of the driving amplitude $\Xi_{\mathrm{exc}}(t)$ (units: m, cf. equ. (5.1)) can be written as:

$$\Xi_{\mathrm{exc}}(t) = K_3 A_{\mathrm{exc}}(t) z_{\mathrm{ps}}(t) \tag{5.6}$$

K_3 (units: $\mathrm{m\,V}^{-1}$) stands for the linear transfer function of the piezoelectric actuator driving the cantilever. $A_{\mathrm{exc}}(t)$ (units: V) is the APIC output. $z_{\mathrm{ps}}(t)$ is the AC part of the excitation signal. It is provided by the phase shifter when the PLL is engaged. When the steady state is reached, i.e. $t \gg t_{\mathrm{steady}} \simeq 2Q/f_0$, the block output has the form:

$$K_1 z_0(t) = K_1 A_0(t) \sin\left[\omega t + \varphi_0(t)\right]. \tag{5.7}$$

K_1 ($\mathrm{V\,m}^{-1}$) depicts the transfer function of the PSD, which is assumed to be linear within the bandwidth (3 MHz in the real setup). If the damping is kept constant, the amplitude and the phase, $A_0(t)$ and $\varphi_0(t)$, respectively, remain constant as well. This is no longer true once the controllers are engaged. This is why the time dependence has been explicitly preserved in the above equation.

5.2.2.2 Lock-In Amplifier

The simulated LIA does not mimic the detailed operational mode of the real dual phase lock-in that is used to monitor the phase shift of the oscillator (Perkin Elmer 7280). Its purpose is rather to provide a simple way to estimate the phase shift

between the excitation and the oscillation. In particular, the built-in low-pass filter has been simulated as a simple averaging analog circuit, but the bandwidth of the LIA remains adjustable. For monitoring the cantilever phase lag, it has been set equal to 2.5 kHz. The reference signal of the LIA is the driving signal of the cantilever with a time-dependent phase of the form ωt. The input signal of the LIA is the output of the bandpass filter z_{bpf}, i.e., a signal that is almost similar to the input of the filter owing to its wide band. The numerical code used to describe in- and off-phase components,[1] X_{LIA} and Y_{LIA}, respectively, is:

$$X_{\mathrm{LIA}}(t) = \frac{\sum_{k=i-n_{\mathrm{LIA}}}^{i} z_{\mathrm{bpf}}(t_k) \times \sin(\omega t)}{n_{\mathrm{LIA}}}$$

$$Y_{\mathrm{LIA}}(t) = \frac{\sum_{k=i-n_{\mathrm{LIA}}}^{i} z_{\mathrm{bpf}}(t_k) \times \cos(\omega t)}{n_{\mathrm{LIA}}}. \tag{5.8}$$

Hence, the phase of the oscillator with respect to the driving excitation is given by:

$$\tan(\varphi(t)) = \frac{X_{\mathrm{LIA}}}{Y_{\mathrm{LIA}}}, \tag{5.9}$$

while the vibration amplitude of the cantilever can also be derived as:

$$A_{\mathrm{LIA}} = 2\sqrt{X_{\mathrm{LIA}}^2 + Y_{\mathrm{LIA}}^2}. \tag{5.10}$$

The LIA that is used in the KPFM setup is implemented with the same code, but with proper input, bandwidth, and reference signals.

5.2.2.3 Code Implementation

The numerical implementation has been performed in ANSI C. The integro-differential equations (5.1) and (5.6) are integrated at their respective sampling frequencies. The monitored signals are the oscillation amplitude A_0 given by the RMS-to-DC converter, the frequency shift Δf given by the PLL, the phase φ given by the LIA (5.9) and the relative damping $QK_3A_{\mathrm{exc}}/A_0 - 1$, deduced from the APIC output.

[1] In- and off-phase components of the LIA are essentially defined upon the structure of its input signal, i.e., here the driving signal of the cantilever which is arbitrarily generated out of a sinus waveform.

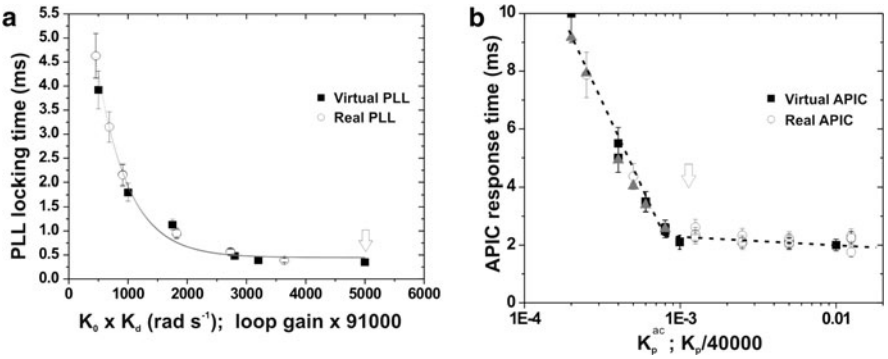

Fig. 5.5 (**a**) Locking time of the simulated (*filled squares*) and real (*empty circles*) PLL vs. loop gains. The arrow indicates the value of the loop gain used experimentally, which corresponds to an optimum behavior of the PLL and a related locking time of about 0.35 ms. The curve is given as a guide to the eye. (**b**) Response time of the APIC vs. K_p^{ac} of the simulated setup and the rescaled K_p gain of the real controller. The two curves match with a reasonable agreement and exhibit two domains: first the response time decreases when increasing K_p^{ac} and then a saturation is reached corresponding to $t_{\mathrm{resp}} \simeq 2$ ms. The *dotted line* is given as a guide to the eye. The saturation is due to the contribution of the RMS-to-DC converter (cf. [58] for details)

5.2.3 Main Results

The dynamic performances of each virtual controller have been investigated carefully and compared to those of the real setup. In Fig. 5.5a, b, the locking time of the simulated and real PLL, and the response time of the simulated and real APIC are reported, respectively. Good agreement is obtained between the locking behavior of both PLLs. The optimum locking time of the PLL is found to be about 0.35 ms. The behavior of the amplitude controller is also found to correctly describe the real setup with an optimum response restricted to 2 ms owing to the intrinsic time constant of the RMS-to-DC converter.

5.3 Numerical Implementation of the KPFM Methods: The nc-AFM/KPFM Simulator

Both KPFM operating modes, i.e., Amplitude-Modulation and Frequency-Modulation, AM- and FM-, respectively, have been implemented within the nc-AFM simulator and can be engaged independently. They are implemented as a set of additional building blocks to those of the simulator. The scheme of the numerical implementation of AM- and FM-KPFM methods is reported in Figs. 5.6 and 5.7, respectively.

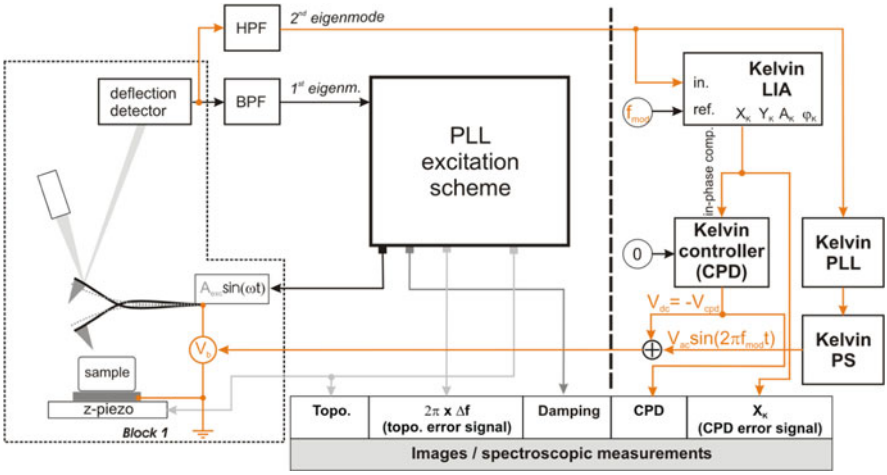

Fig. 5.6 Scheme of the numerical implementation of the AM-KPFM operating mode combined with the nc-AFM simulator

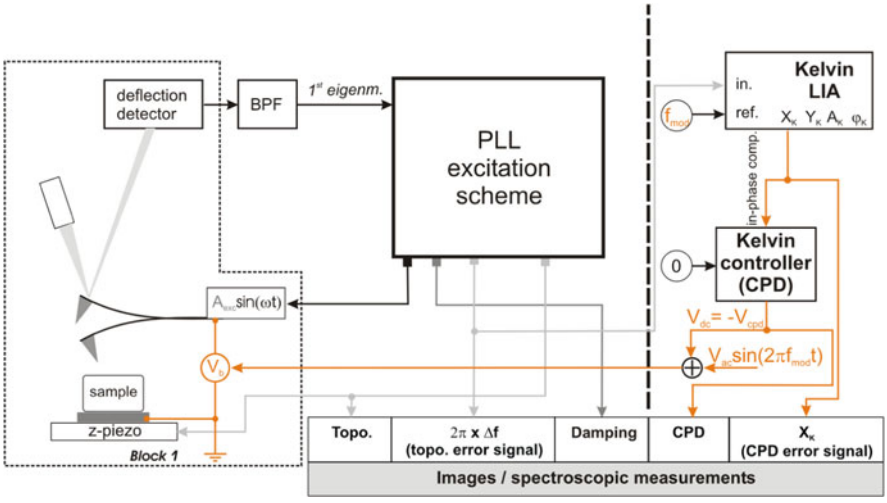

Fig. 5.7 Scheme of the numerical implementation of the FM-KPFM operating mode combined with the nc-AFM simulator

5.3.1 Amplitude-Modulation KPFM (AM-KPFM)

In AM-KPFM, the bias-modulated component is usually the second bending eigenmode of the cantilever, which has been depicted in Fig. 5.6. In this case, the modulation frequency f_{mod} of the applied bias voltage must accurately match the resonance frequency of the mode, f_1 (resonance amplitude A_1). However,

if experiments are to be carried out off-resonance on purpose, i.e., with $f_{\mathrm{mod}} \neq f_1$, the numerical implementation will run as well. When using beam-shaped cantilevers, it is known that $f_1 = 6.24 f_0$, which makes f_1 ranging in the MHz regime: $f_1 = 6.24 \times 150\,\mathrm{kHz} \simeq 940\,\mathrm{kHz}$. The instantaneous position of the cantilever connected to that mode, $z_1(t)$, is ruled out by a similar differential equation as the one of the first eigenmode, except that the actuation force (first term on the right-hand side of (5.1)) is now the electrostatic force $F_{\mathrm{es}}(V_{\mathrm{b}}, z)$, triggered by the modulation of the applied bias voltage $V_{\mathrm{b}} = V_{\mathrm{dc}} + V_{\mathrm{mod}} \sin(2\pi f_{\mathrm{mod}} t)$:

$$\ddot{z_1}(t) + \frac{\omega_1}{Q_1}\dot{z_1}(t) + \omega_1^2 z_1(t) = \frac{\omega_1^2}{k_1}\left[F_{\mathrm{ext}} + F_{\mathrm{int}}(z) + F_{\mathrm{es}}(V_{\mathrm{b}}, z)\right], \tag{5.11}$$

where $Q_1, \omega_1 = 2\pi f_1$ and k_1 are the quality factor, resonance angular frequency and effective stiffness of the mode, respectively. F_{ext} stands for the actuation force of the fundamental bending mode of the cantilever. Owing to the large difference between f_0 and f_1, F_{ext} does not influence $z_1(t)$; however, we have kept it in the equation. As already stated, F_{int} stands for all the non-bias-dependent interaction forces. In the above equation, it is important to notice that F_{es} is not only bias dependent, but also z dependent. Hence, the dynamics of the second eigenmode is complex and non-linear, notably in the short-range regime. However, its usually large Q-value in UHV ($Q_1 \simeq 10{,}000$) combined to the long-range electrostatic interaction allows for the development of the steady state of the eigenmode. Furthermore, although the resonance frequencies of both eigenmodes are far apart, their dynamics are actually coupled by means of the tip-surface separation dependence of the former forces. The instantaneous tip-surface separation $z(t)$ now becomes (cf. Fig. 5.8):

$$z(t) = D - z_0(t) - z_1(t), \tag{5.12}$$

and consequently $z_\mu = D - A_0 - A_1$.

On the numerical level, although $f_1 \gg f_0$, we have kept the sampling frequency standing for the analog parts of the electronics constant, namely $f_{s_2} = 400\,\mathrm{MHz}$. This is still sufficient to integrate the differential equation with an error kept low enough. The splitting between the first and the second eigenmode is performed using a high-pass filter.[2] A simple first-order high-pass filter has been implemented with the differential equation:

$$\dot{z_o}(t) + \omega_c z_o(t) = \dot{z_i}(t), \tag{5.13}$$

where ω_c, z_o, and z_i are the cut-off angular frequency, output and input of the filter, respectively. In the code, we have set $\omega_c = 2\pi \times 200\,\mathrm{kHz}$, while f_0 is always 150 kHz and hence, $f_1 = 940\,\mathrm{kHz}$.

[2]On the experimental level, the AM-KPFM setup requires that the bandwidths of the PSD and of the preamplifier are large enough to allow for the detection of the 2nd eigenmode without attenuation.

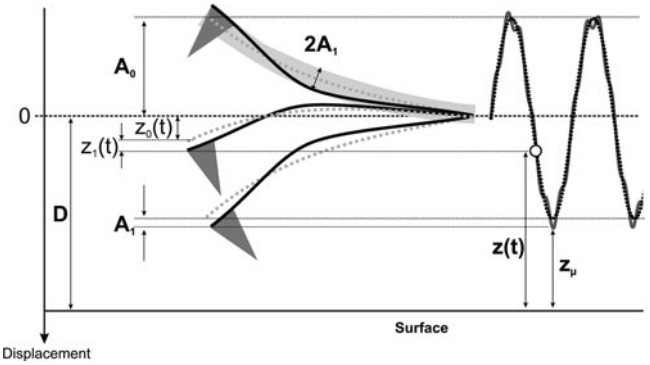

Fig. 5.8 Definition of the geometrical parameters used for the description of the combined vibrations of the fundamental and second eigenmodes of the cantilever in AM-KPFM. The time-dependent vibration is shown on the right-hand side of the figure

The Kelvin LIA detects the vibration amplitude of the second bending eigenmode of the cantilever with a 10 kHz bandwidth. The LIA provides $A_K = 2\sqrt{X_K^2 + Y_K^2}$, which in the case of the AM-KPFM matches A_1. The Kelvin controller has a 2.5 kHz bandwidth. It is a standard proportional and integral controller, the numerical implementation of which is similar to the distance and amplitude controllers of the PLL-excitation scheme. It provides the DC part of the bias that minimizes, or ideally nullifies, the vibration amplitude of the second eigenmode and hereby compensates the CPD. When the tip is biased (sample grounded), $V_{\mathrm{dc}} = -V_{\mathrm{CPD}}$, otherwise $V_{\mathrm{dc}} = +V_{\mathrm{CPD}}$. It is important to notice that the input of the controller is not the signal detected by the Kelvin LIA, A_K, but the in-phase component X_K. The in-phase component is supposed to be used instead of A_K because it can become negative and thus handle negative error signals, while A_K cannot.

The code integrates (5.11) in parallel to the equation of motion for the fundamental flexural eigenmode. The PLL-excitation scheme ensures that the latter mode is continuously actuated at its resonance frequency that shifts as the tip is approached to the surface. Meantime, the second mode undergoes a frequency shift as well. Nevertheless, it is mandatory to maintain the on-resonance excitation for this eigenmode too; otherwise, the vibration amplitude A_K does not match the resonance value, A_1. Experimentally, this requires one to tune precisely the modulation frequency of the bias f_{mod} to recover the on-resonance excitation *as soon as the tip is approached to the surface* and prior to engaging the Kelvin controller and scanning. Performing this step numerically is time consuming as the frequency sweep has to be performed slowly owing to the large value of Q_1. In order to avoid that, an additional PLL, the Kelvin PLL, has been implemented with the goal to continuously track the shift of f_1 while approaching the surface, i.e., as a function of the tip-surface separation. Thus, the AC part of the bias modulation always matches the interaction-shifted resonance frequency of the second eigenmode $\widetilde{f}_{\mathrm{mod}}$: $V_{\mathrm{mod}} \sin(2\pi \widetilde{f}_{\mathrm{mod}} t + \varphi_K)$, φ_K being the phase shift introduced by the Kelvin PLL while processing the input signal. The

numerical implementation of the Kelvin PLL is strictly similar to the one used in the PLL-excitation scheme for the fundamental eigenmode. Then, after a proper phase shifting process, which is insured by the Kelvin phase shifter, the modulation signal $V_{\mathrm{mod}} \sin(2\pi \widetilde{f}_{\mathrm{mod}} t)$ is supplied to the cantilever and hence, the on-resonance condition is maintained. Furthermore, the frequency of the reference signal for the Kelvin LIA, f_{mod}, is continuously updated, which makes the detection of A_1 continuously self-consistent. As said before, this step merely concerns the approach of the tip to the surface. As soon as the required Δf is reached, i.e., prior to engaging the Kelvin controller and scanning or recording a spectroscopic curve, the Kelvin PLL is disengaged and the modulation then continuously performed at the last computed value of $\widetilde{f}_{\mathrm{mod}}$.

5.3.1.1 Maximization of the In-Phase Component of the Kelvin LIA

On the experimental level, in addition to the above comment on the adjustment of $\widetilde{f}_{\mathrm{mod}}$, the phase of the Kelvin LIA is to be adjusted to get always a maximal in-phase signal and hence optimize the measurement of the bias-modulated vibration amplitude. This is an irrelevant issue for the simulator as there is no additional "numerical" phase delay between the LIA and the bias modulation. The phase of the LIA is always exactly the same as the one of the in-phase component. Hence, the in-phase signal is always maximum.

5.3.2 Frequency Modulation KPFM (FM-KPFM)

Unlike in AM-KPFM, the FM-KPFM method does not rely on the detection of a mechanical resonance of the cantilever, but on the detection of the bias-induced modulation of the frequency shift of the fundamental eigenmode of the cantilever. However in this case, the numerical implementation is made easier as no Kelvin PLL is required. The numerical scheme is reported in Fig. 5.7. In FM-KPFM, the modulation frequency of the bias is performed at low frequency, typically $f_{\mathrm{mod}} = 1\,\mathrm{kHz}$. In order to understand how the bias modulation induces the modulation of the Δf, let us consider the following elements. To first order, it is known that the interaction-shifted resonance frequency $\widetilde{f}_0$ of the fundamental bending eigenmode of the cantilever under the influence of an interacting force with the general form $F_{\mathrm{int}}(z)$ may be written as:

$$\widetilde{f}_0 = \frac{1}{2\pi}\sqrt{\frac{k_0 - \partial F_{\mathrm{int}}/\partial z}{m_0}} = f_0\left(1 - \frac{1}{2k_0}\frac{\partial F_{\mathrm{int}}}{\partial z}\right) \Longleftrightarrow \Delta f = \widetilde{f}_0 - f_0 = -\frac{1}{2k_0}\frac{\partial F_{\mathrm{int}}}{\partial z}. \tag{5.14}$$

If one assumes that the interaction force includes an electrostatic component with the usual capacitive form: $F_{\mathrm{int}}(z) \propto F_{\mathrm{es}}(V_{\mathrm{b}}, z) = 1/2\partial C/\partial z V_{\mathrm{b}}^2$ with $V_{\mathrm{b}} = V_{\mathrm{dc}} - V_{\mathrm{cpd}} + V_{\mathrm{mod}} \sin(2\pi f_{\mathrm{mod}} t)$, then it can readily be seen that a modulation at f_{mod} and $2\,f_{\mathrm{mod}}$ will occur in the force and hence, in the frequency shift (5.14). The

DC bias voltage nullifying the modulated component of the Δf at f_{mod} gives the CPD. In other words, in FM-KPFM, the amplitude of the bias-induced modulation of the Δf has the same role as the bias-induced resonance of the second eigenmode of the cantilever (resonance amplitude A_1) in AM-KPFM. The underlying idea of the FM-KPFM method is that it is not sensitive to the electrostatic force like in AM-KPFM (A_1 being proportional to the strength of F_{es}), but rather to its gradient (readily visible in (5.14)). Owing to the lower modulation frequency, the Kelvin LIA has a lower, 500 Hz, bandwidth.

5.3.3 Methodology with the nc-AFM/KPFM Simulator

The sequence of simulation of a spectroscopic curve or an image in FM- or AM-KPFM is detailed in Fig. 5.9. It follows accurately the experimental protocols and is cast into three main steps:

1. The steady state of the cantilever is calculated for a tip-surface separation corresponding to twice the vibration amplitude of the first bending mode of the cantilever (typically 8 nm peak-to-peak). Then (1) the PLL is engaged, (2) the phase lag of the phase shifter is adjusted to maximize the oscillation amplitude (on-resonance condition), (3) the APIC is engaged, and (4) the bias modulation is engaged (i.e., $f_{\mathrm{mod}} \neq 0$ and $V_{\mathrm{mod}} \neq 0$) to trigger the long-range electrostatic force (see (5.5)). Note that if the AM-KPFM is engaged, the Kelvin PLL must be engaged as well. At this point, the cantilever is operated in nc-AFM and the surface may be approached. At this distance, this should yield an almost zero long-range interaction if the tip would carry no charge. However, in the atomistic description of the tip as described in the next section (Sect. 5.4), the tip carries an intrinsic charge of $+1$ that induces a long-range electrostatic background force. Thus, a DC voltage, $V_{\mathrm{dc}}^{\mathrm{ref}} = -0.91$ V, is applied to the tip to compensate for it and nullify the LCPD at large tip–sample separation (>2 nm). $V_{\mathrm{dc}}^{\mathrm{ref}}$ can be interpreted as the opposite of the macroscopic CPD of the electrodes-bulk NaCl system. Thus, the bias voltage applied to the tip is $V_{\mathrm{b}} = V_{\mathrm{dc}} + V_{\mathrm{dc}}^{\mathrm{ref}} + V_{\mathrm{mod}} \sin(2\pi f_{\mathrm{mod}} t)$. Then the approach is engaged down to an arbitrary value of tip-surface separation.
2. The Kelvin controller and the distance controller are engaged sequentially. Impulse response tests are then performed with the amplitude controller and the distance controller to assess their time constant and make sure that they are in a critically damped regime. It is important to perform these tests when the tip is close to the surface. Then, imaging artifacts that would be due to an inadequate choice of the gains of the controllers are unlikely to occur.
3. The spectroscopic curve (i.e., Δf vs. V_{dc} in FM-KPFM, or A_1 vs. V_{dc} in AM-KPFM) or the scan is engaged. Note that if operating in AM-KPFM, the Kelvin PLL is disengaged first and $\widetilde{f}_{\mathrm{mod}}$ kept constant and equal to the latest value computed during the approach, as stated before. If a spectroscopic curve is to be performed, then the Kelvin controller and the distance controller are disengaged

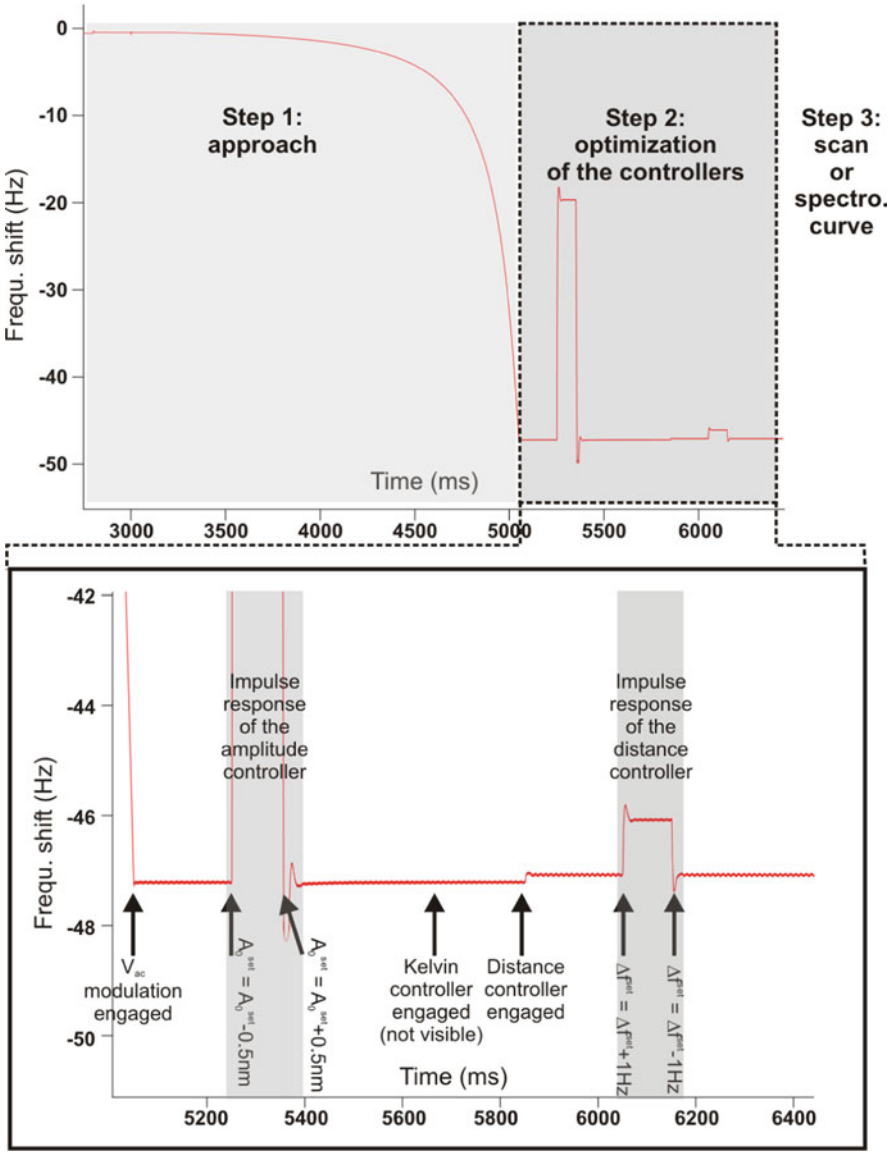

Fig. 5.9 Sequence of simulation of a spectroscopic curve or an image with the nc-AFM/KPFM simulator. When the tip is approached to the surface, the time constant of the controllers is carefully adjusted to make sure that they do not influence the subsequent measurements

(AM- or FM-KPFM). The AC modulation may remain engaged or not. The spectroscopic curve is acquired by continuously sweeping the DC part of the bias, first from 0 down to negative values and then upward. For that purpose, we use a sweep speed of about 200 mV s^{-1}, which is slow enough to prevent nonadiabatic effects from occurring.

5.4 Atomistic Simulations of Bias Voltage-Dependent Force Fields

The two following sections report the results obtained when combining the nc-AFM/KPFM simulator and atomistic calculations of the bias voltage and distance-dependent interaction force field computed between a metallic tip carrying an ionic cluster and the (001) facet of a NaCl crystal, as sketched in Fig. 5.10a. For that work, the nc-AFM/KPFM has been used in the FM-KPFM mode. Most of the elements detailed below are reported in [36]. We first give the expression of the Madelung surface potential for the ionic crystal and then describe the atomistic simulations of the tip-surface interaction. Finally, the results of the calculations performed with the nc-AFM/KPFM simulator are given.

5.4.1 *Madelung Surface Potential of an Alkali Halide*

In order to assess how quantitative the KPFM measurements on the atomic-scale can be, it is important to estimate the physical observable to which the LCPD might be connected to, namely the Madelung surface potential V_s of the alkali halide crystal. V_s can be estimated on the base of the work by Watson et al. [68] and may be written in the form [19]:

$$V_s(x, y, z_\mu) = -\frac{q}{\pi\epsilon_0 a'} \cosh\left[\frac{2\pi}{a'}\delta^{\perp}(V_b)\right] \widetilde{\chi}(x, y) e^{-\frac{2\pi}{a'} z_\mu} \tag{5.15}$$

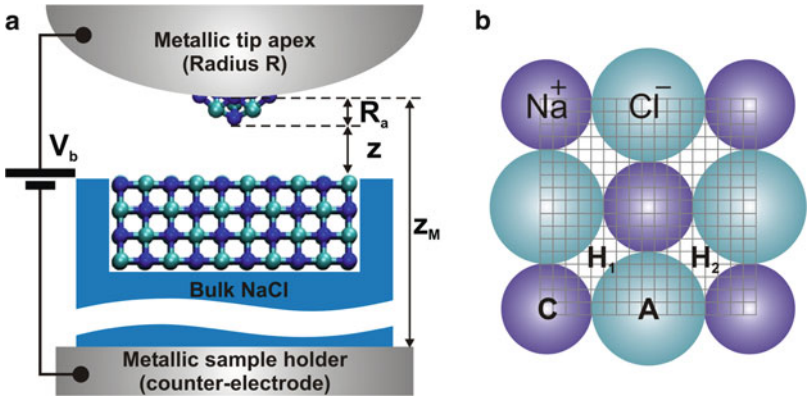

Fig. 5.10 (**a**) Sketch of the numerical tip-surface setup. We have set $z_m = 5$ mm compared to z which scales in the sub-nm range. (**b**) Sketch of the NaCl unit cell showing the 17×17 mesh used to calculate the (x, y, z, V) four-dimensional tip-surface force field. Four particular sites have been investigated: anionic (A), cationic (C), and hollow (H_1, H_2) sites

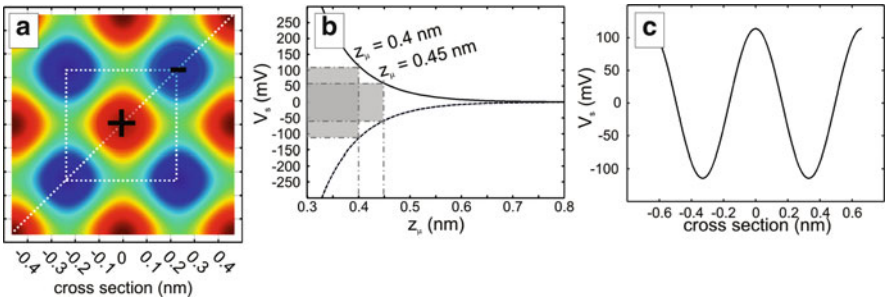

Fig. 5.11 (**a**) Madelung surface potential calculated from (5.15) for $z_\mu = 4$ Å. The vertical contrast ranges from −100 (*blue spots*) to +100 mV (*red spots*). The *dotted square* stands for the unit cell shown in Fig. 5.10b, i.e., centered on top of a cation. (**b**) Distance dependence of the potential on top of an anion (*dotted curve*) and on top of a cation (*solid curve*) showing the exponential decay of the potential. At $z_\mu = 0.4$ nm, the total magnitude of the potential is $\simeq$220 mV and becomes $\simeq$140 mV for $z_\mu = 0.45$ nm. (**c**) Cross section along the dotted diagonal line shown in (**a**)

with: $\widetilde{\chi}(x, y) = \cos\left[\frac{2\pi}{a'}(x - x_0)\right] + \cos\left[\frac{2\pi}{a'}(y - y_0)\right]$, a spatial modulation term. x_0 and y_0 are the x and y coordinates of the center of the asperity projected onto the unit cell. Setting $x_0 = y_0 = 0$ locates the asperity and therefore the tip on top of an anion. a' is a geometrical parameter connected to the lattice constant of the crystal, a, according to: $a' = a\sqrt{(2)/2}$. $\delta^{\perp}(V_b)$ depicts the vertical displacement (i.e., in the perpendicular direction compared to the plane of the crystal) of the ion owing to its ionic polarizability. z_μ depicts the distance from the plane of the crystal above which the surface potential is estimated. z_μ will state for the distance between the lowest turning point of the tip oscillation cycle and the surface, as stated before. The above expression exhibits the expected exponential decaying behavior as a function of z_μ. The potential is reported in Fig. 5.11 for $a = 0.66$ nm, $\delta^{\perp} = 11$ pm and $z_\mu = 4$ Å [19].

5.4.2 *Atomistic Simulations of the Bias Voltage-Dependent Force Field*

The calculations of the force field were performed using atomistic simulations as implemented in the code SCIFI [38]. The interatomic forces are computed from a sum of pairwise Buckingham potentials acting between ions. These are treated atomistically in a shell model with coupled oppositely charged cores and shells in order to describe their polarizabilities. The SCIFI code also allows for the inclusion of metallic electrodes at the tip and below the surface. The interaction of these with ions in the surface and tip are treated by the method of images [38]. Using this approach, we can simulate the polarization of conductors and resultant atomic geometries in the system as a function of tip position and applied bias voltage.

Parameters for the species considered were taken from [69]. All cores and shells were allowed to relax completely with respect to interatomic and image forces with a convergence criterion of 1 meV/Å per ion, the magnitude of the force difference with voltage and distance being of the order of several tenths of an eV/Å. Hence, in the present simulations we take into account ionic relaxation, and electronic and ionic polarization as a function of both atomic interactions and applied bias.

The properties of the NaCl(001) surface are well understood and can be well represented by a slab of four atomic layers containing 10×10 ions, with those in the bottom layer and edges kept fixed (cf. Fig. 5.10a). The NaCl slab is embedded within a semi-infinite, 5 mm thick, slab merely treated by means of its dielectric constant. For the tip, a 64-atom cubic cluster of NaCl is embedded into a metallic sphere of radius $R = 5$ nm and oriented such that the [111] direction is perpendicular to the surface with a Na atom at the apex. The main condition for finding a suitable tip beyond comparing to experimental contrast is the stability of the tip-surface system. Here, we refer to the onset of tip and surface atom instabilities, i.e., large irreversible displacements that would either cause a tip crash in experiments or directly introduce numerical instabilities due to the difficulty in finding the equilibrium geometry. We considered many tip models, and the most stable configuration of the tip is found when the cluster protrudes from the end of the sphere with a height $R_a = 0.3$ nm (cf. Fig. 5.10a). This tip carries an intrinsic charge of $+1$ due to its stoichiometry, inducing an opposite charge in the vicinity of the metallic part of the tip. The NaCl atoms within the sphere are frozen and play no role in the calculation of image forces. They act as ghost metal atoms stabilizing the tip apex. The metallic part of the tip is biased with respect to the counter-electrode holding the crystal.

In order to compute images with the simulator, the NaCl unit cell was meshed with a 17×17 grid (cf. Fig. 5.10b). For each pixel of the mesh, the distance dependence (z-dependence) of the atomistic force field is computed by 10 pm steps from 0.3 to 2.0 nm (171 samples) and the bias dependence (V-dependence) by 100 mV steps from -3.4 to $+2.3$ V (57 samples). It must be noticed that each (z, V) couple of coordinates provides not only the value of the force, but also the position of the core and of the shell of each ion of the setup (464 in total). This results in a very large amount of data to store and handle, about 600 GB uncompressed. The simulation runs are farmed onto a cluster of several hundred workstations, with each grid point and voltage combination run on a single core for every tip height. On Intel 2.5 GHz processors or equivalent, this takes about an hour and calculating the full map takes about 16,000 h of CPU time. Post-processing of the data takes a similar amount of time.

To make the simulations with the nc-AFM/KPFM simulator more accurate and reduce the numerical noise further, the atomistic force field is post-processed as follows. For each pixel of the mesh, the (z, V) force matrix that is built from the raw data is z- and V- interpolated with a Cubic Spline function by 5 pm and 10 mV steps, respectively. In addition to the short-range atomistic force field, the long-range interaction including Van der Waals and electrostatic contributions as described in

Sect. 5.2 is added and the cut-off distance setting the size of the lookup table is set arbitrarily to 8 nm. Above 8 nm, the van der Waals and electrostatic long-range contributions are not set to 0, but estimated out of their analytical expressions, (5.4) and (5.5), respectively. Therefore, the total 4-dimensional lookup table of the force field to be used with the simulator consists of $x \times y \times z \times V = 17 \times 17 \times (8\,\text{nm} - 0.3\,\text{nm})/0.005\,\text{nm} \times (2.3\,\text{V} - (-3.4\,\text{V}))/0.01\,\text{V} \simeq 255 \cdot 10^6$ samples, which requires 8 GB of RAM on the host computer (Intel Core2Duo, 2.5GHz/proc.). With the parameters detailed above, approaching the tip to the surface typically takes 5 min. Computing a spectroscopic curve takes about 30 min and computing an image about 2 h. The spectroscopic curves shown below have been computed on top of four particular sites of the mesh: an anionic site A, a cationic site C, and the two hollow sites H_1 and H_2, which are made inequivalent owing to the orientation of the cluster with respect to the surface symmetry.

Force vs. distance curves computed above the four sites with $V_{\text{dc}} = 0\,\text{V}$ are shown in Fig. 5.12a. Below 0.45 nm, tip/surface instabilities on top of anionic and hollow sites occur. Above 0.45 nm, the curves differ significantly, although exhibiting similar features to those reported with almost equivalent setups [20, 22, 70]. Force vs. V_{dc} curves measured at $z_\mu = 0.45\,\text{nm}$ are shown in Fig. 5.12b for the four sites. The maxima of the curves differ between sites (cf. dotted lines): $-304\,\text{pN}$ at $1.22\,\text{V}$ (site C) and $-506\,\text{pN}$ at $1.06\,\text{V}$ (site A). The curves systematically deviate from the capacitive, parabolic-like, behavior which stems from the polarization of the ions at the tip–surface interface. To assess this, the displacements of the cores of the foremost Na^+ ion of the tip ($\delta^{\text{T}}_{\text{Na}}$) when placed above a Na^+ ($\delta^{\text{S}}_{\text{Na}}$) and above a Cl^- ($\delta^{\text{S}}_{\text{Cl}}$) of the slab as a function of V_{dc} are shown in Fig. 5.12c, d, respectively. They are measured at $z_\mu = 0.45\,\text{nm}$. A positive displacement means that the ion is displaced upward (e.g., toward the tip when considering an ion of the slab). We only have focused on the displacements of the cores of the ions that were judged as the most significant, although the polarization process involves all the ions of the interface and their shells. For the sake of clarity, we have also sketched the ionic displacements in Fig. 5.12e, f.

The calculations show that on top of Na^+ at zero bias, the foremost cation of the tip is attracted toward the surface: $\delta^{\text{T}}_{\text{Na}} = -8.5\,\text{pm}$. Simultaneously, the Na^+ of the slab undergoes a moderate displacement toward the tip: $\delta^{\text{S}}_{\text{Na}} = +2\,\text{pm}$. This behavior stems from the balance between the short-range chemical interaction and the local electrostatic interaction due to the intrinsic charge of the tip, merely compensated by $V^{\text{ref}}_{\text{dc}}$ at large distance. With $V_{\text{dc}} > 0$, the foremost cation of the tip remains attracted to the surface, while the Na^+ is repelled within the slab. The short-range electrostatic force is then strengthened between the tip cation and the four Cl^- closest neighbors of the Na^+ of the slab, while the latter is repelled from the tip because of the overall less favorable chemical and electrostatic interaction. With $V_{\text{dc}} < 0$, the electrostatic force becomes dominant and mostly repulsive for the same reason as before. Then the set of Cl^- and Na^+ ions are repelled within the slab.

On top of Cl^- at zero bias, the favorable combination between the chemical interaction and the local electrostatic interaction due to the intrinsic charge of the tip partly compensated by $V^{\text{ref}}_{\text{dc}}$ produces significant displacements of the ions at

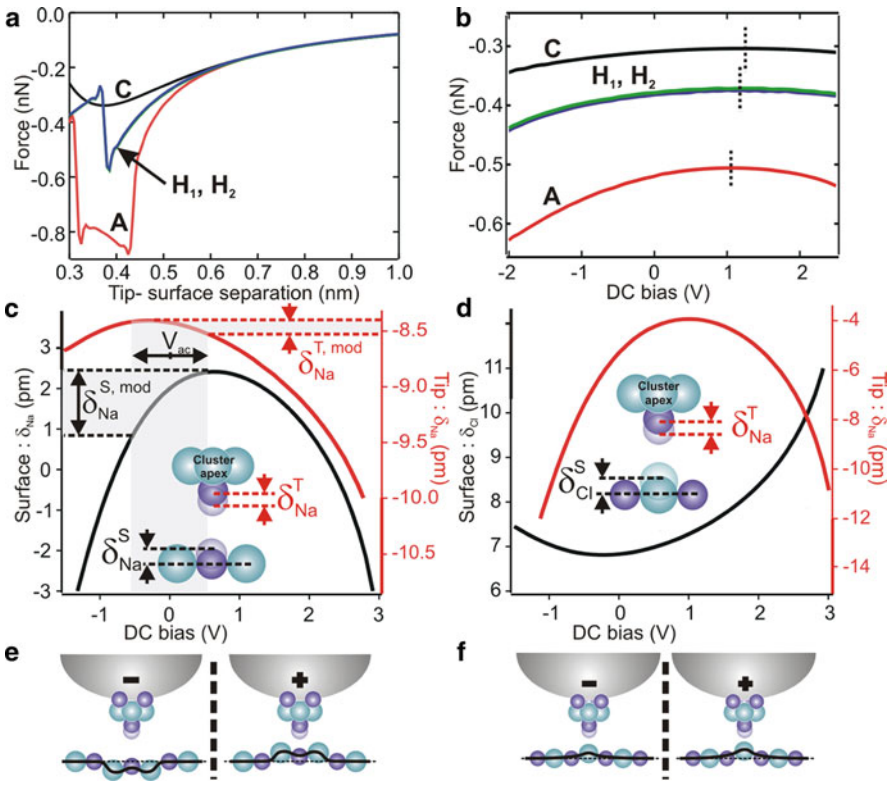

Fig. 5.12 (**a**) Force vs. distance curves measured above the four sites of the unit cell at $V_{dc} = 0$ V. Below 0.45 nm, the tip becomes unstable. (**b**) Force vs. V_{dc} curves at $z_\mu = 0.45$ nm. The dependence is not parabolic. (**c**) V_{dc} dependence of the displacement of the foremost Na^+ ion of the tip, δ^T_{Na}, at $z_\mu = 0.45$ nm on top of Na^+ of the slab and corresponding δ^S_{Na} displacement. The AC bias modulation (*gray*) triggers the dynamic displacement of the ions at the interface ($\delta^{T,S,mod}_{Na}$). (**d**) Same as c- except that the tip is now placed on top of Cl^-. (**e**) Scheme of the ionic displacements induced by the tip on top of Na^+ as a function of the sign of the bias voltage. (**f**) Same as (**e**) except that the tip is now on top of Cl^-

the interface ($\delta^T_{Na} = -6$ pm; $\delta^S_{Cl} = +7$ pm). With $V_{dc} > 0$, the local electrostatic interaction increases the mutual attraction between ions. With $V_{dc} < 0$, the Cl^- of the slab is less attracted by the tip due to the repulsive electrostatic interaction, but the tip cation remains attracted by the surface, likely because the chemical interaction is still large enough.

These conclusions stress that, when the KPFM controller is engaged, the AC modulation of the bias triggers complex dynamic displacements of the cluster/surface ions. As predicted in [19], these displacements support the LCPD signal and explain the deviation from the usual capacitive parabolic law of the force vs. bias voltage curve. Indeed, when performing the following simulations while freezing the ionic polarization, no KPFM contrast occurs (data not shown).

5.5 Results with the nc-AFM/KPFM Simulator

The main parameters for the simulations shown in this section are: oscillation amplitude: 8 nm peak-to-peak, cantilever resonance frequency: 150 kHz, cantilever stiffness: 30 N m^{-1}, Q-factor: 30,000, scan size: 1.03 × 1.03 nm^2, scan speed: 1.5 s/line. The FM-KPFM mode was implemented with a 500 Hz bandwidth lock-in amplifier and a 50 Hz bandwidth controller. The AC bias modulation is $V_{\text{mod}} = 0.5\,\text{V}$ and $f_{\text{mod}} = 1\,\text{kHz}$.

5.5.1 Spectroscopic Curves

The distance dependence of the LCPD has first been investigated by means of spectroscopic curves. When the tip is biased, the maximum of the Δf vs. V_{dc} curve gives a DC voltage opposite to that of the LCPD: $V_{\text{dc}} = -V_{\text{LCPD}}$. In Fig. 5.13a, spectroscopic curves measured on top of each site for a tip-surface separation $z_\mu = 0.45\,\text{nm}$ are shown. As expected from the force vs. V_{dc} curves, the spectroscopic curves deviate from the parabolic-like behavior (shown for site A, dotted gray curve) and the positions of the maxima differ upon sites. Furthermore, the latter positions do not match those of the force vs. V_{dc} curves. However, such an effect is expected to occur as soon as the z and V dependencies of the interaction force cannot be separated, i.e., $F(z, V_{\text{dc}}) \neq h(z)g(V_{\text{dc}})$.[3] A shift of +0.87 V is measured from site A to site C, consistently with the larger repulsive electrostatic force observed above cations. These measurements have been reproduced for various tip-surface separations and gathered in Fig. 5.13b. When increasing the separation, the LCPD first decreases and then increases to converge toward 0 at large distance, as stated before. Below 0.6 nm, the curves unbundle and differ significantly upon sites (gray area). These curves are equivalent to Δf vs. distance curves that are driving the magnitude of the topography contrast. Hence, a site-dependent KPFM contrast is indeed expected while scanning for tip-surface separations smaller than 0.6 nm.

[3]The expressions of the DC value of the bias voltage that maximizes $\Delta f(z, V_{\text{b}})$ and the force $F(z, V_{\text{b}})$ with $V_{\text{mod}} = 0$, i.e., within the framework of spectroscopic curves in FM- and AM-KPFM, respectively are given by: $(\partial \Delta f(z, V_{\text{b}})/\partial V_{\text{dc}})|_{V_{\text{mod}}=0} = 0(1)$ and $(\partial F(z, V_{\text{b}})/\partial V_{\text{dc}})|_{V_{\text{mod}}=0} = 0(2)$, respectively. The expression of Δf is derived from the approach by Giessibl [71]: $\Delta f(z, V_{\text{b}}) \propto \int_0^{T_0} F(z, V_{\text{b}}) \sin(\omega_0 t)\text{d}t$ with: $V_b = V_{\text{dc}} - V_{\text{CPD}} + V_{\text{mod}} \sin(\omega_{\text{mod}} t)$. If the force has the usual quadratic-like form: $F(z, V_{\text{b}}) = h(z) \times V_{\text{b}}^2$ (e.g., $F = \frac{1}{2}\partial C/\partial z V_{\text{b}}^2$), then conditions (1) and (2) yield equivalently to $V_{\text{dc}} = V_{\text{CPD}}$. However, if the force has a less usual fully polynomial form, as this is the case when dealing with SRE forces [19,36]: $F(z, V_{\text{b}}) = h(z) \times [A(z)V_{\text{b}}^2 + B(z)V_{\text{b}} + C(z)]$, then conditions (1) and (2) give: $V_{\text{dc}} = V_{\text{CPD}} - I'/(2J')$ (with $I' = \int_0^{T_0} B(z)h(z)\sin(\omega_0 t)\text{d}t$ and $J' = \int_0^{T_0} A(z)h(z)\sin(\omega_0 t)\text{d}t$) and $V_{\text{dc}} = V_{\text{CPD}} - B(z)/(2A(z))$, respectively. Therefore the maxima of both spectroscopic methods differ. The main reason is that the force is dynamically z-dependent (which makes the compensated CPD z-dependent as well, as seen with the above equation), while Δf is averaged over the oscillation cycle, hereby averaging the force as well.

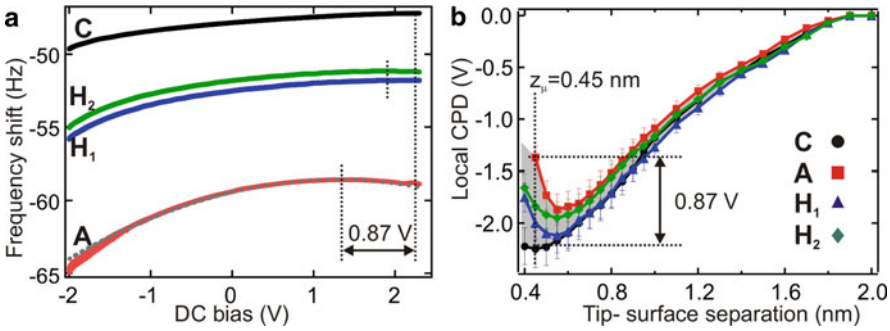

Fig. 5.13 (**a**) Spectroscopic curves computed above the four sites at $z = 0.45$ nm. A shift of 0.87 V is noticed between anionic (A) and cationic (C) sites. (**b**) Distance dependence of the LCPD above the four sites derived from the spectroscopic curves. In the short-range regime, the LCPD exhibits a resonance-like and site-dependent behavior

The magnitude of the LCPD contrast can be derived as well. At $z = 0.45$ nm (dotted line), a maximum of 0.87 V is expected. At equivalent height, the Madelung surface potential is 0.14 V (cf. Fig. 5.11b). This resonance-like effect has been predicted theoretically [36] and reported experimentally [27]. It relies on a subtle balance between short-range and long-range electrostatic forces, both weighting in the manner the LCPD is compensated.

5.5.2 *Topography and LCPD Images*

Finally, topography and LCPD images have been computed (cf. Fig. 5.14a–c, respectively). Images shown in Figs. 5.14a (38 pm full scale) and 5.14b (0.56 V full scale) have been simultaneously computed with the distance controller engaged. The scan has been engaged on top of a cation at $z_\mu = 0.45$ nm, corresponding to $\Delta f_{\text{set}} = -47.22$ Hz. The dotted area depicts the unit cell shown in Fig. 5.10b. Topography and LCPD images show cations as depressions, consistently with spectroscopic curves. The magnitude of the contrasts as well as the distance range are in good agreement with our former experimental observations (30 pm, 0.1 V) [19]. Figure 5.14c (0.86 V full scale) is an LCPD image computed with similar conditions as (b), but at constant height $z = 0.45$ nm, i.e., with the distance controller disengaged. The magnitude of the contrast matches the predicted behavior (cf. Fig. 5.13b, dotted line). In Fig. 5.14d is reported the magnitude of the LCPD contrast as a function of the tip-surface separation (left-hand side). The curve is deduced from scans for which the distance regulator was engaged. The average value of the LCPD (mean contrast) has been reported as well (right-hand side). It follows accurately the evolution of the average LCPD derived from the spectroscopic curves (cf. Fig. 5.13b). The contrast expands around the average value while keeping confined within the gray area, the size of which is controlled by the

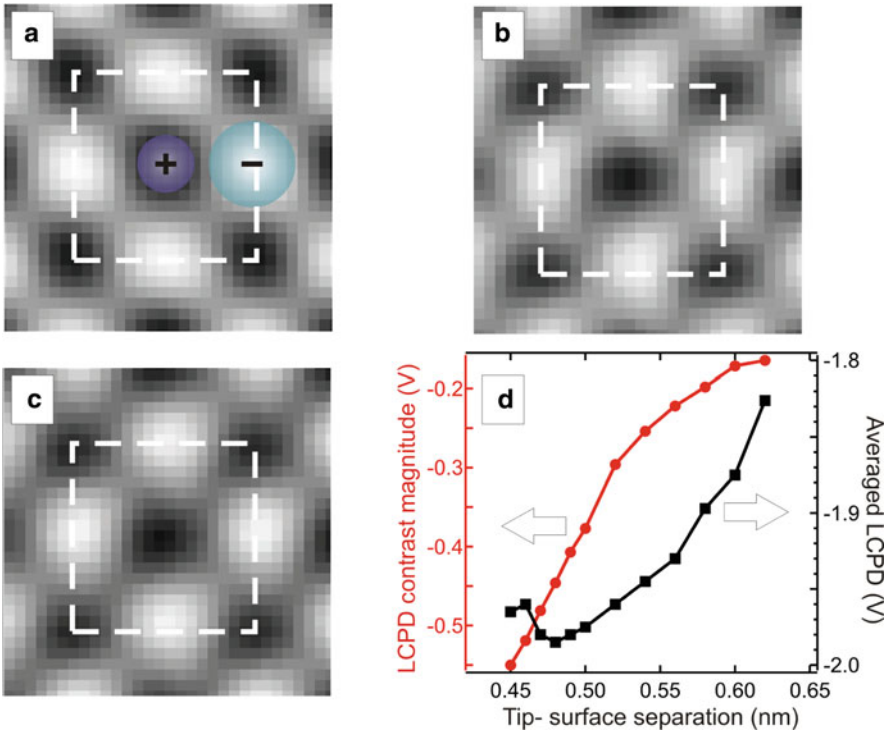

Fig. 5.14 (**a**) Topography image computed with the nc-AFM/KPFM simulator. The vertical contrast is 38 pm. (**b**) Simultaneously computed LCPD image. The contrast ranges from −2.24 to −1.69 V (0.56 V full scale). In both channels, cations are imaged as depressions and anions as protrusions. (**c**) LCPD image computed at constant height, $z_\mu = 0.45$ nm. The contrast ranges from −2.24 to −1.38 V (0.86 V full scale), consistently with the expected range deduced from Fig. 5.13b. (**d**) Evolution of the magnitude of the LCPD contrast (*dots*) and of the mean LCPD (*squares*) as a function of the distance

combination between short-range electrostatic and chemical forces. We infer from the above elements that relevant information about the LCPD is not only carried by the magnitude of the KPFM contrast, but also by its average value.

5.6 Conclusions and Outlook

The focus of this chapter was to present recent numerical developments targeted at helping the interpretation of the atomic-scale contrast in KPFM, which inherently requires (1) an accurate atomistic description of the force field occurring between the tip and the surface, and (2) a proper numerical implementation of the control electronics of the nc-AFM/KPFM setup. In the case of the bulk ionic crystal discussed here, it has been shown that short-range electrostatic forces occur in the

range of 4–6 Å above the surface and differ between cationic and anionic sites. When combined with the chemical short-range forces, these are responsible for the simultaneous topographical and CPD atomic-scale contrast. However, SRE forces are self-consistently correlated with the chemical forces as the modulated bias voltage triggers ionic displacements at the tip–surface interface. Therefore, because the occurrence of the atomic-scale KPFM contrast relies on the latter displacements, the magnitude of the LCPD differs from the Madelung surface potential at equivalent height, *although the spatial periodicity of both observables remains the same, i.e., the one of the ionic lattice*. Thus, the quantitative interpretation of the atomic-scale CPD contrast must be done within the context of SRE forces and not in terms of physical observables such as the Madelung surface potential or the local work function. This is all the more true in that the effects are strongly dependent of the tip shape and size, which has also been reported experimentally (cf. footnote ♯29 in [72]).

An important part of the problem that was not addressed here is the contribution of long-range electrostatic interactions to the observed LCPD. The influence of these on the magnitude of the KPFM contrast has not yet been investigated in detail on the numerical level, despite that the effects are theoretically predicted [36]. Another issue deals with the use of KPFM on the atomic scale to map the chemical identity of atoms. The underlying idea is to assess how sensitive the atomic-scale CPD contrast is to the tip termination and intrinsic charge. If the CPD contrast remains qualitatively unchanged from one tip to the other (e.g., cations=dark contrast, anions=bright contrast, as shown here), then the KPFM channel could unravel in a straightforward and univocal manner the delicate issue of chemical identification, which usually requires a thorough analysis. The two latter issues are currently being addressed. “There’s plenty of room at the bottom”, R. Feynman, meeting at Caltech on December 29, 1959.

Acknowledgements LN, FB, and CL wish to thank E. Meyer, T. Glatzel and S. Kawai from the Department of Physics of the University of Basel for stimulating discussions and acknowledge support from the ANR with the PNANO project MolSiC (ANR-08-P058-36). ASF wishes to thank L.N. Kantorovich for useful discussions and acknowledges support from the Academy of Finland and ESF FANAS programme.

References

1. A. Kikukawa, S. Hosaka, R. Imura, Rev. Sci. Instrum. **67**(4), 1463 (1996)
2. S. Kitamura, M. Iwatsuki, Appl. Phys. Lett. **72**, 3154 (1998)
3. S. Sadewasser, M. Lux-Steiner, Phys. Rev. Lett. **91**, 266101 (2003)
4. S. Sadewasser, T. Glatzel, R. Shickler, Y. Rosenwaks, M. Lux-Steiner, Appl. Surf. Sci. **210**((1–2)), 32 (2003)
5. S. Sadewasser, P. Carl, T. Glatzel, M.C. Lux-Steiner, Nanotechnology **15**, S14 (2004)
6. J. Polesel-Maris, A. Piednoir, T. Zambelli, X. Bouju, S. Gauthier, Nanotechnology **15**, S24 (2004)

7. C. Sommerhalter, T. Matthes, T. Glatzel, A. Jäger-Waldau, M.C. Lux-Steiner, Appl. Phys. Lett. **75**, 286 (1999)
8. Y. Rosenwaks, R. Shikler, T. Glatzel, S. Sadewasser, Phys. Rev. B **70**, 085320 (2004)
9. H. Hoppe, T. Glatzel, M. Niggemann, A. Hinsch, M.C. Lux-Steiner, N.S. Sariciftci, Nanoletters **5**, 269 (2004)
10. S. Kitamura, K. Suzuki, M. Iwatsuki, Appl. Surf. Sci. **140**, 265 (1999)
11. Y. Sugawara, T. Uchihashi, M. Abe, S. Morita, Appl. Surf. Sci. **140**, 371 (1999)
12. S. Kitamura, K. Suzuki, M. Iwatsuki, C. Mooney, Appl. Surf. Sci. **157**, 222 (2000)
13. K. Okamoto, K. Yoshimoto, Y. Sugawara, S. Morita, Appl. Surf. Sci. **210**, 128 (2003)
14. K. Okamoto, Y. Sugawara, S. Morita, Jpn. J. Appl. Phys. **42**, 7163 (2003)
15. T. Arai, M. Tomitori, Phys. Rev. Lett. **93**, 256101 (2004)
16. F. Krok, K. Sajewicz, J. Konior, M. Goryl, P. Piatkowski, M. Szymonski, Phys. Rev. B **77**(23), 235427 (2008)
17. A. Sasahara, C.L. Pang, H. Onishi, J. Phys. Chem. B **110**, 13453 (2006)
18. G. Enevoldsen, T. Glatzel, M. Christensen, J. Lauritsen, F. Besenbacher, Phys. Rev. Lett. **100**, 236104 (2008)
19. F. Bocquet, L. Nony, C. Loppacher, T. Glatzel, Phys. Rev. B **78**, 035410 (2008)
20. R. Hoffmann, L. Kantorovich, A. Baratoff, H. Hug, H.J. Güntherodt, Phys. Rev. Lett. **92**, 146103 (2004)
21. R. Hoffmann, C. Barth, A. Foster, A. Shluger, H. Hug, H.J. Güntherodt, R. Nieminen, M. Reichling, J. Am. Chem. Soc. **127**, 17863 (2005)
22. M. Lantz, R. Hoffmann, A. Foster, A. Baratoff, H. Hug, H.R. Hidber, H.J. Güntherodt, Phys. Rev. B **74**, 245426 (2006)
23. R. Hoffmann, D. Weiner, A. Schirmeisen, A. Foster, Phys. Rev. B **80**, 115426 (2009)
24. Y. Sugimoto, P. Pou, M. Abe, P. Jelinek, R. Péerez, S. Morita, O. Custance, Nature **446**, 64 (2007)
25. A. Foster, C. Barth, C. Henry, Phys. Rev. Lett. **102**, 256103 (2009)
26. C. Leendertz, F. Streicher, M.C. Lux-Steiner, S. Sadewasser, Appl. Phys. Lett. **89**, 113120 (2006)
27. S. Burke, J. LeDue, Y. Miyahara, J. Topple, S. Fostner, P. Grütter, Nanotechnology **20**, 264012 (2009)
28. H. Jacobs, P. Leuchtmann, O. Homan, A. Stemmer, J. Appl. Phys. **84**(3), 1168 (1998)
29. J. Colchero, A. Gil, A. Beró, Phys. Rev. B **64**, 245403 (2001)
30. H. McMurray, G. Williams, J. Appl. Phys. **91**(3), 1673 (2002)
31. T. Takahashi, S. Ono, Ultramicroscopy **100**, 287 (2004)
32. E. Palacios-Lidón, J. Abellán, J. Colchero, C. Munuera, C. Ocal, Appl. Phys. Lett. **87**, 154106 (2005)
33. U. Zerweck, C. Loppacher, T. Otto, S. Grafström, L. Eng, Phys. Rev. B **71**, 125424 (2005)
34. U. Zerweck, C. Loppacher, T. Otto, S. Grafström, L. Eng, Nanotechnology **18**, 084006 (2007)
35. K. Wandelt, Appl. Surf. Sci. **111**, 1 (1997)
36. L. Nony, F. Bocquet, C. Loppacher, T. Glatzel, Nanotechnology **20**, 264014 (2009)
37. R. Pérez, I. Stich, M. Payne, K. Terakura, Phys. Rev. B **58**, 10835 (1998)
38. L. Kantorovich, A. Foster, A. Shluger, A. Stoneham, Surf. Sci. **445**, 283 (2000)
39. R. Bennewitz, A. Foster, L. Kantorovich, M. Bammerlin, C. Loppacher, S. Schär, M. Guggisberg, E. Meyer, A. Shluger, Phys. Rev. B **62**(3), 2074 (2000)
40. C. Barth, A. Foster, M. Reichling, A. Shluger, J. Phys. Condens. Matter **13**, 2061 (2001)
41. A. Foster, A. Shluger, R. Nieminena, Appl. Surf. Sci. **188**, 306 (2002)
42. P. Dieska, I. Stich, R. Pérez, Phys. Rev. Lett. **91**, 216401 (2003)
43. W. Hofer, A. Foster, A. Shluger, Rev. Mod. Phys. **75**, 1287 (2003)
44. O. Pakarinen, C. Barth, A. Foster, R. Nieminen, C. Henry, Phys. Rev. B **73**, 235428 (2006)
45. L. Kantorovich, T. Trevethan, Phys. Rev. Lett. **93**, 236102 (2004)
46. T. Trevethan, L. Kantorovich, Nanotechnology **15**, S34 (2004)
47. T. Trevethan, L. Kantorovich, Nanotechnology **15**, S44 (2004)

48. T. Trevethan, L. Kantorovich, J. Polesel-Maris, S. Gauthier, Nanotechnology **18**, 084017 (2007)
49. T. Trevethan, A. Shluger, Nanotechnology **20**, 264019 (2009)
50. T. Trevethan, M. Watkins, L. Kantorovich, A. Shluger, J. Polesel-Maris, S. Gauthier, Nanotechnology **17**, S5866 (2006)
51. Y. Sugimoto, P. Jelinek, P. Pou, M. Abe, S. Morita, R. Perez, O. Custance, Phys. Rev. Lett. **98**, 106104 (2007)
52. T. Trevethan, M. Watkins, L. Kantorovich, A. Shluger, Phys. Rev. Lett. **98**, 028101 (2007)
53. T. Trevethan, L. Kantorovich, J. Polesel-Maris, S. Gauthier, A. Shluger, Phys. Rev. B **76**, 085414 (2007)
54. N. Martsinovich, L. Kantorovich, Phys. Rev. B **77**, 205412 (2008)
55. T. Trevethan, A. Shluger, J. Phys. Chem. C **112**, 19577 (2008)
56. M. Watkins, T. Trevethan, M. Sushko, A. Shluger, J. Phys. Chem. C **112**, 4226 (2008)
57. L. Nony, A. Foster, F. Bocquet, C. Loppacher, Phys. Rev. Lett. **103**, 036802 (2009)
58. L. Nony, A. Baratoff, D. Schär, O. Pfeiffer, A. Wetzel, E. Meyer, Phys. Rev. B **74**, 235439 (2006)
59. M. Gauthier, R. Pérez, T. Arai, M. Tomitori, M. Tsukada, Phys. Rev. Lett. **89**(14), 146104 (2002)
60. G. Couturier, R. Boisgard, L. Nony, J.P. Aimé, Rev. Sci. Instrum. **74**(5), 2726 (2003)
61. G. Couturier, R. Boisgard, D. Dietzel, J.P. Aimé, Nanotechnology **16**, 1346 (2005)
62. J. Polesel-Maris, S. Gauthier, J. Appl. Phys. **97**, 044902 (2005)
63. J. Kokavecz, Z. Toth, Z. Horvath, P. Heszler, A. Mechler, Nanotechnology **17**, S173 (2006)
64. C. Loppacher, M. Bammerlin, F. Battiston, M. Guggisberg, D. Müller, H.R. Hidber, R. Lüthi, E. Meyer, H.J. Güntherodt, Appl. Phys. A **66**, S215 (1998)
65. R.E. Best, *Phase Locked Loops: Design, Simulation and Applications*, 4th edn. (Mc Graw-Hill, New York, 1999)
66. M. Guggisberg, M. Bammerlin, C. Loppacher, O. Pfeiffer, A. Abdurixit, V. Barwich, R. Bennewitz, A. Baratoff, E. Meyer, H.J. Güntherodt, Phys. Rev. B **61**, 11151 (2000)
67. D. Rapaport, *The Art of Molecular Dynamics Simulation* (Cambridge University Press, Cambridge, 1995)
68. R. Watson, J. Davenport, M. Perlam, T. Sham., Phys. Rev. B **24**, 1791 (1981)
69. A. Shluger, A. Rohl, D. Gay, R. Williams, J. Phys. Condens. Matter **6**, 1825 (1994)
70. A. Schirmeisen, D. Weiner, H. Fuchs, Phys. Rev. Lett. **97**, 136101 (2006)
71. F.J. Giessibl, Phys. Rev. B **61**, 9968 (2000)
72. L. Gross, F. Mohn, P. Liljeroth, J. Repp, F. Giessibl, G. Meyer, Science **324**, 1428 (2009)

Part II
Selected Applications

Chapter 6
Electronic Surface Properties of Semiconductor Surfaces and Interfaces

R. Shikler

Abstract In a world where the physical size of semiconductor devices is in the nano-region it is very important to understand the electronic properties of semiconductor surfaces and interfaces. These properties can be inferred indirectly from the measurement of work function variations across the surface. Kelvin probe force microscopy (KPFM) is a powerful tool that measures variations of work function and electrostatic potential distribution with nanometer resolution. In this chapter we review several important works that address the relation between KPFM measurements and the electronic or opto-electronic properties of the surfaces measured. We will start by explaining the dependence of the work function on the surface and specifically on surface states. This will be followed by a review on the work done on semiconductor surfaces and interfaces using KPFM. The focus is on correlating surface and interface properties with electro-optic device performance. This chapter is mostly focused on the works done on inorganic semiconductors with only a few examples on organic semiconductors.

6.1 Introduction

The ever decreasing dimensions of semiconductor devices increase the influence of the processes at their surfaces and interfaces compared to the bulk contribution. Therefore, understanding the electronic properties of semiconductor surfaces/interfaces is crucial for further development in this field. In general, an interface is defined as a boundary between media with different physical properties. For example, the interface between a semiconductor and vacuum or gas is referred

R. Shikler (✉)
Department of Electrical and Computer Engineering, Ben-Gurion University of the Negev, P.O. Box 653, Beer-Sheva 84105, Israel
e-mail: rshikler@ee.bgu.ac.il

S. Sadewasser and T. Glatzel (eds.), *Kelvin Probe Force Microscopy*, Springer Series in Surface Sciences 48, DOI 10.1007/978-3-642-22566-6_6,

to as a "free surface." or just a "surface." The interface between a semiconductor and another solid is usually referred to as an "interface." However, we shall sometimes use the term "surface" to denote any boundary. One of the basic properties of semiconductor surfaces is their work function. In this chapter we will try to understand the relation between the work function and the electronic properties of semiconductor surfaces.

One of the definitions for the work function of a metal, often used by experimentalists, is the difference between the barrier height on the metal–vacuum interface and the Fermi energy. This definition, however, does not specify the kinds of energies which contribute to the barrier height. In 1935 and 1936 Wigner and Bardeen have theoretically shown that the work function consists of two contributions: (1) an internal contribution from the bulk and (2) a contribution from a surface dipole barrier [1, 2]. Work done by Hölzl et al. [3] and Kiejna et al. [4] have demonstrated that for Tungsten for example, the work function can vary from 4.23 eV for the (1 1 3) surface to 5.7 eV for the (0 1 1) surface. These variations can affect various properties of the surface like atom absorption, see for example [4].

A similar picture holds for the case of semiconductors. The work function of a semiconductor is a property of its surface; it is largely affected by the electrical properties of the semiconductor surface. A comprehensive description of this subject can be found in many text books, for example by Many et al. [5], Mönch [6], Lüth [7] and Sze [8].

The termination of the periodic structure of a semiconductor at its free surface may form surface localized electronic states within the semiconductor bandgap and/or a double layer of charge, known as a surface dipole. The appearance of surface-localized states induces charge transfer between bulk and surface in order to establish thermodynamic equilibrium between the two. The charge transfer results in a non-neutral region (with a non-zero electric field) in the semiconductor bulk, usually referred to as the surface space charge region (SCR). This region may extend quite deeply into the bulk. Similar considerations are applied to a semiconductor interface.

The fixed charge trapped in surface states originates from bulk free carriers in the bands. We therefore expect the carrier density in the vicinity of the surface to deviate from its equilibrium value and result in a surface SCR. The surface may be found in three different regimes:

(a) Accumulation, where the majority carrier concentration at the surface is larger than its bulk value.
(b) Depletion, where the majority carrier concentration at the surface is smaller than its equilibrium value, but larger than the minority carrier concentration at the surface.
(c) Inversion, where the majority carrier concentration at the surface is smaller than the minority carrier concentration at the surface.

For example, case (b) is depicted in Figure 6.1 for the case of a p-type semiconductor. It is clearly shown that due to downward bending at the surface the distance between the Fermi level (E_F) and the conduction band minimum (E_c) is smaller

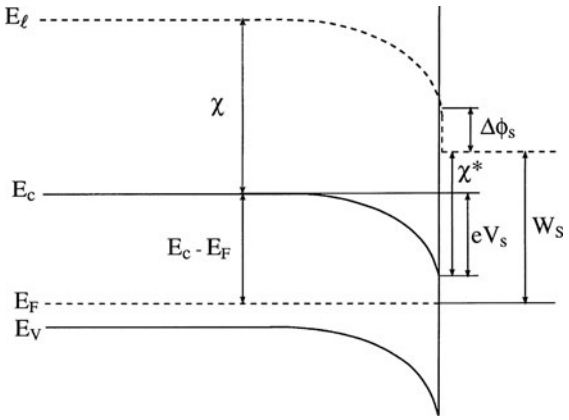

Fig. 6.1 Schematic diagram of the electronic band structure at a semiconductor surface [9]

at the surface with respect to the bulk. This implies that at the surface the density of electrons is larger than its bulk value. Additional quantities that are shown are the surface dipole ($\Delta\phi_s$) that causes the work function to change at the surface, the electron affinity (χ^*) and the work function (W_s). The SCR is also clearly visible in Figure 6.1 as the area where the bands are bent, i.e., where an electric field is present.

The SCR is obtained by solving the Poisson equation. The presence of a non-zero charge density implies a non-zero electric field and potential [8]. Therefore, even under equilibrium conditions the surface potential, denoted as V_s, is different from the electrostatic potential far away in the bulk. This explains the fact that the bands are bent in the vicinity of the surface (this variation manifests itself in a change of the work function because the value of $(E_c - E_F|_s)$, i.e., the distance between the conduction band minimum and the Fermi energy at the semiconductor surface is different from its bulk value). By definition, the energy band is lower the higher the electrical potential is, so that a positive V_s corresponds to downward-bent bands as seen in Figure 6.1. Because we are measuring the variation in the work function we are interested primarily in V_s and not in the exact "shape" of the surface SCR, i.e., the dependence of the electric potential on the distance from the surface. For a given set of semiconductor bulk and surface properties, the value of V_s is dictated by charge neutrality:

$$Q_{ss} = -Q_{sc}, \tag{6.1}$$

where Q_{ss} is the net surface charge and Q_{sc} is the net charge in the SCR (both per unit area). This is because the underlying crystal is the sole supplier of the surface charge. For the calculation of V_s we must know the functional dependence of Q_{ss} and Q_{sc} on V_s (see, for example, Kronik et al. [9]). This explains why by measuring the variation in the work function we can deduce the charge at the surface and the relating electronic properties.

The density and population of surface states may vary across the sample surface, and also the underlying doping concentration may vary (for example in pn structures see below). This means that Q_{ss} and also the surface potential V_s are not constant across the surface. In other words, variation of various sample parameters like doping concentration, surface states density, energy position of surface states, etc. can lead to spatial variations of the work function and therefore, of the contact potential difference (CPD). Another possibility is the presence of surface or interface dipoles. These dipoles can be created by partial charge transfer at the semiconductor/air interface in the presence of adsorbants (e.g., due to "tails" of interface state wave functions) [10–13].

One issue that influences the interpretation of results of Kelvin probe force microscopy (KPFM) measurements is the physical limitation of their lateral resolution. This is very important as the physical size of electronic devices become smaller and smaller. It is accepted that the finite tip size in scanning probe microscopies (SPMs) can have a profound effect on the obtained topographic image. Deconvolution of the tip shape from the image can be determined by several approaches [14–16]. The tip shape can then be used to restore the true surface topography from the measured image. In electrostatic force-based microscopes, the effect of the measuring tip is much larger because the measured forces have an infinite range. Tip effects in electrostatic force and KPFM were discussed and analyzed by several authors [17]. One of the simplest models was suggested by Hochwitz et al. [18], who modeled the tip by a series of (staircase) parallel plate capacitors. Hudlet et al. [19] have presented an analytical evaluation of the electrostatic force between a conductive tip and a metallic surface, while Belaidi et al. [20] have calculated the forces and estimated the resolution in a similar system. Jacobs et al. [21, 22] have extended the calculations for the case of a semiconductor sample, by replacing its surface by a set of ideal conductors with mutual capacitances between them. Another approach using integral equation-based boundary element method combined with modeling the semiconductor by an equivalent dipole-layer and image-charge model was reported by Strassburg et al. [23]. The key conclusion of these works is that the lateral resolution of the KPFM technique can be estimated to be below 20 nm thus giving it a certification as a high spatial resolution microscopy technique. A concise treatment of these issues can be found in Chap. 4 of this book. These theoretical works were complemented in recent years with many experimental works that demonstrated the KPFM ability to measure variations in $V_s(\vec{r})$ on a nanometric scale [24–38].

In the remainder of this chapter we will review these results and explain how a qualitative relation between the measured work function variations and the electrical properties of the surface is obtained. This relation can then be used to explain the influence of the surface on the performance of opto-electronic devices ranging from LED through solar cells to organic TFT. We specifically state that this is a qualitative relation as without exact knowledge of the bulk properties and the method used to fabricate the surface it is impossible to calculate a quantitative one.

6.2 KPFM Measurements of *pn* Junctions

Following the first measurements using KPFM of metal work functions [39–41] one of the basic and important structures that gained a lot of attention is a cleaved *pn*-junction. Devices whose structure is that based on a *pn*-structure like sample having a basic *pn* LED [24, 26, 28] and a laser diode [27] were cleaved and scanned on the cleaved surface as shown in Fig. 6.2.

The predicted built-in bias across the cleaved sample can be calculated using the doping concentrations [8]:

$$V_{\mathrm{bi}} = \frac{k_{\mathrm{B}}T}{e} \ln\left(\frac{N_A N_D}{n_i^2}\right), \tag{6.2}$$

where k_{B} is the Boltzman constant, T the temperature, e the electron charge, N_A and N_D the doping concentrations on the p and n side, respectively and n_i the semiconductor intrinsic density. For example, the sample reported by Shikler et al. [24] that was grown using liquid phase epitaxy,[1] the expected value is $V_{\mathrm{bi}}^{b} = 2\,\mathrm{V}$, however, the measured difference is only $V_{\mathrm{bi}}^{s} = 1.33\,\mathrm{V}$ (the b and s superscripts stand for bulk and surface values) as it can be seen in Figure 6.3 [24].

The lower $V_{\mathrm{bi}}^{\mathrm{s}}$ (compared to $V_{\mathrm{bi}}^{\mathrm{b}}$) is most probably due to two main reasons: band bending due to semiconductor surface states, and/or external charge on the sample surface. Surface states (due to imperfect cleavage and/or oxides on the air exposed sample) can trap holes (electrons) on the cleaved surfaces of the p (n) sides of the junction, creating depletion type band bending opposite in sign on each side of the junction. Thus the bands will bend up in the n-doped region and down in the p-doped region, with the net result being a reduction of $V_{\mathrm{bi}}^{\mathrm{s}}$. The reduction of the built-in voltage on the surface may be used to derive the surface band bending and/or the surface charge on the cleaved crystal. However, the surface states distribution on

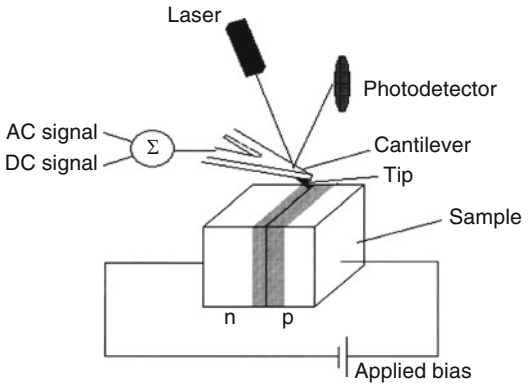

Fig. 6.2 Schematic of the cleaved GaP sample measurement setup under applied forward bias. Equilibrium measurements were conducted with $V_a = 0\,\mathrm{V}$

[1] Elma inc. 103460, Moscow, Zelenograd, Russia.

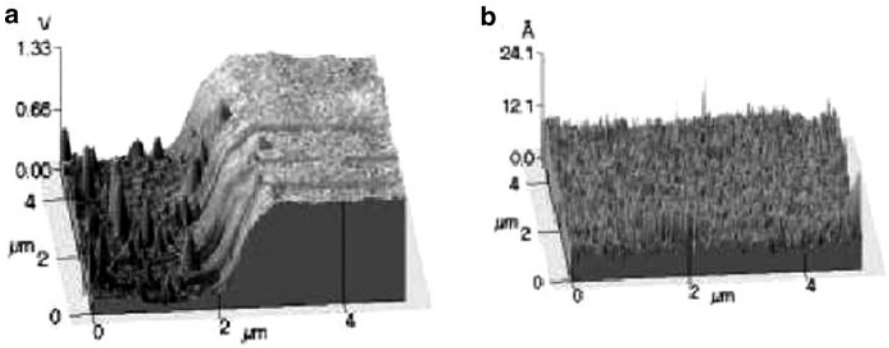

Fig. 6.3 (**a**) Contact potential difference measurements and (**b**) topography of a cleaved GaP *pn*-junction in equilibrium [24]

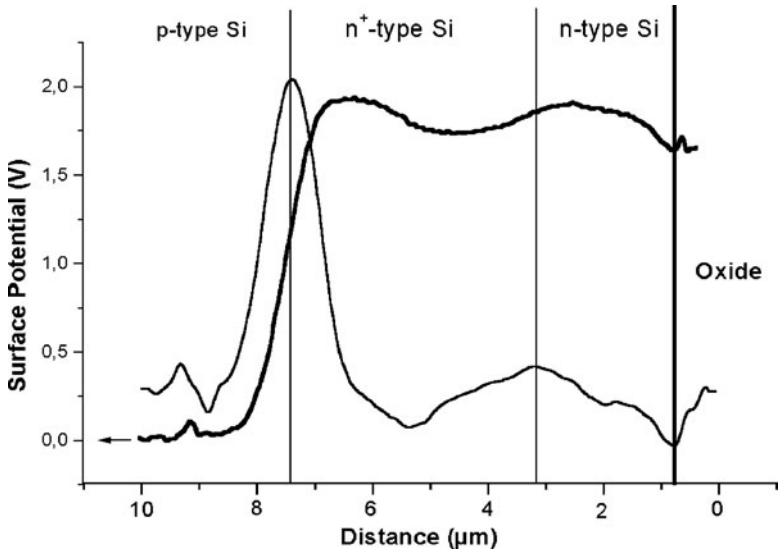

Fig. 6.4 Surface contact potential variations (*bold line*) and surface electric field (*thin solid line*) for reverse diode polarization as function of spatial location on the $pn^{+}n$ junction [29]

the cleaved junction surface is not known and therefore, the band bending can only be estimated by solving the Poisson equation assuming a constant distribution of surface charge [26]. The same phenomenon of reduction in the built-in voltage was also reported by Lévêque et al. [27]. When a forward bias is applied to the junction the built-in potential decreases, however the decrease is not the same as the applied bias. Similar results were reported for reverse bias by Doukkali et al. [29]. In their study they applied a reverse bias of 2 V to a $pn^{+}n$ junction with expected built-in bias at equilibrium of 0.88 V and measured instead of 2.8 V difference just under 2 V as can be seen in Figure 6.4.

The ability to detect the presence of surface states (surface charge) is very important especially for electro-optic devices like LED's and laser diodes. In these devices, part of the light is emitted through the cleaved plane. The emitted light can then be absorbed by the surface states which can lead to reduction in the emitted light intensity. We will shortly elaborate on this issue.

An important fact that can be observed in Figure 6.3 is the inhomogeneous distribution of the potential in the junction plane. Figure 6.3a shows small peaks on the left side of the junction that do not correspond to any topographic feature in Figure 6.3b. Moreover, on the right side of the junction there is a small protrusion at the middle of the right edge. When the junction was forward biased at V_a = 1.54 and 1.62 V the following was observed: some of the peaks at the left side disappear while others decrease in height compared to the average value at the left part of the junction. On the right side the small protrusion becomes larger when compared to the average value of the CPD on the right side as can be seen in Figure 6.5. These results show that the response of the surface is inhomogeneous which can lead in the case of LED to inhomogeneous emission of light.

The above studies lead naturally to the idea of measuring the interaction of light and surface states using KPFM. The basic of solar cells is the photovoltaic effect, where an electron hole pair created by light absorption separates and diffuses to the contacts. A specific variant of the photovoltaic effect is called surface photovoltaic effect. The surface photovoltage (SPV) is defined as the illumination-induced change in the surface potential. This effect, observed at Si and Ge surfaces, was first reported in a short note by Brattain in 1947 [42], followed by a detailed account some years later [43]. Combining the KPFM setup with optical pumping for SPV measurements with high spatial resolution was proposed by Weaver et al. [40]. Since then there were several studies in this area. Shikler et al. [25, 26] showed that light absorption by surface states can be responsible for the inversion of a *pn*-junction at the surface of a GaP LED. This effect, that is not possible in the bulk, is clearly shown in Figure 6.6.

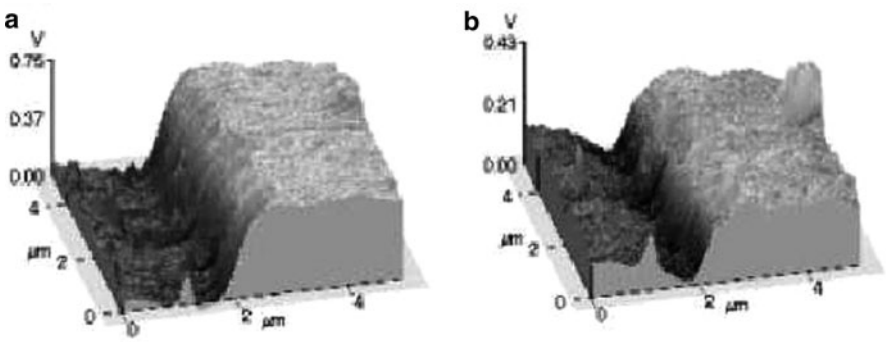

Fig. 6.5 CPD measurements of the GaP *pn*-junction under (**a**) 1.54 V and (**b**) 1.62 V forward bias [26]

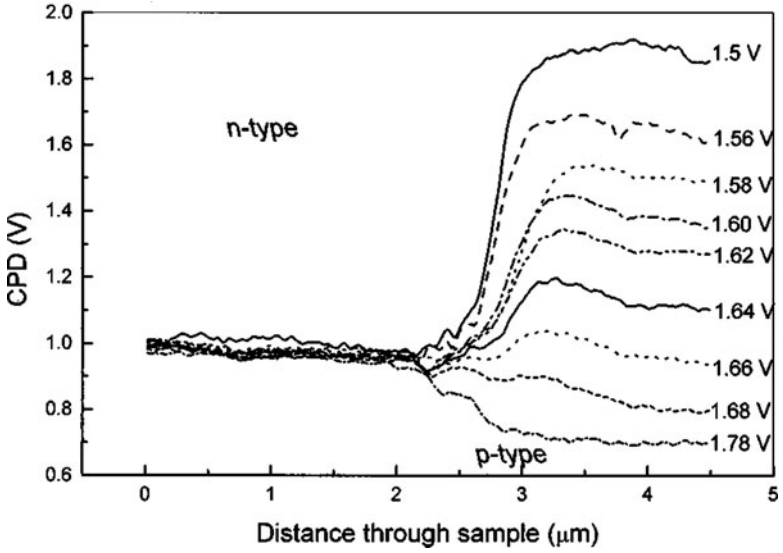

Fig. 6.6 Potential distribution across an GaP LED pn-junction under nine different applied forward bias [26]

The magnitude of $V_{\mathrm{bi}}^{\mathrm{s}}$ changes by about 1.1 V in the bias range between 1.5 and 1.78 V. This large change is unexpected based on the theory of pn-junctions [8]; this theory shows that V_{bi} in the bulk should decrease linearly with a proportionality factor of 1 with increasing forward bias. In principle, a change in $V_{\mathrm{bi}}^{\mathrm{s}}$ which is much larger than the external applied bias can be due to two reasons:

- Reabsorption of light emitted inside the device
- Charging or discharging of surface states

It was found that there is indeed a state whose energy is 2.16 eV below the conduction band minimum that has a transition that can increase the band bending at the p side of the junction as seen in Figure 6.6. Re-absorption of the LED internal emission increases the band bending at the cleaved surface. This may lead to several effects:

1. *High surface reverse currents.* As a result of the inverted junction on the surface, when the LED is biased in the forward direction, the junction on the surface will be under reverse bias. This will increase the device saturation current.
2. *Higher surface recombination rate.* Larger surface depletion fields increase the effective recombination velocity [44]. This will decrease the device efficiency.
3. *Change of the refractive index at the surface.* Large surface electric fields will change the refractive index at the surface due to the linear electro-optic effect. Changes of the surface refractive index will affect the LED radiation pattern.

An additional result, reported in this work, is the direct measurement of minority carrier diffusion length at the surface under illumination. This value is important for devices that are very thin in which it has the dominant length.

6.3 KPFM Measurements of Thin Film Solar Cells, the Role of Grain Boundaries

Recently, Streicher et al. [45] reported on locally resolved SPV on Zn-doped $CuInS_2$ thin films that are used for solar cells. In this work the authors report on a comparative study of pure $CuInS_2$ (CIS) and Zn-doped $CuInS_2$ (CIS:Zn) thin films using surface photovoltage spectroscopy (SPS) in combination with a KPFM setup.

In Figure 6.7 we see a series of normalized SPV spectra taken at different positions along the samples. The ability to take these spectra at nanoscale resolution is due to the combination of KPFM and optical pumping. Using this setup, the authors have shown that polycrystalline $CuInS_2$ and Zn-doped $CuInS_2$ thin films show homogeneous SPV across the sample surface. This indicates that the Zn doping does likely not result in local variations of the band gap. This is a very important result, since variation in the band gap can affect the efficiency of cells . The presence of the Zinc doping manifest itself in the presence of sub bandgap states that it can be described by an Urbach tail with $E_U \approx 74$ meV [46].

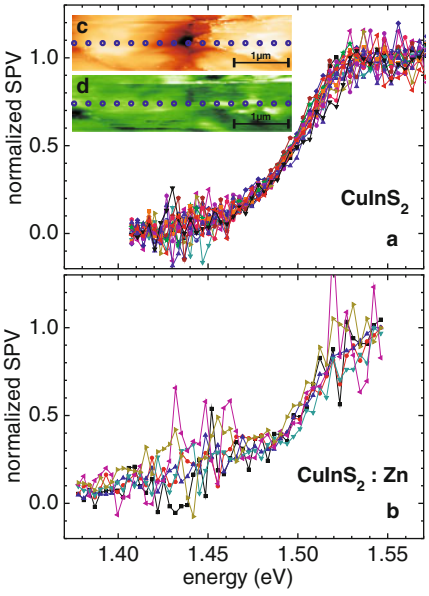

Fig. 6.7 Series of SPV spectra normalized to the maximum SPV of each spectrum for (**a**) pure $CuInS_2$ and (**b**) $CuInS_2$:Zn. The inset shows the position where the spectra on the $CuInS_2$ sample were taken in (**c**) topography and (**d**) work function [45]

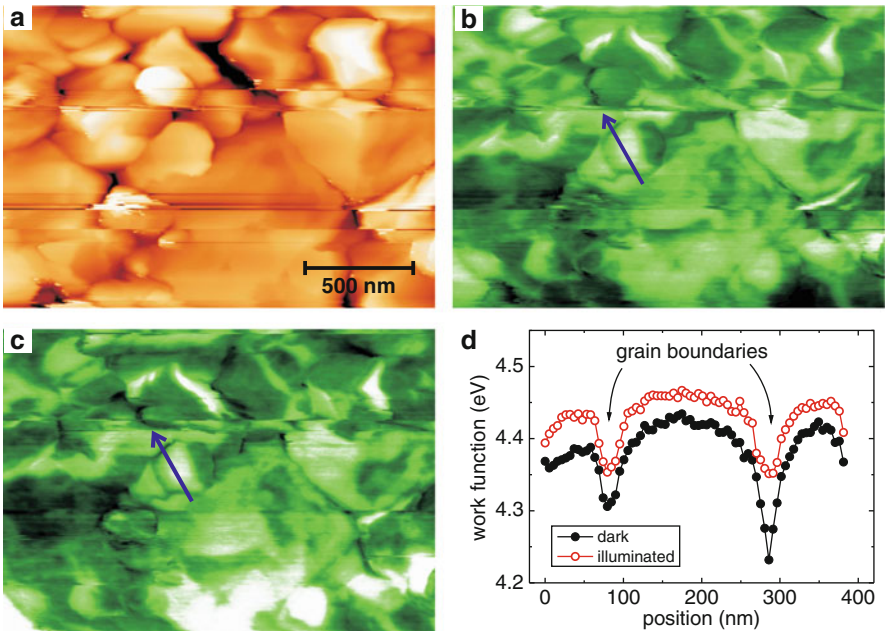

Fig. 6.8 KPFM measurement of a PVD grown $CuGaSe_2$ film. (**a**) Topography ($\Delta z = 360$ nm), (**b**) work function in the dark ($\Phi = 4.23$–4.50 eV) and (**c**) under illumination ($\Phi = 4.20$–4.50 eV). (**d**) Line profile along the *arrow* in (**b**) and (**c**), showing a drop in the work function at the grain boundaries [33]

Many thin films used as absorber in photovoltaic devices are polycrystalline materials. It is of interest to study the role played by the grain boundaries of these films. Sadewasser [33, 47] had reported on microscopic measurements of the individual grain boundaries in Cu–III–VI_2 chalcopyrite. Figure 6.8 shows AFM and KPFM images of a $CuGaSe_2$ film taken in the dark and under illumination. From the images we can infer that there is a dip in the work function at the grain boundaries. We also see the overall SPV response is positive and that it is larger at the grain boundaries than in the grain bulk. This indicates that the boundaries are probably charged. Such charged grain boundaries could increase current collection in the device, thereby compensating for the negative effects of recombination at the grain boundaries defects.

Similar results were reported for CdS/CdTe polycrystalline solar cells by Visoly-Fisher et al. [48, 49]. In their work they have observed the presence of a barrier for hole transport across grain boundaries in solar-cell quality CdTe, a conclusion supported by KPFM data. The barrier height varies between different grain boundaries. This barrier is expected to affect intergrain hole transport of the photocurrent. The demonstrated superiority of polycrystalline over single crystalline CdTe/CdS cells therefore implies that other mechanisms of current collection are operative in these cells (see Fig. 6.9).

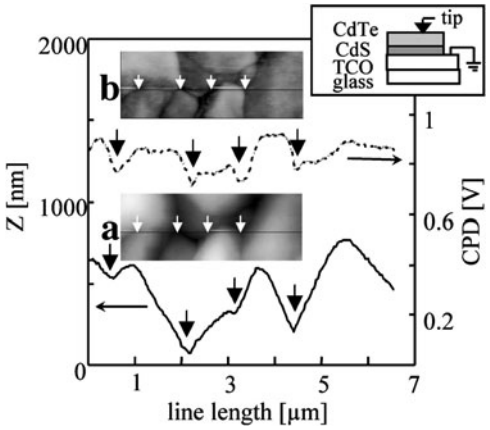

Fig. 6.9 (**a**) AFM topography image and line scan, and (**b**) KPFM image and line scan of a CdTe surface, taken simultaneously. The *lines* in the images indicate the locations of the line scans. The *arrows* indicate the locations of grain boundaries. Scan size was 2.4 µm × 6.7 µm, using a TiO_{2-x}-coated Si tip (Micromasch). The tip-sample separation was 30 nm, and the ac voltage amplitude was ∼6 V. The inset (*top right corner*) shows the schematic arrangement of the measurement. *TCO*: Transparent conducting oxide (here SnO_2:F)

Further measurements on the role of thin CdS films on Cu(In,Ga)Se_2 (CIGSe) solar cells showed that the deposition of a few nm thick CdS on a CIGSe solar cell can improve the quantum efficiency [50]. The authors found that the growth of a thin semiconductor film on top of a polycrystalline substrate can lead to nanoscale material modification around the substrate grain boundaries. When a thin layer of CdS was deposited on the top of CIGSe cells the resulting SPV is smaller and indicates a reduction of recombination as it can be seen in Figure 6.10. This effect is more pronounced at the grain boundaries.

6.4 KPFM Measurements on Organic Materials

To complete this review it will be beneficial to describe some of the work done with KPFM on organic materials. We will start by extending the topic of grain boundaries to the case of polycrystalline organics that are frequently used for thin film transistors (TFTs) [51–53].

Tello et al. [52] investigated charge trapping at the intergrain region (IGR) of pentacene made TFT. Organic field-effect transistors have experienced an impressive development in the last decade which has allowed the appearance of high performance devices with mobilities comparable to those of amorphous silicon [54]. One of the materials that has attracted major attention is pentacene. Mobilities as high as 3–5 $cm^2\,Vs^{-1}$ have been demonstrated in pentacene TFTs [55] and much attention has been devoted to the study of the correlation between the morphology and the

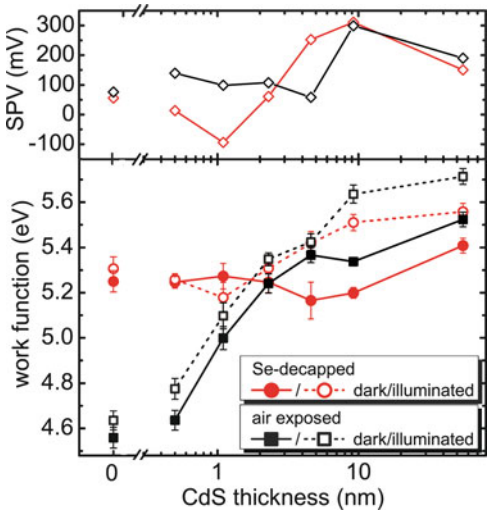

Fig. 6.10 Work function values (*lower graph*) of thin CdS films on a polycrystalline CIGSe film, determined in the dark and under illumination. The *error bars* indicate the full width at half maximum (FWHM) of a Gaussian distribution of the work function values and the *upper part* shows the values of the surface photovoltage [50]

charge transport properties [56]. In their work, they presented a KPFM study performed on transistors with different film thicknesses of the pentacene active layer in order to understand the effect of the film microstructure on the trapping of charges.

An example of an AFM and KPFM measurement in equilibrium and under bias of a TFT made from pentacene is shown in Figure 6.11. It is clear that the surface potential for V_{gs} = 0 V in this unbiased device is equal to 0V both in the pentacene grains and within the IGRs. When a negative bias is applied to the gate electrode, the surface potential in the pentacene grains does not vary, while a negative gate voltage dependent surface potential is measured in the IGRs. As the gate voltage becomes more negative, the potential in the IGRs reaches a minimum value (for $V_{gs} = -25$ V) and then increases again, although it does not go back to 0 V even at the highest bias.

These results provide clear evidence that in very thin pentacene films with island morphology bias stress-induced charge trapping occurs primarily in the thin IGRs between the pentacene islands. In these regions, only an incomplete charge accumulation can be formed and high gate voltages are required to charge portions of the film that are electrically unconnected to the rest of the film at lower gate bias. Once created, the trapped charges cannot be de-trapped in a short time scale. This result answers an important technological question about the operational stability of these devices which is limited by undesirable threshold voltage shifts during prolonged application of bias. The undesirable shift can be correlated with the charge trapping in the polycrystalline pentacene film. The correlation between the trapped charge and the topography indicates that the growth process plays an important role in determining the stability of the device.

The correlation of charge trapping and topographic structure was further observed in pBTTT TFT's [53]. In this work different mesophases exhibit different morphologies resulting in different surface potential distributions and different charge trapping in operating TFT.

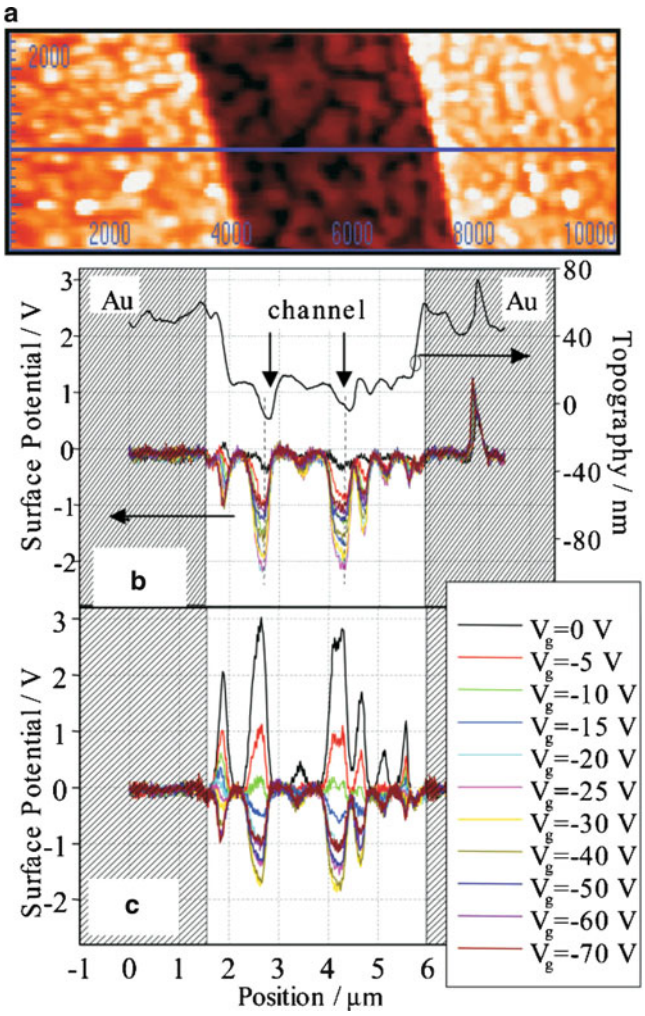

Fig. 6.11 (**a**) Topographic view of an unbiased pentacene TFT sample. The line scans were performed along the *blue line*. The scan area is approximately 2 µm × 10 µm. (**b**) Surface potential profile across the *blue line* at various gate voltages in a previously unbiased sample. The corresponding topographic profile is also shown. The *black arrows* point at the places where the IGRs are. (**c**) Surface potential across the same line, measured immediately after (**b**) [52]

6.5 Concluding Remarks

In this chapter we have reviewed some of the work done on inferring electronic properties of surfaces from KPFM measurements. The works presented show how KPFM measurements can be translated into valuable information regarding electronic and opto-electronic properties that take place in semiconductor devices.

Due to the high spatial resolution of the technique, nanoscale features can be studied and the physics of the processes that govern device performance can be deduced on nanometer scale.

References

1. E. Wigner, J. Bardeen, Phys. Rev. **48**, 84 (1935)
2. J. Bardeen, Phys. Rev. **49**, 653 (1936)
3. Hölzl, F.K. Schulte, *Work Function of Metals, Springer Tracts in Modern Physics*, vol. 85 (Springer, Berlin, 1979)
4. A. Kiejna, K.F. Wojiechwski, Prog. Surf. Sci. **11**, 293 (1981)
5. A. Many, Y.Goldstein, N.B. Grover, *Semiconductor Surfaces*, 2nd edn. (North-Holland, Amsterdam, 1971)
6. W. Mönch, *Semiconductor Surfaces and Interfaces* (Springer, Berlin, 1993)
7. H. Lüth, *Surfaces and Interfaces of Solids*, 2nd edn. (Springer, Berlin, 1993)
8. S. Sze, *Physics of Semiconductor Devices* (Wiley, New York, 1985)
9. L. Kronik, Y. Shapira, Surf. Sci. Rep. **37**, 1 (1999)
10. J. Tersoff, Phys. Rev. B **30**, 4874 (1984)
11. J. Tersoff, Phys. Rev. Lett. **56**, 2755 (1986)
12. W. Lambrecht, B. Segall, O. Anderson, Phys. Rev. B **41**, 2813 (1990)
13. N. Christensen, Phys. Rev. B **37**, 4528 (1988)
14. P. Markiewicz, M. Goh, Langmuir **10**, 5 (1994)
15. P. Markiewicz, S. Cohen, A. Efimov, D. Ovichinnikov, A. Bukharaev, Probe Microsc. **1**, 355 (1999)
16. J.S. Villarubia, J. Res. Natl. Inst. Stand. Technol. **102**, 425 (1997)
17. Y. Rosenwaks, R. Shikler, T. Glatzel, S. Sadewasser, Phys. Rev. B **70**, 085320 (2004)
18. T. Hochwitz, A. Henning, C. Levey, C. Daghlian, J. Slinkman, J. Vac. Sci. Technol. B **14**(1), 457 (1996)
19. S. Hudlet, M.S. Jean, C. Guthmann, J. Berger, Eur. Phys. J. B **2**, 5 (1998)
20. S. Belaidi, F. Lebon, P. Girard, G. Lévêque, S. Pagano, Appl. Phys. A **66**, 239 (1998)
21. H. Jacobs, P. Leuchtmann, O.J. Homan, A. Stemmer, J. Appl. Phys. **84**(3), 1168 (1998)
22. H.O. Jacobs, A. Stemmer, Surf. Interface Anal. **27**(5–6), 361 (1999)
23. E. Strassburg, A. Boag, Y. Rosenwaks, Rev. Sci. Instr. **76**(8), 083705 (2005). doi:10.1063/1.1988089. URL http://link.aip.org/link/?RSI/76/083705/1
24. R. Shikler, T. Meoded, N. Fried, Y. Rosenwaks, Appl. Phys. Lett. **74**(20), 2972 (1999)
25. T. Meoded, R. Shikler, N. Fried, Y. Rosenwaks, Appl. Phys. Lett. **75**(16), 2435 (1999)
26. R. Shikler, T. Meoded, N. Fried, B. Mishori, Y. Rosenwaks, J. Appl. Phys. **86**(1), 107 (1999)
27. G. Lévêque, P. Girard, E. Skouri, D. Yarekha, Appl. Sur. Sci. **157**, 251 (2000)
28. M. Shvebelman, P. Urenski, R. Shikler, G. Rosenman, Y. Rosenwaks, M. Molotskii, Appl. Phys. Lett. **80**(10), 1806 (2002)
29. A. Doukkali, S. Ledain, C. Guasch, J. Bonnet, Appl. Surf. Sci. **235**, 507 (2004)
30. S. Sadewasser, T. Glatzel, R. Shikler, Y. Rosenwaks, M. Lux-Steiner, Appl. Sur. Sci. **210**, 32 (2003)
31. C. Barth, C.R. Henry, Nanotechnology **17**(7), S155 (2006)
32. C.S. Jiang, H.R. Moutinho, M.J. Romero, M.M. Al-Jassim, L.L. Kazmerski, Appl. Phys. Lett. **88**(6), 061909 (2006)
33. S. Sadewasser, Thin Solid Films **515**, 6136 (2007)
34. R. Oliver, Rep. Prog. Phys. **71**, 076501 (2008)
35. A. Lochthofen, W. Mertin, G. Bacher, L. Hoeppel, S. Bader, J. Off, B. Hahn, Appl. Phys. Lett. **93**, 022107 (2008)

36. C. Lin, T. Merz, D. Doutt, M. Hetzer, J. Joh, J. del Alamo, U. Mishra, L. Brillson, Appl. Phys. Lett. **95**, 033150 (2009)
37. C. Baumgart, M. Helm, H. Schmidt, Phys. Rev. B **80**(8), 085305 (2009)
38. L. Liu, G. Li, Appl. Phys. Lett. **96**, 083302 (2010)
39. Y. Martin, D. Abraham, H. Wickramasinghe, Appl. Phys. Lett. **52**(13), 1103 (1988)
40. J. Weaver, D. Abraham, J. Vac. Sci. Technol. B **9**(3), 1559 (1991)
41. J. Weaver, H. Wickramasinghe, J. Vac. Sci. Technol. B **9**(3), 1562 (1991)
42. W.H. Brattain, Phys. Rev. **72**, 345 (1947)
43. W. Brattain, J. Bardeen, Bell System Tech. J. **32**, 1 (1953)
44. B. Bedny, N. Badus, Semiconductors **27**, 431 (1993)
45. F. Streicher, S. Sadewasser, T. Enzenhofer, H.W. Schock, M. Lux-Steiner, Thin Solid Films **517**, 2349 (2009)
46. F. Urbach, Phys. Rev. **92**, 1324 (1953)
47. C. Leendertz, F. Streicher, M. Lux-Steiner, S. Sadewasser, Appl. Phys. Lett. **89**, 113120 (2006)
48. I. Visoly-Fisher, S.R. Cohen, D. Cahen, Appl. Phys. Lett. **82**(4), 556 (2003)
49. I. Visoly-Fisher, S.R. Cohen, D. Cahen, C.S. Ferekides, Appl. Phys. Lett. **83**(24), 4924 (2003)
50. T. Glatzel, M. Rusu, S. Sadewasser, M. Lux-Steiner, Nanotechnology **19**, 145705 (2008)
51. H. Huang, H.Wang, J. Zhang, D. Yan, Appl. Phys. A **95**, 125 (2009)
52. M. Tello, M. Chiesa, C. Duffy, H. Sirringhaus, Adv. Func. Mater. **18**, 3907 (2008)
53. T. Hallam, M. Lee, N. Zhao, I. Nandhakumar, M. Kemerink, M. Heeney, I. McCulloch, H. Sirringhaus, Phys. Rev. Lett. **103**, 256803 (2009)
54. G. Horowitz, Adv. Mater. **10**, 365 (1998)
55. H. Klauk, M. Halik, U. Zschieschang, G. Schmid, W. Radlik, W.Weber, J. Appl. Phys. **92**, 5259 (2002)
56. Y.Y. Lin, D. Gundlach, S. Nelson, T. Jackson, IEEE Trans. Elec. Dev. **44**, 1325 (1997)

Chapter 7
Surface Properties of Nanostructures Supported on Semiconductor Substrates

F. Krok, J. Konior, and M. Szymonski

Abstract The surface electronic properties, related to nanostructures grown on semiconductor substrates, are presented. Major experimental results were obtained in UHV with the use of Kelvin probe force microscopy (KPFM). Investigated systems include epitaxial nanostructures assembled on InSb(0 0 1) by submonolayer deposition of Au, semiconductor nanostructures grown on lattice-mismatched semiconductor substrates, semiconductor surfaces with surface modification and nanostructuring induced by ionizing irradiation, and dielectric structures grown on InSb(0 0 1). A new efficient algorithm for the evaluation of electrostatic forces in the tip–plane system is also presented. As a theoretical step, the results of contact potential difference values for tip–plane systems are presented and compared with the experimental data, showing good agreement between theory and experiment. We also analyze and discuss the important issue of high resolution contrast obtained, with the use of the KPFM method. In particular, using the Au/InSb(0 0 1) system as an example, we address a key problem of the limits of lateral resolution in KPFM. Then, the subject of the quasi-spectroscopic KPFM measurements is being discussed, together with the phenomenon of the so-called short-range bias-dependent electrostatic interactions.

7.1 Introduction

In the advent of nanotechnology, the growth of nanostructures on substrate surfaces has been extensively studied driven by the interest in new physical and chemical properties of structures of reduced dimensions. A recent tendency in miniaturization of electronic devices, as well as exciting prospects of new emerging technologies are

F. Krok (✉) · J. Konior, · M. Szymonski
Institute of Physics, Jagiellonian University, ul. Reymonta 4, 30-059 Krakow, Poland
e-mail: franciszek.krok@uj.edu.pl

S. Sadewasser and T. Glatzel (eds.), *Kelvin Probe Force Microscopy*, Springer Series in Surface Sciences 48, DOI 10.1007/978-3-642-22566-6_7,

prompting a huge interest in the science of nanostructured materials. In particular, there is a need to develop efficient methods for preparation of functionalized surfaces with desired structural and electronic properties. Standard spectroscopic techniques used for the surface characterization, like for example, determination of surface voltage, surface barrier height, interface trap density or doping density, are insufficient when applied to the characterization of nanometer size objects due to their limited spatial resolution. Particularly, the measurement of the nanometer-scale surface potential distribution is necessary for analyzing nanodevice properties. Therefore, there is a need for developing nondestructive, diagnostic tools that can probe into a variety of surface related properties, down to a nanometer scale range. In this chapter we demonstrate that the Kelvin probe force microscopy (KPFM) technique can be used for the characterization of nanosized structures deposited on semiconductor surfaces. The KPFM technique, based on dynamic force microscopy (DFM) principles, gives information on topography and potential distribution of the sample with high spatial resolution.

The chapter is organized as follows. In Sect. 7.2, the KPFM experimental system is described together with the optimization procedure of the feedback parameters for CPD measurements. In Sect. 7.3, the KPFM studies of surface properties of metallic and semiconductor nanostructures assembled on semiconductor substrates are shown. In Sect. 7.4, the results of KPFM imaging of the ion beam-induced nanostructuring of semiconductor surfaces are presented. Then, in Sect. 7.5, based on the example of dielectric films grown on InSb(0 0 1), we discuss the issue of ultimate sensitivity and lateral resolution of the KPFM technique. The experimental CPD contrasts are compared with predictions of the theoretical model (Sect. 7.5.2) of the tip–sample electrostatic interactions. In Sect. 7.6, using KPFM imaging of Au/InSb(0 0 1) as an example, we provide experimental evidence of KPFM sensitivity to short-range and bias-dependent interactions, acting between the tip and the surface. Finally, Sect. 7.7 summarizes the chapter.

7.2 Experimental

The essential part of the results presented in this chapter was obtained with a home-build KPFM, which is basically a modified VP2 AFM/STM Park Scientific Instruments (PSI) device. The KPFM measurements were performed in UHV (pressure $\sim 5 \times 10^{-11}$ mbar) and at room temperature (RT). Figure 7.1a presents a schematic plot of the VP2 STM/AFM set-up with the modification allowing for simultaneous contact potential difference (CPD) measurements (the electronics within the dashed line). In the measurements, the topography was acquired using a non-contact FM mode, with silicon (boron-doped) piezoresistive cantilevers, purchased from Park Scientific Instruments. Prior to the measurements the tip was cleaned in the UHV conditions following the procedure described in [1]. The tip of conical shape with a half opening angle of about 20°, has an apex radius of about 20 nm, as checked by high resolution scanning electron microscopy (SEM).

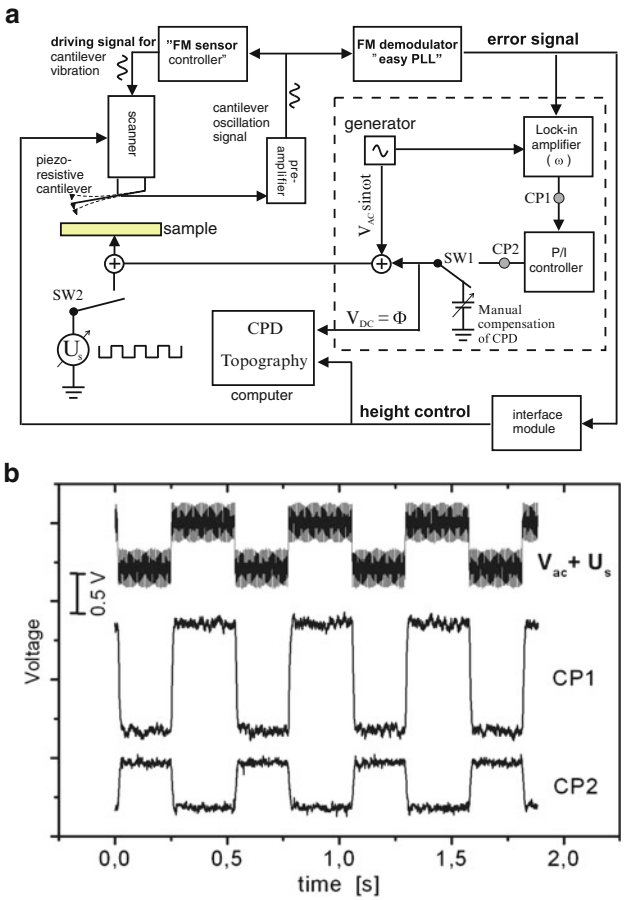

Fig. 7.1 (**a**) Schematic circuit diagram of the VP2 PSI setup with the modifications allowing for the operation in FM–KPFM mode in UHV (the scheme of electronics within the *dashed line*). (**b**) Signals which are tracked during the procedure of optimization of the electronic feedback parameters allowing for optimum performance of the CPD compensation. For fine tuning of the feedback, first the feedback loop is opened (SW1 set to manual) and an external square-wave voltage (SW2 – closed) is applied to the sample – see the upper signal ($V_{ac} + U_S$). Then, the lock-in parameters are optimized until the lock-in output signal (signal CP1) reflects the external square-wave voltage shape. Finally, with closed feedback loop (SW1 closed) the PI controller gains are optimized until its output signal (signal CP2) tracks the external voltage source

During the experiments, the frequency shift Δf with respect to the resonant frequency (detuning), was set in the range between −3 and −110 Hz, and a constant oscillation amplitude A was kept in the range between 20 and 50 nm; the scanning rate was 0.2–0.5 scanline per second. For the CPD measurements, the feedback electronics containing a sine-wave voltage generator, a lock-in amplifier (Stanford Research Systems, SR510) and PI controller was implemented to the original VP2

set-up. During the normal KPFM mode operation, the sample was biased with a *dc*-voltage plus an *ac*-voltage of angular frequency ω, with $f = \omega/2\pi = 600\,\text{Hz}$, and amplitude $V_{\text{ac}} = 300\,\text{mV}$. The time-dependent tip-sample interaction, with an angular frequency ω, induces a variation of the FM demodulator (Nanosurf "easyPLL") output. This ω-component is detected through the x-component of a lock-in amplifier, then a feedback loop (Kelvin PI controller) is used to add a *dc*-voltage to the sample in order to compensate the CPD between the tip and the sample. As a result, the acquired *dc*-map represents the distribution of the measured sample surface potential. By definition, throughout the chapter, the bright contrast on the CPD maps (the higher CPD) represents areas of a higher work function. In order to ensure the stable potential measurements and high sensitivity of the system, special care has been taken for proper optimization of the feedback parameters. In the electronics circuit, the access signal check points are added (see Fig. 7.1a) to control the output signals of the lock-in amplifier (CP1) and the PI controller (CP2). There are also two switches: SW1 to turn off the feedback for manual compensation of the CPD and SW2 to apply a square-wave voltage to the sample. In the following, we describe the procedure of optimization of the electronic feedback parameters, allowing for optimum performance of the CPD compensation. The procedure is performed upon the approach of the cantilever to the surface and before scanning the surface. First, with SW1, the circuit loop is opened and the *dc*-voltage is changed manually, until the CP1 signal becomes zero (the compensation of local CPD). Next, with the help of SW2, a square-wave voltage is supplied to the sample surface and the lock-in amplifier is tuned. The sensitivity, time constant, and phase shift of the lock-in amplifier are adjusted until the regular square-wave signal at CP1 is obtained. Then, for final tuning of the feedback with the help of SW1, the feedback loop is closed and the PI controller gains are optimized until the signal at CP2 tracks the external square-wave voltage. The signals are shown in Figure 7.1b. Once this is done, the external voltage is disconnected with SW2 and the system is ready to perform the measurements in the KPFM mode.

7.3 Self-Assembling on Semiconductor Surfaces

7.3.1 Epitaxial Au Nanostructures Assembled on InSb(0 0 1)

Metal nanostructures on surfaces are very often studied in view of their possible applications in various fields, including nanoelectronics. In particular, they could be essential for fabrication of atomic scale conductive interconnects providing electric contact with basic elements of molecular electronic devices, such as single organic molecules and molecular circuits [2]. From a practical perspective, semiconductors and insulators are the most interesting substrates, since their geometrical and electronic structures are well known and large atomically flat terraces of such materials can be prepared with sufficient precision. As a consequence, there is

an intense activity aiming to develop efficient methods for patterning on large scale substrates and films, with regular arrays of nanostructures having functional properties. Suitable solutions for such a task might be provided by thermally-assisted assembling processes occurring at atomically ordered surfaces of $A_{III}B_V$ semiconductors. In particular, gold seems to be a good candidate for manufacturing nanometer-scale flat metallic patches on surfaces and/or conductive nanowires, aligned by the strongly anisotropic structure of the surface reconstruction rows and ridges of the metal-terminated (0 0 1) face of $A_{III}B_V$ semiconductors [3]. In the case of submonolayer deposition of Au on reconstructed InSb(0 0 1), Goryl et al. [4] reported on formation, morphology, and composition of Au nanostructures strongly dependent on the substrate temperature during deposition, or post-growth thermal annealing. They have found that Au deposition on the substrate kept at 400 K results in the formation of rectangular islands with edges on average 15 nm long, oriented along $\langle 0\,1\,1 \rangle$ and $\langle 1\bar{1}0 \rangle$ crystallographic surface directions (see Fig. 7.2a). The

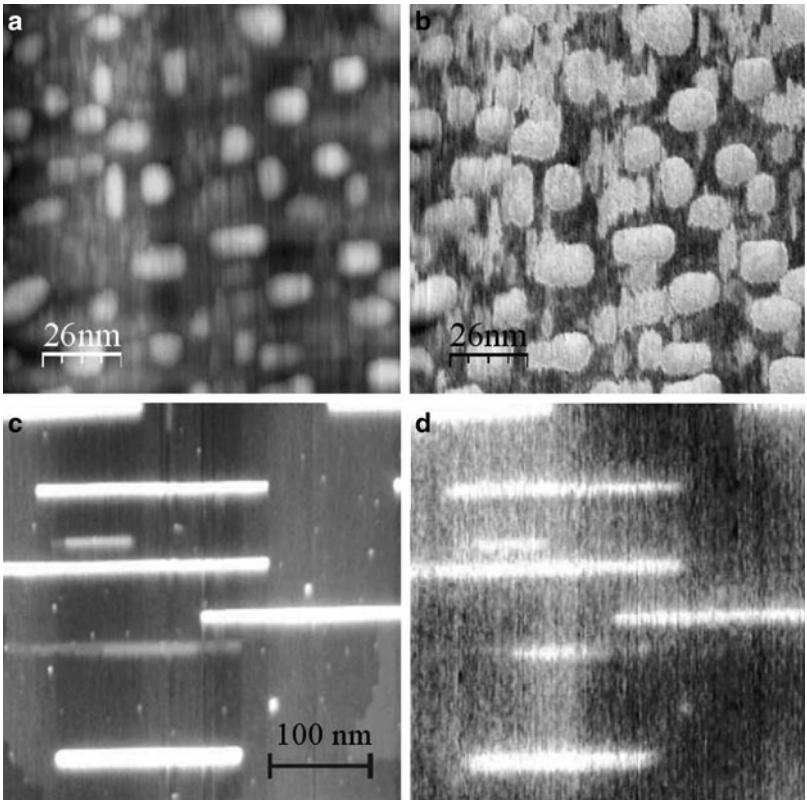

Fig. 7.2 Nanostructures created by Au deposition (<1 ML) on InSb(0 0 1) surfaces at temperatures of (**a**) 400 K and (**c**) 600 K with corresponding CPD maps (**b**) and (**d**), respectively. Sizes of the images: (**a**)–(**b**) 130×130 nm^2 and (**c**)–(**d**) 400×400 nm^2. Reproduced with permission from [3] and [4]

average height of the islands is of 1 nm. Although the reconstructed InSb(0 0 1)c (8×2) surface is strongly anisotropic and has the characteristic ridge-row structure along the ⟨110⟩ direction [5], there is no statistically significant preference in creating islands along atomic troughs on the InSb surface. This is consistent with previous reports, which state that large Au adsorbate clusters can disrupt the structure of the substrate and, therefore, they do not exhibit anisotropy along the ⟨1 1 0⟩ direction [6]. Also, the topography image shows that a certain amount of the deposited material is spread over the surface (between well defined islands), perhaps bound in the troughs of the reconstructed c(8×2) InSb(0 0 1) surface. A LEED pattern obtained for such a system indicates the c(8×2) reconstruction, characteristic for the clean substrate, although of somewhat lower quality, which might indicate that gold is not intermixing with the substrate material. Therefore, one could think that both the islands and the material accumulated between them are built of gold, not mixed with the substrate material. This hypothesis is confirmed by a CPD image presented in Figure 7.2b, showing a high quality contrast and a relatively low noise level. It is also evident that both the islands and the features between the islands have higher work function than the one corresponding to the substrate material. This is corroborated by the fact that the work function of Au(0 0 1) ($\phi = 5.2$ eV [7]) is higher than that of clean InSb(1 1 0) ($\phi = 4.7$ eV [8]).

For Au nanostructure assembling the substrate temperature seems to be the most important factor. A general tendency is that the higher the deposition temperature, the better organization of the nanostructures is observed. This is most likely due to the increase of gold atom diffusion with the temperature. Increasing the sample temperature during deposition by additional 200 K results in formation of narrow, long structures (nanowires) with a length up to 800 nm (see Fig. 7.2c). The nanowire orientation follows the ⟨110⟩ direction on the reconstructed InSb(0 0 1) surface. The nanowires are of different height and at both ends they have wings of lower height than the central part of the nanowires. The local CPD mapping of the nanostructures (Fig. 7.2d) exhibits a lack of contrast in the CPD signal over the wings and the nanowires with heights not exceeding two atomic layers. Only the nanowires with heights larger than 2 ML show an increased CPD with respect to the InSb(0 0 1) substrate surface. The KPFM measurements strongly indicate a non uniform chemical composition along the nanowires. The lack of the CPD contrast over the lower parts indicates that they are of the same chemical composition as the surrounding substrate surface. Accordingly, atomically resolved imaging of the wings (see Fig. 4 in [3]) closely resembles the structure of the substrate atomic reconstruction. The same behavior has been found for the nanowires with a height not exceeding 2 ML. Only the upper parts of the nanowires (>2 ML) have a regular 1×1 structure with the CPD clearly different from the substrate surface. Although this is a strong indication that the upper part of the nanowire is composed of gold atoms, recent STM measurements of nanowires assembled in a Au/InSb(0 0 1) system at 600 K do not support this expectation [9]. The STM images acquired with the chemical contrast on atomic-scale level have proven that the upper part of the nanowires is composed of two kinds of atomic species, most likely due to the formation of an InAu alloy phase. The height dependent composition of the

structures sheds light on the mechanism of self-organization of Au atoms on the InSb surface upon the deposition process [3].

Subsequent annealing of the system could produce further modification of its structure and atomic composition. It has been established that the post-growth annealing of the initial gold islands at a temperature of 600 K results in the formation of an InAu alloy phase [10]. Figure 7.3a, b presents the topography and the simultaneously acquired CPD map of the system of gold islands grown at 400 K and subsequently annealed to 600 K for 2 h. The islands preserved their initial rectangular shape, but their average size is almost doubled (16 nm across in comparison to 9 nm across as deposited) and the material accumulated previously in the substrate troughs, seen in Fig. 7.2a, disappeared. The corresponding CPD image, contrary to the KPFM measurements of the as-grown islands, shows significantly lower surface potential on the islands, as compared to the substrate. The inversion of the CPD contrast suggests a composition change of the islands. It seems that upon annealing in the presence of the gold overlayer there is a disruption of the cation–anion bonds on the substrate surface, leading to segregation of indium atoms

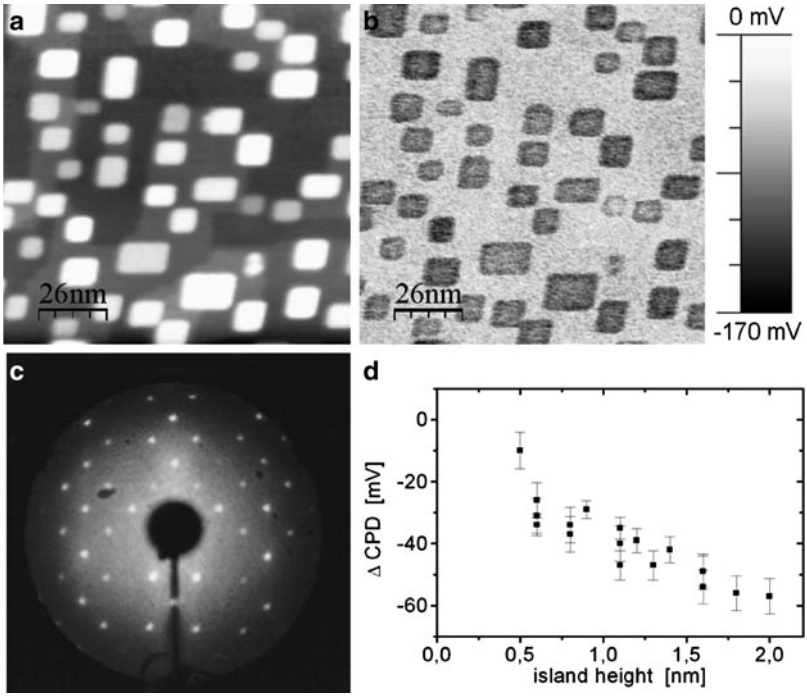

Fig. 7.3 (**a**) Topography and (**b**) CPD map of the Au/InSb(0 0 1) system grown at 400 K and later annealed to 650 K for 2 h. (**c**) Corresponding LEED image with the c(4×4) pattern characteristic for Sb-rich InSb surface reconstruction. (**d**) CPD signal dependence on the island height extracted from (**b**). The CPD gradually decreases with the island height and finally saturates at about −55 mV for the height of 2 nm. Reproduced with permission from [11]

and their dissolution in the Au islands [10]. Interdiffusion of surface In atoms into the islands should result in an enrichment of the substrate surface by Sb atoms. This hypothesis is supported by a LEED pattern of the annealed system (Fig. 7.3c) exhibiting the c(4×4) symmetry characteristic for a Sb-rich reconstruction. Since the islands cover less than 30% of the surface and the pattern is very bright, it is safe to assume that the LEED pattern comes predominantly from the substrate.

The surface potential of the islands depends on their height, as depicted in Figure 7.3d, in such a way that the higher islands exhibit lower CPD with respect to the substrate surface. The measured island surface potential monotonically decreases with the island height and finally saturates at the level of about −55 mV for an island height of about 2 nm. Such a dependence of the metal overlayer work function on the overlayer thickness, with its subsequent saturation at some level, is commonly observed. For example, in the Au/W(0 0 1) system [12], the measured work function saturates at a value corresponding to the one of bulk Au, at the minimum coverage of 3 ML of Au. Moreover, the high-resolution KPFM imaging of the islands shows that the work function is not uniform across the island and it is lower on the island edges than in its central part. A laterally resolved CPD measurement on a single island step is shown in Fig. 7.4b. As expected, the CPD signal along the island edge is reduced with respect to the island top surface. From the ΔCPD histogram (Fig. 7.4c), the relative decrease of the CPD at the edge is about 11 mV. It is well known from macroscopic contact potential (CP) investigations that stepped metal surfaces exhibit a lower work function when compared to flat surfaces [13], which can be simply explained in the frame of the jellium model approximation [14]. It is known that a considerable smoothing of the electron density occurs at stepped metal surfaces [15] due to the fact that the energy of an electron in the vicinity of a large flat plane is lower than when it is surrounded by complicated morphologies like, for example, a step edge. This means that charge flows from hills into the valleys formed by the surface atoms of the step edge (see Fig. 7.4d). Consequently, on the hill a net positive charge arises whereas at the valley there is a net negative charge inducing the dipole moments at the steps and finally, the decrease of the work function.

7.3.2 Semiconductor Nanostructures Grown on Lattice-Mismatched Semiconductor Substrates

Due to its unique capabilities, KPFM is often used for the characterization of self-assembled semiconductor nanostructures [like quantum wires (QWrs) and dots (QDs)] grown on lattice-mismatched semiconductor substrates. Such nanostructures are widely studied not only for better understanding of low-dimensional electron systems [16] but also due to important applications in electronic and photonic design and manufacturing [17, 18]. Further interest in studying nanometer-size QDs stems from their extraordinary abilities for charge storage [19], cold electron

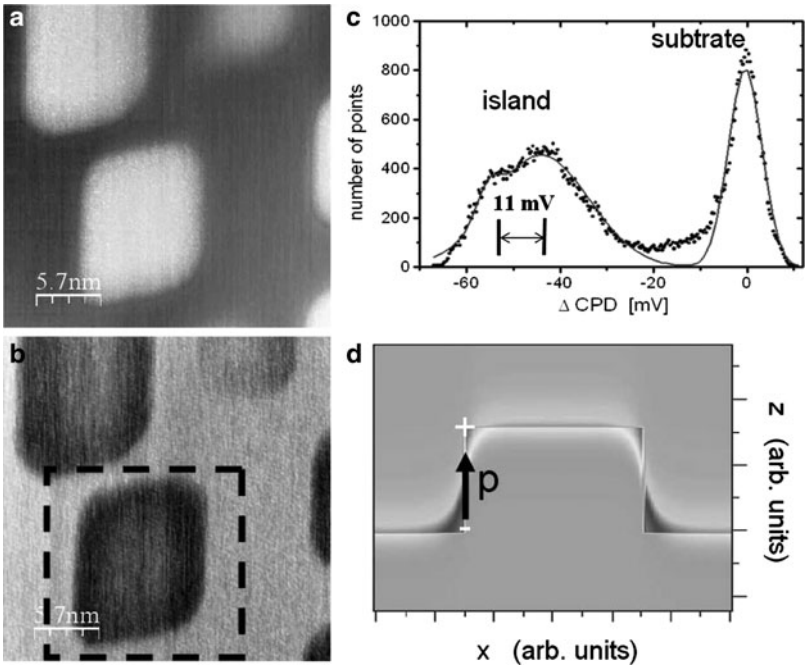

Fig. 7.4 (**a**) High-resolution topography image of the Au/InSb(001) system after annealing to 650 K with (**b**) corresponding CPD map. The measured CPD signal is not uniform across the whole island. (**c**) CPD histogram taken over the marked area in (**b**). The contact potential on the island edge is about 11 mV lower compared to the top of the island as can be seen from the histogram. (**d**) The decrease of the CPD signal at the edge is attributed to the dipole moments which are localized at the step in the frame of the jellium model approximation for stepped metal surfaces. The drawing in (**d**) is from [14]

emission [20], and photoluminescence [21]. The work function of a single QD is an important parameter for such a device because it is related to the barrier height for the carrier injection into, or for the carrier ejection from the QD. The KPFM is a powerful tool for investigation of the local electronic states and transport properties of modern nanoelectronic devices. Salem et al. [22] used the KPFM, under ambient conditions, to investigate the CPD of nanocrystalline silicon (nc-Si) dots with various sizes before and after dot charging. nc-Si dots of 2–8 nm were grown by plasma decomposition of SiH_4 on a thin SiO_2 layer, covering the Si(100) substrate surface. The local charge injection to the dots was performed using the biased tip in the contact mode. Figure 7.5 shows the topography and CPD images of the nc-Si dots as-grown ((a) and (b)) and after the charging process ((c) and (d)), respectively. It is seen that the charging process does not change the substrate surface potential, whereas it influences the local surface potential of the dots. The change of the dot CPD depends on the dot size, i.e., larger dots have a higher potential value. These experimental findings indicate that the KPFM allows for detection of the quantity

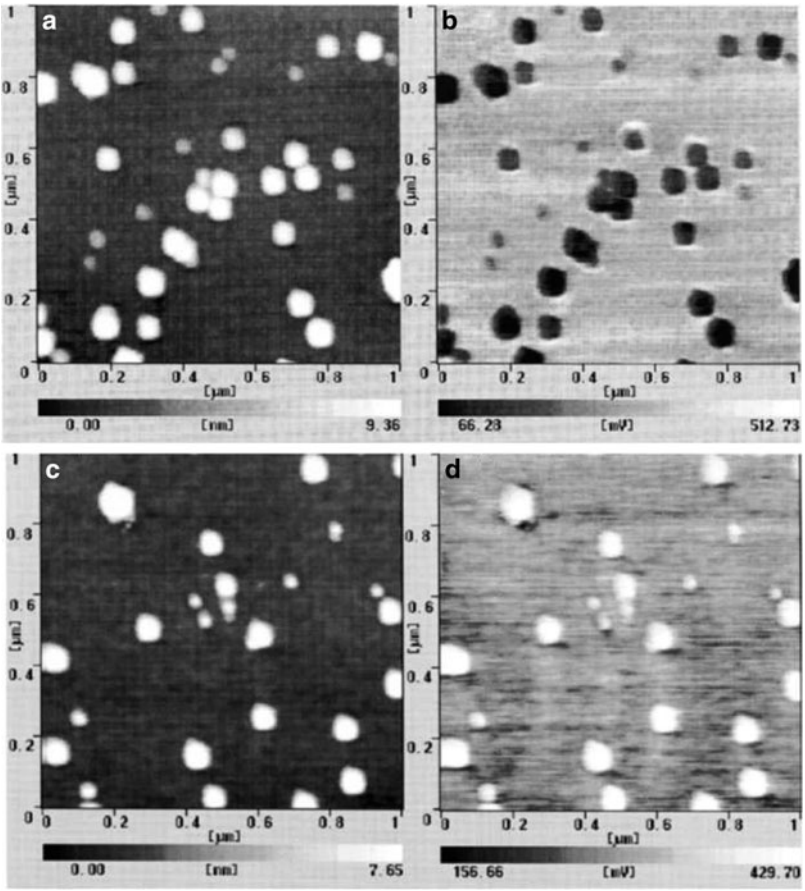

Fig. 7.5 (**a**) Topographic and (**b**) corresponding surface potential images for nc-Si dots before and (**c**) and (**d**) after dots charging, respectively (Reprinted with permission from [22]. Copyright 2007, American Institute of Physics)

of the charge confined in nanostructured objects. Measuring the CPD changes as a function of the dot diameter and comparing the results with the calculated charging energy of separated dots, the number of injected electrons can be evaluated. It has been found [22] that one electron could be stored in a nc-Si dot of diameter up to 2.8 nm, whereas there can be three electrons in dots having diameters from 4.7 to 7.4 nm.

Yamauchi et al. [23] used KPFM in UHV to investigate the correlation between the size and the local work function of InAs QDs, grown on GaAs(0 0 1). The QDs of height from 1.3 to 7.2 nm and lateral size from 20 to 40 nm have been grown by molecular beam epitaxy (MBE). The measured values of the InAs QDs CPD depend on the dot height, as shown in Figure 7.6. The height dependence of the

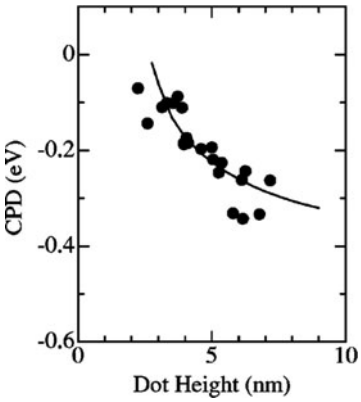

Fig. 7.6 Dot height dependence of the CPD for InAs QDs. *Closed circles* and the *solid curve* indicate the measured CPD and the calculated one, respectively. The numerical calculations of the dot height dependence of the surface potential were performed taking into account a quantum disk model for the quantum size effect [24]. The presented CPD is expressed in values relative to the wetting layer (WL) value (Reprinted with permission from [23]. Copyright 2007, American Institute of Physics)

CPD is interpreted in terms of the quantum size effects, by which the amount of charge accumulated in the QD is determined by the discrete energy levels of the QD. That is, in thermodynamic equilibrium, due to the difference of the Fermi energies of InAs and GaAs, the carriers (mostly electrons) in the InAs/GaAs heterostructure should be transferred from a GaAs to an InAs dot. Then, the charge distribution induced by the charge transfer creates an electrostatic potential on the QD surface. Carriers in the InAs QD are confined in the nanometer-scale region and the discrete energy levels are created. The net number of carriers transferred into the InAs dots depends on the energy difference between the discrete levels in the dot and the conduction-band bottom of the substrate. Therefore, the local surface potential of the QDs created by the charge distribution depends on the dot height through the number of discrete energy levels.

7.4 Surface Modification and Nanostructuring Induced by Laser Ablation and Ion Beams

Apart from self-assembling of the deposited material presented in the previous sections, there is another convenient technique for surface nano-manufacturing. For decades, it has been known that the interaction of particles and photons with solids leads to modification of their surfaces and formation of regular, periodic nanostructure patterns like ripples, dots, or wires [25, 26]. It appears that the

particular shape and size of such structures can be controlled by a proper choice of the irradiation conditions [27, 28].

In the case of laser-induced ablation, the ripple or dot patterns result from non uniform melting, due to intensity variations in the interference pattern between the incident laser field and the surface or capillary wave of same frequency, induced in the target [29]. Reif et al. [30] reported the use of KPFM to study the electronic properties of a nanostructured silicon surface produced by femtosecond laser ablation. Figure 7.7a presents the chains of regularly arranged spherical nanodots with a diameter of about 120 nm produced on silicon surface at an intermediate dose (1,000 pulses at 1.1×10^{12} W cm^{-2}). Such a morphology is of interest for possible applications as a template for biomolecule immobilization. Although the target is composed of a single element material, the KPFM measurements revealed a variation of the surface potential of the nanostructured Si surface, as it is shown in Fig. 7.7b, where the CPD of the laser-induced nanodots is decreased by about 50 mV with respect to the untreated substrate. It is proposed that the CPD map reflects the local change of the sample contact potential, since experiments on similar structures on metalized dielectrics showed that purely topological variations alone could not result in a variation of the CPD signal. In order to explain the origin of the observed contrast in the CPD of laser ablated silicon, the dependence of the CPD signal variation on the dopant concentration of the irradiated silicon crystals has been measured. The obtained results indicate that a dopant segregation due to partial liquefaction is the main mechanism responsible for the change of the surface potential on the laser ablated silicon surfaces [30].

In the case of ion bombarded solids, the main processes involved in nanostructuring are: surface sputtering, mass transport processes due to momentum transfer

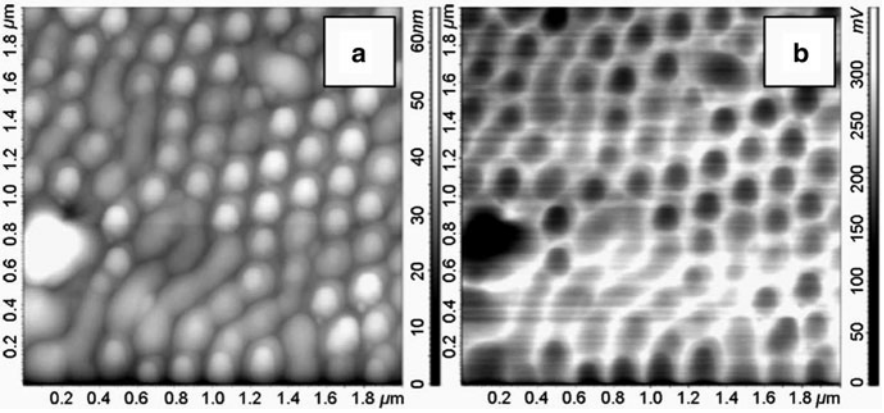

Fig. 7.7 (**a**) Typical morphology of femtosecond laser ablated silicon (a circular laser polarization) exhibiting chains of spherical nanodots with a diameter of about 120 nm and (**b**) the simultaneously recorded CPD map. The surface potential of the nanodots is lower by about 50 mV as compared to the one of the surrounding area. The measurement was performed at ambient conditions. Reproduced with permission from [30]

in the collision cascades in the target, and diffusion (thermally or beam enhanced) on the irradiated surfaces. Typically, for the normal ion beam incidence dot patterns are observed [31], whereas for the oblique incidence periodic height modulations (ripple structures) are observed [32]. The above behavior is also seen for the InSb(0 0 1) surface where dot-like and wire-like structures of diameter of a few tens of nanometers are created [33]. Apart from the morphological evolution, ion bombardment can also induce changes in the elemental composition of irradiated multi-component surfaces. Due to preferential sputtering, partial sputtering yields depend on the atomic masses and surface binding energies of the constituents [34]. Such theoretical predictions are consistent with an experimentally observed large non-stoichiometry for the InP surface [35], possibly because of the large mass difference between In and P atoms. However, for compounds with similar masses of the constituents, like GaAs or InSb, this theory is not able to predict partial sputtering yield ratios.

KPFM can provide valuable information on the composition of ion-induced nanostructures on InSb(0 0 1). In Figure 7.8, the topography and the CPD images of a InSb(0 0 1) surface irradiated with an Ar ion beam at 4 keV and a fluence of 2.1×10^{16} ions/cm^2, are shown. In the topography image (Fig. 7.8a), there are two dots interconnected with a long wire. There is also a small cluster close to the wire. In the CPD image (Fig. 7.8b), the corresponding CPD signal contrast indicates that all those structures are made of a material with a different work function with respect to the surrounding InSb substrate. For both, the wire and the dots, the work function is lower than for the substrate area. The decrease of the work function is size dependent, as illustrated by the line profile across the surface contact potential image (Fig. 7.8c). The potential of the larger dot is lower by about 50 mV with respect

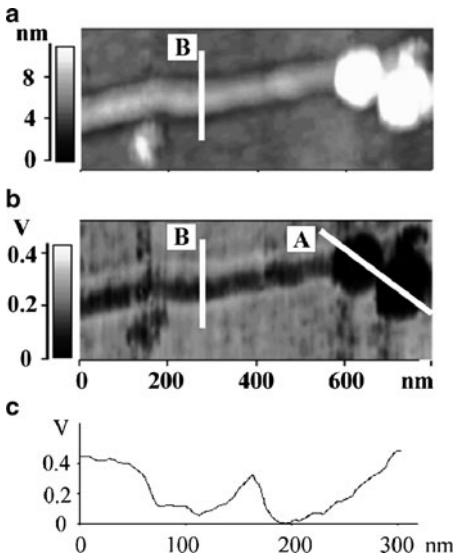

Fig. 7.8 (**a**) Topography and (**b**) CPD images of nanostructures developed on a InSb(0 01) surface irradiated with a 4 keV Ar ion beam and acquired with KPFM. (**c**) Line profile of the CPD map of the dots, taken along the line marked by A. From [33]

to the potential of the neighboring smaller dot. The CPD contrast of the wire, on average, is less than half of the dots (Figs. 7.8c and 7.9). However, the differences in CPD values cannot be directly ascribed to the differences in the relative composition of In and Sb in the nanostructures. The electrostatic force is a long-range interaction and, as a result, the obtained surface potential distribution can also be affected by averaging effects due to a finite tip size. Results of several other experiments, in which ion irradiated InSb surfaces were investigated with spectroscopic methods indicate that the surfaces are enriched in indium [36]. However, a lack of the lateral resolution in the spectroscopic measurements does not allow for a direct determination of the form in which the excess indium atoms are accumulated on the bombarded surface. We have compared these results with the KPFM measurements performed on the nanostructured InSb(0 0 1) surface. KPFM could reveal that the wires and the dots are made of a material with a different work function than that for the irradiated InSb (see Fig. 7.8b). The lower work function of the nanostructures compared with that of the substrate, indicates the excess of indium, since the work function of In ($\phi_{\mathrm{In}} = 4.12\,\mathrm{eV}$) is lower than that of the irradiated InSb(0 0 1) surface ($\phi_{\mathrm{irrad.InSb}} = 4.6\,\mathrm{eV}$ [37]).

Indium enrichment of the wires and dots means that there are metallic-type structures generated on the semiconductor substrate [38]. In such a case, the condition of thermodynamic equilibrium implies that the Fermi levels of the two materials must coincide with each other. This condition is fulfilled due to a charge transfer and band bending near the interface in analogy with that on the interface between a bulk metal and a semiconductor (Schottky barrier model). The direction of electron flux in a metal–semiconductor contact depends upon the relative values of work functions of the two materials and the electrons will travel from the material with the smaller work function to the material with the higher one. As in the present

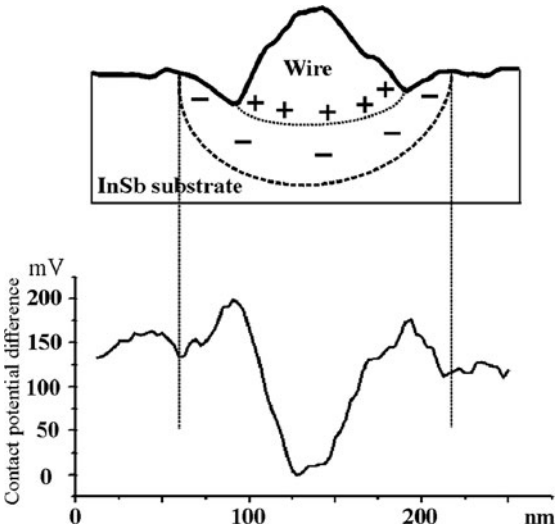

Fig. 7.9 Line profiles of the wire topography (*upper graph*) with the corresponding profile of the CPD signal (*lower graph*). The profiles are taken along the lines marked with B in Figure 7.8a, b, respectively. In the upper graph a substrate region enriched in electrons is drawn schematically. From [33]

case, $\phi_{\text{nanostructure}} < \phi_{\text{substrate}}$, the electrons are transferred from the nanostructures to the substrate. As a result, the metal–semiconductor interface is charged and there is a certain region in the semiconductor substrate enriched in electrons. Figure 7.9 shows the line profile (cross-section) of the wire (taken along line B in Fig. 7.8), with the corresponding cross-section of the wire's CPD image. The deep minimum in the CPD signal, corresponding to the potential of the wire, is accompanied by two "shoulders" on its both sides. The signal at the shoulder maxima is higher by about 50 mV in comparison with the potential of the InSb substrate. In the CPD image (Fig. 7.8b) the "shoulders" are visible as two bright stripes, aligned along the broad dark stripe, corresponding to the CPD of the wire. The maximum of the "shoulders" corresponds to the border between the wire and the substrate. It is likely that the increased CPD signal in the shoulders reflects the charged metal-semiconductor interface. We have associated the width of the CPD "shoulders" (from their onset to their maximum) with the thickness of the substrate region enriched in electrons. In Figure 7.9, a cross-section of the substrate region enriched in electrons is drawn schematically. The termination of the enriched region on the surface implies that the substrate areas on both sides of the wire should be negatively charged. In fact, the increased magnitude of the CPD signals on both sides of the wire support the concept that the areas around the wire are negatively charged. This was already shown by Sommerhalter et al. [39], who demonstrated that in the CPD image the bright contrast corresponds to negatively charged areas.

7.5 Dielectric Structures Grown on InSb(0 0 1)

Apart from metallic and semiconductor nanostructures on surfaces, the KPFM technique has been also used to study the properties of insulating films on semiconductor surfaces. In particular, alkali halide films are often considered as model systems and they have been studied extensively in recent years. This is both, because of their interesting physical properties and because of their importance as insulator/semiconductor interfaces in all technologies for electronics. It has been established that alkali halide films can be grown epitaxially on $A_{III}B_V$ compound semiconductors [40]. This is due to a strong chemical bond between the halogen ion and the A_{III} atom on the substrate surface, and due to the possibility of choosing the $A_{III}B_V$ compound with a lattice (zincblende type) matched closely to the lattice of the given alkali halide (rock-salt type). An example of a closely matched alkali halide/$A_{III}B_V$ adsorption system is KBr/InSb(0 0 1): InSb has the lattice constant 6.47 Å and KBr has the lattice constant 6.58 Å.

A typical topographical image of the KBr/InSb(0 0 1) surface is shown in Figure 7.10a. The coverage of KBr is about 0.2 ML. The substrate surface is composed of large, atomically flat terraces. The monatomic substrate steps are oriented along the main substrate surface crystallographic directions of $\langle 1\,1\,0\rangle$ and $\langle 1\bar{1}0\rangle$.

KBr is aggregated into monoatomically thick islands (visible on the image as brighter features) which are elongated along the $\langle 1\,1\,0\rangle$ crystallographic direction.

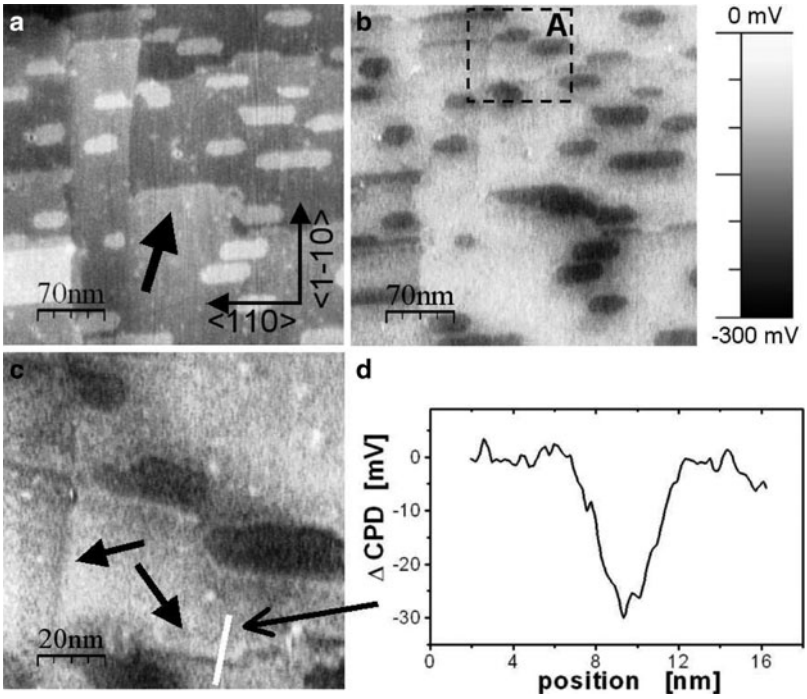

Fig. 7.10 (**a**) Topography and (**b**) CPD images of KBr islands grown on a InSb(0 0 1) surface acquired with KPFM. The *black arrow* in (**a**) indicates the KBr island which is topographically not resolved from the substrate terrace and can be identified only with the help of the CPD image. (**c**) High-resolution CPD image of the zone marked with A in (**b**). Together with the decreased CPD signal corresponding to the KBr islands, a dark zigzag line (indicated by the *black arrows*) corresponding to the substrate terrace edges and reflecting the variation of electrostatic potential along the substrate monatomic steps is observed. (**d**) Line profile of the CPD taken along the white line indicated in (**c**). From [41]

The island shapes indicate that the diffusion of KBr molecules during the film growth is highly anisotropic; this is due to the structure of the substrate surface, which is composed of atomic rows along the ⟨1 1 0⟩ direction [5]. The KBr molecules aggregate into compact islands of different lateral size but uniform in height (i.e., of 1ML thickness). The average lateral dimensions of islands can be controlled by the amount of deposited material, i.e., the surface coverage. Depending on the nominal surface coverage of KBr, islands as small as a few nm^2 and as large as $100 \times 100\,nm^2$ can be created, with the coverage in the range from 0.2 to 0.7 ML of KBr, respectively.

A CPD image of the KBr/InSb(0 0 1) surface, acquired simultaneously with the surface topography is shown in Figure 7.10b. The dark features on the CPD map correspond to the KBr islands. The darker contrast on the KBr islands (lower voltage) corresponds to a locally decreased work function of the islands,

as compared to the substrate. There are a few features of the system under study which are discussed below.

First, there is a straightforward observation, emerging from the comparison of Figure 7.10a, b, which demonstrates the advantage of using KPFM for imaging heterogeneous surfaces. That is, there are some KBr islands (marked by the arrow in Fig. 7.10a), which have grown up attached to the substrate terrace edge and they are topographically not distinguishable from the substrate terrace. They can be recognized only if the CPD signal is acquired simultaneously with the topography.

Second, by compensating the electrostatic interaction, KPFM can image the true topography of heterogeneous structures, contrary to what is measured with the conventional dynamic force microscopy (DFM) technique [42]. For DFM, the surface topography is acquired by keeping the total interaction between the vibrating cantilever and the sample constant. In the case of imaging heterogeneous structures, the visible topography is highly influenced by the difference of the electrostatic interaction between the probe and the imaged surface areas of different composition. For the KBr/InSb the "height" of the KBr islands measured in the DFM images (the sample bias kept constant) is about 2.57 Å, whereas KPFM reads a "height" of about 3.19 Å. The last value is in good agreement with the height of a monatomic terrace step on the KBr(0 0 1) crystal surface ($\sim$ 3.32 Å) as measured with DFM alone.

Third, the high-resolution CPD map presented in Figure 7.10c reveals that the two KBr islands, separated by 4 nm from each other, can easily be distinguished. Moreover, in the CPD map seen in Figure 7.10c, together with the "dark islands" corresponding to the KBr overlayers, there is a decrease of the surface potential visible in a form of a zigzag line (see the black arrows in the image). The zigzag line corresponds to the substrate terrace edges and it reflects the variation of the electrostatic potential (ES) across the monatomic steps. The variation of the ES indicates trapping of electrical charge at step states which induces pinning of the Fermi level [39]. The measured drop of the CPD (decrease of the work function) indicates that the steps are positively charged. In Figure 7.10d the cross section of the CPD values, taken along the white line indicated in Figure 7.10c, shows a drop in the CPD signal of about 30 mV. However, the measured value of the reduction of the surface potential should not be directly assigned to the magnitude of a variation of the electrostatic potential. Most likely the true local ES variation is much higher but the measured value is highly influenced by averaging due to the large tip size. This can be also deduced from the line profile, the spatial resolution in the KPFM measurements is of 5 nm.

7.5.1 Accuracy of KPFM Signal Measurements

There is yet another issue we would like to point out on the example of KPFM imaging of the KBr/InSb(0 0 1) system. That is, in the CPD images shown in Figure 7.10b ,c, the shapes of the KBr islands are well defined, although the surface potential on the substrate and the island sites is not homogeneous. The

inhomogeneity of the surface potential results from the influence of the averaging effect on the measured CPD values, due to the finite tip size. The CPD signal gets lowered when measured close to or between the islands. The non-uniformity of the substrate work function points out to the issue of the accuracy of CPD signal measurements. There are two effects that may influence the correctness of CPD measurements and they should be considered as stemming from the long-range nature of the electrostatic forces. First, the averaging of the measured CPD is due to the contribution of the whole tip, which is much larger than the island itself. Thus, the region surrounding the island contributes to the measured CPD values. Second, the tip vibrations make the obtained CPD values averaged over the whole tip trajectory.

To determine the relative change of the KBr island work function with respect to the substrate surface work function, we first employ the point Kelvin probe force spectroscopy (KPFS). In Figure 7.11 the Kelvin probe force spectroscopy performed on the InSb(0 0 1) surface covered with a submonolayer of KBr film is shown. To perform the KPFS measurements, at first, the surface is imaged to obtain the topography. Subsequently, the scan range is set to zero and the probe is moved to the desired location (over the substrate surface to point A) for the KPFS. Then, the feedback loop is disabled and the sample bias is scanned over a certain range. Simultaneously, the error signal (detuning) from the PLL demodulator is collected. Since the tip–sample distance is kept constant during the KPFS measurements (disabled feedback loop), the detuning signal versus bias voltage curve is characteristic of a pure electrostatic force in the tip–sample system. Subsequently, the measurement is repeated over the KBr island [point (B)]. In both cases a parabolic dependence of the detuning signal on the bias voltage is obtained since the electrostatic force is a quadratic function of the bias voltage (see Fig. 7.11b). The maxima correspond to the sample bias, for which the CPD between the chosen areas on the surface and the tip is nullified. Although the absolute values of the tip work function is unknown, the difference in the surface potentials of the two different locations on the sample surface can be measured. The relative difference of the sample bias voltage, corresponding to the parabola maximum,

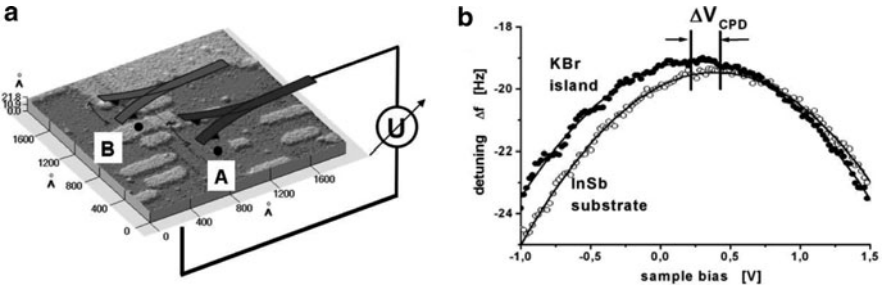

Fig. 7.11 Principle of the Kelvin probe force spectroscopy performed on the KBr/InSb(001) system. In (**a**) the topography of the KBr/InSb surface with the two points marked with A (substrate) and B (KBr island) where the dependence of detuning versus sample bias voltage were taken and are presented in (**b**). From [43]

provides the difference in the contact potentials of the surface sites, where the spectroscopy is performed. The KPFS measurements prove that the work function of the KBr film (or the KBr/InSb interface) is lower by about 210 meV with respect to the work function of the bare and clean InSb surface.

A wide range of KBr island sizes, grown on InSb, offers great opportunities for studying the lateral resolution, as well as for checking the accuracy of the KPFM contrast. For studying the limits of the CPD signal accuracy in FM–KPFM measurements, we have analyzed the dependence of CPD, as taken over the KBr islands, on lateral island dimensions. We selected the islands with the length to width ratio not higher than 1.5 and then we assumed the islands to be of equivalent quadratic shape. In Figure 7.12, the measured CPD, as a function of the KBr island size (i.e., the island side length), is shown. It is clear that the measured CPD depends on the size of the islands and CPD saturates for the island size larger than 100 nm.

The value of the saturated CPD in FM–KPFM corresponds to the values measured with point KPFS and indicates that there is no observable tip-induced band bending effect for the system under study, as demonstrated recently by Rosenwaks et al. [44]. We have found that the observed saturation of the CPD for islands of size around 100 nm is in good agreement with the previously reported lateral resolution of FM–KPFM of 50 nm, obtained by Zerweck et al. [45], when only a single boundary of a KCl island grown on Au was imaged. When even smaller KBr islands are imaged, the tip obviously also senses the contact potential of the substrate and hence the CPD is significantly reduced. According to the experimental data, when the size of the KBr islands is comparable to the size of the tip apex (i.e., about 20 nm) the CPD signal provides only about 50% of the correct potential value (see Fig. 7.12).

7.5.2 Theoretical Model of Electrostatic Tip–Sample Interaction

In order to analyze and understand the KPFM experimental results, the electrostatic forces in tip–plane systems have to be evaluated with sufficient accuracy and reasonable computing effort. The main difficulty in such a computation is due to

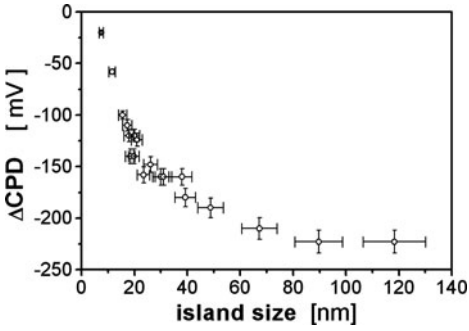

Fig. 7.12 Measured CPD over the KBr islands versus the island size. The evaluated tip–sample distance is of 1 nm

the large variation of the geometrical scale, as the tip–plane distance, tip size, and the plane dimension differ in orders of magnitude. Also, non-constant potential distributions on a plane – which are due to differences in the work function of various materials placed onto the plane – may introduce further difficulties. In the simplest case, considered in most of the theoretical investigations, the plane has a fixed electrostatic potential relative to an axially symmetric tip placed above the plane. Except for the simple cases of high symmetry tips, such as a sphere [46], analytical solutions for such problems are not usually possible. As a result, almost all important results were obtained by various numerical [47–52] or quasi-analytical [45,53,54] methods. In [55], we have presented an efficient method for calculating the electrostatic force in tip–plane systems. The method is suitable for an arbitrary surface potential distribution and it consists of two basic steps. First, the Green function formalism is applied to integrate out exactly the potential distribution in the plane, reducing the task to an effective electrostatic boundary value problem for the tip surface only.

In the second step, the resulting effective problem is solved by a standard numerical scheme. It should be stressed that on the contrary to many previously published methods [45, 47–54], the developed approach is not limited to a constant value of the plane potential and, furthermore, does not require the tip to be axially symmetric.

To analyze the effect of experimental conditions on the accuracy of FM–KPFM results, we calculated numerically the CPD values for an idealistic tip–surface geometry and for non-uniform potential distributions on the surface. As the first step of the calculation, an electrostatic tip–surface force was evaluated with an efficient method suitable for an arbitrary surface potential distribution. In the following part of this subsection, the essential elements of the developed method [55] and calculated results are presented.

7.5.2.1 Outline of the Method

The system considered is built of an infinite plane surface, at $z = 0$, and the tip placed in the region $z > 0$. The approximation to an infinite plane seems sufficient for most applications, where the plane segment is much larger than the tip size and the tip–surface distance. The electrostatic potential distribution in the plane is denoted by $V_1(x, y)$ and the potential of the tip surface is fixed at V_0. The above described original electrostatic potential problem is known in electrostatics as the Dirichlet boundary value problem and it was shown in [55], finding the tip surface charge density $\sigma(\mathbf{r})$ is equivalent to solving the following linear integral equation:

$$V_0 = \Phi_1(\mathbf{r}) + \frac{1}{4\pi\epsilon_0} \oint_{TS} G(\mathbf{r}, \mathbf{r}')\sigma(\mathbf{r}')\, \mathrm{d}S', \tag{7.1}$$

with the unknown surface charge density function $\sigma(\mathbf{r})$ being limited to only the tip–surface ($\mathbf{r} \in TS$). The physical meaning of (7.1) is the following. The electrostatic

potential on the tip–surface, being equal V_0, has two sources: the plane potential distribution $V_1(x, y)$ and the tip surface charge density $\sigma(\mathbf{r})$. The function $\Phi_1(\mathbf{r})$ includes all the contribution from the plane and is given by the following surface integral involving $V_1(x, y)$ and the outward normal derivative of the electrostatic Green function $G(\mathbf{r}, \mathbf{r}')$:

$$\begin{aligned}\Phi_1(\mathbf{r}) &\stackrel{\text{def}}{=} -\frac{1}{4\pi}\oint_{z'=0}\frac{\partial G(\mathbf{r},\mathbf{r}')}{\partial n'}V_1(x',y')\,\mathrm{d}x'\,\mathrm{d}y' \\ &= +\frac{1}{4\pi}\oint_{z'=0}\frac{\partial G(\mathbf{r},\mathbf{r}')}{\partial z'}V_1(x',y')\,\mathrm{d}x'\,\mathrm{d}y'. \end{aligned} \tag{7.2}$$

Here $G(\mathbf{r}, \mathbf{r}')$ is the exact electrostatic Green function [56]:

$$G(\mathbf{r},\mathbf{r}') = \frac{1}{|\mathbf{r}-\mathbf{r}'|} - \frac{1}{|\mathbf{r}-\mathbf{r}'_1|}, \tag{7.3}$$

with the vectors $\mathbf{r} = [x, y, z]$, $\mathbf{r}' = [x', y', z']$, and $\mathbf{r}'_1 = [x', y', -z']$. The integral term of the right side in (7.1) is the tip surface charge density contribution to the electrostatic potential on the tip surface. It is composed of two subterms, one follows from the Coulomb law, while the second presents the image charge contribution [therefore, there are two terms present in (7.3)]. Equation (7.1) is exactly equivalent to the original problem formulated for the plane plus tip surface system with an arbitrary potential distribution on the plane. Moreover, as we proved in [55], for any rectangle type region in the plane, the integral in (7.2) may be evaluated analytically.

7.5.2.2 Numerical Implementation

After the plane contribution to the potential is integrated out exactly and the term $\Phi_1(\mathbf{r})$ is evaluated, any of the existing numerical methods may be used to solve the resulting integral equation. The method we used is similar to the so-called surface charge method [50] and with this method, calculation of the force on the tip proceeds as follows. The tip surface is first divided into N small surface segments ΔS_i, each with the central point at $\mathbf{r}_i$ and with constant surface charge density σ_i. Then, using (7.1) for these points, the following set of N linear equations is obtained:

$$V_0 - \Phi_1(\mathbf{r}_j) = \sum_{i=1}^{N} F_{ji}\sigma_i, \tag{7.4}$$

with the free term contribution $\Phi_1(\mathbf{r}_j)$ computed from (7.2) and $j = 1, 2, \ldots, N$. The matrix elements F_{ji} are defined as:

$$F_{ji} = \frac{1}{4\pi\epsilon_0}\oint_{\Delta S_i} G(\mathbf{r}_j,\mathbf{r}')\,\mathrm{d}S', \tag{7.5}$$

and for a given tip–plane geometry, the elements F_{ji} are evaluated and stored for subsequent use. The system of linear equations (7.4) is the main formula for the numerical implementation of the method and shows explicitly its advantage by limiting computation to the finite tip surface, thus eliminating from the numerical part of the infinite plane. Once the system of N linear equations (7.4) is numerically solved, the surface charge densities σ_i are known and the force acting on the tip may be evaluated:

$$\mathbf{F} = \frac{1}{2\epsilon_0} \sum_{i=1}^{N} \sigma_i^2 \Delta S_i \hat{\mathbf{n}}_i , \tag{7.6}$$

with $\hat{\mathbf{n}}_i$ being the unit vector normal to the tip surface at $\mathbf{r}_i$.

7.5.2.3 Main Calculated Results

To test the proposed method, a system with typical and realistic geometry was investigated. Figure 7.13 shows geometrical details of the system studied, in which the tip consists of a cone with spherical end segments. The lower apex has radius $r_{\text{tip}} = 10\,\text{nm}$, the total tip length is $L_{\text{tip}} = 10\,\mu\text{m}$, the cone half angle is $\Theta = 10°$, and the bottom point of the tip has the coordinates $[x_c, y_c, d_{\text{min}}]$.

For simplicity, the cantilever was not included in the calculation. This might be taken into account by extending the tip–surface region, thus increasing the number of the matrix elements defined by (7.5).

As the first application, we considered a single potential step along the line $y = 0$ in the plane $z = 0$:

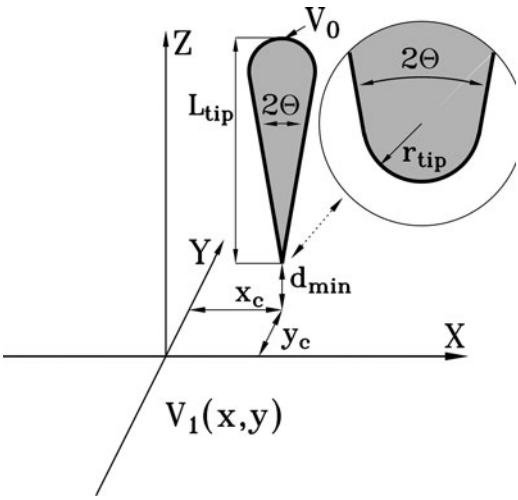

Fig. 7.13 Geometry of the tip–plane system studied in this work, with details of the tip apex geometry shown in the inset. The potential distribution on the plane is marked as $V_1(x, y)$ and the tip surface has the potential V_0. (Reprinted with permission from [55]. Copyright 2007, American Institute of Physics)

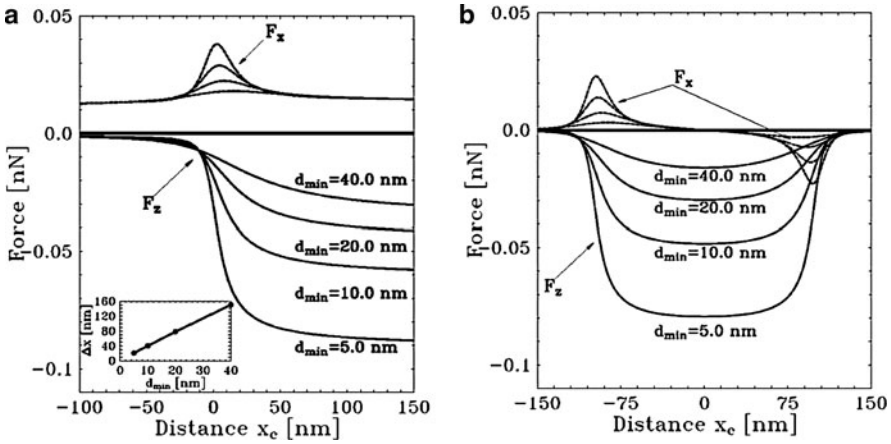

Fig. 7.14 (**a**) Force components F_x and F_z as functions of the x-axis distance x_c between the tip apex and the potential step position, as defined by (7.7). The system considered is shown in Figure 7.13 and is described in the text. F_x values (*dashed lines*) change monotonically with $d_{\min}$, the distance from tip apex to plane. F_x and F_z are of comparable magnitude in the region close to a potential step. (**b**) Force components F_x and F_z as functions of the x-axis distance x_c between the tip apex and the center of the potential island, as defined by (7.9). The system considered is shown in Figure 7.13 and is described in the text. The magnitude of the force components F_x and F_z increases monotonically with decreasing $d_{\min}$ and is of comparable size. (Reprinted with permission from [55]. Copyright 2007, American Institute of Physics)

$$V_1(x, y) = \begin{cases} 0 \text{ for } x < 0, \\ 1 \text{ V for } x > 0. \end{cases} \tag{7.7}$$

The computed force components F_x and F_z are presented in Figure 7.14a ($F_y = 0$ by symmetry).

F_z agrees both qualitatively and quantitatively with the results presented in [57]. As expected, the x-component of the force saturates asymptotically with $F_{-\infty} = 0$ and F_∞ finite, reflecting the potential step. Then, the resolution of the discontinuity determination may be defined in terms of F_z as follows:

$$\Delta x = x_{1-\alpha} - x_\alpha, \tag{7.8}$$

where x_β ($\beta = \alpha$ or $\beta = 1 - \alpha$) are determined from the conditions $F_z(x_\beta) = \beta F_\infty$ [57]. The values of Δx were calculated for $\alpha = 0.25$ and they are presented in the inset of Figure 7.14a, showing a linear dependence on the tip–plane separation, as in [57].

The variation of a lateral force component F_x with x was generally neglected in previous studies [57]. However, the results presented in Figure 7.14a demonstrate that any potential step introduces nonzero lateral components of the electrostatic force, with values not negligible when compared with the vertical component F_z.

This obviously could effect the tip movement and, as a consequence, the physical picture obtained in the experiment. This conclusion is supported by experimental work, where lateral forces were investigated [58] and shown to be important, when the tip approaches a step or an impurity island. These experiments detected lateral forces in the order of 0.05 nN, which is of the same order of magnitude as the values of F_x presented in Figure 7.14a. These results suggest the possibility of determining the position of potential steps using lateral force data, which would complement the method based on F_z values only.

As the second test of the method, a square potential island was considered:

$$V_1(x, y) = \begin{cases} 1\,\mathrm{V} & \text{for } |x| < a/2 \text{ and } |y| < a/2, \\ 0 & \text{elsewhere,} \end{cases} \tag{7.9}$$

with the edge size $a = 200$ nm. Results for the calculated force components, F_x and F_z, are presented in Figure 7.14b.

The function $F_z(x)$ shown in Figure 7.14b tends to zero at large distances, falling to a minimum above the spot. However, for each value of the tip-plane distance $d_{\min}$, the minimum value of F_z does not reach the corresponding saturation level as shown in Figure 7.14a. Therefore, with finite potential islands the magnitude of F_z is smaller and spot-size dependent. Hence, as the island size decreases, the determination of island boundaries from vertical force data becomes more difficult than for step edges.

Now, the following remarks can be made about the values of F_x. There are two potential jumps, at $x = \pm a/2$, and they produce the two peaks of F_x. These peaks, similar to the one presented in Figure 7.14a for the single step, have approximately Lorentzian line shapes and are antisymmetric with respect to $x = 0$, i.e., $F_x = -F_{-x}$, with magnitudes peaking around $x = \pm a/2$. As with the potential step, the peaks in the magnitude of F_x, may be used to estimate the island boundaries. The difference is that, unlike in the case of the potential step, $|F_x|$ decays rapidly to zero for large values of $|x|$.

The last but not least: a numerical advantage of the proposed method is that convergence is achieved with the same number of surface segments for both the potential distributions given by (7.7) and (7.9). This should be compared with numerical force calculations using both the plane and the tip, where typical matrix sizes would be at least an order of magnitude larger.

7.5.3 Numerical Simulation of KPFM Contrast

7.5.3.1 Contact Potential Difference Evaluation

Based on the presented theoretical model of the electrostatic tip–sample interaction we calculated the CPD signal acquired in FM–KPFM. We consider a metallic

tip with potential V_0 placed at a certain height above the surface (x–y plane) and vibrating with the resonant frequency f_0. In the plane, there is a potential distribution $V_1(x, y)$ in the form of one or more islands, each having a fixed value of the electrostatic potential V_i, where $i = 1, 2, \ldots, N$; the rest of the plane has a potential value equal to zero. In such a system, the electrostatic energy W_{el} is given by the formula [56]:

$$W_{\mathrm{el}} = \frac{1}{2} \sum_{i,j=0}^{N} C_{ij} V_i V_j, \tag{7.10}$$

where C_{ij} is a relative capacitance of a pair of conductors i and j. The component F_z of the electrostatic force acting on the tip is given by the expression:

$$F_z \stackrel{\mathrm{def}}{=} -\frac{\partial W_{\mathrm{el}}}{\partial z} = -\frac{1}{2} \sum_{i,j=0}^{N} \frac{\partial C_{ij}}{\partial z} V_i V_j, \tag{7.11}$$

where z is the tip–surface distance. From (7.11) it follows that for fixed potentials V_i ($i = 1, 2, \ldots, N$), F_z is a quadratic function of the tip potential V_0:

$$F_z = \alpha + \beta V_0 + \gamma V_0^2, \tag{7.12}$$

where α, β, and γ are geometry dependent parameters.

In the general case of KPFM, the value of the oscillation amplitude A can be so large that the improved formula for the frequency shift Δf, as derived by the classical perturbation theory [59], has to be used:

$$\frac{\Delta f}{f_0} = -\frac{1}{\pi k A} \int_{-1}^{1} F_z[d_{\min} + A(1 + u)] \frac{u \, \mathrm{d}u}{\sqrt{1 - u^2}}. \tag{7.13}$$

From (7.12) used together with (7.13), it follows that the calculated value of $\Delta f / f_0$ is a quadratic function of V_0, but with modified coefficients α_1, β_1, and γ_1, which result from a corresponding integration of F_z in (7.13). Therefore, the CPD may be written as:

$$\mathrm{CPD} = -\frac{\beta_1}{2\gamma_1}. \tag{7.14}$$

The reviewed general nonlinear method for the CPD evaluation has been used for a direct comparison with the experimental values, as obtained in [40, 41] for KBr islands on the InSb(0 0 1) surface. The results are plotted in Figure 7.15. In the calculations, we used the experimental value of the amplitude of oscillation $A = 40\,\mathrm{nm}$ and fixed the tip–surface distance at $d_{\min} = 1\,\mathrm{nm}$. The only varying paramter was the tip radius, for which we have chosen three values, namely, $r_{\mathrm{tip}} = 5$, 10, and 20 nm.

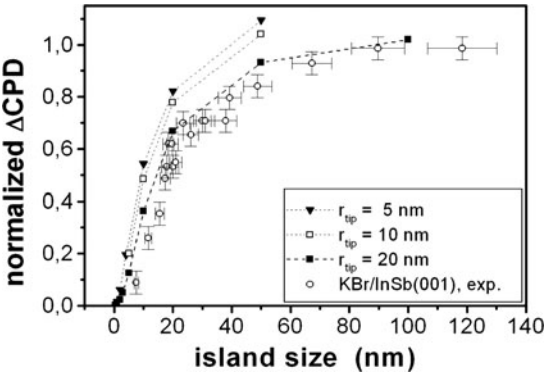

Fig. 7.15 Calculated contact potential difference together with the experimental results for KBr islands on InSb(0 0 1), as a function of the island size. The theoretical results were calculated for fixed values of the vibration amplitude $A = 40\,\text{nm}$, the tip–surface distance $d_{\min} = 1\,\text{nm}$ and $x_c = y_c = 0$, and for three given values of the tip apex radius r_{tip}. The curves between the symbols are guides to eye only

The best agreement between the calculation and experiment is reached if a value of $r_{\text{tip}} = 20\,\text{nm}$ is selected. The results of Figure 7.15 suggest that there might be a possibility of determining the tip geometry parameters from the CPD behavior, when measurement and calculation are performed for a series of island sizes. The results of more detailed calculation of the CPD for different surface potential distributions (potential islands) have been presented in [60], to which we refer the interested reader for complete details.

7.6 High Resolution KPFM Measurements

7.6.1 Limits of Lateral Resolution in FM–KPFM

Once we have discussed the capability of FM–KPFM to map the true values of the surface potential, the second question arises, concerning the observed lateral resolution of the CPD contrast in the sub-nanometer scale as it has been recently reported in a few experiments [61–64]. The atomic contrast in the CPD signal is an evidence that some short-range electrostatic forces are probed with KPFM. To explore in more detail the issue for which interactions are detected by the KPFM, we have performed FM–KPFM imaging of nanostructures formed during the deposition of gold on semiconductor surfaces. Figure 7.16 shows the topography (a) and CPD images (b) of Au grown on InSb(0 0 1), respectively. For the experimental conditions used, gold grows predominantly in the form of rectangular islands with a typical height of a few monolayers of Au (about 2.0 nm), and there is a certain amount of material spread over the substrate surface (i.e., between the islands).

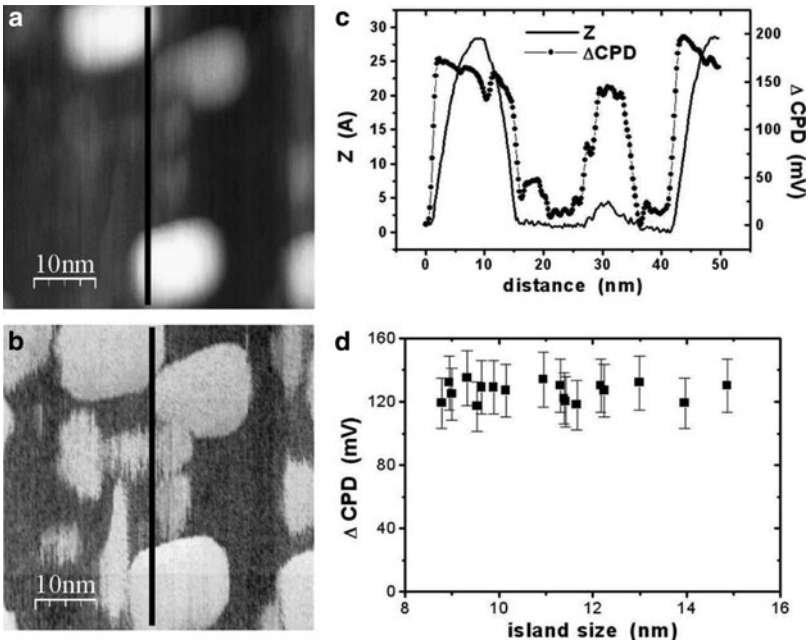

Fig. 7.16 (**a**) FM–KPFM topography and (**b**) corresponding CPD map of 0.2 ML Au grown on a InSb(0 0 1) surface at 400 K ($f_0 = 249.0$ kHz, $\Delta f = -6$ Hz). (**c**) topography (*solid line*) and CPD (*solid circles*) profiles taken along the lines on images (**a**) and (**b**). (**d**) Measured CPD versus lateral size of the 2 nm high Au islands

From the comparison between the topography and CPD images it follows that the CPD map provides more details concerning the developed surface topography. Some small features, which are difficult to recognize in the topography image, due to a large variation of the image in the z-direction, are easily recognized with the help of CPD signal. Moreover, almost the same CPD contrast, for Au islands and spread material, indicates that they are of the same chemical composition. Thus, KPFM is able to give information about the chemical composition of the surface, provided there is some reference marker on the imaged surface, i.e., the Au islands in this study. The gold topography features show a higher surface potential in comparison with the substrate surface, according to what is generally expected due to the higher work function of gold with respect to a clean InSb surface. However, despite a large difference in the amount of material constituting both the islands and the features seen between the islands as well as the difference in their lateral dimensions, both kind of structures exhibit almost the same CPD. This is in contrast to the observed dependence of the work function on Au film coverage. For example, for the Au/W(0 0 1) system [12], the measured work function saturates at a value corresponding to the one of bulk Au, at the least coverage of 3 ML Au.

Figure 7.16c presents topography (solid line) and CPD (solid circles) line profiles along the lines shown in the two 2D images in Figure 7.16a, b. The profiles depict

that the areas of increased CPD correspond to the areas of the topographic features at their bases. The CPD signal changes simultaneously with the topographic one, but the CPD profile is steeper. The CPD signal reaches its saturation levels, in both uphill and downhill direction of the islands, much faster than the topography signal. Since in KPFM the topography image is due to the van der Waals and chemical interactions between the tip and the sample, with the relative contribution depending on the actual tip–apex shape, one can draw two conclusions. First, the observed changes of the CPD signal, faster than the topography ones, indicate that the Kelvin controller for surface potential compensation probes interactions which have the interaction range shorter than that of the van der Waals interaction. Second, the weak dependence of the CPD on the volume of the imaged Au features indicates that the interaction is limited to the tip apex and the closest single surface gold atoms. These conclusions are further supported by the observed lack of the dependence of the CPD on the Au island size. As Figure 7.16d clearly demonstrates, the FM–KPFM measurements of the 2.0 nm thick Au islands of lateral edge sizes ranging from 8 up to 15 nm, resulted in almost the same CPD, whereas for the KBr/InSb system such a change of the KBr island size was reflected in a change of the CPD by a factor of 2 (see Fig. 7.12).

7.6.2 Characterization of the Short-Range Bias Dependent Interactions: Quasispectroscopic KPFM Measurements

In order to evaluate the range of interaction contributing to the observed "high quality" of the CPD (as seen in Fig. 7.16b), we have performed "quasi-spectroscopic" measurements for the Au/InSb(0 0 1) system. We have found that for certain growth conditions on the InSb(0 0 1) surface, gold organizes itself in form of flat and elongated islands (nanowires) of about 1 nm height and a few hundreds nanometers length. Therefore, this system provides a good template for performing the required quasi-spectroscopic FM–KPFM measurements as described below.

When using SPM at room temperature, it is usually difficult to perform reliable spectroscopy measurements over a specific surface site, since the thermal drift and/or piezoscanner creep give large uncertainty, both for "in-plane" tip position, as well as in its height determination. To overcome this problem, we have performed FM–KPFM measurements of the Au nanowires grown on the InSb(0 0 1) surface in two distinct regimes of the imaging. In the first regime, we could acquire a clear topography image of the Au islands with corresponding sharp CPD contrast, while in the other regime, the same Au islands can still be seen in the topography but can be hardly resolved in the corresponding CPD map. The former conditions correspond to imaging with relatively large detuning, in this case $\Delta f = -15\,\mathrm{Hz}$ (tip "close" to the surface), whereas the latter ones correspond to imaging with a much smaller detuning of $\Delta f = -3\,\mathrm{Hz}$ (the tip retracted from the surface). The system was stable and we could repeat this kind of imaging several times. The

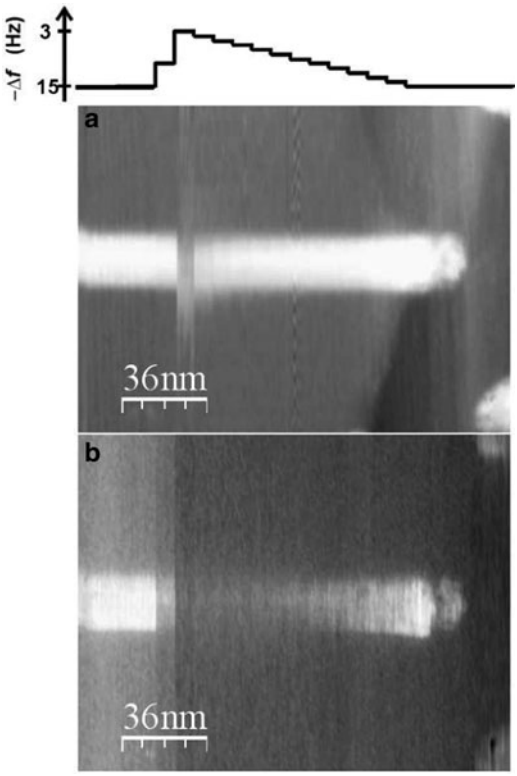

Fig. 7.17 (**a**) FM–KPFM topography and (**b**) corresponding CPD map of a Au island (nanowire) grown on a InSb(0 0 1) surface at 560 K ($f_0 = 358.4$ kHz). Above the image a schematic of the changes of the detuning magnitude during the acquisition of the images is shown. For better visualization of the apparent change of the island height the topography image was flattened with a line-by-line subtraction of an offset line in the fast scan direction. Reprinted with permission from [64]

imaging was performed with the fast scan direction being always perpendicular to the nanowire. Then, a sample surface with relatively low density of islands has been chosen to obtain in the AFM image frame that has only a single Au nanowire. While imaging the nanowire, after acquisition of every few tens of scan lines, the detuning was gradually changed by 1 Hz between the two distinguished values of Δf, namely, -15 and -3 Hz. The results are shown in Figure 7.17a, b (topography and CPD maps), respectively, with the corresponding scheme of the detuning changes. From the cross section of the topography image taken along the slow scan direction, the tip–surface separation changes have been extracted and attributed to the corresponding changes of the detuning.

Next, from the cross sections taken along the fast scan direction, the apparent island height and corresponding CPD for a given detuning have been evaluated. Having calibrated the tip–surface distance change versus the detuning change, the dependences of the island height and the CPD on the relative tip-surface separation change were obtained, as shown in Figure 7.18. The zero value in the abscissa axis corresponds to the closest distance between the tip and the sample ($\Delta f = -15$ Hz).

The decreasing of the detuning down to $\Delta f = -3$ Hz resulted in the increase of the tip–surface separation by 2.2 nm. The apparent island height exhibits a slow

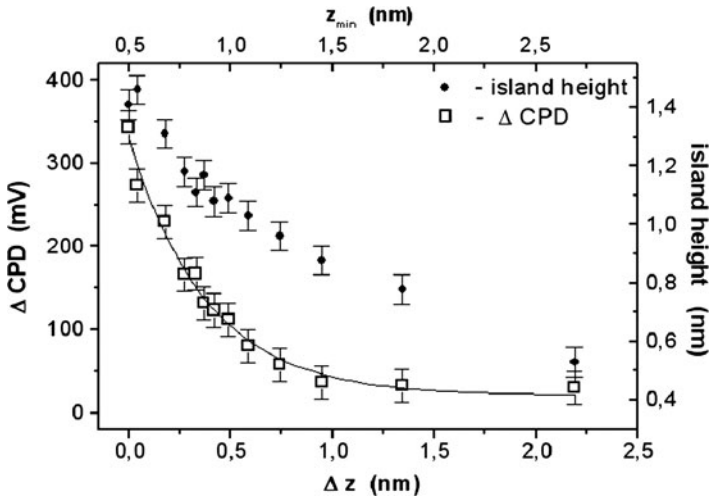

Fig. 7.18 Dependences of the apparent Au island height and corresponding CPD on the tip–surface separation change. The upper abscissa axis, $z_{\min}$, is the evaluated distance of the closest tip–surface approach. The data were extracted from the quasispectroscopic measurements presented in Fig. 7.17. Reprinted with permission from [64]

decrease as the tip is retracted from the surface, whereas the CPD exhibits a faster exponential-like decay dependence on the tip–sample separation. The exponential fit CPD $\sim \exp(-\Delta z/\lambda)$ reveals the decay length of the CPD signal of $\lambda = 0.38$ nm. The faster disappearance of the CPD signal than the topography contrast as the tip is retracted from the surface indicates that the interactions contributing to the measured CPD are of shorter range than the van der Waals ones. The observed saturation of the CPD signal on the level of about 30 mV at higher tip–surface separation we associate with the contribution of the "true" CPD due to the long range electrostatic interactions between the tip and the Au island. We have evaluated the distance between the surface and the tip apex at its turning point (the closest approach) of the oscillation cycle, $z_{\min}$, taking into account van der Waals interactions only. We have considered the following expression for the corresponding frequency shift derived for the van der Waals interaction between a sphere of radius R and infinite plane [65]:

$$\Delta f_{\mathrm{VdW}}/f_0 = -\frac{HR}{12kAz_{\min}(2z_{\min}A)^{1/2}}, \tag{7.15}$$

where we used the experimental values of the cantilever spring constant $k = 20\,\mathrm{N\,m^{-1}}$, the Hamaker constant [66] $H = 8 \times 10^{-21}$ J, $R = 20$ nm and the oscillation amplitude $A = 20$ nm. From these data, we have evaluated the closest approach of the tip to the surface at the $\Delta f = -3$ Hz as $z_{\min} = 2.7$ nm (Fig. 7.18).

The results presented provide the experimental evidence that in the FM–KPFM technique some short-range, bias-dependent interactions between the tip and the

surface may be detected. These interactions eventually contribute to the observed "high quality" CPD contrast. A rough estimate of the tip–sample separation during the imaging of the Au/InSb(0 0 1) system indicates that the interactions are detected when the tip–surface separation is of the order of 1 nm or smaller. For the tip being "far enough" from the surface, only long-range electrostatic interactions are bias-dependent. In this case, FM–KPFM provides the CPD signal related to the surface potential distribution on the sample and the measured CPD contrast depends on the experimental conditions, such as the ratio of the tip and surface structure dimensions. This is demonstrated for the KBr/InSb(0 0 1) system, where the measured CPD contrast depends on the KBr island size. This observation is then supported by the predictions of the theoretical model presented in Sect. 7.5.2.1, which takes into account only long-range electrostatic interactions between the tip and the surface.

When some other bias-dependent interactions between the tip and the surface are active, the interpretation of the experimental CPD contrast is more complicated. In this case, the measured CPD signal does not reflect the voltage which compensates the CPD between the tip and the sample. Rather, it corresponds to the voltage for which the sum of the long-range electrostatic interaction (due to the CPD between the tip and the sample) and the short-range interactions (related to the front tip atom and surface) has its minimum. In particular, the measured CPD signal does not reflect the distribution of the work function on the imaged surface.

7.7 Summary

In this chapter we have presented the surface properties, related to nanostructures supported on semiconductor substrates. The main part of the experimental results, presented above, was obtained by KPFM in UHV. The investigated systems include:

- Epitaxial nanostructures assembled on InSb(0 0 1) by submonolayer deposition of Au.
- Semiconductor nanostructures grown on lattice-mismatched semiconductor substrates.
- Semiconductor surfaces with surface modification and nanostructuring induced by ionizing irradiation.
- Dielectric structures grown on InSb(0 0 1).

We have also presented a new efficient algorithm for evaluation of electrostatic forces in the tip–plane system. Based on this method, we calculated the CPD values for the considered tip–plane systems and compared the theoretical results with the experimental data. We have presented these results, which show a good agreement with the experiment.

In the last part of the chapter, we have analyzed and discussed the important issue of high resolution measurements. Particularly, using the Au/InSb(001) system as an

example, we have addressed the key problem of the limits of lateral resolution. Then, the subject of the quasispectroscopic KPFM measurements has been discussed. Finally, we have discussed the phenomenon of the so-called short-range bias-dependent electrostatic interactions.

Acknowledgements This work was supported by the Polish Ministry of Science and Higher Education within the framework of program of European Science Foundation, ESF, EUROCORE – FANAS, project Active Control of Friction, ACOF. We thank M. Goryl and K. Sajewicz for providing the images from their work, and P. Piatkowski for helping in the upgrade of VP2 system.

References

1. M. Tomitori, T. Arai, Appl. Surf. Sci. **140**, 432 (1999)
2. C. Joachim, J.K. Gimzewski, A. Aviram, Nature **408**, 541 (2000)
3. M. Szymonski, M. Goryl, F. Krok, J.J. Kolodziej, F. Buatier de Mongeot, Nanotechnology **18**, 044016 (2007)
4. M. Goryl, J.J. Kolodziej, F. Krok, P. Piatkowski, B. Such, M. Szymonski, Microelectron. Eng. **81**, 394 (2005)
5. J.J. Kolodziej, B. Such, M. Szymonski, F. Krok, Phys. Rev. Lett. **90**, 226101 (2003)
6. M.O. Schweitzer, T.S. Jones, C.F. McConville, N.V. Richardson, Surf. Sci. **287-288**, 545 (1993)
7. P.J. Feibelman, D.R. Hamann, Phys. Rev. B **29**, 6463 (1984)
8. G.W. Gobeli, F.G. Allen, Phys. Rev. **137**, 245 (1965)
9. G. Goryl - PhD thesis, Jagiellonian University 2011
10. Y. Shapira, F.Xu, D.M. Hill, J.H. Weaver, Appl. Phys. Lett. **51**, 118 (1987)
11. M. Goryl, F. Krok, J.J. Kolodziej, P. Piatkowski, B. Such, M. Szymonski, Vacuum **74**, 223 (2004)
12. G.W. Graham, Phys. Rev. B **32**, 2640 (1985)
13. H. Wagner, in *Solid Surface Physics: Physical and Chemical Properties of Stepped Surfaces*, vol. 85 of Springer Tracts in Modern Physics (Springer, Berlin, 1979)
14. H. Ibach, W. Schmickler, Phys. Rev. Lett. **91**, 016106 (2003)
15. R. Smoluchowski, Phys. Rev. **60**, 661 (1941)
16. H. Sakaki, Solid State Commun. **92**, 119 (1994)
17. D. Leonard, M. Krishnamurthy, C.M. Reaves, S.P. Denbaars, P.M. Petroff, Appl. Phys. Lett. **63**, 3203 (1993)
18. J.-Y. Marzin, J.-M. Gerard, A. Izrael, D. Barrier, G. Bastard, Phys. Rev. Lett. **73**, 716 (1994)
19. B.J. Hinds, T. Yamanaka, S. Oda, J. Appl. Phys. **90**, 6402 (2001)
20. K. Hishiguchi, X. Zhao, S. Oda, J. Appl. Phys. **92**, 2748 (2002)
21. K. Arai, S. Oda, Phys. Status Solidi C **0**, 1254 (2003)
22. M.A. Salem, H. Mizuta, S. Oda, Appl. Phys. Lett. **85**, 3262 (2004)
23. T. Yamauchi, M. Tabuchi, A. Nakamura, Appl. Phys. Lett. **84**, 3834 (2004)
24. T. Yamauchi, Y. Ohyama, Y. Matsuba, M. Tabuchi, A. Nakamura, Appl. Phys. Lett. **79**, 2465 (2001)
25. A. Yabe, H. Niino, in *Laser Ablation of Electronic Materials*, ed. by E. Fogarassy, S. Lazare (Elsevier, Amsterdam, 1992), p. 199
26. W.L. Chan, E. Chason, J. Appl. Phys. **101**, 121301 (2007)
27. J. Reif, F. Costache, M. Bestehorn, in *Recent Advances in Laser Processing of Materials*, ed. by J. Perrier, E. Millon, E. Fogarassy (Elsevier, Amsterdam, 2006) p. 275
28. M.A. Makeev, R. Cuerno, A.-L. Barabasi, Nucl. Instrum. Meth. B **197**, 185 (2002)
29. Z. Guosheng, P.M. Fauchet, A.E. Siegman, Phys. Rev. B **26**, 5366 (1982)

30. J. Reif, M. Ratzke, O. Varlamova, F. Costache, Mater. Sci. Eng. B **134**, 114 (2006)
31. S. Facsko, T. Dekorsy, C. Koerdt, C. Trappe, H. Kurz, A. Vogt, H.L. Hartnagel, Science **285**, 1551 (1999)
32. C.M. Demanet, J.B. Malherbe, N.G. van der Berg, V. Sankar, Surf. Interf. Anal. **23**, 433 (1995)
33. F. Krok, Vacuum **83**, 745 (2008)
34. P. Sigmund, Phys. Rev. **184**, 383 (1969)
35. J. Massies, L. Dazaly, J. Appl. Phys. **55**, 3136 (1984)
36. M. Bouslama, C. Jardin, M. Ghamnia, Vacuum **46**, 143 (1995)
37. F. Krok, J.J. Kolodziej, B. Such, P. Piatkowski, M. Szymonski, Appl. Surf. Sci. **210**, 112 (2003)
38. M. Szymonski, F. Krok, P. Struski, J. Kolodziej, B. Such, Progress in Surf. Sci. **74**, 331 (2003)
39. Ch. Sommerhalter, Th.W. Matthes, Th. Glatzel, A. Jaeger-Waldau, Appl. Phys. Lett. **75**, 286 (1999)
40. J.J. Kolodziej, B. Such, P. Czuba, F. Krok, P. Piatkowski, M. Szymonski, Surf. Sci. **506**, 12 (2002)
41. F. Krok, P. Piatkowski, J.J. Kolodziej, B. Such, P. Struski, P. Czuba, M. Szymonski, Surf. Science **566–568**, 63 (2004)
42. S. Sadewasser, M. Ch. Lux-Steiner, Phys. Rev. Lett. **91**, 266101 (2003)
43. B. Such, F. Krok, M. Szymonski, in *Scanning Force Microscopies for Imaging and Characterisation of Nanostructured Materials*, ed. by A. Korkin, E. Gusev, J.K. Labanowski, S. Luryi. Nanotechnology for Electronic Materials and Devices (Springer, Berlin 2007)
44. Y. Rosenwaks, R. Shikler, Th. Glatzel, S. Sadewasser, Phys. Rev. B **70**, 085320 (2004)
45. U. Zerweck, Ch. Loppacher, T. Otto, S. Grafstrom, L.M. Eng, Phys. Rev. B **71**, 125424 (2005)
46. L.N. Kantorovich, A.S. Foster, A.L. Shluger, A.M. Stoneham, Surf. Sci. **445**, 283 (2000)
47. G. Mesa, E. Dobado-Fuentes, J.J. Sáenz, J. Appl. Phys. **79**, 39 (1996)
48. G. Mesa, J.J. Sáenz, Appl. Phys. Lett. **68**, 1169 (1996)
49. S. Gómez-Monivas, L.S. Froufe-Pérez, A.J. Caamano, J.J. Sáenz, Appl. Phys. Lett. **79**, 4048 (2001)
50. S. Watanabe, K. Hane, T. Ohye, M. Ito, T. Goto, J. Vac. Sci. Technol. **11**, 1774 (1993)
51. H.O. Jacobs, H.F. Knapp, S. Müller, A. Stemmer, Ultramicroscopy **69**, 39 (1997)
52. H.O. Jacobs, P. Leuchtmann, O.J. Homan, A. Stemmer, J. Appl. Phys. **84**, 1168 (1998)
53. A. Gil, J. Colchero, J. Gómez-Herrero, A.M. Baró, Nanotechnology **14**, 332 (2003)
54. S. Hudlet, M. Saint Jean, C. Guthmann, J. Berger, Eur. Phys. J. **2**, 5 (1998)
55. J. Konior, J. Appl. Phys. **101**, 084907 (2007)
56. J.D. Jackson, *Classical Electrodynamics* (Wiley, New York, 1998)
57. S. Belaidi, F. Lebon, P. Girard, G. Leveque, S. Pagano, Appl. Phys. A **66**, S239 (1998)
58. O. Pfeiffer, R. Bennewitz, A. Baratoff, E. Meyer, Phys. Rev. B **65**, 161403 (2002)
59. F. J. Giessibl, Phys. Rev. B, **56**, 24 (1997)
60. K. Sajewicz, F. Krok, J. Konior, Jap. J. Appl. Phys. **49**, 025210 (2010)
61. Y. Sugawara, T. Uchihashi, M. Abe, S. Morita, Appl. Surf. Sci. **140**, 371 (1999)
62. S. Kitamura, K. Suzuki, M. Iwatsuki, C. Mooney, Appl. Surf. Sci. **157**, 222 (2000)
63. K. Okamoto, K. Yoshimoto, Y. Sugawara, S. Morita, Appl. Surf. Sci. **210**, 128 (2003)
64. F. Krok, K. Sajewicz, J. Konior, M. Goryl, P. Piatkowski, M. Szymonski, Phys. Rev. B **77**, 235427 (2008)
65. M. Guggisberg, M. Bammerlin, Ch. Loppacher, O. Pfeiffer, A. Abdurixit, V. Barwich, R. Bennewitz, A. Baratoff, E. Meyer, H.-J. Guntherodt, Phys. Rev. B **61**, 11151 (2000)
66. L. Bergstrom, Adv. Colloid Interface Sci. **70**, 125 (1997)

Chapter 8
Optoelectronic Studies of Solar Cells

S. Sadewasser

Abstract Solar cells are a most promising candidate to supply future energy needs in a sustainable and renewable way. Currently, solar cell devices based on semiconductor materials achieve the highest power conversion efficiencies. A typical solar cell consists of a semiconductor pn-junction where the semiconductor band gap is in the range between 1 and 2 eV, well adapted to absorb a large part of the solar spectrum. Issues as band alignment and spatial homogeneity of the materials are essential in providing the optimum achievable efficiencies. Kelvin probe force microscopy has been applied to a wide range of solar cell materials and devices, ranging from crystalline and amorphous silicon to polycrystalline CdTe and $Cu(In,Ga)(S,Se)_2$ to organic semiconductors and molecules. On these systems, KPFM has been applied in different ways, from surface characterization to effects of illumination to cross-sectional studies. From many of these local work function measurements, understanding of functional principles and limiting factors has been gained. This chapter reviews the results that have been obtained by Kelvin probe force microscopy on solar cell devices and materials and describes how the gained understanding promotes the improvement of solar cell devices for renewable energy conversion.

8.1 Introduction to Solar Cells

The world's energy demand is continuously increasing and it is clear that fossil fuels will in the future not be able to supply sufficient energy. The only solution to this energy problem is the conversion of our energy systems to renewable energies. One

S. Sadewasser (✉)
International Iberian Nanotechnology Laboratory - INL, Avda. Mestre José Veiga s/n, 4715-330 Braga, Portugal
e-mail: sascha.sadewasser@inl.int

S. Sadewasser and T. Glatzel (eds.), *Kelvin Probe Force Microscopy*, Springer Series in Surface Sciences 48, DOI 10.1007/978-3-642-22566-6_8,

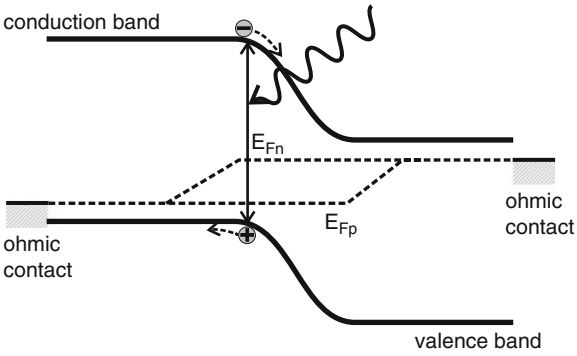

Fig. 8.1 Band diagram of the pn-junction in a solar cell

of the prime suppliers of such renewable energy is the sun, and it is predicted that conversion of the radiation from the sun into usable energy will cover a main part of our future energy needs. One way is the direct conversion of sunlight into electricity by means of photovoltaic solar cells [1, 2]. The development of the currently most widespread solar cells started half a century ago. This crystalline silicon solar cell, however, has the disadvantage that it is based on an indirect band gap semiconductor, which results in the requirement to fabricate solar cells with a sufficient thickness of about 300 μm. Subsequent developments implement direct band gap materials, thereby providing the possibility to use less material and fabricate thinner devices. Such thin film solar cells consist of amorphous silicon, Cu(In,Ga)Se_2, CdTe, III–V semiconductors or organic materials.

At the core of a semiconductor solar cell is a pn-junction. When light with energy larger than the semiconductor band gap (E_g) is absorbed in the semiconductor material, the generated electron-hole pair is separated by the built-in field of the pn-junction. A schematic band diagram of a pn-junction is shown in Fig. 8.1. The generated electron is driven toward the n-doped semiconductor side, while the hole goes into the p-type side. Under illumination, the junction is in nonequilibrium conditions and the Fermi level splits into the quasi Fermi levels of the electrons and holes. The open circuit voltage of the solar cell is then given by the separation of the Fermi level between n- and p-type side of the junction.

In the case of silicon-based solar cells, several different approaches can be distinguished. The single crystalline Si solar cell is based on a wafer, where typically the major part of the wafer is p type and the top-part (thickness ∼200 nm), through which the cell is illuminated, is doped n^+ type. The cell has to be sufficiently thick to provide efficient light absorption in the indirect band gap material. At the same time, the large thickness imposes a requirement on the purity of the material to avoid recombination and provide for sufficiently long diffusion lengths of the generated charge carriers. In addition to the basic pn-junction setup, several improvements have been achieved by designing the cell accordingly. These include a p^+ back surface field layer, a highly structured front side for better light trapping,

and point contacts at the back contact side to reduce recombination losses [1]. A significant cost reduction in the fabrication can be achieved using polycrystalline silicon. An efficiency reduction has to be accepted, since defects, as for example grain boundaries reduce the electronic quality of the material. In this respect, the electronic properties of grain boundaries and their systematic modification are important. Another Si-based solar cell uses amorphous silicon (a-Si:H), which typically contains hydrogen to passivate dangling bonds. While the indirect band gap of crystalline Si amounts to E_g(x-Si) $= 1.1$ eV, that of a-Si:H is direct and somewhat larger, E_g(a-Si:H) $\cong 1.7$ eV; therefore, light absorption in a-Si:H is more effective, opening the possibility to fabricate thin film solar cells. Typically, an a-Si:H solar cell consists of an intrinsic a:Si layer sandwiched between thin p^+ and n^+ contacts on either side. The cell thus provides a fairly thick region with an electric field, serving to separate and drive out the generated charge carriers [1].

Highly efficient thin film solar cells using polycrystalline absorbers are based either on the chalcopyrite compound Cu(In,Ga)$(S,Se)_2$ or on CdTe/CdS. Both materials are direct band gap semiconductors and provide sufficiently high light absorption to be used in thin film photovoltaics. The compound material Cu(In,Ga)$(S,Se)_2$ (CIGSSe) is typically deposited onto a Mo-coated glass substrate serving as a back contact. Deposition processes for the p-type CIGSSe include thermal evaporation in vacuum, sputter deposition of the metals and subsequent selenization and/or sulfurization, or various chemical approaches. Best solar cells achieve currently 20% efficiency grown with the composition $Cu(Ga_{0.3}In_{0.7})Se_2$ using a three-stage coevaporation process [3]. The solar cell device is completed by a thin ($\sim$50 nm) CdS buffer layer and an i-ZnO/n-ZnO window layer. In case of CdTe-based thin film solar cells, the device is typically fabricated as a superstrate solar cell, where a transparent conductive oxide serves as the front contact. An n-type CdS layer then forms the pn-junction with the subsequent p-type CdTe. A metal contact (i.e., Ni-Al) serves as the back contact.

For III–V semiconductor-based solar cells crystalline material is used. Based on a wafer, various layers of III–V material are typically grown by metal-organic vapor phase epitaxy (MOVPE) to form the device structure. Mainly these solar cells are built as double or triple junction devices, where different III–V materials with different band gaps are stacked with the goal to harvest a larger part of the solar spectrum. In a triple junction device, for example (Ga,In)As, Ge, and $GaInP_2$ could be used. The different cells are then separated by tunnel junctions built up from highly doped III–V layers. Issues to consider in such devices are lattice matching, strain and stress in the various layers, interface quality, and current matching of the series connected individual cells.

Besides these semiconductor pn-junction-based devices, another more recent approach uses organic materials as absorbing layers. Such organic molecules promise a cost effective and easy fabrication of solar cells. Little material has to be used, since the organic molecules used exhibit excellent light absorption properties. The solar cells consist of a combination of donor and acceptor molecules and light absorption leads to the generation of an exciton. After its diffusion to the interface between the donor and acceptor molecules, the exciton is separated and the two

charge carriers are led to the external contacts via the respective molecules [4]. Either a combination of polymers can be used, or frequently also an approach based on small molecules as for example C_{60} and Cu-Phthalocyanine (Cu-Pc). Currently, efficiencies of organic solar cells are limited to about 5% [5].

8.2 Nanometer Optoelectronic Surface Studies

8.2.1 Cu(In,Ga)(S,Se)$_2$-Based Solar Cells

The *pn*-junction in a solar cell is the critical interface for charge carrier separation, and a large density of defects at this interface is detrimental for the efficiency of the device. The *p*-type CIGSSe absorber forms the *pn*-junction with the *n*-type CdS and ZnO window layers; therefore, the absorber surface is of high interest for the device performance (see Chap. 8.1). In this respect, the KPFM presents a well-suited characterization technique to investigate the morphology and the local electronic properties of the chalcopyrite surface. The surface cleanness is a critical point in such studies, as a reliable measurement of the work function requires clean surfaces [6]. Therefore, surfaces to be meaningfully characterized by KPFM should be either prepared or cleaned under UHV conditions. Due to experimental restrictions, it is not always possible to transfer samples under vacuum conditions. When exposed to air, Cu-chalcopyrite surfaces oxidize, forming various native oxide species, as In_2O_3, Ga_2O_3, and SeO_x, but also Na_2CO_3 [7]. Several preparation techniques for obtaining clean surfaces in UHV are described below.

The effect of the surface condition on KPFM experiments is demonstrated by comparing studies of different sample surfaces and surface preparations. The most straightforward method to obtain a UHV-clean sample surface is to grow the chalcopyrite thin film inside the same UHV chamber. The topography and work function of an as-prepared $CuGaSe_2$-film by a two-stage growth process using physical vapor deposition (PVD) are shown in Fig. 8.2a, b, respectively [8]. Solar cells processed from these absorbers show efficiencies up to 5%. The granular structure of the polycrystalline thin film with a typical grain size of $\approx$500 nm is seen. The work function shows variations within 250 meV; the distribution of work functions is best seen in a histogram as shown in Fig. 8.3a. A single peak in the distribution can be fitted by a Gauss distribution with a maximum at $\Phi = 5.45$ eV and a full width at half maximum (FWHM) of $\approx$0.06 eV.

For most investigations, samples from an in-vacuum deposition and transfer are not available. Therefore, other ways of obtaining clean as-grown surfaces in UHV are necessary. One option is transfer in an inert-gas atmosphere (i.e., Ar or N_2), which avoids surface oxidation and adsorbate contamination. As an example, a $CuGaSe_2$ surface prepared on a Mo/glass substrate in a chemical vapor deposition (CVD) reactor is shown in Fig. 8.4 [9]. The granular structure in the topography is comparable to the previous case; however, the work function shows a clear

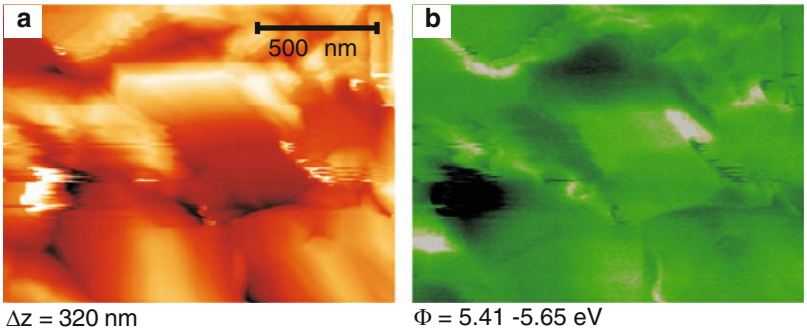

Fig. 8.2 KPFM measurement of a $CuGaSe_2$ thin film deposited in a UHV-PVD and transferred under UHV conditions. The topography (**a**) shows the granular structure ($\Delta z \approx 320$ nm) and the work function (**b**) varies from $\Phi \approx 5.41$–5.65 eV [8]

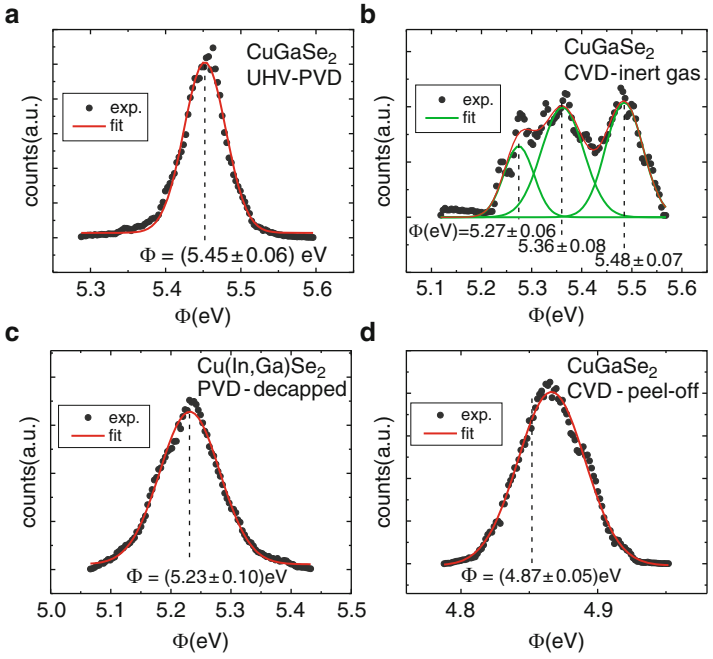

Fig. 8.3 Histograms showing the work function distribution obtained by KPFM for (**a**) UHV-PVD grown $CuGaSe_2$ [8], (**b**) CVD-grown $CuGaSe_2$ transferred in inert-gas atmosphere [9], (**c**) co-evaporated and Se-decapped $Cu(In,Ga)Se_2$ [10], (**d**) CVD-grown $CuGaSe_2$ rear-side obtained by peel-off in UHV [11, 12]

distinction between the values for different facets of the crystallites. This is also clearly observed in the corresponding histogram, presented in Fig. 8.3b. A number of different peaks can be observed, each corresponding to a distinct work function

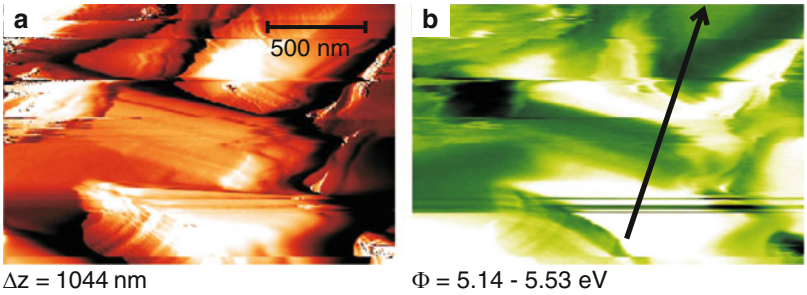

Fig. 8.4 KPFM measurement of a $CuGaSe_2$ thin film deposited by CVD and transferred in Ar-atmosphere. The topography (**a**) shows the granular structure and the work function (**b**) varies from $\Phi \approx 5.14$–5.53 eV, showing distinct values for different facets [9]

value of a specific facet [9]. The assignment of the specific facets was achieved by comparing the geometric angles of numerous facets to literature values using a textured $CuGaSe_2$ sample grown by MOVPE onto a single crystalline ZnSe(110) surface [13].

Another option for transferring a sample from the growth system to the UHV analysis chamber without oxidation and contamination is to overgrow the surface with a protective layer, which can be removed inside the UHV. A well-suited option for this overlayer is a Se-capping layer of a few hundred nanometers thickness, which is deposited after film growth by the same Se-source used for the chalcopyrite deposition. Such a film can be transported in air without oxidation of the burried chalcopyrite, and the protective layer can be evaporated by sample heating inside the UHV chamber. Hunger et al. [14, 15] have shown by photoemission spectroscopy (PES) that the resulting chalcopyrite surface is free of oxides and other contamination and shows a composition similar to UHV-prepared samples. We have followed this route using a co-evaporated $Cu(In, Ga)Se_2$ thin film. Topography and work function images [10] obtained by KPFM show similar results to the previous samples, and the histogram of the work function image is presented in Fig. 8.3c.

Another approach for obtaining a clean surface in UHV is the preparation by peel-off [11, 16]. In this technique, use is made of an intermediate van-der-Waals compound at the chalcopyrite/Mo interface. During the deposition process, an $MoSe_2$ film develops on the surface of the Mo-layer. This layered compound shows weak bonding between van-der-Waals planes building up its crystalline structure. Gluing a supporting structure (i.e., a glass or metal foil) to the top of the chalcopyrite thin film, it can be lifted off from the Mo/glass substrate. The obtained rear-side chalcopyrite surface is free of Mo remnants, as confirmed by PES studies [11]. The work function shows a fairly narrow range of values as can be seen in the histogram in Fig. 8.3d. It is apparent that the above-observed work function variation according to distinct facets is not observed in the present case, pointing to a homogeneous texturing of the small initial grains.

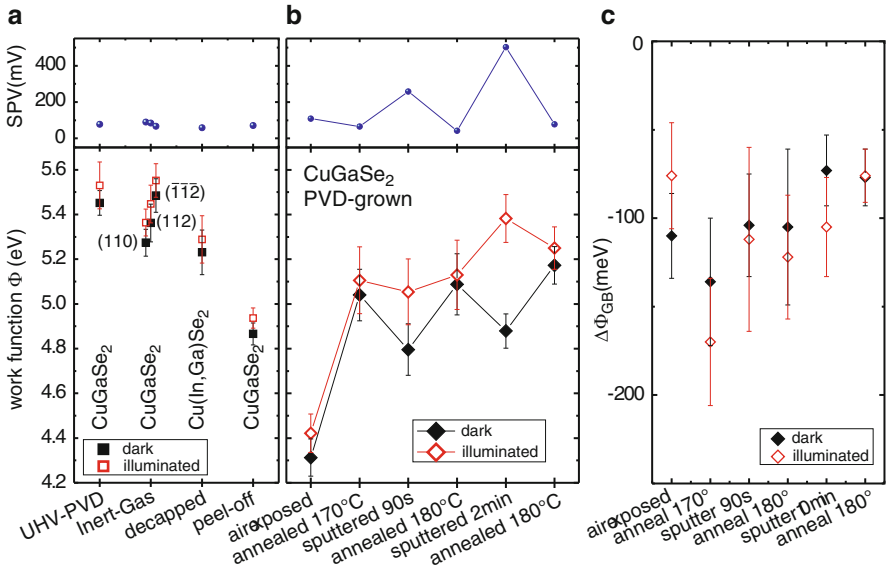

Fig. 8.5 Overview of the work function of (**a**) differently prepared surfaces of various chalcopyrite thin films (as indicated in the figure). (**b**) Sputter and annealing cleaning procedure for an air-exposed PVD-grown $CuGaSe_2$ thin film. The *lower panels* show the work function in dark and under illumination and the *upper panels* show the surface photovoltage (SPV) [12]. (**c**) Development of the work function dip $\Delta\Phi_{GB}$ at grain boundaries upon the same sputter and annealing treatment as shown in (**b**). See Chap. 8.3.2 for details

The work function values obtained by Gauss-fitting the histograms in Fig. 8.3 are shown comparatively in Fig. 8.5a for the differently prepared surfaces. A strict comparison is rather difficult and not very meaningful, as the growth processes are not identical and therefore also the materials composition and doping level is likely different; in the case of preparation by decapping, the In-containing $Cu(In,Ga)Se_2$ was used. Nevertheless, the obtained work function is fairly comparable for all samples showing values between ~5.2 eV and 5.6 eV. For the peeled-off $CuGaSe_2$, a lower value is obtained. A PES study on this backside surface revealed traces of oxygen and carbon, which was ascribed to contamination of the Mo substrate before the chalcopyrite deposition [11]; additionally, the Cu-rich initial growth of the 2-step grown $CuGaSe_2$ might affect the work function on the rear-side. Also given in Fig. 8.5a are the work function values obtained under illumination (open symbols), from which the surface photovoltage (SPV) can be computed, shown in the upper panel of Fig. 8.5a. The SPV shows a fairly constant value of ≈80 mV for all surfaces. This indicates a depletion at the free chalcopyrite surface and consequently a downward band bending due to positively charged surface defects, in accordance with the *p*-type doping usually observed for chalcopyrites.

In many cases, samples can only be entered into the UHV after having been exposed to air. In this case, a surface cleaning is necessary. This can well be

performed by sputtering and annealing. Otte et al. [17] have performed PES studies on $CuInSe_2$ and $CuGaSe_2$ showing that soft sputtering with low energies up to 60 min results in cleaning from surface oxides and contamination, leading to a surface stoichiometry close to 1:1:2. A KPFM study was performed with subsequent sputter and annealing cycles to clean the surface of a $CuGaSe_2$ sample grown in a PVD system [18] and exposed to air, prior to introduction into the UHV-KPFM [12]. Subsequent to an initial measurement, the sample was cleaned by first annealing it at 170°C for 1 h, then sputtering the surface with Ar-ions at 500 keV for 90 s (incident angle varied between 45 and 90° to the surface), again annealing (180°C for 30 min), another sputtering step (500 eV for 10 min) and a final annealing step at 180°C for 30 min. After each treatment, the sample surface was imaged by KPFM. Measurements were performed in dark and under illumination. An overview of the obtained work function values is presented in Fig. 8.5b; the given values correspond to the Gauss peak position and the error bar to the FWHM of the Gauss distribution fitted to the corresponding work function histograms, according to the procedure shown in Fig. 8.3.

The initially low work function of ∼4.31 eV is increased to ∼5.00 eV after removal of the contamination water layer by the first annealing treatment. Subsequent sputtering lowers the work function slightly, despite the further cleaning, which is expected, i.e., the removal of oxides on the surface. A high SPV of ∼260 mV is observed for the sputtered sample, indicating the presence of electrically active surface defects, presumably created due to the Ar-ion impact. Under illumination, this sample reaches nearly the same work function as the annealed sample, indicating that band bending is efficiently reduced. The subsequent annealing treatment increases the work function and only a small SPV is observed. Upon annealing, surface atoms become more mobile resulting in defect healing. This reduces the band bending and accordingly also the SPV. Subsequent sputtering and annealing steps change the work function slightly, showing again the sputter-induced defects and high SPV. These results show that by sputter-annealing cycles an effective surface cleaning can be obtained, at least from the electronic point of view. For testing the chemical composition PES studies are necessary. Recently, a study on epitaxial $CuGaSe_2$ showed that upon sputtering and simultaneous annealing at 300°C, a (2×4) reconstructed surface is obtained, free of contamination and with a composition close to a 1:1:2 surface stoichiometry [19].

For the solar cell device, it would be more interesting to image the interface between absorber and buffer layer. However, scanning probe microscopy is a surface sensitive technique, and thus obtaining information about the interface is not straightforward. Nevertheless, using locally resolved surface photovoltage, also the electronic behavior of a burried interface can be investigated [20].

In this respect, two studies were performed. As a representative of the interface between absorber and buffer, the $CuGaSe_2$/ZnSe interface was investigated, prepared by growing $CuGaSe_2$ onto the (110) face of freshly cleaved ZnSe single crystals by CVD. The work function and surface photovoltage were obtained from KPFM measurements in the dark and under illumination with super band gap light. These data were obtained independently for the ZnSe(110) substrate and

the $CuGaSe_2$ thin film. Combining these information, a schematic band diagram for the $CuGaSe_2$/ZnSe heterostructure was proposed [9]. Additionally, the time dependence of the surface photovoltage of the samples was studied. The surface photovoltage transients in the dark could be described by a thermally activated process with one distinct energy level at mid-gap of the $CuGaSe_2$ [21].

An extension of the surface photovoltage measurement was achieved by combination with a light source with variable wavelength. This surface photovoltage spectroscopy in combination with the local measurement of the KPFM allows to obtain a more detailed information of the surface optoelectronic properties [22, 23]. In a study on $CuInS_2$ with and without Zn-doping, it was found that Zn is distributed homogeneously throughout the sample surface by comparison of individual spectra in different surface positions [24]. Detailed analysis of the SPV spectra revealed a band gap of $\sim$1.48 eV for both undoped and Zn-doped $CuInS_2$. However, for the Zn-doped sample a clear sub-band gap SPV signal was detected, which could be described by a Urbach-tail with an Urbach energy of $\sim$74 meV. This indicates an enhanced disorder in the crystal structure due to the additional Zn doping [24].

8.2.2 Organic Solar Cells

Surface studies of organic solar cells by KPFM can provide valuable information about the material structure. In organic solar cells, the donor and acceptor materials are often deposited in the form of a blend; therefore, the intermixing of the two materials can be effectively studied by KPFM. Glatzel et al. [25] and Hoppe et al. [26] have studied the classic organic solar cell blend consisting of MDMO-PPV and PCBM, where the latter is a fullerene derivative representing the electron acceptor and the former serves as the donor. The authors compare the effect of two different solvents for spin-casting the organic blends onto the ITO substrate. Pure acceptor and donor films show homogeneous work function distributions, as does the blend casted with chlorobenzene as a solvent. Nevertheless, despite the similar and homogeneous work function of all three samples, only the blend shows a distinct photovoltaic effect under illumination with a laser at 442 nm. The measured SPV results from an effective charge separation in the donor and acceptor blend and amounts to $\sim$300 mV. In contrast to this, the toluene-cast film shows a clear surface topography resulting from several hundred nanometers large clusters of PCBM, which are mostly covered by the donor MDMO-PPV. For these films, the surface photovoltage shows positive values for regions where the PCBM clusters are covered with the donor layer, and negative values where the clusters are exposed to the surface. This shows that effective charge separation is only reached when the donor–acceptor junction is formed. However, this junction performs much better in the well-mixed chlorobenzene-cast organic blends, showing a homogeneous and large SPV [25, 26].

A similar study and similar conclusions were presented by Palermo et al. [27] for the donor–acceptor combination of P3HT and T5OHM, respectively.

Here illumination with white light results in charge separation at the interface with electron accumulation in the acceptor crystals and hole accumulation in the donor matrix. This effect changes the work function difference between donor and acceptor from 25 mV in the dark to 75 mV under illumination. Furthermore, by time-dependent experiments with light being switched on and off, the authors concluded that charging and discharging proceed on a similar time scale of 5–20 s, extracted from exponential fits to the CPD signal. The slightly slower discharge was attributed to charge trapping.

Coffey and Ginger [28] presented a study on F8BT/PFB polymer solar cells using electrostatic force microscopy (EFM). In addition to the above presented studies, they investigated the dynamic behavior of charge separation using time resolved measurements. After excitation of the blended films with light pulses, the temporal evolution of the EFM signal was observed, and the authors concluded that right at the interface between F8BT and PFB the charging rate is slower. These microscopic charging rates were shown to correlate well with macroscopic external quantum efficiency measurements for a series of blend ratios of F8BT:PFB ranging between 0 and 100%.

8.3 Grain Boundaries in Thin Film Solar Cells

One specific feature of polycrystalline solar cells that has received considerable attention is the electrostatic properties of grain boundaries in polycrystalline semiconductor layers. Thin film solar cells consist of polycrystalline materials and contain an abundance of grain boundaries. The role of these grain boundaries is still under discussion and many studies using KPFM have been performed, with the goal to study the electrostatic properties of GBs, and the possible presence of charges [29]. A general discussion of the physics of grain boundaries in chalcopyrite semiconductors has been presented by Rau et al. [30].

8.3.1 Si-Based Solar Cells

Despite the relatively large grain size in polycrystalline Si solar cells, the grain boundaries still have a detrimental effect on the device efficiency. It is therefore highly useful to obtain local information about the electronic structure of grain boundaries. With KPFM the potential at grain boundaries in polycrystalline Si has been measured in the dark and under illumination [31]. To avoid influence of the detection laser of the AFM system, a piezo-resistive cantilever was used, thus replacing the optical beam deflection detection method by a piezo-electric detection method. A potential peak was found at the grain boundaries when measured in the dark as well as when measured under monochromatic laser illumination. The photovoltage (the difference between illuminated and dark measurement) showed a different size for different grain boundaries [31].

Using a pulsed illumination at different pulse frequencies, Takihara et al. [32] extracted the minority carrier lifetime with local resolution. Using this method, they performed measurements across grain boundaries of polycrystalline Si, finding a gradually decreasing minority carrier lifetime toward the grain boundary. At the grain boundary a lifetime of $\sim$100 µs was found, only half the value found on the grains. This drop goes along with a drop in the photovoltage at the grain boundary [31, 32]. It was concluded that the examined $\Sigma 3$ grain boundary acts as a recombination site, thus degrading the solar cell performance.

With the goal to understand the mechanism of passivation of grain boundaries in polycrystalline solar cells upon H_2O vapor treatment, Honda et al. [33] performed KPFM measurements on treated and untreated samples. After the H_2O treatment, a potential peak found at the grain boundaries was reduced to half its size, from $\sim$80 mV to $\sim$40 mV. Measurements of the Hall mobility showed an increased mobility upon the treatment, leading to the conclusion that the water vapor passivates the grain boundaries leading to the lower potential peak. This behavior and the mechanism of passivation is concluded to be different from passivation by nitrogen or hydrogen annealing [33].

8.3.2 Cu(In,Ga)(S,Se)$_2$-Based Solar Cells

The role of grain boundaries in polycrystalline chalcopyrite thin films has received considerable attention. KPFM was used in many studies to improve the understanding of the grain boundary properties. Results from KPFM experiments were in many cases compared to different models for the understanding of their properties. One model is based on charged defects in the position of the grain boundaries [34]. The defects will cause band bending which repels or attracts the respective charge carriers and will be a source for recombination. In difference to this electronic grain boundary model, a model based on structural considerations and density-functional theory calculations proposed the presence of a Cu-deficiency in the grain boundary plane, leading to a valence band offset [35, 36]. The valence band offset would repel holes and therefore reduce recombination of the minority carriers in the grain boundaries. Yet another model proposes that a large lattice relaxation around the defects in the grain boundary plane results in a shift of the defect levels from within the band gap to the bands [37]. Thus, those defects are not active electronically, which reduces recombination and could therefore explain the high device efficiencies obtained for these polycrystalline solar cells. To study the impact of these models on the solar cell device, two-dimensional device simulations were used; these propose that independent of the model, a rather large band bending or band offset is required to provide for an improvement of the device efficiency [38–40]. The goal of the many KPFM studies on these materials was to obtain experimental information about the electronic properties of the grain boundaries in these materials.

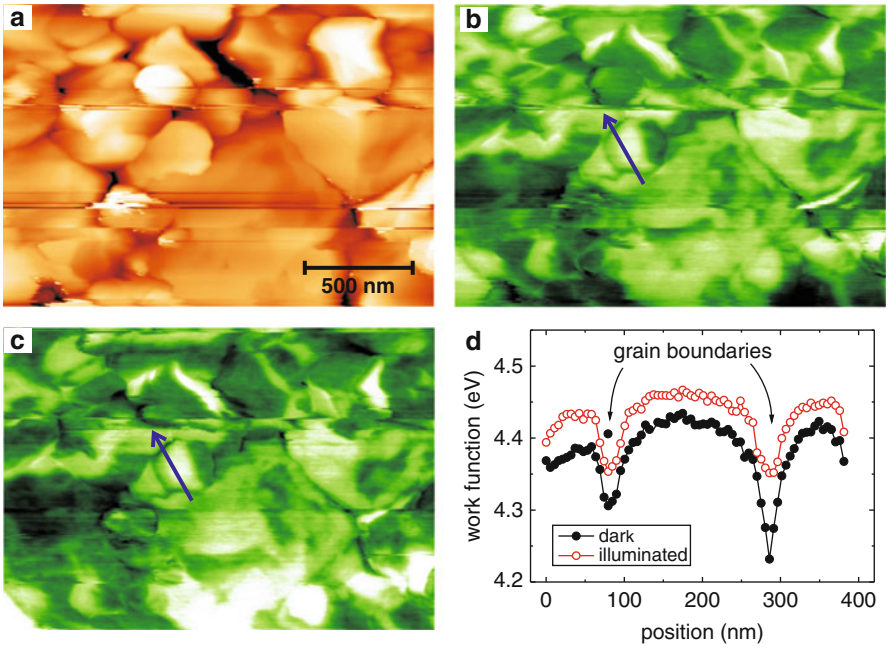

Fig. 8.6 KPFM measurement of a PVD grown $CuGaSe_2$ film. (**a**) Topography ($\Delta z = 360$ nm), (**b**) work function in the dark ($\Phi = 4.23-4.50$ eV) and (**c**) under illumination ($\Phi = 4.20-4.50$ eV). (**d**) Line profile along the *arrow* in (**b**) and (**c**), showing a drop in the work function at the GBs [41]

Initial KPFM experiments determining the surface potential across individual GBs were performed on a $CuGaSe_2$ thin film grown onto Mo-covered glass by PVD. The sample was transferred through air into a UHV-KPFM system [41]. The topography of the polycrystalline thin film is shown in Fig. 8.6a, exhibiting the typical granular structure. The corresponding work function measured under dark conditions is shown in Fig. 8.6b. Dark lines at the positions of the GBs surround areas of nearly constant work function. A line profile across two GBs is shown in Fig. 8.6d by the solid black circles. Similar results were found on a $Cu(In,Ga)Se_2$ film measured in air [42]. The shape of the work function dip at the GBs agrees very closely with the results obtained from simulations [43]. Thus, this result of the KPFM experiment does not provide sufficient information for a distinction of the applicability of the structural or the electronic GB model described above. To obtain additional information, measurements under super band gap illumination were performed; the same sample area as in Fig. 8.6b is shown under illumination in Fig. 8.6c. The respective line profile is shown by the open red circles in Fig. 8.6d. The work function under illumination is slightly increased by $\sim$50 mV, which can be attributed to a reduced surface band bending. Furthermore, it can be observed that the work function dip at the right GB is decreased with respect to the dark measurement, indicating a different electronic behavior of the two GBs.

As shown in Fig. 8.5, the work function measured with KPFM is very sensitive to the surface condition and the surface treatment. Thus, one concern with the obtained work function dip at the grain boundaries would be the state of the surface. However, as shown in Fig. 8.5c, the size of the dip is nearly independent of the sputter or annealing treatment the surface was exposed to. This demonstrates that the specific surface condition does not have a severe influence on the measurement of the GB potential, and that the dip is a property of the grain boundary itself and not of the surface condition at the grain boundary.

The influence of segregated Na at the absorber surface on KPFM experiments was studied by comparing untreated and water-rinsed surfaces. Jiang et al. [42] found sharper and deeper dips in the work function at the positions of GBs after cleaning the sample surface by rinsing with deionized water. Treatment with NH_4OH or $NH_4OH + CdSO_4$ resulted in a lower work function change at the GBs or even a flat work function image, respectively [44]. The influence of Na at the GBs was addressed also in a common study by KPFM and density functional theory calculations of the grain boundary atomic structure [37]. The theoretical calculations predict a high segregation probability for Na at the GBs; since Na acts as a shallow donor, a reduced work function should result for films grown in the presence of Na. The comparative KPFM study on Cu(In,Ga)Se_2 films grown on soda-lime glass and Na-free glass confirms this prediction [37].

A more concise study looked at differences between individual GBs. Measurements were performed on the back side of a $CuGaSe_2$ thin film, obtained by peel-off in UHV [45]. Differences in the observed GB potentials and light-induced activities were attributed to different GB structures. GBs showing a dip in the work function which remains unchanged upon illumination could be explained by the structural GB model [35] assuming an interface dipole. However, GBs showing light-induced changes were attributed to charged defects according to the electronic GB model [34].

The influence of a variation in the Ga/(In+Ga) ratio was studied by Jiang et al. [46]. They found for $CuInSe_2$ a work function drop of ∼150 mV at the GBs, which drops sharply to 0 mV at the Ga/(In+Ga) ratio ≈0.3, for which the highest power conversion efficiencies are obtained. However, due to the significantly smaller grain size for higher Ga contents, the KPFM measurements will be subject to a larger averaging effect [43], which likely has an impact on these findings. For Cu(In,Ga)Se_2 films with an optimal Ga-content of 30%, variation in the GB properties of differently textured films was shown using KPFM and cathodoluminescence (CL) [47]. While a randomly textured film shows a work function dip of ∼300 meV, a preferentially (220/204)-textured film shows no work function dip or even a slight work function peak. From CL experiments performed on samples from the same batches, stronger non-radiative recombination is observed for randomly and (112)-textured films, whereas (220/204)-textured films show a reduced electronic activity; the latter absorber layers result in devices exhibiting higher efficiency.

A few studies show the relation between structural and electronic properties of GBs, using single GBs obtained by growth of epitaxial chalcopyrite layers on GaAs bicrystals. Those samples were investigated by electron back scatter diffraction

(EBSD), Hall effect, and KPFM. A first study was performed on a $CuGaSe_2$ bicrystal containing a twin grain boundary [48, 49]. Contrary to the results on polycrystalline samples reported above, no work function dip could be observed in KPFM experiments. The charge carrier mobility across the GB was deduced from Hall measurements and shows an activated behavior with a barrier of $\sim$30 meV for majority carrier transport. These observations support the structural GB model [35], at least for the investigated twin GB ($\Sigma 3$) which according to structural considerations contains a low defect concentration.

A closer look at the KPFM experiments on polycrystalline material reveals that also here not all GBs show a work function dip. Thus, it appears likely that a wide variation of grain boundary orientations exists in the polycrystalline layers, where different orientations result in different electronic properties. This was addressed by studying bicrystals with GBs of different orientations, namely $\Sigma 9$ and $\Sigma 17$. In contrast to the $\Sigma 3$ twin GB, a $\Sigma 9$ GB in $CuGaSe_2$ does show a work function dip in the KPFM experiments [50, 51]. The dip is measured to be 30–90 meV and indicates the presence of charges at the grain boundary. The barrier for transport as determined by the Hall-mobility results to $\sim$100 meV and is thus slightly larger than the band bending observed in the KPFM experiment [51]. The difference between transport barrier and charge-induced band bending of the $\Sigma 3$ and $\Sigma 9$ grain boundaries is however similar, possibly indicating a constant contribution from the grain boundary structure in form of a valence band offset.

The above-described studies investigated the properties of GBs at the surface of the pure absorber film; however, the state of the GB could be influenced by the further deposition processes during the device fabrication, especially when considering that diffusion along GBs is considerably facilitated with respect to bulk diffusion. To investigate such an influence, UHV-clean $Cu(In,Ga)Se_2$ films onto which CdS was evaporated under UHV conditions were studied as a function of the deposited CdS layer thickness [10, 52]. For thin CdS films up to 10 nm, a region of 100–200 nm around the GBs exhibits a lower work function than regions on top of the grains; these regions are considerably wider than the work function dips observed in the pure absorber films. This observation was interpreted as a S-deficient CdS around the GBs (lower work function) from which sulfur has diffused into the GB resulting in an efficient passivation of GB defects. When using oxidized $Cu(In,Ga)Se_2$ films, these effects could not be observed and devices resulted in a lower efficiency as compared to devices from UHV-clean absorber films. A considerable Cd and S diffusion into a $CuGaSe_2$ absorber was independently confirmed by measuring the elemental distribution as a function of the depth into the absorber film [53].

8.3.3 CdTe-Based Solar Cells

Much less work has been presented regarding the study of GBs in CdTe-based solar cells using KPFM. Visoly-Fisher et al. [54] have used a combination of scanning capacitance and Kelvin probe force microscopy to study the electronic structure

of GBs in polycrystalline p-type CdTe layers deposited by closed space vapor transport. From the capacitance imaging, a depletion of holes around the grain boundaries was determined. For some specific grain boundaries even an inversion to n-type conductivity was observed [55]. Based on these measurements, schematic band diagrams of the GB region would show a downward band bending at the GBs. Measurements with KPFM were also performed on the same samples using a two-pass mode. In these experiments, a lower CPD was observed at the GBs, confirming the previous findings by scanning capacitance microscopy: a depletion of holes at the GBs and therefore a downward band bending at the GBs in the p-type CdTe thin film. In this respect, the findings for the CdTe layers are very similar to the ones for the chalcopyrite-based materials described in the previous section.

8.4 Cross-Sectional Device Characterization

A possibility to study the electronic properties inside a solar cell device is to perform KPFM experiments along the cross section of a device. This technique is well established for Si and III–V semiconductor structures and devices. In principle, cross-sectional KPFM experiments on solar cell devices allow to image the potential distribution inside the device. As the KPFM measures the local work function, i.e., the distance between the local vacuum level and the Fermi level, the obtained results are useful for the construction of a band diagram. Of special interest are the potential profiles across the contacts and the pn-junction. However, care has to be taken with data interpretation, as imaged potential profiles present a convolution of the inner potential and the surface potential, modified by surface reconstruction, surface defects, and surface charges.

8.4.1 Si-Based Solar Cells

Cross-section studies on Si solar cells have been conducted on amorphous, microcrystalline, and multicrystalline material with the goal to investigate the internal field distribution in the devices.

A first study investigated the field distribution in a microcrystalline $p-i-n$ structure deposited by hot-wire CVD [56]. From the measured potential distribution, the electric field can be obtained by calculation of the derivative. The authors find an inhomogeneous field distribution, with a weaker field in the middle of the intrinsic region. This experimental information was then used to simulate the distribution of dopants in the structure, finding a graded donor and a constant acceptor distribution. At the contact between the p-type Si and the n-type transparent conductive oxide layer, even a reverse diode was found.

Jiang et al. investigated the distribution of the electrical potential of amorphous Si (a-Si:H) and a-SiGe:H $p-i-n$ solar cells [57, 58]. In the experiments the device

is grown on top of a GaAs substrate to provide a flat surface after cleavage of the substrate. The CPD is then measured with the KPFM at different applied bias voltages across the device. From the comparison of the field distribution in a-Si:H solar cells for devices with different thickness, the authors conclude that the best field characteristic is provided for layers below ∼500 nm thickness [57]. For devices with ∼250 nm thick i-layers, the potential decreases linearly across the devices, whereas for thicker devices a stronger voltage drop is found at the i/n transition region. Similar experiments were performed to compare a-Si:H and a-SiGe:H $p{-}i{-}n$ structures. Here a stronger field was found at the respective p/i and i/n interfaces in the a-Si:H device, where the nonuniform field distribution could be reduced by implementation of buffer layers at the transitions [58]. For the a-SiGe:H device, the field distribution was found to be more inhomogeneous, with a much stronger field at the p side of the i-layer, which was attributed to a charge accumulation due to increased defect density at this position.

The same authors presented also a study on multicrystalline Si solar cells incorporating a pn-junction [59]. Again the potential distribution in the device was measured for different applied bias-voltages and the respective electric field distribution was determined. Comparison to device simulations was used to identify the junction location in the device; however, deviations of ∼40 nm in position were found. The authors also present a two-dimensional image of the junction in the device, finding that the shape of the junction follows the shape of the surface. Thus, in these multicrystalline solar cells, the pn-junction is concluded to be at the same depth from the surface throughout the device.

8.4.2 *Cu(In,Ga)(S,Se)$_2$-Based Solar Cells*

For Si and III–V single crystalline semiconductor devices, cleavage presents an excellent approach to prepare cross sections suitable for scanning probe experiments. However, cleavage of the glass substrate used in chalcopyrite thin film solar cells in combination with the poor adhesion of the chalcopyrite layer to the Mo back contact results in a fairly large roughness of the cleavage face. It has also been found that cleavage occurs along the grain boundaries, resulting in additional roughness [60]. Therefore, in many studies polished cross-section samples were used for KPFM experiments [61]. For this purpose, a complete device is cut into two halves and glued face-to-face. By sputter cleaning of the cross section surface proper electronic surface properties could be restored [61]. Samples without sputter cleaning exhibit a reduced CPD contrast of only ∼100 meV between the different layers [61].

Figure 8.7 shows the development of the work function of the various materials used in a $CuGaSe_2$ solar cell device [62] subject to different sputter cleaning steps [61]. Solid symbols correspond to measurements in the dark, while open symbols represent the work function under illumination. The increased work function of the $CuGaSe_2$ layer under illumination corresponds to a reduced band bending at

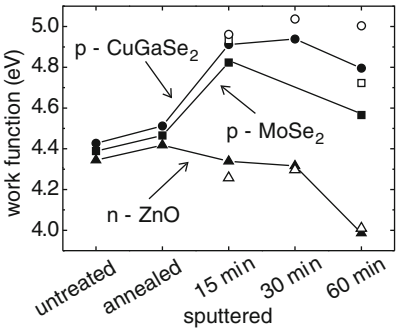

Fig. 8.7 Work function of the different materials in a CVD-grown $CuGaSe_2$ solar cell after different surface treatments. The open symbols represent the values under super band gap illumination ($\sim$60 mW, $\lambda = 442$ nm). Reprinted from [61] with permission

the *p*-type semiconductor surface. The strong change for longer sputtering times is attributed to preferential sputtering of some elements and to a resulting change in surface stoichiometry [17]. The work function changes upon sputtering the cross section are in agreement with those shown in Fig. 8.5. However, highly doped *n*-ZnO shows almost no change for the different sputter steps; due to the high doping, surface defects have a much weaker influence on the surface band bending.

A comparative study between two $CuGaSe_2$ solar cell devices has been performed, where a Ga-rich grown $CuGaSe_2$ absorber was compared to a Cu-rich absorber [61, 63]. To obtain best power conversion efficiencies, Ga-rich absorbers are used, while Cu-rich mostly result in poor device efficiencies, many times due to short circuits in the device. The cross-sectional KPFM experiments on the polished surface after a suitable sputter cleaning showed a contrast of $\sim$570 meV between the work function of *p*-$CuGaSe_2$ and *n*-ZnO, which increased to $\sim$700 meV under illumination (see Fig. 8.8). For the device functionality, the CdS buffer layer and its electronic effect on the device is of special interest. However, the 50-nm-thick CdS layer is incorporated in between the *p* and *n* side, right at the junction. At this point the strongest potential drop in the KPFM measurement is observed and a reasonable assignment of a work function for the CdS layer is not possible. Nevertheless, at the interface between the absorber and the Mo back contact, an additional work function contrast could be observed. This additional layer of $\sim$100 nm thickness shows a distinct work function from the Mo and the $CuGaSe_2$ and was attributed to $MoSe_2$, which develops during the CVD growth of the absorber material. It was independently confirmed by transmission electron microscopy [61].

The study on the Cu-rich grown $CuGaSe_2$ device revealed rich information and interesting insights in the reasons for device failure when the absorber material is grown under Cu-rich conditions. A work function image is shown in Fig. 8.9a. Clearly a different contrast can be observed for the ZnO window with the low work function, the buffer layer, and the absorber material. Even three different grains can be identified, indicated by the numbers “1” through “3.” In comparison

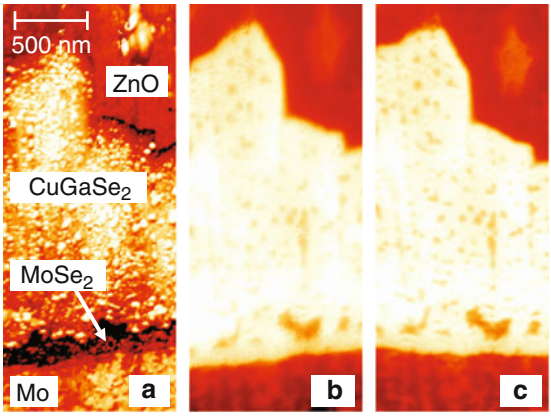

Fig. 8.8 Cross-sectional UHV-KPFM images ($1{,}200 \times 2{,}800\,\mathrm{nm}^2$) of a CVD-grown $CuGaSe_2$ solar cell after 15 min Ar-ion sputtering (500 eV). (**a**) Topography (height scale = 45 nm), (**b**) work function (Φ = 4.44–5.01 eV) and (**c**) work function (Φ = 4.48–5.18 eV) under illumination ($\sim$60 mW, λ = 442 nm) [61]

to scanning energy dispersive X-ray diffraction (EDX) measurements on the same sample position, the grains were assigned to different phases, where grains "1" and "2" were $CuGaSe_2$ and grain "3" was found to be $Cu_{2-x}Se$, which also shows a clearly higher work function than the $CuGaSe_2$. An interesting feature is seen at the grain boundary between the two $CuGaSe_2$ grains "1" and "2." Here the work function shows an increase (see Fig. 8.9b) as opposed to the findings presented in Chap. 8.3. This increased work function was assigned to a $Cu_{2-x}Se$ phase that also segregated at the grain boundary; this phase is likely p^+-type, conductive, and therefore also responsible for the shorts between the *n*-ZnO and the Mo back contact. Another interfacial phase is found at the transition from the $CuGaSe_2$ grain "1" to the *n*-ZnO window layer. As seen from the work function line profile in Fig. 8.9c, a barrier for minority carrier transport into the ZnO window layer is observed. The authors attributed the higher work function of this buffer to a Cu_xS-phase. It was suggested that during the chemical bath deposition of the CdS buffer layer, a $Cu_{2-x}Se$ surface layer was converted into a Cu_xS-phase [63]. No such barrier was observed at the transition from the $Cu_{2-x}Se$-grain to the ZnO window layer, as seen in Fig. 8.9d.

The effect of a different buffer/window layer was investigated in a cross-sectional study using the absorber material $Cu(In,Ga)(S,Se)_2$ [64]. Again, the potential distribution along the complete solar cell device structure after polished cross-section preparation was measured by KPFM. The authors compared solar cells without the CdS buffer layer, where the *i*-ZnO part of the window layer was exchanged for a (Zn,Mg)O layer of the same thickness ($\sim$100 nm). While the work function of the *i*-ZnO appears similar to that of the *n*-ZnO, the (Zn,Mg)O shows a lower work function, thereby making the potential drop at the *pn*-interface somewhat larger. In order to account for possible resolution limitations in the work

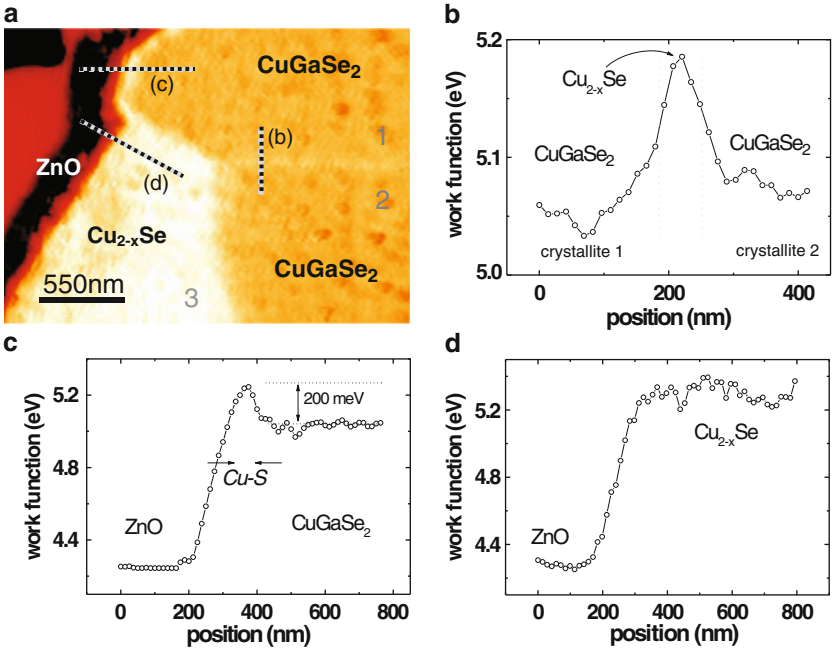

Fig. 8.9 KPFM measurement of a Cu-rich CVD-grown $CuGaSe_2$ solar cell device cross section. (**a**) Work function image showing the several materials and phases. (**b**) Line profile showing the presence of a $Cu_{2-x}Se$ foreign phase at the grain boundary between two $CuGaSe_2$ grains. (**c**) Transition from the ZnO window to the $CuGaSe_2$ with the electronic barrier due to the CuS phase. (**d**) Transition from the ZnO to the $Cu_{2-x}Se$ grain showing no barrier [63]

function imaging of small structures also simulations were performed. The contrast change as a function of tip-sample distance was found to agree well between simulations and experiment. This provides the possibility to estimate the full built-in voltage of the device without the influence of tip-averaging effects due to the long-range electrostatic force (see Chap. 2).

The Ga-distribution in a $Cu(In_{1-x},Ga_x)S_2$ solar cell device was investigated in a combined study by KPFM and EDX in a scanning electron microscope (SEM). The EDX measurements revealed a two layer structure within the $Cu(In_{1-x},Ga_x)S_2$ absorber layer, showing a significantly enhanced Ga-content toward the Mo back contact. By comparison to the KPFM image, taken at the same position as the EDX-SEM image, a sharp increase in the CPD coincides with the increase in the gallium concentration. This increase in the electric potential at the transition from the Ga-rich back layer to the In-rich front layer results in an electric field oriented such that it causes an acceleration of electrons toward the indium-rich region of the absorber layer, i.e., away from the back contact of the solar cell. This back surface field provides for a reduction of back contact recombination and explains the improved carrier collection, especially for those carriers generated by near band edge photons deep inside the absorber [65].

For a study on a cleaved cross section, a special preparation of a solar cell device on a GaAs substrate was undertaken [66]. In this study, special attention was given to the pn-junction between the Cu(In,Ga)Se_2 absorber and the CdS buffer layer. Analysis of the electrical potential profiles obtained from the KPFM measurements along the cleaved cross sections demonstrated that the pn-junction is a buried homojunction and does not coincide with the metallurgical junction between the materials. The electronic pn-junction is located 30–80 nm from the interface in the Cu(In,Ga)Se_2 layer [66]. This is advantageous for the device performance, as at the metallurgical junction considerably more electronic defects are expected than inside the homogeneous Cu(In,Ga)Se_2 material; a reduced recombination at the interface should be the result.

8.4.3 III–V-Based Solar Cells

As mentioned above, III–V materials present an excellent specimen for cross section preparation by simple cleavage of the device structure. Typically, III–V devices are grown along the ⟨001⟩ direction and the typical cleavage plane is the {110} surface, which then exposes the cross section through the device structure.

Jiang et al. [67] have studied a $GaInP_2$ solar cell and extracted the potential profile across the device structure. Comparison of the experimental result to a one-dimensional Poisson simulation of the device reveals that the experimental KPFM profile shows less details than the simulated potential profile. This was on one hand attributed to the limited resolution of the KPFM measurements, which were performed in air, and on the other hand to surface contamination and oxidation of the exposed $GaInP_2$ cross section. The surface defects created due to oxidation and contamination result likely in Fermi level pinning, thereby modifying the measured potential profile [67]. The $GaInP_2$ junction was also investigated as part of a tandem solar cell in combination with a GaAs bottom cell [67, 68]. Potential profiles were measured as a function of externally applied bias voltage across the device with and without illumination, providing different illumination energy to absorb either in the bottom or in the top cell. While illumination flattens the band bending of the illuminated top cell, the voltage drop occurs in all cases at the cell which is not illuminated [68].

The III–V compound GaInNAs was investigated as a possible candidate for the fourth junction in a multi-junction solar cell [69]. The junction is realized as a $p{-}i{-}n$ junction to ease current matching to the rest of the device. To decrease surface roughness induced by the high In content, Bi is investigated as a surfactant during the growth. However, the Bi also results in an electronic effect, observed for example in the internal quantum efficiency (IQE), which indicates a different junction position as a function of the Bi content [69]. Using KPFM, the potential profile through the device structure was measured, thus allowing the direct experimental determination of the junction position, which was found to be in good agreement to the indirect determination from the IQE measurements.

A cross-sectional KPFM study under ultrahigh vacuum (UHV) conditions on a III–V structure has been presented by Schwarzman et al. [70]. The authors investigated a quantum well solar cell device by KPFM and secondary electron imaging in high-resolution scanning electron microscopy (HRSEM) and compared experimental results to device simulations. The solar cell was a strain-balanced $In_{0.17}GaAs/GaAsP_{0.06}$ multiquantum well structure consisting in 8-nm-thick $In_{0.17}GaAs$ wells separated by 45-nm-thick $GaAsP_{0.06}$ barriers. Both HRSEM and KPFM could resolve the potential profile of the individual wells; however, the KPFM profile shows a weaker contrast between well and barrier than expected from the device simulations. The authors also conducted a deconvolution procedure for the KPFM potential profile which considers the averaging effect of the scanning AFM tip [71]. This deconvolution demonstrates that the measured potential profile only exhibits half the depth of the potential wells, showing that after deconvolution the KPFM result is in good agreement with the device simulation [70].

8.5 Summary

This chapter described the application of KPFM for the investigation of solar cell materials and devices. KPFM provides access to the structural and electronic properties of these devices, usually consisting in layers of different material or intermixed materials. Performing KPFM with additional illumination provides the possibility to study the device or parts thereof under simulated operating conditions. Two main approaches were described, on one hand, studies were presented on the surface of the absorber material, or the various other layers of which the device structure is built up. In these studies, the effects of polycrystallinity, the optoelectronic properties of grain boundaries, or the electronic structure of crystal facets on the surface were investigated. On the other hand, studies of cross sections of the complete devices provide valuable information on the potential profiles through the device structure. This is of high importance as the electric field distribution can be inferred, which is responsible for proper charge carrier separation. But also material inhomogeneities and impurity phases can be investigated and their possible effect on device efficiency studied. The large number of KPFM studies on solar cell materials and devices throughout the recent years shows that the nanoscale electronic and structural characterization of such electronic devices provides valuable information for the understanding and improvement of solar cells. It is expected that also in the future KPFM remains an important tool for such characterization of solar cells.

References

1. H.J. Lewerenz, H. Jungblut, *Photovoltaik* (Springer, Berlin, 1995)
2. A.L. Fahrenbruch, R.H. Bube, *Fundamentals of Solar Cells* (Academic, New York, 1983)
3. I. Repins, M.A. Contreras, B. Egaas, C. DeHart, J. Scharf, C.L. Perkins, B. To, R. Noufi, Prog. Photovolt Res. Appl. **16**, 235 (2008)
4. Ch.J. Brabec, N.S. Sariciftci, J.C. Hummelen, Adv. Funct. Mat. **11**, 15 (2001)

5. F. Yang, M. Shtein, S. Forrest, J. Appl. Phys. **98**, 014906 (2005)
6. Ch. Sommerhalter, Th.W. Matthes, Th. Glatzel, A. Jäger-Waldau, M.Ch. Lux Steiner, Appl. Phys. Lett. **75**, 286 (1999)
7. R. Würz, M. Rusu, Th. Schedel-Niedrig, M.Ch. Lux-Steiner, H. Bluhm, M. Hävecker, E. Kleimenov, A. Knop-Gericke, R. Schögl, Surf. Sci. **580**, 80 (2005)
8. S. Sadewasser, K. Ishii, Th. Glatzel, M.Ch. Lux-Steiner, in *Polycrystalline Semiconductors VII- Bulk Materials, Thin Films, and Devices*, ed. by T. Sameshima, T. Fuyuki, H.P. Strunk, J.H. Werner (Scitech Publ., Uettikon am See, Switzerland, 2003), p. 319
9. S. Sadewasser, Th. Glatzel, M. Rusu, A. Meeder, D. Fuertes Marrón, A. Jäger-Waldau, M.Ch. Lux-Steiner, Mater. Res. Soc. Symp. Proc. **668**, H5.4.1 (2001)
10. M. Rusu, Th. Glatzel, A. Neisser, C.A. Kaufmann, S. Sadewasser, M.Ch. Lux-Steiner, Appl. Phys. Lett. **88**, 143510 (2006)
11. D. Fuertes Marrón, A. Meeder, S. Sadewasser, R. Würz, C.A. Kaufmann, Th. Glatzel, Th. Schedel-Niedrig, M.Ch. Lux-Steiner, J. Appl. Phys. **97**, 094915 (2005)
12. S. Sadewasser, Phys. Stat. Sol. (a) **203**, 2571 (2006)
13. S. Sadewasser, Th. Glatzel, M. Rusu, A. Jäger-Waldau, M.Ch. Lux-Steiner, Appl. Phys. Lett. **80**, 2979 (2002)
14. R. Hunger, T. Schulmeyer, A. Klein, W. Jaegermann, K. Sakurai, A. Yamada, P. Fons, K. Matsubara, S. Niki, Surf. Sci. **557**, 263 (2004)
15. T. Schulmeyer, R. Kniese, R. Hunger, W. Jaegermann, M. Powalla, A. Klein, Thin Solid Films **451–452**, 420 (2004)
16. R. Würz, D. Fuertes Marrón, A. Meeder, A. Rumberg, S.M. Babu, Th. Schedel-Niedrig, U. Bloeck, P. Schubert-Bischoff, M.Ch. Lux-Steiner, Thin Solid Films **431–432**, 398 (2003)
17. K. Otte, G. Lippold, D. Hirsch, A. Schindler, F. Bigl, Thin Solid Films **361–362**, 498 (2000)
18. S. Schuler, S. Nishiwaki, J. Beckmann, N. Rega, S. Brehme, S. Siebentritt, M.Ch. Lux-Steiner, in 29th IEEE Photovoltaic Specialist Conference (IEEE, New Orleans, 2002), p. 504
19. Th. Deniozou, N. Esser, S. Siebentritt, Surf. Sci. **579**, 100 (2005)
20. L. Kronik, Y. Shapira, Surf. Sci. Rep. **37**, 1 (1999)
21. S. Sadewasser, Th. Glatzel, M. Rusu, A. Meeder, A. Jäger-Waldau, M.Ch. Lux-Steiner, Proc. of the 17th European Photovoltaic Solar Energy Conference, München, 2001, p. 1155
22. S. Saraf, R. Shikler, J. Yang, Y. Rosenwaks, Appl. Phys. Lett. **80**, 2586 (2002)
23. F. Streicher, S. Sadewasser, M.Ch. Lux-Steiner, Rev. Sci. Instrum. **80**, 013907 (2009)
24. F. Streicher, S. Sadewasser, T. Enzenhofer, H.-W. Schock, M.Ch. Lux-Steiner, Thin Solid Films **517**, 2349 (2009)
25. Th. Glatzel, H. Hoppe, N.S. Sariciftci, M.Ch. Lux-Steiner, M. Komiyama, Jap. J. Appl. Phys. **44**, 5370 (2005)
26. H. Hoppe, Th. Glatzel, M. Niggemann, A. Hinsch, M.Ch. Lux-Steiner, N.S. Sariciftci, Nano Lett. **5**, 269 (2005)
27. V. Palermo, G. Ridolfi, A.M. Talarico, L. Favaretto, G. Barbarella, N. Camaioni, P. Samori, Adv. Funct. Mater. **17**, 472 (2007)
28. D.C. Coffey, D.S. Ginger, Nat. Mater. **5**, 735 (2006)
29. S. Sadewasser, Thin Solid Films **515**, 6136 (2007)
30. U. Rau, K. Taretto, S. Siebentritt, Appl. Phys. A **96**, 221 (2008)
31. M. Takahira, T. Igarashi, T. Ujihara, T. Takahashi, Jap. J. Appl. Phys. **46**, 5548 (2007)
32. M. Takahira, T. Takahashi, T. Ujihara, Appl. Phys. Lett. **93**, 021902 (2008)
33. S. Honda, T. Mates, B. Rezek, A. Fejfar, J. Kočka, J. Non-Cryst. Solids **354**, 2310 (2008)
34. J.Y.W. Seto, J. Appl. Phys. **46**, 5247 (1975)
35. C. Persson, A. Zunger, Phys. Rev. Lett. **91**, 266401 (2003)
36. C. Persson, A. Zunger, Appl. Phys. Lett. **87**, 211904 (2005)
37. Y. Yan, C.-S. Jiang, R. Noufi, S.-H. Wei, H.R. Moutinho, M.M. Al-Jassim, Phys. Rev. Lett. **99**, 235504 (2007)
38. W.K. Metzger, M. Gloeckler, J. Appl. Phys. **98**, 063701 (2005)
39. M. Gloeckler, J.R. Sites, W.K. Metzger, J. Appl. Phys. **98**, 113704 (2005)
40. K. Taretto, U. Rau, J.H. Werner, Thin Solid Films **480–481**, 8 (2005)

41. S. Sadewasser, Th. Glatzel, S. Schuler, S. Nishiwaki, R. Kaigawa, M.Ch. Lux-Steiner, Thin Solid Films **431–432**, 257 (2003)
42. C.-S. Jiang, R. Noufi, J.A. AbuShama, K. Ramanathan, H.R. Moutinho, J. Pankow, M.M. Al-Jassim, Appl. Phys. Lett. **84**, 3477 (2004)
43. C. Leendertz, F. Streicher, M.Ch. Lux-Steiner, S. Sadewasser, Appl. Phys. Lett. **89**, 113120 (2006)
44. C.-S. Jiang, R. Noufi, K. Ramanathan, H.R. Moutinho, M.M. Al-Jassim, J. Appl. Phys. **97**, 053701 (2005)
45. D. Fuertes Marrón, S. Sadewasser, Th. Glatzel, A. Meeder, M.Ch. Lux-Steiner, Phys. Rev. B **71**, 033306 (2005)
46. C.-S. Jiang, R. Noufi, K. Ramanathan, J.A. AbuShama, H.R. Moutinho, M.M. Al-Jassim, Appl. Phys. Lett. **85**, 2625 (2004)
47. G. Hanna, Th. Glatzel, S. Sadewasser, N. Ott, H.P. Strunk, U. Rau, J.H. Werner, Appl. Phys. A **82**, 1 (2006)
48. S. Siebentritt, S. Sadewasser, M. Wimmer, C. Leendertz, T. Eisenbarth, M.Ch. Lux-Steiner, Phys. Rev. Lett. **97**, 146601 (2006)
49. S. Siebentritt, T. Eisenbarth, M. Wimmer, C. Leendertz, F. Streicher, S. Sadewasser, M.Ch. Lux-Steiner, Thin Solid Films **515**, 6168 (2007)
50. M. Hafemeister, S. Siebentritt, S. Sadewasser, Ch. Frank-Rotsch, M.Ch. Lux-Steiner, in *Thin-Film Compound Semiconductor Photovoltaics-2007*, ed. by T. Gessert, K. Durose, C. Heske, S. Marsillac, T. Wada. Mater. Res. Soc. Symp. Proc. vol. 1012 (Warrendale, PA, 2007), pp. Y09-04
51. M. Hafemeister, S. Siebentritt, J. Albert, M.Ch. Lux-Steiner, S. Sadewasse, Phys. Rev. Lett. **104**, 196602 (2010)
52. Th. Glatzel, M. Rusu, S. Sadewasser, M.Ch. Lux-Steiner, Nanotechnology **19**, 145705 (2008)
53. M. Rusu, M. Bär, S. Lehmann, S. Sadewasser, L. Weinhardt, C.A. Kaufmann, E. Strub, J. Röhrich, W. Bohne, I. Lauermann, Ch. Jung, C. Heske, M.Ch. Lux-Steiner, Appl. Phys. Lett. **95**, 173502 (2009)
54. I. Visoly-Fisher, S.R. Cohen, D. Cahen, Appl. Phys. Lett. **82**, 556 (2003)
55. I. Visoly-Fisher, S.R. Cohen, K. Gartsman, A. Ruzin, D. Cahen, Adv. Func. Mat. **16**, 649 (2006)
56. A. Breymesser, V. Schlosser, D. Peiró, C. Voz, J. Bertomeu, J. Andreu, J. Summhammer, Sol. Energy Mater. Sol. Cells **66**, 171 (2001)
57. C.-S. Jiang, H.R. Moutinho, M.J. Romero, M.M. Al-Jassim, Y.Q. Xu, Q. Wang, Thin Solid Films **472**, 203 (2005)
58. C.-S. Jiang, H.R. Moutinho, Q. Wang, M.M. Al-Jassim, B. Yan, J. Yang, S. Guha, Mat. Res. Soc. Symp. Proc. **808**, A9.42.1 (2004)
59. C.-S. Jiang, H.R. Moutinho, R. Reedy, M.M. Al-Jassim, A. Blosse, J. Appl. Phys. **104**, 104501 (2008)
60. C. Ballif, H.R. Moutinho, F.S. Hasoon, R.G. Dhere, M.M. Al-Jassim, Ultramicroscopy **85**, 61 (2000)
61. Th. Glatzel, D. Fuertes Marrón, Th. Schedel-Niedrig, S. Sadewasser, M.Ch. Lux-Steiner, Appl. Phys. Lett. **81**, 2017 (2002)
62. D. Fischer, T. Dylla, N. Meyer, M.E. Beck, A. Jäger-Waldau, M.Ch. Lux-Steiner, Thin Solid Films **387**, 63 (2001)
63. D. Fuertes Marrón, Th. Glatzel, A. Meeder, Th. Schedel-Niedrig, S. Sadewasser, M.Ch. Lux-Steiner, Appl. Phys. Lett. **85**, 3755 (2004)
64. Th. Glatzel, H. Steigert, S. Sadewasser, R. Klenk, M.Ch. Lux-Steiner, Thin Solid Films **480–481**, 177 (2005)
65. R. Mainz, F. Streicher, D. Abou-Ras, S. Sadewasser, R. Klenk, M.Ch. Lux-Steiner, Phys. Stat. Sol. (a) **206**, 1017 (2009)
66. C.-S. Jiang, F.S. Hasoon, H.R. Moutinho, H.A. Al-Thani, M.J. Romero, M.M. Al-Jassim, Appl. Phys. Lett. **82**, 127 (2003)

67. C.-S. Jiang, H.R. Moutinho, D.J. Friedman, J.F. Geisz, M.M. AlJassim, J. Appl. Phys. **93**, 10035 (2003)
68. C.-S. Jiang, D.J. Friedman, J.F. Geisz, H.R. Moutinho, M.J. Romero, M.M. Al-Jassim, Appl. Phys. Lett. **83**, 1572 (2003)
69. A.J. Ptak,R. France, C.-S. Jiang, R.C. Reedy, J. Vac. Sci. Technol. B **26**, 1053 (2008)
70. A. Schwarzman, E. Grunbaum, E. Strassburg, E. Lepkifker, A. Boag, Y. Rosenwaks, Th. Glatzel, Z. Barkay, M. Mazzer, K. Barnham, J. Appl. Phys. **98**, 084310 (2005)
71. E. Strassburg, A. Boag, Y. Rosenwaks, Rev. Sci. Instrum. **76**, 083705 (2005)

Chapter 9
Electrostatic Force Microscopy Characterization of Low Dimensional Systems

Yoichi Miyahara, Lynda Cockins, and Peter Grütter

Abstract The electrostatic potential profile is of great importance in nanoscale electronic devices. The effect of the random potential caused by dopants or other defects becomes an increasingly more important problem as device size continues to shrink and as devices exploiting quantum effects emerge. We review the past studies on the potential profile in semiconductor heterostructures by Kelvin probe force microscopy (KPFM) and electrostatic force microscopy (EFM), focusing on the technical aspects of the experiments. We then describe measurements of the spatial and temporal fluctuations of the electrostatic potential in an InP/InGaAs heterostructure sample by EFM and KPFM using frequency modulation mode atomic force microscopy (AFM). We also describe a new EFM technique capable of detecting charge with single-electron resolution and show that such techniques can be used for quantitative spectroscopic measurements of discrete electronic states such as those in quantum dots. Finally, we compare EFM and KPFM with two non-AFM-based scanning probe techniques with highly sensitive potentiometry and electrometry capability.

9.1 Fluctuations of the Electrostatic Potential in Semiconductor Low-Dimensional Structures

It is of great importance to characterize the electrostatic potential profile in systems containing semiconductor heterostructures as various types of electronic devices, such as field effect transistors and semiconductor lasers, are built on such structures. In particular, further miniaturization of such electronic devices down to a few tens of nanometers makes it possible to develop new kinds of electronic devices exploiting quantum effects such as quantum dots and quantum point contacts.

Y. Miyahara (✉) · L. Cockins · P. Grütter
Department of Physics, McGill University, 3600 rue University, Montreal, H3A 2T8, Canada
e-mail: miyahara@physics.mcgill.ca

S. Sadewasser and T. Glatzel (eds.), *Kelvin Probe Force Microscopy*, Springer Series in Surface Sciences 48, DOI 10.1007/978-3-642-22566-6_9,

In these nanometer scale devices, the effects of electrostatic potential fluctuations in both space and time become crucial for proper operation. As the operation of the device relies on precise control of the electrostatic potential, which is usually performed by applying external voltages to the gate electrodes, background electrostatic fluctuations, either spatial or temporal, can cause serious undesirable effects. For example, a device may exhibit unexpected behavior, such as the formation of a triple quantum dot in a double quantum dot device [1], and/or low-frequency switching noise [2], both of which greatly degrade device performance. It has also been discussed recently that temporal charge fluctuations can be an important source of decoherence in charge qubits [3, 4].

In the case of silicon Metal-Oxide-Semiconductor Field Effect Transistor (Si-MOS-FET) devices, the situation is similar. As the size of the Si-MOS-FET is reduced to the lower tens of nanometers scale, the device size becomes comparable to the characteristic length of the potential fluctuations caused by randomly placed dopants or charged defects in the silicon oxide and oxide/Si interface. This leads to undesirable effects such as a large variability of device parameters such as the threshold voltage [5]. Temporal random charge fluctuations are also known to cause $1/f$ noise limiting low frequency noise performance. A similar issue has also been identified on graphene-based transistors where the random potential in a supporting substrate (typically SiO_2/Si) limits their performance due to their high sensitivity to the surrounding environment [6]. The effects of the random potential become crucial in attempts to realize Si-MOS-based quantum dots, which are of interest as potential solid-state implementations of quantum computing, because of a possible long coherence time [7]. The use of a random potential to create quantum dots has also been proposed [8].

Kelvin probe force microscopy (KPFM) and electrostatic force microscopy (EFM) are powerful tools for investigating the local electrostatic potential and have been used for characterizing such technically relevant systems as two-dimensional electron gases (2DEG) [9–11], high-κ dielectric films on silicon [12–14], and graphene [15, 16]. KPFM and EFM have also been applied to cross sections of technically relevant heterostructures such as $p-i-n$ junction and multiple quantum well laser diodes. The details can be found in a recent review [17]. Because of its importance in the development of quantum/nano electronic devices, other scanning probe techniques capable of giving similar information have also been developed and successfully applied to various systems [18, 19].

In the following sections, we first review the past KPFM and EFM studies on low-dimensional systems, mainly a 2DEG formed in semiconductor heterostructures. We then describe the observation of random electrostatic potential fluctuations by both dc electrostatic force microscopy (dc-EFM) and KPFM using frequency modulation mode atomic force microscopy (FM-AFM). We discuss an interesting relationship between dc-EFM and KPFM and the implications for topography imaging by FM-AFM. Finally, we present the measurement of temporal fluctuations by dc-EFM as a new application for nanoelectronic device research.

To conclude this chapter, a summary is presented of single-electron sensitive electrostatic force microscopy (e-EFM) and two other scanning probe techniques,

which are not based on AFM: scanning single electron transistor microscopy and scanning charge accumulation microscopy (SCAM).

9.1.1 Kelvin Probe Force Microscopy on Semiconductor Heterostructures

Spatially random potential fluctuations in semiconductor heterostuctures are an important subject of research in two different contexts: one in the development of electronic device applications, and the other in the more fundamental context of the quantum Hall effect (QHE).

The effect of the random potential caused by randomly positioned dopants on a 2DEG was postulated as a source of localized states, which play an essential role in the QHE [20]. Nixon and Davies [21] calculated this effect on a realistic 2DEG numerically and depicted the resulting localized states along with the random potential profile. A large number of experimental investigations have been reported since then. We will briefly review the experimental researches done by KPFM and EFM.

There is a substantial body of literature on the observation of the local potential profile in a 2DEG using AFM [10, 22–29]. These measurements were made on high quality 2DEGs formed in a GaAs/$Al_xGa_{1-x}As$ heterostructure interface at cryogenic temperature. The 2DEGs are located below the surface, typically at a depth of around 100 nm (500 nm in [29]). The local potential profile was measured by either ac electrostatic force microscopy (ac-EFM) or frequency modulation mode KPFM (FM-KPFM).

In ac-EFM, cantilever oscillations are excited by coupling the sample and the AFM tip via an electrostatic force. This force is controlled by applying a time varying (ac) voltage as well as a dc bias voltage between tip and 2DEG [30]. The ac modulation frequency, equal to/near the cantilever resonance frequency, is used to enhance the force detection sensitivity through the high quality factor of the AFM cantilever. When the dc bias voltage is regulated with a feedback circuit such that the electrostatic force signal is minimized, the resulting minimizing voltage can be interpreted as the contact potential difference between the tip and sample. This mode of operation was first proposed by Nonnenmacher et al. [31] and was later referred to as amplitude modulation mode KPFM (AM-KPFM). In order to keep the detection sensitivity constant, the oscillation of the cantilever can be driven by self-excitation and a positive feedback loop [22–26] or a phase lock loop (PLL excitation) [29] with a constant ac modulation amplitude. The self-excitation mode keeps the oscillation frequency at the cantilever resonance frequency even when the resonance frequency, is affected by the tip–sample interaction.

FM-KPFM has also been used for this type of measurement [24, 27, 28, 32]. The cantilever oscillation is self-excited mechanically with a piezoelectric actuator with a positive feedback loop [33]. In this case, the oscillation frequency tracks the cantilever resonance frequency which is being altered by the tip–sample interaction.

The change in the resonance frequency (resonance frequency shift) is a measure of the tip–sample interaction. In FM-KPFM, an ac modulation voltage with frequency well below the cantilever resonance frequency is applied between the tip and sample and the resulting modulation of the resonance frequency shift is detected by a lock-in amplifier [34]. The detected modulation is used as input to a dc potential feedback loop, which minimizes the electrostatic interaction by canceling the contact potential difference. It has been argued that FM-KPFM has a higher spatial resolution while AM-KPFM requires a much smaller ac modulation amplitude because of the enhancement of the force detection sensitivity by the high cantilever Q factor [35].

All the experiments mentioned above were performed with a constant-height mode scan at a tip–sample distance of a few tens of nanometers to reduce the influence from the topography. Here, the properties of buried structures (a 2DEG in this case) were probed using the variety of tecniques mentioned above. Most of the experiments focused on a local voltage distribution, in particular a local Hall voltage profile near the sample edge, which is important to understand the microscopic mechanism of electrical conduction in a 2DEG in the QHE regime. The measured signal due to the local contact potential is a disturbance for these measurements and therefore had to be compensated for by measuring a reference contact potential profile on a separate scan [24, 25] or both contact potential and Hall voltage profiles simultaneously using two different modulation frequencies [22, 23]. Hedberg et al. have demonstrated that the ac-EFM technique can be used to study the spatial variation in the density of states of a deep 2DEG which is located 500 nm below the surface by showing Shubnikov-de Haas oscillation observed in the force signal [29].

Crook et al. have used the AM-KPFM technique to characterize the charge pattern created on the surface of GaAs/$Al_xGa_{1-x}As$ heterostructure samples by controlled contact electrification with an AFM tip [10]. The charge patterns, which remain stable at low temperature, depleted the underlying 2DEG to define quantum electronic devices such as quantum dots and quantum point contacts. The technique is named Erasable Electrostatic Lithography (EEL) as the fabricated devices can be erased by light illumination [36]. They observed dissipating charge on the GaAs surface under illumination as well as a random potential profile in the background at 150 mK [10].

9.1.2 Large Spatial Fluctuations in Electrostatic Potential on Epitaxially Grown InAs/InGaAs/InP Heterostructures Observed by FM-AFM

9.1.2.1 Experimental Details

We have studied the electrostatic potential fluctuations in InAs quantum dot/InGaAs/InP heterostructures with a low-temperature AFM [37]. The samples are epitaxially grown by chemical beam epitaxy [38] and have an InGaAs quantum well (QW) in

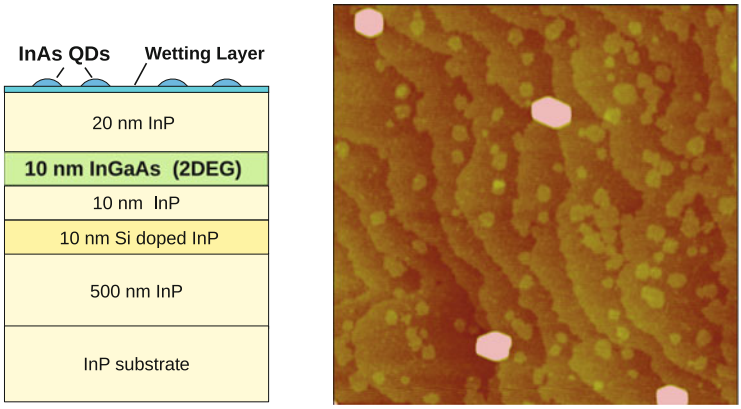

Fig. 9.1 (**a**) Structure of InGaAs/InP heterostructure sample with InAs QDs. (**b**) Topography images of InAs quantum dot sample grown on InP. ($1 \times 1\,\mu$m, height scale 4 nm)

which a two-dimensional electron gas (2DEG) is formed. The $In_{0.47}Ga_{0.53}As$ QW is formed 20 nm below the surface. A 10 nm thick Si-doped InP layer is grown 10 nm below the QW with a 10 nm undoped InP layer in-between. In this system, InAs self-assembled quantum dots (QD) can also be grown on the InP surface due to lattice mismatch. The schematic of the sample structure is shown in Fig. 9.1a.

Figure 9.1b shows a typical surface topography image of the InP/InGaAs/InP heterostructure sample. The image was taken in the amplitude modulation (AM) mode (tapping mode) in air at room temperature by a commercial AFM (Multimode, Veeco). It shows a smooth surface with monoatomic steps and facetted InAs quantum dots.

All the following AFM images were acquired with a home-built low temperature AFM [37] at either 77 or 4.5 K in 3×10^{-3} mbar of He gas atmosphere to better thermalize the sample. We used commercial Si AFM cantilevers (NCLR, Nanosensors). We coated the tip-side of the cantilevers with 20 nm Pt using a 10 nm thick Ti adhesion layer by sputtering to ensure good electrical conductivity at low temperature. The nominal resonance frequency of the coated cantilevers is 160 kHz and the quoted spring constant is $40 \sim 50\,\mathrm{N\,m^{-1}}$. The quality factor, Q, of the cantilevers is typically 8,000 at room temperature, 30,000 at 77 K and 100,000 at 4.5 K. We found that these quality factors were not limited by the dilute He gas atmosphere.

In frequency modulation (FM) imaging mode [33], a commercial oscillator controller and phase-lock loop frequency detector (easyPLLplus, Nanosurf) are used in the self-oscillation mode with a amplitude controller for a constant oscillation amplitude. For AM-mode imaging, the active Q control technique is needed to reduce a high Q factor to an appropriate value (about ~1,000) [39, 40]. The details of the technique are discussed in the following as this mode of operation (AM-mode

imaging in vacuum) has not been commonly employed. In both operating modes, an oscillation amplitude of 16 nm_{p-p} was typically used.

9.1.2.2 Active Q-Damped Amplitude Modulation Mode Imaging

In vacuum, the typical Q factor of commonly used AFM cantilevers reaches 10,000 or higher. AM-mode operation is impossible with cantilevers having such a high Q factor because of a long amplitude settling time (e.g., $\tau = Q/\pi f_0 \sim 63$ ms for $Q = 30{,}000$ and $f_0 = 150$ kHz) [33]. In order to circumvent this problem, we implemented an active Q control technique [39, 40] to decrease the effective Q factor in order to obtain a fast enough amplitude response for AM-mode operation.

Active Q control has been mostly used to increase the effective Q of cantilevers immersed in liquid environments to achieve higher and more stable imaging [41]. The same technique can also be used to decrease the effective Q by switching the phase shift by 180° in the oscillation control electronics. This active damping technique was applied to increase the imaging speed in AM-mode operation in air where the intrinsic Q of 150 was reduced to 7 [42].

Figure 9.2 shows a schematic diagram of the active Q controlled AM-mode AFM. The added component to the normal AM-mode AFM is the self-excitation loop, which consists of a phase shifter and variable gain amplifier (shown in the box in the figure) to form a feedback loop for the cantilever deflection signal. This feedback loop can be positive or negative depending on the setting of the phase shifter. The positive (negative) feedback leads to an increase (decrease) in effective Q factor.

We use the phase shifter and variable gain amplifier in a commercially available oscillator controller (EasyPLLplus, Nanosurf), which was originally designed to

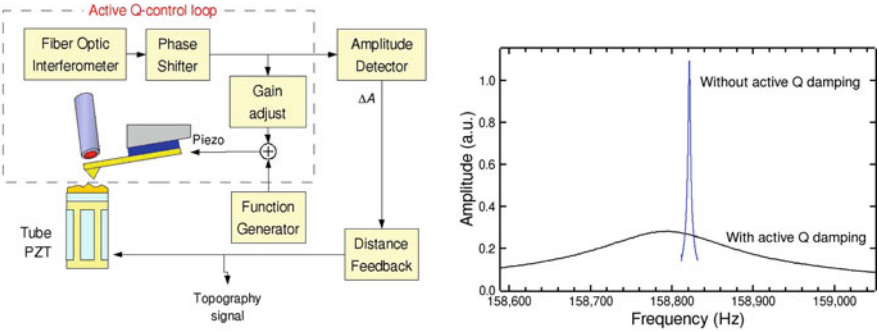

(a) Block diagram of Q control technique

(b) Cantilever resonance

Fig. 9.2 (**a**) Block diagram of active Q-damped amplitude modulation mode AFM. (**b**) Cantilever resonance curves with/without active Q damping. $Q = 59{,}000$ before and $Q = 960$ after active Q damping

be used for FM-mode operation. An external summing amplifier was used to add the self-excitation signal to an external drive signal from a signal generator. In order to decrease the effective Q, we first adjust the phase so that the cantilever starts self-oscillating at its resonance frequency by minimizing the drive amplitude as is done in the normal FM-mode operation. Then we invert the phase by 180° to switch to active-Q damping mode operation. The self-oscillating loop is now working as a negative feedback as opposed to the previous case, and the higher feedback gain leads to a lower effective Q factor. We reduced an intrinsic Q factor of more than 10,000 to an effective Q factor of less than 1,000 (Fig. 9.2b), which enables a reasonable scanning speed using typical AFM cantilevers with a resonance frequency of a few 100 kHz.

A low-pass filter is often needed to suppress the oscillation from higher oscillation modes (usually from second flexural mode). The highest possible gain (which means the minimum possible Q) is limited by the self-oscillation of other mechanical vibrational modes, most often those of the cantilever itself.

9.1.2.3 Comparison Between Topographic Images Taken in FM-Mode and AM-Mode

Figure 9.3a, b shows the topography of the InAs QD sample in constant-amplitude AM-mode with active Q damping and in constant-frequency shift (Δf) FM-mode in vacuum at 77 K, respectively. The AM-AFM image (Fig. 9.3a) shows clear topographic structure with monoatomic steps and facetted QDs, which is comparable to the one shown in Fig. 9.1b. In FM-mode imaging, however, it was impossible to get images such as shown in Fig. 9.3a since a more negative Δf set-point led to unstable imaging due to the intermittent stops of the cantilever oscillation induced by the sudden topographic change associated with the QDs.

The importance of the electrostatic force in topographic imaging with FM-AFM was recognized as soon as the FM-AFM technique was used for high-resolution topography imaging. A constant dc bias voltage is usually applied between the tip and sample to minimize the electrostatic force while imaging. This minimization technique was often found to be sufficient for high-resolution FM-AFM imaging of homogeneous samples [43].

On the InAs QD/InGaAs/InP heterostructure sample, however, it is not enough to apply a constant dc bias voltage to get real topographic images of good quality with FM-mode. Fig. 9.3b shows a typical topography image of the same sample as shown in Fig. 9.1b taken with FM-mode at a bias voltage of −0.3 V, which minimizes the average electrostatic interaction. The image looks more blurry and the flat terraces in Fig. 9.3 show much more roughness. As we will see later, it turns out that these features originate from spatially inhomogeneous electrostatic interactions, which exhibit a large spatial variation. This is in contrast to imaging in the AM-mode, where the tip and sample were simply electrically connected (i.e., zero bias voltage applied) and thus no particular attempt was made to minimize the electrostatic force. The AM-AFM imaging mode is not as sensitive to the

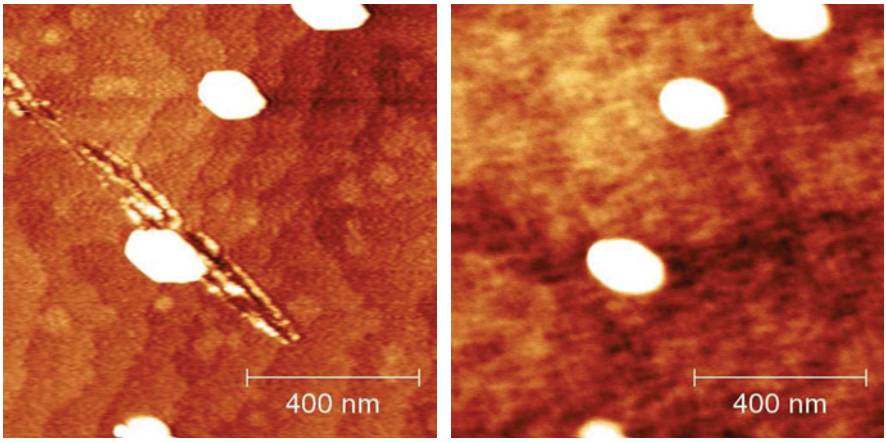

(a) actively Q-damped AM-mode (b) FM-mode

Fig. 9.3 Topography images of an InAs quantum dot sample grown on InP/InGaAs/InP heterostructure substrate taken at 77 K. (**a**) Taken by AM-mode with active Q damping. The effective Q was 960 and the amplitude set-point was 98% of the free oscillation amplitude. The excitation frequency was chosen to be the resonance frequency of the cantilever ($f_0 = 158{,}790$ Hz). The scratch was made by an accidental tip crash. (**b**) FM-mode image taken at 77 K on the same area as (**a**). ($\Delta f = -7.5$ Hz, $V_{\text{bias}} = -0.3$ V, $Q = 56{,}000$). Both images were taken in the same experimental run ((**b**) first and then (**a**)) with the same tip and the same oscillation amplitude of 16 $\text{nm}_{\text{p-p}}$. The height scale is 2 nm for both images

electrostatic force as FM-AFM. This different sensitivity to the electrostatic force can easily be qualitatively understood. In the AM-AFM case, the tip goes into the repulsive interaction regime (intermittent contact) for typical operating conditions (assuming an amplitude set point ∼90% of the free amplitude and a small dc bias voltage) [44]. Under these conditions, the resulting change in oscillation amplitude is largely determined by short-range interaction and thus is less sensitive to the longer-range electrostatic interaction. The FM-AFM, however, is sensitive to long-range electrostatic interactions. If not compensated for, it is often difficult to take images on heterogeneous samples because the cantilever oscillation can become unstable.

We conclude that AM-imaging mode with active Q damping is a useful operating mode in vacuum to obtain the real topography of electrostatically heterogeneous samples with minimal influence of the electrostatic force.

9.1.2.4 Bias Dependence of FM-AFM Image

In order to clarify the origin of the apparent roughness found in the FM-AFM image (Fig. 9.3b), we investigated the topography images as a function of the bias voltage, V_{bias}. Figure 9.4 shows the constant Δf topography images taken at

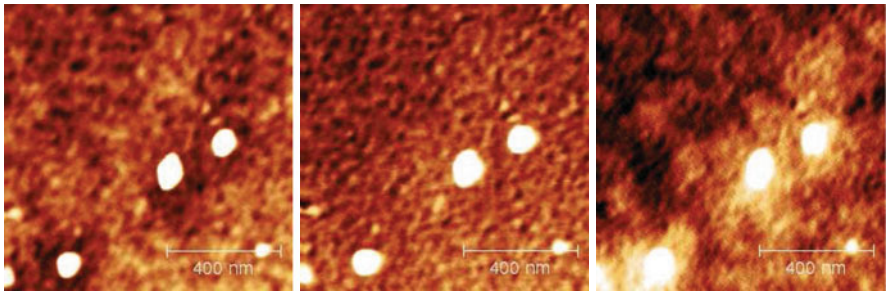

Fig. 9.4 Constant frequency shift topography images of an InAs quantum dot/InP heterostructure sample taken at different bias voltages, V_{bias} at $T = 4.5$ K. (**a**) $V_{\mathrm{bias}} = -1.0$ V and $\Delta f = -2.43$ Hz, (**b**) $V_{\mathrm{bias}} = -0.1$ V and $\Delta f = -0.69$ Hz, (**c**) $V_{\mathrm{bias}} = 0.8$ V and $\Delta f = -3.01$ Hz, The mean tip-sample distance was set to be the same for all the images. The height scale is 2 nm for all the images

different V_{bias}. The mean tip-sample distance was set to be the same for all the images by choosing the Δf set-point (determined from a reference Δf-V_{bias} curve taken at a position over the sample (the similar curve as shown in Fig. 9.5d). All of the images in Fig. 9.4 show the characteristic apparent roughness well above the instrumental noise floor. We notice many similar features in the background roughness. Furthermore, the contrast of the features is bias voltage dependent. In particular, the background around the QDs increases from Fig. 9.4a–c, indicating the contrast is of electrostatic origin.

The same behavior is observed on the sample without InAs QDs. Figure 9.5 shows the constant Δf topography images taken at $V_{\mathrm{bias}} = 1.0, -0.6$ and -1.0 V. These images could be taken at a more negative Δf set-point (smaller tip-sample distance) than the previous images because there are no QDs on the sample surface. This explains why Fig. 9.5b shows a more clearly resolved surface topography with atomic steps. ($V_{\mathrm{bias}} = -0.6$ V corresponds to the minimizing V_{bias} deduced from a $\Delta f - V_{\mathrm{bias}}$ curve.) On the other hand, Fig. 9.5a shows a random pattern and Fig. 9.5c shows a mixture of the topography in (b) and the random pattern in (a).

With this set of images, we demonstrate that the random background pattern clearly shown in Fig. 9.5a originates from the random spatial fluctuation of the surface potential. In passing we point out that increasing V_{bias} increases the apparent topographic roughness and can eventually mask the underlying topography completely. This can be understood as follows. The force acting on an AFM probe can be expressed as $F_{\mathrm{tot}} = F_{\mathrm{cap}} + F_{\mathrm{res}}$, where the first term is the capacitive force and the second term is the force independent of the applied bias voltage and is due to all other force components. F_{res} is usually dominated by chemical bonding forces and van der Waals forces and is responsible for real topographic information. The capacitive force, F_{cap}, can be derived from the partial derivative of the total electrostatic energy (energy stored in the tip-sample system plus the work done by

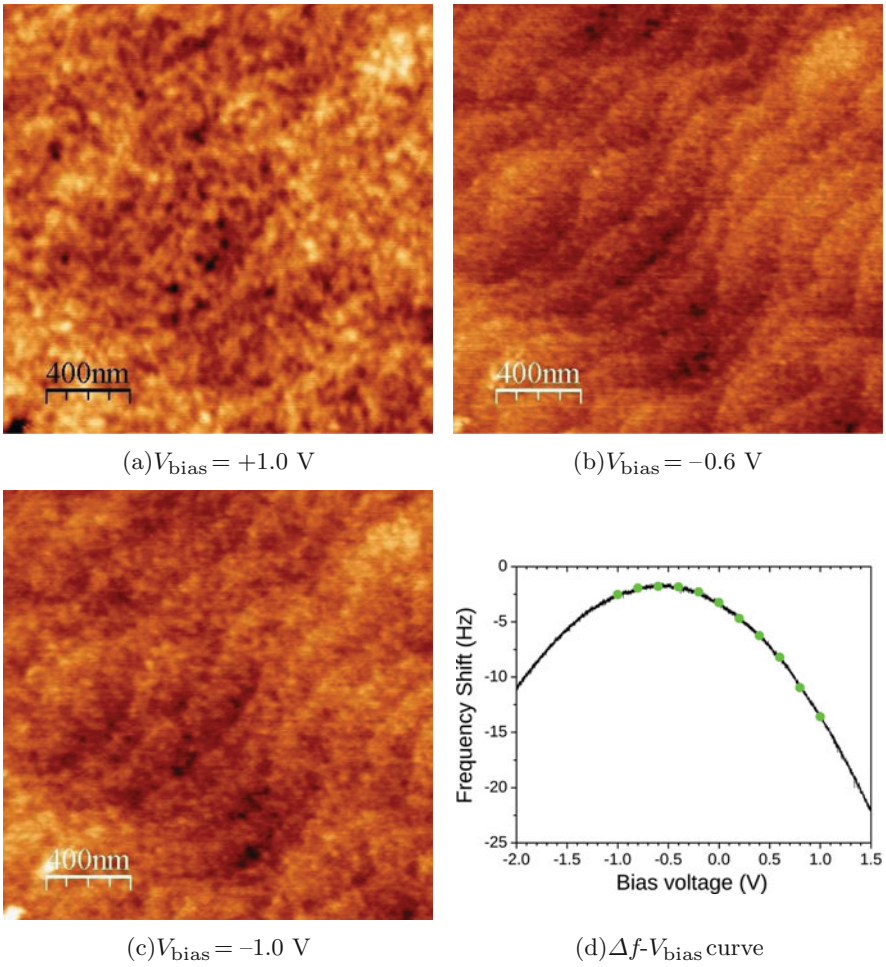

(a) $V_{\mathrm{bias}} = +1.0$ V (b) $V_{\mathrm{bias}} = -0.6$ V

(c) $V_{\mathrm{bias}} = -1.0$ V (d) Δf-V_{bias} curve

Fig. 9.5 Constant frequency shift topography images of InP heterostructure sample taken at different bias voltages, V_{bias} at $T = 77$ K. (**a**) $V_{\mathrm{bias}} = +1.0$ V and $\Delta f = -13.7$ Hz, (**b**) $V_{\mathrm{bias}} = -0.6$ V and $\Delta f = -1.83$ Hz, (**c**) $V_{\mathrm{bias}} = -1.0$ V and $\Delta f = -2.33$ Hz, The mean tip-sample distance was set to be the same for all the images. (**d**) Δf-V_{bias} curve used for setting the tip-sample distance. The curve is taken at a position on the sample and the Δf set-point is determined the curve to set the same distance at each V_{bias}

the voltage source) [45] and can thus be expressed as:

$$F_{\mathrm{cap}}(z, V_{\mathrm{bias}}) = -\frac{1}{2}\frac{\partial C}{\partial z}(V_{\mathrm{bias}} - V_{\mathrm{CPD}}(x, y))^2 \tag{9.1}$$

for a metallic tip and sample under a constant bias voltage condition, where z is the tip-sample distance and (x,y) is the lateral position of the tip. This expression

is also valid for systems containing dielectric materials between the tip and counter electrode if there are no fixed charges (cf. system with fixed charges can be described by (9.3)). For a small oscillation amplitude, the frequency shift is expressed as $\Delta f = \frac{f_0}{2k}\frac{\partial F}{\partial z}$. The total frequency shift is $\Delta f_{\mathrm{tot}} = \Delta f_{\mathrm{res}} + \Delta f_{\mathrm{cap}}$, where

$$\Delta f_{\mathrm{cap}} = -\frac{f_0}{4k}\frac{\partial^2 C}{\partial z^2}(V_{\mathrm{bias}} - V_{\mathrm{CPD}}(x, y))^2. \tag{9.2}$$

The constant Δf topography images include "electrostatic roughness" caused by the spatially nonuniform local contact potential difference, $V_{\mathrm{CPD}}(x, y)$. The effect of the spatially varying capacitance $\partial^2 C/\partial z^2(x, y)$ is small in a sample with little variation in topography. Therefore, changing V_{bias} changes the contribution of the electrostatic force to the total apparent topography as shown in Fig. 9.5. Although the importance of this effect has already been demonstrated previously on inhomogeneous samples [46, 47] as a contrast inversion in the apparent topography, such an inversion is correlated with the real topographic feature of the samples. In the case of the InP heterostructure sample, however, the electrostatic roughness appears random and uncorrelated with the real surface topography. It is important to realize that the electrostatic roughness can overwhelm the real topography, leading to a complication in interpreting the observed topography taken with FM-mode.

9.1.2.5 Relation Between dc-EFM Contrast and Surface Potential

In order to prove the nature of the electrostatic roughness observed in Fig. 9.5, we performed FM-KPFM imaging on the same surface just after taking the images in Fig. 9.5. We notice a significant resemblance between the V_{CPD} image (Fig. 9.6b) and the topography image taken with $V_{\mathrm{bias}} = +1\,\mathrm{V}$ (Fig. 9.5a). In order to compare the V_{CPD} image with the electrostatic contrast of the topography image (Fig. 9.5a) more clearly, the topography image taken at the minimizing potential ($V_{\mathrm{bias}} = -0.6\,\mathrm{V}$) (Fig. 9.5b) is subtracted to remove the topographic contribution. The resulting difference image (Fig. 9.6d) strikingly resembles the V_{CPD} image obtained by FM-KPFM. This similarity allows us to conclude that the observed electrostatic contrast in the dc-EFM image indeed reflects the spatially varying contact potential difference, $V_{\mathrm{CPD}}(x, y)$. In fact, a constant Δf image taken with a substantial V_{bias} applied can be regarded as a dc electrostatic force microscopy (dc-EFM) image as the total force is dominated by the capacitive force, F_{cap}.

We can use dc-EFM to observe the spatial fluctuations of the surface potential with a higher spatial resolution than FM-KPFM because $F_{\mathrm{cap}}(x, y)$ can be increased by increasing V_{bias}, leading to a higher sensitivity to $V_{\mathrm{CPD}}(x, y)$. KPFM imaging mode, however, is necessary for quantitative measurement of surface potentials. A spatial resolution of $\sim$ 20 nm is achieved in Fig. 9.6d using the subtraction of dc-EFM images acquired at different biases. A higher scanning speed can be achieved in dc-EFM than FM-KPFM because it is not limited by the slow response of the Kelvin feedback loop. Finally, a further potential advantage of dc-EFM over FM-KPFM is that there is no need for ac modulation which induces an additional

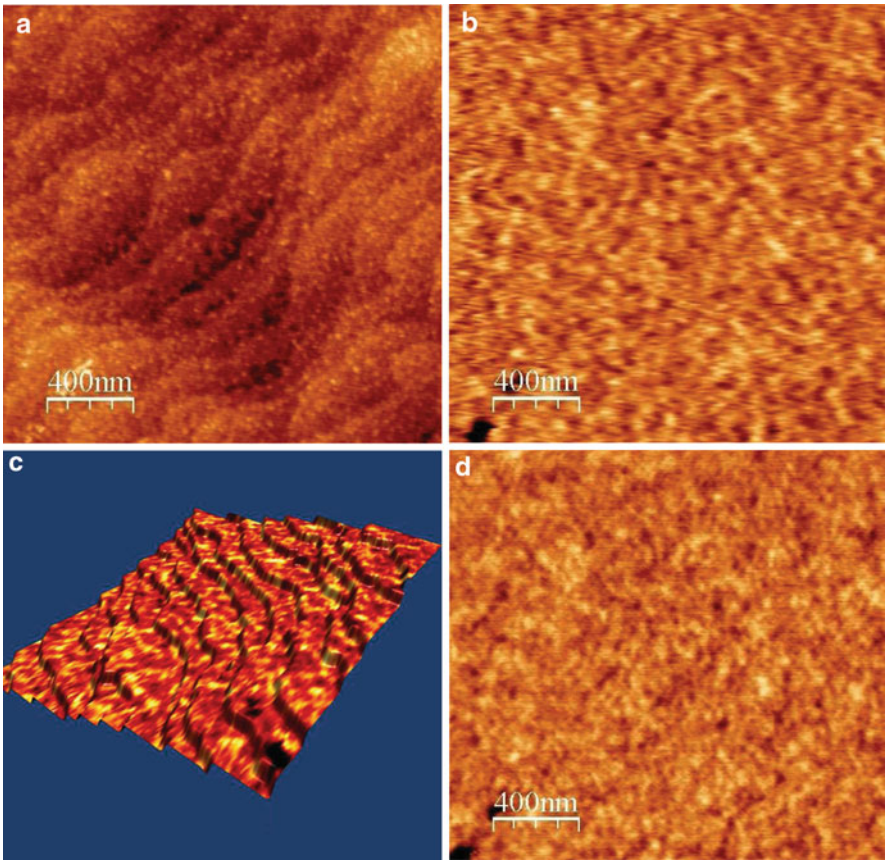

Fig. 9.6 (**a**) Topography and (**b**) surface potential images on an InP 2DEG sample by FM-KPFM. (**a**) and (**b**) were taken simultaneously. Height scale of (**a**) and (**b**) are 2 nm and 1.2 V, respectively. ($\Delta f = -13$ Hz, $V_{ac} = 1\,V_{p-p}$ with the modulation frequency of 1 kHz.) (**c**) Surface potential image (**b**) overlaid as a color code on the smoothed topography image (**a**). (**d**) Difference image of the topography images taken at $V_{bias} = +1.0$ V (Fig. 9.5a) and $V_{bias} = -0.6$ V (Fig. 9.5b)

electrostatic force component ($\frac{1}{2}\frac{\partial C}{\partial z}V_{ac}^2$) [48]. Since this component cannot be canceled by the Kelvin feedback, it can mask the electrostatic force component carrying V_{CPD} information or can introduce an artifact caused by the topography [49].

The potential fluctuations observed in Fig. 9.6b are as high as $\sim 1 V_{p-p}$. As shown in the V_{CPD} map overlaid on the topography (Fig. 9.6c), there is no clear correlation between the V_{CPD} and the topography, indicating that the origin of the fluctuations is below the surface. By combining this information with the higher spatial resolution of dc-EFM, we can deduce a local electric field on the order of $10^7\,V\,m^{-1}$. An electric field of this magnitude is large enough to influence the orientation of

molecules on the surface as well as the behavior of charged carriers on/below the surface.

Similar spatial surface potential fluctuations have been observed on high-κ dielectric materials [12–14] and partially oxidized Si(111)7×7 surfaces [50]. These kinds of experiments could benefit from the described combination of dc-EFM and FM-KPFM techniques.

9.2 Temporal Fluctuations of the Surface Potential Under Light Illumination

The dc-EFM technique can also be used for measuring the temporal fluctuations of the surface potential [51]. Figure 9.7a, b show dc-EFM topography images taken on InAs QD/InP with 780 nm laser irradiation on (a) and off (b). The image with the

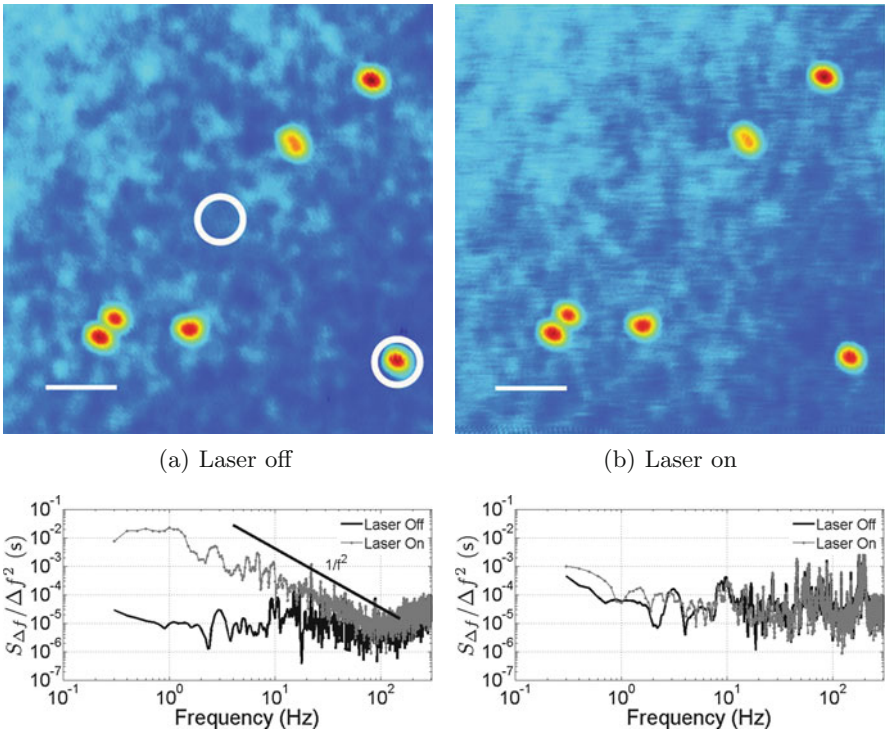

(a) Laser off (b) Laser on

(c) Noise power spectrum on WL (d) Noise power spectrum on QD

Fig. 9.7 Effect of laser irradiation on dc-EFM topography. (**a**) Laser on and (**b**) off. Both images were taken with constant frequency shift ($\Delta f = -31.66$ Hz) with $V_{\text{bias}} = 2$ V at 4.5 K. Scale bars = 200 nm. The EFM image with the laser on (**b**) shows noise (streaks) along the fast scan (horizontal) direction. (**c**) Power spectrum density (PSD) of Δf signal taken over the WL (circled in the center of (**a**)). (d) PSD over the QD (lower circle in (**a**)). From [51]

laser illumination (b) shows many streaks along the fast scan (horizontal) direction. The streaks are found to be caused by fluctuations in the electrostatic force as it mostly disappears in the image taken with $V_{\text{bias}} = V_{\text{CPD}}$ (image not shown).

The noise in the frequency shift, Δf, was characterized by acquiring Δf over the QD and the wetting layer (WL) for 10 s at a constant tip–sample distance of approximately 9 nm. The power spectrum density (PSD) of the Δf noise shows an increase in the low frequency range (<100 Hz) with laser irradiation over the WL but not the QD (Fig. 9.7c, d). The low frequency part of the PSD follows a $1/f^2$ dependence indicating generation-recombination (G-R) noise [52] from photo-excited electron-hole pairs. The spatial separation of electron-hole pairs by the built-in electric field in the space-charge layer leads to the relaxation of the surface band bending, which leads to the fluctuating electrostatic force [53].

Figure 9.8 shows the position dependence of the G-R noise around the QD. It demonstrates that the spatial resolution of the noise measurement by dc-EFM can be as good as 20 nm, which is limited by the tip diameter. The lack of G-R noise over the QDs can be explained by the strong confinement potential of the QD preventing the spatial separation of electron-hole pairs.

In some locations on the WL, random telegraph noise was observed for lower light intensities as shown in Fig. 9.8b. Here, the noise arises from a few fluctuating charges due to trapping and detrapping of localized defect states. The trapping and recombination dynamics of the photo-excited carriers is of great importance in developing photovoltaic devices [54]. The local noise measurement by EFM along with its topography imaging capability can be very useful in the characterization of these devices and their constituent materials.

Low frequency noise measurements with EFM have also been employed to investigate the dynamics of glassy polymers such as the dielectric relaxation and fluctuation [55–59]. In these experiments, the dc-EFM technique was used to measure the Δf noise, which originated from thermal fluctuations of molecular polarization in polymer film samples. A tip–sample distance of typically 20–50 nm

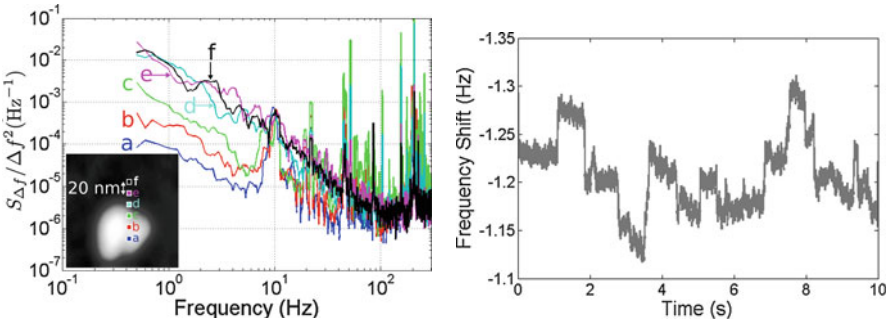

(a) Position dependence (b) Random telegraph noise

Fig. 9.8 Position dependence of Δf noise. (**a**) PSD of Δf noise taken around the QD. (**b**) Random telegraph noise in Δf observed on WL for low light intensity. From [51]

was used to detect only the long-range electrostatic interaction. Vidal Russell and Israeloff observed the unusual time dependence in the PSD spectra of the Δf as well as occasional occurrences of a random telegraph signal [56]. They ascribe these observations to the switching of configurations in individual molecular clusters. Crider et al. used KPFM to measure local dielectric properties including the dielectric fluctuation. They obtained space-time images of polarization fluctuations on the glassy polymer [57].

Similar noise measurements with a soft cantilever oscillating parallel to the surface have also been reported [58, 59]. Yazdanian et al. measured the Δf noise and the cantilever dissipation caused by electric field fluctuations from the dielectric fluctuations in polymer samples. They observed that the Δf noise is quadratically dependent on the bias voltage and confirmed that their results agree with linear response theory. An interesting connection between the Δf noise and dissipation through fluctuation-dissipation theorem was discussed [59]. As is discussed in [59], Δf noise contains more information on the fluctuating field than the cantilever dissipation as the latter probes only the Fourier component of electric field fluctuation at the cantilever resonance frequency.

9.3 Single-Electron Sensitive Electrostatic Force Microscopy/Spectroscopy

9.3.1 Single-Electron Electrostatic Force Microscopy/Spectroscopy on Quantum Dots

AFM was shown to be capable of detecting electric charge with single-electron charge sensitivity shortly after its invention. Schönenberger and Alvarado demonstrated that AFM can detect the decay of the electric charge deposited in Si_3N_4 film with single-electron resolution by using an ac-EFM technique [60].

More recently, dc-EFM using FM-mode operation has been applied to detect the electric charge stored in QDs with single-electron resolution [61–66]. In these experiments, single-electron tunneling between individual QDs and a back electrode were observed in Δf and the dissipation signal. Imaging as well as spectroscopic measurements of the single-electron charging was demonstrated on various QDs. This technique was demonstrated to be capable of quantitative spectroscopy of electronic energy levels in QDs [66], and possess capabilities such as a sensitivity to degenerate electronic levels (shell structure) and excited-state spectroscopy [67].

Figure 9.9a shows a schematic of the experimental setup used in these experiments. Considering the free energy of the system shown in Fig. 9.9b, the electrostatic force, F_{el}, acting on the AFM tip [64] can be calculated:

$$F_{\mathrm{el}} = \frac{1}{(C_{\mathrm{tip}} + C_{\mathrm{sub}})^2} \frac{\partial C_{\mathrm{tip}}}{\partial z} \left\{ \frac{q^2}{2} - C_{\mathrm{sub}} q V_{\mathrm{B}} + \frac{1}{2} C_{\mathrm{sub}}^2 V_{\mathrm{B}}^2 \right\} \tag{9.3}$$

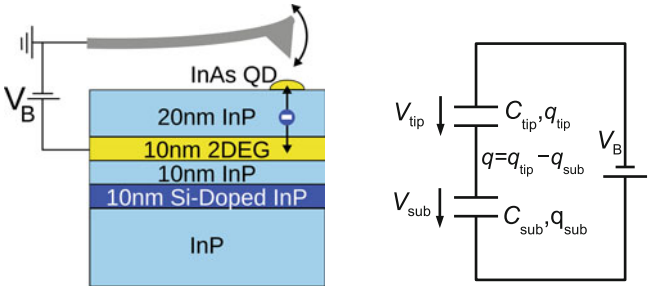

(a) Experimental setup (b) Equivalent circuit

Fig. 9.9 (**a**) Experimental setup for single-electron detection experiment. (**b**) Equivalent circuit of the setup

$$= \frac{1}{2}\frac{\partial C_{\parallel}}{\partial z}\left(\frac{q}{C_{\mathrm{sub}}} - V_{\mathrm{B}}\right)^2, \tag{9.4}$$

where q is the stored charge in the InAs QD and $C_{\parallel} = \frac{C_{\mathrm{tip}}C_{\mathrm{sub}}}{C_{\mathrm{tip}}+C_{\mathrm{sub}}}$. The first term in (9.3) accounts for the interaction between the charge in the QD and its image charge in the tip, but it is negligibly small. The third term accounts for the capacitive force that we have already discussed earlier and shows up as a parabolic background in the Δf-V_{B} curve. The second term is responsible for the detection of the charge in the QD and is referred to as the single-electron force. Although (9.4) resembles the formula for the capacitive force in (9.1), the effect of q on the electrostatic force is qualitatively different as q varies with V_{B} via the electron tunneling through the insulating InP layer. If q is static (i.e., not dependent on V_{bias}), the effect of q can be observed as a shift of the Δf-V_{B} curve. This shift, caused by a single-electron charge, has been observed on single Au atoms on a NaCl/Cu substrate with the dc-EFM technique using a quartz tuning fork AFM where the Au atoms were in two different charge states (neutral Au^0 or Au^-) [68].

At low temperature where the charging energy, $E_{\mathrm{C}} = e^2/2C_{\mathrm{tip}}$ (e: electron charge) is much larger than the thermal energy, $k_{\mathrm{B}}T$, single-electron tunneling occurs at $V_{\mathrm{B}} = \frac{e}{C_{\mathrm{tip}}}(n+1/2)$ (n: integer, number of electrons), leading to a switching of F_{el} such as $F_{\mathrm{el}}(n) \leftrightarrow F_{\mathrm{el}}(n+1)$. This switching of the single-electron force is cycled by the oscillating tip, which effectively modulates the voltage across the InP tunnel barrier. The switching character of F_{el} appear as dips in Δf-V_{B} that are superposed on a parabolic background as shown in Fig. 9.10a. Figure 9.10b shows that the corresponding peaks appear in the dissipation-V_{B} curve as well. The dissipation classically arises from the delayed response of the single-electron force ($\propto q$) due to the finite tunneling rate of the single-electron tunneling process [66, 67]. As is known from the FM-AFM theory [69], Δf and dissipation measure the in-phase and 90° out-of-phase components of $F_{\mathrm{el}}(t)$, respectively. It means that

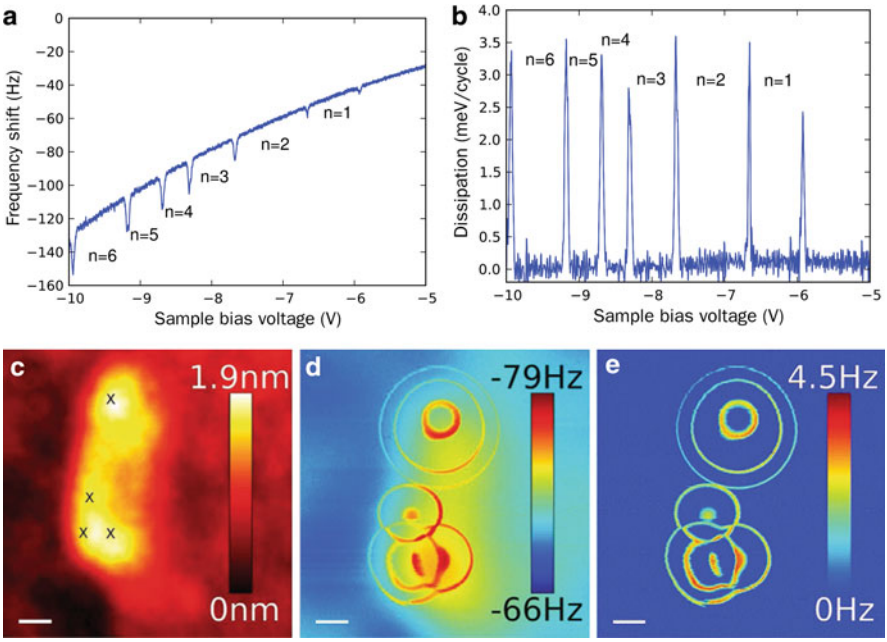

Fig. 9.10 (**a**)Δf-V_B curve and (**b**) Dissipation-V_B curve taken on an InAs QD. n is the number of electrons in the QD. (**c**) Topography of InAs QD. (**d**) Constant-height Δf image of the QD in (**c**). (**e**) Constant-height dissipation image of the QD in (**c**). (**c**) and (**d**) were taken with $V_{bias} = -8\,V$ at a tip–sample distance of 20 nm. Scale bar in (**c**)–(**e**) is 20 nm

the tunneling rate can be obtained from the relative intensity of the Δf dips and the dissipation peaks.

Figure 9.10d, e show the Δf and dissipation images taken around the QD shown in Fig. 9.10c with a constant V_{bias} of $-8\,V$ in constant-height mode scan. Both images show the concentric rings around the QD. These rings correspond to the Δf dips and dissipation peaks in the voltage spectra (Fig. 9.10a, b). The ring furthest from the center corresponds to the first peak ($n = 1$). The rings themselves are contour lines of constant chemical potential in the QD. The better contrast in the dissipation image (e) is due to the fact that the dissipation is not sensitive to the capacitive force (the third term in (9.3)), which gives rise to the background attributed to the topography of the QD observable in Fig. 9.10d.

The imaging capability of this method illustrates the advantage of the technique over conventional transport spectroscopy: It enables one to identify the origin of the peaks when multiple QDs are involved. Without images like Fig. 9.10e, it is cumbersome to identify which peak in the voltage spectra belong to which QD. The images also provide us with a simple way to extract the inter-QD coupling energy, which is of great importance for multiple-QD devices [66]. These images also demonstrate that an individual topographic QD can support multiple confinement potentials.

Similar images of single-electron charging have also been obtained by using scanning gate microscopy (SGM) technique. In SGM, the AFM tip is used only as a mobile local gate and the conductance of the device of interest is measured at each tip position. Similar concentric ring patterns showing single-electron charging in lithographically defined QDs have been reported [61, 70–72]. However, as the SGM technique requires the devices to be wired to external electrodes for conductance measurements, its applicability is rather limited.

9.3.2 Single-Electron Tunneling Force Microscopy/Spectroscopy on Insulator Surfaces

Single-electron tunneling between an AFM tip and individual trap states in insulator surfaces have been observed by Williams's group using the dc-EFM technique [73, 74]. In these experiments, the tip needs to be brought much closer to the sample surface than in the experiments described in the last section. Single-electron tunneling can occur when the tip reaches the closest point to the surface during the oscillation. The single-electron tunneling results in a step-like change in Δf. By applying a dc bias voltage between the tip and backelectrode, a spectroscopic measurement of localized electronic states can be performed. Bussmann and Williams observed localized electronic states in a SiO_2 thin film via identifying sharp steps in the Δf versus bias voltage curves [73, 74] and also observed stochastic single-tunneling events at a fixed bias voltage in the time trace of Δf [74]. Bussmann et al. adopted the FM-KPFM technique for similar measurements and obtained spatial maps of the localized states on SiO_2 [75, 76]. Similar experiment on Au nanoparticles have also been recently reported [77]. This technique is useful for investigating the isolated electronic states that are not tunnel-coupled to nearby electrodes.

9.4 Related Scanning Probe Techniques

For highly sensitive charge or electric potential measurements, there are two other non-AFM based scanning probe techniques: scanning single electron transistor microscopy and scanning charge accumulation microscopy.

9.4.1 Scanning Single Electron Transistor Microscopy

Single-electron transistor microscopy (SSET) was first reported by Yoo et al. [18]. Single electron transistors (SET) are known to be the most sensitive electrometers and have been used for various applications such as single-electron charge detection

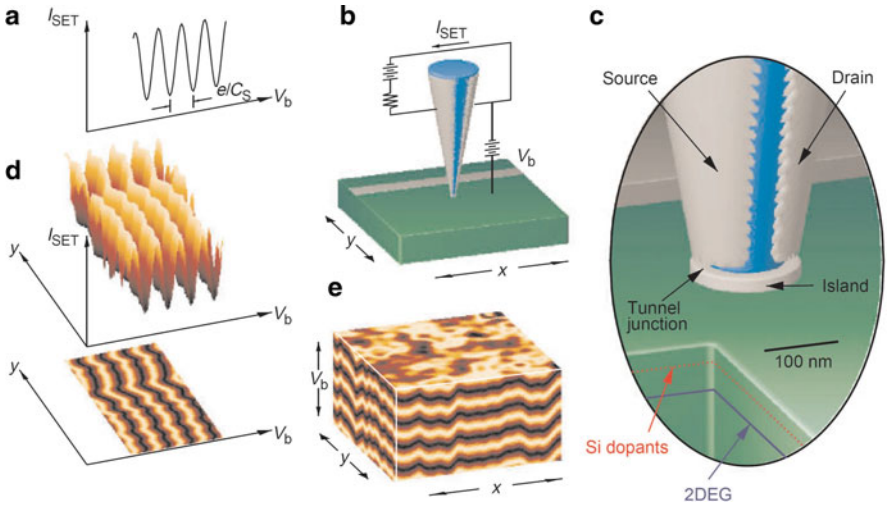

Fig. 9.11 (**a**) Current oscillations of a SET. (**b**) Schematic of SSET technique. (**c**) Magnified view of the SSET tip and the sample structure. (**d**) SET current as a function of the tip position and bias voltage. (**e**) Potential profile of $Ga/Al_xGa_{1-x}As$ structure sample at different bias voltages. From [18]. Reprinted with permission from AAAS

in lithographically defined QDs [78] and as a high-sensitivity displacement sensor for a nanoscale mechanical resonator [79]. In the SSET experiment, a SET using an Al/Al oxide tunnel junction is fabricated on a tapered optical fiber tip (Fig. 9.11c). The fiber tip is scanned over the sample surface with a typical tip–sample distance of $\sim$100 nm. A change in electrostatic potential under the probe modulates the current flowing in the SET (Fig. 9.11a). This signal can be interpreted as a surface potential qualitatively or can be used to control the sample bias voltage with a feedback circuit for nullifying the SET current as in KPFM (Fig. 9.11b). Yoo et al. reported a surface potential resolution better than 1 mV and a spatial resolution of $\sim$100 nm, which is limited by the tip size. They observed spatial fluctuations of the surface potential due to the randomly located dopant atoms in a $GaAs/Al_xGa_{1-x}As$ heterostructure sample. They also demonstrated that the technique can resolve individual charges created via weak light illumination [18].

The SSET technique has been successfully applied to the microscopic investigation of the QHE, such as the observation of the edge state [80] and localized states [81, 82] predicted theoretically. It has been more recently used to investigate the electron-hole puddles created by the random potential and localization on graphene [83].

In spite of these successes, the technique has not been widely adopted. Some of the drawbacks are that it requires a temperature less than a few Kelvin which limits its application, and that it cannot take good topography images because of the large tip diameter ($\sim$100 nm shown in Fig. 9.11c) . These drawbacks along with a difficult fabrication process keeps this technique from being widely adopted. An attempt has

recently been made to integrate a SET with a quartz tuning fork [84] to overcome these drawbacks but its application has not been reported yet.

9.4.2 Scanning Charge Accumulation Microscopy

Another scanning probe technique with a highly sensitive electrometry capability is known as SCAM [19]. Technically, it is nothing more than an ac current probe with a sharp metallic tip, but a custom-built highly sensitive current amplifier with a cryogenic high electron mobility transistor (HEMT), makes the technique very unique [85]. An ac voltage with a frequency of $\sim$100 kHz and an amplitude 4–6 $\mathrm{mV_{rms}}$ is applied between the tip and sample and the resulting ac current is measured by a lock-in amplifier. The output of the lock-in amplifier gives the impedance of the tip–sample system. A charge sensitivity of 0.02 $e/\sqrt{\mathrm{Hz}}$ was achieved. As the impedance of the system is influenced mainly by the charge motion in the sample, the technique is sensitive to the electronic properties of buried structures in the sample such as a 2DEG.

SCAM has been applied to interesting phenomena in the QHE regime such as electron puddles [19, 86], the observation of random potentials [19, 87], and the charging of tip-induced single-electron bubbles [88]. The spectroscopy of small numbers of Si dopants in a GaAs/$\mathrm{Al_{0.4}Ga_{0.7}As}$ heterostructure have been performed recently and the peculiar electronic levels of Si dopant molecules have been identified [89].

It is worth noting that SCAM can be used for the original Kelvin probe measurement by measuring the ac current induced when the tip is oscillated mechanically (vibrating capacitor method). The technique is based on a simple electrical measurement and thus has the important advantage of being able to sweep the frequency of the ac modulation. It enables the investigation of the frequency response of samples (i.e., impedance measurement), which still remains very difficult with AFM-based techniques which rely on the mechanical resonances of the AFM cantilevers.

As is the case in SSET, the integration of this technique with an AFM would open up interesting applications particularly in the characterization of nanoscale electronic devices.

9.5 Conclusion

We have given an overview of the applications of the EFM and KPFM techniques to semiconductor low-dimensional structures. There has been a substantial body of experimental studies on the potential profile in 2DEGs with both EFM and KPFM. The interest comes mainly from the view point of mesoscopic physics. In particular, a substantial effort has been made to better understand the microscopic mechanism of the QHE. Various experimental techniques have been developed for this end,

most of them for buried structures such as a 2DEG formed in semiconductor heterointerfaces.

We have described the effect of a spatially nonuniform electric potential on FM-mode imaging. We have shown that constant Δf topography images are sensitive to the electrostatic force and that therefore such images taken under a high bias voltage can be interpreted as a surface potential profile by comparing it with the potential profile taken with FM-KPFM. This imaging mode (dc-EFM) can thus be used to measure the surface potential profile with a higher spatial resolution and signal-to-noise ratio than KPFM imaging. KPFM, however, is necessary for quantitative measurement of the V_{CPD}. We have also demonstrated that the active-Q damped AM-AFM mode can be a useful tool for obtaining good topography resolution of samples with tall topographic features such as QDs.

Charge noise measurements by dc-EFM have been discussed. This technique allows to investigate the dynamics of fluctuating charges and thus can be instrumental in characterizing electronic and photovoltaic devices where the dynamics of charge carriers is essential. The effect of fluctuating charges on the decoherence of charge-based qubits can also potentially be addressed by this technique.

Finally, we described single-electron sensitive charge sensing measurements. The single-electron charging spectroscopy described in Sect. 9.3 allows the quantitative determination of energy levels in a quantum system such as a QD and provides the tunneling rate to a nearby electrode. The imaging capability of this technique is helpful to understand the complex charging spectra from multiple QDs and can be used to determine the coupling between QDs. The underlying physics in the technique is of fundamental interest in the emerging field of nanoelectromechanical systems [90] as the interaction between the oscillating AFM tip and tunneling electrons can be described as the back action of a quantum system on the AFM cantilever. This technique can be a versatile tool to study the back action of a quantum system such as quantum dots and individual molecules on a macroscopic system (the AFM cantilever), thus allowing interesting experimental insights into the field of quantum cavities and quantum limited measurements [91].

These EFM-based techniques have two major advantages over other more conventional characterization techniques such as electrical transport measurements. One is that it is a noncontact technique and the other is that it does not require patterned electrodes. These features make it attractive and suitable for investigating nanoscale entities such as quantum dots, defects and individual molecules, which might eventually constitute new types of electronic devices.

References

1. L. Gaudreau, S. Studenikin, A. Sachrajda, P. Zawadzki, A. Kam, J. Lapointe, M. Korkusinski, P. Hawrylak, Phys. Rev. Lett. **97**(3), 36807 (2006). doi:10.1103/PhysRevLett.97.036807. URL http://link.aps.org/doi/10.1103/PhysRevLett.97.036807

2. M. Pioro-Ladrière, J. Davies, A. Long, A. Sachrajda, L. Gaudreau, P. Zawadzki, J. Lapointe, J. Gupta, Z. Wasilewski, S. Studenikin, Phys. Rev. B **72**(11), 1 (2005). doi:10.1103/PhysRevB.72.115331. URL http://link.aps.org/doi/10.1103/PhysRevB.72.115331
3. T. Itakura, Y. Tokura, Phys. Rev. B **67**(19), 195320 (2003). doi:10.1103/PhysRevB.67.195320. URL http://link.aps.org/doi/10.1103/PhysRevB.67.195320
4. J. Bergli, Y.M. Galperin, B.L. Altshuler, New J. Phys. **11**(2), 025002 (2009). doi:10.1088/1367-2630/11/2/025002. URL http://stacks.iop.org/1367-2630/11/i=2/a=025002?key=crossref.937cc0b57df62f086c4461484728f29d
5. A. Asenov, A. Brown, J. Davies, S. Kaya, G. Slavcheva, IEEE Trans. Electron. Dev. **50**(9), 1837 (2003). URL http://ieeexplore.ieee.org/lpdocs/epic03/wrapper.htm?arnumber=1224485
6. J.H. Chen, C. Jang, S. Adam, M.S. Fuhrer, E.D. Williams, M. Ishigami, Nat. Phys. **4**(5), 377 (2008). doi:10.1038/nphys935. URL http://www.nature.com/doifinder/10.1038/nphys935
7. E.P. Nordberg, G.A. Ten Eyck, H.L. Stalford, R.P. Muller, R.W. Young, K. Eng, L.A. Tracy, K.D. Childs, J.R. Wendt, R.K. Grubbs, J. Stevens, M.P. Lilly, M.A. Eriksson, M.S. Carroll, Phys. Rev. B **80**(11), 115331 (2009). URL http://link.aps.org/abstract/PRB/v80/e115331
8. O. Makarovsky, A.G. Balanov, L. Eaves, A. Patanè, R.P. Campion, C.T. Foxon, R.J. Airey, Phys. Rev. B **81**(3), 035323 (2010). doi:10.1103/PhysRevB.81.035323. URL http://prb.aps.org/abstract/PRB/v81/i3/e035323
9. T. Vančura, S. Kičin, T. Ihn, K. Ensslin, M. Bichler, W. Wegscheider, Appl. Phys. Lett. **83**(13), 2602 (2003). URL http://link.aip.org/link/?APL/83/2602/1
10. R. Crook, C. Smith, S. Chorley, I. Farrer, H. Beere, D. Ritchie, Physica E **34**(1–2), 686 (2006). URL http://linkinghub.elsevier.com/retrieve/pii/S1386947706002013
11. G. Valdrè, D. Moro, D. Lee, C.G. Smith, I. Farrer, D.A. Ritchie, R.T. Green, Nanotechnology **19**(4), 45304 (2008). URL http://stacks.iop.org/0957-4484/19/045304
12. R. Ludeke, E. Gusev, J. Appl. Phys. **96**(4), 2365 (2004). URL http://link.aip.org/link/JAPIAU/v96/i4/p2365/s1&Agg=doi
13. J.M. Sturm, A.I. Zinine, H. Wormeester, B. Poelsema, R.G. Bankras, J. Holleman, J. Schmitz, J. Appl. Phys. **97**(6), 63709 (2005). doi:10.1063/1.1870113. URL http://link.aip.org/link/JAPIAU/v97/i6/p063709/s1&Agg=doi
14. J. Sturm, A. Zinine, H. Wormeester, R. Bankras, J. Holleman, J. Schmitz, B. Poelsema, Microelectron. Eng. **80**, 78 (2005). URL http://linkinghub.elsevier.com/retrieve/pii/S016793170500153X
15. S.S. Datta, D.R. Strachan, E.J. Mele, A.T.C. Johnson, Nano Lett. **9**(1), 7 (2009). doi:10.1021/nl8009044. URL http://www.ncbi.nlm.nih.gov/pubmed/18613730
16. Y.J. Yu, Y. Zhao, S. Ryu, L.E. Brus, K.S. Kim, P. Kim, Nano Lett. **9**(10), 3430 (2009). doi:10.1021/nl901572a. URL http://www.ncbi.nlm.nih.gov/pubmed/19719145
17. W. Melitz, J. Shen, A.C. Kummel, S. Lee, Surf. Sci. Rep. **66**(1), 1 (2011). doi:10.1016/j.surfrep.2010.10.001. URL http://dx.doi.org/10.1016/j.surfrep.2010.10.001
18. M.J. Yoo, T.A. Fulton, H.F. Hess, R.L. Willett, L.N. Dunkleberger, R.J. Chichester, L.N. Pfeiffer, K.W. West, Science **276**(5312), 579 (1997). doi:10.1126/science.276.5312.579. URL http://www.sciencemag.org/cgi/doi/10.1126/science.276.5312.579
19. S.H. Tessmer, P.I. Glicofridis, R.C. Ashoori, L.S. Levitov, M.R. Melloch, Nature **392**(6671), 51 (1998). doi:10.1038/32112. URL http://dx.doi.org/10.1038/32112
20. B.I. Halperin, Phys. Rev. B **25**(4), 2185 (1982). doi:10.1103/PhysRevB.25.2185. URL http://link.aps.org/doi/10.1103/PhysRevB.25.2185
21. J. Nixon, J. Davies, Phys. Rev. B **41**(11), 7929 (1990). doi:10.1103/PhysRevB.41.7929. URL http://link.aps.org/doi/10.1103/PhysRevB.41.7929
22. K.L. McCormick, M. T. Woodside, M. Huang, P.L. McEuen, C. Duruoz, J. Harris Jr, Physica B **249–251**, 79 (1998). doi:10.1016/S0921-4526(98)00071-4. URL http://linkinghub.elsevier.com/retrieve/pii/S0921452698000714
23. K. McCormick, M. Woodside, M. Huang, M. Wu, P. McEuen, C. Duruoz, J. Harris, Phys. Rev. B **59**(7), 4654 (1999). doi:10.1103/PhysRevB.59.4654. URL http://link.aps.org/doi/10.1103/PhysRevB.59.4654

24. P. Weitz, E. Ahlswede, J. Weis, K.V. Klitzing, K. Eberl, Appl. Surf. Sci. **157**(4), 349 (2000). URL http://www.sciencedirect.com/science/article/B6THY-403790W-Y/2/45f769f959db7436330cd7e502094690
25. P. Weitz, E. Ahlswede, J. Weis, K.V. Klitzing, K. Eberl, Physica E **6**(1–4), 247 (2000). URL http://www.sciencedirect.com/science/article/B6VMT-3YSY07V-23/2/190637d1d8c82dc273e9b72a66060d52
26. M. Woodside, C. Vale, K. McCormick, PL, Physica E **6**(1–4), 238 (2000). doi:10.1016/S1386-9477(99)00115-0. URL http://linkinghub.elsevier.com/retrieve/pii/S1386947799001150
27. E. Ahlswede, P. Weitz, J. Weis, K.V. Klitzing, K. Eberl, Physica B **298**(1–4), 562 (2001). URL http://www.sciencedirect.com/science/article/B6TVH-4344GH6-41/2/10e88fb8768479257fb665cc0e9d981c
28. F. Dahlem, E. Ahlswede, J. Weis, K. v. Klitzing, Phys. Rev. B **82**(12), 121305(R) (2010). doi:10.1103/PhysRevB.82.121305. URL http://prb.aps.org/abstract/PRB/v82/i12/e121305
29. J.A. Hedberg, A. Lal, Y. Miyahara, P. Grutter, G. Gervais, M. Hilke, L. Pfeiffer, K.W. West, Appl. Phys. Lett. **97**(14), 143107 (2010). doi:10.1063/1.3499293. URL http://link.aip.org/link/APPLAB/v97/i14/p143107/s1&Agg=doi
30. B.D. Terris, J.E. Stern, D. Rugar, H.J. Mamin, Phys. Rev. Lett. **63**(24), 2669 (1989). doi:10.1103/PhysRevLett.63.2669. URL http://link.aps.org/doi/10.1103/PhysRevLett.63.2669
31. M. Nonnenmacher, M.P. O'Boyle, H.K. Wickramasinghe, Appl. Phys. Lett. **58**(25), 2921 (1991). doi:10.1063/1.105227. URL http://link.aip.org/link/APPLAB/v58/i25/p2921/s1&Agg=doi
32. E. Ahlswede, J. Weis, K.V. Klitzing, K. Eberl, Physica E **12**(1–4), 165 (2002). doi:10.1016/S1386-9477(01)00267-3. URL http://linkinghub.elsevier.com/retrieve/pii/S138694770100267373
33. T.R. Albrecht, P. Grutter, D. Horne, D. Rugar, J. Appl. Phys. **69**(2), 668 (1991). doi:10.1063/1.347347. URL http://link.aip.org/link/JAPIAU/v69/i2/p668/s1&Agg=doi
34. S. Kitamura, M. Iwatsuki, Appl. Phys. Lett. **72**(24), 3154 (1998). doi:10.1063/1.121577. URL http://link.aip.org/link/APPLAB/v72/i24/p3154/s1&Agg=doi
35. U. Zerweck, C. Loppacher, T. Otto, S. Grafstrom, L.M. Eng, Phys. Rev. B **71**(12), 125424 (2005). URL http://link.aps.org/abstract/PRB/v71/e125424
36. R. Crook, A.C. Graham, C.G. Smith, I. Farrer, H.E. Beere, D.A. Ritchie, Nature **424**(6950), 751 (2003). doi:10.1038/nature01841. URL http://www.ncbi.nlm.nih.gov/pubmed/12917677
37. M. Roseman, P. Grutter, Rev. Sci. Instrum. **71**(10), 3782 (2000). doi:10.1063/1.1290039. URL http://link.aip.org/link/RSINAK/v71/i10/p3782/s1&Agg=doi
38. P. Poole, J. McCaffrey, R. Williams, J. Lefebvre, D. Chithrani, J. Vac. Sci. Technol. B **19**, 1467 (2001). URL http://link.aip.org/link/?JVTBD9/19/1467/1
39. J. Mertz, O. Marti, J. Mlynek, Appl. Phys. Lett. **62**(19), 2344 (1993). doi:10.1063/1.109413. URL http://link.aip.org/link/APPLAB/v62/i19/p2344/s1&Agg=doi
40. B. Anczykowski, J. Cleveland, D. Krüger, V. Elings, H. Fuchs, Appl. Phys. A **66**(7), S885 (1998). doi:10.1007/s003390051261. URL http://www.springerlink.com/openurl.asp?genre=article&id=doi:10.1007/s003390051261
41. H. Hölscher, D. Ebeling, U.D. Schwarz, in *Q-controlled Dynamic Force Microscopy in Air and Liquids*. NanoScience and Technology (Springer, Berlin, 2007), pp. 75–97. doi:10.1007/978-3-540-37316-2. URL http://www.springerlink.com/content/u201221p217t262k/
42. T. Sulchek, R. Hsieh, J.D. Adams, G.G. Yaralioglu, S.C. Minne, C.F. Quate, J.P. Cleveland, A. Atalar, D.M. Adderton, Appl. Phys. Lett. **76**(11), 1473 (2000). doi:10.1063/1.126071. URL http://link.aip.org/link/APPLAB/v76/i11/p1473/s1&Agg=doi
43. S. Morita, R. Wiesendanger, E. Meyer (eds.), *Noncontact Atomic Force Microscopy* (Springer, Berlin, 2002)
44. R. García, A. San Paulo, Phys. Rev. B **60**(7), 4961 (1999). URL http://link.aps.org/doi/10.1103/PhysRevB.60.4961
45. L N Kantorovich et al., J. Phys.: Condens. Matter **12**(6), 795 (2000). doi:10.1088/0953-8984/12/6/304. URL http://stacks.iop.org/0953-8984/12/i=6/a=304

46. S. Sadewasser, M. Lux-Steiner, Phys. Rev. Lett. **91**(26), 1 (2003). doi:10.1103/PhysRevLett.91.266101. URL http://link.aps.org/doi/10.1103/PhysRevLett.91.266101
47. S.A. Burke, J.M. LeDue, Y. Miyahara, J.M. Topple, S. Fostner, P. Grutter, Nanotechnology **20**(26), 264012 (2009). URL http://stacks.iop.org/0957-4484/20/264012
48. K. Okamoto, Y. Sugawara, S. Morita, Appl. Surf. Sci. **188**(3–4), 381 (2002). URL http://linkinghub.elsevier.com/retrieve/pii/S0169433201009539
49. M. Lee, W. Lee, F.B. Prinz, Nanotechnology **17**(15), 3728 (2006). doi:10.1088/0957-4484/17/15/019. URL http://stacks.iop.org/0957-4484/17/i=15/a=019?key=crossref.495ccf607fae35e6d68dc8dd61337e4a
50. J. Sturm, H. Wormeester, B. Poelsema, Surf. Sci. **601**(19), 4598 (2007). doi:10.1016/j.susc.2007.07.016. URL http://linkinghub.elsevier.com/retrieve/pii/S0039602807007911
51. L. Cockins, Y. Miyahara, P. Grutter, Phys. Rev. B **79**(12), 121309 (2009). URL http://link.aps.org/abstract/PRB/v79/e121309
52. M.J. Deen, F. Pascal, J. Mater. Sci. Mater. Electron. **17**(8), 549 (2006). URL http://www.springerlink.com/index/10.1007/s10854-006-0001-8
53. G. Dumitras, H. Riechert, H. Porteanu, F. Koch, Phys. Rev. B **66**(20), 1 (2002). URL http://link.aps.org/doi/10.1103/PhysRevB.66.205324
54. D.C. Coffey, D.S. Ginger, Nat. Mater. **5**, 735 (2006)
55. L.E. Walther, E.V. Russell, N.E. Israeloff, H.A. Gomariz, Appl. Phys. Lett. **72**(24), 3223 (1998). URL http://link.aip.org/link/?APL/72/3223/1
56. E.V. Russell, N.E. Israeloff, Nature **408**(6813), 695 (2000). URL http://www.ncbi.nlm.nih.gov/pubmed/11130066
57. P.S. Crider, N.E. Israeloff, Nano Lett. **6**(5), 887 (2006). URL http://pubs.acs.org/doi/abs/10.1021/nl060558q
58. S.M. Yazdanian, J.A. Marohn, R.F. Loring, J. Chem. Phys. **128**(22), 224706 (2008)
59. S.M. Yazdanian, N. Hoepker, S. Kuehn, R.F. Loring, J.A. Marohn, Nano Lett. **9**(6), 2273 (2009). doi:10.1021/nl9004332. URL http://dx.doi.org/10.1021/nl9004332
60. C. Schönenberger, S.F. Alvarado, Phys. Rev. Lett. **65**(25), 3162 (1990). doi:10.1103/PhysRevLett.65.3162. URL http://prl.aps.org/abstract/PRL/v65/i25/p3162_1
61. M.T. Woodside, P.L. McEuen, Science **296**(5570), 1098 (2002). doi:10.1126/science.1069923. URL http://www.ncbi.nlm.nih.gov/pubmed/12004123
62. J. Zhu, M. Brink, P.L. McEuen, Appl. Phys. Lett. **87**, 242102 (2005)
63. J. Zhu, M. Brink, P.L. McEuen, Nano Lett. **8**(8), 2399 (2008). URL http://pubs.acs.org/doi/abs/10.1021/nl801295y
64. R. Stomp, Y. Miyahara, S. Schaer, Q. Sun, H. Guo, P. Grutter, S. Studenikin, P. Poole, A. Sachrajda, Phys. Rev. Lett. **94**(5), 56802 (2005). doi:10.1103/PhysRevLett.94.056802. URL http://link.aps.org/doi/10.1103/PhysRevLett.94.056802
65. Y. Azuma, M. Kanehara, T. Teranishi, Y. Majima, Phys. Rev. Lett. **96**(1), 16108 (2006). doi:10.1103/PhysRevLett.96.016108. URL http://link.aps.org/doi/10.1103/PhysRevLett.96.016108
66. L. Cockins, Y. Miyahara, S.D. Bennett, A.A. Clerk, S. Studenikin, P. Poole, A. Sachrajda, P. Grutter, PNAS **107**(21), 9496 (2010). doi:10.1073/pnas.0912716107. URL http://www.pnas.org/cgi/content/abstract/107/21/9496
67. S.D. Bennett, L. Cockins, Y. Miyahara, P. Grütter, A.A. Clerk, Phys. Rev. Lett. **104**(1), 2 (2010). doi:10.1103/PhysRevLett.104.017203. URL http://link.aps.org/doi/10.1103/PhysRevLett.104.017203
68. L. Gross, F. Mohn, P. Liljeroth, J. Repp, F.J. Giessibl, G. Meyer, Science **324**(5933), 1428 (2009). URL http://www.sciencemag.org/cgi/content/abstract/324/5933/1428
69. H. Hölscher, B. Gotsmann, W. Allers, U. Schwarz, H. Fuchs, R. Wiesendanger, Phys. Rev. B **64**(7), 1 (2001). URL http://link.aps.org/doi/10.1103/PhysRevB.64.075402
70. A. Pioda, S. Kicin, T. Ihn, M. Sigrist, A. Fuhrer, K. Ensslin, A. Weichselbaum, S.E. Ulloa, M. Reinwald, W. Wegscheider, Phys. Rev. Lett. **93**, 216801 (2004)
71. P. Fallahi, A.C. Bleszynski, R.M. Westervelt, J. Huang, J.D. Walls, E.J. Heller, M. Hanson, A.C. Gossard, Nano Lett. **5**, 223 (2005)

72. A.C. Bleszynski, F.A. Zwanenburg, R.M. Westervelt, A.L. Roest, E.P.A.M. Bakkers, L.P. Kouwenhoven, Nano Lett. **7**(9), 2559 (2007). URL http://www.ncbi.nlm.nih.gov/pubmed/17691848
73. E. Bussmann, D.J. Kim, C.C. Williams, Appl. Phys. Lett. **85**(13), 2538 (2004). URL http://link.aip.org/link/APPLAB/v85/i13/p2538/s1&Agg=doi
74. E. Bussmann, C.C. Williams, Appl. Phys. Lett. **88**, 263108 (2006). URL http://link.aip.org/link/?APPLAB/88/263108/1
75. E.B. Bussmann, N. Zheng, C.C. Williams, Nano Lett. **6**(11), 2577 (2006). doi:10.1021/nl0620076. URL http://www.ncbi.nlm.nih.gov/pubmed/17090094
76. J.P. Johnson, N. Zheng, C.C. Williams, Nanotechnology **20**(5), 55701 (2009). URL http://stacks.iop.org/0957-4484/20/055701
77. N. Zheng, J.P. Johnson, C.C. Williams, G. Wang, Nanotechnology **21**(29), 295708 (2010). doi:10.1088/0957-4484/21/29/295708. URL http://www.ncbi.nlm.nih.gov/pubmed/20601769
78. W. Lu, Z. Ji, L. Pfeiffer, K.W. West, A.J. Rimberg, Nature **423**(6938), 422 (2003). URL http://dx.doi.org/10.1038/nature01642
79. R.G. Knobel, A.N. Cleland, Nature **424**(6946), 291 (2003). URL http://dx.doi.org/10.1038/nature01773
80. A. Yacoby, H.F. Hess, T.A. Fulton, L.N. Pfeiffer, K.W. West, Solid State Commun. **111**(1), 1 (1999). doi:10.1016/S0038-1098(99)00139-8. URL http://linkinghub.elsevier.com/retrieve/pii/S0038109899001398
81. N.B. Zhitenev, T.A. Fulton, A. Yacoby, H.F. Hess, L.N. Pfeiffer, K.W. West, Nature **404**(6777), 473 (2000). URL http://dx.doi.org/10.1038/35006591
82. S. Ilani, J. Martin, E. Teitelbaum, J.H. Smet, D. Mahalu, V. Umansky, A. Yacoby, Nature **427**(6972), 328 (2004). doi:10.1038/nature02230. URL http://www.ncbi.nlm.nih.gov/pubmed/14737162
83. J. Martin, N. Akerman, G. Ulbricht, T. Lohmann, J.H. Smet, K. von Klitzing, A. Yacoby, Nat. Phys. **4**(2), 144 (2007). doi:10.1038/nphys781. URL http://www.nature.com/doifinder/10.1038/nphys781
84. H.T.A. Brenning, S.E. Kubatkin, D. Erts, S.G. Kafanov, T. Bauch, P. Delsing, Nano Lett. **6**(5), 937 (2006). URL http://dx.doi.org/10.1021/nl052526t
85. P.I. Glicofridis, Subsurface charge accumulation imaging of the quantum hall liquid. Ph.D. thesis, Massachusetts Institute of Technology (2001)
86. G. Finkelstein, P. Glicofridis, R. Ashoori, M. Shayegan, Science **289**(5476), 90 (2000). doi:10.1126/science.289.5476.90. URL http://www.sciencemag.org/cgi/content/abstract/289/5476/90
87. I. Maasilta, S. Chakraborty, I. Kuljanishvili, S. Tessmer, M. Melloch, Phys. Rev. B **68**(20), 205328 (2003). doi:10.1103/PhysRevB.68.205328. URL http://link.aps.org/doi/10.1103/PhysRevB.68.205328
88. G.A. Steele, R.C. Ashoori, L.N. Pfeiffer, K.W. West, Phys. Rev. Lett. **95**(13), 136804 (2005)
89. I. Kuljanishvili, C. Kayis, J.F. Harrison, C. Piermarocchi, T.A. Kaplan, S.H. Tessmer, L.N. Pfeiffer, K.W. West, Nat. Phys. **4**(3), 227 (2008). URL http://dx.doi.org/10.1038/nphys855
90. M.P. Blencowe, Contemp. Phys. **46**(4), 249 (2005). URL http://www.informaworld.com/openurl?genre=article&doi=10.1080/00107510500146865&magic=crossref||D404A21C5BB053405B1A640AFFD44AE3
91. T.J. Kippenberg, K.J. Vahala, Science **321**(5893), 1172 (2008)

Chapter 10
Local Work Function of Catalysts and Photoelectrodes

H. Onishi and A. Sasahara

Abstract The charge transfer from a nanometer-sized transition metal particle to a catalyst support is thought to affect reactions over metal particles. We propose application of a Kelvin probe force microscope (KPFM) to observe the charge transfer particle-by-particle. Observed lateral distributions of the contact potential difference are interpreted to be the local work function affected by the electric dipole moments at the particle-support interface. Our recent results demonstrating successful applications with Na adatoms, Cl adatoms, Pt adatoms and particles, and Ni particles evaporated on TiO_2(110) are reviewed. Positive and negative shifts of the work function were observed on the adatoms and particles as expected. An organometallic compound, N3 dye, adsorbed on the TiO_2 surface was also examined to simulate a photoelectrode of dye-sensitized solar cells. When the electrode was irradiated with visible light, some dye molecules presented a negative shift of the work function. Electron injection from the dye to the surface is proposed to cause the negative shift. These results offer promising applications of KPFM in catalyst and photoelectrode research.

10.1 Introduction

The world today is supported by a number of artificial processes for material and energy conversion. Heterogeneous catalysts provide an important class of examples that assist chemical reactions on demand. Most catalysts contain nanometer-sized transition metal particles interfaced with metal oxide support particles. The charge transfer from a metal particle to the support particle is thought to affect reactions over the metal surface. Macroscopic methods, e.g., X-ray photoelectron

H. Onishi (✉) · A. Sasahara
Department of Chemistry, Kobe University, Rokko-dai, Nada, Kobe 657-8501, Japan
e-mail: oni@kobe-u.ac.jp

S. Sadewasser and T. Glatzel (eds.), *Kelvin Probe Force Microscopy*, Springer Series in Surface Sciences 48, DOI 10.1007/978-3-642-22566-6_10,

spectroscopy, are used to characterize the extent of charge transfer by observing chemical shifts. The observed chemical shifts are averaged over the catalyst. However, the metal particles cannot be homogeneous on catalysts. Particles of different sizes are interfaced with different portions (terraces, steps, kinks) of the support. When the transferred charge is quantified on individual particles, significant progress is made in catalysts characterization. We have proposed the application of the Kelvin probe force microscope (KPFM) to observe the charge transfer particle-by-particle. Atomistic resolutions of KPFM have been reported on Au/Si [1], Si [2, 3], Ge/Si [4], alkali halides [5], TiO_2 [6], MgO [7, 8], dopants in Si [9], Au and Ag adatoms [10], Au nanoclusters [11], and grain boundaries of $Cu(In,Ga)Se_2$ [12]. Applications to carbon nanotube FETs [13], quantum dots [14], surface photovoltage tracking [15] have also been successfully done.

When a particle donates electrons to the support, an electric dipole moment appears at the interface. The moment is directed outward from the support to the particle, as illustrated in Fig. 10.1. The work function of the catalyst is defined as the minimum energy required to remove one electron from the Fermi level of the support. This energy is sensitive to the electrostatic field at the interface. The minimum energy reduces with the outward-directed dipole moment, because the electron traveling across the interface is accelerated by the field. The work function thereby presents a local, negative shift on the electron-donating particle. On the other hand, a positive shift is expected with an electron-accumulating particle. The particle-induced shifts of the work function can be observed using a Kelvin probe force microscope. Our recent efforts in applying the microscope to catalyst models, Na adatoms, Cl adatoms, Pt adatoms and particles deposited on $TiO_2(110)$ surfaces are reviewed in Sects. 10.2–10.5.

Another class of devices focused on in Sect. 10.6 includes dye-sensitized photoelectrodes for low-cost, flexible solar cells [16]. Dyes are adsorbed on a semiconducting film and irradiated by solar light. Electrons photoexcited in the dye are injected into the film and transferred to an external circuit, as illustrated in Fig. 10.2. The photon-to-current conversion efficiency has exceeded 11% with a Ru-containing dye adsorbed on TiO_2 films [17]. The conversion efficiency is determined by the forward electron transport from the dye to the films, and by the backward transport from the films to the ionized dye [18]. As metal particles of catalysts, adsorbed dye molecules cannot be homogeneous over the films. The efficiency of

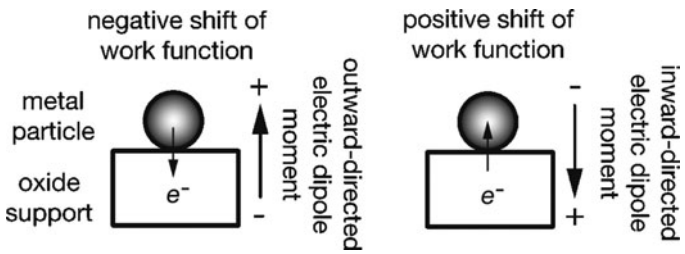

Fig. 10.1 Work function shifts induced by electron transfer at a particle-support interface

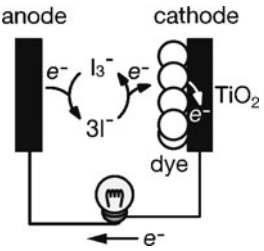

Fig. 10.2 Typical dye-sensitized solar cell composed of a photocathode, anode and iodine-containing solution

the forward and backward transfers is sensitive to the local structures of the dye-film interface. Some dyes are thorough in terms of their electron injection, while others are not. By injecting an electron into the film, a dye molecule is positively ionized and produces an electric dipole moment directed from the film to the dye. The work function of the dye-sensitized film thereby shifts negatively. We have attempted and succeeded to identify which dyes are photoionized on a TiO_2(110) surface by observing local shifts of the work function.

10.2 Na Adatoms

Sodium is a representative catalyst promoter and extensively studied on metal oxide surfaces [19]. The electron transfer from Na additives to catalysts is received to enhance the dissociation of molecular reactants. The expected electron transfer from Na adatoms to an oxide support are examined using a KPFM on a rutile TiO_2(110) surface [20]. Sodium atoms are thermally vaporized in a vacuum and deposited on the TiO_2 surface at room temperature (RT). X-ray photoelectron spectroscopy studies [21] revealed that Na adatoms are fully ionized at low coverages. The TiO_2 surface receives the released electrons, and the surface Ti cations are reduced from the $+4$ state to the $+3$ state.

Figure 10.3a, b show the topography and work function map of a TiO_2 surface with 0.17 Na adatoms nm^{-2}, respectively. Images presented in this chapter were observed by an ultrahigh vacuum microscope (JSPM4500A, JEOL) with Si cantilevers of 300 kHz resonance frequency (NCS12,Mikro Masch). Individual adatoms are identified as protrusions in the topography. The bright rows on the background represent bridge oxygen-atom rows. The adatoms are placed between oxygen-atom rows, and we expect the adatoms are on five-fold surface Ti cations, as illustrated in (c). Deposition on the Ti-atom rows is consistent with what was observed in a previous STM study [22]. The contrast of the work function map is presented so that areas with large work functions are shown as bright areas. As shown by typical cross sections of (b1) and (a1), the work function is reduced by 0.2–0.3 eV on Na adatoms. The Na adatoms are almost fully ionized to Na^+ at this coverage

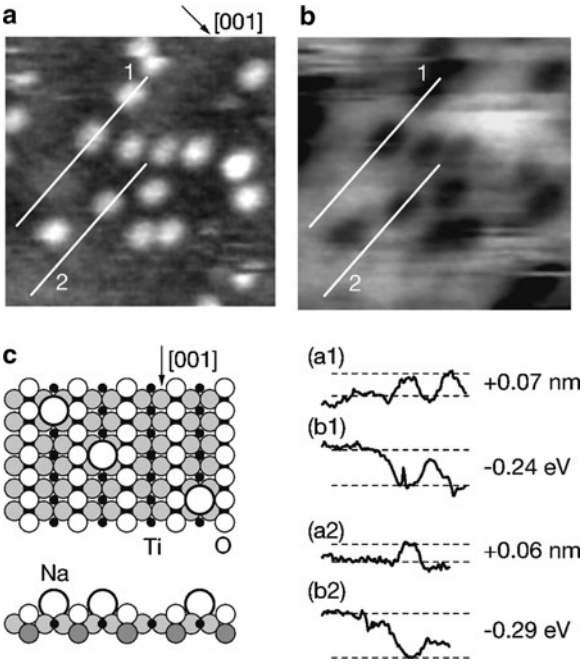

Fig. 10.3 Na adatoms vacuum-deposited on a TiO_2(110) surface after [20]. The physical topography (**a**) and local work function (**b**) are shown with the cross sections on lines 1 and 2. Image size: $10 \times 10\,nm^2$, frequency shift Δf: -76 Hz, peak-to-peak oscillation amplitude A_{p-p}: 5.8 nm, ac modulation frequency and voltage: 2 kHz and 2 V. A ball model of adatoms is illustrated in (**c**)

according to the reported Na 1s core level shift [21]. When one adatom is fully ionized, the surface receives one electron. An electric dipole moment appears with the positive charge above the surface and with the complementary negative charge below the surface. The work function of the surface reduces with the electric double layer of this polarity. The sign of the observed work function shift is consistent with the prediction.

The absolute shift of work function was not uniform, ranging from 0.2 to 0.4 eV. Figure 10.4 presents the distribution observed on 108 adatoms. The non-uniform shifts reflect the strength distribution of Na-induced dipole moments. The extent of electron transfer from Na to TiO_2 is thus heterogeneous. Oxygen vacancies and hydrogen adatoms on the TiO_2 surface are possible origins of the heterogeneity. Some surface O atoms are lost on vacuum-annealed TiO_2 surfaces. Two Ti atoms neighboring an oxygen vacancy are reduced from the 4+ state to the 3+ state. A residual water molecule dissociates on the vacancy to make two hydroxyl species on the bridge O-atom row [23]. The vacancies and hydroxyls are identified in the STM topography as small protrusions between adjacent Ti-rows. Protrusions were present in a density of $0.4\,m^{-2}$ on the surface of Fig. 10.3. Some Na adatoms may be neighbors of the vacancies and hydroxyl species.

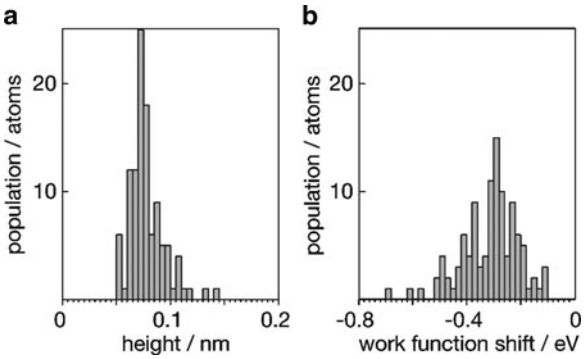

Fig. 10.4 Distribution of (**a**) the image height and (**b**) work function shift of Na adatoms after [20]

The extent of electron transfer is thus affected. Another origin is the adsorption site of Na adatoms. Three adatoms are illustrated in Fig. 10.3c just on top of five-fold coordinated surface Ti atoms. If adatoms are shifted along or perpendicular to the Ti-atom row, the efficiency of the electron transfer is perturbed.

10.3 Cl Adatoms

Evaporated chlorine was examined as an electronegative catalyst poison [24]. A TiO_2(110) surface was prepared in a vacuum and exposed at RT to a mixture of 5% Cl_2 and 95% Ar. Hebenstreit et al. [25] found that an impinging Cl_2 dissociates on the surface to generate two Cl adatoms. The adatoms are adsorbed on five-fold coordinated surface Ti atoms. The Cl_2-exposed TiO_2 surfaces were subjected to careful STM observation to identify surface species prior to work function mapping. Figure 10.5a shows the STM image of the surface exposed to the Ar-diluted Cl_2 gas for 200 L. Protrusions appear with the number density of 0.41 nm^{-2}, and the density increased to 0.67 nm^{-2} on a 3,600-L exposed surface. The protrusions appear on Ti-atom rows, which is represented by bright lines in the STM topography. The protrusions are assigned to Cl adatoms adsorbed on Ti-atom rows. Larger particles are islands of reduced titanium oxide, TiO_x, which are inevitably formed in the vacuum annealing [26].

Figure 10.5b, c show the topography and work function map of the Cl_2-exposed TiO_2 surface of (a). Three different types, one major and two minor, are identified from the comparison of the topography and the work function. Major species A are not recognized in the topography and are observed as bright spots with a uniform diameter of 1.0 nm in the work function map. Four atoms of species A are marked with arrows in (c). The work function increased on species A relative to that of the surrounding TiO_2 surface. The shifts are distributed from +0.05 to +0.12 eV with an average of +0.08 eV, as shown in the histogram in (d). The number density of

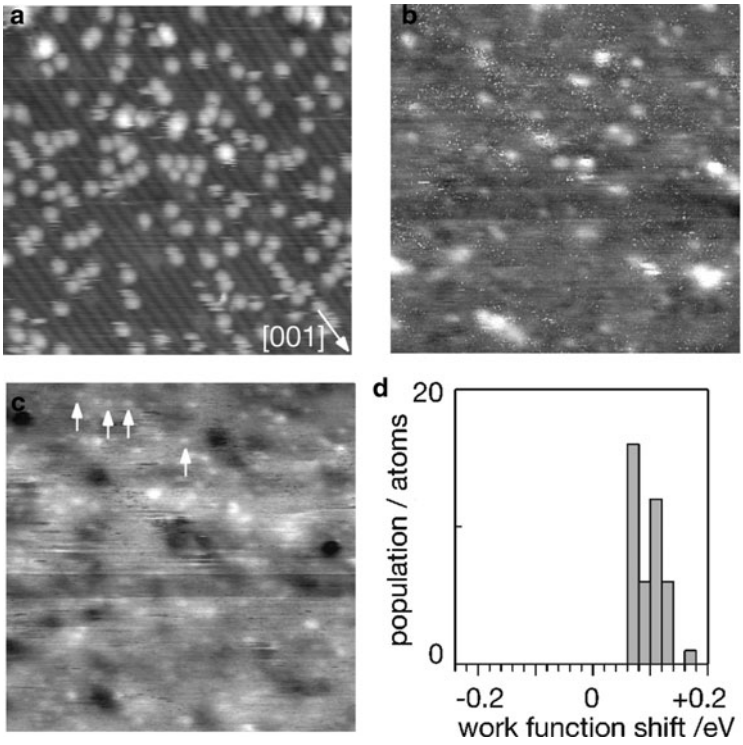

Fig. 10.5 Chlorine adatoms adsorbed on a $TiO_2(110)$ surface after [24]. (**a**) STM image of $20 \times 20\,nm^2$, (**b**) physical topography and (**c**) work function map of $30 \times 30\,nm^2$. Δf: -68 Hz, A_{p-p}: 6.8 nm, ac modulation frequency and voltage: 2 kHz and 2 V. Four of the Cl adatoms are marked with *arrows* in (**c**). (**d**) Distribution of Cl-induced work function shifts

species A was $0.32\,nm^{-2}$, whereas the Cl adatom density in the STM topography of Fig. 10.4 was $0.41\,nm^{-2}$. The agreement of the density allows us to assign species A to Cl adatoms. The positive sign of the shift is consistent with the expected electron accumulation by Cl adatoms.

Here we consider the extent of electron accumulation. Electric dipole moments of strength μ are distributed over the TiO_2 surface with number density σ. With the parallel plate condenser model, the work function shifts by $\Delta\phi = \sigma\mu/\varepsilon_0$. According to an ultraviolet photoelectron spectroscopy study [27], the macroscopic work function of $TiO_2(110)$ increased by 0.7 eV with 1.6×10^{18} Cl adatoms m^{-2}. The dipole moment per Cl adatom μ_{Cl} is thus 4×10^{-30} C m. This moment is small when compared with the moment derived by a Na adatom. When the $TiO_2(110)$ surface is covered with a c(4 × 2)-ordered Na overlayer, the work function decreased by 3 eV [21]. The adatom density of the c(4 × 2) overlayer is 1.3×10^{18} Na-atoms m^{-2} [22]. The dipole moment per Na adatom μ_{Na} is 2×10^{-29} C m. The local shift of the work function observed with KPFM was +0.08 eV for the Cl adatom and −0.35 eV for the Na adatom. The ratio of the absolute shift, 8/35,

agrees with the ratio of $\mu_{Cl}/\mu_{Na} = 0.2$. This agreement strengthens our assumption that the adatom-induced electron transfer results in a miniaturized electric double layer.

10.4 Pt Adatoms and Particles

Platinum was thermally evaporated on a TiO_2(110) surface at RT. Single Pt atoms appeared in the initial stage of deposition followed by particle nucleation. The work function of the adatoms [28] and particles [29] was compared.

A TiO_2(110) surface prepared in the vacuum was exposed to a Pt vapor source for 30 s to receive Pt adatoms. Figure 10.6a shows the topography of a 10-nm square of the exposed surface. Platinum adatoms are identified as protrusions of an atomistic size. Some protrusions are half-truncated due to migration in imaging scans. A similar sign of migration was not observed with Na and Cl adatoms. This suggests that Pt adatoms are less tightly bound on the surface. The bright lines of the surface represent oxygen-atom rows. The majority of Pt adatoms, adatom A, appear on the Ti-atom rows. A minor fraction of adatoms, adatom B, are on the O-atom rows. The topographic height of A and B are 0.09 and 0.10 nm relative to the O-atom rows. Three of adatoms B are marked with arrowheads in (a). Histogram (c) shows the height distribution. We assign adatoms B to single Pt atoms placed on an oxygen vacancy.

The work function distribution of a separate 10-nm square is presented in Fig. 10.6b. The work function is reduced on the Pt adatoms, as was observed with Na adatoms. This suggests that the electron transfer occurs from the adatoms to the surface. As shown in histogram (d) for 71 adatoms, the work function of adatom A shifted by −0.25 eV. The work function shifts of adatom B, which are represented by the hatched portions, are centered at −0.27 eV. The different shifts on A and B are presumably due to the different local structures of the adatoms. The electron donated from an adatom A is received by one Ti atom underneath. When a bridge O atom is removed, two sixfold coordinated Ti atoms lose one oxygen ligands. An adatom B is in the place of the removed O atom and is coordinated by the two Ti atoms.

Figure 10.7a, b show the topography of the TiO_2 surfaces following exposure to the Pt source for 10 and 120 min [29]. The number of bright particles, assigned to Pt particles of different sizes, increases with exposure time. The topography of Fig. 10.7c was observed on a surface exposed to Pt vapor for 10 min and then annealed in the vacuum for 3 min at 830 K. When compared with the topography of Fig. 10.7a, the size of Pt particles increased upon the annealing. The number of particles decreased and some particles are found at steps.

Figure 10.8a, b show the topography and work function distribution of a 10-min deposited surface with no annealing. The particle height, diameter, and local work function are determined using cross sections, some of which are shown in the figure. The height and diameter are distributed from 0.2–0.4 nm and 2–3 nm in

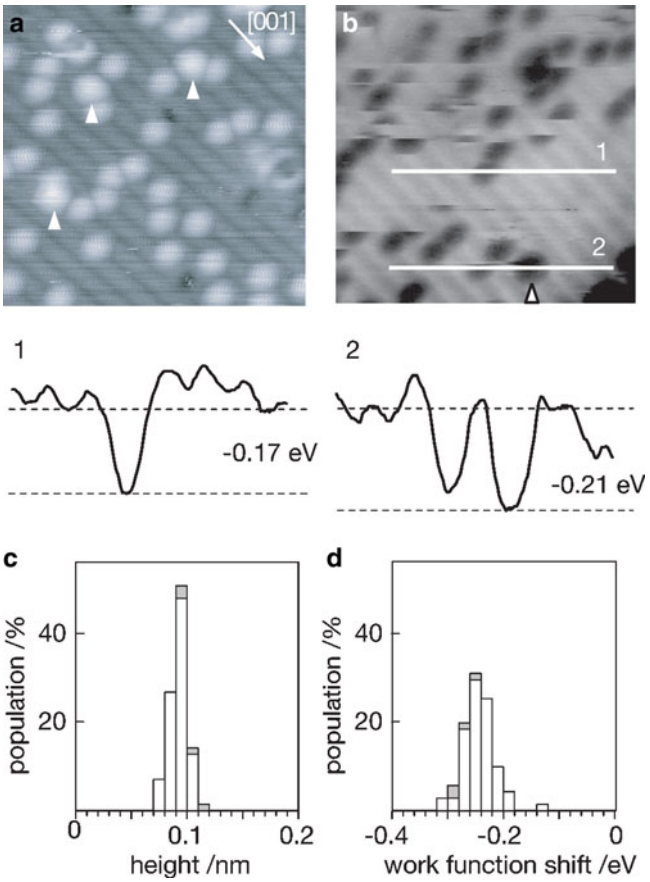

Fig. 10.6 Pt adatoms adsorbed on a TiO_2(110) surface after [28]. A vacuum-prepared TiO_2 surface was exposed to a Pt vapor source for 30 s. (**a**) Physical topography of a 10-nm square and (**b**) the local work function of a separate 10-nm square with the cross sections on lines 1 and 2. Δf: −78 Hz, A_{p-p}: 6.6 nm, ac modulation frequency and voltage: 2 kHz and 2 V. The distribution of the image height and work function shifts of Pt adatoms are presented in (**c**) and (**d**). The open and hatched portions represent adatom A and adatom B

the histograms of (c). The number of Pt atoms is estimated to be 10^2 per particle on the basis of the height and diameter. The local work function on the particles always negatively shifts relative to that on the TiO_2 surface. The negative shift is related to electric dipole moments caused by the electron transfer from the Pt particles to the TiO_2 surface. This is consistent with a previous electron paramagnetic resonance study [30] in which evidence for Pt^+ accompanied with Ti^{3+} was provided on Pt-loaded TiO_2 catalysts. The fraction of filled Pt 5d states is estimated with X-ray absorption near edge structures. A smaller filled fraction was found on Pt-loaded TiO_2 catalysts than on a Pt foil [31]. This also supports the finding of the electron transfer occurring from Pt particles to TiO_2 surfaces.

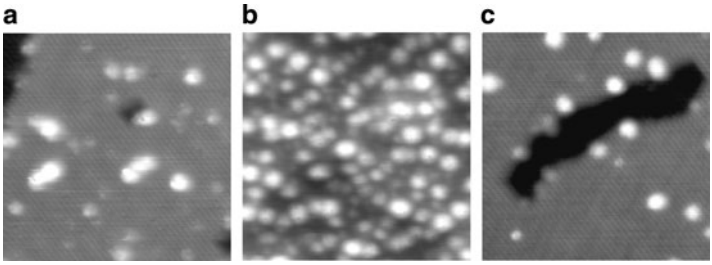

Fig. 10.7 Pt particles adsorbed on a TiO_2(110) surface after [29]. A vacuum-prepared TiO_2 surface was exposed to the Pt source for (**a**) 10 and (**b**) 120 min. The constant frequency-shift topography of $30 \times 30\,nm^2$ is presented. The surface of (**a**) was annealed in the vacuum at 830 K for 3 min. The topography of the annealed surface is shown in (**c**)

The amount of negative shift depends on the lateral size of the particles. Figure 10.8d shows the observed shifts proportional to the interface area of particles. This shows an important finding; the vacuum-deposited Pt particles of different sizes are homogeneous in respect to electron transfer. When a constant number of electrons is transferred per Pt atom, the strength of the dipole moments is proportional to the number of Pt atoms interfacing the TiO_2 surface. This is what was found as shown in Fig. 10.8d. Some particles were deposited on steps, while others were found on terraces. The shifts observed with particles on the steps, which are depicted as dots in the figure, overlap the shifts of particles on the terraces. Whether a Pt particle is deposited on a terrace or on a step does not affect the extent of electron transfer.

The electrostatic force pulling the tip to the surface is proportional to the squared tip-surface distance in the flat plate capacitor model. The long-ranged electrostatic force causes lateral averaging artifacts in KPFM results of small objects [32–34]. The artifacts can contribute to the systematic shifts depicted in Fig. 10.8d. Even if the artifacts are present the conclusion is not affected; the Pt particles of different size and of different adsorption sites are homogeneous.

The Pt particles turned to be heterogeneous when annealed in the vacuum. Figure 10.9a, b show the topography and work function distribution of the surface of Fig. 10.8 subsequently annealed at 830 K for 1 min. The particle height and diameter were only slightly affected by the annealing as seen in histogram (c). On the other hand, the work function distribution changed dramatically. Some particles present positive shifts, while the others still show negative shifts. The linear relationship with the particle size is completely lost as shown in Fig. 10.9d.

When the particle-TiO_2 interface is modified by the annealing, the extent of electron transfer can be affected. In this picture, the observed heterogeneous shifts result from heterogeneous compositions, atomistic structures, and oxidation states of the particle-TiO_2 interfaces. Transition metal particles can be encapsulated by TiO_x layers when metal-loaded TiO_2 catalysts are reduced at elevated temperatures [35, 36]. The height, diameter and shape of our particles were insensitive to the annealing. Encapsulation was thus less likely.

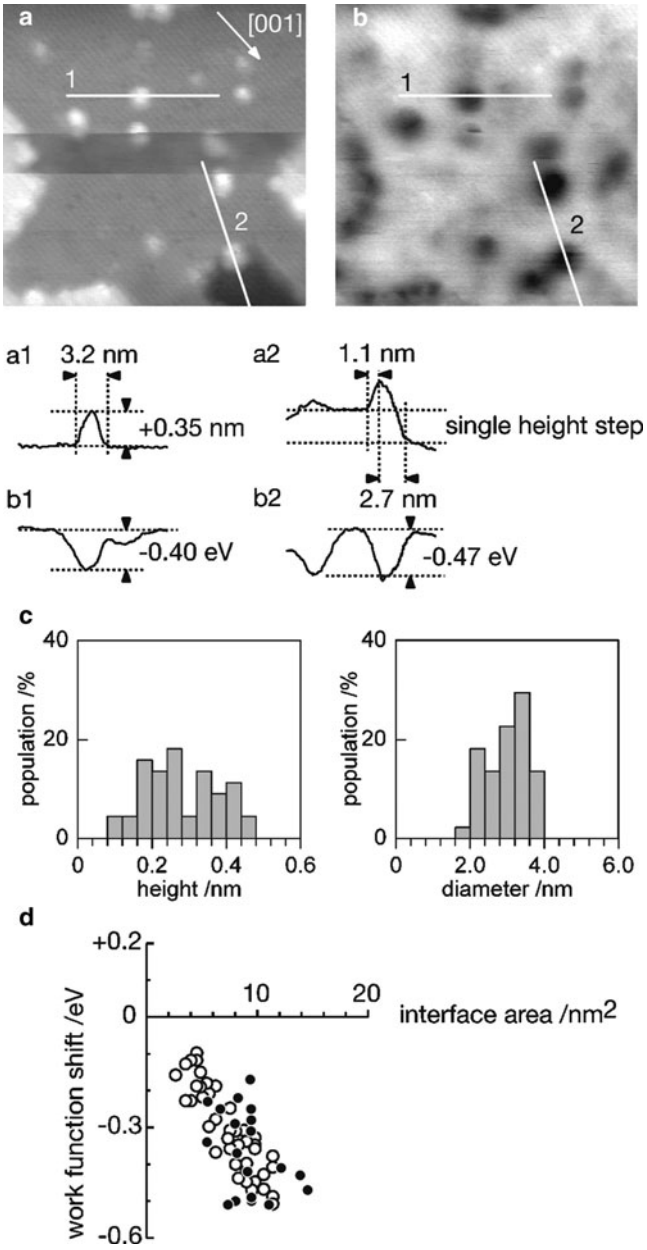

Fig. 10.8 Pt particles on a $TiO_2(110)$ surface after [29]. A vacuum-prepared TiO_2 surface was exposed to the Pt source for 10 min. The topography (**a**) and local work function (**b**) are shown with the cross sections on lines 1 and 2. Image size: $30 \times 30\,nm^2$, Δf: -58 Hz, A_{p-p}: 6.8 nm, ac modulation frequency and voltage: 2 kHz and 2 V. The distribution of the particle height and diameter are shown in (**c**). The work function shifts are plotted in (**d**) as a function of the particle-surface interface area. Shifts of particles on terraces are shown as *open circles*, and shifts of particles on steps are depicted as *dots*

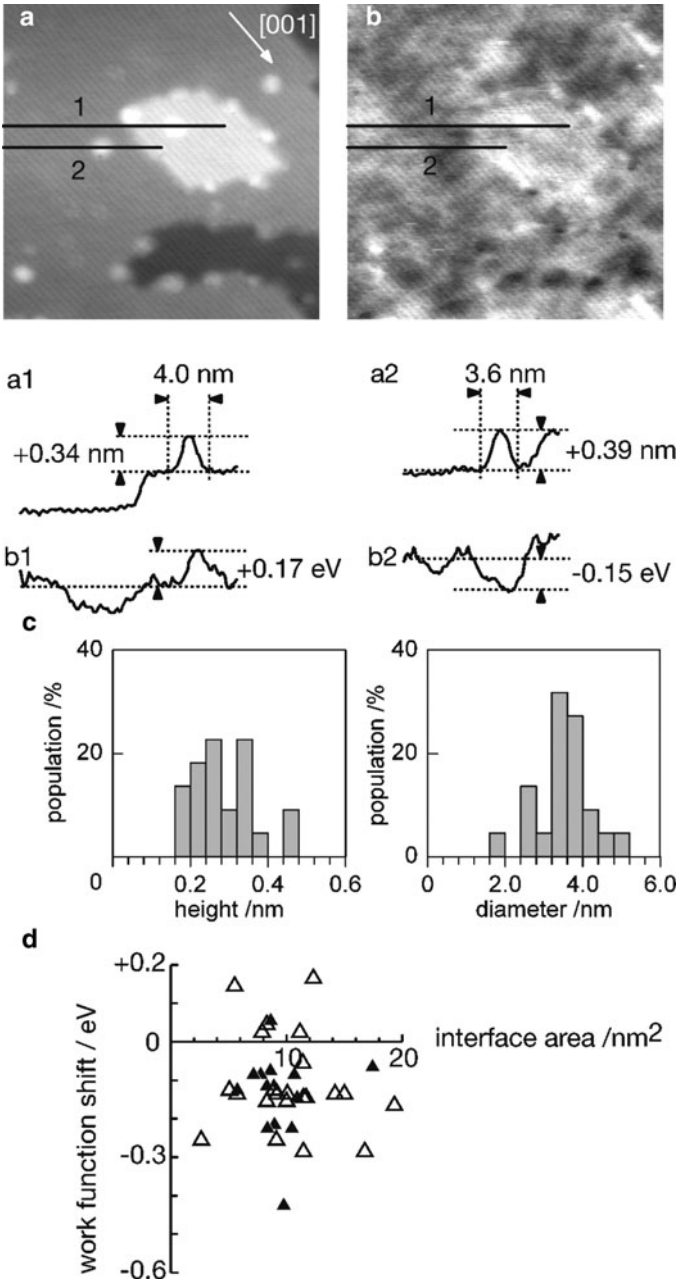

Fig. 10.9 Vacuum-annealed Pt particles on a $TiO_2(110)$ surface after [29]. The surface of Fig. 10.8 was annealed at 830 K for 1 min. (**a**) Topography and (**b**) local work function with cross sections on lines 1 and 2. Image size: $30 \times 30\,nm^2$, Δf: −58 Hz, A_{p-p}: 6.8 nm, ac modulation frequency and voltage: 2 kHz and 2 V. (**c**) Distribution of the particle height and diameter. (**d**) Work function shifts as a function of the particle-surface interface area. Shifts of particles on terraces and on steps are depicted as *open* and *filled triangles*

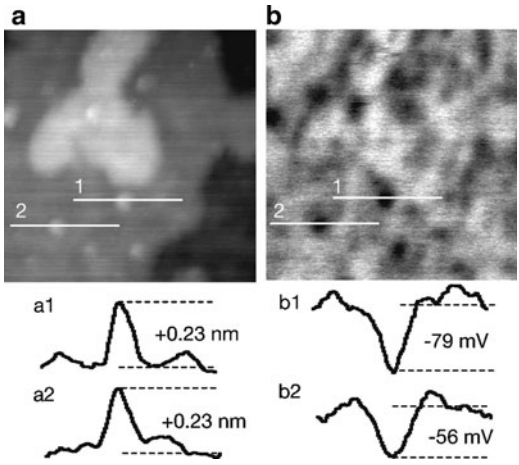

Fig. 10.10 Nickel particles on a $TiO_2(110)$ surface after [37]. (**a**) Topography and (**b**) local work function with cross sections on lines 1 and 2. Image size: $50 \times 50\,nm^2$, Δf: −48 Hz, A_{p-p}: 5.8 nm, ac modulation frequency and voltage: 2 kHz and 2 V

10.5 Ni Particles

Another transition metal, nickel, was vacuum-deposited on a $TiO_2(110)$ surface and observed by the microscope [37]. Nickel particles of 5 nm in diameter are identified in the topography of Fig. 10.10a. The local work function again presented negative shifts as shown in (b). The amount of the shift was less than that observed on the Pt particles. Nice lateral resolution of topography and local work function is expected with a sharp tip. Observed corrugations of work function are enhanced when imaged with a sharp tip. This tip-dependent artifact causes problems in quantitative comparison on different surfaces scanned by tips. Comparison of objects imaged in one frame is free from the tip problem.

10.6 Organometallic Dye

One of the most efficient sensitizer dyes, Ru(4,4'-dicarboxy-2,2'-bipyridine)$_2$ $(NCS)_2$ which is commonly called N3, was adsorbed on an atomically flat $TiO_2(110)$ surface and examined by KPFM. Two bipyridine ligands and two thiocyanate ligands are coordinated to the Ru center metal as illustrated in Fig. 10.11a with the light absorption spectrum in panel (b). One dye molecule contains four carboxyl (COOH) groups, some of which are dissociatively adsorbed on TiO_2 surfaces [38]. Unlike the metals examined in the preceding sections, the organometallic dye is thermally unstable, and it is difficult to deposit it in the vacuum. In preparing practical electrodes, TiO_2 films are immersed into a dye solution and dried.

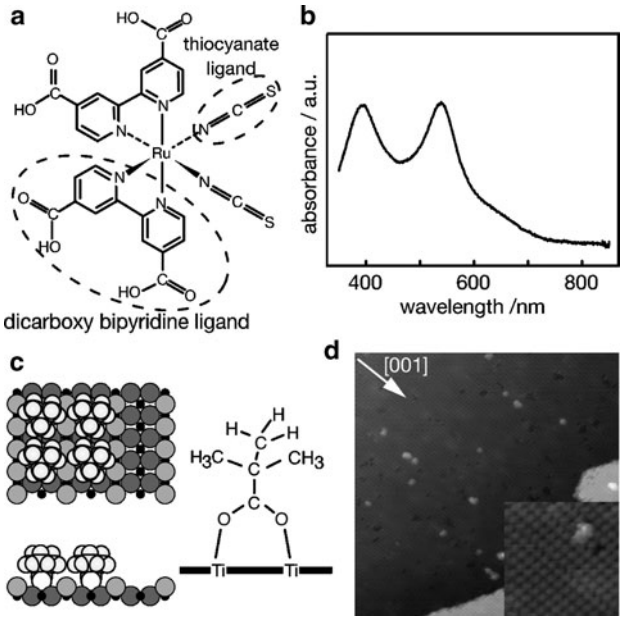

Fig. 10.11 (**a**) Structure and (**b**) light absorption of N3 dye. (**c**) Pivalate-covered $TiO_2(110)$ surface with the structure of an adsorbed pivalate. (**d**) STM topography of a pivalate-covered surface. Image size: $50 \times 50\,nm^2$, sample bias voltage: +1.0 V, tunnel current: 1.0 nA. The inset shows a zoomed-in image of $7.5 \times 7.5\,nm^2$

We attempted to simulate the wet process to sensitize our single crystalline TiO_2 surface. If the atomically flat, low-surface-area TiO_2 accommodates contaminants including H_2O and CO_2, it is not easy to identify individual dye molecules. The atomically flat surface was prepared in the vacuum, exposed to pivalic acid vapor, removed from the vacuum chamber, and immersed in a dye solution. A pivalic acid molecule, $(CH_3)_3CCOOH$, is dissociated on the TiO_2 surface to a pivalate anion,[1] $(CH_3)_3CCOO^-$ and a proton. One pivalate anion occupies two Ti^{4+} cations with the OCO plane perpendicular to the surface [39]. When the surface Ti^{4+} cations are fully occupied, bulky and hydrophobic groups of atoms, $(CH_3)_3C$, are exposed on the topmost surface as illustrated in panel (c). We expect that the pivalate-covered $TiO_2(110)$ surface is free from hydrophilic contaminants even when exposed to laboratory air [40,41]. The STM topography of a pivalate-covered surface is shown in panel (d). Individual pivalate anions are resolved as long-range ordered particles in the inset.

A pivalate-covered $TiO_2(110)$ surface was immersed in an acetonitrile solution of N3 of $0.02\,mmol\,l^{-1}$, washed with the solvent, and imaged in the vacuum [42]. On the surface immersed for 2 min, particles larger than the pivalate appeared at

[1] Pivalate is sometimes called trimethylacetate (TMA).

a number density of 0.07 nm^{-2} are shown in the STM image of Fig. 10.12a. The number of large particles increased with the immersion time. The height and lateral size of the particles were positively dependent on the immersion time suggesting N3 aggregation. Particles were assigned to single or aggregated N3 on the basis of lateral size. Particles of a minimum lateral size, 1.5 nm, were assigned to single N3 molecules embedded in the pivalate monolayer.

Panels (b) and (c) present the topography and local work function of the N3-adsorbed surface observed in the dark. The single and aggregated N3 molecules were assigned based on their lateral size in the topography. The image height distribution of single and aggregated objects, 796 objects in total, is shown in (d) relative to the pivalate monolayer. One maximum appears at 0.3–0.4 nm in the distribution, which represents objects assignable to single N3. Aggregated N3 presents a broad distribution at 0.4–0.7 nm. The local work function of the objects was positively shifted from that of the surrounding pivalate monolayer. The distribution of the work function shift is presented in histogram (e). The single N3 and aggregated N3 show a sharp peak at +0.1 eV. The work function of the TiO_2(110) surface is 5.3 eV according to an ultraviolet photoelectron spectroscopy study [43]. When the pivalate monolayer is present on top of the surface, the work function was shifted by −0.8 eV due to electric double layer induced by the pivalate monolayer [44]. The N3-induced shift of +0.1 eV relative to the pivalate-covered surface is ascribed to slightly different dipole strengths of N3 and pivalate.

An N3-adsorbed TiO_2(110) surface was placed on the microscope stage in the vacuum and irradiated by a 300 W Xe arc lamp. The ultraviolet portion of the irradiation was eliminated with a glass filter. The visible light intensity on the surface was estimated to be 1.5 mW cm^{-2} at 420–850 nm wavelengths. A set of the topography and local work function under light irradiation is presented in Fig. 10.13a, b. Single and aggregated N3 are identified in the topography, and the image height distribution of 409 objects is shown in (c).

The local work function was affected by light irradiation. A certain portion of N3 objects presented negative shifts as depicted in (b). Histograms of the work function shift (d) indicate two peaks centered at −0.04 and +0.07 eV. A major fraction, 76%, of the N3 objects is included in the negative peak. The other minor fraction is intact at +0.07 eV being insensitive to irradiation. The observed, light-induced negative shift of the local work function appeared both on single and aggregated N3 objects. It is interesting to compare what happened on the steps and on terraces. Among the 409 objects, 133 entities are adsorbed on single-height steps. There was no sign that work function shifts are related to adsorption sites. The light-induced shift of the work function lasted for several hours in the vacuum when the irradiation stopped. After remaining overnight in the dark, the light-induced shifts disappeared.

The negative shifts of the work function are interpreted with the electron injection from a photoexcited N3 to the TiO_2 surface. The positively ionized N3 and injected electron make an electric dipole moment, as created by Na adatoms. The negative sign of work function shifts is consistent with the moments of this direction.

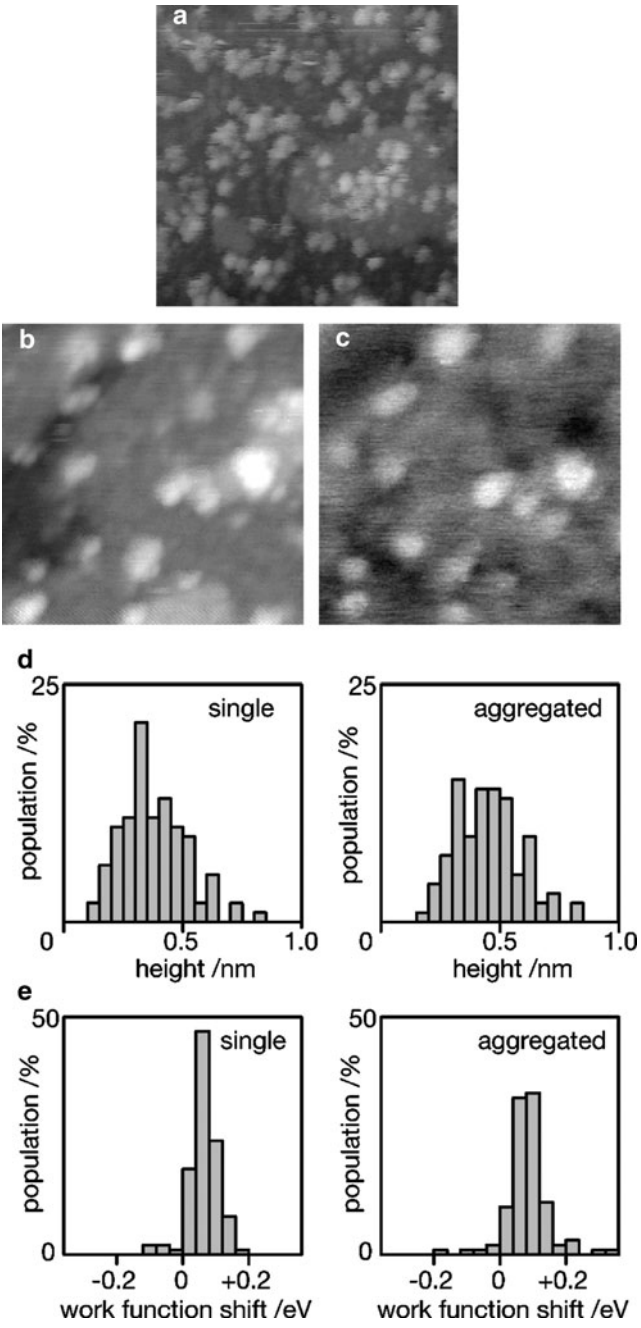

Fig. 10.12 Pivalate-covered $TiO_2(110)$ surface immersed in the acetonitrile solution of N3 for 2 min after [42]. (**a**) STM topography, image size: $50 \times 50\,nm^2$, sample bias voltage: +1.0 V, tunnel current: 1.0 nA. (**b**) Topography and (**c**) local work function observed in the dark. Image size: $30 \times 30\,nm^2$, Δf: −70 Hz, A_{p-p}: 6.2 nm, ac modulation frequency and voltage: 2 kHz and 2 V. (**d**) Image height distribution of single and aggregated N3 and (**e**) corresponding work function shifts

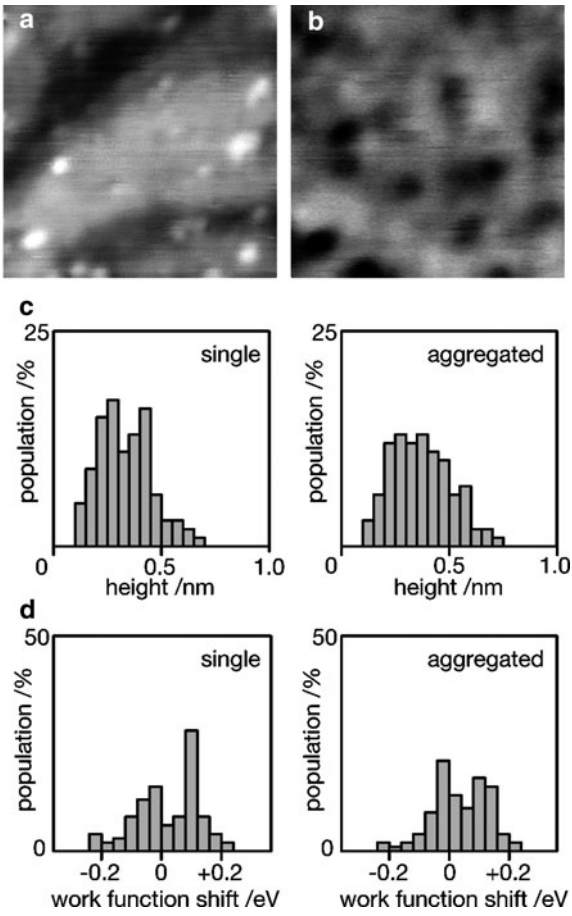

Fig. 10.13 N3-adsorbed TiO_2 surface under visible light irradiation after [42]. (**a**) Topography and (**b**) local work function, image size: $30 \times 30\,\mathrm{nm}^2$, Δf: $-70\,\mathrm{Hz}$, $A_{\mathrm{p-p}}$: 6.3 nm, ac modulation frequency and voltage: 2 kHz and 2 V. (**c**) Image height distribution of single and aggregated N3 and (**d**) the corresponding work function shifts

A transient state, neutral N3 in an electronic excited state, is difficult to image by the microscope. The frequency of photoexcitation is $0.1\,\mathrm{s}^{-1}$ in our light flux, much smaller than the rate of quenching to the ground state, $10^{10}\,\mathrm{s}^{-1}$ [45].

Here, we consider the backward electron transfer from the electron-injected TiO_2 to the ionized $N3^+$. The $N3^+$ cation is neutralized by back transfer of the injected electrons in the millisecond time scale [46, 47]. The rate of the backward transfer is suppressed on our dye-sensitized electrode. Otherwise most $N3^+$ cations would have been imaged to be neutralized. We thus assume the injected electrons are trapped somewhere in the TiO_2 wafer. Based on this assumption, the number of N3 objects sensitive to light irradiation is related to the number of electron traps. On the other hand, the probability of electron injection can also be sensitive to

the environment of individual dyes. The electron transport from the excited N3 is controlled by molecular orbitals overlapped with the surface states of TiO_2. The injection probability is different from one N3 to another. It is currently difficult to further identify the reasons for the different sensitivities.

10.7 Summary and Perspectives

Kelvin probe force microscopy was applied to characterize Na, Cl, Pt, Ni and N3 adsorbed on an atomically flat TiO_2 surfaces. Positive and negative shifts of the local work function were observed and qualitatively interpreted with electron transfer across the adsorbate-surface interfaces. The ability of KPFM has been demonstrated in revealing heterogeneity of nanometer-sized objects, as evidenced with vacuum-annealed Pt particles and light-irradiated N3.

Two issues are raised for further investigation. Our interpretation with miniaturized electric double layers is based on high school physics. This does work on micrometer-sized objects. Some criticism of this interpretation involves its accuracy with nanometer-sized objects. The tip-object distance is required to be less than the lateral size of objects for high-resolution imaging with KPFM. Quantum mechanical contributions cannot be ignored in canceling the contact potential difference [32–34, 48, 49]. When an atomistic resolution is not necessary, which is the case with some applications, the tip-object distance can be intentionally increased to suppress the quantum mechanical artifacts. Another direction of developments is operation with more realistic models of catalysts and electrodes. The catalyst surface is oxidized or reduced by vapor environments. In-situ mapping of the local work function provides the chemical states of nanometer-sized objects in working states. A new generation of microscopes [50] is now being developed to significantly enhance the force sensitivity. KPFM imaging of Pt nanoparticles has been achieved in laboratory air [51]. Imaging of micrometer-sized crystals would also be promising using the advanced microscopes. These extensions would offer a much wider observable range of catalysts and photoelectrodes than that observed on single crystals.

Acknowledgements The authors were encouraged by Wang Jung Chun and Makoto Misonoo to initiate the studies presented in this chapter. A number of studies were performed over a 7-year period at Kanagawa Academy of Science and Technology and at Kobe University in the collaboration with Chi Pang, Masatoshi Ikeda, Kumiko Hiehata, Keita Fujio, Naoki Koide and Liyuan Han. Discussion with Christian Roppacher and Kenjiro Kimura was helpful to review the experimental results. Support by Core Research for Evolutional Science and Technology from the Japan Science and Technology Agency, and a Grant-in-Aid for Scientific Research on Priority Areas [477] "Molecular Science for Supra Functional Systems" from the Ministry of Education, Culture, Sports, Science and Technology, Japan are acknowledged. The work of the photoelectrodes described in Sect. 10.6 was additionally supported by the New Energy and Industrial Technology Development Organization in association with the Ministry of Economy, Trade and Industry, Japan.

References

1. S. Kitamura, K. Suzuki, M. Iwatsuki, C.B. Mooney, Appl. Surf. Sci. **157**, 222 (2000)
2. T. Shiota, K. Nakayama, Jpn. J. Appl. Phys. **41**(10B), L1178 (2002)
3. K. Okamoto, K. Yoshimoto, Y. Sugawara, S. Morita, Appl. Surf. Sci. **210**, 128 (2003)
4. T. Eguchi, Y. Fujikawa, K. Akiyama, T. An, M. Ono, T. Hashimoto, Y. Morikawa, K. Terakura, T. Sakurai, M.G. Lagally, Y. Hasegawa, Phys. Rev. Lett. **93**, 266102 (2004)
5. C. Barth, C.R. Henry, Phys. Rev. Lett. **98**, 136804 (2007)
6. G.H. Enevoldsen, T. Glatzel, M.C. Christensen, J.V. Lauritsen, F. Besenbacher, Phys. Rev. Lett. **100**, 236104 (2008)
7. T. König, G.H. Simon, H.P. Rust, M. Heyde, J. Phys. Chem. C **113**, 11301 (2009)
8. T. König, G.H. Simon, H.P. Rust, G. Pacchioni, M. Heyde, H.J. Freund, J. Am. Chem. Soc. **131**(48), 17544 (2009)
9. M. Ligowski, D. Moraru, M. Anwar, T. Mizuno, R. Jablonski, M. Tabe, Appl. Phys. Lett. **93**(14), 142101 (2008)
10. L. Gross, F. Mohn, P. Liljeroth, J. Repp, F.J. Giessibl, G. Meyer, Science **324**(5933), 1428 (2009)
11. C. Barth, C.R. Henry, Appl. Phys. Lett. **89**, 252119 (2006)
12. C. Leendertz, F. Streicher, M. Lux-Steiner, S. Sadewasser, Appl. Phys. Lett. **89**, 113120 (2006)
13. Y. Miyato, K. Kobayashi, K. Matsushige, H. Yamada, Jpn. J. Appl. Phys. **44**(4A), 1633 (2005)
14. S. Shusterman, A. Raizman, A. Sher, Y. Paltiel, A. Schwarzman, E. Lepkifker, Y. Rosenwaks, Nano Lett. **7**(7), 2089 (2007)
15. F. Streicher, S. Sadewasser, M. Lux-Steiner, Rev. Sci. Instrum. **80**, 013907 (2009)
16. M. Grätzel, J. Photochem. Photobiol. A **164**(1–3), 3 (2004)
17. Y. Chiba, A. Islam, Y. Watanabe, R. Komiya, N. Koide, L. Han, Jpn. J. Appl. Phys. **45**(25), L638 (2006)
18. A. Hagfeldt, M. Graetzel, Chem. Rev. **95**(1), 49 (1995)
19. W. Henrich, P. Cox, *The Surface Science of Metal Oxides* (Cambridge University Press, Cambridge, 1994)
20. A. Sasahara, H. Uetsuka, H. Onishi, Jpn. J. Appl. Phys. **43**(7B), 4647 (2004)
21. H. Onishi, T. Aruga, C. Egawa, Y. Iwasawa, Surf. Sci. **199**(1–2), 54 (1988)
22. H. Onishi, Y. Iwasawa, Catal. Lett. **38**, 89 (1996)
23. O. Bikondoa, C.L. Pang, R. Ithnin, C.A. Muryn, H. Onishi, G. Thornton, Nat. Mater. **5**, 189 (2006)
24. K. Hiehata, A. Sasahara, H. Onishi, Jpn. J. Appl. Phys. **47**(7), 6149 (2008)
25. E.L.D. Hebenstreit, W. Hebenstreit, H. Geisler, C.A. Ventrice, D.A. Hite, P.T. Sprunger, U. Diebold, Surf. Sci. **505**, 336 (2002)
26. H. Onishi, K. ichi Fukui, Y. Iwasawa, Bull. Chem. Soc. Jpn. **68**(9), 2447 (1995)
27. D. Vogtenhuber, R. Podloucky, J. Redinger, E.L.D. Hebenstreit, W. Hebenstreit, U. Diebold, Phys. Rev. B **65**, 125411 (2002)
28. A. Sasahara, C.L. Pang, H. Onishi, J. Phys. Chem. B **110**(27), 13453 (2006)
29. A. Sasahara, C.L. Pang, H. Onishi, J. Phys. Chem. B **110**(35), 17584 (2006)
30. T. Salama, H. Hattori, H. Kita, K. Ebitani, T. Tanaka, J. Chem. Soc. Faraday Trans. **89**, 2067 (1993)
31. D.R. Short, A.N. Mansour, J.W. Cook, D.E. Sayers, J.R. Katzer, J. Catal. **82**(2), 299 (1983)
32. S. Ono, T. Takahashi, Jpn. J. Appl. Phys. **43**(7B), 4639 (2004)
33. U. Zerweck, C. Loppacher, T. Otto, S. Grafström, L. Eng, Phys. Rev. B **71**, 125424 (2005)
34. F. Krok, K. Sajewicz, J. Konior, M. Goryl, P. Piatkowski, M. Szymonski, Phys. Rev. B **77**, 235427 (2008)
35. S.J. Tauster, S.C. Fung, R.T.K. Baker, J.A. Horsley, Science **211**(4487), 1121 (1981)
36. O. Dulub, W. Hebenstreit, U. Diebold, Phys. Rev. Lett. **84**, 3646 (2000)
37. A. Sasahara, K. Hiehata, H. Onishi, Catal. Surv. Asia **13**, 9 (2009)

38. P. Falaras, M. Gratzel, A.H.L. Goff, M. Nazeeruddin, E. Vrachnou, J. Electrochem. Soc. **140**(6), L92 (1993)
39. A. Sasahara, H. Uetsuka, H. Onishi, Surf. Sci. **481**(1–3), L437 (2001)
40. T.a. Ishibashi, H. Uetsuka, H. Onishi, J. Phys. Chem. B **108**(44), 17166 (2004)
41. C.L. Pang, T. aki Ishibashi, H. Onishi, Jpn. J. Appl. Phys. **44**(7B), 5438 (2005)
42. M. Ikeda, N. Koide, L. Han, A. Sasahara, H. Onishi, J. Phys. Chem. C **112**(17), 6961 (2008)
43. H. Onishi, T. Aruga, C. Egawa, Y. Iwasawa, Surf. Sci. **193**(1–2), 33 (1988)
44. K. Hiehata, A. Sasahara, H. Onishi, Nanotechnology **18**(8), 084007 (2007)
45. Y. Tachibana, J.E. Moser, M. Gratzel, D.R. Klug, J.R. Durrant, J. Phys. Chem. **100**(51), 20056 (1996)
46. D. Kuciauskas, M.S. Freund, H.B. Gray, J.R. Winkler, N.S. Lewis, J. Phys. Chem. B **105**(2), 392 (2001)
47. K. Takeshita, Y. Sasaki, M. Kobashi, Y. Tanaka, S. Maeda, A. Yamakata, T.a. Ishibashi, H. Onishi, J. Phys. Chem. B **107**(17), 4156 (2003)
48. T. Arai, M. Tomitori, Phys. Rev. Lett. **93**, 256101 (2004)
49. S. Sadewasser, P. Jelinek, C.K. Fang, O. Custance, Y. Yamada, Y. Sugimoto, M. Abe, S. Morita, Phys. Rev. Lett. **103**, 266103 (2009)
50. T. Fukuma, T. Ichii, K. Kobayashi, H. Yamada, K. Matsushige, Appl. Phys. Lett. **86**(3), 034103 (2005)
51. R. Kokawa, M. Ohta, K. Watanabe, K. Kobayashi, H. Yamada, A. Sasahara, H. Onishi, to be submitted

Chapter 11
Electronic Properties of Metal/Organic Interfaces

Christian Loppacher

Abstract A detailed understanding of the interface dipole formation between organic molecules and metal electrodes is a key issue for the fabrication of organic devices. This chapter will give an overview of the work done in this field. A comparison of macroscopic methods and KPFM, both used for the characterization of the electronic properties of molecular assemblies on these surfaces, will show that KPFM is capable of revealing the same quantitative results, however, with a nanometer scale resolution. Several examples will be used to point out the importance of exactly knowing the nanoscopic organization and orientation of these molecular assemblies to be able to fabricate reproducible devices with a few or even single molecules.

11.1 Introduction

Nowadays, thin films of organic molecules are widely used for the fabrication of macroscopic devices such as light emitting diodes (LED), solar cells, and chemical sensors, to name only a few. Smaller elements like organic field-effect transistors (OFET) or even single molecular devices with various functionalities are explored in research and are already working on test benches (for an overview in organic electronic devices see [1] and references therein). A key issue in all of these applications is the control of the electronic properties at the metal/organic interface which, of course, first needs a detail understanding of the processes involved.

C. Loppacher (✉)
Aix-Marseille Université, IM2NP, Centre Scientifique de Saint-Jérôme, Avenue Escadrille Normandie-Niemen, Case 151, 13397 Marseille CEDEX 20, France

CNRS, IM2NP (UMR 6242), Marseille-Toulon, France
e-mail: Christian.Loppacher@im2np.fr

S. Sadewasser and T. Glatzel (eds.), *Kelvin Probe Force Microscopy*, Springer Series in Surface Sciences 48, DOI 10.1007/978-3-642-22566-6_11,

Organic materials have a wide band gap (2–3 eV) and a small thermally excited carrier concentration. Thus, a priori, Fermi level (E_f) alignment and band bending as observed at semiconductor interfaces are not given. At many metal/organic interfaces, it is rather a dipole layer at the interface due to charge transfer, chemical reaction, or other charge rearrangements that dominates the interface properties (see, e.g., [2]).

Let us first address the question of what is desired for best device operation. In most electronic devices, a good ohmic contact with a low injection barrier height is required. Therefore, the metal electrode and the organic functional layer must be well chosen to provide the desired energy level alignment. The contact resistance depends on many factors such as the work function of the metal electrode used, the properties of the organic material (ionization potential, IP; electron affinity, EA; etc.), and of course on the interface properties (vacuum-level shift, band bending, and interface-dipole formation) [3]. Therefore, device-specific tailoring of metal/organic interfaces is addressed in many studies. Solutions for selected metal/organic contacts are presented, and systematic studies were performed to choose the combination of metal electrode and organic material which would give the best performance. For multilayer devices such as solar cells, it is not only the contacts but rather the gradient of the built-in potential within the space charge layer (band bending in thicker region) which is crucial for optimizing the efficiency of charge separation. In this chapter, we will not address the problems that arise in doped organic multilayer devices but rather the effects that occur at the direct metal/organic contact.

The effects that occur at metal/organic interfaces are manifold and can often not be regarded as isolated problems. A few are more substrate related and may occur as a modification of the metal work function (ϕ_m). ϕ_m can change as a result of surface rearrangements or screening due to mirror charges. Some other effects are more adsorbate related. For example, band bending within the organic adsorbate layer was observed to be both gradual and linear [4], intermolecular interaction can lead to depolarization due to neighboring molecules, or molecular assembly. The latter can influence the interface properties as a function of molecular conformation or orientation, of order and disorder, of packaging density, but also due to defects in films and grain boundaries. Most of the named effects depend on both substrate and adsorbate as for example also chemical binding or dipole formation.

From an electronic point of view, all the above-described effects will lead to the formation of different types of contacts: an ohmic contact, a Schottky–Mott contact, or the dipole formation at the interface, for example. In many cases, a clear separation between these types of contacts is not possible since for the same materials of electrode and organic material, it can depend on many factors such as the film thickness, the structural arrangement of the organic material, and many more.

11.1.1 Ohmic Contact

Low-resistance, stable contacts are required at the interface of organic electronic devices. An ohmic contact is both linear and symmetric in its current-voltage characteristics. In a simple picture, electrodes made from metals whose work function is close to the organic adsorbate electron affinity (EA) should most easily form ohmic contacts. As mentioned above, the contact resistance depends on the details of the interfacial chemistry. Therefore, chemical reaction and surface reconstruction are some of the factors that make the reproducible formation of ohmic contacts challenging.

11.1.2 Schottky–Mott Contact

The Schottky–Mott contact is a textbook model for a semiconductor/metal interface [5, 6]. In a semiconductor, conduction and valence bands as well as a well-defined forbidden energy gap are formed. Electrons are free to move throughout the solid and thermal equilibrium is achieved. The Schottky–Mott model assumes common vacuum level (VL) and alignment of the Fermi levels E_f as a result of band bending at the semiconductor/metal interface. Its current-voltage characteristic is nonlinear and asymmetric; it has rectifying properties similar to semiconducting p-n junctions. In the case of organic material with a wide gap in the order of 2–3 eV and thus larger than the thermal energy, the concentration of thermally excited carriers is extremely small. Therefore, thermal equilibrium with E_f alignment and band bending in the organic layer close to the organic/metal interface cannot be assumed a priori. Especially for thin organic layers, it is mostly the vacuum level shift (dipole formation) at the interface described in the following that dominates the electronic properties for charge carrier injection.

11.1.3 Dipole Formation at Interface

As mentioned above, a common VL at organic/metal interfaces is often not achieved, but rather a VL shift leading to the formation of an electric dipole layer Δ. This layer can safely be assumed to be a pure interface property concentrated to a single or very few monolayers only; it is a consequence of a lack of mobile charge carriers in the organic material. For thicker layers, it often occurs in combination with band bending and E_f alignment [7].

The origins for this dipole layer formation are manifold: polarization of molecules, charge transfer across the interface, charge rearrangement or redistribution of the electron cloud [8], interfacial chemical reaction (chemisorption), dipole alignment, pillow effect and image forces, and many more. In the case of organic

molecules, these properties show a strong dependence on molecular ordering, packaging density, defects, molecular conformation, adsorption sites, to name only a few. Thus, for a detailed understanding of the interface properties, macroscopic methods must be complemented with nanoscale investigations to exactly determine all nanoscale geometrical and electronic parameters.

11.1.4 Macroscopic Methods

Up to now, most systematic studies (see Sect. 11.2) on the organic/metal interface have been performed with macroscopic methods such as the Kelvin Probe (KP), photoelectron spectroscopy (PES) and in special UV photoelectron spectroscopy (UPS), or inverse photoelectron spectroscopy (IPES). All the above-mentioned methods either use the emission of electrons or they rely on well-conducting samples. Therefore, for organic/metal interfaces that often have a reduced conductivity, their application must be done very carefully. In the following sections, IPES, PES, and the KP method will briefly be discussed including the different properties that can be retrieved from these techniques.

11.1.4.1 Kelvin Probe

The macroscopic Kelvin Probe (KP) was developed by Lord Kelvin in 1898 [9]. As depicted in Fig. 11.1a, two plane electrodes of metals with different work function ϕ_1 and ϕ_2 are placed close and parallel to each other to form a capacitor. When the electrodes are connected, Fermi level E_f alignment is achieved and a voltage:

$$V = \frac{\phi_1 - \phi_2}{e}$$

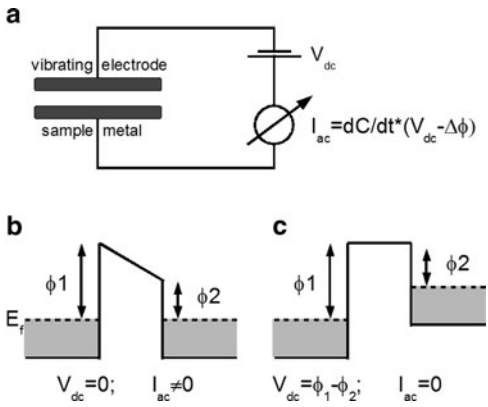

Fig. 11.1 (**a**) A metallic sample surface and a plane electrode are connected with a *dc*-voltage source as well as a current meter. (**b**) Mechanically vibrating the electrode will create a displacement current I_{ac} when $V_{dc} = 0$. (**c**) I_{ac} can be nullified by compensating the contact potential difference V_{CPD} by applying $V_{dc} = \phi_1 - \phi_2$

corresponding to the work function difference between the two metals is built up across the capacitor as it gets charged by the displacement current (Fig. 11.1b). e is the elementary charge of an electron. The total charge Q in the capacitor is $Q = C \cdot V$. It depends on the capacity of the plate capacitor $C = \varepsilon \cdot A/d$ with the permittivity ε, the surface of the plates A, and the distance d between them. As C is a function of the distance d, it varies when d is modulated as a function of time. As a result, the charge is modulated which leads to an ac-displacement current $I_{\mathrm{ac}} = \mathrm{d}Q/\mathrm{d}t$. The latter is measured and can be nullified when an additional dc-voltage equivalent to $-V_{\mathrm{cpd}}$ is added in the circuit to make the voltage across the capacitor $V = V_{\mathrm{cpd}} + V_{\mathrm{dc}} = 0$ equal to zero (Fig. 11.1c). Thus, KP nullifies the displacement current between two metal plates by applying an appropriate V_{dc} which gives a direct measure for the work function difference between the two electrodes. If one electrode is made of an inert, well-defined metal with calibrated work function, quantitative results are obtained. KP integrates over the size of the electrodes; although it relies on measuring a current, it has been shown that it correctly maps the surface potential also for poor conducting surfaces [4, 10].

11.1.4.2 Photoelectron Spectroscopy

PES uses a monochromatic photon source to illuminate the sample surface [11, 12]. For UPS, most instruments use gas discharge lamps with an energy of either 21.2 eV (He-I) or 40.8 eV (He-II). These energies are sufficient to emit electrons from occupied states due to the photoelectric effect. The energies of these emitted electrons are analyzed with a spectrometer to determine their original electronic state in the solid. Electrons emitted from the surface escape from the topmost layers with a depth of a few nanometers only, and thus UPS is very surface sensitive.

For metallic surfaces, the electrons with the highest kinetic energy in the analyzer originate from the Fermi level E_f and can be used to calculate the work function ϕ of the sample. Using careful analysis for increasing film thicknesses, further organic/metal interface properties such as the vacuum level (VL) shift relative to the substrate E_f (dipole formation), or the ionization potential (IP) can be determined.

11.1.4.3 Inverse Photoelectron Spectroscopy

Inverse PES (IPES) is a complementary method to PES to gain information on the empty states of the surface. In IPES, the sample surface is exposed to an electron beam and the emitted photons are analyzed in energy. The energies of the emitted photons are characteristic for the decay processes of the incident electrons into all of the unoccupied electronic states below their initial energy. In such a way, IPES will give a picture of the unoccupied electronic states above E_f. Especially, the electron affinity (EA) or the position of the lowest unoccupied molecular orbital (LUMO) can be estimated. The incident electron beam has a very low penetration depth; thus IPES is sensitive to a few atomic layers only.

For organic material especially with low conductivity, PES and IPES must carefully be evaluated since charging of the surface and final state screening can influence the energy of emitted or collected electrons. Furthermore, radiation damage can make it impossible to apply these methods for certain materials.

11.1.5 Nanoscopic Methods: Kelvin Probe Force Microscopy

In the past years, many techniques based on scanning force microscopy (SFM) have been developed to investigate electronic properties on the nanometer scale (for an overview, see, e.g., [13]). Conducting probe SFM [14], scanning capacitance microscopy [15], electrostatic force microscopy (EFM) [16], and Kelvin probe force microscopy (KPFM) [17, 18] (KPFM) have been developed and can be used to measure the properties such as current flows, resistance, capacitance, electrostatic forces, charge distribution, surface potential, and voltage drops on the nanometer scale. All of these SFM-based methods can provide simultaneous topographic imaging. The lateral resolution achieved, however, depends on the probes used as well as the distance between tip and sample during the measurements.

For imaging surface potentials or charge distribution, local work function, and electrostatic forces, KPFM is the method which provides the best spatial resolution. The details on the physical effects that determine the imaging process in KPFM and on how exactly the method can be implemented are described elsewhere (see Chap. 2). Here it is just reminded that the imaging process of KPFM relies on minimizing the electrostatic force or its gradient between the tip and the sample by applying an appropriate *dc*-voltage V_{dc} between tip and sample. The measured value of V_{dc} corresponds to the local contact potential difference (LCPD). In order to extract quantitative values out of the acquired signal, either areas on the surface or a well-characterized tip have to been taken for calibration (e.g., with known work function). Although KPFM can be used to measure the LCPD on even an atomic length scale (see Chap. 13), its quantitative resolution is in the order of the diameter of the tip front end. Note that KPFM is fundamentally different from macroscopic Kelvin Probe (KP) in which a current is nullified and hence conducting samples are needed. KPFM perfectly works for poorly conducting organic material or for insulating samples; however, charging can lead to an offset of the measured local values.

11.2 Macroscopic Studies

The macroscopic characterization methods described above have been intensively used to characterize the organic/metal interface to gain insight into the details of the contact formation of organic layers to metallic electrodes.

One large group of studies is focussing on the organic/metal interface for rather thick organic layers and is discussing mostly the effects of band-bending, interface dipole formation, as well as the Fermi level alignment at these interfaces. PES and the macroscopic Kelvin Probe (KP) are used to investigate the properties of these interfaces. A general review on the electronic properties at organic/metal interfaces is given by Ishii et al. in [19]. For the KP, it has been stated that it is well suited to measure Fermi level shifts at organic/metal interfaces, and that Fermi level alignment is not achieved in many cases [7, 10, 20] due to the formation of an interface dipole layer. Furthermore, for increasing thicknesses KP can be used to observe band bending or effects due to screening [4]. The conclusion that Fermi level alignment is not always achieved is supported by various PES studies which can give a little more insight into the details of the interface properties. For example, it has been shown that the interface dipole is confined to a few nanometers only, and that it linearly depends on the difference between the ionization potential and the transport gap in the case of phthalocyanines with different degree of fluorination [21, 22]. In these studies, besides the formation of a dipole layer, different contributions are identified which are responsible for the potential drop at the interface: modification of metal work function (mirror force or surface rearrangement) and potential drop in the organic layer (band bending).

Other studies focus more on the very first layer of an organic material adsorbed on metal surfaces. For example, it has been shown by KP that Ag electrodes can be chemically tailored via the adsorption of different self-assembled monolayers (SAM) to control the electronic interface properties of organic diodes [23]. Various studies have been performed to measure the work function change of metals upon deposition of organic layers [7], in many cases, a linear dependence between the metal work function and the interface dipole is found [2, 20, 24]. Both positive and negative dependencies are found. For most systems studied, the interface dipole is confined to the very first layer. However, the strength and the orientation of the dipole depend on various parameters. For example Venkataraman et al. [25] used different alkanethiols to tune surface chemical gradients by changing the coverage, the orientation, or the component gradient. The observed shifts in binding energy are due to interface charge redistribution, surface coverage, chemical nature, and molecular orientation. For monolayer SAM, the electronic interface properties can be tuned using different alkanethiols with either different terminal groups [26] or different chain lengths [27]. Also, the side groups of porphyrin molecules can change the work function shifts on various metal surfaces as demonstrated by Alkauskas et al. [28]. Furthermore, De Renzi concludes that the molecular level alignment is influenced by the value of the local work function, which in real, inhomogeneous surfaces, substantially differs from the typically measured average value [29]. One other effect is spontaneous dipole alignment which can occur for multilayers of polar molecules such as N_2O [30] or Alq_3 on gold [31]. In the latter study, the aligned dipoles formed a giant surface potential of several tens of volts.

In summary, the most prominent effects at the interface of ultrathin organic films with a metal substrate are the following: Fermi level alignment is not necessarily achieved but rather a dipole layer at the interface is formed. In most cases, this layer

is confined to the very first monolayer only. Furthermore, the size of the dipole layer often linearly depends on the metal substrate work function. Theoretical studies can be used to identify the origins of the dipole formation. For example at the Alq_3/Al interface: (1) charge transfer, (2) mirror force, (3) push back effect due to Pauli repulsion between metal and molecular electrons, (4) chemical interaction, (5) interface state, and (6) permanent dipole of adsorbates are determining the dipole formation [32]. It is therefore not always the direction of a charge transfer that determines the orientation of the dipole, but rather the redistribution of the electronic cloud as a function of the above-mentioned effects [8].

In most of the above-mentioned macroscopic studies that investigate the origin of the interface dipole formation, it is pointed out that it is crucial to exactly know the substrate surface reconstruction, the precise adsorption site of the molecule, its conformation as well as the intermolecular assembly. These nanoscale geometrical information in combination with the local electronic properties can be acquired by noncontact atomic force microscopy (nc-AFM) in combination with KPFM.

11.3 Nanoscopic Studies

KPFM can be used to measure many electronic properties such as local dopant concentrations [33, 34], surface charging due to photoinduced charge separation [35–37], interface dipole formation between a metal surface and an organic layer [38, 39], or an ionic thin film [40], electronic band bending at semiconducting interfaces [41–46], contrast due to differently terminated or reconstructed surface orientations on the facets of a nanocrystal [47], at grain boundaries [48], and on ordered and disordered surfaces [49], to name only a few of the first experimental results. These examples show that the contrast provided by KPFM reveals important information in addition to the sample surface topography.

11.3.1 Quantitative Results by KPFM

As mentioned in Sect. 11.1.5, for a quantitative interpretation of the measured KPFM contrast, the tip work function must be known. Furthermore, although nanoscale information is obtained, a quantitative interpretation is only valid if either the observed nanoscale object is larger than the tip front end or if quantitative values can be obtained by comparing the measured data with the results obtained from KPFM image simulations using effective tip geometries and optimizing the local CPD distribution [50–53].

For ultrathin alkali halides on metal surfaces [51] as well as for C_{60} molecules on various metal substrates [54], it has been shown that KPFM reveals quantitative values on a nanometer scale that are in agreement with the macroscopically acquired results by UPS and KP.

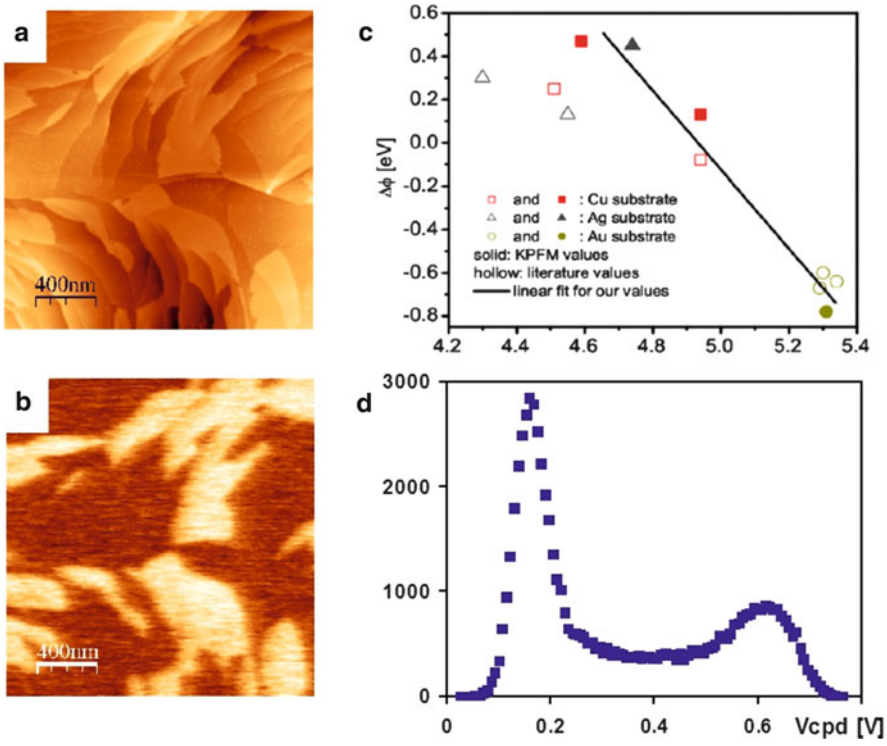

Fig. 11.2 (**a**) NC-AFM topography image (2 × 2 μm, *z*-scale 1 nm) and (**b**) simultaneously recorded KPFM signal of 0.5 monolayer C_{60} on Ag(111). (**c**) Overview of different experimental results for work function changes of clean metal substrates after deposition of C_{60}. (**d**) Histogram of the values recorded in (**b**), the distance between the two peaks corresponds to a work function change of $\Delta\phi = +0.45$ eV [54]

In the latter study by Zerweck et al. [54], the adsorption of C_{60} on various metal substrates was investigated by KPFM. C_{60} is a molecule widely used for different applications in organic electronic devices, and furthermore, C_{60} can be used to tune the interface properties between a metal substrate and an organic layer [55–57]. The KPFM experiments for Ag(111), Au(111), Cu(100), and Cu(111) single crystal substrates by Zerweck et al. were measuring the work function difference between the metal substrate and one monolayer thick islands of C_{60} on only partially covered samples (Fig. 11.2).[1] Figure 11.2a, b shows the topography and the Kelvin signal, respectively, for the Ag(111) surface partially covered with C_{60}. The clear Kelvin contrast in Fig. 11.2b can be evaluated by taking a histogram of the voltages applied by the KPFM as depicted in Fig. 11.2d. Triple-Gaußian[2] peak fitting reveals the

[1] For image evaluation, WSxM [58] was used.

[2] The third peak is used to account for the background noise.

distance between the two peaks which for the present example corresponds to the contact potential difference (CPD) (V_{CPD}) between the pure Ag(111) surface and the areas covered by 1 ML of C_{60} ($\Delta\phi = +0.45$ eV). The calibration of the data was done by taking the work function for the pure Ag(111) substrate from literature [59] as a reference which is then attributed to the value measured for the pure Ag(111) substrate. The results for all investigated metal surfaces are displayed in Fig. 11.2c where they are compared to the values obtained macroscopically by KP and by UPS [20, 60–63]. The scatter of the values for the bare metal work function for copper and silver might be due to the fact that these surfaces are not that noble and tend to react with residual gases present even in ultrahigh vacuum (UHV). All the same, this study showed that, first, nanoscale KPFM experiments are in very good agreement to the macroscopically acquired ones, second, what is valid for most organic molecules physisorbed on metal substrates: the interface dipole layer which is formed linearly depends on the substrate work function (see Sect. 11.1.3), and third, quantitative resolution in KPFM can be obtained on a length scale as small as 10 nm. This high resolution was achieved when using ultra sharp well-conducting AFM tips that were covered with an ultrathin chromium layer [54].

Different nanoscale KPFM studies support the importance of exactly knowing the geometrical and chemical properties of the investigated organic/metal contacts since many parameters can change the strength or even the direction of the interface dipole. Cui et al. [64] showed that the interface dipole layer at carbon nanotube/Au contacts can reversibly change its direction as the environment changes from air to vacuum or an oxygen-free environment. Miyazaki et al. [65] observed that the structural order of methylquinquethiophene (M5T) strongly influences the electrical resistance of the film. Furthermore, these authors observed the formation of a first monolayer of M5T on platinum electrodes with a hight resistance, higher than the one observed for example at grain boundaries. Yamada et al. [66] studied layers of organic molecules on Pt substrates. Different surface potentials were observed for the first as well as the second monolayer. The authors explain these results by a charge transfer for the first monolayer and an induced polarization for the second one. Finally, the dipole moment normal to the substrate obtained by ab initio MO (molecular orbital) calculations were also used to predict the surface potentials of patterned SAM [67].

Besides these studies of organic layers directly adsorbed on metal substrates, there have also been a few reports on KPFM applied to organic material on insulating substrates. Palermo et al. [68] report on acceptor–donor phase segregated blend films adsorbed on mica. In these films, each component clearly possesses significantly different nanoscale electronic properties from its neat film. This is due to molecular ordering as well as due to the interaction between the two components. The molecular ordering and orientation with respect to the substrate also influenced the CPD measured for PTCDA on ultrathin KBr films on Ag(111) as observed by Loppacher et al. [69] (see Sect. 11.3.2). In other experiments, Glatzel et al. [70] measured a clear contrast in the KPFM signal between molecules and gold nanoclusters on the insulating surface of KBr. The contrast formation is explained by variations of the local surface potential or the local dipole moment.

In the following, some examples will be discussed where either the orientation of the adsorbed molecules with respect to the surface or their organization on the surface influence the measured CPD. All investigated samples were prepared under UHV conditions and measured in situ with a commercial low-temperature AFM (Cryogenic SFM Omicron Nanotechnology GmbH) at 80 K.

11.3.2 Orientational Dependence

The first example we are going to discuss is the adsorption of PTCDA (3,4,9,10-perylene-tetracarboxylic-dianhydride) on partially KBr covered Ag(111) [69]. The aim of this work was to use an ultrathin insulating layer (KBr) between the metal substrate and the organic molecules to control the vertical interaction (adsorbate–substrate) and therefore to influence the growth mode of the organic adsorbates. It was shown that the delicate balance between adsorbate–adsorbate (lateral) and adsorbate–substrate (vertical) interactions is indeed strongly influenced by the ultrathin KBr layer leading to a completely different molecular arrangement of PTCDA on the first and the second monolayer of KBr. A similar conclusion was drawn by Ramoino et al. [71] for the adsorption of porphyrins adsorbed on NaCl layers with different thicknesses on Cu(111). Simulations of the results by Loppacher et al. [69] with an extended Ising-type model reproduced the experimental patterns very well, especially the size of the observed molecular aggregates corresponds to the experimental values. Apparently, small aggregates are formed when the vertical and lateral interaction are competing, and larger ones are formed as soon as one of the interactions dominates. Besides the different sizes, in the smaller aggregates PTCDA formed rods in which the PTCDA molecules were laterally π-stacked and in the larger aggregates planar growth with the π-orbital parallel to the surface was observed.

Figure 11.3a, b displays the topography and KPFM signal for PTCDA adsorbed on a one (upper left part) and two monolayer (lower right part) thick KBr film on the Ag(111) substrate. The separation between the two areas of 1 and 2 ML thick KBr underneath the molecules is indicated by the dashed line. The molecules adsorb in two different conformations in a planar geometry and in rods where the molecules are oriented perpendicular to the substrate. The KPFM contrast in Fig. 11.3b shows three different levels, the darkest color corresponds to the KBr covered Ag(111) substrate, the medium one corresponds to the conformation in rods, and the brightest one is measured above the molecules adsorbed in planar geometry on the ultrathin KBr film. A difference in approximately 0.1 V (lowering of the work function) was observed between each, the KBr covered Ag(111), the molecules adsorbed in a planar conformation on the thin insulating film, and molecules adsorbed in stacks. These values can be taken from the histogram of the measured CPD values (Fig. 11.3e). Figure 11.3c, d shows the formation in rods (topography) as well as the planar growth of PTCDA (dissipation image in the area depicted in Fig. 11.3a). Interestingly, there is PTCDA in rods on both the first and the second ML KBr

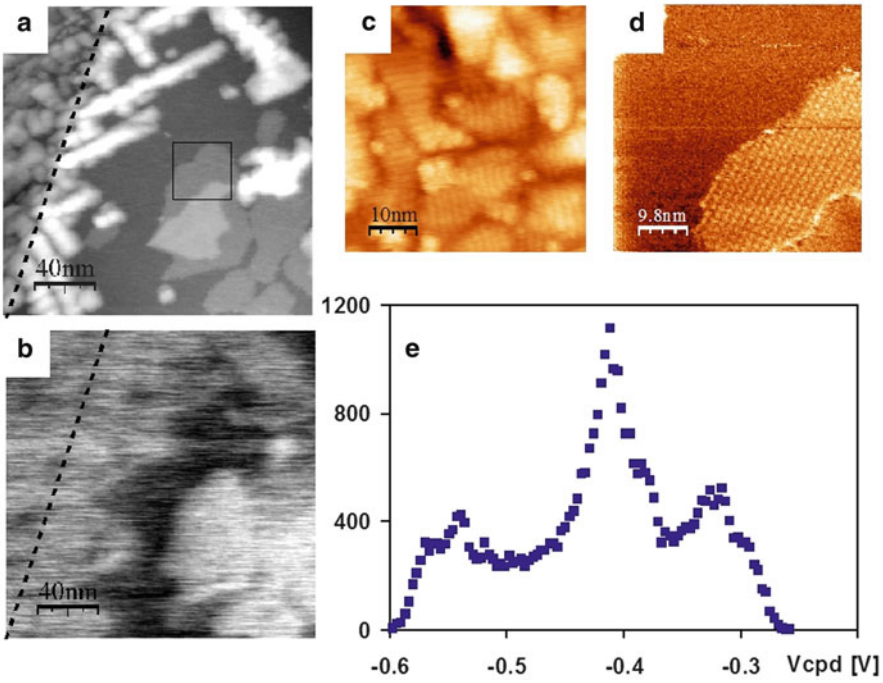

Fig. 11.3 (**a**) Topography (200 nm × 200 nm, *z*-scale 1.4 nm) of PTCDA on 1 ML (*upper left part*) and 2 ML (*lower right part*) of KBr/Ag(111). (**b**) KPFM image simultaneously acquired to the topography in (**a**) showing three different levels that are evaluated by the histogram displayed in (**e**). (**c**) and (**d**) show molecular resolution images for the two different assemblies found on this surface: (**c**) the formation of rods with the molecules π-stacked parallel to the surface (on 1 ML KBr/Ag(111), *z*-scale 0.5 nm), and (**d**) planar growth as observed mostly on 2 ML of KBr/Ag(111) (dissipation image) [69]

above which the CPD values are identical. Although, it is not the thickness of the underlying KBr film which determines the local CPD values but rather the orientation and the assembly of the molecules. A quantitative evaluation of the local work function can be made from the measured CPD values as follows: first, the work function of Ag(111) is taken from literature (4.74 eV [59]) and the work function difference between pure and KBr covered Ag(111) is measured before PTCDA deposition (−1.04 eV). This results in a reference value for the work function of KBr-covered Ag(111) of 3.6 eV. The PTCDA on KBr in rods increases this work function by ≈0.1 eV, and the PTCDA adsorbed in planar geometry increases the work function by ≈0.2 to an absolute value of 3.7 eV and 3.8 eV, respectively. These evaluations must be made with care, since due to the reactivity of the Ag(111) surface it is not guaranteed that after the deposition of KBr the work function of Ag(111) is not altered. Hence, taking literature values for metal work functions can lead to wrong absolute values; however, the measured local differences are correct.

The second example we will discuss is the adsorption of porphyrin molecules on highly ordered pyrolytic graphite (HOPG) [72]. Porphyrin compounds have been of interest for many years due to the facile ability to engender and tune optical and electrical functionality by varying the nature of the porphyrin ring central metal ion and modulating porphyrin σ- and π-system electronic structure through introduction of appropriate substituents at the macrocycle β- or meso-positions [73]. Many substituted porphyrin systems have been established to self-assemble on metal surfaces [74, 75]. Nikiforov et al. [72] deposited 0.6 monolayer (ML) of 5,15-bis (2′,6′-bis(3,3-dimethyl-1-butylocy)phenyl) porphyrin (compound **1**) [76] on the atomically smooth surface of HOPG.

Figure 11.4a depicts the resulting topography image which shows one part of a large island of porphyrin surrounded by the clean HOPG substrate. Typically, the molecules assembled in islands with sizes in the order of 1 μm; however, their

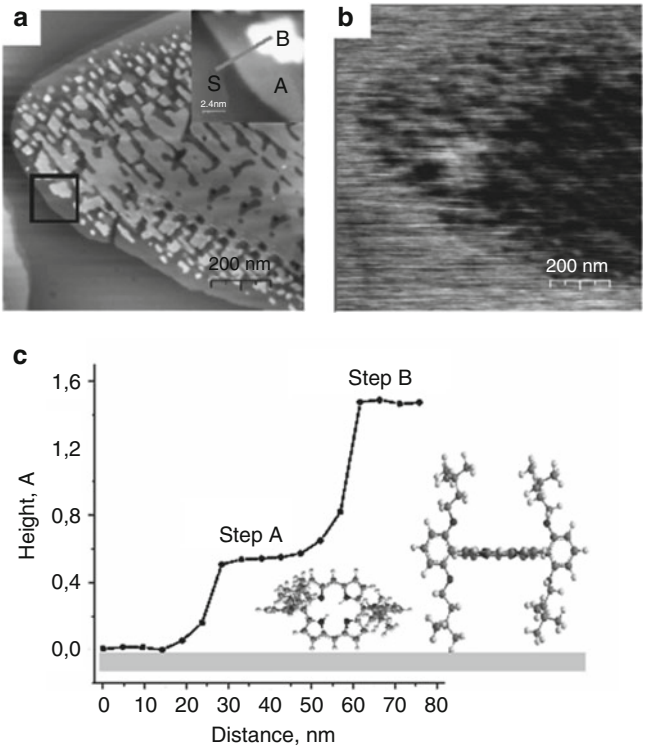

Fig. 11.4 (**a**) NC-AFM topography (z-scale 2.4 nm) and (**b**) KPFM image (z-scale 80 mV) (**b**) (1 μm × 1 μm) of 0.6 ML of porphyrin molecules adsorbed on HOPG. The inset in (**a**) shows a close up view of the topography image in the area indicated by the *black square*. A line profile drawn along the *gray line* marked in the inset is displayed in (**c**). A careful height analysis leads to the conclusion that in areas A the porphyrin ring is oriented perpendicular to the surface and in areas B with higher step height, the porphyrin ring is oriented parallel to the sample surface. In the latter case, there is a stronger dipolar coupling between the porphyrin ring and the surface [72]

organization was not homogeneous. What at first glance looks like a second ML of molecules which develops on the first one in the form of smaller islands is in fact a different conformation of the molecules in still the very first ML. A careful height analysis taken from the inset in Fig. 11.4a and displayed in Fig. 11.4c reveals two different step heights: 0.6 and 1.55 nm. The height of step A corresponds to the width of the porphyrin ring (∼0.7 nm), while that of step B matches the length spanned by the two 3,3-dimethyl-1-butyloxy groups which lie above and below the porphyrin plane. Both islands A and B are highly ordered, and an evaluation of their ordering using images with molecular resolution (not shown) reveals lattice parameters which confirm the following conclusions: The molecules in island A assemble with their porphyrin rings oriented perpendicular to the substrate, while in island B the porphyrin rings lie parallel to the substrate surface. These structures are similar to the "face on" and the "edge on" stacking modes of porphyrin molecules observed in monolayers and the solid state [77–80].

The interesting result of the above-described experiments is that there is a difference in the surface potential measured by KPFM for the two molecular arrangements. Figure 11.4b shows the KPFM signal simultaneously acquired to the topography signal displayed in Fig. 11.4a. For the island A with the porphyrin rings perpendicular to the surface, the molecular ML shows the same work function as the one above the clean HOPG substrate. However, for the molecular layer with the porphyrin rings parallel to the HOPG surface, the surface work function is lowered by ∼50 mV. This is due to the fact that when the porphyrin ring is parallel to the surface, the π-symmetric orbital of the porphyrin and underlying substrate facilitate charge delocalization. A comparison between the expected dipole moment calculated by a simple model and the dipole moment deduced from the measured work function difference (∼50 mV) leads the authors to the conclusion that significant charge screening occurs at the porphyrin–HOPG interface for the islands of type B. When the charge density of the porphyrin lies perpendicular to the surface (island type A), the magnitude of the dipolar interaction is diminished greatly and no measurable change of the surface potential is observed. This study indicates that in a metal-porphyrin-metal device configuration, molecules oriented with the porphyrin ring parallel to the surface will demonstrate an increased hole injection barrier with respect to analogous structures oriented perpendicular to the surface. Thus, differences in surface potential that derive from molecular configuration have important implications for molecular and organic electronics.

11.3.3 Dependence on Molecular Arrangement

As mentioned in Sect. 11.1, the effects that occur at metal/organic interfaces are manifold. Often, they are both substrate and adsorbate related as it is for example in the case of chemical binding or dipole formation. In the above-described experiments, the orientation of the adsorbed molecule's π-orbital with respect to the surface changes the local work function. Hence, for the investigated organic/metal

contacts, the charge injection barrier will strongly depend on the morphology at the interface. Different other parameters can influence the interface properties such as order and disorder, packaging density, but also defects in films and grain boundaries. In the following, we are going to discuss an example which shows that both the packaging density and an order–disorder transformation can vary the local surface potential.

Milde et al. [81] used KPFM to investigate the work function changes that are generated by the adsorption of different structural phases of octachloro zinc phthalocyanine ($ZnPcCl_8$) on Ag(111). Phthalocyanines are a common class of organic dyes used for applications in optoelectronic devices, but might equally be used in molecular electronic devices due to their chemical stability, self-assembly behavior, and electronic properties [82–84]. The latter can be modified by substitution of the eight hydrogen atoms with either electron donors or acceptors, or by complementation with different metal atoms or metal complex cores [21, 85]. Standard phthalocyanine is known to show a good self-assembly behavior, but in a subtle balance between intermolecular and molecule-substrate balance. In a study by Abel et al. [86], the intermolecular interaction of ZnPc was enlarged by substitution of hydrogen with halogenides, which lead to a more complex self-assembly behavior of the synthesized $ZnPcCl_8$ with different phases. Within the first ML $ZnPcCl_8$ on Ag(111), distinct structural phases were formed which could be attributed to the formation of 8, 4, and 0 intermolecular hydrogen–halogen bonds [87].

In the work by Milde et al. [81], 0.5 ML of $ZnPcCl_8$ were deposited on the clean Ag(111) surface, and the sample was cooled down to 80 K after 10 min to preserve a surface on which the phases P1 and P2 coexisted. Note that at room temperature, the organization of the molecules develops toward P3 via the gas phase [86, 87]. In P1, the molecules are arranged in a rhombic phase showing no hydrogen–chlorine bonds. P2 is an asymmetric phase with four intermolecular bonds. Typically, for a submonolayer coverage, the molecules are arranged in rather large, highly ordered ML thick islands. Most of these islands have smaller peninsulas which occur at a changed voltage in the KPFM signal compared to the mother island. Figure 11.5a, c depicts the topography and KPFM signal of such an area, where all the Ag(111) substrate, P1 and P2 are imaged. The identification of the phases P1 and P2 was done by images with molecular resolution (not shown). The measured lattice constants were in excellent agreement with the ones observed by Abel et al. [86]. The observed work function change between the Ag(111) and an ML of $ZnPcCl_8$ in phase P1 is $\Delta\phi_{P1} = -(103 \pm 22)$ meV and in phase P2 $\Delta\phi_{P2} = -(54 \pm 20)$ meV.

As mentioned in Sect. 11.3.1, taking as a reference the work function from literature of a surface which tends to react with residual gases is quite delicate. Therefore, the authors evaluated the difference between the two surface potentials acquired above the phases P1 and P2 $\Delta\phi_{21} = \phi_{P2} - \phi_{P1} = (49 \pm 22)$ meV. This measured value can be used according to Iwamoto et al. [88] to calculate a charge density difference between the two phases of $\Omega_{21,m} = (0.026 \pm 0.014)(e^{-1}nm^{-2})$. For comparison, the authors performed density functional theory calculations using SIESTA [89, 90] to deduce the molecular density in the different phases as well as

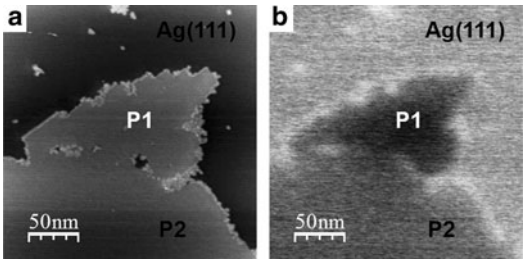

Fig. 11.5 (**a**) Topography (z-scale 0.8 nm) and (**b**) KPFM image (250 nm × 250 nm) of 0.5 ML $ZnPcCl_8$ adsorbed on the Ag(111) surface. Images with molecular resolution (not shown) were used to deduce the areas in which the molecules are organized in the rhombic phase P1 showing no hydrogen–chlorine bonds, and in the asymmetric phase P2 with four intermolecular bonds. The observed work function change between the Ag(111) and an ML of $ZnPcCl_8$ is $\Delta\phi_{P1} = -(103 \pm 22)$ meV in phase P1 and $\Delta\phi_{P2} = -(54 \pm 20)$ meV in phase P2 [81]

the charge per molecule. The latter is almost the same for all phases ($\sim 0.66\,e^-$ per molecule) and can be used with the molecular density to compute a charge density difference $\Omega_{21,c} = (0.033 \pm 0.002)(e^{-1}nm^{-2})$ which is well within the uncertainty of the one calculated from the measured values ($\Omega_{21,m}$, see above). Thus, the difference in work function measured by KPFM on these two differently assembled molecular layers can be attributed to a difference in charge density, which is a direct consequence of the intermolecular bonds.

Besides the difference in work function between highly ordered molecular layers of P1 and P2, there were also disordered layers that showed a much larger surface potential than the ordered ones. The size of disordered areas increased when the substrate temperature was increased during molecular deposition. Figure 11.6 shows an area with ordered (P1 and P2) and disordered (D) molecular layers as well as with pure Ag(111). The images in Fig. 11.6a, c were recorded before the images in Fig. 11.6b, d. Between the two, a scan in a smaller square area (indicated by the arrow) with increased tip sample interaction was performed. In the scanned area (40 nm × 40 nm), the slightly higher topography clearly shows that the molecules have undergone an order–disorder transition, and the KPFM signal shows an increased potential similar to the one observed in the disordered areas (D). In the disordered areas, it is most probable that the molecules are not adsorbed with their π-orbital parallel to the surface. The reversed sign of the work function change on disordered islands compared to the ordered ones indicates a completely different binding mechanism, since the symmetry of the molecule does not allow for a static dipole moment. Such a rise in work function upon $ZnPcCl_8$ deposition on Ag(111) was also observed by UPS [91]; however, in these experiments the ordering of the molecules is unknown and there might even be multilayer islands on the surface.

On the one hand, this order–disorder transition could be seen as a possibility for nanolithography; on the other hand, it shows how important it is to determine the exact morphology of the investigated samples on a molecular length scale. For $ZnPcCl_8$ on Ag(111) it is not only the density of the molecular assembly but also

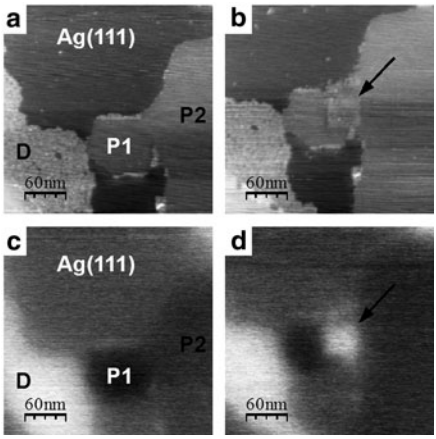

Fig. 11.6 (**a**) and (**b**) Topography (300 nm × 300 nm, *z*-scale 0.7 nm) and (**c**) and (**d**) corresponding KPFM images of 0.5 ML $ZnPcCl_8$ adsorbed on Ag(111). Areas of pure substrate, the phases P1 and P2, as well as a disordered phase D can be identified. Images (**b**) and (**d**) have been recorded after a small square area (indicated by the *arrow*) has been scanned with much higher frequency shift as usual. During this scan with much higher tip sample interaction, the tip induced an order–disorder transformation. This one can be observed both in the subsequently recorded (**b**) topography and (**d**) KPFM image [81]

the orientation with respect to the surface and the ordering of the molecules which has to be considered to understand the interface dipole layer formation.

11.4 Conclusion

In summary, this chapter described the effects that occur at metal/organic interfaces. In the first part, an overview of the work done by macroscopic methods is given. From an electronic point of view, three different types of contacts can be distinguished: an ohmic contact, a Schottky–Mott contact, or a dipole layer. These effects have been systematically studied by means of macroscopic methods such as the KP, PES, and IPES. KP gives a direct measure for the work function, PES and IPES can be used to estimate the vacuum level (VL) shift relative to the substrate E_f (dipole formation), the ionization potential (IP), the electron affinity (EA), or the position of the LUMO. Macroscopic methods either use the emission of electrons or they rely on well-conducting samples. Thus, for organic layers with reduced conductivity, their application must be done with care. The most important conclusions drawn from macroscopic studies of organic/metal interfaces are the following: Fermi level alignment is not necessarily achieved but rather a dipole layer at the interface is formed, the latter is confined to the very first monolayer only. The size of the dipole layer shows a linear dependence on the metal substrate

work function. The origins for dipolar layer formation can be charge transfer, mirror forces, push back effects, chemical interaction, interface states, permanent dipole of adsorbates, and many more. It is not always the direction of a charge transfer that determines the orientation of the dipole, but rather the redistribution of the electronic cloud. These properties strongly depend on the local environment; therefore, it is crucial to exactly know the geometrical and chemical properties of the investigated interface.

The second part of this chapter is dedicated to the nanoscopic KPFM method. First of all, it is shown that KPFM reveals quantitative values for the local work function. This was demonstrated by comparing locally acquired KPFM values with results from macroscopic methods for a variety of metal/organic (C_{60}) interfaces [54]. Furthermore, some studies were discussed where either the orientation of the adsorbed molecules with respect to the surface or their organization on the surface influenced the measured CPD. The influence of the orientation was demonstrated with the help of two examples. The first was the adsorption of PTCDA on Ag(111) covered by an ultrathin KBr film with a thickness of 1 or 2 ML [69]. It was shown that the CPD observed above differently organized molecules was independent of whether the molecules were adsorbed on the first or the second ML of KBr/Ag(111), but rather depended on the orientation of the molecules with respect to the surface. The second example discussed the adsorption of porphyrin molecules on HOPG [72]. Again, it was found that the CPD strongly depended on the orientation of the adsorbed molecules π-orbital with respect to the surface. The dependence on the molecular arrangement was shown for the case of different structural phases of octachloro zinc phthalocyanine (ZnPcCl8) on Ag(111) [81]. Although these structural phases were assisted by intermolecular hydrogen–halogen bonds (which did not significantly influence their electronic properties), it was primarily the packaging density in these phases which led to the observed work function differences. Besides the packaging density, this study also showed that an order–disorder transformation can vary the local surface potential.

Thus, KPFM is a very versatile tool to characterize metal/organic interfaces. It is indispensable to exactly know the molecular organization and orientation. However, for a complete picture of the complex effects that occur at these interfaces, KPFM must be complemented either with macroscopic methods or with theoretical calculations.

References

1. L. Fu, L. Cao, Y. Liu, D. Zhu, Adv. Coll. Int. Sci. **111**, 133 (2004)
2. H. Ishii, E. Morikawa, S. Tang, D. Yoshimura, E. Ito, K. Okudaira, T. Miyama, S. Hasegawa, P. Sprunger, N. Ueno, K. Seki, V. Saile, J. Electr. Spectrosc. Relat. Phenom. **101–103**, 559564 (1999)
3. L. Buergi, T.J. Richards, R.H. Friend, H. Sirringhaus, J. Appl. Phys. **94**, 6129 (2003)
4. H. Ishii, N. Hayashi, E. Ito, Y. Washizu, K. Sugi, Y. Kimura, M. Niwano, Y. Ouchi, K. Seki, Phys. Status Solidi A **201** (2004)

5. N.F. Mott, Math. Proc. Cambridge Philos. Soc. **34**, 568 (1938)
6. W. Schottky, Phys. Z. **41**, 570 (1940)
7. K. Seki, N. Hayashi, H. Oji, E. Ito, Y. Ouchi, H. Ishii, Thin Solid Films **393**, 298 (2001)
8. T. Leung, C. Kao, W. Su, Phys. Rev. B **68**, 195408 (2003)
9. L. Kelvin, Phil. Mag. **46**, 82 (1898)
10. M. Pfeiffer, K. Leo, N. Karl, J. Appl. Phys. **80**, 6880 (1996)
11. S. Huefner, *Photoelectron Spectroscopy: Principles and Applications Book Description* (Springer, Berlin, 2003)
12. A.M. Ellis, M. Feher, T.G. Wright, *Electronic and Photoelectron Spectroscopy: Fundamentals and Case Studies* (Cambridge University Press, Cambridge, 2005)
13. D.A. Bonnell, R. Shao, Curr. Opin. Solid State Mater. Sci. **7**, 161 (2003)
14. T.W. Kelley, E.L. Granstöm, C.D. Frisbie, Adv. Mater. **11**, 261 (1999)
15. J.R. Matey, J. Blanc, J. Appl. Phys. **57**, 1437 (1985)
16. B.D. Terris, J.E. Stern, D. Rugar, H.J. Mamin, Phys. Rev. Lett. **63**, 2669 (1989)
17. M. Nonnenmacher, M.P. O'Boyle, H.K. Wickramasinghe, Appl. Phys. Lett. **58**(25), 2921 (1991)
18. J.M.R. Weaver, D.W. Abraham, J. Vac. Sci. Technol. B **9**(3), 1559 (1991)
19. H. Ishii, , K. Sugiyama, E. Ito, K. Seki, Adv. Mater. **11**, 605 (1999)
20. N. Hayashi, H. Ishii, Y. Ouchi, K. Seki, J. Appl. Phys. **92**(2), 3784 (2002)
21. H. Peisert, M. Knupfer, J. Fink, Appl. Phys. Lett. **81**, 2400 (2002)
22. H. Peisert, M. Knupfer, T. Schwieger, G. Fuentes, D. Olligs, J. Fink, J. Appl. Phys. **93**, 9683 (2003)
23. I. Campbell, S. Rubin, T. Zawodzinksi, J. Kress, R. Martin, D. Smith, Phys. Rev. B **54**, 14321 (1996)
24. A. Kahn, N. Koch, W. Gao, J. Polymer Sci. Part B: Polymer Phys. **41**, 2529 (2003)
25. N. Venkatamaran, S. Zurcher, A. Rossi, S. Lee, N. Naujoks, D. Spencer, J. Phys. Chem. C **113**, 5620 (2009)
26. H. Mcnally, D. Janes, B. Kasibhatla, C. Kubiak, Superlatt. Microstr. **31**, 239 (2002)
27. J. Lü, E. Delamarche, L. Eng, R. Bennewitz, E. Meyer, H.J. Güntherodt, Langmuir **15**, 8184 (1999)
28. A. Alkauskas, L. Ramoino, S. Schintke, M. von Arx, A. Baratoff, H.J. Güntherodt, T.A. Jung, J. Phys. Chem. B **109**, 23558 (2005)
29. V.D. Renzi, Surf. Sci. **603**, 1518 (2009)
30. R. Balog, P. Cicman, N. Jones, D. Field, Phys. Rev. Lett. **102**, 073003 (2009)
31. E. Ito, Y. Washizu, N. Hayashi, H. Ishii, N. Matsuie, K. Tsuboi, Y. Ouchi, Y. Harima, K. Yamashita, K. Seki, J. Appl. Phys. **92**, 7306 (2002)
32. S. Yanagisawa, K. Lee, Y. Morikawa, J. Chem. Phys. **128**, 244704 (2008)
33. A.K. Henninga, T. Hochwitz, J. Slinkman, J. Never, S. Hoffmann, P. Kaszuba, C. Daghlian, J. Appl. Phys. **77**(5), 1888 (1995)
34. N. Duhayon, P.E.M. Fouchier, T. Clarysse, W. Vandervorst, D. Alvarez, S. Schoemann, M. Ciappa, M. Stangoni, W. Fichtner, P. Formanek, M. Kittler, V. Raineri, F. Giannazzo, D. Goghero, Y. Rosenwaks, R. Shikler, S. Saraf, S. Sadewasser, N. Barreau, T. Glatzel, M. Verheijen, S.A.M. Mentink, M. von Sprekelsen, T. Maltezopoulos, R. Wiesendanger, L. Hellemans, J. Vac. Sci. Technol. B **22**(1), 385 (2004)
35. T. Meoded, R. Shikler, N. Fried, Y. Rosenwaks, Appl. Phys. Lett. **75**(16), 2435 (1999)
36. M. Fujihira, Annu. Rev. Mater. Sci. **29**, 353 (1999)
37. C. Loppacher, U. Zerweck, S. Teich, E. Beyreuther, T. Otto, S. Grafström, L.M. Eng, Nanotechnology **16**, S1 (2005)
38. J. Lü, E. Delamarche, L. Eng, R. Bennewitz, E. Meyer, H.J. Güntherodt, Langmuir **15**, 8184 (1999)
39. H. Sugimura, K. Hayashi, N. Saito, O. Takai, N. Nakagiri, Jpn. J. Appl. Phys. **40**, 4373 (2001)
40. C. Loppacher, U. Zerweck, L.M. Eng, Nanotechnology **15**, S9 (2004)
41. O. Vatel, M. Tanimoto, J. Appl. Phys. **77**(6), 2358 (1995)
42. A. Kikukawa, S. Hosaka, R. Imura, Appl. Phys. Lett. **66**(25), 3510 (1995)

43. I.G. Hill, A. Rajagopal, A. Kahn, Appl. Phys. Lett. **73**(5), 662 (1998)
44. C. Sommerhalter, T. Matthes, T. Glatzel, A. Jäger-Waldau, M.C. Lux-Steiner, Appl. Phys. Lett. **75**(2), 286 (1999)
45. R. Shikler, T. Meoded, N. Fried, Y. Rosenwaks, Appl. Phys. Lett. **74**(20), 2972 (1999)
46. T. Glatzel, D.F. Marrón, T. Schedel-Niedrig, S. Sadewasser, M.C. Lux-Steiner, Appl. Phys. Lett. **81**(11), 2017 (2002)
47. S. Sadewasser, T. Glatzel, M. Rusu, A. Jäger-Waldau, M. Lux-Steiner, Appl. Phys. Lett. **80**(16), 2979 (2002)
48. C.S. Jiang, R. Noufi, J.A. AbuShama, K. Ramanathan, H.R. Moutinho, J. Pankow, M.M. Al-Jassim, Appl. Phys. Lett. **84**(18), 3477 (2004)
49. Y. Leng, C.C. Williams, L.C. Suand, G.B. Stringfellow, Appl. Phys. Lett. **66**(10), 1264 (1995)
50. J. Colchero, A. Gil, A. Berό, Phys. Rev. B **64**, 245403 (2001)
51. U. Zerweck, C. Loppacher, T. Otto, S. Grafström, L.M. Eng, Phys. Rev. B **71**, 125424 (2005)
52. T. Glatzel, L. Zimmerli, S. Koch, B. Such, S. Kawai, E. Meyer, Nanotechnology **20**, 264016 (2009)
53. T. Machleidt, E. Sparrer, D. Kapusi, K.H. Franke, Meas. Sci. Technol. **20**, 084017 (2009)
54. U. Zerweck, C. Loppacher, T. Otto, S. Grafström, L.M. Eng, Nanotechnology **18**, 084006 (2007)
55. J. Lee, Appl. Phys. Lett. **88**, 073512 (2006)
56. M. Nonomura, I. Hiromitsua, S. Tanaka, Appl. Phys. Lett. **88**, 042111 (2006)
57. X. Feng, C. Huang, V. Lui, R. Khangura, Z.H. Lua, Appl. Phys. Lett. **86**, 143511 (2005)
58. I. Horcas, Rev. Sci. Instr. **78**, 013705 (2007)
59. D.R. Linde, *CRC Handbook of Chemistry and Physics* (Boca Raton, FL, 1992)
60. K.D. Tsuei, J.Y. Yuh, C.T. Tzeng, R.Y. Chu, S.C. Chung, K.L. Tsang, Phys. Rev. B **56**, 15412 (1997)
61. C.T. Tzeng, W.S. Lo, J.Y. Yuh, R.Y. Chu, K.D. Tsuei, Phys. Rev. B **61**, 2263 (2000)
62. S. Veenstra, A. Heeres, G. Hadziioannou, G. Sawatzky, H. Jonkman, Appl. Phys. A **75**, 661666 (2002)
63. S.W. Cho, J.H. Seo, C.Y. Kim, K.H. Yoo, K. Jeong, C.N. Whang, Y. Yi, S.J. Kang, M. Noh, Appl. Phys. Lett. **88**, 151103 (2006)
64. X. Cui, M. Freitag, R. Martel, L. Brus, P. Avouris, Nanoletters **3**, 783 (2003)
65. T. Miyazaki, K. Kobayashi, K. Ishida, S. Hotta, T. Horiuchi, H. Yamada, K. Matsushige, Jap. J. Appl. Phys. **42**, 4852 (2003)
66. H. Yamada, T. Fukuma, K. Umeda, K. Kobayashi, K. Matsushige, Appl. Surf. Sci. **188**, 391 (2002)
67. N. Saito, K. hayashi, H. Sugimura, O. Takai, N. Nakagiri, Surf. Interf. Analysis **34**, 601 (2002)
68. V. Palermo, S. Morelli, M. Palma, C. Simpson, F. Nolde, A. Herrmann, K. Mullen, P. Samori, ChemPhysChem **7**, 847 (2006)
69. C. Loppacher, U. Zerweck, L.M. Eng, S. Gemming, G. Seifert, C. Olbrich, K. Morawetz, M. Schreiber, Nanotechnology **17**, 1568 (2006)
70. T. Glatzel, L. Zimmerli, S. Koch, S. Kawai, E. Meyer, Appl. Phys. Lett. **94**, 063303 (2009)
71. L. Ramoino, M. von Arx, S. Schintke, A. Baratoff, H.J. Guntherodt, T. Jung, Chem. Phys. Lett. **417**, 22 (2006)
72. M.P. Nikiforov, U. Zerweck, P. Milde, C. Loppacher, T.H. Park, H.T. Uyeda, M.J. Therien, L. Eng, D. Bonnell, Nano Lett. **8**, 110 (2008)
73. *The Porphyrins*, David Dolphin (Editor), Academic Press, New York, (1978)
74. L. Scudiero, D.E. Barlow, U. Mazur, K.W. Hipps, J. Am. Chem. Soc. **123**, 4073 (2001)
75. L. Scudiero, D.E. Barlow, K.W. Hipps, J. Phys. Chem. B **106**, 996 (2002)
76. H.T. Uyeda, Y. Zhao, K. Wostyn, I. Asselberghs, K. Clays, A. Persoons, M.J. Therien, J. Am. Chem. Soc. **124**, 13806 (2002)
77. J. Otsuki, E. Nagamine, T. Kondo, K. Iwasaki, M. Asakawa, K. Miyake, J. Am. Chem. Soc. **127**, 10400 (2005)
78. T. Terui, T. Kamikado, Y. Okuno, H. Suzuki, S. Mashiko, Curr. Appl. Phys. **4**, 148 (2004)
79. A. Ogunrinde, K. Hipps, L. Scudiero, Langmuir **22**, 5697 (2006)

80. Y. Zhou, B. Wang, M. Zhu, J. Hou, Chem. Phys. Lett. **403**, 140 (2005)
81. P. Milde, U. Zerweck, L. Eng, M. Abel, L. Giovanelli, L. Nony, M. Mossoyan, L. Porte, C. Loppacher, Nanotechnology **19**, 305501 (2008)
82. Z. Bao, A. Lovinger, A. Dodabalapur, Appl. Phys. Lett. **69**, 3066 (1996)
83. B. Crone, A.D.Y.Y. Lin, R. Filas, Z. Bao, A. LaDuca, R. Sarpeshkar, H.E. Katz, W. Li, Nature **403**, 521 (2000)
84. S.R. Forrest, Chem. Rev **97**, 1793 (1997)
85. T. Manaka, M. Iwamoto, Thin Solid Films **438**, 157 (2003)
86. M. Abel, V. Oison, M. Koudia, C. Maurel, C. Katan, L. Porte, ChemPhysChem **7**, 82 (2006)
87. M. Koudia, M. Abel, C. Maurel, A. Bliek, D. Catalin, M. Mossoyan, J. Mossoyan, L. Porte, J. Phys. Chem. B **110**, 10058 (2006)
88. M. Iwamoto, E. Itoh, Thin Solid Films **331**, 15 (1998)
89. D. Sanchez-Portal, P. Ordejon, E. Artacho, J.M. Soler, Int. J. Quantum. Chem. **65**, 543 (1997)
90. J. Soler, E. Artacho, J.D. Gale, A. Garcia, J. Junquera, P. Ordejon, D. Sanchez-Portal, J. Phys. Condens. Matter **14**, 2745 (2002)
91. P. Amsalem, L. Giovanelli, J. Themlin, M. Koudia, M. Abel, V. Oison, Y. Ksari, M. Mossoyan, L. Porte, Surf. Sci. **601**, 4185 (2007)

Chapter 12
KPFM and PFM of Biological Systems

B.J. Rodriguez and S.V. Kalinin

Abstract Surface potentials and electrostatic interactions in biological systems are key elements of cellular regulation and interaction. Examples include cardiac and muscular activity, voltage-gated ion channels, protein folding and assembly, and electroactive cells and electrotransduction. The coupling between electrical, mechanical, and chemical signals and responses in cellular systems necessitates the development of tools capable of measuring the distribution of charged species, surface potentials, and mechanical responses to applied electrical stimuli and vice versa, ultimately under physiological conditions. In this chapter, applications of voltage-modulated atomic force microscopy (AFM) methods including Kelvin probe force microscopy (KPFM) and piezoresponse force microscopy (PFM) to biological systems are discussed. KPFM is a force-sensitive non-contact or intermittent-contact mode AFM technique that allows electrostatic interactions and surface potentials to be addressed. Beyond long-range electrostatic interactions, the application of bias can lead to a mechanical response, e.g., due to linear piezoelectric coupling in polar biopolymers or via more complex electrotransduction and redox pathways in other biosystems. The use and development of PFM, based on direct electromechanical detection, to biological systems will also be addressed. The similarities and limitations of measuring surface potentials and electromechanical coupling in solution will be outlined.

B.J. Rodriguez (✉)
Conway Institute of Biomolecular and Biomedical Research, University College Dublin, Belfield, Dublin 4, Ireland
e-mail: brian.rodriguez@ucd.ie

S.V. Kalinin
Materials Science and Technology Division and Center for Nanophase Materials Science, Oak Ridge National Laboratory, Oak Ridge, TN 37831, USA
e-mail: brian.rodriguez@ucd.ie

S. Sadewasser and T. Glatzel (eds.), *Kelvin Probe Force Microscopy*, Springer Series in Surface Sciences 48, DOI 10.1007/978-3-642-22566-6_12,

12.1 Introduction

12.1.1 Electric Potentials and Electromechanics in Biosystems

Electrostatic interactions and electromechanical coupling in biological systems are key to biological structure and functionality, and span length scales from the single molecule to the cellular level and beyond [1–6]. The most widely known examples include muscle contraction, hearing, and voltage-gated ion channels. The electrostatics of proteins, membranes, and their interactions with each other and their environment have been broadly studied [7–13]. It is thought that charged surface residues impact protein folding and stability [14], and that long-range electrostatic forces drive initial nonspecific protein-protein associations [15]. The surface potential of cellular membranes varies according to the lipid composition, and the negative surface charge on the inner plasma membrane plays a role in cellular signaling to initiate, e.g., phagosome formation [16, 17]. The electric potential differences across a membrane regulate the proton transfer process of proton pumps [18, 19]. Electric fields associated with membranes often extend beyond the associated membrane deep into the cytosol as was recently shown for mitochondrial membranes [20], and models have been proposed which describe a three dimensional electric field cellular signaling network with the nucleus at the center of a cytoskeletal network [21]. Membrane surface charges also influence the formation of calcium microdomains [22], place constraints on protein anchoring [23] and import [24], and regulate membrane protein function, including electroconformational coupling [25–27] and the gating of ion channel proteins [28–30]. The complexity of the electrostatic interactions on a single membrane level can be illustrated in Fig. 12.1a. Note that the presence of the proteins in the membrane will affect local charge distributions making the membrane potential laterally inhomogeneous. In addition, deformation of the membrane will change potential distributions due to the flexoelectric effect.

These electrostatic interactions are fundamental to biological processes at the molecular and cellular levels, and the improper generation or sensing of electric signals can indicate significant deviations in biological function. Recently, it was shown that a reduction in the neuronal membrane potential is associated with Alzheimer's [32]. Similarly, membrane potentials are tied to cell cycle and death [33]. Beneficial and detrimental effects of external fields on tissue formation and repair have been studied in detail [34, 35].

Clearly, electric fields and electrostatic interactions are an integral component of the complete biophysical picture. These electrical signals are strongly linked to mechanical responses, e.g., as a conformational change in a protein or cellular electrotransduction and the mechanisms by which a cell converts an electrical signal to a chemical or mechanical response. Similarly, mechanical stimuli can result in an electrical signal. This class of interactions are described as electromechanical coupling and can take multiple forms, ranging from relatively simple mechanisms such as membrane flexoelectricity and biopolymer piezoelectricity [36, 37] to auditory

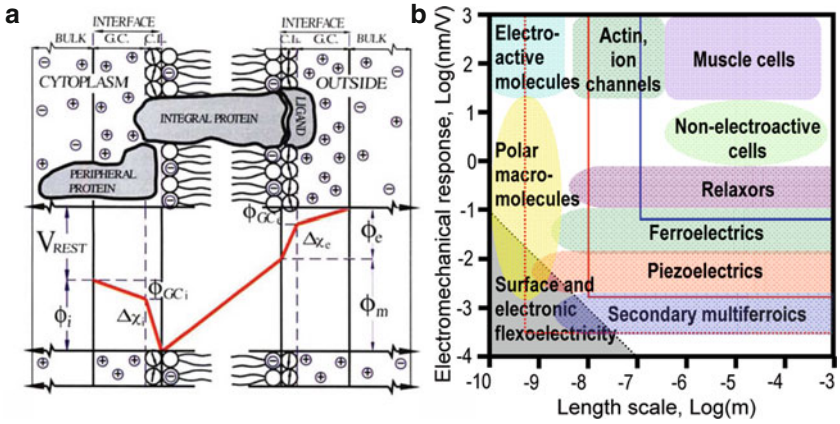

Fig. 12.1 (**a**) Electrostatics across a cellular plasma membrane. At each membrane interface, the negative charge of the polar heads of the phospholipids is compensated by a cationic Gouy–Chapman (GC) layer separated by a compact layer (CL) of strongly polarized water molecules. Electric potential (ϕ) is the sum of the potential across the CL ($\Delta\chi$) and the GC (ϕ_{GC}). (**b**) Electromechanical coupling in functional materials. The solid blue and red lines correspond to estimated limits of nanoindentation and atomic force microscopy, respectively, while the dashed red lines correspond to the ultimate limits that can be achieved through the instrumentation development including resonant-enhanced modes, low-noise beam deflection position systems, and high-stability platforms. Panel (**a**) reproduced with permission from [6]. Copyright 1996, John Wiley & Sons, Inc. Panel (**b**) adapted with permission from [31]. Copyright 2008, Elsevier

and sensory activity that amplifies high-frequency signals [5]. Note that in biological systems, the traditional separation of electromechanical interactions into long-range electrostatic forces and electromechanical piezoelectric and electrostrictive interactions is challenging. For example, the presence of mobile ions will render electrostatic interactions short-ranged and screened at the scale of the corresponding Debye length. Furthermore, the interplay between ionic field motion and specific adsorption gives rise to a broad range of electrocapillary phenomena that can be interpreted differently dependent on the scale of the observation (e.g., local electrostatic interactions and tissue-level piezoelectric coupling). Correspondingly, we aim to keep the discussion general to include all forms of electromechanical coupling in biosystems.

Typical values of electromechanical response for a wide range of functional materials and systems are shown in Fig. 12.1b. Piezoelectricity is the linear coupling in a material between a mechanical strain and an electric polarization (or a redistribution of charge), or, conversely, between an applied field and a mechanical deformation, both more generally referred to as electromechanical coupling, and has been observed in calcified tissues such as bone. This has prompted speculation that piezoelectricity could be partially responsible for biomineralization (the formation and mineralization of bone and dental tissues) and bone remodeling (the process of bone tissue renewal, which depends on the regulation of osteoclast and osteoblast

activity). In fact, a key missing element of understanding mechanotransduction in bone cell regulation is how bone cells sense mechanical stimuli of different magnitudes, direction, and duration [38]. Wolff's law [39] states that bone develops and adapts (self-organizes) to mechanical stresses to produce a structure best-suited to withstand the applied stress. Thus, the direction-dependent piezoelectricity of collagen, which generates an electric potential proportional to an applied stress, is an intriguing mechanism by which osteoclast and osteoblast cells can sense where bone should be resorbed or formed, respectively.

This relation between mechanics and change in potential underscores the importance of being able to measure both electrical and electromechanical interactions in biological systems. The coupling between electrical, mechanical, and chemical signals and responses in molecular and cellular systems necessitates the development of tools capable of measuring the distribution of charged species, surface potentials, and mechanical responses to applied electrical stimuli and vice versa, ultimately under physiological conditions. Atomic force microscopy (AFM) [40] is ideally suited to measure electrostatic and electromechanical interactions owing to the high lateral and force resolution it offers. Below, we discuss the implementation of two complementary voltage-modulated AFM methods, namely, Kelvin probe force microscopy (KPFM) as a method to study electrostatic interactions and piezoresponse force microscopy (PFM) as a method to study electromechanical coupling in biosystems. We emphasize that while for low-resolution ambient and ultra-high vacuum imaging, these techniques can be clearly differentiated (noncontact and contact regimes, respectively), for high-resolution studies achieving molecular and atomic resolution [41] and for studies in liquid environments (no jump-to-contact instability), this separation is somewhat artificial, and both electrostatic and electromechanical interactions must be taken into account to give a full picture of voltage-induced mechanical responses as deduced from the measured signals.

12.1.2 Voltage Modulation SPM for Electrical and Electromechanical Measurements

12.1.2.1 Kelvin Probe Force Microscopy

In this section, the use of electrostatic force microscopy (EFM) and KPFM to measure electric fields and contact potential differences are briefly discussed. These intermittent or noncontact voltage-modulated AFM techniques are widely used scanning probe microscopy (SPM)-based techniques for the determination of electric interactions and electronic structure, including surface potentials, band bending, and surface state densities, especially in inorganic and organic semiconductors and often in ultra-high vacuum. Detailed descriptions of EFM [42, 43] and KPFM [44–46] can be found elsewhere, including this book.

There are several approaches to implementing EFM and KPFM. Often these techniques utilize an approach developed by Terris et al. [42] and Saurenbach et al. [43] which uses a mechanically driven cantilever and a voltage modulation applied to the tip, allowing topographic and electrostatic images to be acquired simultaneously, or in sequential line scans using a lift-height or interleave approach. The key distinctions between the techniques are that in EFM, generally the electrostatic and capacitive forces on the tip are measured as the changes in the dynamic response of a mechanically driven, electrically biased cantilever. In KPFM, the cantilever is driven by periodic ac bias, and a feedback loop is used which minimizes the amplitude of the force on the cantilever (amplitude modulation KPFM) or the force gradient (frequency modulation KPFM [47–49]). In KPFM, the electric potential on the conductive SPM probe is modulated as $V_{\text{tip}} = V_{\text{dc}} + V_{\text{ac}}\cos(\omega t)$, where V_{dc} is the static potential offset, V_{ac} is the driving voltage, and the driving frequency ω is typically chosen close to the free cantilever resonance. The tip bias results in the capacitive tip–surface force, $F_{\text{el}} = C_z'(V_{\text{tip}} - V_s - \Delta\text{CPD})^2$, where C_z' is the (unknown) tip–surface capacitance gradient, V_s is the electrostatic surface potential, and ΔCPD is the contact potential difference between the tip and the surface. Depending on the experimental configuration, the voltage modulation can be applied either during the interleave scan (i.e., when the tip retraces the predetermined surface topography while maintaining constant tip–surface separation), or during the acquisition of topographic information (at a different frequency). A lock-in amplifier is used to select the first harmonic component of the electrostatic force on the tip, $F_{\text{el}}(1\omega) = C_z'V_{\text{ac}}(V_{\text{dc}} - V_s - \Delta\text{CPD})$. In KPFM, a feedback loop is engaged to keep this component zero by adjusting the static offset of the tip potential, V_{dc}. The condition $F_{\text{el}}(1\omega) = 0$ is satisfied when $V_{\text{dc}} = V_s + \Delta\text{CPD}$, i.e., when the microscope-controlled compensation potential is equal to the (unknown) local surface potential. On a (nominally) grounded surface, KPFM allows direct detection of the materials-specific contact potential, containing the contributions from surface dipole layers, non-equilibrium surface charges, etc. The theory of spatial resolution, the effect of topographic inhomogeneities (topographic cross-talk), and the image formation mechanism in KPFM for conductive and semiconductive materials have been studied extensively [50]. The resulting images are of the combined electric and capacitive force on the probe and cantilever in the case of EFM, and the bias which minimizes these forces or force gradients in the case of KPFM. This bias is related to the contact potential difference between the tip material or coating and the sample and the electronic structure of the sample. In solution, this can further be related to the isoelectric point. A schematic for interleave-mode KPFM is shown in Fig. 12.2a. Note that the KPFM signal is controlled by the tip–surface force acting across the tip-sample gap and does not depend on the field inside the material (Fig. 12.2c). Furthermore, for most materials, the mismatch between the dielectric constants of the imaging environment and the material implies that the potential drops significantly in the tip–surface gap. In intermittent-contact KPFM, both electrostatic and electromechanical to the signal contributions are present.

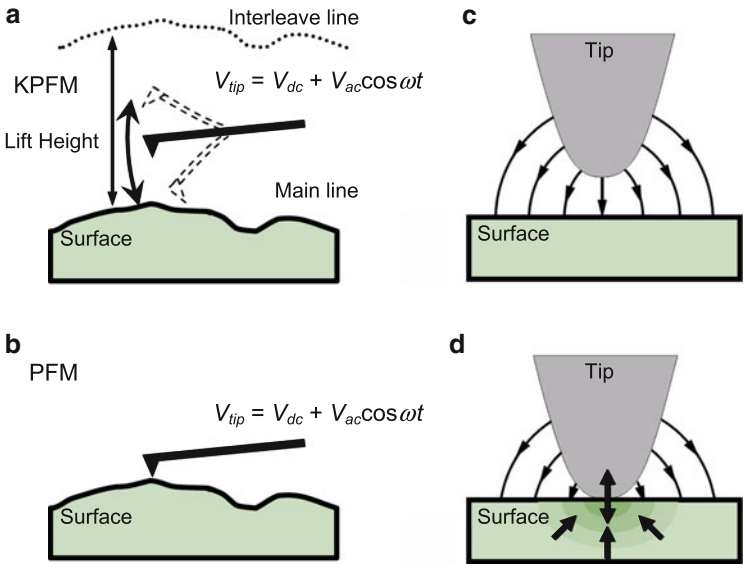

Fig. 12.2 Schematics showing (**a**,**c**) KPFM and (**b**,**d**) PFM imaging principles. (**c**) In KPFM, electrostatic forces act on the tip in the tip–surface gap. (**d**) In PFM, electrostatic and electromechanical (double arrow) forces are present. Strain is indicated in (**d**). (**c**,**d**) Adapted with permission from [51]. Copyright 2006, American Physical Society

12.1.2.2 Piezoresponse Force Microscopy

Piezoresponse force microscopy is a voltage-modulated contact-mode AFM technique. In PFM [52–59], an electrically conductive tip traces surface topography using standard deflection-based feedback, during which time, a sinusoidal electrical bias, $V_{\text{tip}} = V_{\text{dc}} + V_{\text{ac}}\cos(\omega t)$, is applied to the tip. The electromechanical response of the surface, e.g., the local piezoelectrically induced mechanical deformation of the sample due to the applied field, is detected as the first harmonic component of the bias-induced tip deflection, $d_{1\omega}\cos(\omega t + \varphi)$, as shown in Fig. 12.2b. The response amplitude, $d_{1\omega}$, is a measure of the local electromechanical activity of the surface, while the phase of the piezoresponse, φ, provides information on the polarization direction or polar orientation below the tip. In the case of ferroelectric materials, for c^- domains (polarization vector pointing downward) the application of a positive tip bias results in the expansion of the sample and surface oscillations are in phase with the tip voltage, $\varphi = 0$. For c^+ domains, $\varphi = 180°$. In the case of piezoelectric biomaterials, the phase is coupled to polar orientation yielding similar phase responses. The PFM signal is usually plotted as a pair of amplitude-phase, $A = d_{1\omega}/V_{\text{ac}}$, φ, images, or as a mixed piezoresponse (PR) signal, $\text{PR} = A\cos\varphi$. This AFM-based approach for measuring electromechanical response was first

demonstrated by Günther and Dransfeld on thin copolymer films of polyvinylidene fluoride and trifluoroethylene [60].

Both flexural and torsional components of tip displacement can be probed, giving rise to out-of-plane (vertical) and in-plane (lateral) PFM (VPFM and LPFM, respectively). By combining VPFM data with (ideally two orthogonal) LPFM data sets, the data can be represented in a vector form [61], enabling an approach for determining the three-dimensional direction of polarization in, e.g., thin films [62], crystals [63], and ferroelectric capacitors [64].

Note that the operation of PFM is complementary to that of conventional SPMs as shown in Fig. 12.3. For scanning tunneling microscopy (STM), an electrical bias is applied to a metal tip, and the tunneling current is measured, while in the case of AFM, a force is applied, and the resulting tip-deflection is measured. In PFM, an electrical bias is applied to a tip, and the tip deflection resulting from the deformation of the sample surface due to the bias-induced strain is detected. Notably, the surface deformation is dependent only on the potential drop in the material, and is not affected by the tip size. Hence, while both PFM and KPFM use a modulated voltage applied to a conducting cantilevered tip, in one case the mechanical response of material to the applied bias is measured, while in the other, the electric forces are measured or minimized to gain insight into the electronic structure. In principle, both mechanisms can operate at the same time; however, in contact mode where the tip-sample stiffness is high, bias-induced strains dominate, while in noncontact mode, electrostatic forces dominate since the tip-sample stiffness is small. As an example, KPFM can be used on conductive surfaces whereas PFM cannot. Clearly there is the possibility of an overlap, as the applied bias can lead to a mechanical deformation in the case of piezoelectric materials, and electromechanical deformations can lead to redistribution of charge and changes in surface potentials. However, these second-order effects are usually small.

In an ambient environment, the tip interacts with the surface through electrostatic forces and short-range electromechanical interactions and the piezoresponse (PR) signal can be written as a combination of the two interactions,

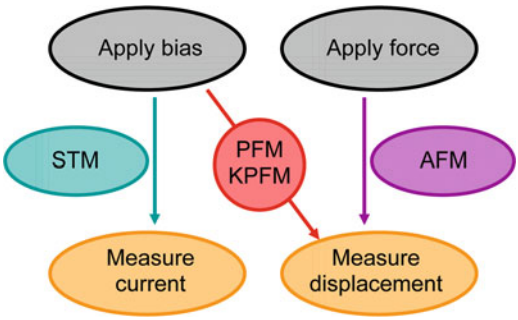

Fig. 12.3 Classification of SPM techniques based on the type of stimulus and response. In PFM and KPFM, a bias is applied to the AFM tip and displacements resulting from electromechanical and electric forces are measured. Adapted with permission from [36]. Copyright 2007, Annual Reviews

PR=PR$_{em}$+PR$_{el}$ [51]. In the low-frequency limit, the electromechanical component is

$$\mathrm{PR}_{\mathrm{em}} = \alpha_a(h)\tilde{d}_{33}\frac{k_1}{k_1 + k}, \tag{12.1}$$

where $\tilde{d}_{33}$ is the effective electromechanical response of material, $\alpha_a(h)$ is the ratio of the ac tip potential to the ac surface potential of the ferroelectric (i.e., the potential drop in the tip–surface gap), k_1 is the spring constant of the tip–surface junction, and k is the spring constant of the cantilever. In ambient or vacuum, the electrostatic forces are long-range, $F_{\mathrm{el}}^{\mathrm{amb}} = (1/2)C_z'(z)(V_t - V_s)^2$, where V_t is the tip potential, V_s is the surface potential, and $C_z'(z)$ is the tip–surface capacitance gradient. The electrostatic contribution is

$$\mathrm{PR}_{\mathrm{el}}^{\mathrm{amb}} = \left(\frac{C'_{\mathrm{sphere}} + C'_{\mathrm{cone}}}{k_1 + k} + \frac{C'_{\mathrm{cant}}}{24\,k}\right)(V_{\mathrm{dc}} - V_s), \tag{12.2}$$

where C'_{sphere}, C'_{cone}, and C'_{cant} are the capacitance gradients due to the spherical and conical parts of the tip and cantilever, respectively. V_{dc} is the dc potential offset of the tip bias, and h is the tip–surface separation. In a sphere-plane model for small separations, $C'_{\mathrm{sphere}}(h) = \pi\epsilon_0 R/h$, where R is the tip radius of curvature. In ambient, $\alpha_a(h) = 1$ for $h < 0$ (contact), i.e., the response is independent of the penetration depth [65], and $\alpha_a(h) << 1$ for $h > 0$ (non-contact). The numerical values of coefficients in (12.2) depend on the mode of cantilever oscillations.

As discussed above, the implementation of both PFM and KPFM relies on the application of a bias to measure electromechanical coupling and electrostatic interactions, respectively. In the case of PFM, the applied ac bias leads to a surface deformation which is detected by the AFM cantilever. In KPFM, the applied ac bias allows electrostatic forces to be measured and minimized through the additional application of a dc offset. The image formation mechanisms are the effects of the combined electric, capacitive, and electromechanical forces on the probe and cantilever in the case of KPFM and PFM, with long-range forces dominating the signal for KPFM, whereas short-range forces dominate for contact-mode PFM. An example of simultaneously acquired PFM and KPFM of model ferroelectric systems are shown in Fig. 12.4 [66]. Note that in ambient, PFM yields higher resolution than KPFM since it measures strong contact forces and not long-range electrostatic forces. Often, PFM and KPFM contrast can be related (e.g., for ferroelectric domain structures [Fig. 12.4]); however, in other cases they can differ significantly.

12.2 KPFM of Biosystems

In this section, the measurements of electrostatic interactions in biological systems are explored. The applications of KPFM to measure surface potentials at the single molecular to the assembled lipid bilayer and protein membrane level are discussed.

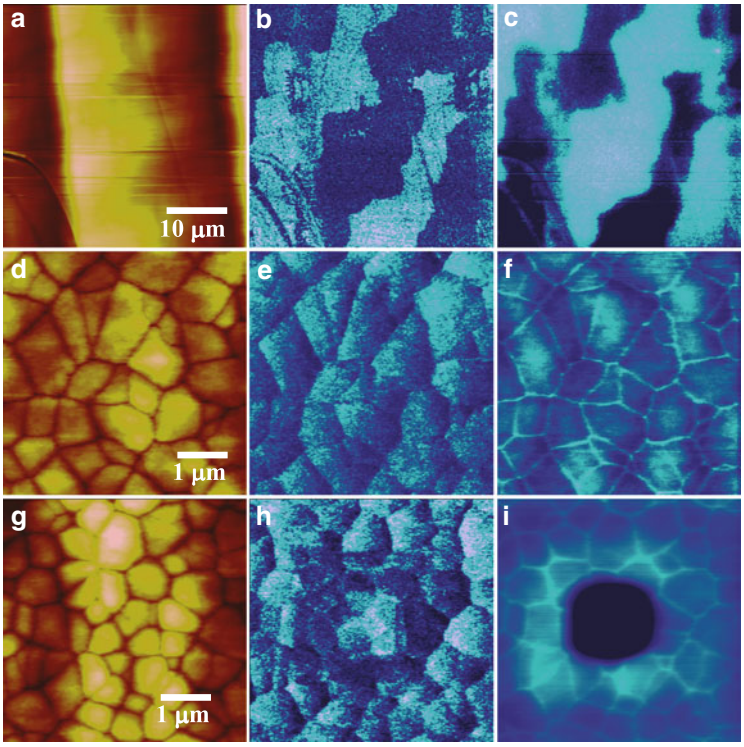

Fig. 12.4 (**a**,**d**,**g**) Surface topography, (**b**,**e**,**h**) piezoresponse, and (**c**,**f**,**i**) KPFM images of a $BaTiO_3$ (100) crystal surface (**a**–**c**) and $Pb(ZrTi)O_3$ film (**d**–**i**), respectively. Panels **g**–**i** have been acquired after the application of 10 V during a $2.5 \times 2.5\ \mu m^2$ scan and −10 V during a $1 \times 1\ \mu m^2$ scan. Reproduced with permission from [66]. Copyright 2002, American Physical Society

12.2.1 Organic Molecules

Surface potential measurements have been performed on a variety of molecular surfaces including self-assembled monolayers [67–72], Langmuir–Blodgett films [73–77], organic ferroelectric oligomers [78], and organic nanostructures [79, 80]. KPFM has been used extensively to measure electronic structure of organic molecules films and structures, and thorough reviews can be found in [81, 82] and in Chap. 11 of this book.

12.2.2 Biomolecular Systems

As discussed in Sect. 12.1, charge and surface potentials play an active role in both biological structure and function. The measurement of these interactions in cellular

biology has been primarily membrane-based, using voltage-sensitive dyes, and fluorescence and patch/voltage clamp techniques [83–89]. Recently, encapsulated voltage dyes have been used to map the electric field within a cell [20], and voltage/patch clamp techniques have been extended to subcellular structures with a smart patch-clamp system [90]. For proteins, scanning Kelvin probe [91–93] and nanoprobe [94–97] have been used by several groups to measure surface potentials of dispersed proteins and microarrays on scales ranging from $\sim$ 1 cm to 100s of nm. In order to extend this technique to the nanoscale, as a precondition to resolve single molecules and charged groups within molecules or charged domains in membranes, a nanoscale local probe is required. An early attempt at measuring electrostatics in biosystems with an etched tungsten wire tip was made by Leng and Williams [99]. In this section, the uses of KPFM to measure biomolecular surface potentials in static and dynamic systems are discussed.

12.2.2.1 KPFM of Static Systems

Several attempts have been made to image electrostatic interactions and surface potential of biosystems using SPM (see [98] for a review). The charged backbone and necessity of fast sequencing has made DNA a popular target of KPFM measurements. Gil et al. deposited gold electrodes on DNA-coated mica and used KPFM to investigate the conductivity of DNA [100]. By applying bias to the electrodes, and measuring KPFM of DNA connected to an electrode it was determined that λ-DNA is not conductive.

Kwak et al. used a molecular combing method based on silane-modified Si substrates and the hydrodynamic force of a receding meniscus (i.e., self-orientation effect when the substrate is removed from solution) to prepare stretched single DNA molecules for KPFM measurements [101]. The contact potential difference of the sample was measured against a chemically hexadecanethiol-modified conducting AFM tip. The topography of the stretched DNA is shown in Fig. 12.5a. In Figs.

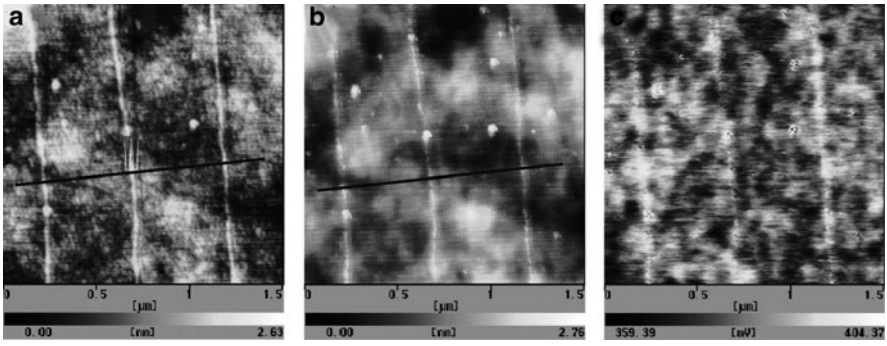

Fig. 12.5 (**a**) Topographic image and simultaneously obtained (**b**) topographic and (**c**) KPFM images. Reproduced with permission from [101]. Copyright 2003, Elsevier

12.5b and c, the simultaneously measured topography and KPFM images of the same region are shown. All images were measured at 48.9% relative humidity. Variations in Fig. 12.5c can be due to the mixed monolayer of NH_2^- and CH_2=CH-terminated silanes. The stretched DNA strands can be seen to have a higher contact potential difference than the surrounding surface, suggesting that dipole moments formed between the surface water layer and the negatively charged DNA backbones point away from the substrate.

Mikamo-Satoh et al. reported a modified EFM study of DNA strands containing T7 RNA polymerase, which binds at a specific location on the DNA to synthesize mRNA [102]. The topography and potential images are shown in Figs. 12.6a and b, respectively. The electric potential image (Fig. 12.6b) shows dark contrast for both DNA and the polymerase transcription complex corresponding to low electric potential. Despite having different heights, the potentials for the transcription complex and tangled DNA are similar (~ -0.37 V), while the potential for isolated DNA is ~ -0.48 V as shown in the line profiles in Figs. 12.6c and d, indicating that the accumulation of DNA on the surface induces a local potential increase. Analysis of the results indicate as before an upward pointing electric dipole at the DNA due to distortion arising from a collapsed coaxial structure and partial ionization of phosphate groups with the surface water layer.

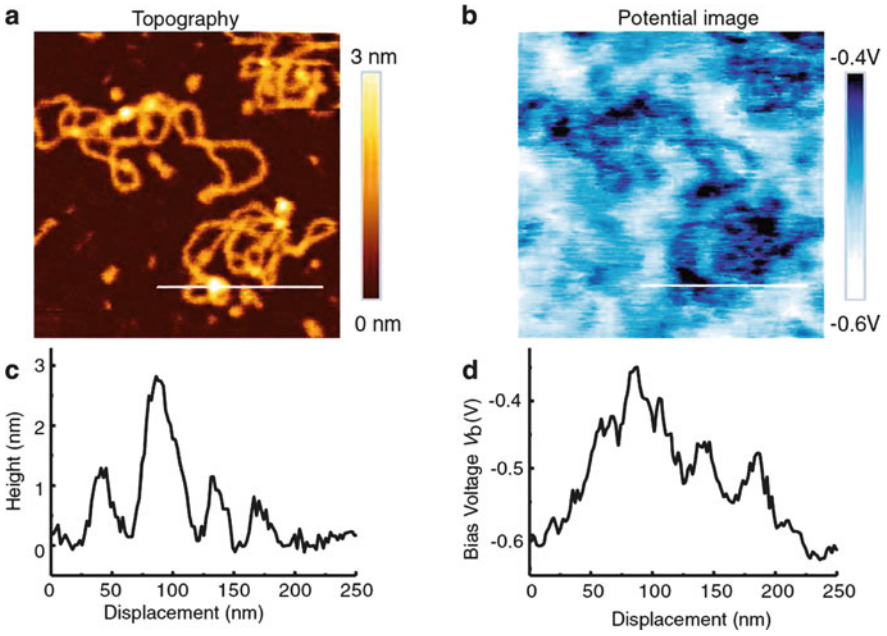

Fig. 12.6 (**a**) Topography and (**b**) electric potential images of DNA and transcription complexes of DNA. (**c**) Section profile of the topography showing 1.4 and 2.8 nm heights of DNA and transcription complex, respectively. (**d**) Section profile of the potential showing potential values of -0.45 V, -0.35 V, and -0.6 V for DNA, transcription complex, and mica, respectively. Reproduced with permission from [102]. Copyright 2009, Institute of Physics

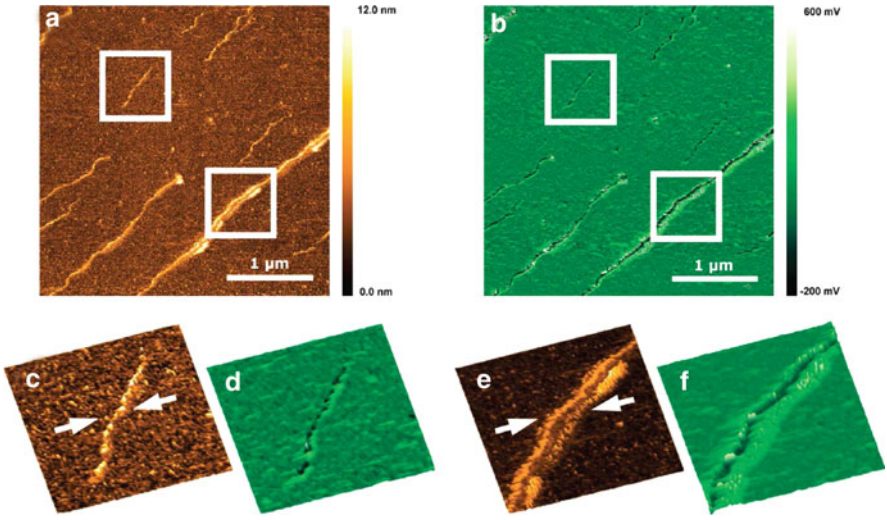

Fig. 12.7 (**a**) Topography image of single and multiple DNA strands on a silicon surface. (**b**) Corresponding KPFM scan of the same area showing a more negative potential for the DNA strands than the substrate. Regions of the (**c**,**e**) topography and (**d**,**f**) KPFM scans showing (**c**,**d**) single and (**e**,**f**) multiple DNA strands. Reproduced with permission from [103]. Copyright 2009, American Chemical Society

KPFM of DNA molecules and counterions have been reported recently by Leung et al. [103, 104] using a dual frequency mode. In Fig. 12.7a, the height image shows single and multiple DNA strands. The corresponding KPFM image (Fig. 12.7b) shows that the DNA is always at a more negative potential than the substrate. Upon closer inspection of single (Figs. 12.7c and d) and multiple (Figs. 12.7e and f) DNA strands, it is apparent that there is a slight increase in positive potential at the edges of the DNA. The authors attribute this to the presence of buffer salt deposits which have dried adjacent to the DNA. A shell of positively charged counterions gives DNA its stability. The multiple DNA strands have a more negative measured surface potential, and the associated counterions have a higher positive potential than those for a single DNA strand.

Note that KPFM of biological systems can be strongly affected by surface topography irregularities that can provide a discernible contrast even on a chemically uniform surface. An example of this topographic cross-talk on an as-deposited gold surface was reported by Efimov and Cohen [105]. Recent studies of the cross-talk effect are reported in Chap. 4. The practical consequence of the presence of cross-talk is that the cross-talk should be taken into account in the interpretation of KPFM data.

KPFM can be applied to any biomolecule which has charge or dipole moment. Another example of KPFM measurements of charged biomolecules was reported by Leung et al. [103]. In Fig. 12.8a, the topography image of avidin molecules adsorbed on silicon is shown. From the KPFM image (Fig. 12.8b) it is apparent that

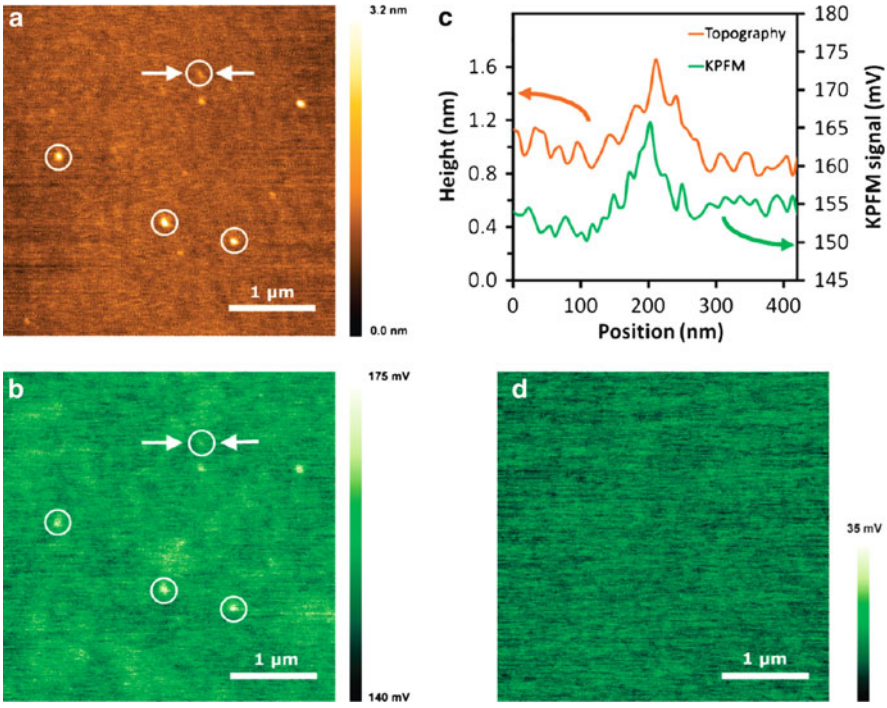

Fig. 12.8 (**a**) Topography and (**b**) KPFM images of avidin molecules (*circled*) deposited on a silicon substrate (**c**) Line profiles of the avidin molecule at the location indicated by arrows in (**b**). (**d**) KPFM image of a bare silicon substrate. Reproduced with permission from [103]. Copyright 2009, American Chemical Society

these avidin molecules have a positive surface potential 10–15 mV higher than the substrate. This is further illustrated via line profiles of the topography and KPFM signal across an avidin molecule (Fig. 12.8c). In the absence of avidin molecules, no such surface potential variation can be seen (Fig. 12.8d). This observation supports the attribution of the signal in Fig. 12.8b to intrinsic surface potential variations rather than cross-talk.

Another example of KPFM applied to the characterization of surface potentials of biomolecules is the study of human plasma fibrinogen deposited on highly ordered pyrolytic graphite (HOPG) presented by Ohta et al. [106] and shown in Fig. 12.9. Typical examples of topographic images of single fibrinogen molecules and fibrinogen fibrils of singe molecule widths are shown in Figs. 12.9a and b, respectively. KPFM images of the surface potential of isolated or aggregated fibrinogen molecules are shown in Fig. 12.9c. In Fig. 12.9d, KPFM of fibrinogen aggregated into fibers are shown, which demonstrate a periodic surface potential dependence, indicated by arrows, corresponding to the different polypeptide domains present in fibrinogen.

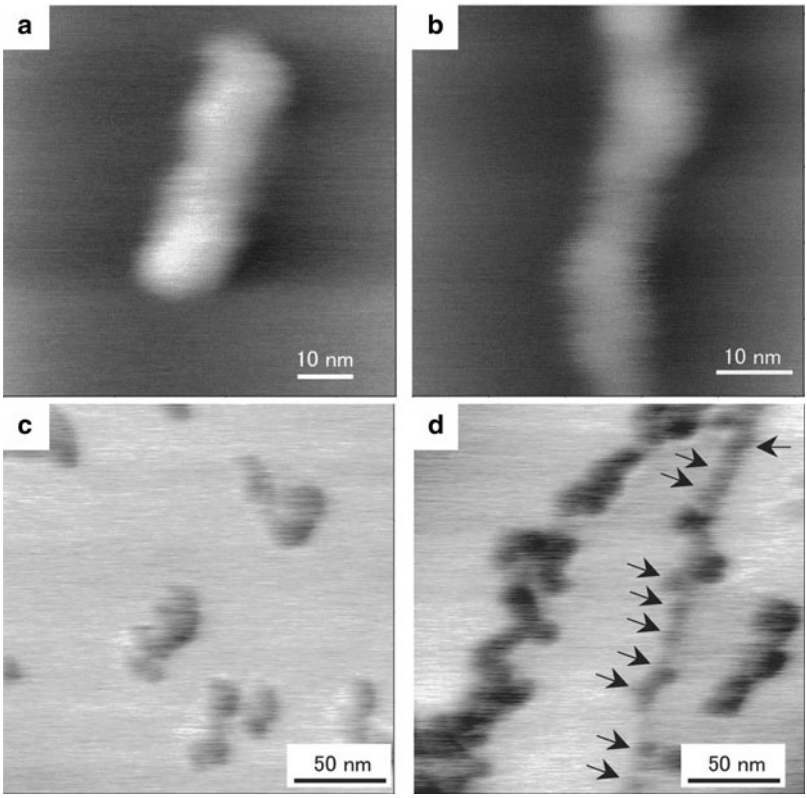

Fig. 12.9 (**a**,**b**) Topography images of a single fibrinogen molecule and a single-molecule wide fibrinogen fibril. (**c**) KPFM image of isolated and aggregated fibrinogen molecules adsorbed on a HOPG substrate. (**d**) KPFM image of fibrinogen aggregates composed of fibers. Reproduced with permission from [106]. Copyright 2006, Elsevier

The group of Gomila has made several significant contributions to electrical-based characterization of supported biomembranes using non-contact dual-pass approaches to measure dielectric constants [107, 108]. In one approach, based on nanoscale capacitance microscopy [109], the topography is measured in the first pass in a standard dynamic mode and the height is retraced in the second pass at a constant-height to measure the variation in local capacitance. The dielectric constant can then be determined from the capacitance and scan height[107]. In other words, the second harmonic of the force on the tip is a measure of the dielectric constant. In the second approach [108], standard DC EFM is used with an appropriate analytical model to determine the dielectric constant with knowledge of the applied bias, the bias-induced deflection, and the lift-height. Both approaches have been demonstrated on purple membrane fragments and the obtained values for the dielectric constant are in good agreement (Fig. 12.10).

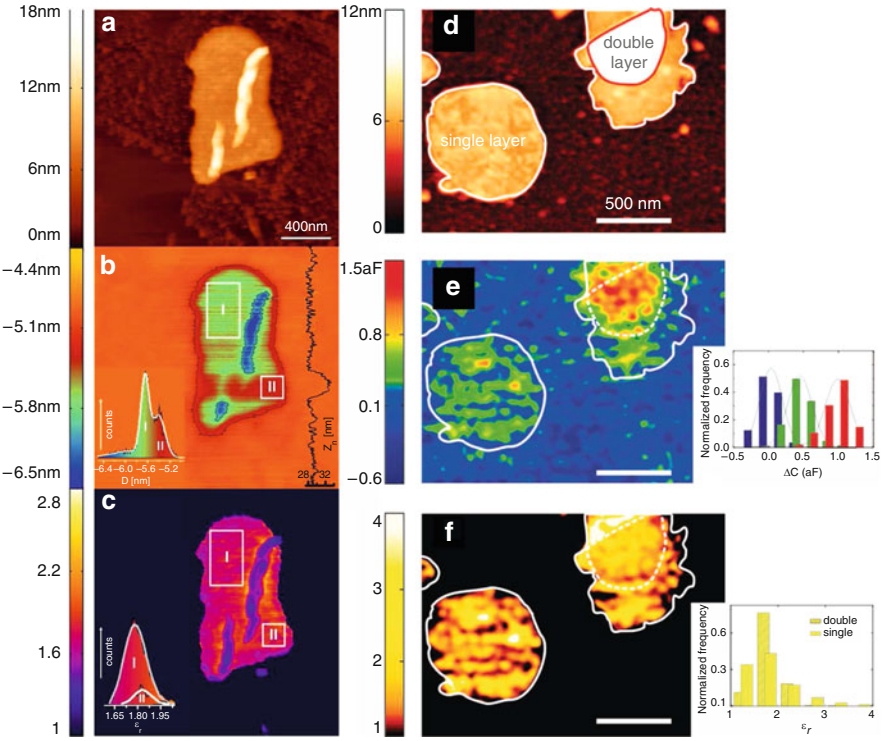

Fig. 12.10 Dielectric constant measurements on single and double layer purple membranes using (**a**–**c**) DC EFM and (**d**–**f**) nanoscale capacitance approaches. (**a**) Topography, (**b**) DC EFM cantilever deflection, and (**c**) the extracted dielectric constant of a single layer patch. Histograms in (**b**,**c**) show the distribution of the cantilever deflection and the dielectric constant on the purple membrane, respectively. (**d**) Topography, (**e**) local capacitance, and the extracted dielectric constant of single and double layer purple membranes. (**a**–**c**) Reproduced with permission from [108]. Copyright 2009, Institute of Physics. (**d**–**f**) Reproduced with permission from [107]. Copyright 2009, American Chemical Society

12.2.2.2 KPFM of Dynamic Chemical Phenomena

While static KPFM images measured on uneven surfaces can always contain cross-talk, observation of dynamic changes of potential that leave the topography invariant are generally much more reliable. The examples of such studies include polarization switching in ferroelectric materials [110] and photo-induced phenomena in semiconductors [49, 111, 112]. Similarly, the potential of KPFM extends beyond the imaging of static biomolecules – it can also be applied to detect changes in surface potential as a result of specific chemical or optical events, as will be discussed now. Sinensky and Belcher used a combination of dip pen lithography and KPFM to extend the Kelvin probe measurements for microassays to the nanoscale [113]. In this manner, local changes in charge densities due to the formation of specific

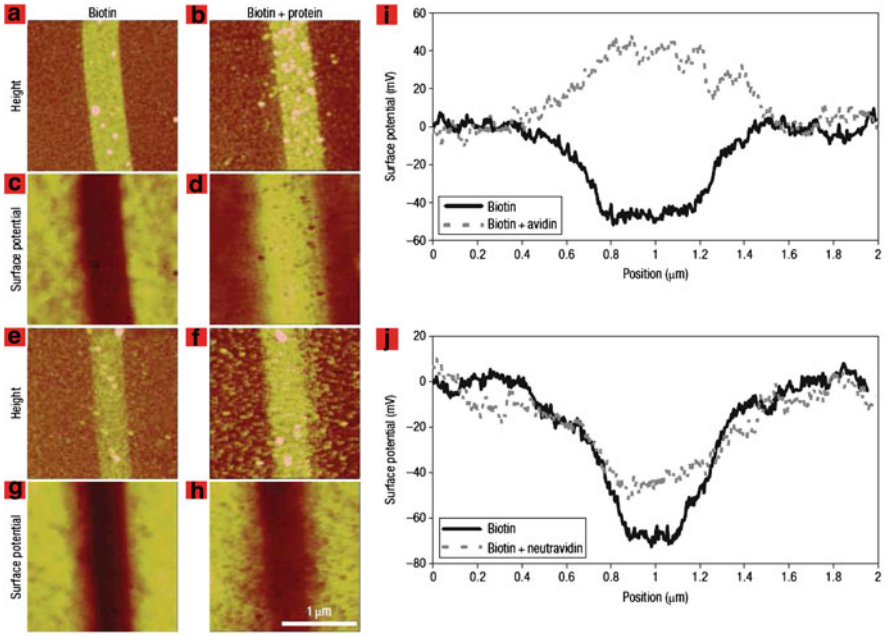

Fig. 12.11 (**a**–**d**) Topography and KPFM images of the patterned biotin sample before and after exposure to avidin. (**e**–**h**) Topographic and KPFM images of the immobilized biotin sample before and after exposure to neutravidin. (**i**), (**j**) Line profiles of the surface potential. Reproduced with permission from [113]. Copyright 2007, Nature Publishing Group

biomolecular complexes (the presence of specific bound target biomolecules) can be identified without labeling or special chemistries. They looked specifically at avidin-biotin binding and DNA probes.

The effect of binding of avidin and neutravidin with surface- immobilized biotin on surface potential is illustrated in Fig. 12.11. The topography and KPFM images of a surface patterned with biotin are shown in Figs. 12.11a and c, while the changes in topography and surface potential after the binding of avidin are shown in Figs. 12.11b and d. Comparing the KPFM images before and after the binding, it is clear that the addition of avidin causes the surface potential of the biomolecular region to invert with respect to the background. The topographic and surface potential images of the sample before and after neutravidin exposure are shown in Figs. 12.11e and h. In this case, the potential does not appear to have been affected significantly by the addition of neutravidin. These differences are further illustrated in Figs. 12.11i and f which show cross sections of the potential images. The presence of the charged avidin molecule (see Fig. 12.8) is detectible by KPFM.

In another example of using KPFM to measure changes in surface potential due to the formation of specific biomolecular complexes, Sinensky and Belcher used patterned DNA probe strands taken from anthrax and exposed the DNA to

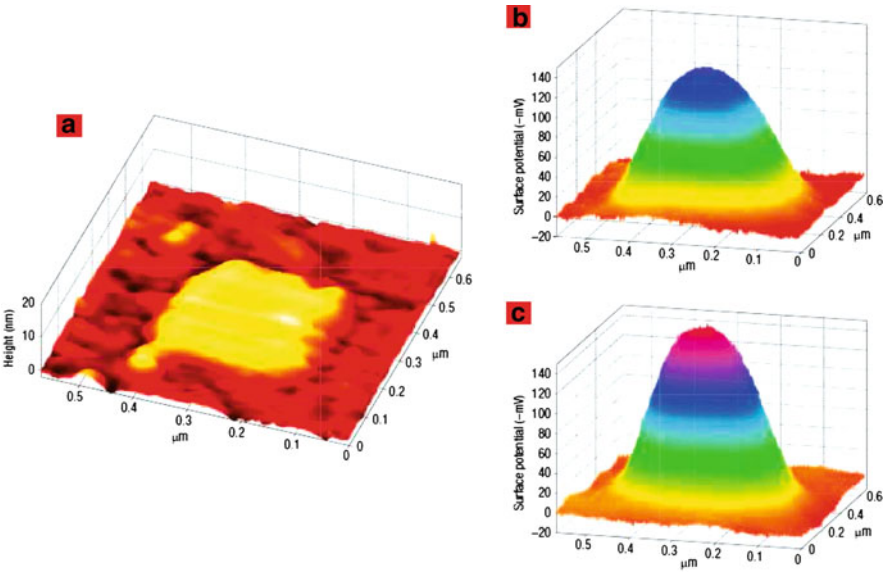

Fig. 12.12 (**a**) Topography image of a dip pen lithography-patterned anthrax DNA probe. (**b**) and (**c**) KPFM images before and after exposure to the complementary anthrax DNA sequence, respectively. Reproduced with permission from [113]. Copyright 2007, Nature Publishing Group

complementary and noncomplementary DNA targets [113]. When a micron-sized anthrax probe is exposed to its complementary target, the surface potential doubles, but when the anthrax probe is exposed to a noncomplementary malaria target no change in surface potential is observed. The same result is observed with a malaria DNA probe; only the complementary target leads to a surface potential doubling. In Fig. 12.12, KPFM results are shown before and after DNA hybridization for a submicron anthrax probe. In this case, surface potential doubling is not observed most likely resulting from the reduced concentrations for small features [113]. Note that the negative surface potential of DNA has been corroborated by other studies [103]. The authors further explored the scan rate and height dependence on the KPFM signal, noting the measurements must be performed close (10s of nm) to the sample surface to achieve high sensitivity and resolution, while the scan rate could be increased from 1 μm/s to 1,172 μm/s and still resolve micron-sized features, demonstrating the potential for nanoarray analysis by KPFM.

Gao and Cai have taken this approach one step further by demonstrating the potential of KPFM as a tool to detect interactions between DNA and proteins [114]. They used an AFM nanolithography approach to create protein patterns of lysozyme. When the lysozyme is incubated with an anti-lysozyme aptamer, the aptamer binds to the edge of the lysozyme, but when incubated with a randomly generated DNA strand, there is no binding to the lysozyme. KPFM was used to study this aptamer–lysozyme binding using a high aspect ratio Ag_2Ga needle tip.

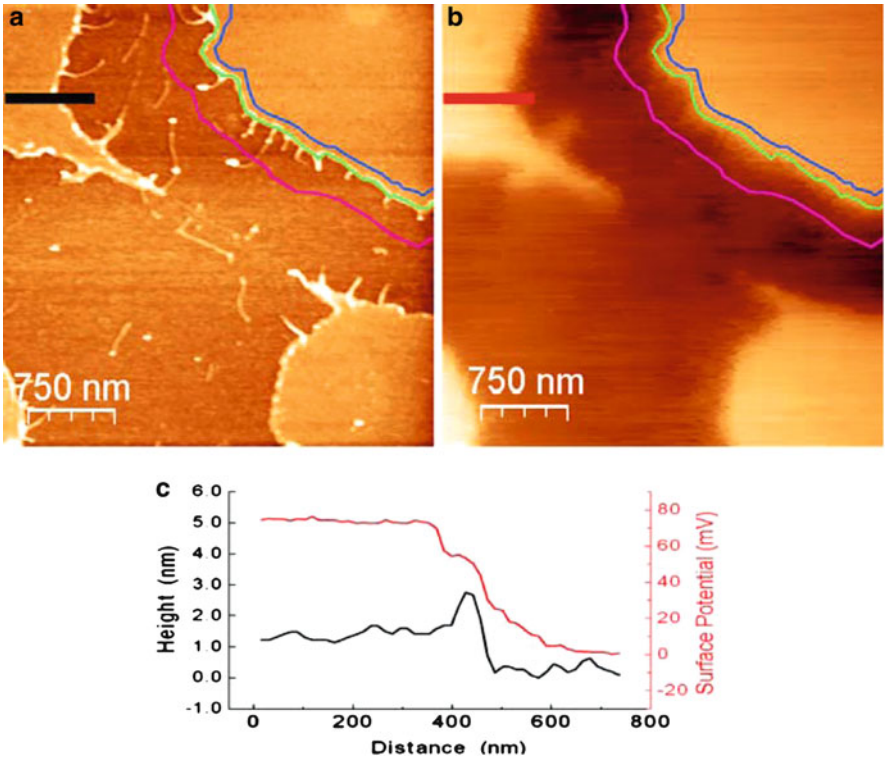

Fig. 12.13 (**a**) Topography and (**b**) surface potential images of the lysozyme pattern after incubation with aptamers. (**c**) Line profiles of the topography and surface potential across the aptamer-lysozyme complex. Reproduced with permission from [114]. Copyright 2009, Springer

Topography and KPFM images of the aptamer-incubated lysozyme patterns are shown in Fig. 12.13. As demonstrated by the line profiles of the topography and KPFM images (Fig. 12.13c), the peak in the topography due to the aptamer–lysozyme complex corresponds to a step in the surface potential. The surface potential of the complex is lower than that of the lysozyme itself and higher than that of the substrate. The authors state that this step was not visible using conventional KPFM tips. Analysis of the surface potentials reveals a 12 mV difference between the lysozyme and the aptamer–lysozyme complex. Richards et al. used KPFM to characterize the functionalization of GaP(100) surfaces with linker molecules and single strand and complementary DNA [200]. They showed a certain tunability in the modification of the surface potential of the GaP surface by varying the initial concentration of the linker molecule.

12.2.2.3 KPFM of Light-Induced Phenomena

KPFM has also been extended to detect changes in surface potential as a result of illumination in optically active proteins and protein membranes. Lee et al.

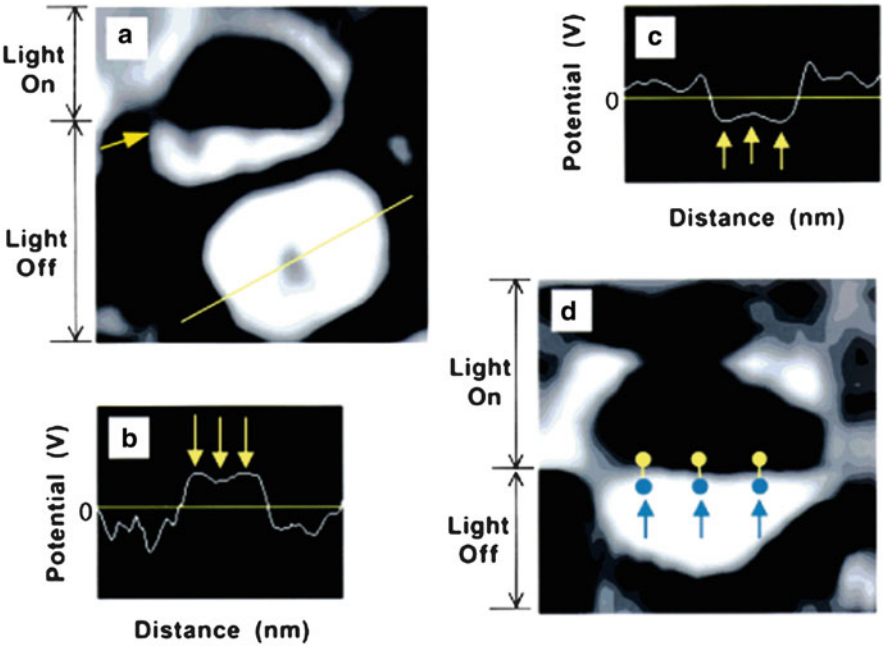

Fig. 12.14 (**a**) KPFM image of two photosynthetic reaction centers. (**b**,**c**) Dark and illuminated voltage-distance profiles, respectively, along the indicated line in (**a**). In (**d**) the illumination is turned off mid-scan during the acquisition of the KPFM image of a single reaction center. Reproduced with permission from [115]. Copyright 2000, American Chemical Society

demonstrated the potential of KPFM for the measurement of photovoltages generated from single photosynthetic reaction centers on an organosulfur molecular layer coated, gold coated mica substrate as a function of illumination [115]. They report a reversal of the potential from positive to negative upon illumination while the topography remains unchanged. KPFM images of a photosynthetic reaction center are shown in Fig. 12.14. In Fig. 12.14a the lower reaction center was imaged in a dark state. Line profiles for this reaction center are shown in Figs. 12.14b and c in darkness and under illumination, respectively, showing the potential reversal. In Fig. 12.14d, a single reaction center is shown which is imaged partially under illumination. Frolov et al. extended this approach by demonstrating that a photoelectronic device could be fabricated by direct binding of a reaction center onto a metallic substrate without the need for a surfactant and without losing the capacity to generate a photovoltage [116]. The group of Lee has also used KPFM to investigate reaction center proteoliposomes [117], the air-liquid interface of liquid containing proteoliposomes [118], and bacterial spores [119].

Bacteriorhodopsin, the light-driven protein pump in the purple membrane of *Halobacterium salinarium* has also been investigated by KPFM [120, 121]. Knapp et al. reported KPFM of the purple membrane on mica and HOPG substrates [120].

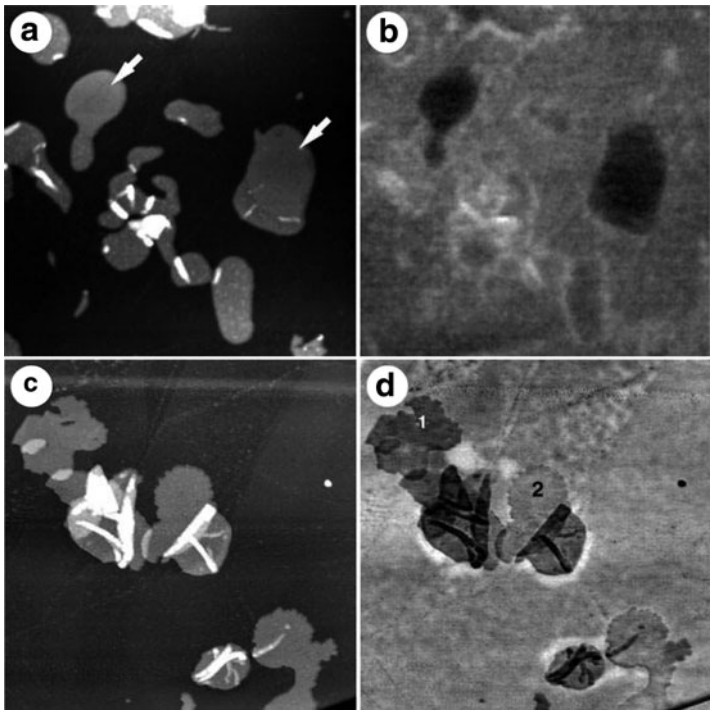

Fig. 12.15 (**a**) Topography and (**b**) surface potential of purple membrane imaged on mica at 64% relative humidity (5.5 μm × 5.5 μm). (**c**) Topography and (**d**) surface potential of purple membrane imaged on HOPG at 41% relative humidity (5.3 μm × 5.3 μm). Reproduced with permission from [120]. Copyright 2002, John Wiley & Sons, Inc

Topography and surface potential images of purple membrane are shown in Fig. 12.15 for mica (Fig. 12.15a, b) and HOPG (Fig. 12.15c, d). They found the surface potential of the extracellular side of the purple membrane to be more negative than the cytoplasmic side. Knapp et al. also measured the patch voltage of representative patches relative to the HOPG background as a function of illumination, reporting that the extracellular patch surface potential increased by 3–5 mV while the cytoplasmic patch potential decreased by 3–5 mV under illumination. Lee et al. measured surface potentials of the extracellular side of wild type and mutant bacteriorhodopsin membranes at a relative humidity of 65–70% as a function of illumination and buffer solution pH, reporting photoinduced surface potentials of 63 mV and 37 mV for the mutant and wild types, respectively, at pH 10.5 and 48 mV and $\sim$ 0 mV at pH 7 [121].

While surveying the use of KPFM for the characterization of biological systems, we have explored KPFM to look at single molecules, proteins, biomolecular complexes, and most recently patches of membrane protein. Beyond these systems, KPFM has been used to study surface potential mapping in lipid bilayer systems

[122, 123, 125] the primary component of cellular membranes. Leonenko et al. have used KPFM to study the mixed lipid protein pulmonary surfactant that assembles at the air-lung interface [122]. The surface potential at this interface may have relevance to the interaction between airborne particles and surfaces of the lung. Topography and surface potential images of pulmonary surfactant deposited on a mica substrate are shown in Fig. 12.16. Figures 12.16a and b, and are measured without added cholesterol, while Figs. 12.16c–f are surfactant films with 5% cholesterol (by weight). The observed contrast in Fig. 12.15b is explained in terms of the arrangement of stacks of lipid bilayers and their associated dipoles. The monolayer regions are dark ($\sim -0.6\,\mathrm{V}$) and relatively uniform, while the topographic features are generally less negative. In contrast, for the surfactant-containing cholesterol, the monolayer region appears to show some segregation into domains of different surface potential. It is suggested that a similar effect could be involved in sphingolipid-cholesterol rafts of the plasma membrane. The effect of cholesterol and surfactant protein C on surfactant assembly and surface potential is studied in more detail in [123, 124] and [125], respectively [201]. Recently, the group has explored the differences between different KPFM techniques for characterizing the surface potentials of biomolecular films [200].

12.3 PFM of Biosystems

12.3.1 Historical Background

Many biological materials are piezoelectric due to the combination of polar bonds and optical activity inherent to all biopolymers. Electromechanical properties (triboelectricity) ascribed to piezoelectric properties were first demonstrated in biological materials in 1941 [126], and subsequently, the piezoelectric effect was identified in a wide variety of biomaterials including bone, tendon, skin, tooth dentin, blood vessel walls, myosin, actin, amylose, chitin, fibrin, wood cellulose, and DNA [127–131]. The first published report on piezoelectricity in bone in 1957 by Fukada and Yasuda [132] sparked intense research on bone piezoelectricity [133, 134], and it was speculated that piezoelectricity could be responsible for the formation and regeneration of calcified tissues [135, 136]. The organizational complexity of bone [137] and limitations in characterization had sidelined this area of investigation (e.g., the symmetry of piezoelectric response could not be determined absolutely, and minute changes in sample preparation yielded changes in the measured coupling constants) until the advent of AFM-based techniques for electromechanical measurements.

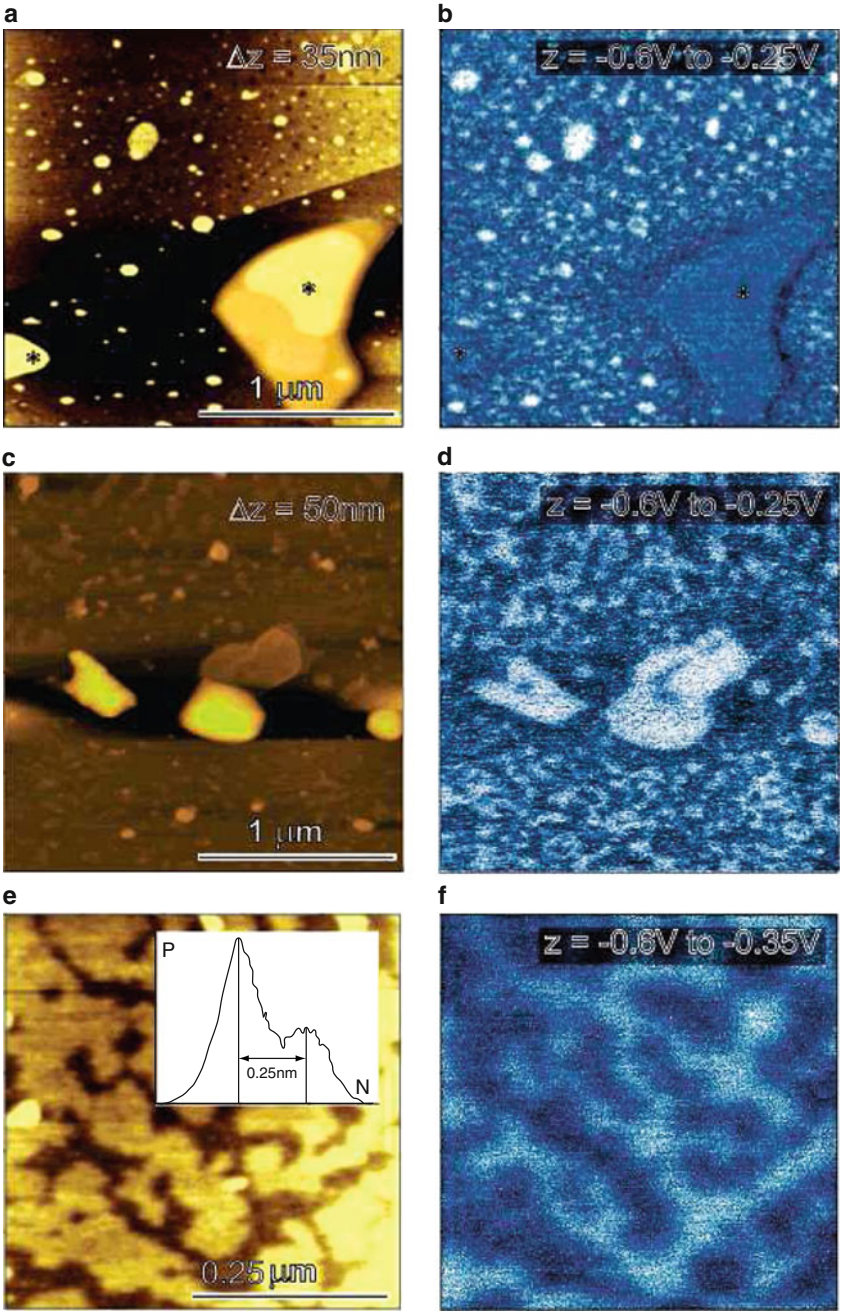

Fig. 12.16 (**a**), (**b**) Topography and surface potential images, respectively, of pulmonary surfactant with 0% cholesterol. (**c**), (**e**) Topography and (**d**), (**f**) surface potential images of pulmonary surfactant with 5% cholesterol. Reproduced with permission from [122]. Copyright 2006, American Chemical Society

12.3.2 PFM of Collagen

In order to understand bioelectromechanics on the nanoscale and to relate piezoelectricity to biological functionality, a nanoscale probe of local piezoelectricity is needed. With recent advances in SPM, it has become possible to investigate piezoelectricity in biological materials at the micro- to nanoscale, and subsequently, piezoelectricity has been measured in a wide variety of calcified and non-calcified connective tissues [138–145]. Recent reports have shown piezoelectricity from single, isolated collagen fibrils [146, 147].

The first nanoelectromechanical measurements of biomaterials were reported by Halperin et al. [138]. They reported piezoelectric values of wet and dry cortical bone and imaged the variation in the response near a Haversian canal (Fig. 12.17). The next advancement came in a series of papers from Kalinin et al., Gruverman et al., and Rodriguez et al. [139–142] where piezoelectric properties of a variety of biosystems including tooth dentin, embedded proteins in enamel, butterfly wing scales, and purified collagen were reported (see [148] for a review).

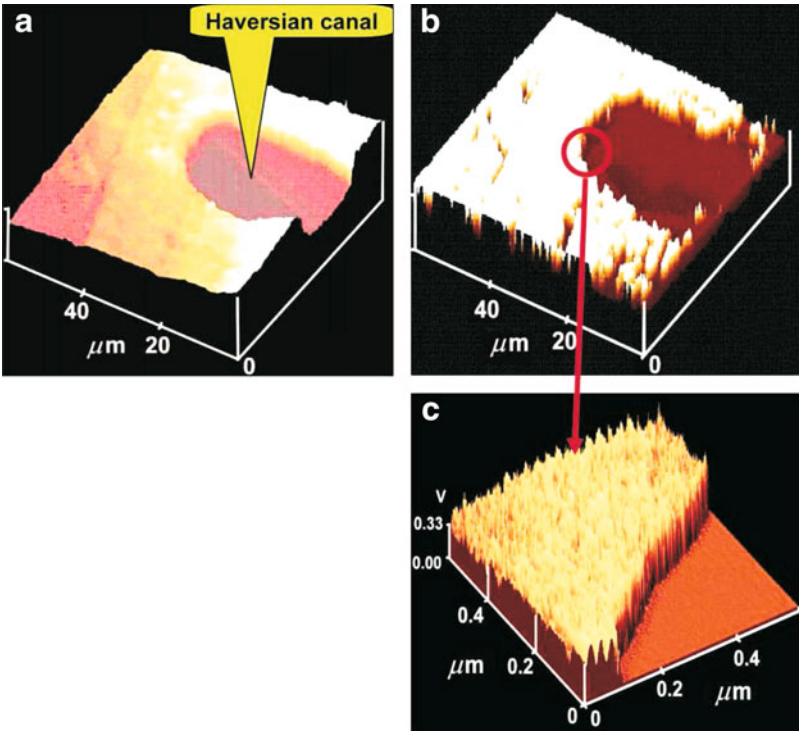

Fig. 12.17 (**a**) Topography image and (**b**) and (**c**) piezoresponse images of mature human cortical bone near the Haversian canal. Reproduced with permission from [138]. Copyright 2004, American Chemical Society

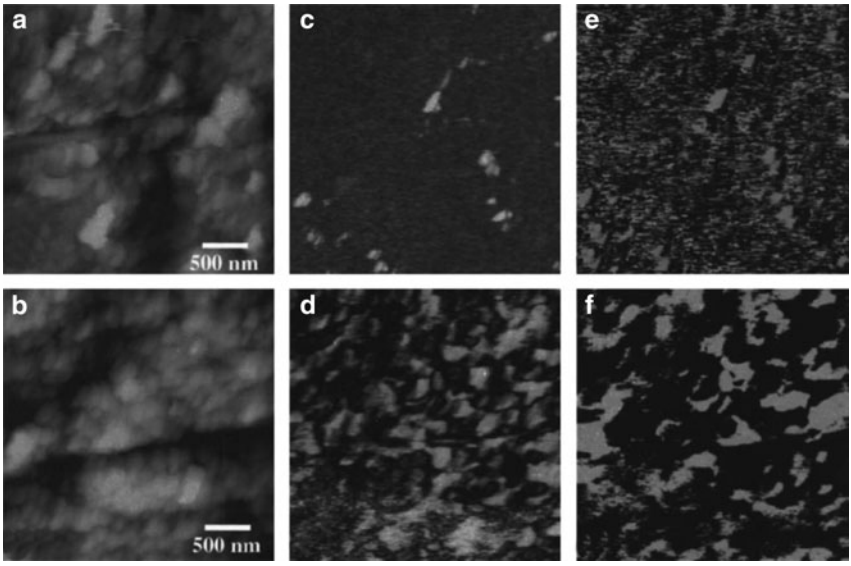

Fig. 12.18 (**a**), (**b**) Topographic and (**c**), (**d**) PFM amplitude and (**e**), (**f**) phase images of human tooth (**a**), (**c**), (**e**) enamel and (**b**), (**d**), (**f**) dentin. Reproduced with permission from [139]. Copyright 2005, American Institute of Physics

The piezoelectric activity in dentin was attributed to the collagen, while that of butterfly wing scales to the protein chitin. Topographic and PFM amplitude and phase images of human tooth enamel and dentin are shown in Fig. 12.18. Recall that the PFM amplitude image provides information on the local piezoelectric activity, while the PFM phase image reveals the orientation of the underlying piezoelectric components. Only isolated response is obtained from the enamel, while analysis of the dentin reveals regions with nearly uniform response having different orientations. As both enamel and dentin contain a hard mineral and a soft protein phase, and the protein content in dentin is much higher than that in enamel, the more uniform response observed in the dentin is attributed to the protein content, primarily type I collagen.

To verify this, Gruverman et al. investigated piezoelectricity in tooth dentin in more detail, using etching to remove the surface mineral component and subsequent bleaching to reveal collagen fibrils [143]. The piezoresponse can clearly be seen to depend on the collagen fibril orientation (Fig. 12.19).

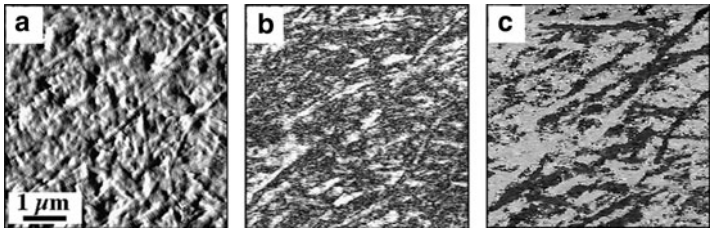

Fig. 12.19 (**a**) AFM deflection image of an etched and bleached dentin surface. (**b**) PFM amplitude and (**c**) phase images of the same dentin surface. Reproduced with permission from [143]. Copyright 2007, Elsevier

Subsequently, Habelitz et al. used PFM to address whether collagen is present in peritubular dentin [144]. Using a combination of VPFM and LPFM and sagittal and oclussal cross sections of tooth dentin, they show a lack of piezoelectricity from peritubular dentin which they attribute to an absence of collagen in the region surrounding the dentin tubules.

These studies focused primarily on piezoelectricity in dental tissues. Recently, Minary-Jolandan and Yu extended PFM to the single collagen fibril [146, 147]. Shown in Figs. 12.20a and b are lateral PFM phase images of a type I collagen fibril. The fibril in Fig. 12.20b has been physically rotated by 180° with respect to Fig. 12.20a and the PFM phase signal has changed accordingly. Figures 12.21a and c show topographic images of a single collagen fibril. The corresponding lateral PFM amplitude images are shown in Figs. 12.21b and d showing apparent intrinsic piezoelectric heterogeneity within a collagen fibril which coincides with the gap and overlap periodicity.

Harnagea et al. analyzed the lateral and vertical response from a fibril in detail, confirming the expected shear piezoelectricity in collagen fibrils, and attributing vertical signal to cantilever buckling [149]. Piezoelectricity in fibrils of type I collagen has been attributed to the hexagonal packing of collagen monomers in a fibrillar structure with periodicity arising from the stacking of the monomers; however, it should be noted that collagen in non-fibrillar form also exhibits piezoelectricity [142]. In Fig. 12.22, PFM images of purified type I collagen in non-fibrillar form deposited on a platinized silicon substrate are shown.

12.3.3 PFM of Other Biosystems

The use of PFM to investigate electromechanical coupling in biosystems has not been limited to biopolymers such as collagen, but has also been applied to systems such as tobacco mosaic viruses (TMVs) [150]. The observed PFM contrast of TMVs was analyzed in terms of topographic crosstalk, differences in elastic properties, and the intrinsic electromechanical coupling due to the piezoelectric and flexoelectric

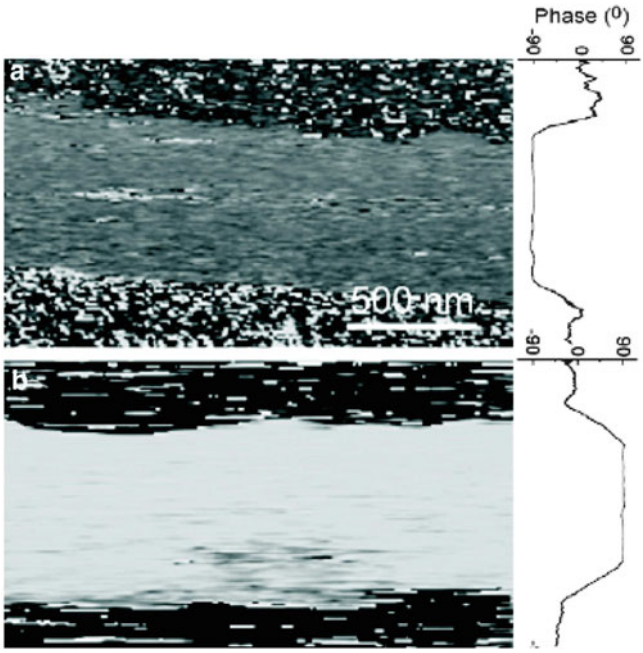

Fig. 12.20 (**a**) Lateral PFM phase images of a type I collagen fibril (**a**) before and (**b**) after the sample was rotated by 180°. Reproduced with permission from [146]. Copyright 2009, Institute of Physics

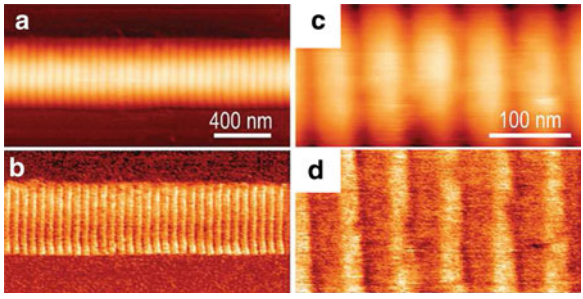

Fig. 12.21 (**a**) and (**c**) Topographic images of a collagen fibril. (**b**) and (**d**) lateral PFM amplitude images of the same collagen fibril. Reproduced with permission from [147]. Copyright 2009, American Chemical Society

effects. Kalinin et al. concluded that the contrast was dominated by flexoelectric coupling, and further demonstrated the use of PFM-based techniques for electrical manipulation of these nanosized viruses, as shown in Fig. 12.23, in which one TMV has been removed from a virus network via the application of a dc bias pulse.

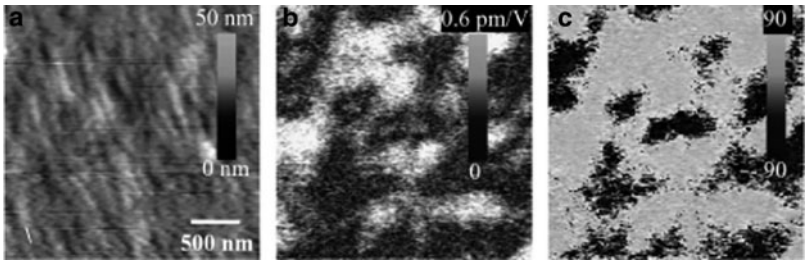

Fig. 12.22 (**a**) Topography and (**b**) vertical PFM amplitude and (**c**) phase images of a type I collagen film deposited on a platinized silicon substrate. Reproduced with permission from [142]. Copyright 2006, Elsevier

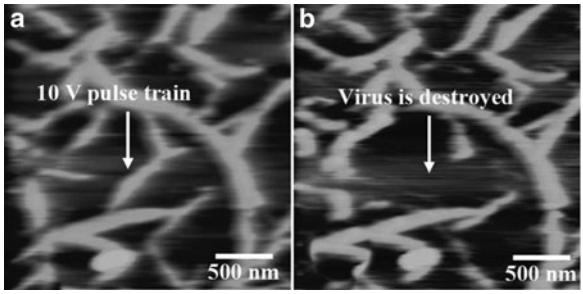

Fig. 12.23 Surface topography (**a**) before and (**b**) after electrical manipulation of a tobacco mosaic virus. Reproduced with permission from [150]. Copyright 2006, American Institute of Physics

12.3.4 Challenges

A key challenge for electromechanical studies of biopiezoelectrics is the smallness of the coupling coefficients and thereby, the signal-to-noise ratio. Several approaches have been developed to address this issue, as the application of larger bias to elicit a larger response is generally not an option for biological samples. A common solution in dynamic SPMs is to make use of the resonance enhancement of the cantilever to enhance weak mechanical responses. In PFM, this approach was pioneered by Harnagea [151]. However, the use of resonance-enhancement in PFM is limited, since variations in the tip-sample contact stiffness can cause strong coupling between the topography and the apparent PFM signal, making data interpretation difficult. This has led to the development of dual-frequency [152] and band excitation (BE) [153] PFM modes and dual-cantilever systems [154] to increase the signal-to-noise ratio. The use of BE-PFM of ferroelectric materials has been summarized in recent publications [155, 156].

12.4 Liquid Imaging

The obvious challenge for electromechanical and electrostatic SPM measurements of biological systems is imaging in a liquid environment. While the combination of liquid imaging with voltage-modulated SPM techniques seems at first to be a mismatch, the convergence has come from two directions, namely the strong reduction of the adhesive van der Waals force and the absence of capillary forces in liquids, and the necessity to maintain a natural environment for viable biological systems. Note that for imaging in an ambient environment, the van der Waals and capillary forces and the associated jump-to-contact instability separate the "contact" regime with large system stiffness (where electromechanical responses dominate) and the "noncontact" regime with low sample stiffness (where electrostatic forces dominate), a division largely absent in liquids. The second aspect that naturally arises in the context of voltage modulation methods in conductive media is the propensity of these systems for ionic diffusion and electrochemical reactions even at modest (∼1–2 V) potential. In comparison, driving voltages in PFM and KPFM are often in the 2–10 V range, suggesting the possible contribution of electrochemical reactions to the imaging process.

At the same time, electric forces in solution play an important role in, e.g., electrical double layers, lipid membranes, and biomolecules [157, 158]. Electric forces in solution are used for a variety of applications, including trapping and manipulating cells and viruses at the microscale [159, 160] and nanofabrication through electrophoretic [161] and electrostatic [162] assembly. Electrostatic interactions are dominated by non-dissipative capacitive forces in ambient [45]. In liquid, complex effects due to electrical double layers, electrochemical reactions, mobile ions, ionic currents, and convective motion of the liquid must be taken into account [163, 164], necessitating experimental methods to probe electrically driven force interactions in liquids.

In this section, efforts to measure electrostatic and electromechanical interactions in a liquid environment are discussed in detail, from attempts to measure electrostatic forces using force distance curves, to voltage-modulated approaches, and to electromechanical imaging of biopolymers in solution.

12.4.1 Measurements of Electric Potential in Solution

As outlined in Sect. 12.2, KPFM has recently been applied to the study of surface potentials and electrostatic interactions in biological systems in air and as a function of relative humidity. In general, proteins, biopolymers, and cells are soft materials, and tapping mode in air can be quite destructive to the sample due to the high forces involved, provided the sample remains intact in air. In addition, functional properties can become inactive for certain biological samples imaged in air and also depending on the support or substrate. Also, capillary forces due to the presence of surface

water layers are detrimental to resolution. Similarly, the resolution of electrostatic and surface potential measurements can be limited due to long-range electrostatic forces, which interact with not only the tip locally, but also the entire probe and cantilever beam non-locally. Tapping mode in liquid [165] overcomes some of these limitations and allows for improved resolution and imaging with lower forces. Ideally, only a true noncontact technique would guarantee minimal surface damage. Perhaps more importantly, the role of surface potential and electrostatics in biosystems are most relevant in physiological environments. Interestingly, tapping mode AFM in liquid has been used to visualize surface charge as early as 1998 [202].

Several attempts have been made to measure and analyze electrostatic interactions of biosystems in liquid including force distance mapping and electrostatic balancing with electrolyte solution [166–168]. Müller et al. have used electrostatic balancing with pH and electrolyte solution to improve topographic images of biomolecular membranes [169]. By varying the ionic strength and noting the differences between each image, Philippsen et al. were able to generate difference maps that revealed the electrostatic potential of transmembrane channels [170]. Sotres and Baró used a similar, albeit spectroscopic, mapping approach to measure isodistance maps of the electrical double layer forces of a DNA molecule [171]. Similar approaches based on chemical force microscopy and spectroscopy with functionalized tips have also been used to determine electrostatic forces [172, 173].

Recently, several attempts by the group of Hafner have been made to measure electrostatic forces (charge density maps) of lipid bilayers and DNA in 1–3 mM ionic concentrations using a lift-mode approach [174–176]. In the first line scan, the topography is measured, and in the second, the topography is retraced at a certain constant lift-height from the sample surface (Fig. 12.24a). By choosing the appropriate lift-height for the concentration used, the second line scan will be affected only by the electric double layer. Note that an electrical bias is not applied and the cantilever is not conducting. Through careful calibration of the probe used, the measurement can be made quantitative [175, 176]. A numerical simulation of the field distribution for a tip in an electrolyte solution near a mica-support lipid bilayer film is shown in Fig. 12.24b, and simultaneously-obtained topography and charge density map images of lipid domains are shown in Figs. 12.24c and d.

In KPFM, a dc bias is applied to minimize electrostatic forces or force gradients. As such, to implement KPFM in solution, a dc bias will need to be applied in solution. The application of nonlocal dc bias in solution has been used by Müller and Engel to visualize voltage-gated closure of ion channels by AFM, as shown in Fig. 12.25 [177], and the application of nonlocalized and localized dc bias has been demonstrated for ferroelectric switching [178] by direct biasing of the tip. Insulating conductive probes have also been used to image membranes during the application of bias to a conducting substrate [179].

There are very few examples of voltage-modulated EFM or KPFM imaging in solution. Hirata et al. reported a slightly modified KPFM, electrochemical AFM hybrid for the measurement of surface potential of a mixed, self-assembled thiol film on gold in water [180]. Lynch et al. have used dielectrophoretic force

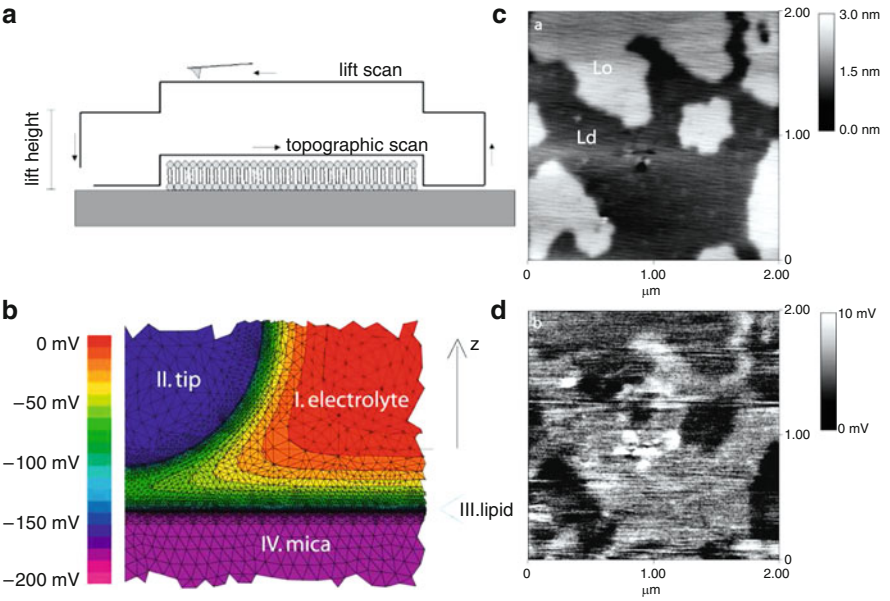

Fig. 12.24 (**a**) Schematic showing the tip path during lift-mode liquid EFM. (**b**) Numerical simulations of the tip-sample interaction in an electrolyte solution. (**c**) Surface topography image of liquid ordered (L_o) and liquid disordered (L_d) lipid domains. (**d**) Liquid EFM image of the charge density map of the same location demonstrating that the L_o phase is more positive than the L_d phase. Panel (**a**) reproduced with permission from [174]. Copyright 2003, American Chemical Society. Panels (**b**–**d**) reproduced with permission from [175]. Copyright 2007, the Biophysical Society

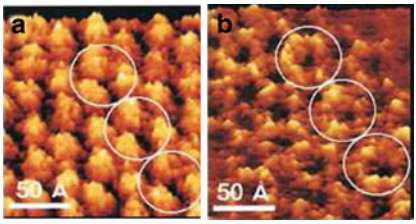

Fig. 12.25 Trigonally packed porin trimers (**a**) before and (**b**) after the application of a membrane potential demonstrating a voltage-induced conformational change. Reproduced with permission from [177]. Copyright 1999, Elsevier

microscopy with conducting, biased tips to measure local membrane capacitance of *Escherichia coli* cells in water [181]. Using an approach similar to scanning impedance microscopy (SIM) [182, 183], alternating electrostatic forces have also been measured in a liquid environment using SPM with an ac bias applied to the tip and a microelectrochemical cell formed by two periodically biased electrodes [51].

The implementation of traditional KPFM in solution requires both the application of ac and dc biases with concomitant suppression of unwanted electrochemical processes at the tip–surface junction. The strategies to achieve this goal include the development of insulated and shielded probes (reducing the electrochemically active areas), the use of materials with high overpotentials for water dissociation, and the use of high frequencies. The latter approach can be extended to the use of intermodulation techniques, in which the information on nonlinear (in bias) forces is acquired through the frequency mixing between two high-frequency signals. Additionally, SPMs based on the use of ionically conductive solution [184–186] can potentially be developed to probe bias-induced strain effects. Approaches based on scanning electrochemical potential microscopy may also prove relevant [187]. Finally, one of the most promising techniques is based on a KPFM technique which measures surface potential without using a bias-voltage feedback [203]. This dual-harmonic approach has already been used in a liquid environment [204].

12.4.2 Piezoresponse Force Microscopy

Future work in the area of relating PFM to biofunctionality necessitates electromechanical imaging in a liquid environment. As a first step in this direction, PFM imaging of a ferroelectric sample has been demonstrated in a liquid environment [51]. Both long-range electrostatic forces and capillary interactions were minimized in liquid, resulting in a localization of the ac field to the tip–surface junction and allowing 3 nm resolution to be achieved. PFM images in liquid of a lead zirconate titanate bulk ceramic surface are shown in Fig. 12.26.

As shown previously in Figs. 12.2c and 12.2d, the capacitive tip–surface electrostatic interaction in ambient is present for both noncontact and contact modes of operation, while electromechanical coupling is present only in the contact mode [double arrow in Fig. 12.2d]. In liquid, however, the PFM contrast is strongly mediated by the presence of mobile ions that screen electrostatic tip–surface interactions. For the sphere-plane system [188],

$$F_{\mathrm{el}}^{l}(z) = \frac{\epsilon\epsilon_0 R}{\lambda_D} \frac{2V_t V_s \exp(h/\lambda_D) - (V_t^2 + V_s^2)}{\exp(2h/\lambda_D) - 1}. \tag{12.3}$$

Electrostatic interactions in liquid are short-range due to screening by mobile ions and decay exponentially for $h > \lambda_D$ (Fig. 12.27a, b). Thus, the electrostatic contribution to the PFM signal in liquid is (for $h > 0$)

$$\mathrm{PR}_{\mathrm{el}}^{\mathrm{liq}} = \frac{\epsilon\epsilon_0 R}{\lambda_D} \frac{2V_s \exp(h/\lambda_D)}{\exp(2h/\lambda_D) - 1} \frac{1}{k_1^l + k}, \tag{12.4}$$

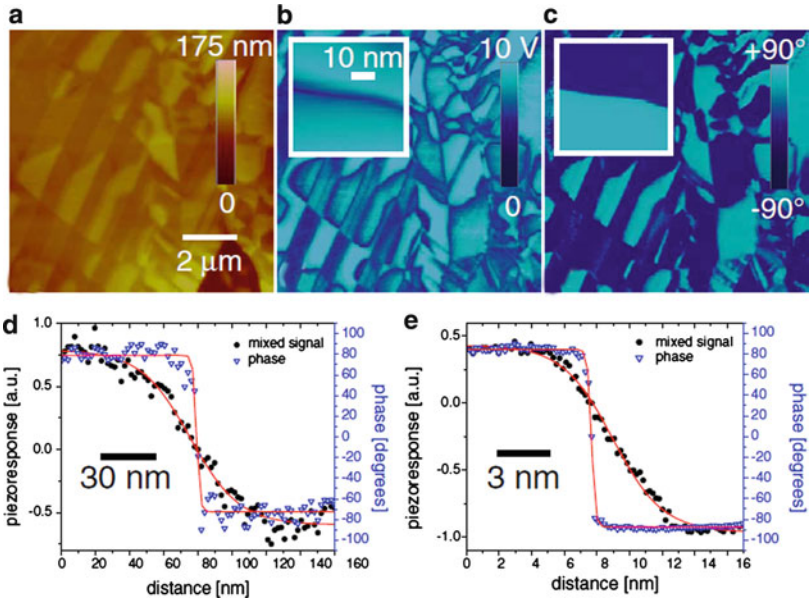

Fig. 12.26 (**a**) Topography, (**b**) PFM amplitude, and (**c**) PFM phase images of a lead zirconate titanate ceramic measured in water. Insets show high resolution PFM images. Domain wall cross-sections of PFM signals in (**d**) air and (**e**) water. Reproduced with permission from [51]. Copyright 2006, American Physical Society

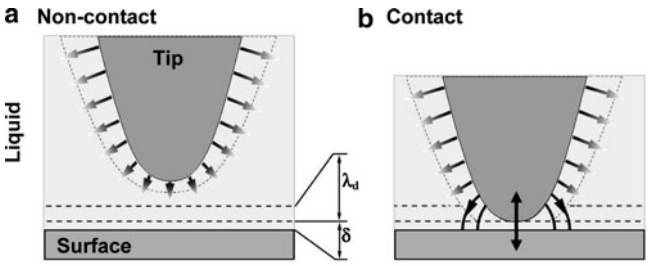

Fig. 12.27 (**a**) For noncontact SPM techniques, electrostatic forces are minimized in liquid. (**b**) In contact mode, electrostatic forces are also minimized in liquid; however, electromechanical coupling [double arrow in (**b**)] is present. The reduced electrostatic force allows improvements in PFM resolution in liquid. Adapted with permission from [51]. Copyright 2006 by the American Physical Society

where k_1^l is tip–surface spring constant in liquid. The contribution from the conical part of the tip and cantilever is absent for $R >> \lambda_D$. Note that the increase in response observed at the contact point in liquid is due to additional electrostatic coupling in the double layer. The response decreases with increasing force due to the increased contact stiffness.

The electromechanical response in liquid is described by (12.1), where the tip–surface spring constant now includes the effect of the liquid layer. The screening coefficient is $\alpha(h) = 1$ in (12.1) for $h << \lambda_D$, i.e., when the tip touches the surface, and is $\alpha(h) = 0$ if the electric double layers around the tip and the surface do not overlap. Thus, the electromechanical response (12.1) in solution gradually decays at distances on the order of the Debye length of the solution, and the electrostatic contribution is significantly minimized as compared to ambient or vacuum imaging (Fig. 12.27b).

Through the application of an ac bias in ambient or liquid environments, the electromechanical coupling can be investigated. In the case of ferroelectric materials in an ambient environment, an applied dc voltage of sufficient magnitude will lead to the nucleation of a ferroelectric domain directly under the tip. In solution, a transition of ferroelectric switching behavior from localized to uniform switching depending on the choice of the solvent has been observed, establishing that imaging is possible at conductivities far larger than allowed for localized switching [178]. Furthermore, these results illustrate the degree to which the spatial extent of a dc field can be controlled in solution. Through the choice of solvent and bias magnitude and duration, it has been shown that it is possible to nucleate a single domain, switch an entire sample surface, and even partially switch a large region (Fig. 12.28). Application of local dc pulses using conventional metal-coated cantilevers is possible only in less conductive nonaqueous solvents such as isopropanol or methanol, which has relevance for the implementation of KPFM in solution.

Liquid PFM has subsequently been applied to a number of biosystems, including lysozyme and insulin fibrils and adenocarcinoma cells [189]. Shown in Fig. 12.29 are topographic and PFM amplitude and phase images of a lysozyme fibril, illustrating the dependence of the measured signal on the applied bias. Note that the topography does not change with bias, while the PFM amplitude signal increases with increasing bias, and the phase response is stronger for higher bias. The fibril does not appear to degrade with repeated scanning or application of ac bias, suggesting the applicability of PFM even on soft biosystems. Some internal structure is discernable in the PFM amplitude images, while the PFM phase response is uniform within a fibril. Similar behavior has been observed for insulin fibrils. The strong dependence of the PFM phase contrast on the driving amplitude and small phase shifts ($<<180°$ typical of changes in polar orientation) between dissimilar regions suggest a significant contribution of electric double layer forces and elasticity to the PFM signal. This is not surprising considering most biopolymers are shear piezoelectrics, and the out-of-plane piezoelectric response can be expected to be small. With regards to adenocarcinoma cells, only weak contrast between different cells or at cell boundaries is observed in the PFM amplitude image, while cells with higher height profiles appear to have a slightly different PFM phase response than surrounding cells (not shown). These observations suggest the possibility of a strong elastic contribution to the PFM signal. The high conductivity of the growth media and imaging solution results in uniform biasing of the liquid. To avoid this problem, the imaging should be performed using insulated or shielded probes, in which the central part of the tip is insulated from the solution except

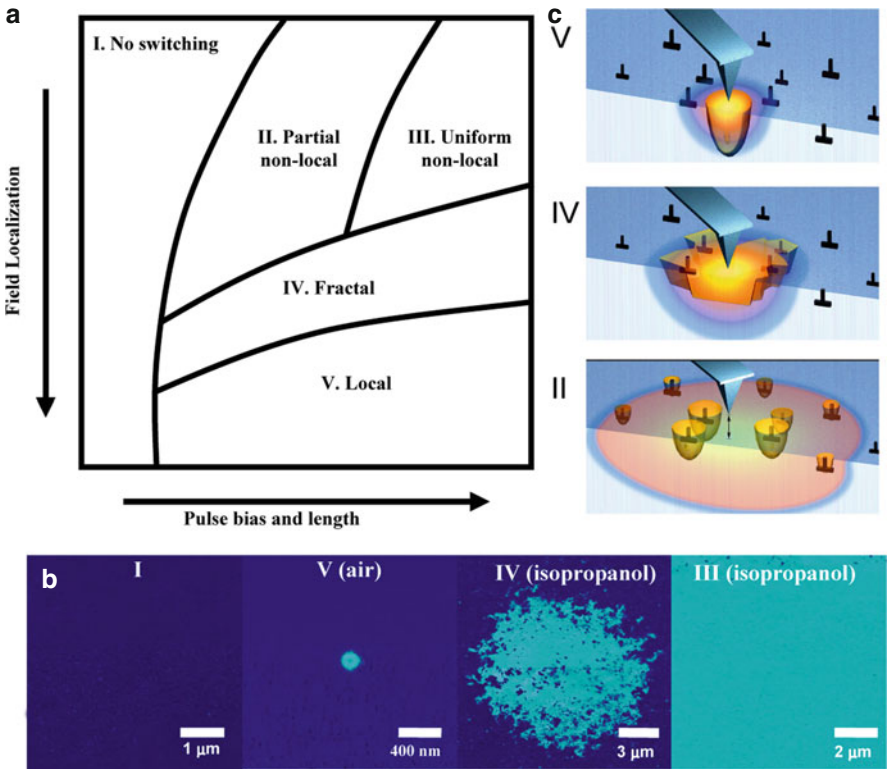

Fig. 12.28 (**a**) Schematic parameter diagram of possible switching modes vs. field localization and pulse parameters. (**b**) PFM phase images illustrating domain morphology in regions I, III, IV, and V and the choice of solvent for the phase map in (**a**). (**c**) Schematics of switching in local, fractal, and non-local cases. Adapted with permission from [178]. Copyright 2007, American Physical Society

for the region near the probe apex. In addition, a much different response should be expected from electroactive cells such as cardiac myocites, neuronal cells, and pancreatic beta cells.

There are several major challenges with understanding PFM images in biosystems in solution. First, the electromechanical response depends on the orientation of the polar bonds within the biosystem and the direction the electric field is applied, requiring some knowledge of the biomolecular assembly. Second, the relatively low electromechanical coupling coefficients combined with the potentially reduced signals in solution and complications from topographic crosstalk, differences in elastic properties, other electromechanical couplings such as flexoelectricity in membranes, and the presence of an electrical double layer all make interpretation of the signal and separation of signal components challenging.

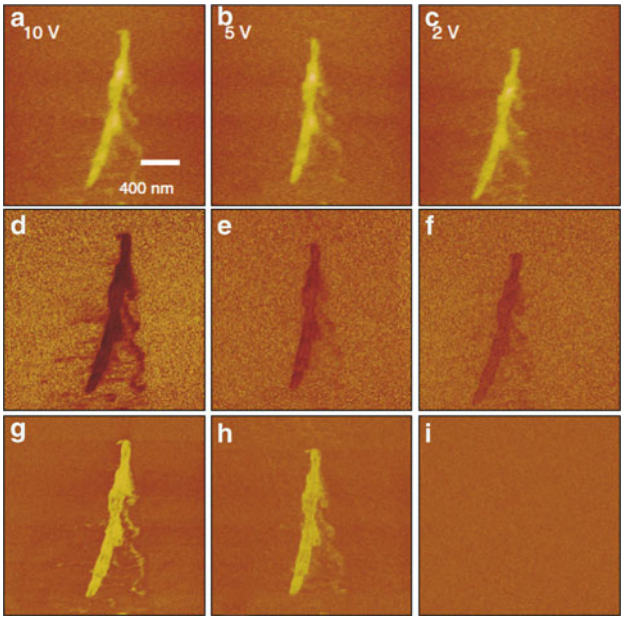

Fig. 12.29 (**a–c**) Topographic, (**d–f**) PFM phase, and (**g–i**) PFM amplitude images of a lysozyme fibril as a function of applied ac bias. Reproduced with permission from [189]. Copyright 2007, Institute of Physics

Nikiforov et al. have begun to address these challenges using BE-PFM in solution. In one instance, they have demonstrated functional recognition imaging of two bacteria types using a combined statistical analysis of the broadband electromechanical response using principal component analysis and a recognition neural network [190]. The technique is demonstrated on model *Micrococcus lysodeikticus* and *Pseudomonas fluorescens* bacteria (Fig. 12.30).

BE-PFM in solution was further applied to study electromechanical coupling in amyloid fibrils [191]. Again, a statistical approach based on principal component analysis is used; this time to separate elastic and electromechanical contributions from the broadband electromechanical signal. The authors demonstrate that in the bulk of the fibril, the electromechanical response is dominated by double-layer effects (consistent with the shear piezoelectricity of biomolecules), while a number of electromechanically active hot spots are observed, possibly related to structural defects, which allow a nonzero out-of-plane piezoresponse. In Fig. 12.31, spatially resolved BE-PFM maps of the electromechanical response amplitude, the quality factor, and resonance frequency are shown.

Beyond these early observations, there are several challenges for the interpretation and applicability of PFM of biosystems in a liquid environment. To explore the biofunctionality of piezoelectricity in biosystems, ideally, the measurements should be performed under physiologically relevant environments; however, it should be

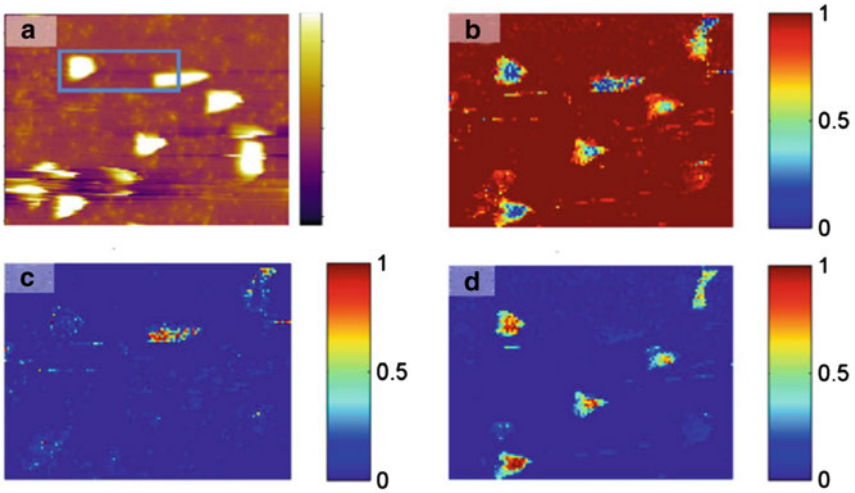

Fig. 12.30 (**a**) Topography image of bacteria on poly-L-lysine-coated mica. The area within the rectangle in (**a**) was used to train the neural network. Neural netork recognition maps for the (**b**) background, (**c**) *P. fluorescens*, and (**d**) *M. lysodeikticus*. Reproduced with permission from [190]. Copyright 2009, Institute of Physics

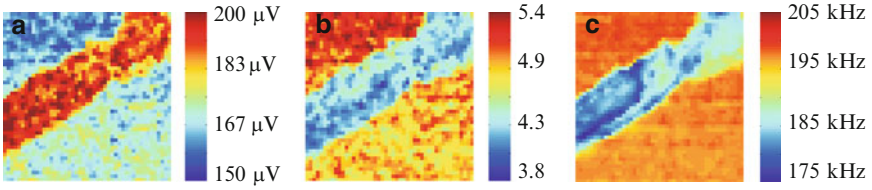

Fig. 12.31 Spatially resolved maps of the (**a**) amplitude, (**b**) quality factor, and (**c**) resonance frequency of electromechanical response of an amyloid fibril. Reproduced with permission from [191]. Copyright 2010, American Chemical Society

noted that the signal in PFM can be reduced significantly in ionic solutions, as demonstrated in Fig. 12.32. Furthermore, biological surfaces in solution are subject to hydration layers which can potentially prevent the detection of shear piezoelectric deformations and limit the bias applied directly to the sample.

As with PFM imaging in air, routes are under investigation to enhance the signal-to-noise ratio for PFM imaging in solution. This is particularly challenging, as a liquid environment is not necessarily compatible with the application of the high bias necessary to increase the signal. Similarly, the use of resonance enhancement in liquid environments is hampered by significant cross-talk between mechanical and electromechanical responses, making data interpretation and quantification difficult.

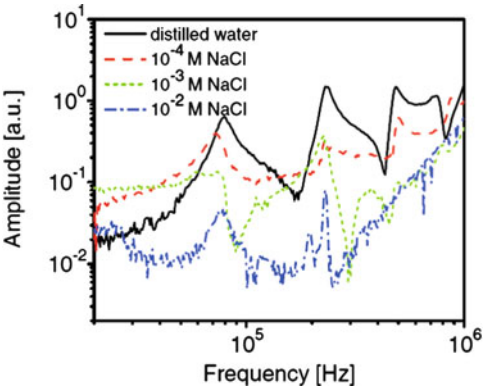

Fig. 12.32 Piezoresponse amplitude signal as a function of frequency and salt concentration. Reproduced with permission from [51]. Copyright 2006, American Physical Society

12.4.3 At the Intersection of Electrostatics and Electromechanics

The similarities between voltage-modulated electric and electromechanical AFM modes provide a unique opportunity in liquid environments, where the spatial extent of long-range electrostatic forces can be controlled through the choice of the imaging solution. Thus, it may be possible to image electromechanical coupling during the contact portion of the cantilevered tip motion. As such, depending on the imaging medium and parameters, it may be possible to control the image formation mechanism. Several preliminary results are presented below.

In the case of dual-modulation AFM, in which the tip is modulated both mechanically and electrically, it is possible to image a sample in tapping or intermittent-contact and measure information related to the electric or electromechanical interactions. The mechanical motion of the tip is driven at the first free resonance of the cantilever, while the electrical signal is chosen at the second resonance of the cantilever (close to the first contact resonance, as shown in Fig. 12.33b). This approach follows previous implementations of "dual ac" modes [192, 193], but in this case one of the excitations is electrical [42]. This bimodal intermittent contact PFM approach has been first applied to model ferroelectric samples [194]. The approach is outlined schematically in Fig. 12.33, whereby both mechanical and electrical modulations are used (Fig. 12.33a). The piezoelectric response, the effective stiffness, and the electrostatic force (in ambient and liquid environments) are plotted as a function of tip-sample separation in Figs. 12.33c and d.

Shown in Fig. 12.34 are bimodal PFM images of topography and the amplitude of the electromechanical response signal of a purple membrane patch, revealing a change in contrast at features exhibiting topographic contrast. Further work is required to distinguish between electric, elastic, and electromechanical contributions to the signal.

Topography, PFM amplitude, and PFM phase images of human tooth dentin in air are shown in Figs. 12.35a–c, respectively. Intertubular dentin is piezoelectric, while

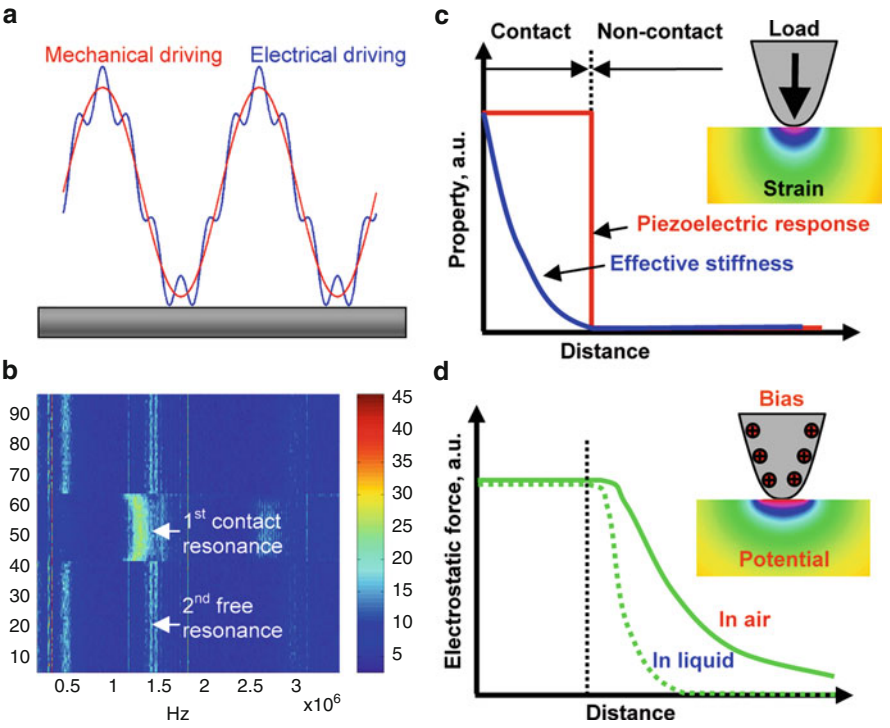

Fig. 12.33 (**a**) Schematic showing mechanical and electrical modulations. (**b**) Two- dimensional map of the measured signal as a function of electrical modulation frequency and tip-sample separation. Sketches of c the response and effective stiffness as a function of tip-sample separation, and of (**d**) the electrostatic force as a function of distance in liquid and air. Reproduced with permission from [194]. Copyright 2009, Institute of Physics

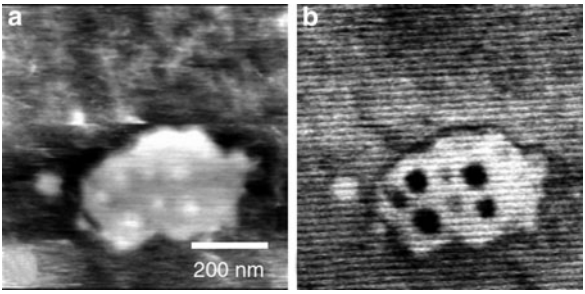

Fig. 12.34 Bimodal PFM mode images of bacteriorhodopsin imaged in buffer solution with a metal coated tip. Shown are (**a**) surface topography (6 nm z-scale) and (**b**) the amplitude of the electromechanical response signal. Reproduced with permission from [189]. Copyright 2007, Institute of Physics

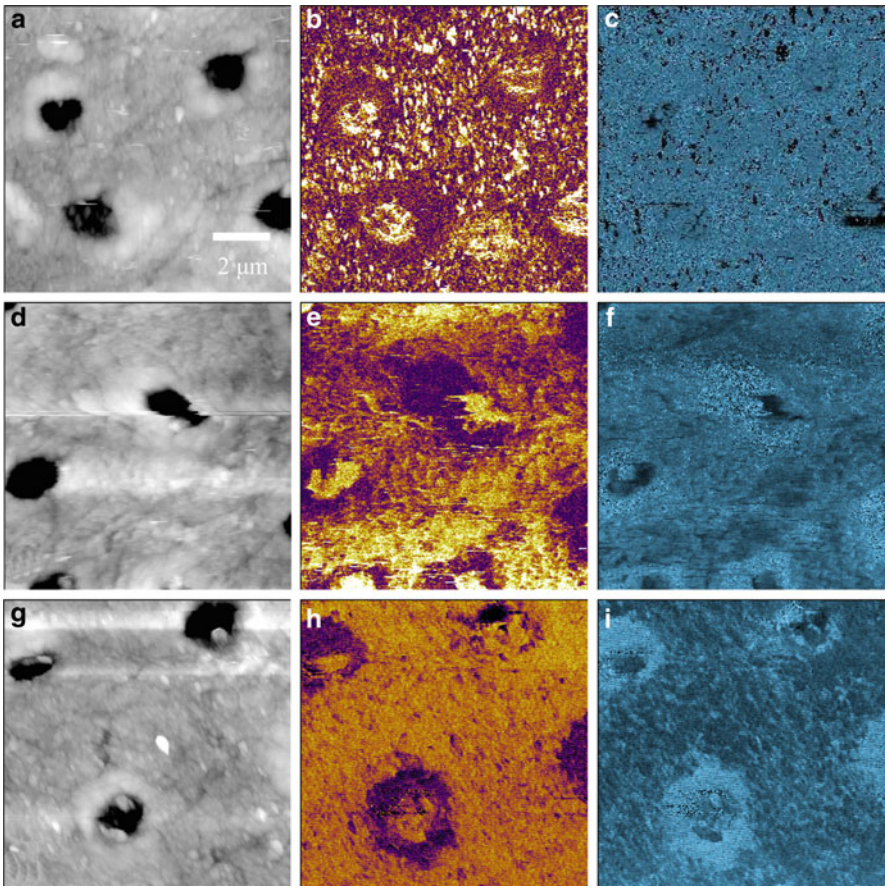

Fig. 12.35 (**a**), (**d**), (**g**) Topography, (**b**), (**e**), (**h**) amplitude, and (**c**), (**f**), (**i**) phase images of dentin in ambient contact mode PFM, liquid contact mode PFM, and liquid bimodal PFM, respectively. Reproduced with permission from [194]. Copyright 2009, Institute of Physics

the peritubular dentin is not, resulting in clear contrast in the PFM amplitude image. Topography, PFM amplitude, and PFM phase images of tooth dentin in deionized water are shown in Figs. 12.35d–f, respectively. The response variations between intertubular and peritubular regions are both still visible. Finally, topography and bimodal PFM images in DI water are shown in Figs. 12.35g–i. While the contrast is further reduced compared to contact mode PFM in liquid, the overall morphology of the intermittent-contact PFM images of dentin is similar to the contact mode PFM, suggesting the feasibility of the approach.

12.5 Summary and Outlook

PFM and KPFM are rapidly emerging as promising techniques for probing electromechanical coupling and electrostatic interactions in biological systems. Dynamic phenomena in biological systems from tissue to cellular, subcellular and molecular levels are typically associated with electromechanical transformations [195]. Thus, PFM and KPFM potentially open pathways for studies of electrophysiology on cellular and molecular levels, signal propagation in neurons, action potentials, etc. Liquid PFM and KPFM may provide novel opportunities for high-resolution studies of imaging biological systems in physiological environments on nanometer and ultimately molecular levels.

Toward this end, there are several challenges that must first be overcome including applying localized bias in solution and separating elastic from electromechanical signals. The former can be addressed through the continued development of probes with electrostatic shielding [164, 179, 196, 197]. The later can be addressed through the continued development of novel imaging modes [153, 194, 198, 199].

Acknowledgements BJR acknowledges the support of UCD Research and Science Foundation Ireland (grant no. 10/RFP/MTR2855). This research was sponsored (BJR, SVK) by the Center for Nanophase Materials Sciences, Oak Ridge National Laboratory, managed and operated by UT-Battelle, LLC for the Office of Basic Energy Sciences, U.S. Department of Energy.

References

1. B. Honig, A. Nicholls, Science **268**, 1144 (1995)
2. A. DeLoof, Int. Rev. Cytol. **88**, 251 (1986)
3. R. Plonsey, R.C. Barr, *Bioelectricity: A Quantitative Approach* (Kluwer, New York, 2000)
4. H.G.L. Coster, J. Biol. Phys. **29**, 363 (2003)
5. F. Sachs, W.E. Brownell, G. Petrov, MRS Bull. **34**, 665 (2009)
6. M. Olivotto, A. Arcangeli, M. Carlà, E. Wanke, Bioessays **18**, 495 (1996)
7. M.F. Perutz, Science **201**, 1187 (1978)
8. K.A. Sharp, B.H. Honig, Annu. Rev. Biophys. Biophys. Chem. **19**, 301 (1990)
9. B.H. Honig, W.L. Hubbell, R.F. Flewelling, Annu. Rev. Biophys. Biophys. Chem. **15**, 163 (1986)
10. G.C. Brown, FEBS Lett. **260**, 1 (1990)
11. S. McLaughlin, Curr. Top. Membr. Transp. **9**, 71 (1977)
12. S. McLaughlin, Annu. Rev. Biophys. Biophys. Chem. **18**, 113 (1989)
13. D.S. Cafiso, Curr. Opin. Struct. Biol. **1**, 185 (1991)
14. S.S. Strickler, A.V. Gribenko, T. R. Keiffer, J. Tomlinson, T. Reihle, V.V. Loladze, G.I. Makhatadze, Biochemistry **45**, 2761 (2006)
15. C. Tang, J. Iwahara, M. Clore, Nature **444**, 383 (2006)
16. T. Yeung S. Grinstein, Immunol. Rev. **219**, 17 (2007)
17. T. Yeung, M. Terebiznik, L. Yu, J. Silvius, W. M. Abidi, M. Philips, T. Levine, A. Kapus, S. Grinstein, Science **313**, 347 (2006)
18. A.V. Pisliakov, P.K. Sharma, Z.T. Chu, M. Haranczyk, A. Warshel, PNAS **105**, 7726 (2008)
19. Z. Hejnowics, K. Trebacz, A. Sievers, Plant Cell. Environ. **18**, 471 (1995)
20. K.M. Tyner, R. Kopelman, M.A. Philbert, Biophys. J. **93**, 1163 (2007)

21. M. Mazzani, J. O. Bustamante, H. Oberleithner, Physiol. Rev. **81**, 1 (2001)
22. L. Catacuzzeno, B. Fioretti, F. Franciolini, Biophys. J. **95**, 2160 (2008)
23. S. McLaughlin, A. Aderem, Trends Biochem. Sci. **20**, 272 (1995)
24. S.D. Zakharov, T.I. Rokistkaya, V.L. Shapovalov, Y.N. Antonenko, W.A. Cramer, Proc. Natl. Acad. Sci. USA **99**, 8654 (2002)
25. T.Y. Tsong, R.D. Astumian, Progr. Biophys. Mol. Biol. **50**, 1 (1987)
26. T.Y. Tsong, R.D. Astumian, Annu. Rev. Physiol. **50**, 273 (1988)
27. T.Y. Tsong, Annu. Rev. Biophys. Biophys. Chem. **19**, 83 (1990)
28. D. Oliver, C.-C. Lien, M. Soom, T. Baukrowitz, P. Jonas, B. Fakler, Science **304**, 265 (2004)
29. W.A. Catterall, Annu. Rev. Biochem. **55**, 953 (1986)
30. M. Grabe, H. Lecar, Y.N. Jan, L.Y. Jan, Proc. Natl. Acad. Sci. USA **101**, 17640 (2004)
31. S.V. Kalinin, B.J. Rodriguez, S. Jesse, P. Maksymovych, K. Seal, M. Nikiforov, A.P. Baddorf, A.L. Kholkin, R. Proksch. Mater Today **11**, 16 (2008)
32. B.J. Blanchard, V.L. Thomas, V.M. Ingram, Biochem. Biophys. Res. Commun. **293**, 1197 (2002)
33. J.S. Kim, L. He, J.J. Lemasters, Biochem. Biophys. Res. Commun. **304**, 463 (2003)
34. G.T. Rogers, J. Appl. Electrochem. **12**, 379 (1982)
35. M. Levin, Bioelectromagnetics **24**, 295 (2003)
36. S.V. Kalinin, B.J. Rodriguez, S. Jesse, B. Mirman, E. Karapetian, E.A. Eliseev, A.N. Morozovska, Annu. Rev. Mater. Sci. **37**, 189 (2007)
37. S.V. Kalinin, N. Setter, A. Kholkin, MRS Bull. **34**, 634 (2009)
38. K.K. Papachroni, D.N. Karatzas, K.A. Papavassiliou, E.K. Basdra, A.G. Papavassiliou, Trends Mol. Med. **15**, 208 (2009)
39. H.M. Frost, Anat. Rec. **226**, 403 (1990)
40. G. Binnig, C. F. Quate, C. Gerber, Phys. Rev. Lett. **56**, 930 (1986)
41. S. Sadewasser, P. Jelinek, C.-K. Fang, O. Custance, Y. Yamada, Y. Sugimoto, M. Abe, S. Morita, Phys. Rev. Lett. **103**, 266103 (2009)
42. B.D. Terris, J.E. Stern, D. Rugar, H.J. Mamin, Phys. Rev. Lett. **63**, 2669 (1989)
43. F. Saurenbach, B.D. Terris, Appl. Phys. Lett. **56**, 1703 (1990)
44. M. Nonnenmacher, M.P. O'Boyle, H.K. Wickramasinghe, Appl. Phys. Lett. **58**, 2921 (1991)
45. T. Glatzel, M.Ch. Lux-Steiner, E. Strassburg, A. Boag, Y. Rosenwaks, in *Principles of Kelvin Probe Force Microscopy*, ed. by S.V. Kalinin, A. Gruverman. Scanning Probe Microscopy: Electrical and Electromechanical Phenomena on the Nanoscale, vol. 1 (Springer Science and Business Media, New York, 2007), pp. 113–131
46. C. Leung, H. Kinns, B.W. Hoogenboom, S. Howorka, P. Mesquida, Nano Lett. **9**, 2769 (2009)
47. S. Kitamura, M. Iwatsuki, Appl. Phys. Lett. **72**, 3154 (1998)
48. C. Loppacher, U Zerweck, L M Eng, Nanotechnology **15**, S9 (2004)
49. C. Loppacher, U. Zerweck, S. Teich, E. Beyreuther, T. Otto, S. Grafström, L.M. Eng, Nanotechnology **16**, S1 (2005)
50. C. Baumgart, M. Helm, H. Schmidt, Phys. Rev. B **80**, 085305 (2009)
51. B.J. Rodriguez, S. Jesse, A.P. Baddorf, S.V. Kalinin, Phys. Rev. Lett. **96**, 237602 (2006)
52. A. Gruverman, O. Auciello, H. Tokumoto, J. Vac. Sci. Technol. B **14**, 602 (1996)
53. A. Gruverman, O. Auciello, H. Tokumoto, Appl. Phys. Lett. **69**, 3191 (1996)
54. T. Hidaka, T. Maruyama, M. Saitoh, N. Mikoshiba, M. Shimizu, T. Shiosaki, L. A. Wills, R. Hiskes, S. A. Dicarolis, J. Amano, Appl. Phys. Lett. **68**, 2358 (1996)
55. A. Gruverman, O. Auciello, H. Tokumoto, Annu. Rev. Mat. Sci. **28**, 101 (1998)
56. M. Alexe, A. Gruverman (eds.) *Nanoscale Characterization of Ferroelectric Materials*. (Springer, Berlin, 2004)
57. S. Hong, (ed.) *Nanoscale Phenomena in Ferroelectric Thin Films*. (Kluwer Academic Publishers, Norwell, MA, 2004)
58. M. Alexe, C. Harnagea, D. Hesse, U. Gösele, Appl. Phys. Lett. **75**, 1793 (1999)
59. M. Alexe, A. Gruverman, C. Harnagea, N.D. Zakharov, A. Pignolet, D. Hesse, J.F. Scott, Appl. Phys. Lett. **75**, 1158 (1999)
60. P. Günther, K. Dransfeld, Appl. Phys. Lett. **62**, 1137 (1992)

61. S.V. Kalinin, B.J. Rodriguez, S. Jesse, J. Shin, A.P. Baddorf, P. Gupta, H. Jain, D.B. D.B. Williams, A. Gruverman, Microsc. Microanal. **12**, 206 (2006)
62. A. Roelofs, U. Böttger, R. Waser, F. Schlaphof, S. Trogisch, L.M. Eng, Appl. Phys. Lett. **77**, 3444 (2000)
63. L.M. Eng, H.-J. Güntherodt, G. Rosenman, A. Skliar, M. Oron, M. Katz, D. Eger, J. Appl. Phys. **83**, 5973 (1998)
64. B.J. Rodriguez, A. Gruverman, A.I. Kingon, R.J. Nemanich, J.S. Cross, J. Appl. Phys. **95**, 1958 (2004)
65. S.V. Kalinin, E. Karapetian, M. Kachanov, Phys. Rev. B **70**, 184101 (2004)
66. S.V. Kalinin, D.A. Bonnell, Phys. Rev. B **65**, 125408 (2002)
67. H. Sugimura, K. Hayashi, N. Saito, N. Nakagiri, O. Takai, Appl. Surf. Sci. **188**, 403 (2002)
68. H. Sugimura, N. Saito, N. Maeda, I. Ikeda, Y. Ishida, K. Hayashi, L. Hong, O. Takai, Nanotechnology **15**, S69 (2004)
69. J. Lü, E. Delamarche, L. Eng, R. Bennewitz, E. Meyer, H.J. Güntherodt, Langmuir **15**, 8184 (1999)
70. N. Saito, K. Hayashi, H. Sugimura, O. Takai, N. Nakagiri, Surf. Interface Anal. **34**, 601 (2002)
71. T. Ichii, T. Fukuma, K. Kobayashi, H. Yamada, K. Matsushige, Nanotechnology **15**, S30 (2004)
72. H. McNally, D.B. Janes, B. Kasibhatla, C.P. Kubiak, Superlatt. Microstruct. **31**, 239 (2002)
73. M. Fujihira, H. Kawate, J. Vac. Sci. Technol. B **12**, 1604 (1994)
74. L.F. Chi, S. Jacobi, H. Fuchs, Thin Solid Films **284**, 403 (1996)
75. M. Fujihira, Annu. Rev. Mater. Sci. **29**, 353 (1999)
76. N. Reitzel, T. Hassenkam, K. Balashev, T. R. Jensen, P. B. Howes, K. Kjaer, A. Fechtenkötter, N. Tchebotareva, S. Ito, K. Müllen, T. Bjørnholm, Chem. Eur. J. **7**, 4894 (2001)
77. P. Karageorgiev, B. Stiller, D. Prescher, B. Dietzel, B. Schulz, L. Brehmer, Langmuir **16**, 5515 (2000)
78. H. Yamada, T. Fukuma, K. Umeda, K. Kobayashi, K. Matsushige, Appl. Surf. Sci. **188**, 391 (2002)
79. V. Palermo, M. Palma, Ž Tomović, M. D. Watson, R. Friedlein, K. Müllen, P. Samorì, Chem. Phys. Chem. **6**, 2371 (2005)
80. A. Liscio, V. Palermo, D. Gentilini, F. Nolde, K. Müllen, P. Samorì, Adv. Funct. Mater. **16**, 1407 (2006)
81. V. Palermo, M. Palma, P. Samorì, Adv. Mater. **18**, 145 (2006)
82. V. Palermo, A. Liscio, M. Palma, M. Surin, R. Lazzaronic, P. Samorì, Chem. Commun. 2007, 3326 (2007)
83. R. Buhler, W. Sturmer, H.J. Apell, P. Lauger, J. Membr. Biol. **121**, 141 (1991)
84. J. Zhang, R.M. Davidson, M.D. Wei, L.M. Loew, Biophys. J. **74**, 48 (1998)
85. P. Gogan, I. Schmiedel-Jakob, Y. Chitti, S. Tyc-Dumont, Biophys. J. **69**, 299 (1995)
86. L.B. Cohen, B.M. Salzberg, H.V. Davila, W.N. Ross, D. Landowne, A.S. Waggoner, C.H. Wang, J. Membr. Biol. **19**, 1 (1974)
87. J.Y. Wu, Y.W. Lam, C.X. Falk, L.B. Cohen, J. Fang, L. Loew, J.C. Prechtl, D. Kleinfeld, Y. Tsau, Histochem. J. **30**, 169 (1998)
88. M.S. Siegel, E.Y. Isacoff, in *Green fluorescent proteins for measuring voltage*, ed. by R. Yuste, A. Konnerth. Imaging in Neuroscience and Development: A Laboratory Manual (Cold Spring Harbor Laboratory Press, Cold Spring Harbor, NY, 2005), pp. 573
89. A. Kuznetsov, V.P. Bindokas, J.D. Marks, L.H. Philipson, Am. J. Physiol. Cell Physiol. **289**, 224 (2005)
90. J. Gorelik, Y. Gu, H.A. Spohr, A.I. Shevchuk, M.J. Lab, S.E. Harding, C.R.W. Edwards, M. Whitaker, G.W.J. Moss, D.C.H. Benton, D. Sánchez, A. Darszon, I. Vodyanoy, D. Klenerman, Y. E. Korchev, Biophys. J. **83**, 3296 (2002)
91. D. Laoudji, C. Guasch, E. Renault, R. Bennes, J. Bonnet, Anal. Bioanal. Chem. **381**, 1476 (2005)
92. D.C. Hansen, K.M. Hansen, T.L. Ferrell, T. Thundat, Langmuir **19**, 7514 (2003)
93. I.D. Baikie, P.J.S. Smith, D.M. Porterfield, P.J. Estrup, Rev. Sci. Instrum. **70**, 1842 (1999)

94. M. Thompson, L.E. Cheran, Faraday Discuss. **116**, 23 (2000)
95. L.E. Cheran, S. Sadeghi, M. Thompson, Analyst **130**, 1569 (2005)
96. L.E. Cheran, M. Chacko, M.Q. Zhang, M. Thompson, Analyst **129**, 161 (2004)
97. M. Thompson, L.-E. Cheran, M. Zhang, M. Chacko, H. Huo, S. Sadeghi, Biosens. Bioelectron. **20**, 1471 (2005)
98. I. Lee, E. Greenbaum, in *Electrical Scanning Probe Microscopy of Biomolecules on Surfaces and at Interfaces*, ed. by S.V. Kalinin, A. Gruverman. Scanning Probe Microscopy: Electrical and Electromechanical Phenomena on the Nanoscale, vol. 2, (Springer Science and Business Media, New York, 2007) pp. 601
99. Y. Leng, C.C. Williams, Colloids and Surfaces A **93**, 335 (1994)
100. A. Gil, P.J. de Pablo, J. Colchero, J. Gómez-Herrero, A.M. Baró, Nanotechnology **13**, 309 (2002)
101. K.J. Kwak, S. Yoda, M. Fujihira, Appl. Surf. Sci. **210**, 73 (2003)
102. E. Mikamo-Satoh, F. Yamada, A. Takagi, T. Matsumoto, T. Kawai, Nanotechnology **20**, 145102 (2009)
103. C. Leung, H. Kinns, B.W. Hoogenboom, S. Howorka, P. Mesquida, Nano Lett. **9**, 2769 (2009)
104. C. Leung, D. Maradan, A. Kramer, S. howorka, P. Mesquida, B.W. Hoogenboom, Appl. Phys. Lett. **97**, 203703 (2010)
105. A. Efimov, S.R. Cohen, J. Vac. Sci. Technol. A **18**, 1051 (2000)
106. R. Ohta, N. Saito, T. Ishizaki, O. Takai, Surf. Sci. **600**, 1674 (2006)
107. L. Fumagalli, G. Ferrari, M. Sampietro, G. Gomila, Nano Lett. **9**, 1604 (2009)
108. G. Gramse, I. Casuso, J. Toset, L. Fumagalli, G. Gomila, Nanotechnology **20**, 395702 (2009)
109. L. Fumagalli, G. Ferrari, M. Sampietro, I. Casuso, E. Martinez, J. Samitier, G. Gomila, Nanotechnology **17**, 4581 (2006)
110. X.Q. Chen, H. Yamada, T. Horiuchi, K. Matsushige, S. Watanabe, M. Kawai, P.S. Weiss, J. Vac. Sci. Technol. B **17**, 1930 (1999)
111. D.C. Coffey, D.S. Ginger, Nat. Mater. **5**, 735 (2006)
112. L. Kronik ,Y. Shapira, Surf. Interface Anal. **31**, 954 (2001)
113. A.K. Sinensky, A.M. Belcher, Nature Nanotech. **2**, 653 (2007)
114. P. Gao, Y. Cai, Anal. Bioanal. Chem. **394**, 207 (2009)
115. I. Lee, J.W. Lee, A. Stubna, E. Greenbaum, J. Phys. Chem. B **104**, 2439 (2000)
116. L. Frolov, Y. Rosenwaks, C. Carmeli, I. Carmeli, Adv. Mater. **17**, 2434 (2005)
117. T. Kuritz, I. Lee, E.T. Owens, M. Humayun, E. Greenbaum, IEEE Trans. Nano. Biosci. **4**, 196 (2005)
118. I. Lee, J.W. Lee, A. Stubna, E. Greenbaum, J. Phys. Chem. B **107**, 14225 (2003)
119. I. Lee, E. Chung, H. Kweon, S. Yiacoumi, D.C. Joy, A.V. Palumbo, C. Tsouris, Microsc. Microanal. **15**, 1132 (2009)
120. H.F. Knapp, P. Mesquida, A. Stemmer, Surf. Interface Anal. **33**, 108 (2002)
121. I. Lee, E. Greenbaum, S. Budy, J.R. Hillebrecht, R.R. Birge, J.A. Stuart, J. Phys. Chem. B **110**, 10982 (2006)
122. Z. Leonenko, M. Rodenstein, J. Döhner, L.M. Eng, M. Amrein, Langmuir **22**, 10135 (2006)
123. Z. Leonenko, S. Gill, S. Baoukina, L. Monticelli, J. Doehner, L. Gunasekara, F. Felderer, M. Rodenstein, L. M. Eng, M. Amrein, Biophys. J. **93**, 674 (2007)
124. E. Finot, Y. Leonenko, B. Moores, L. Eng, M. Amrein, Z. Leonenko, Langmuir **26**, 1929 (2010)
125. F. Hane, B. Moores, M. Amrein, Z. Leonenko, Ultramicroscopy **109**, 968 (2009)
126. A. J. P. Martin, Proc. Phys. Soc. **53**, 186 (1941)
127. E. Fukada, J. Phys. Soc. Japan **10**, 149 (1955)
128. V.A. Bazhenov, Piezoelectric Properties of Wood (Consultant Bureau, New York, 1961)
129. H.S. Nalwa, *Ferroelectric Polymers: Chemistry, Physics and Applications* (Dekker, New York, 1995)
130. E. Fukada, R. Prog. Polym. Phys. **38**, 1 (1995)
131. E. Fukada, IEEE Trans. Ultrason. Ferroelectr. Freq. Control **47**, 1277 (2000)
132. E. Fukada, I. Yasuda, J. Phys. Soc. Jpn. **12**, 1158 (1957)

133. E. Fukada, I. Yasuda, Jpn. J. Appl. Phys. **3**, 117 (1964)
134. S.B. Lang, Nature **212**, 704 (1966)
135. C.A.L. Bassett, Calc. Tiss. Res. **1**, 252 (1968)
136. A.A. Marino, R.O. Becker, Nature **228**, 473 (1970)
137. S. Weiner, H.D. Wagner, Annu. Rev. Mater. Res. **28**, 271 (1998)
138. C. Halperin, S. Mutchnik, A. Agronin, M. Molotskii, P. Urenski, M. Salai, G. Rosenman, Nano Lett. **4**, 1253 (2004)
139. S.V. Kalinin, B.J. Rodriguez, S. Jesse, T. Thundat, A. Gruverman, Appl. Phys. Lett. **87**, 053901 (2005)
140. S.V. Kalinin, B.J. Rodriguez, J. Shin, S. Jesse, V. Grichko, T. Thundat, A.P. Baddorf, A. Gruverman, Ultramicroscopy **106**, 334 (2006)
141. A. Gruverman, B.J. Rodriguez, S.V. Kalinin, J. Scann. Probe Micros. **1**, 1 (2006)
142. B.J. Rodriguez, S.V. Kalinin, J. Shin, S. Jesse, V. Grichko, T. Thundat, A.P. Baddorf, A. Gruverman, J. Struct. Bio. **153**, 151 (2006)
143. A. Gruverman, D. Wu, B.J. Rodriguez, S.V. Kalinin, S. Habelitz, Biochem. Biophys. Res. Commun. **352**, 142 (2007)
144. S. Habelitz, B.J. Rodriguez, S.J. Marshall, G.W. Marshall, S.V. Kalinin, A. Gruverman, J. Dent. Res. **86**, 908 (2007)
145. V.R. Binetti, J.D. Schiffman, O.D. Leaffer, J.E. Spanier, C.L. Schauer, Integr. Biol. **1**, 324 (2009)
146. M. Minary-Jolandan, M.-F. Yu, Nanotechnology **20**, 085706 (2009)
147. M. Minary-Jolandan, M.-F. Yu, ACS Nano **3**, 1859 (2009)
148. A. Gruverman, B.J. Rodriguez, S.V. Kalinin, in *Electromechanical Behavior in Biological Systems at the Nanoscale*, ed. by S.V. Kalinin, A. Gruverman. Scanning Probe Microscopy: Electrical and Electromechanical Phenomena on the Nanoscale, vol. 2, (Springer Science and Business Media, New York, 2007), pp. 615
149. C. Harnagea, M. Valléres, C.P. Pfeffer, D. Wu, B.R. Olsen, A. Pignolet, F. Légaré, A. Gruverman, Biophys J. **98**, 3070 (2010)
150. S.V. Kalinin, S. Jesse, W. Liu, A.A. Balandin, Appl. Phys. Lett. **88**, 153902 (2006)
151. C. Harnagea, A. Pignolet, M. Alexe, D. Hesse, IEEE Trans Ultrason, Ferroelectr, Freq Control **53**, 2309 (2006)
152. B.J. Rodriguez, C. Callahan, S.V. Kalinin, R. Proksch, Nanotechnology **18**, 475504 (2007)
153. S. Jesse, S.V. Kalinin, R. Proksch, A. P. Baddorf, B.J. Rodriguez, Nanotechnology **18**, 435503 (2007)
154. B. Zeyen, K. Virwani, B. Pittenger, K.L. Turner, Appl. Phys. Lett. **94**, 103507 (2009)
155. S. Jesse, S.V. Kalinin, Nanotechnology **20**, 085714 (2009)
156. S. Jesse, P. Maksymovych, S.V. Kalinin, Appl. Phys. Lett. **93**, 112903 (2008)
157. J.N. Israelashvili, *Intermolecular and Surface Forces* (Academic, London, 1985)
158. M.E. Davis, J.A. McCammon, Chem. Rev. **90**, 509 (1990)
159. T.P. Hunt, R.M. Westervelt, Biomed. Microdev. **8**, 227 (2006)
160. A. Docoslis, L.A. Tercero Espinoza, B. Zhang, L.-L. Cheng, B.A. Israel, P. Alexandridis, N.L. Abbott, Langmuir **23**, 3840 (2007)
161. R.C. Hayward, D.A. Saville, I.A. Aksay, Nature **404**, 56 (2000)
162. K. Hu, A.J. Bard, Langmuir **13**, 5418 (1997)
163. H.-J. Butt, Biophys. J. **60**, 1438 (1991)
164. T.J. Smith, K.J. Stevenson, in *Electrochemical SPM: Fundamentals and Applications*, ed. by S.V. Kalinin, A. Gruverman. Scanning Probe Microscopy: Electrical and Electromechanical Phenomena on the Nanoscale, vol. 1 (Springer Science and Business Media, New York, 2007) pp. 280–314
165. C.A.J. Putman, K.O. Van der Werf, B.G. De Grooth, N.F. Van Hulst, J. Greve, Appl. Phys. Lett. **64**, 2454 (1994)
166. H.-J. Butt, Biophys. J. **60**, 777 (1991)
167. H.-J. Butt, Biophys. J. **60**, 1438 (1991)
168. V.G. Levandy, M.L. Belaya, D.A. Pink, M.H. Jericho, Biophys. J. **70**, 1745 (1996)

169. D.J. Müller, D. Fotiadis, S. Scheuring, S.A. Müller, A. Engel, Biophys. J. **76**, 1101 (1999)
170. A. Philippsen, W. Im, A. Engel, T. Schirmer, B. Roux, D.J. Müller, Biophys. J. **82**, 1667 (2002)
171. J. Sotres, A.M. Baró, Appl. Phys. Lett. **93**, 103903 (2008)
172. A. Noy, D.V. Vezenov, C.M. Lieber, Annu. Rev. Mater. Sci. **27**, 381 (1997)
173. J. Seog, D. Dean, A.H.K. Plaas, S. Wong-Palms, A.J. Grodzinsky, C. Ortiz, Macromolecules **35**, 5601 (2002)
174. A.S. Johnson, C.L. Nehl, M.G. Mason, J.H. Hafner, Langmuir **19**, 10007 (2003)
175. Y. Yang, K.M. Mayer, J.H. Hafner, Biophys. J. **92**, 1966 (2007)
176. Y. Yang, K.M. Mayer, N.S. Wickremasinghe, J.H. Hafner, Biophys. J **95**, 5193 (2008)
177. D.J Müller, A. Engel, J. Mol. Biol. **285**, 1347 (1999)
178. B.J. Rodriguez, S. Jesse, A.P. Baddorf, S.-H. Kim, S.V. Kalinin, Phys. Rev. Lett. 98, 247603 (2007)
179. P.L.T.M. Frederix, M. R. Gullo, T. Akiyama,A. Tonin, N. F. de Rooij, U. Staufer, A. Engel, Nanotechnology **16**, 997 (2005)
180. Y. Hirata, F. Mizutani, H. Yokoyama, Surf. Interface Anal. **27**, 317 (1999)
181. B.P. Lynch, A.M. Hilton, C.H. Doerge, G.J. Simpson, Langmuir **21**, 1436 (2005)
182. S.V. Kalinin, D.A. Bonnell, Appl. Phys. Lett. **78**, 1306 (2001)
183. S.V. Kalinin, D.A. Bonnell, J. Appl. Phys. **91**, 832 (2002)
184. P.K. Hansma, B. Drake, O. Marti, S.A. Gould, C.B. Prater, Science **243**, 641 (1989)
185. M. Böcker, B. Anczykowski, J. Wegener, T.E. Schäffer, Nanotechnology **18**, 145505 (2007)
186. P. Novak, C. Li, A.I. Shevchuk, R. Stepanyan, M. Caldwell, S. Hughes, T.G. Smart, J. Gorelik, V.P. Ostanin, M.J. Lab, G.W.J. Moss, G.I. Frolenkov, D. Klenerman, Y.E. Korchev, Nat. Meth. **6**, 279 (2009)
187. www.veeco.com/pdfs/datasheets/DS57-SECPM_-_04153_189.pdf
188. W.R. Bowen, A.N. Filippov, A.O. Sharif, V.M. Starov, Adv. Colloid. Interface Sci. **81**, 35 (1999)
189. S.V. Kalinin, B.J. Rodriguez, S. Jesse, K. Seal, R. Proksch, S. Hohlbauch, I. Revenko, G.L. Thompson, A.A. Vertegel, Nanotechnology **18**, 424020 (2007)
190. M.P. Nikiforov, V.V. Reukov, G.L. Thompson, A.A. Vertegel, S. Guo, S.V. Kalinin, S. Jesse, Nanotechnology **20**, 405708 (2009)
191. M.P. Nikiforov, G.L. Thompson, V.V. Reukov, S. Jesse, S. Guo, B.J. Rodriguez, K. Seal, A.A. Vertegel, S.V. Kalinin, ACS Nano **4**, 689 (2010)
192. R. Proksch, Appl. Phys. Lett. **89**, 113121 (2006)
193. T.R. Rodríguez, R. García, Appl. Phys. Lett. **84**, 449 (2004)
194. B.J. Rodriguez, S. Jesse, S. Habelitz, R. Proksch, S.V. Kalinin, Nanotechnology **20**, 195701 (2009)
195. R. Plonsey, R.C. Barr, *Bioelectricity: A Quantitative Approach* (Plenum Press, New York, 1988)
196. B.T. Rosner, D.W. van der Weide, Rev. Sci. Instrum. **73**, 2505 (2002)
197. B.J. Rodriguez, S. Jesse, K. Seal, A.P. Baddorf, S.V. Kalinin, P. Rack, Appl. Phys. Lett. **91**, 093130 (2007)
198. T. Fukuma, S.P. Jarvis, Rev. Sci. Instrum. **77**, 043701 (2006)
199. S.P. Jarvis, A. Oral, T.P. Weihs, J.B. Pethica, Rev. Sci. Instrum. **64**, 3515 (1993)
200. D.N. Richards, D.Y. Zemlyanov, R.M. Asrar, Y.Y. Chokshi, E.M. Cook, T.J. Hinton, Z. Lu, V.Q. Nguyen, N.K. Patel, J.R. Usher, S. Vaidyanathan, D.A. Yeung, A. Ivanisevic, J. Phys. Chem. C **114**, 15486 (2010)
201. B. Moores, F. Hane, L. Eng, Z. Leonenko, Ultramicroscopy **110**, 708 (2010)
202. D.M. Czajkowsky, M.J. Allen, V. Elings, Z. Shao, Ultramicroscopy **74**, 1 (1998)
203. O. Takeuchi, Y. Ohrai, S. Yoshido, H. Shigekawa, Jap. J. Appl. Phys. **46**, 5626 (2007)
204. N. Kobayashi, H. Asakawa, T. Fukuma, Rev. Sci. Instrum. **81**, 123705 (2010)

Chapter 13
Measuring Atomic-Scale Variations of the Electrostatic Force

Th. Glatzel

Abstract Kelvin Probe Force Microscopy (KPFM) has proven its ability to map the surface electrostatic potential at nanometer scale with a resolution of a few mV. Recently, even atomic-scale details in KPFM images have been reported; however, complete understanding of basic processes leading to such resolution is still not developed.

Within this chapter experimental and theoretical works dealing with atomic and molecular resolution are reviewed and presented. Recent studies have shown that the atomic-scale contrast in KPFM can be attributed to short-range electrostatic forces. The electrostatic interaction is therefore strongly influenced by the geometrical and chemical composition of the tip-apex. Nevertheless, it will be shown, that site-dependent information of the electrostatic interaction can be drawn down to the atomic scale. In KPFM a detailed analysis of the cross talk between the height measurement and the detected electrostatic forces is unavoidable. Therefore, possible influences and error sources will also be introduced and discussed.

13.1 Introduction

Kelvin Probe Force Microscopy (KPFM) is a scanning probe technique permitting the measurement and compensation of electrostatic forces between a probe and a sample [1, 2]. It is based on a regular noncontact Atomic Force Microscope (nc-AFM) which is generally strongly influenced by electrostatic forces resulting from work function differences of the tip and the surface materials [3, 4]. This technique has proven its ability to map the surface electrostatic potential at nanometer scale with a resolution of a few mV [5–7]. The application of

Th. Glatzel (✉)
Department of Physics, University of Basel, Klingelbergstr. 82, 4056 Basel, Switzerland
e-mail: thilo.glatzel@unibas.ch

S. Sadewasser and T. Glatzel (eds.), *Kelvin Probe Force Microscopy*, Springer Series in Surface Sciences 48, DOI 10.1007/978-3-642-22566-6_13,

multiple simultaneously available probing channels of the surface, such as nc-AFM topography and KPFM images, is of great interest in multiple fields of science [8, 9]. The complimentary information obtained through such studies aids in the interpretation of the images recorded and may prove as a path to provide direct chemical identification of the surface atoms and species imaged.

Sadewasser et al. have shown that the use of KPFM is mandatory in nc-AFM measurements to obtain a reliable height information in a sample with several different materials [3]. Recently also several groups published KPFM measurements showing atomic contrast variations which are controversially discussed. Kitamura et al. showed for the first time atomic contrast of the Si(111)-(7 × 7) reconstructed surface and explained it by an atomic potential difference which reflects the local electron density on the surface while the average contact potential difference (CPD) corresponds to the work function [10–12]. With an comparable setup, frequency modulated KPFM (FM-KPFM), Okamoto et al. imaged the Si(111)-($5\sqrt{3} \times 5\sqrt{3}$)-Sb system showing a contrast between the Si surface and the Sb adatoms. They concluded that the FM-KPFM images mainly reflect the force distribution on the surface rather than the CPD distribution [13, 14]. While another work by Sasahara et al. explained the atomic contrast observed by FM-KPFM on a TiO_2 surfaces with Pd adatoms again by a change of work function due to a difference in the local electron transfer [15].

Since the CPD is by definition a macroscopic property of the tip-surface system, there is currently an intense debate concerning the origin and authenticity of atomic-scale resolution in KPFM. It has previously been advocated that the measured KPFM signal is dependent on the tip-surface imaging distance [14, 16], which implies the possibility of cross-talk occurring when recording KPFM and topographic nc-AFM images simultaneously. Nevertheless, recent experimental and theoretical studies on ionic bulk crystals by AM-KPFM (amplitude modulated KPFM) show a clear evidence for atomically resolved short-range electrostatic force variations of the KBr(100) surface [17–19]. For details see also Chap. 5.

Starting from a general description of the local contact potential difference (LCPD) in the first Sect. 13.2 of this Chapter a detailed overview of the atomically resolved KPFM experiments and their explanations will be given in Sect. 13.3. Possible artifacts as well as optimal measurement conditions will be discussed in the last Sect. 13.4.

13.2 Concept of the Local Work Function

Electron emission and work function measurements can be seen as the beginning of experimental surface science [20]. The work function is very sensitive to the microscopic structure of the surface, i.e., the crystallographic orientation and the structural and chemical condition and as such a valuable quantity for the characterization of surfaces [21–23]. In several publications Wandelt et al. introduced the local character of the work function of real surfaces [24–26]. The definition

of a local work function became useful with the discovery of appropriate local work function probes, namely the photo electron spectroscopy of adsorbed xenon (PAX), the scanning tunneling spectroscopy (STS), and KPFM. In PAX the electron binding energies of xenon atoms adsorbed on non-uniform surfaces are derived by photoemission. They are sensitive to the local work function of the respective adsorption site. As a consequence separated photoemission lines can be resolved corresponding to xenon atoms coexisting on differing surface patches. In order to perform STS measurements and get informations about the local work function, the tunneling current has to be measured as a function of the separation between the tip and a selected point of the sample surface [27–29].

The work function Φ of an infinite homogeneous metal surface is defined as the energy difference between two states of the (semi-infinite) solid at T = 0 K. In the initial state the electron is in the highest occupied level of the neutral ground state of the solid, i.e., at the Fermi level E_F. In the final state the solid is ionized with the electron being at infinity in vacuum at rest, i.e., at the so-called vacuum level E_{vac}. The energy of the electron in the solid described by the uniform-charge-background (jellium) model can be divided in two contributions, the influence of the electrostatic surface-dipole barriers and the chemical bonding [21, 30]. The first contribution arises from the existence of the surface dipole layer: a negative charge density $n_-(z)$ (z normal to the surface) leaks beyond the geometrical surface plane ($z = 0$) thereby creating an excess of negative charge in front of the surface and simultaneously an excess of positive charge $n_+(z)$ on the inside. Any charged particle crossing this surface dipole undergoes a change $\Delta\phi$ in potential energy $\phi(z)$. Both the "thickness" of the dipole layer and, as a consequence, the z-dependence of $\phi(z)$ are rather short-ranged, i.e., of the order of a few Å only [21]. The second contribution arises within the solid due to a lowering of the energy of the electron by the chemical potential μ, i.e., formation of the solid. Thus the work function is given by

$$\Phi = E_{vac} - E_F = \Delta\phi - \mu. \tag{13.1}$$

Upon removing the electron from the solid the electron induces a positive polarization near the surface such that negative charge is repelled. The resultant surface charge can be described as a positive "image point charge" at the same distance inside the solid ($-z$) as the electron is outside the surface ($+z$). The Coulomb interaction between electron and image charge leads to an attractive image potential ϕ_{im} which vanishes only at infinity as considered in the definition of the work function above.

This theoretical concept of the work function neglects several features of real surfaces. Real surfaces are never (a) infinitely extended and (b) completely homogeneous with respect to charge distribution parallel to the surface. Real surfaces are (a) of limited size, (b) made up by discrete atoms (not necessarily in one plane), and (c) mostly include chemical and structural defects (e.g., heteroatoms and steps). The atomistic structure and, in particular, heterogeneities are equivalent to a lateral modulation of the charge density within the surface, i.e., $n_\pm(x, y, z)$ [31–33],

resulting in a variation of $\phi(z)$ and, hence, $\Delta\phi$ parallel to the surface. A few Å away from the surface the energy difference

$$\Phi_{local} = \phi(x, y, z) - E_F = \Delta\phi(x, y, z) - \mu \tag{13.2}$$

thus, acquires the character of a "local work function" which varies with x and y parallel to the surface. More detailed information about the local character of the work function can be found in the stimulating summary of K. Wandelt [26].

13.2.1 Mesoscopic Measurements of the Work Function

After the invention of the AFM [34] and the further development to the KPFM [1, 2] the resolution in the work function signal continuously increased. Various measurements to characterize the technique itself as well as device and surface properties were performed on the microscopic and nanometer length scale. In this section some essential results on semiconducting surfaces resolving local work function variations close to the atomic level (mesoscopic) are presented and discussed. Kitamura et al. published in 1998 nc-AFM studies of the Si(111) surface combined with uncompensated FM-KPFM measurements [10]. While the topography revealed an atomic contrast only a difference between the (7 × 7) and (5 × 2) reconstruction could be observed in the local electrostatic force signal on nanometer length scale. In this measurement no dc-compensation was used, instead directly the ω-component of the electrostatic force (see (2.15)) was plotted.

Figure 13.1a and b shows the ω-component and topography measured by nc-AFM/FM-KPFM on Si(111) containing (7 × 7) and (5 × 2) phases, in an area of 500 × 500 nm^2, respectively. Details are visible in Fig. 13.1c and (d) in an area of 100 × 100 nm^2. The observed surface structure resulted from the evaporation of Au from the cantilever onto the sample surface due to radiant heat when the sample was flashed in close proximity. An ac-bias voltage of 1 kHz frequency with an amplitude of 3 V_{pp} was applied to the tip, while no feedback dc voltage was used.

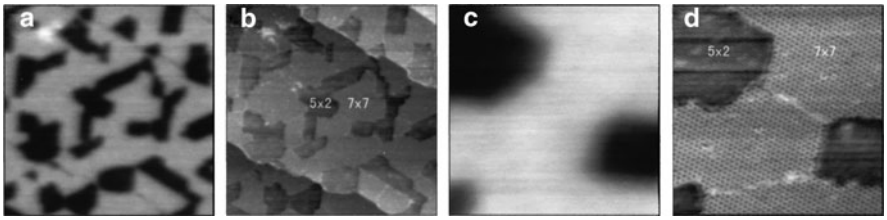

Fig. 13.1 ω-component (**a**,**c**) and topography (**b**,**d**) measured by nc-AFM/FM-KPFM on Si(111) containing (7 × 7) and (5 × 2) phases. Scan size: 500 × 500 nm^2 (**a**,**b**) and 100 × 100 nm^2 (**c**,**d**). Image parameters: f_{ac} = 1 kHz, and V_{ac} = 3 V_{pp} [10]

The data presented in Fig. 13.1 displays directly the change of the output voltage taken from the lock-in amplifier. Therefore, the measurements do not correspond to the actual CPD but are directly related to the ω-component of the electrostatic force. The bias polarity was set so that the CPD images are darkened when the sample bias voltage is negative. The bright and dark regions in the images of the ω-component correspond to (7×7) and (5×2) phases, respectively. The real potential difference between the phases, estimated by a rough manual adjustment of V_{dc} was approximately 0.5 eV [10].

Shiota et al. [35] observed on a quenched Si(111) surface a triangular surface structure. A feedback loop to compensate the effect of the electrostatic force was not applied during the observation (Fig. 13.2a). The $A - A'$ markers in this figure label monoatomic step edges. Bright triangular and dark areas corresponding to (7×7) and (1×1) reconstructed domains coexist on the quenched Si(111) surface. In order to identify the atomic arrangement topographic measurements were performed in an enlarged area of $20 \times 20\,\text{nm}^2$ showing a clear (7×7) reconstructed structure. Nevertheless, the height information between the different domains does not correlate well with known and calculated values. Therefore, the authors measured the surface potential distribution in the same area again by FM-KPFM presented in Fig. 13.2b and c. Similar to Kitamura et al. they used an electrostatic excitation signal at 1 kHz frequency and with an amplitude of 3 V_{pp} applied to the tip. By comparing the pure nc-AFM image of Fig. 13.2a with the KPFM image of Fig. 13.2b it was found that the surface potential of the (7×7) domains has larger values than that of the (1×1) domains. The corresponding topography Fig. 13.2c shows that the height of the quenched Si(111) surface with the (7×7) domains is around 50 pm lower than the (1×1) area, which is close to the expected values. The results show again clearly the beneficial impact of KPFM in the determination of correct height information even on mesoscopic length scales like these nanometer-sized domains. Since most of the height information is strongly influenced by electrostatic forces varying between materials as well as different surface reconstructions.

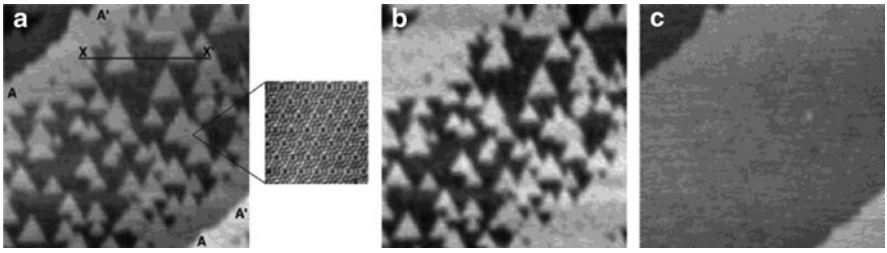

Fig. 13.2 (**a**) nc-AFM topography of a quenched Si(111) surface without electrostatic force compensation in an area of $1,520 \times 1,520\,\text{nm}^2$. The triangular structures are the (7×7) reconstructed domains. (**b**) and (**c**) are the potential distribution and the topography of the same area measured by FM-KPFM and nc-AFM, simultaneously. Image parameters: $f_{ac} = 1$ kHz, and $V_{ac} = 3\ V_{pp}$ [35]

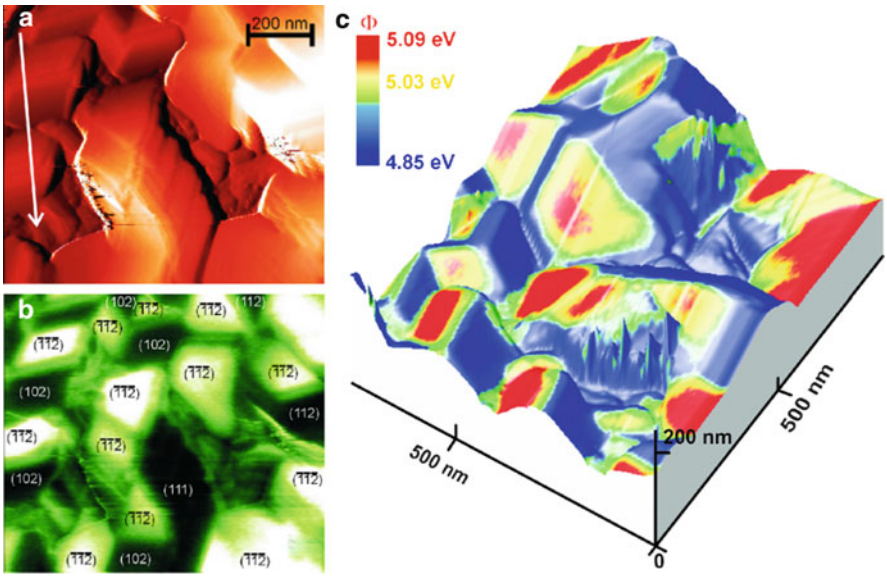

Fig. 13.3 KPFM measurement of polycrystalline $CuGaSe_2$ thin films on a ZnSe(110) substrate. (**a**) The topography showing distinct crystal facets on the (220) oriented film ($\Delta z = 384$ nm). (**b**) The simultaneously measured work function shows constant values for the various facets ($\Phi = 4.85...5.09$ eV). The crystallographic orientation of the facets is assigned based on the angles to other facets and to the surface normal (reprinted from [23])

Another study showing a detailed analysis of the influence of reconstruction was performed on the surface of $CuGaSe_2$ absorber material grown on a ZnSe(110) substrate [23]. The analyzed polycrystalline film was oriented along the (220) direction. In the AM-KPFM study, absolute work function values on differently oriented facets of the grains were determined. Distinct values with differences between the facets as small as 30 meV and up to 255 meV were clearly observed (Fig. 13.3). The differences were explained by a different surface dipole, determined by the orientation and termination of the surface. Moreover, due to the oriented growth, it was possible to determine the orientation of the facets, thereby allowing the direct assignment of the work function values to the surface orientation.

Besides the variations of the local work function depending on the surface reconstruction also measurements at the mesoscopic length scale of step edges where analyzed [36]. In Fig. 13.4 the topography and the work function measured by AM-KPFM of p- and n-type doped GaAs(110) are presented. Additionally, averaged line profiles are plotted. It is clearly seen that local work function changes are associated with the steps, a depression is observed on the p-type sample, whereas the n-type GaAs(110) shows a local work function increase along the step edge. This was explained by the authors with localized charge-induced downward and upward band bending at the step edges. Thus, the steps are found to be positively charged on p-type doped and negatively charged on n-type doped materials.

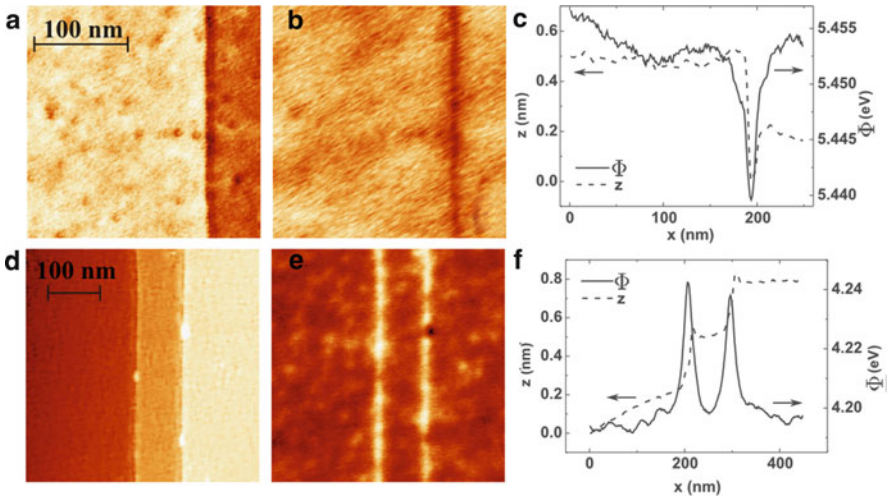

Fig. 13.4 AM-KPFM measurements on UHV cleaved n-type (**a**–**c**) and p-type (**d**–**f**) GaAs(110). The topography (**a**) shows a n-type GaAs monolayer step ($\Delta z = 0.55$ nm). The simultaneously measured work function (**b**) shows a downward band bending at the step edge ($\Phi = 5.44 - 5.46$ eV). (**d**) topography of two separate monolayer steps of p-type GaAs ($\Delta z = 0.83$ nm) and (**e**) the corresponding work function which shows an upward band bending at the step edges ($\Phi = 4.19 - 4.24$ eV). The profiles in (**c**) and (**f**) show an average value of the respective data perpendicular to the step edges [36]

The presented measurements show some examples of KPFM measurements at length scales in the region of several tenth of nanometers. In certain cases the results can directly be related to macroscopic work function values determined by theoretical calculations or macroscopic measurements of the work function. The last example already shows the limit of the technique which is the convolution of the detected electrostatic force signal with the geometry of the detecting cantilever. By taking the shape of the cantilever into account absolute charge densities at the step edges can nevertheless be obtained [6]. Going one step further leads us to the question if localized surface dipoles induced by single molecules or molecular self assemblies can also be quantitatively detected by KPFM.

13.2.2 Molecular Variations of the Local Contact Potential Difference

Molecular electronics relies on electrical contacts of the molecular assemblies. While electrical properties of single molecules can be measured by means of break-junction techniques or STM, the properties of larger structures are not easily accessible. Molecular assemblies grown on metallic substrates have to be electrically decoupled, which is feasible by the deposition of alkali-halide thin films

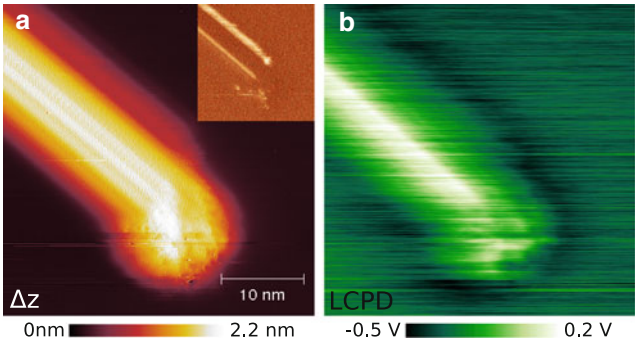

Fig. 13.5 Topography (**a**) and LCPD (**b**) images with a size of 30×30 nm^2 of the interface between stacked porphyrin molecules and an Au nanocluster. For contrast enhancement the derivative of the topography was added to (**a**). The inset of (**a**) shows the dissipation signal ranging up to 1.6 eV/cycle at certain brighter areas above the molecular structure. Scan parameters: $f_{1st} = 173.013$ kHz, $\Delta f_{1st} = -11$ Hz, $A_{1st} = 10$ nm, $f_{ac} = 1.086$ MHz, and $V_{ac} = 500$ mV. [51]

as an insulating spacer [37, 38]. Nevertheless, a complete decoupling can only be achieved by using several monolayers thick or even bulk insulators which requires AFM for measurements. In the past years many attempts to observe molecular self assemblies on insulating materials have been performed. It has been discovered that the high mobility of organic molecules on non-metallic surfaces can be lowered by inducing radiation defects [39, 40] or modified molecular structures [41–44]. The question is, can we use KPFM to identify combined structural and electronic properties of the adsorbed molecules? Several studies of imaging molecular self assemblies by KPFM on insulating surfaces were performed under ambient [8, 45] as well as UHV conditions, e.g., [7, 46–49] but nearly single molecular resolution was observed only recently [50, 51]. While Chap. 11 describes more mesoscopic variations of the LCPD on molecular structures we will in the following concentrate more on reviewing high-resolution measurements.

Figure 13.5 shows such a measurement of a contact between an Au cluster and a molecular assembly of cyano-porphyrines [51]. The LCPD image in Fig. 13.5b resolves clear differences among the KBr surface, the Au nano-cluster and the molecular wires. The different materials can be distinguished by means of the LCPD. Differences of $\approx$250 mV between the KBr surface and the Au nano-clusters and of $\approx$220 mV between Au nano-cluster and the molecular wire were measured. Furthermore, different LCPD values at the wire $\Delta V_{LCPD} = 180 \pm 20$ mV are observed and explained by an asymmetric molecular orientation, which would have a direct influence on the strength of the local dipole moment and therefore also on the LCPD. The difference in dipole moment densities (Δp) is related to the LCPD by $\Delta V_{LCPD} = 1/\epsilon_0 \Delta p$ which results in 0.5 Dnm^{-2}. Assuming a molecule density of 0.72 nm^{-2} [41] yields to an average dipole moment density difference per molecule of 0.36 D, which is a reasonable value taking the absolute dipole moment of a single cyanoporphyrin of 4.37 D into account. Nevertheless, it was stated, that besides the well-known averaging effect [52] KPFM measurements at very close

proximity to the surface (<1 nm) are also strongly distance dependent and therefore absolute predictions are only feasible combined with theoretical considerations. However, in the present measurements the LCPD is mainly influenced by the averaging effect which reduces the measured LCPD difference, and therefore the determined dipole moment difference can be assumed to be a lower limit.

In Fig. 13.6 another measurement of such a molecular porphyrin wire is shown. The substrate in that case is not a single crystal but a thin NaCl layer on a Cu(111) surface. Within this image NaCl steps with and without decoration can be found. At the first sight the molecular ordering looks the same for every step edge, but having a closer look to the surface potential in Fig. 13.6b reveals two different types of step decoration. One which leads to an increased potential of around 20 mV and the other exhibits a decreased potential of around 40 mV compared to the surface potential measured at the bare NaCl surface. In Fig. 13.6c an averaged line scan indicated

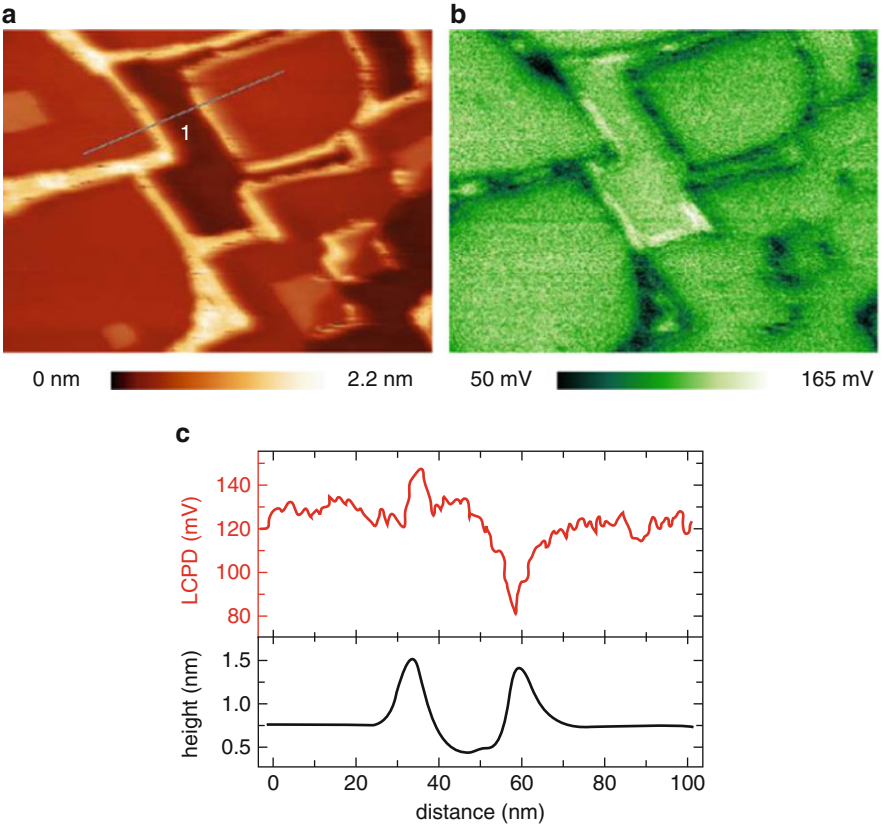

Fig. 13.6 Topography (**a**) (200 × 150 nm^2) with the simultaneously measured surface potential image (**b**) of a NaCl thin film with porphyrin wires on Cu(111). In the graph (**c**) the line section taken from the same position of (**a**) and (**b**) are shown. Image parameters: $f_{1st} = 170.317$ kHz, $A_{1st} = 10$ nm, $\Delta f_{1st} = -8$ Hz, $f_{ac} = 1004.810$ kHz, and $V_{ac} = 500$ mV [53]

in the topography image is shown. Also in the topography a difference of the step decoration is observed, the molecules which have a decreased surface potential are also around 10 pm reduced in height compared to the others. These findings are explained by differently oriented molecules attached to NaCl step edges which was not observed on a crystalline NaCl nor on KBr surfaces [53].

Even higher resolution was observed by Ichii et al. of a CuPc monolayer on a bare Au(111) surface presented in Fig. 13.7a [54]. Although submolecular resolution was not achieved in that case, a clear molecularly resolved image was obtained. Figure 13.7b shows the LCPD obtained simultaneously with the topography in FM-KPFM mode using 600 Hz and 10 V_{pp} for the electrical excitation. Some horizontal

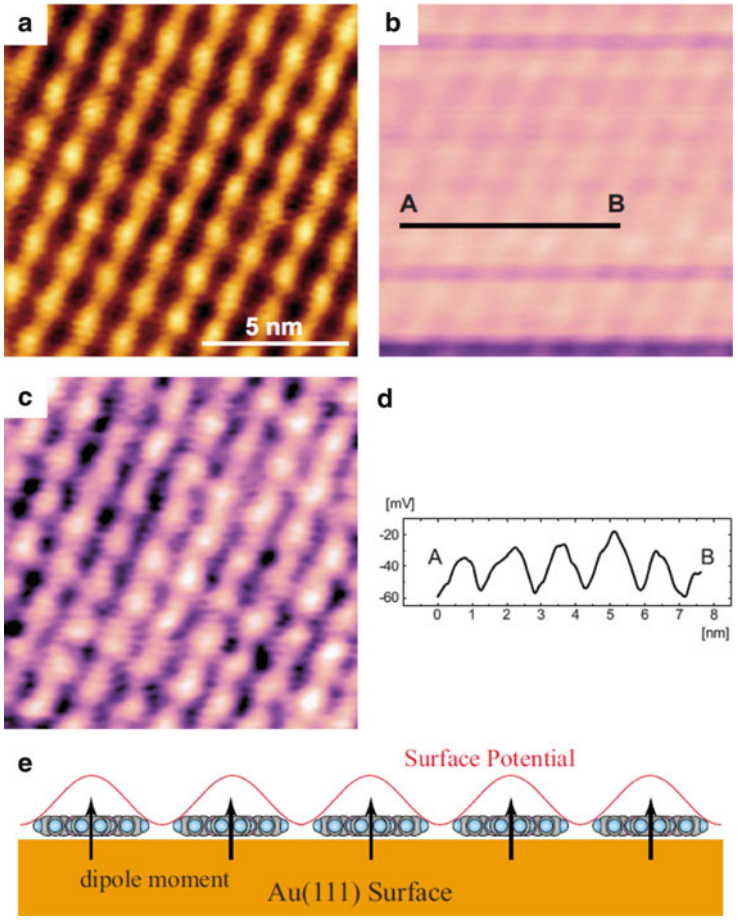

Fig. 13.7 nc-AFM/FM-KPFM measurements, topography (**a**), LCPD (**b**), and image processed LCPD (**c**) of a CuPc monolayer on an Au(111) surface with a size of 12×12 nm^2. (**d**) Cross-section measured along the A-B line indicated in (**b**). (**e**) Model of the molecular dipole moment. Image parameters: $f_{1st} \approx 300$ kHz, $A_{1st} \approx 5$ nm, $\Delta f_{1st} = -170$ Hz, $f_{ac} = 600$ Hz, and $V_{ac} = 10$ V. [54]

jumps due to abrupt changes, most probably due to local changes of the tip apex, were removed by image processing to increase the local contrast (Fig. 13.7c). The image clearly shows molecular-scale LCPD variations indicating a higher surface potential (bias applied to the sample) at the molecules. The difference between the CuPc molecules and the intermolecular region was approximately 30 mV, as shown in the cross-sectional profile. This result was explained by the electric dipole moment on the interface between the CuPc molecules and the Au substrate as illustrated schematically in Fig. 13.7e. Nevertheless, a quantitative determination of the local dipole moment was not possible due to unknown tip contributions to the signal. The origin of the interface dipole moment was related to a higher concentration of electrons in the molecules and/or rearrangements of the electron clouds at the Au surface [54].

Another example for single molecular resolution in KPFM on molecular assemblies is shown in Fig. 13.8. Truxene molecules [55] were evaporated on a KBr single crystal surface and analyzed by AM-KPFM at RT. To form this single layer molecular assembly the sample was annealed at 150° for 15 min. As shown in the chemical structure of truxene (Fig. 13.8c) the molecules have three CN-groups inducing a relatively strong dipole moment. It is known that the binding of the molecules to ionic surfaces is strongly enhanced by electrical interactions [44]. In the topographical image a clear hexagonal arrangement of the molecules can be seen. Even so submolecular resolution was obtained a clear determination of the molecular arrangement could not be determined. Most likely the three CN-groups are directed toward the KBr surface. The LCPD image in Fig. 13.8b shows a clear contrast of 200 mV between the molecules and the substrate and even a weak submolecular contrast is observed. In contrast to the studies of CuPc on Au(111) discussed before, here the molecules have a lower LCPD than the substrate indicating a more positive localized charge, which is in perfect agreement with the expected direction of the dipole moments. A more careful analysis of the data might even lead to a structural model of the absorbed molecules. Nevertheless,

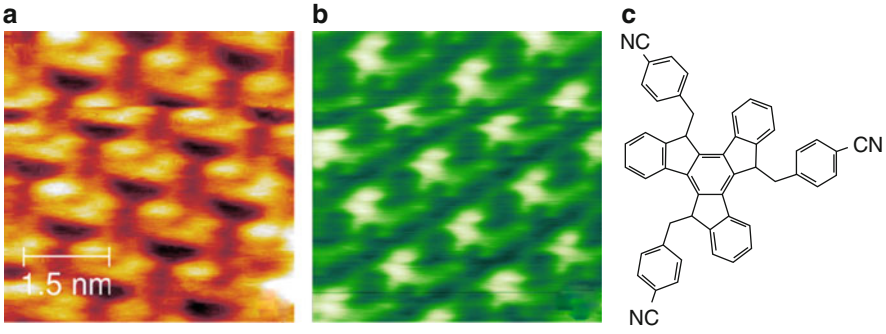

Fig. 13.8 Topography (**a**) and LCPD (**b**) measured by AM-KPFM of truxene molecules (**c**) on a KBr single crystal with a size of 5×5 nm^2. The LCPD shows a clear submolecular contrast as well as a decreased surface potential at the molecules. Image parameters: $\Delta z = 150$ pm, LCPD $= -300...100$ mV, $\Delta f_{1st} = -11.6$ Hz, $A_{1st} = 10$ nm, $V_{ac} = 1$ V_{pp}, $f_{ac} = 938.634$ kHz

a quantitative analysis of the data can only be performed by a fundamental analysis of the short-range electrostatic interaction including tip apex and local substrate deformations as well as possible averaging effects.

13.3 Measurements at the Atomic Scale

In Sect. 13.2 the concept of the local work function as well as experiments giving a clear evidence for surface potential variations at the molecular or even submolecular range were presented and discussed. These variations are mainly induced by local charge variations due to varying molecular orientations, changed electron densities or different coupling to the substrate. These electrical properties have a direct influence on the work function which can also be measured far away from the surface covered by a comparable but homogeneous molecular film. One step further, in this section experiments will be presented showing LCPD variations at the atomic scale. Some of the results were discussed very critically within the last decade, since the work function concept does not include a local character ranging down to a single atomic site. Nevertheless, several authors presented atomic-scale KPFM measurements explained by different approaches.

13.3.1 The Silicon(111)-(7 × 7) Surface

One of the most analyzed surface by nc-AFM in UHV is the reconstructed Si(111)-(7 × 7) surface [56, 57]. Recently, even atom identification on a Sn and Pb covered Si(111) surface was reported [58]. Also atomically resolved KPFM measurements were obtained mainly on this substrate which are presented and discussed in this section.

In Figure 13.9 an early nc-AFM/FM-KPFM experiment from Kitamura et al. [10] with a scan range of $20 \times 20\ nm^2$ is shown. The FM-KPFM measurement was obtained simultaneously to the topography (Fig. 13.9b) in standard FM technique

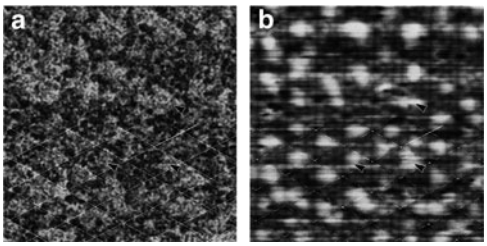

Fig. 13.9 Simultaneously acquired LCPD (**a**) and topography (**b**) of the Si(111)-(7 × 7) surface with Ag deposits with a scan size of $20 \times 20\ nm^2$. Image parameters: $V_{ac} = 3\ V_{pp}$, $f_{ac} = 2$ kHz [10]

on a Si(111)-(7 × 7) surface covered partly with Ag. The mesh shown at the bottom corresponds to a (7 × 7) unit cell and most of the bright regions correspond to Ag clusters as marked by the arrows. Since a voltage feedback loop was applied to the tip potential the voltage contrast in Fig. 13.9a represents the inverted LCPD, brighter values are areas with a lower local work function. Thus, the LCPD image was observed with atomic level resolution, not only discriminating the Ag clusters deposited on the faulted half of the Si(111)-(7 × 7) unit cells but also showing a higher local work function of the (7 × 7) structure than that of the Ag clusters by approximately 10 mV. Even so the contrast is very weak, this measurement was one of the first atomically resolved KPFM measurements.

Following these studies Okamoto et al. used a Si(111)-$(5\sqrt{3} \times 5\sqrt{3})$-Sb reconstructed surface [13] to identify and distinguish Si and Sb atoms. They performed FM-KPFM measurements using a Si-cantilever cleaned by Ar-ion bombardment. Figure 13.10 shows a nc-AFM measurement of such a surface with a scan size of 12.1 × 8.5 nm^2. Simultaneously the LCPD was measured by FM-KPFM (c), while it is not clear if the dc-bias was applied to the tip or the sample, only qualitative conclusions can be drawn. The Sb adatoms of the structure are visible as bright spots in the topography (a), although the periodicity of the $(5\sqrt{3} \times 5\sqrt{3})$ reconstruction is not complete. A hexagon indicates one unit cell. In the LCPD image (c) the adatoms are imaged as black spots and it can even be seen that there are two kinds of adatoms, i.e., there is a slight height difference in the topography, and an obvious potential difference in the LCPD image. The line section in Fig. 13.10b includes both kinds of adatoms. Those differences where attributed by the authors to the influence by the different atomic species. Thus, the circled adatoms are specified as Si adatoms, since the circles indicate slightly larger adatoms in the topography (a) and darker adatoms in the LCPD (c), it was concluded that Si and Sb atoms could be distinguished

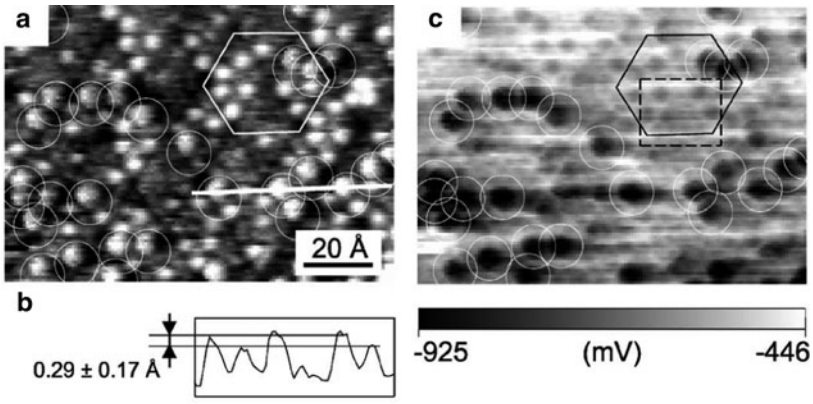

Fig. 13.10 Topography (**a**) of a Sb covered Si(111) sample, the cross section at the white solid line on the topography (**b**), and the LCPD (**c**) image with a size of 12.1 × 8.5 nm^2 obtained by nc-AFM and FM-KPFM. Image parameters: $f_{1st} = 167$ kHz, $A_{1st} = 10.2$ nm, $\Delta f_{1st} = -29$ Hz, $V_{ac} = 1\ V_{rms}$, $f_{ac} = 1$ kHz [13]

through the LCPD image, while the difference was not decisive in the topography. Nevertheless, the authors pointed already out that KPFM possibly measures other kinds of information besides the LCPD. They considered the effect of band bending, which can occur due to the semiconducting character of tip and sample and the usage of quite high ac-bias voltage $V_{ac} = 1\ V_{rms}$ at low frequency $f_{ac} = 1$ kHz. Since in the principle of KPFM, the dependence of the capacitance between tip and sample on the bias voltage is not considered an induced band bending might influence the results. Furthermore, influences like the additional modulation of the tip-sample distance as well as a tunneling current occurring at very close proximity of the conductive tip and the sample might occur. They concluded that Si and Sb adatoms can be distinguished by KPFM due to the difference in their electrical properties, such as work function, ionization energy, electronegativity, or the local distribution of electron density.

Following these exciting results, other groups further improved the resolution in KPFM to study the origin and the quantitative character of the LCPD signal at atomic scale. Figure 13.11 shows a nc-AFM (a) and FM-KPFM (b) measurement of a Si(111)-(7 × 7) surface observed under a constant frequency shift of $\Delta f_{1st} = -78$ Hz and a regulated amplitude of $A_{1st} = 11.1$ nm [59]. The oscillation amplitude dropped during the observation by $A_{1st} = 250$ pm marked in the center of the image. The rapid decrease in the oscillation amplitude indicates that the cantilever tip was brought into soft contact with the surface. After this contact, the nc-AFM image slightly changed by an offset while the contrast of the LCPD image reflecting the tip bias voltage became inverse. The authors explained this contrast inversion by a removal and/or attachment of atoms at the tip-apex changing the short-range interaction between the front most atom at the tip-apex and the Si adatoms at the surface. The results seem to indicate a strong dependence of the LCPD on short-range forces as well as on the tip-apex condition. Nevertheless, it was still unclear if the atomic contrast is only an artifact induced by a local band bending, the tip-sample distance modulation or the tunneling current. Furthermore, the origin of the detected short-range force stayed unclear.

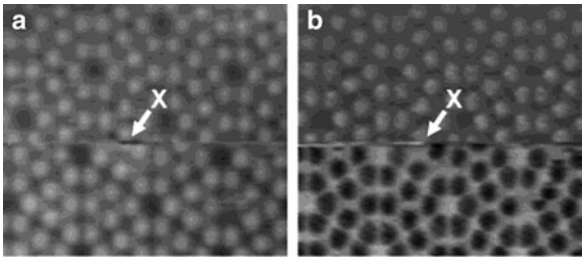

Fig. 13.11 A simultaneously measured nc-AFM (**a**) and FM-KPFM (**b**) image of a Si(111)-(7 × 7) surface with a size of 9 × 10 nm^2. In the center of the image a tip apex change occurred and the contrast of the LCPD inverted while the topography did not. Image parameters: $f_{1st} \approx 350$ kHz, $\Delta f_{1st} = -78$ Hz, $A_{1st} = 11.1$ nm, $V_{ac} = 2\ V_{pp}$, $f_{ac} = 1$ kHz [59]

The first AM-KPFM measurements on Si(111)-(7 × 7) were presented by Kawai et al. in 2010 [60]. The main benefits compared to the FM-KPFM measurements were the reduced ac-bias voltage down to $V_{ac} = 250$ mV omitting the band bending effect while keeping high energy sensitivity and the usage of a high ac-bias frequency to avoid disturbing tip-sample distance modulations. In these studies the ac- and dc-bias voltages were applied to the sample and the ac-frequency was tuned to the second resonance of the cantilever. Figure 13.12a shows a topography obtained with an amplitude A_{1st} of 13 nm at a frequency shift Δf_{1st} of −5.45 Hz in an area of 8.3×8.3 nm^2. The clear atomic contrast indicates that the tip apex had a bare dangling bond without any oxide layer. Figure 13.12b shows the simultaneously detected LCPD map. As can be seen, atomic corrugations were clearly observed. The LCPDs at the adatom and the corner hole CoH were approximately −170 mV and −157 mV, respectively. The adatom had a more negative LCPD than the CoH, and this relationship is consistent with previous results [12, 59]. Furthermore, three foreign atoms presumably related to contamination were clearly observed (Co1 −202 mV, Co2 −210 mV, and Ce1 −182 mV). These adsorbates stayed on their positions for more than 100 min. Contrary to the previous experiments carried out by Kitamura et al. [11] and Shiota et al. [61], the intensity of the atomic contrast

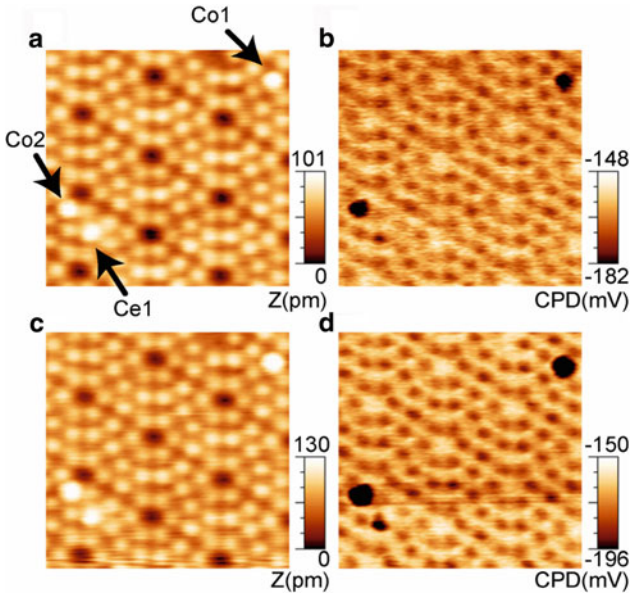

Fig. 13.12 (**a**) and (**c**) are topographies and (**b**) and (**d**) the corresponding LCPD maps taken simultaneously on a Si(111)-(7 × 7) surface (8.3×8.3 nm^2) by AM-KPFM. Three foreign atoms on the corner adatom CoA and center adatom CeA sites are labeled Co1 and Co2, and Ce1, respectively. Measurements (**a**) and (**b**) were taken at $\Delta f_{1st} = -5.45$ Hz, while (**c**) and (**d**) were taken at $\Delta f_{1st} = -6.05$ Hz. Image parameters: $f_{1st} = 150.491$ kHz, $Q_{1st} = 30,000$, $A_{1st} = 13$ nm, $f_{2nd} = 939.182$ kHz, $Q_{2nd} = 12,800$, $V_{ac} = 250$ mV [60]

was changed by the tip-sample distance. Figure 13.12c and d shows the topography and simultaneously detected LCPD map at a smaller tip-sample distance regulated at $\Delta f_{1st} = -6.05$ Hz. The topography corrugation amplitude changed from 65 pm to 100 pm, while the LCPDs at the adatom and the CoH were also changed to −185 mV and −160 mV, respectively. The shift of the LCPD at the adatom was much larger than at the CoH. These shifts were also observed at the contamination sites (Co1 −243 mV, Co2 −259 mV, and Ce1 −209 mV). The measured LCPD was found to be strongly affected by the tip-sample distance, and the amount of the shift was site-dependent. This effect was analyzed in detail by various constant height measurements and was attributed to the influence of short-range electrostatic forces, originating from charges between single atoms.

To unambiguously determine the short-range character obtained by KPFM on different atomic sites local bias-spectroscopy data are a very suitable detection method. Sadewasser et al. performed such rigorous analysis on Si(111) covered by several individual Pb adatoms [97]. Figure 13.13 summarizes a comparison of several spectroscopic measurements over various atomic positions of such a surface.

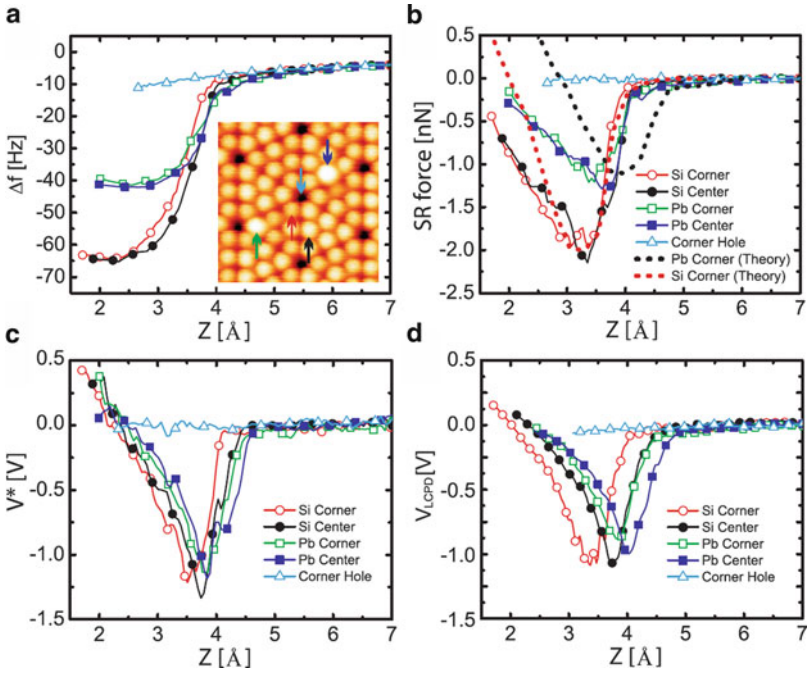

Fig. 13.13 Bias-spectroscopy reveals detailed information on the short-range interaction. (**a**) $\Delta f(z)$ curves extracted from $\Delta f(V_{dc}, z)$ maps (Δf determined at minimum electrostatic interaction for each tip-surface separation $\Delta f(V_{dc} = V^*, z)$) measured over the atomic positions marked with arrows in the inset topography image on Si(111) covered with Pb adatoms. (**b**) Short-range interaction force obtained from the $\Delta f(z)$ curves in (**a**). (**c**) and (**d**) variations of V^* and the V_{LCPD} obtained by activated FM-KPFM circuit with the tip-surface separation, respectively [97]

Figure 13.13a displays $\Delta f(z)$ curves obtained from $\Delta f(V_{dc}, z)$ maps acquired over the atoms pointed by arrows in the inset image. The values of these $\Delta f(z)$ curves quantify the Δf at minimum electrostatic interaction for each tip-surface separation, i.e., $\Delta f(V_{dc} = V^*, z)$, obtained from parabolic fits to the horizontal line profiles of the corresponding $\Delta f(V_{dc}, z)$ map. The short-range forces obtained from these $\Delta f(z)$ curves and the corresponding variation of V^* with the tip-surface separation are displayed in Fig. 13.13b and c, respectively. Surprisingly, $V^*(z)$ shows a considerable drop at the onset of the short-range force from an almost constant value of 180 mV away from the surface down to −1.25 V near the region of the maximum attractive short-range force. Similar behavior is obtained when performing force spectroscopy over the same atoms with identical tip-apex termination but compensating the LCPD at each point of the $\Delta f(z)$ curve by using KPFM (d). The short-range forces obtained by the latter method and from $\Delta f(z)$ curves produced by choosing $V_{dc} = 180$ mV in the $\Delta f(V_{dc}, z)$ maps match the ones displayed in Fig 13.13b. The similarities of the KPFM and bias-spectroscopy images point toward the ac-bias in KPFM having no significant influence on the measured LCPD values, in agreement with the previously discussed AM-KPFM measurements. Furthermore, the authors state that the inspection of all the measured $\Delta f(V_{dc})$ curves obtained from the latter two methods showed no indication of a deviation from a parabolic behavior up to tip-surface separations close to the repulsive part of the short-range interaction force. Thus, they conclude that neither the application of the ac-bias [62], nor the occurrence of a resonant tunneling [63] seem to be responsible for the atomic contrast in LCPD measurements at separations close to the onset of the short-range interaction force.

13.3.2 III–V Semiconductors

Not only Si surfaces were analyzed by KPFM but also surfaces of III–V semiconductors as GaAs and InP. Nevertheless, most of the studies are based on the characterization of devices or mesoscopic structures and are not focused on atomic resolution. One of the first atomically resolved measurements was presented by Sugawara et al. in 1995 [64, 65]. They presented nc-AFM measurements taken in UHV with atomic resolution for the semi-insulating InP(110) surface. They observed atomic-scale point defects at room temperature, and studied thermally induced motion of atoms or defects in real space. Following these achievements they implemented the simultaneous detection of electrostatic and van der Waals forces by electrostatic force microscopy (EFM) [66, 67].

Figure 13.14 shows such simultaneously determined topography and EFM images measured on a GaAs(110) surface. In that case the electrostatic forces are not compensated but measured via the ω-component of the electrostatic force (see (2.15)), which contains not only the dependence on the work function difference but also influences of the capacitance gradient. Therefore, a direct relation to work function differences cannot be drawn. For the EFM imaging in Fig. 13.14b the

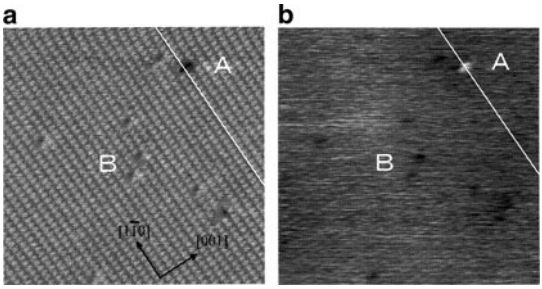

Fig. 13.14 (**a**) Topography and (**b**) EFM measurements of a GaAs(110) surface with a size of $15 \times 15\ nm^2$. Image parameters: $f_{1st} = 159$ kHz, $A_{1st} = 2.9$ nm, $Q_{1st} = 38{,}000$, $\Delta f_{1st} = -231$ Hz, $V_{dc} = +500$ mV applied to the sample, and an ac-frequency of $f_{ac} = 500$ Hz [67]

sample was biased at $V_{dc} = +500$ mV and the electrostatic force was measured at constant height. The topography presented in Fig. 13.14a illustrates the actual capability of true atomic resolution imaging showing atomic-scale point defects as depressions in the height contrast. Two kinds of defects were observed: large and deep defects marked as "A" and small and shallow defects marked as "B". According to STM results the atomic-scale defects on GaAs(110) can be classified into five groups [68]. However, only by the nc-AFM topography the details of the defects cannot be identified. Interestingly, large and deep point defects "A" appeared as bright contrast with respect to the background in the EFM measurement. By varying the sample bias voltage, the authors demonstrated that the bright contrast of the electrostatic force gradient in Fig. 13.14b can be assigned to a positive charge at the atomic-scale point defect.

Another III–V semiconductor which was analyzed at atomic scale by nc-AFM is the InSb(100) surface [69]. Krok et al. focused their analysis on the study of the limits of potential and lateral resolutions in FM-KPFM [70]. They have investigated the clean surface of InSb(100) and the same surface with some submonolayer coverages of KBr and Au. It was found that long- and short-range bias-dependent interactions, acting between the tip and the surface, could be detected and that both interactions contribute to the measured LCPD. For the FM-KPFM measurements, the sample was biased with an ac voltage at a frequency of $f_{ac} = 600$ Hz and a reasonably small amplitude of $V_{ac} = 300$ mV.

In Fig. 13.15 high-resolution measurements of the topography (a) and the LCPD (b) of the bare InSb(001) surface are shown. The reconstructed surface is composed of atomic rows running along the ⟨110⟩ crystallographic direction. Based on earlier studies of the same group [69] the structure can be related to an indium sublattice, where the dominant indium chains, visible as bright lines in the topography, protrude about 120 pm over the rest of the surface. Theoretically only variations in the range of 90 pm are expected [71], which might be explained by a wrong z-calibration, a displacement of the In atoms at the surface due to the tip-sample interaction or by a not fully compensated electrostatic force field. In the

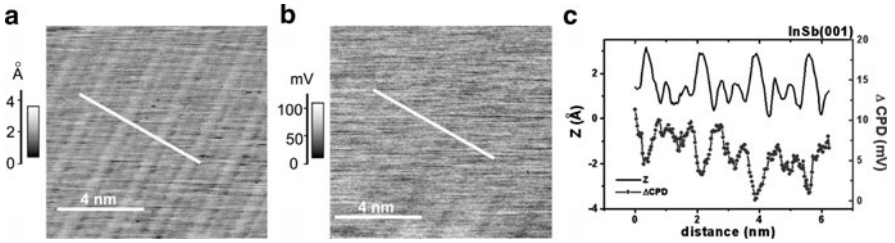

Fig. 13.15 High resolution (**a**) nc-AFM topography and (**b**) FM-KPFM LCPD measurements of a InSb(001) surface with a size of 10×10 nm^2. (**c**) shows profiles of the topography as a solid line and the LCPD as solid circles. The profiles are averaged over a few lines as shown in (**a**) and (**b**). Image parameters: $A_{1st} \approx 20 - 50$ nm, $\Delta f_{1st} = -112$ Hz, $f_{ac} = 600$ Hz, $V_{ac} = 300$ mV [70]

corresponding LCPD measurement (b) similar structures of dark stripes running parallel to the topographic atomic rows can be recognized. In Fig. 13.15c, profiles of the topography (solid line) and the LCPD (solid circles) along the lines in the images are plotted. In the profile of the LCPD signal dips of about 5 mV are observed, which are out of phase with the topographic features corresponding to the dominant indium atomic chains. The authors argue that such lateral modulations of the LCPD signal, which are visible in the range of distances comparable to the surface atom separations, indicate short-range tip-surface forces. These interactions are bias-dependent and most likely related to the tip-apex atom and the surface atom underneath. Finally they conclude that the obtained LCPD cannot be directly related to the CPD between the tip and the surface.

13.3.3 Rutile TiO_2

Also metal oxides having metallic, semiconducting, and insulating properties are of great scientific and technological importance. Rutile TiO_2 has been thoroughly investigated as a model system, and is widely known to form stoichiometric (1×1) phases and slightly reduced (1×2) phases [72]. Both phases have been visualized on a true atomic resolution level by nc-AFM several times, which imaged the surface structures of the uppermost oxygen atoms, including atomic-scale defects [73, 74]. Thus, $TiO_2(110)$ is used both as a material for learning about the contribution of surface electronic states to atomic resolution nc-AFM [75–79] as well as for advanced material properties and the influence of adsorbates [15, 80–84]. While Chap. 10 by Onishi and Sasahara is focused mainly on the study of the change of work function due to the adsorption of metal clusters on rutile TiO_2 we want to present and discuss here mainly the origin of the atomic contrast in the KPFM signal on the same surface.

One of the first measurements of a clear atomic corrugation and an interpretation leading to a KPFM contrast which is induced by a charge transfer from Na-adsorbates to the surface was presented by Sasahara et al. [80]. Figure 13.16

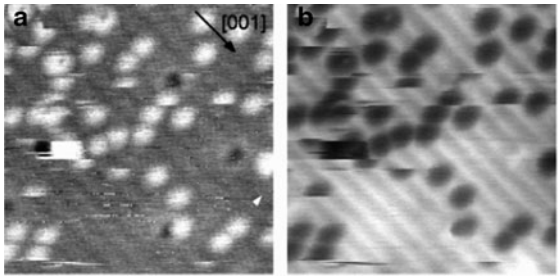

Fig. 13.16 Simultaneously obtained (**a**) topography and (**b**) LCPD image of a TiO_2 surface with a size of 10×10 nm^2 covered by adsorbates. Image parameters: $f_{1st} \approx 300$ kHz, $\Delta f_{1st} = -78$ Hz, $A_{1st} \approx 6.6$ nm, $f_{ac} = 2$ kHz, $V_{ac} = 2$ V [15]

shows a simultaneously recorded topography image (a) and the corresponding LCPD (b) of a $TiO_2(110)$ surface covered by Pt-clusters, respectively. In the topographic image, both the adatom and oxygen atom rows are resolved. The contrast of the LCPD in Fig. 13.16b was adjusted so that areas with larger local work functions are shown brighter. The positions of the Pt adatoms are darker than the surrounding TiO_2 surface, indicating a decrease of the local work function on the Pt adatoms in the range of 250 meV. The authors observed always a smaller local work function above the Pt adatoms than the one of the surrounding TiO_2 surface, even when the contrast between the O atom rows and Ti atom rows was sometimes reversed in the work function map. They concluded that the local work function at the adatoms was locally perturbed by an electric dipole moment directed from the substrate to the vacuum which locally decreases the work function. Even so these results fit very well to the expected physical behavior, still it stayed unclear why the contrast of the images changed while scanning and how quantitative these results are. Enevoldsen et al. discussed these phenomena which was also observed in standard nc-AFM measurements and reduced it to the influence of a localized charge at the tip apex [75,76]. Such a charged tip apex should also have an influence in KPFM measurements which might be used to clarify the contrast mechanisms as well as the tip apex condition.

In Fig. 13.17a and b simultaneously recorded nc-AFM topography and LCPD images by AM-KPFM are shown, respectively. The dark-bright striped pattern visible in the topography reflects the normal appearance of the $TiO_2(1 \times 1)$ surface structure, with alternating rows of bridging oxygen atoms (O(2c)) and in-plane titanium atoms (Ti(5c)) in the [001] surface direction. The same (1×1) pattern is also resolved in the LCPD image (Fig. 13.17b) which shows that additional local contributions to the macroscopic CPD are playing a key role in the image contrast generation. The local potential set up by the individual ions on the $TiO_2(110)$ surface (formally O^{2-} and Ti^{4+}) is added to the CPD background, and the resulting LCPD is clearly detectable. Even though no hydroxyls, which can be used as O(2c) row markers, are resolved, the surface ionic sublattice was identified by the authors by using the information available through the LCPD image. As the tip scans across

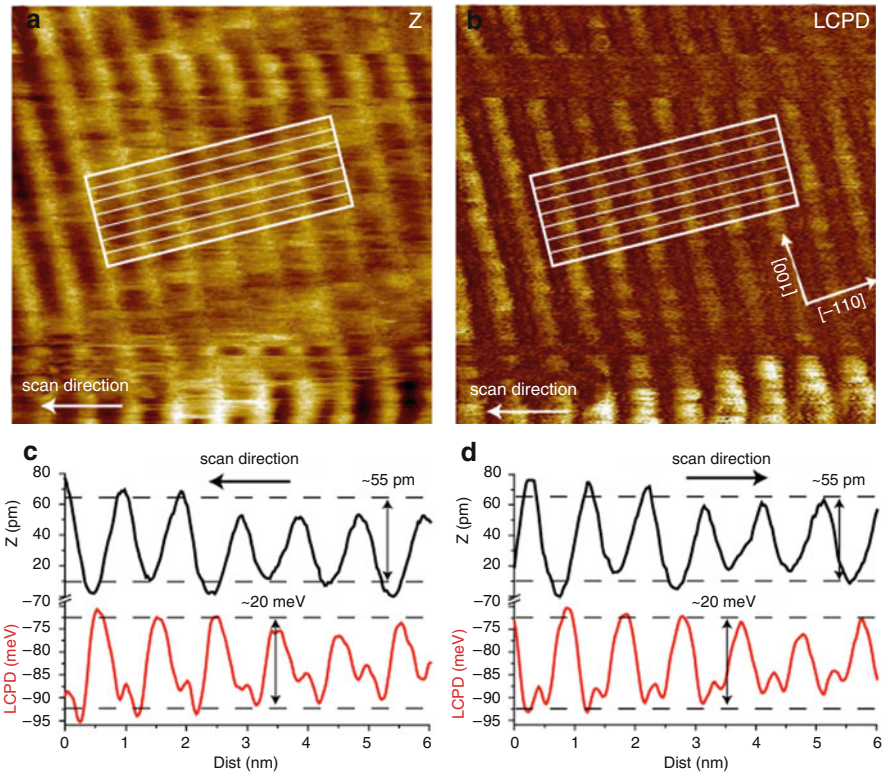

Fig. 13.17 (**a**) nc-AFM/AM-KPFM topography and (**b**) simultaneously recorded LCPD on a TiO_2 surface with a size of 10×8 nm^2. (**c**) and (**d**) 99-line average cross-sections of the topography and the LCPD, as indicated by the white boxes in (**a**) and (**b**) for the forward and backward scan direction. A line-by-line slope-correction filter was applied to (**a**). Image parameters: $f_{1st} = 70.691$ kHz, $\Delta f_{1st} = -212.2$ Hz, $A_{1st} \approx 28$ nm, $f_{ac} = 451.978$ kHz, $V_{ac} = 300$ mV [85]

the O(2c) anions, the electrostatic contribution to the overall interaction causes the KPFM setup to increase the negative bias on the tip, and a direct assignment of the O(2c) rows to the dark rows in the LCPD image and vice versa for the Ti(5c) rows is possible. It was noted by the authors that the absolute values of the LCPD signal ($\approx$20 meV) exhibits a significant distance dependence influenced by averaging effects, which depend both on the closest tip-surface distance and the tip sharpness. From the analysis of cross-sections taken along equivalent paths in the topography and the LCPD images recorded in the forward and backward directions (Fig. 13.17c and d) the authors ruled out that the apparent LCPD atomic resolution could be entirely due to cross-coupling. They assumed that a cross-talk effect would manifest itself in the LCPD channel as a proportional inverse response in the topography trace, which was not the case.

Furthermore, the details of the cross-sections revealed insights in the nature and range of the electrostatic potential associated with the LCPD signal compared to the

short-range chemical forces that produce the atomic contrast in nc-AFM. The LCPD maxima are shifted slightly to the right with respect to the minima in the topography, and since this shift is evident in both scanning directions it is not a delay effect of the loop controller, but related to an asymmetry in the way forces and LCPD signals are detected by the tip. Also, a thorough inspection of the cross-section graphs, revealed additional small peaks in the LCPD signal which are located in between the primary corrugation. These observations were qualitatively described by considering a slightly asymmetric model of the atomic structure of the AFM tip-apex, which consists of a polar material (e.g., SiO_x or TiO_x clusters picked up from the surface), constructed by placing the imaging apex-atom slightly off the vertical symmetry axis of the tip. This seems to be a reasonably realistic model in light of previous observations showing that even a rather small configurational change associated with the movement of single atom or a small cluster may shift the charge on the tip and lead to a pronounced differences in the topography signal without deterioration of the lateral atomic-scale contrast [76]. By means of this simple model, the authors were able to explain the experimental findings, by considering that the imaging-site on the tip for the topography might be located at the outermost tip-apex atom, whereas the LCPD imaging site may be shifted slightly to one side and could be located at the electrostatic center-of-mass somewhere in between two positive tip ions expected at the tip apex.

Random changes in the atomic-scale structure of the AFM tip-apex may occur during scanning, and this in turn leads to changes in the AFM topography and LCPD signals. It is clearly evident in the topography image (Fig. 13.18a) that the image contrast changes twice along the slow scan direction (bottom-to-top), as indicated by the two dashed horizontal black lines. The cross-section graph in Fig. 13.18c

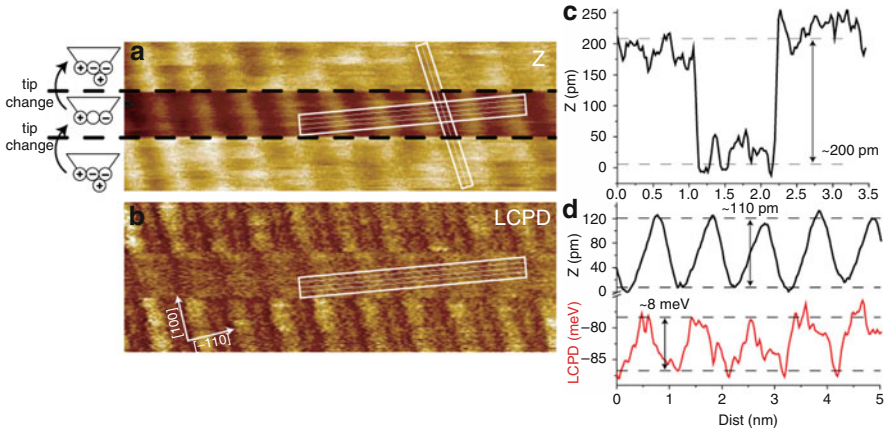

Fig. 13.18 (**a**) and (**b**) Cutouts from Fig. 13.17(**a**) and (**b**) showing two tip changes, indicated by the dashed horizontal black lines, changing the image contrast in both the topography and the LCPD. (**c**) 9-line average cross-section of (**a**) as indicated by the smaller white box (I). (**d**) 21-line average twin cross-sections of (**a**) and (**b**), indicated by the larger white boxes (II) [85]

shows that the changes in the image contrast are associated with tip-jumps of ≈200 pm toward and away from the surface. This change was interpreted by a very simple model shown to the left in Fig. 13.18a as a modification at the single atom level where the tip apex is made one atomic distance shorter, causing the Z feedback loop to move the tip closer to the surface to maintain the frequency-shift set point. At the second tip-change event the original tip-apex structure is regained, causing the z-feedback loop to retract the tip again. In Fig. 13.18d the authors presented cross-sections taken perpendicular to the bright rows in Fig. 13.18a and b. When comparing the corrugation values to those in Fig. 13.17c it is clear that the z corrugation has been more than doubled from ≈50 pm to ≈110 pm, while a comparison of the LCPD corrugation reveals that it has been reduced by more than a factor of two from ≈20 meV to ≈8 meV. This apparent inverse relation between the corrugation amplitudes in AFM topography and LCPD was explained by considering the detailed structure of the tip using the simple tip model. A stronger topography signal, which at the same time gives a vanishing LCPD contrast, may be realized by a slightly blunter model tip consisting of both a negative and a positive part placed near by with an interspacing matching the distance between O and Ti rows on the surface. When a fixed (or induced) positive charge in the tip-apex interacts with an anion in the surface, and at the same time a fixed (or induced) negative charge in the tip interacts with a cation in the surface, the combined effect is either that the induced charges cancel each other or that it is not possible to bias the tip (place surface charges) so that the field between tip and surface is nullified, i.e., a vanishing contrast is seen in the LCPD. The important finding is that the absolute values of the LCPD are determined to a very large degree by the tip sharpness and the conductive nature of the tip (metallic, ionic), and a quantitative comparison between atomic-scale LCPD measurements and surface potentials derived by theory should take this finding into account.

13.3.4 Ionic Surfaces

The difficulty for interpreting the experimental results presented before stems mainly from the lack of theoretical description for the short-range electrostatic forces which are intricately involved in the atomic-scale contrast and the way these forces are processed by the KPFM control circuit. In order to address these questions, an analytical model for the short-range electrostatic interaction between a biased tip and an ionic surface was developed and presented in Chap. 5. In this section we want to extend the experimental findings on this material class to verify that KPFM contrast can lead to qualitative as well as quantitative results at atomic scale. It has previously been advocated that the measured KPFM signal is dependent on the tip-surface imaging distance [14,16], which implies the possibility of cross-talk occurring when recording KPFM and topography nc-AFM images simultaneously.

Facing this question an ionic crystal KBr(100) which is easy to prepare and has a well-known surface structure was used. The insets of Fig. 13.19a and b show the

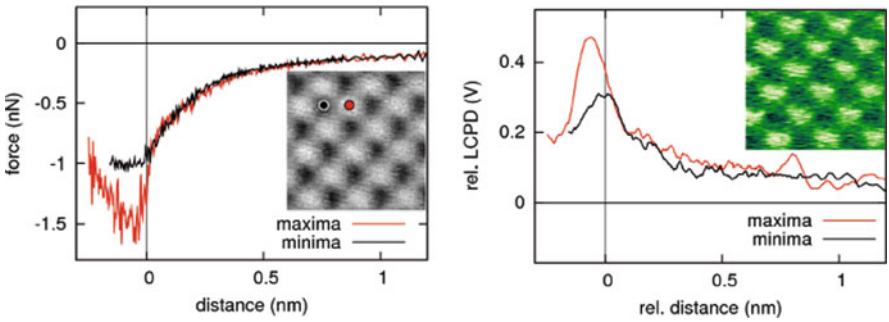

Fig. 13.19 Simultaneously recorded (**a**) force- and (**b**) relative LCPD-distance curves above a protruding and a hollow side (indicated by the dots in the inset) on a KBr(110) surface. The insets showing the topography ($\Delta z = 100$ pm) and the LCPD ($\Delta LCPD = 360$ mV) in an area of 2×2 nm^2. Image parameters: $f_{1st} = 168.205$ kHz, $\Delta f_{1st} = -36$ Hz, $A_{1st} = 10$ nm, $f_{ac} = 1.0406$ MHz, $V_{ac} = 500$ mV

topography and the LCPD signal observed by AM-KPFM on a bulk KBr sample, respectively. To clarify the origin of the contrast we used z-spectroscopy measurements taken on specific atomic sites. The thermal drift during the measurements was reduced by the atom tracking technique. The plot in Fig. 13.19a shows the force calculated by the Sader-Jarvis algorithm [86] from the frequency shift of the first resonance for two positions, a protruding and a hollow side marked by small dots in the inset images. In Fig. 13.19b the simultaneously determined relative LCPD is presented. Below a tip-sample distance of 0.5 nm a clear increase of the LCPD can be observed which has a different behavior for the anionic and cationic site. Nevertheless, it cannot be decided which site corresponds to the anion or cation since no clear evidence from the topography image is possible. However, taking the theoretical considerations from Nony et al. [18, 19] into account (compare also Chap. 5) which are describing the short-range electrostatic interaction between an ionic surface and a AFM tip, we can assign the protrusions to the cationic K^+ and the hollow sites to the anionic Br^- sites. To verify that no cross talk strongly influenced the results bias-spectroscopy measurements above a cation for several distinct tip-surface distances were done. The results show comparable features so that influences due to capacitive cross talk or due to a frequency shift of the second resonance can be neglected.

To further study the influence of the ac-voltage on KPFM results on an ionic crystal, measurements along a two monolayer KBr step edge with different V_{ac} were taken. The main questions addressed by this experiment are, is the local polarization expected to be the origin of the LCPD contrast on ionic crystals dependent on the changing electrostatic field induced by V_{ac} and does the capacitive cross talk which is linearly dependent on the ac-voltage play a crucial role in the contrast formation. More technical details about the cross talk can be found in Sect. 13.4. Figure 13.20 a and b shows the topography and the LCPD, respectively. The V_{ac} was changed according to the indicated arrows and values from 100 to 700 mV.

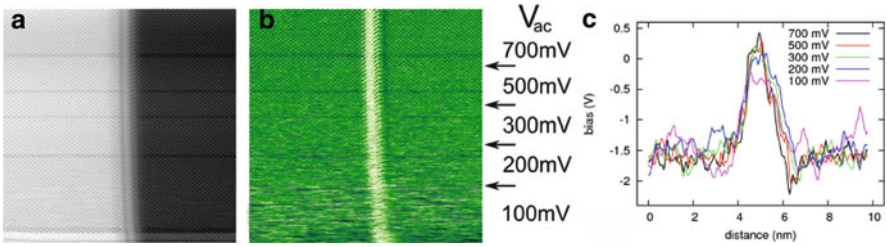

Fig. 13.20 Topography (**a**) and simultaneously detected LCPD (**b**) by AM-KPFM for various different ac-voltages V_{ac} with a size of 25×25 nm^2. The cross-sections in (**c**) taken from the respective regions in (**b**) showing a decreased LCPD at the step edge which is independent for different V_{ac} voltages. Image parameters: $f_{1st} = 154.022$ kHz, $\Delta f_{1st} = -52$ Hz, $A_{1st} = 10$ nm, $f_{ac} = 960.830$ kHz

The scan direction was from bottom to top of the image. In the topography several jumps of ≈300 pm can be noticed which are not correlated to the change of the V_{ac} voltage and are most probably related to atomic jumps at the tip apex. The LCPD does only change marginally with these tip-apex changes compared to the potential drop at the step edge.

The signal to noise ratio of the LCPD measurement is obviously directly coupled to the applied ac-voltage, as expected. For the lowest voltage of 100 mV no atomic corrugation in the LCPD is visible while the drop at the step edge is still observable. One has to notice that the detected signal on a bulk ionic crystal is very small compared to measurements on semiconductors or metals. Therefore, usually higher ac-voltages are preferred to increase the signal to noise ratio, also surface band bending effects like on semiconducting surfaces are not expected. In conclusion, no clear evidence if the atomic variations of the LCPD are directly influenced by the ac-voltage can be drawn, since the variations disappear in the noise. The second question can be addressed more easily. In Fig. 13.20c several line sections across the step edge for the different V_{ac} values are plotted. The difference between the LCPD of the terrace and the step edge increases only slightly from the lowest to the highest ac-voltage. This effect again can mainly be explained by the increased noise since the line sections are averaged over several parallel lines. Therefore an influence due to a capacitive cross talk can be neglected since a linear behavior should be observed otherwise.

13.3.5 KPFM by Tuning-Fork AFM

A relatively new technique for the determination of the LCPD is the tuning-fork based AFM [88–90]. The main difference is the capability to use a full metal tip which might improve the theoretical description of the interaction forces in KPFM. Up to know only a few examples are published [87, 91–95]. M. Heyde et al. optimized a double quartz tuning fork sensor at low temperature for simultaneous

STM and AFM operation [88]. They published several studies of work function changes on thin metal oxides on metal surfaces. The determination of the tip-sample distance on the local work function difference of MgO islands on Ag(001) [93], the drop of the local work function along line defects of thin film aluminum oxide on NiAl(110) [94] as well as the distinction of the charge state of point defects on MgO/Ag(001) [87]. Figure 13.21a shows a nc-AFM image taken at constant frequency shift of a MgO step edge with such point defects and a typical frequency shift vs. bias voltage curve (b) taken on a defect position. In (c) the determined LCPD values of the four types of defects indicated by numbers and

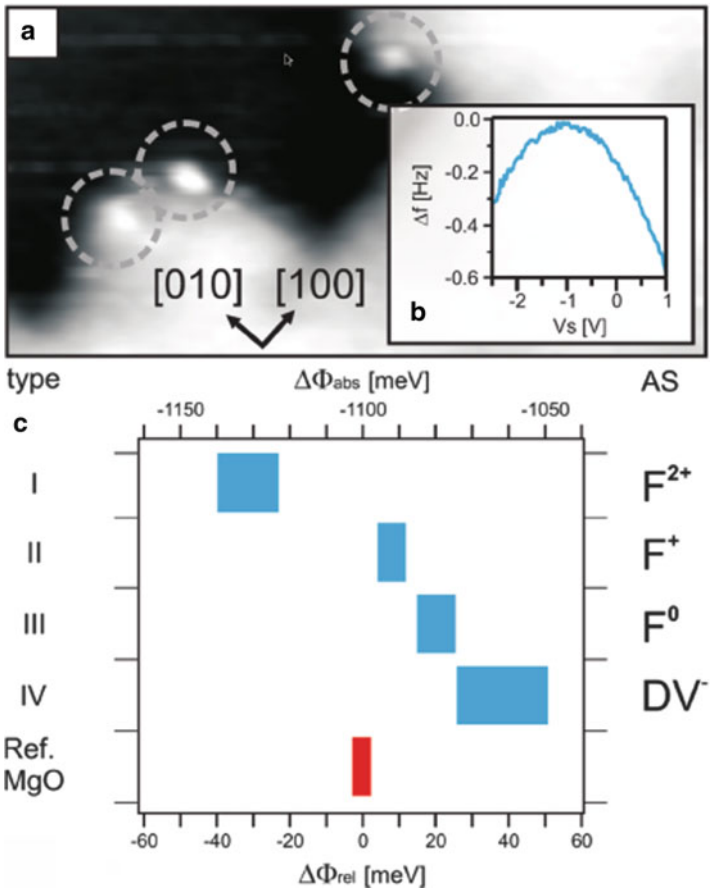

Fig. 13.21 (**a**) Tuning fork nc-AFM image (23.0×11.5 nm^2) taken at constant frequency shift showing a MgO step edge with point defects (indicated by the dashed circles).(**b**) Presents a typical frequency shift vs. bias voltage curve taken on a defect position. (**c**) shows a graph presenting the relative shift of the LCPD $\Delta\Phi_{\mathrm{rel}}$ with respect to the MgO surface (bottom abscissa) and the absolute shift $\Delta\Phi_{\mathrm{abs}}$ with respect to the Ag(001) level (top abscissa). Image parameters: $f_{1st} = 21.200$ kHz, $Q_{1st} = 22{,}000$, $\Delta f_{1st} = -1.6$ Hz, $A_{1st} = 350$ pm [87]

the MgO reference are plotted. The values were determined by the maximum positions of the parabola with respect to a reference measurement on MgO (bottom abscissa) and with respect to the Ag(001) level (top abscissa). Additional and supporting measurements for all defect types were performed with STS. The electronic signature of the defects, i.e., the local density of states (LDOS), has been analyzed complementary by STS directly after the local potential measurements without moving the tip laterally. The combined KPFM and STM measurements clearly show the possibility to characterize and quantify the major and in literature mostly discussed defect types in MgO by their charge state.

Gross et al. identified and manipulated the charge state of a single adatom by a tuning-fork tip [91]. In Fig. 13.22a the frequency shift measured as a function of the bias voltage is plotted for a gold atom sitting on top of an ultrathin NaCl layer on Cu(111). In between the measurement the Au^- was switched to the uncharged state Au^0. The switching event itself was done by applying a bias voltage pulse of about −1 V for a few seconds. To confirm that the switching event has occurred and to verify that the switched atom has not changed its lateral position, STM images were taken before and after this routine (Fig. 13.22b and c). Performing the measurement under these conditions, i.e., without moving the tip, ensures that the observed effects

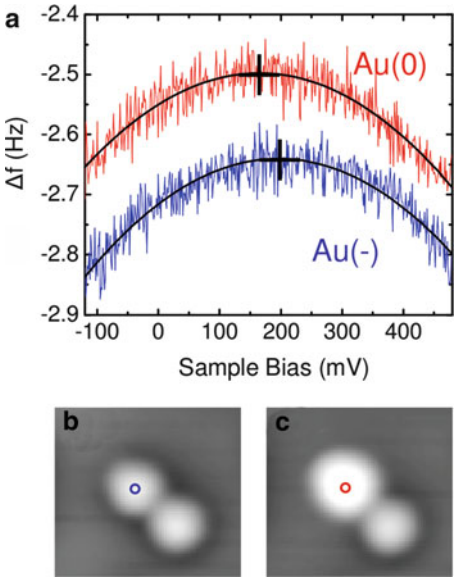

Fig. 13.22 (**a**) Frequency shift measured as a function of the voltage above an Au^- and an Au^0 adatom on an ultrathin NaCl layer deposited on Cu(111). After measuring $\Delta f(V)$ above Au^-, the charge state was switched to Au^0 by applying a bias pulse of V = −1 V for a few seconds. Image parameters: f_{1st} = 23 kHz, Q_{1st} = 50,000, Δz = 580 pm, A_{1st} = 60 pm, f_{ac} = 960.830 kHz. The LCPD values were determined by parabolic fits. STM images (I = 7.4 pA,V = 50 mV, and size 2.9 × 2.7 nm) before (**b**) and after (**c**) the $\Delta f(V)$ measurements confirm the charge-switching event and show no evidence of any lateral movement of the switched Au atoms [91]

are not due to tip changes, different tip heights, or spatial variations of the LCPD of the substrate. They observed that the LCPD of Au^- has shifted by $+27 \pm 8$ meV with respect to Au^0. The shift in the LCPD was explained by a dipole moment directed from the vacuum to the surface, which is induced by the negative Au^-. Hence the work function at the adatom position increases locally, i.e., the sample has to be biased more positively to compensate for the negative charge on the adatom. The absolute value of the LCPD shift depends on the tip-sample separation and tip condition but the direction was found to be unaffected.

While most of the tuning fork-related LCPD measurements are based on spectroscopy a simultaneously measured topography and LCPD image was presented by Bettac et al. [92]. They performed KPFM measurements with a QPlus sensor on a Si(111) surface at 77 K. Figure 13.23 presents an atomically resolved Si(111)-(7 × 7) reconstructed surface imaged in combined nc-AFM and FM-KPFM

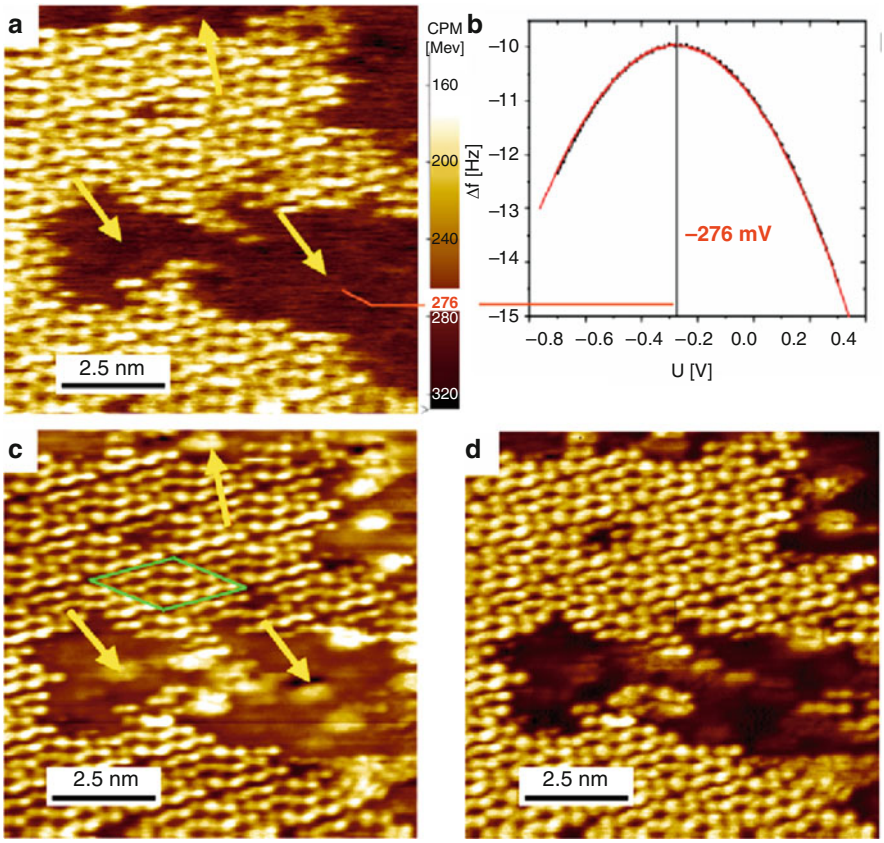

Fig. 13.23 Kelvin probe microscopy on a Si(111) surface. (**a**) LCPD, (**b**) $\Delta f(V)$ measurement at the indicated position, (**c**) topography image, and (**d**) damping signal. Image parameter: $f_{1st} = 47$ kHz, $\Delta f_{1st} \approx -10$ Hz, $A_{1st} = 2$ nm, T = 77 K, $f_{ac} = 500$ Hz, and $V_{ac} = 1$ V [92]

mode. The LCPD as presented in Fig. 13.23a reveals clear CPDs between the clean areas with (7 × 7) reconstruction and the precipitate regions indicated by arrows. In addition, the contact potential map shows the Kelvin probe signal with atomic contrast.

In the preceding section we reviewed and discussed the main experiments showing variations of the electrostatic force at the atomic scale. These effects are only observable in very close proximity to the sample surface, in most cases below 500 pm. Even so a lot of artifacts influencing the measured signals can be expected, the results suggest that by KPFM qualitative information about charge variations at the atomic scale can be obtained. Qualitative comparisons with theoretical calculation suggest that at least the polarity of the detected signal can be related to the observed charge. Up to now quantitative information like the charge density or the ionization energy cannot be obtained. The major hindrance might be the unknown tip-apex configuration which has a major impact on the measured signal. In the following section the major possible artifacts influencing the KPFM measurements will be discussed.

13.4 Influence of Measurement Parameters

The atomic contrast in KPFM measurements is still under controversial debate since the concept used to determine the relevant signals is based on a macroscopic concept of the work function and long-range electrostatic forces. As we discussed in the sections above the number of publications observing atomic corrugations as well as giving fundamental explanations of the contrast mechanisms are increasing. Nevertheless, the technique itself is very sensitive to various experimental artifacts which are important to take into consideration especially while analyzing data on atomic scale. In the following the most prominent influences will be presented and discussed.

13.4.1 Influence of the Tunneling Current

Arai and Tomitori conducted nc-AFM measurements on Si(111) with a piezoresistive Si cantilever. While doing bias-spectroscopy measurements they observed close to the surface deviations from the expected parabolic behavior [63].

Figure 13.24a shows measured Δf plots versus the tip-sample distance and the bias voltage V applied to the sample. At separations larger than 1 nm, the signal is mainly influenced by the van der Waals and the long-range electrostatic forces visible in the pure quadratic bias dependence ($F_{el} = \frac{1}{2}\frac{\partial C}{\partial z}(V - V_{CPD})^2$). Under a constant oscillation amplitude the absolute value of the capacitance gradient $\partial C/\partial z$ increases with decreasing separation owing to a steep increase in capacitance [96]. The minimum value of Δf was determined to be located at $\mathrm{V} = \mathrm{V_{CPD}} = -0.27$ V.

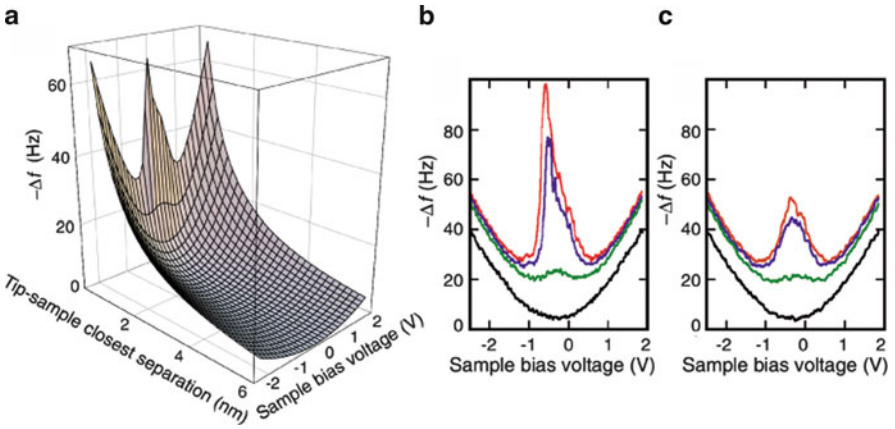

Fig. 13.24 (**a**) Δf spectroscopy curves in dependence of the tip-sample distance and the sample bias voltage, which were measured over a Si adatom on a Si(111)-(7 × 7) surface. (**b**) and (**c**) showing single bias-spectroscopy Δf curves for different tip-sample distances (0.30 (red), 0.33 (blue), 0.43 (green), and 1.5 nm (black)) taken above a Si adatom and over an area without Si surface atoms, respectively [63]

For separations less than about 0.5 nm deviations from the parabolic shape have been observed by the authors indicating a clear bias dependence of the short-range attractive forces [63]. Figure 13.24b and c shows the raw spectra at several separations over a Si adatom and over an area with no Si surface atoms, respectively. In particular, more prominent peaks were found over a Si adatom at specific voltages with decreasing separation. Arai and Tomitori attributed the sharp peaks to quantum mechanical resonances due to a tuning of the energy levels of the surface states from the sample to those of the tip by shifting the Fermi level through changing the bias voltage. The broad peak was explained by resonating states over a lowered tunneling barrier. Taking the principle of KPFM into account, which uses the parabolic shape to determine the minima at the bottom of the curve, it becomes obvious that the atomic contrast in the LCPD signal on Si(111)-(7 × 7) might be related to a hopping between the double minima of the bias-dependent frequency shift. However, recent results have shown, that atomic resolution in the LCPD signal can also be observed without the double feature in the bias dependence [60, 97].

In conclusion, the experimental results available up to now indicate that there might be a dependence of the LCPD signal to the tunneling current, e.g., the overlap of energy levels from surface states of the sample and the tip, respectively. Furthermore, it should be mentioned that for a correctly working KPFM setup a defined potential of the sample and the tip is essential, which might be not the case if the tip or the sample is connected via an IV-converter with a limited bandwidth to a virtual ground.

13.4.2 Influences by V_{ac}

Further effects can be expected by influences of the used ac-bias modulation voltage V_{ac} which is used to modulate the electrostatic forces between sample surface and tip. The fundamental equations describing the basic model for KPFM measurements (2.12)–(2.15) obviously show a direct impact of V_{ac} as well as the capacitance gradient on the static cantilever deflection (dc-component), while on semiconductors additionally an induced surface band bending effect might be expected. The strong influence on KPFM measurements was already noticed in 1995 by Yasutake [98] and was tried to be minimized by simultaneously detecting the 2ω-component as well as reducing V_{ac}. The latter has the drawback that the signal to noise ratio strongly depends on applied ac-bias, which is especially significant in FM-KPFM.

A possibility to reduce this artifact was presented by Uchihashi et al. [66]. Figure 13.25 shows the frequency shift (here $\Delta\nu$) as a function of the tip-sample distance Z on a Si(111) surface. The closed circles correspond to the distance dependence of the frequency shift at an ac-bias voltage of $V_{ac} = 0$ V. The closed triangles correspond to that at $V_{ac} = 1$ V with a frequency of $\omega/2\pi = 300$ Hz applied to the cantilever indicating a clear contribution from the capacitive forces. The open circles correspond to the frequency shift curve after subtracting the 2ω-component (open triangles) from the data obtained at $V_{ac} = 1$ V (closed triangles). After that treatment the variation in the distance dependence is almost coincident with that of the original curve. However, at that time no atomic information was

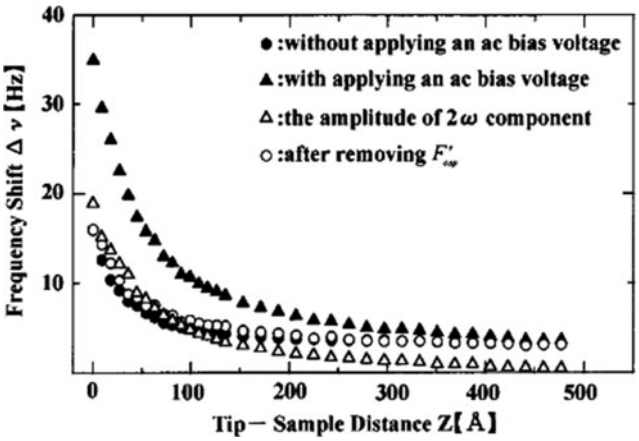

Fig. 13.25 Frequency shift $\Delta\nu$ as a function of the tip-sample distance Z on Si(111). Filled triangles and circles represent the distance dependence with and without an ac-bias voltage, respectively. After subtracting the 2ω-component (*open triangles*) from the curve with an applied ac-bias the distance dependence (*open circles*) follows the original one. Used parameters: $V_{ac} = 1$V, $\omega/2\pi = 300$Hz [66]

attributed to the crosstalk between this ac-bias induced change in the capacitance gradient.

Okamoto and co-workers addressed first this problem and presented simultaneous measurements of the topography, the ω-, as well as the 2ω-component on Si(111)-(7 × 7) [62]. Figure 13.26a–c shows clear atomic resolution in all three channels. While the 2ω-signal shows only variations in the mHz regime, they measured corresponding variations of up to 30 Hz in the frequency shift (roughly 30% of the set point) used for topography control. This means that the "artifact" signal might have a considerable magnitude depending on experimental conditions and should be minimized as well as detected to avoid unwanted changes of the tip-sample distance.

Beside this effect care has to be taken while measuring on semiconductors as well as on surfaces which can be polarized. However, this effect is not jet analyzed at the atomic scale. Sommerhalter et al. [99] have shown that the quantitative determination of the CPD on semiconducting samples can be significantly influenced by the electric field of the applied ac-bias voltage. Figure 13.27 depicts the dependence of the CPD on V_{ac}. The CPD value was obtained from the minimum of the lock-in

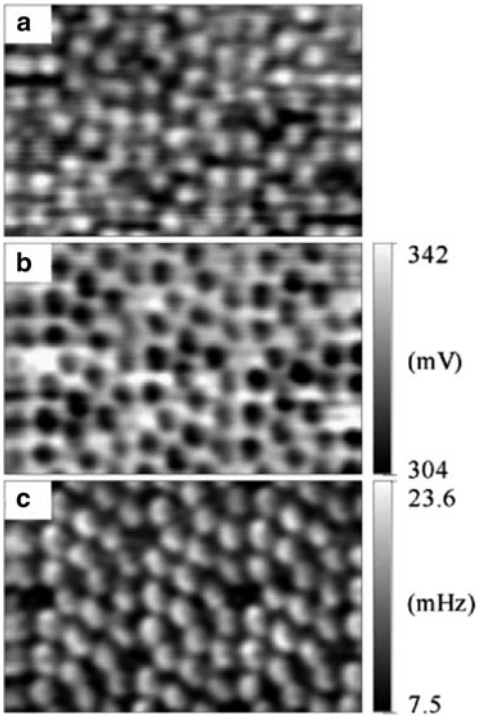

Fig. 13.26 Simultaneously obtained images of (**a**) topography, (**b**) LCPD and (**c**) 2ω-signal on a Si(111)-(7 × 7) surface with a scan size of $10.2 \times 6.6\ nm^2$. Measurement parameters: $f_{1st} = 169.69$ kHz, $\Delta f_{1st} = -105$ Hz, $A_{1st} = 8.1$ nm, $f_{ac} = 1$ kHz, and $V_{ac} = 1\ V_{rms}$ [62]

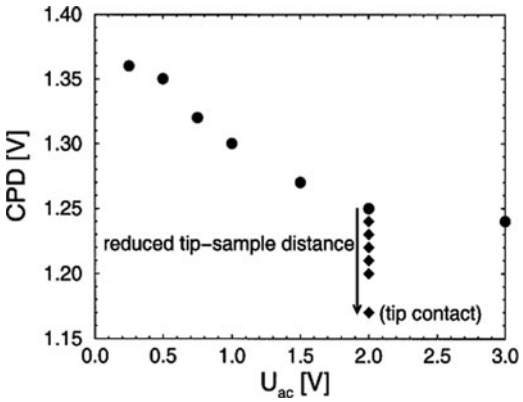

Fig. 13.27 Dependence of the CPD on WSe_2 on V_{ac}. At $V_{ac} = 2.0$ V the frequency shift was decreased from $\Delta f_{1st} = -40$ Hz to $\Delta f_{1st} = -90$ Hz to compensate the additional electrostatic dc force; tip contact occurred at $\Delta f_{1st} = -150$ Hz [99]

signal in FM detection. The measurements were performed on a non-degenerate p-type WSe_2 ($p = 10^{16}$ cm^3) single crystal surface. Due to the layered structure, the (0001) van der Waals surface represents an ideal semiconductor surface free of cleavage-induced defects and surface states. A clear decrease of the measured CPD with increasing ac voltage was observed. The reason for this effect is that the electric field can penetrate into the semiconductor. Therefore, a tip-induced band bending occurs and V_{ac} is partially rectified at the semiconductor surface, resulting in an apparent reduction or increase of the measured CPD for p- or n-type doped samples, respectively. Since this effect strongly depends on the tip-sample distance, the change of the CPD for decreasing distance was measured in addition. As an example, the observed CPD$-z$ values for $V_{ac} = 2.0$ V are depicted along the arrow in Fig. 13.27. Measurements on metallic HOPG also confirmed that this effect was solely caused by the semiconducting sample. In conclusion Sommerhalter et al. showed that up to ac-bias voltages of 300 mV even on semiconductors only minor artifacts are expected [99].

Burke and co-workers have shown evidence of tip-induced polarization in CPD measurements on organic semiconductors [100]. They performed $\Delta f(V)$-spectroscopy measurements and FM-KPFM measurements on PTCDA and observed indications of tip-induced polarization effects of PTCDA appearing both as a "flattening" of the anticipated $\Delta f(V)$ curves and as a weak distance dependence consistent with the expected $1/z^2$ behavior for a polarizable material.

Even so the measurements do not show a clear influence at atomic scale, artifacts have to be taken into account in the determination of the LCPD due to tip-induced polarization and band bending effects. AM-KPFM may offer an improvement over FM-KPFM in this regard by permitting the application of smaller bias modulation voltages, and with an appropriate selection of imaging parameters may offer equivalent or superior resolution to FM-KPFM.

13.4.3 The Influence of Short-Range Forces

Another artifact was addressed by Okamoto et al. [14]. They analyzed the influence of the short-range forces on the detection of the electrostatic forces via FM-KPFM. The ac-bias applied for KPFM induces a modulation of the force signal, which results in a modulation of the cantilever oscillation. The force gradient information for the LCPD compensation is extracted from a small vertical region, even compared with the region of the short-range forces and contains the force distribution on the surface rather than the LCPD distribution.

Figure 13.28a shows the tip oscillation when an ac-bias is exerted between the tip and the sample surface, which consists of the resonance of the cantilever (here ω_0) and the additional oscillation induced by the ac-bias (here ω). The feedback control for the tip-sample distance cannot cancel the cantilever movement since the frequency of the ac-bias is chosen sufficiently faster than the response speed of the feedback controller. The points P and Q indicate the moments when the tip is closest to and furthest from the surface, respectively. The force F_{top} at both points was determined by Okamoto et al. [14] by integrating the force exerted on the tip in one oscillation cycle, it corresponds to the integrals of the force curve over the amplitude at each moment, Z_P and Z_Q, respectively, as shown in Fig. 13.28b. The modulated component of the force signal $f_{\text{top}}(\omega, \Delta V)$, therefore, reflects the averaged force in the region ΔZ. A change of the boundary closer to the surface, i.e., the left boundary in the figure, affects $f_{\text{top}}(\omega, \Delta V)$, while a change of the boundary further from the surface should not, because it is out of the short-range force region. Therefore, $f_{\text{top}}(\omega, \Delta V)$ is a nonlinear function with respect to V through Z. In other words, the topography is controlled via the time averaged force gradient measured at the resonance of the cantilever at a certain oscillation amplitude. A modulation of the amplitude is driven by the applied ac-bias (electrostatic force) as well as by uncompensated short-range forces. The latter is induced by different force sensitivities based on the different oscillation amplitudes

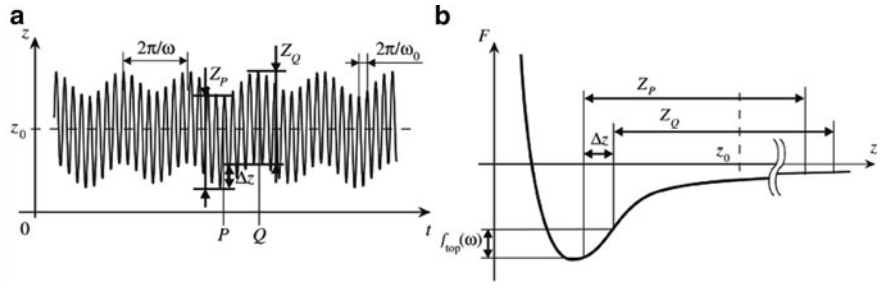

Fig. 13.28 (**a**) In FM-KPFM a cantilever oscillation with the angular frequency ω is induced in addition to the resonant oscillation at ω_0, schematic view. Due to the electrostatic excitation an additional oscillation with an amplitude Δz is induced. (**b**) The resulting frequency shift is proportional to the integral of the force curve over the amplitude Z. The points P and Q are indicators for the closest and furthest approach of the tip to the surface [14]

of the topography and KPFM signals. Therefore, the dc-bias used to compensate the KPFM signal does not only contain the LCPD but is also influenced by other short-range forces. This effect is comparable to the increased sensitivity observed in bimodal AFM [101, 102].

13.4.4 Capacitive Crosstalk

Especially in AM-KPFM where relatively high frequencies are used to modulate the electrostatic forces care has to be taken to avoid influences due to capacitive cross talk. Since the magnitude of the cross talk is linear proportional to the frequency and amplitude of the electrical excitation it can easily be determined. Furthermore, the effect is visible in a bias-spectroscopy curve done by KPFM above a surface as an offset in the amplitude R detected by the Lock-In amplifier. An example is shown in Fig. 13.29 where two graphs are showing the amplitude R, the in-phase signal X and the frequency shift Δf in dependence of the applied tip-sample bias. Since the measurement was taken with a relatively sharp tip on a KBr surface the bias values used to demonstrate the influence are large. In Fig. 13.29a the offset induced by the capacitive cross talk is visible in R since at the CPD we should detect a zero amplitude, which is not the case. This offset is directly transferred to the in-phase signal which is used by the Kelvin controller to determine the CPD. In the present case the dc-bias applied to the sample will be ≈ -20 V instead of 0 V. The influence is especially pronounced in this case (insulating KBr surface) since there is only a weak electrostatic coupling between the tip and the sample and therefore large ac-amplitudes have to be used to get a good signal to noise ratio. For a conductive surface this effect is much smaller and in most cases negligible.

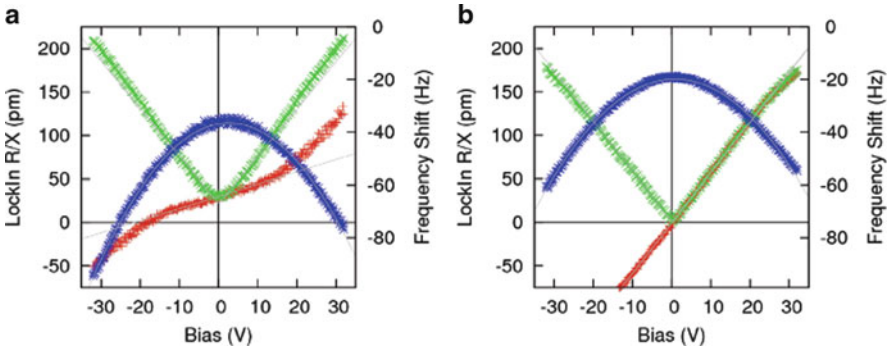

Fig. 13.29 Frequency shift Δf_{1st} and the amplitude R as well as the in-phase signal X of the second resonance of the cantilever ($f_{2nd} \approx 1$ MHz, $V_{ac} = 1$ V) obtained in bias spectroscopy on a KBr sample. (**a**) The capacitive cross talk is not compensated and the phase of the lock-in is not well adjusted. (**b**) External cross talk compensation and well-adjusted parameters

A second effect can be observed in Fig. 13.29a where the phase of the Lock-In is not perfectly adjusted to zero. This phase determined by the time delay between the ac-modulation voltage and the cantilever deflection signal should be adjusted to zero before the compensation to ensure the best signal to noise ratio. In the case of a capacitive cross talk, this phase offset does not only have an influence on the S/N ratio but also on the compensation voltage since the zero-crossing point of the in-phase signal is shifting. Since the phase might change even during the measurement due to a frequency shift of the resonance (only important in resonant AM-KPFM) a contrast in the LCPD can be induced. This effect only becomes important if the tip-sample distance becomes small, so that the tip apex enters the short-range force regime.

To avoid these influences the capacitive cross talk has to be minimized as much as possible. There are several possibilities of a capacitive interaction, first the ac-bias line can couple into the detection lines coming from the photodiode and second also into the z-piezo driving line. Both can be minimized by using appropriately shielded cables and spatially separated lines [99]. This allows for most conductive materials an effective and sufficient minimization of the capacitive cross talk and the related measurement errors. Nevertheless, using insulators reduces the ratio between the detected electrostatic oscillations and the incoming ac-modulation bias so that even small cross talks might have a non-negligible influence on the measured LCPD. Diesinger et al. presented an active compensation of the cross talk in these cases (see also Chap. 3) [103]. By applying a phase stable (but turned by 180°) signal at the same frequency used for the ac-modulation to the normal force signal of the photo detector the cross talk can be fully compensated by adjusting the amplitude of this cross talk compensation signal. Figure 13.29b shows a bias spectroscopy with optimal adjusted lock-in phase and an additional cross talk compensation enabling the correct measurement of the LCPD in AM-KPFM even at high resonances and ac-modulation voltages of up to $V_{ac} = 1$ V.

13.5 Summary

In this chapter the development of the KPFM technique toward molecular and atomic resolution was reviewed and discussed. Since by definition the work function has no clearly defined local character the so-called local work function as well as the related local CPD was introduced. By this definition variations in the mesoscopic length scale of only a few nanometer like potential variations at step edges or local variations of surface dipoles can be explained. But still the experimentally observed atomic contrast on Si, InP, TiO_2, and ionic surfaces is not directly accessible by a general theory. Theoretical considerations of ionic and Si surfaces point toward a local polarization effect induced by the tip used for the KPFM measurements. Experimental findings on these surfaces are described by such models quite well and even allow the identification of ionic species. Nevertheless, there are also clear experimental evidences that the effect of a single charge deposited on an atom on

top of an insulating layer can be detected by this technique, which can up to now not be quantified. In the last part of the chapter we discussed briefly the main origins of possible and unwanted artifacts in KPFM, which might become dominant at atomic-scale measurements.

References

1. J. Weaver, D. Abraham, J. Vac. Sci. Technol. B **9**(3), 1559 (1991)
2. M. Nonnenmacher, M.P. O'Boyle, H.K. Wickramasinghe, Appl. Phys. Lett. **58**(25), 2921 (1991)
3. S. Sadewasser, K. Ishii, T. Glatzel, M. Lux-Steiner, in *Polycrystalline Semiconductors VII, Proceedings, Solid State Phenomena*, vol. 93, ed. by T. Fuyuki, T. Sameshima, H. Strunk, J. Werner (2003), *Solid State Phenomena*, vol. 93, pp. 319–324. 7th International Conference on Polycrystalline Semiconductors, Nara, Japan, Sep 10–13, 2002
4. S. Sadewasser, P. Carl, T. Glatzel, M. Lux-Steiner, Nanotechnology **15**, S14 (2004)
5. C. Sommerhalter, T. Matthes, T. Glatzel, A. Jäger-Waldau, M.C. Lux-Steiner, Appl. Phys. Lett. **75**(2), 286 (1999)
6. Y. Rosenwaks, R. Shikler, T. Glatzel, S. Sadewasser, Phys. Rev. B **70**, 085320 (2004). DOI 10.1103/PhysRevB.70.085320
7. H. Hoppe, T. Glatzel, M. Niggemann, A. Hinsch, M.C. Lux-Steiner, N.S. Sariciftci, Nano Lett. **5**, 269 (2004). DOI 10.1021/nl048176c
8. A. Sinensky, A. Belcher, Nat. Nanotechnol. **2**, 653 (2007). DOI 10.1038/nnano.2007.293
9. T. Glatzel, D.F. Marrn, T. Schedel-Niedrig, S. Sadewasser, M.C. Lux-Steiner, Appl. Phys. Lett. **81**(11), 2017 (2002). DOI http://dx.doi.org/10.1063/1.1506205
10. S. Kitamura, M. Iwatsuki, Appl. Phys. Lett. **72**(24), 3154 (1998). DOI 10.1063/1.121577
11. S. Kitamura, K. Suzuki, M. Iwatsuki, Appl. Surf. Sci. **140**, 265 (1999)
12. S. Kitamura, K. Suzuki, M. Iwatsuki, C.B. Mooney, Appl. Surf. Sci. **157**, 222 (2000)
13. K. Okamoto, K. Yoshimoto, Y. Sugawara, S. Morita, Appl. Surf. Sci. **210**, 128 (2003)
14. K. Okamoto, Y. Sugawara, S. Morita, Jpn. J. Appl. Phys. **42**, 71637168 (2003)
15. A. Sasahara, C. Pang, H. Onishi, J. Phys. Chem. B **110**, 13453 (2006)
16. C. Leendertz, F. Streicher, M.C. Lux-Steiner, S. Sadewasser, Appl. Phys. Lett. **89**, 113120 (2006)
17. F. Bocquet, L. Nony, C. Loppacher, T. Glatzel, Phys. Rev. B **78**, 035410 (2008)
18. L. Nony, F. Bocquet, C. Loppacher, T. Glatzel, Nanotechnology **20**(26), 264014 (2009)
19. L. Nony, A.S. Foster, F. Bocquet, C. Loppacher, Phys. Rev. Lett. **103**(3), 036802 (2009)
20. L. Kelvin, Phil. Mag. **46**, 82 (1898)
21. N.D. Lang, W. Kohn, Phys. Rev. B **3**(4), 1215 (1971)
22. N.D. Lang, A.R. Williams, Phys. Rev. B **25**(4), 2940 (1982)
23. S. Sadewasser, T. Glatzel, M. Rusu, A. Jäger-Waldau, M. Lux-Steiner, Appl. Phys. Lett. **80**(16), 2979 (2002)
24. J. Küppers, K. Wandelt, G. Ertl, Phys. Rev. Lett. **43**(13), 928 (1979)
25. K. Wandelt, J. Vac. Sci. Technol. **2**(2), 802 (1984)
26. K. Wandelt, Appl. Surf. Sci. **111**, 1 (1997). Proceedings of the International Vacuum Electron Sources Conference 1996
27. J.F. Jia, K. Inoue, Y. Hasegawa, W.S. Yang, T. Sakurai, Phys. Rev. B **58**(3), 1193 (1998).
28. R. Wiesendanger, *Scanning Probe Microscopy and Spectroscopy, Methods and Applications* (Cambridge, Cambridge University Press, 1994)
29. G. Binnig, H. Rohrer, C. Gerber, E. Weibel, Appl. Phys. Lett. **40**(2), 178 (1982)
30. N.D. Lang, W. Kohn, Phys. Rev. B **8**(12), 6010 (1973)
31. J.G. Gay, J.R. Smith, F.J. Arlinghaus, Phys. Rev. Lett. **38**(10), 561 (1977)

32. N. Lang, S. Holloway, J. Nrskov, Surf. Sci. **150**(1), 24 (1985)
33. M. Thompson, H. Huntington, Surf. Sci. **116**(3), 522 (1982)
34. G. Binnig, C. Quate, C. Gerber, Phys. Rev. Lett. **56**(9), 930 (1986)
35. T. Shiota, K. Nakayama, Jpn. J. Appl. Phys. **40**(9A/B), L986 (2001)
36. T. Glatzel, S. Sadewasser, R. Shikler, Y. Rosenwaks, M. Lux-Steiner, Mater. Sci. Eng. B **102**, 138 (2003)
37. J. Repp, G. Meyer, S. Stojkovic, A. Gourdon, C. Joachim, Phys. Rev. Lett. **94**, 026803 (2005)
38. L. Gross, F. Mohn, N. Moll, P. Liljeroth, G. Meyer, Science **325**(5944), 1110 (2009)
39. L. Nony, E. Gnecco, A. Baratoff, A. Alkauskas, R. Bennewitz, O. Pfeiffer, S. Maier, A. Wetzel, E. Meyer, C. Gerber, Nano Lett. **4**(11), 2185 (2004)
40. J. Mativetsky, S. Burke, S. Fostner, P. Grütter, Small **3**(5), 818 (2007)
41. S. Maier, L.A. Fendt, L. Zimmerli, T. Glatzel, O. Pfeiffer, F. Diederich, E. Meyer, Small **4**, 1115 (2008)
42. L. Zimmerli, S. Maier, T. Glatzel, E. Gnecco, O. Pfeiffer, F. Diederich, L. Fendt, E. Meyer, J. Phys.: Conf. Ser. **61**(1), 1357 (2007)
43. S. Kawai, S. Maier, T. Glatzel, S. Koch, B. Such, L. Zimmerli, L.A. Fendt, F. Diederich, E. Meyer, Appl. Phys. Lett. **95**(10), 103109 (2009)
44. B. Such, T. Trevethan, T. Glatzel, S. Kawai, L. Zimmerli, E. Meyer, A.L. Shluger, C.H.M. Amijs, P. de Mendoza, A.M. Echavarren, ACS Nano **4**(6), 3429 (2010)
45. V. Palermo, S. Morelli, M. Palma, C. Simpson, F. Nolde, A. Herrmann, K. Möllen, P. Samori, ChemPhysChem **7**, 847 (2006)
46. T. Glatzel, H. Hoppe, N. Sariciftci, M. Lux-Steiner, M. Komiyama, Jpn. J. Appl. Phys. **44**(7B), 5370 (2005)
47. S.A. Burke, J.M. LeDue, J.M. Topple, S. Fostner, P. Grütter, Adv. Mater. **21**, 1 (2009)
48. J. Mativetsky, S. Burke, S. Fostner, P. Grütter, Nanotechnology **18**(10), 105303 (6pp) (2007)
49. S.A. Burke, J.M. Mativetsky, S. Fostner, P. Grütter, Phys. Rev. B **76**(3), 035419 (2007)
50. T. Glatzel, M. Rusu, S. Sadewasser, M. Lux-Steiner, Nanotechnology **19**, 145705 (2008)
51. T. Glatzel, L. Zimmerli, S. Koch, S. Kawai, E. Meyer, Appl. Phys. Lett. **94**(6), 063303 (2009)
52. T. Glatzel, S. Sadewasser, M. Lux-Steiner, Appl. Surf. Sci. **210**(84), 8489 (2003)
53. T. Glatzel, L. Zimmerli, E. Meyer, Isr. J. Chem. **48**(2), 107 (2008)
54. T. Ichii, T. Fukuma, T. Yoda, K. Kobayashi, K. Matsushige, H. Yamada, J. Appl. Phys. **107**(2), 024315 (2010)
55. O. de Frutos, T. Granier, B. Gomez-Lor, J. Jimenez-Barbero, A. Monge, E. Gutierrez-Puebla, A.M. Echavarren, Chem. Eur. J. **8**(13), 2879 (2002)
56. F. Giessibl, Science **267**, 68 (1995)
57. S. Kitamura, M. Iwatsuki, Jpn. J. Appl. Phys. **34**(1B), L145 (1995)
58. Y. Sugimoto, P. Pou, M. Abe, P. Jelinek, R. Prez, S. Morita, O. Custance, Nature **446**, 64 (2007)
59. T. Shiota, K. Nakayama, Jpn. J. Appl. Phys. **41**(10B), L1178 (2002)
60. S. Kawai, T. Glatzel, H.J. Hug, E. Meyer, Nanotechnology **21**(24), 245704 (2010)
61. T. Shiota, K. Nakayama, Appl. Surf. Sci. **202**, 218 (2002)
62. K. Okamoto, Y. Sugawara, S. Morita, Appl. Surf. Sci. **188**, 381 (2002)
63. T. Arai, M. Tomitori, Phys. Rev. Lett. **93**(25), 256101 (2004)
64. Y. Sugawara, M. Ohta, H. Ueyama, S. Morita, Jpn. J. Appl. Phys. **34**(4A), L462 (1995)
65. H. Ueyama, M. Ohta, Y. Sugawara, S. Morita, Jpn. J. Appl. Phys. **34**(8B), L1086 (1995)
66. T. Uchihashi, M. Ohta, Y. Sugawara, Y. Yanase, T. Sigematsu, M. Suzuki, S. Morita, J. Vac. Sci. Technol. B **15**(4), 1543 (1997)
67. Y. Sugawara, T. Uchihashi, M. Abe, S. Morita, Appl. Surf. Sci. **140**, 371 (1999)
68. C. Domke, P. Ebert, M. Heinrich, K. Urban, Phys. Rev. B **54**(15), 10288 (1996)
69. J. Kolodziej, B. Such, M. Szymonski, F. Krok, Phys. Rev. Lett. **90**(22), 226101 (2003)
70. F. Krok, K. Sajewicz, J. Konior, M. Goryl, P. Piatkowski, M. Szymonski, Phys. Rev. B **77**, 235427 (2008)
71. C. Kumpf, D. Smilgies, E. Landemark, M. Nielsen, R. Feidenhans'l, O. Bunk, J.H. Zeysing, Y. Su, R.L. Johnson, L. Cao, J. Zegenhagen, B.O. Fimland, L.D. Marks, D. Ellis, Phys. Rev. B **64**(7), 075307 (2001)

72. H. Onishi, K. Fukui, Y. Iwasawa, Bull. Chem. Soc. Jpn. **68**(9), 2447 (1995)
73. K. Fukui, H. Onishi, Y. Iwasawa, Phys. Rev. Lett. **79**(21), 4202 (1997)
74. M. Ashino, T. Uchihashi, K. Yokoyama, Y. Sugawara, S. Morita, M. Ishikawa, Phys. Rev. B **61**(20), 13955 (2000)
75. J.V. Lauritsen, A.S. Foster, G.H. Olesen, M.C. Christensen, A. Kühnle, S. Helveg, J.R. Rostrup-Nielsen, B.S. Clausen, M. Reichling, F. Besenbacher, Nanotechnology **17**(14), 3436 (2006)
76. G.H. Enevoldsen, A.S. Foster, M.C. Christensen, J.V. Lauritsen, F. Besenbacher, Phys. Rev. B **76**, 205415 (2007)
77. G.H. Enevoldsen, H.P. Pinto, A.S. Foster, M.C.R. Jensen, A. Kühnle, M. Reichling, W.A. Hofer, J.V. Lauritsen, F. Besenbacher, Phys. Rev. B **78**(4), 045416 (2008)
78. G.H. Enevoldsen, H.P. Pinto, A.S. Foster, M.C.R. Jensen, W.A. Hofer, B. Hammer, J.V. Lauritsen, F. Besenbacher, Phys. Rev. Lett. **102**(13), 136103 (2009).
79. R. Bechstein, C. Gonzalez, J. Schütte, P. Jelinek, R. Perez, A. Kühnle, Nanotechnology **20**(50), 505703 (2009)
80. A. Sasahara, H. Uetsuka, H. Onishi, Jpn. J. Appl. Phys. **43**, 4647 (2004)
81. A. Sasahara, C.L. Pang, H. Onishi, J. Phys. Chem. B **110**(35), 17584 (2006)
82. J. Schütte, R. Bechstein, P. Rahe, M. Rohlfing, A. Kühnle, H. Langhals, Phys. Rev. B **79**(4), 045428 (2009)
83. P. Rahe, M. Nimmrich, A. Nefedov, M. Naboka, C. Woll, A. Kühnle, J. Phys. Chem. C **113**(40), 17471 (2009)
84. F. Loske, R. Bechstein, J. Schütte, F. Ostendorf, M. Reichling, A. Kühnle, Nanotechnology **20**(6), 065606 (2009)
85. G. Enevoldsen, T. Glatzel, M. Christensen, J. Lauritsen, F. Besenbacher, Phys. Rev. Lett. **100**, 236104 (2008)
86. J.E. Sader, S.P. Jarvis, Appl. Phys. Lett. **84**(10), 1801 (2004)
87. T. König, G.H. Simon, H.P. Rust, G. Pacchioni, M. Heyde, H.J. Freund, J. Am. Chem. Soc. **131**, 17544 (2009)
88. M. Heyde, M. Kulawik, H.P. Rust, H.J. Freund, Rev. Sci. Instrum. **75**(7), 2446 (2004)
89. F.J. Giessibl, Appl. Phys. Lett. **73**(26), 3956 (1998)
90. S. Hembacher, F.J. Giessibl, J. Mannhart, C.F. Quate, Proc. Natl. Acad. Sci. U. S. A. **100**(22), 12539 (2003)
91. L. Gross, F. Mohn, P. Liljeroth, J. Repp, F.J. Giessibl, G. Meyer, Science **324**(5933), 1428 (2009)
92. A. Bettac, J. Koeble, K. Winkler, B. Uder, M. Maier, A. Feltz, Nanotechnology **20**(26), 264009 (2009)
93. T. König, G.H. Simon, H.P. Rust, M. Heyde, J. Phys. Chem. C **113**(26), 11301 (2009)
94. L. Heinke, L. Lichtenstein, G.H. Simon, T. König, M. Heyde, H.J. Freund, ChemPhysChem **11**, 2085 (2010)
95. L. Heinke, L. Lichtenstein, G.H. Simon, T. König, M. Heyde, H.J. Freund, Phys. Rev. B **82**(7), 075430 (2010)
96. M. Guggisberg, M. Bammerlin, C. Loppacher, O. Pfeiffer, A. Abdurixit, V. Barwich, R. Bennewitz, A. Baratoff, E. Meyer, H.J. Güntherodt, Phys. Rev. B **61**(16), 11151 (2000)
97. S. Sadewasser, P. Jelinek, C.K. Fang, O. Custance, Y. Yamada, Y. Sugimoto, M. Abe, S. Morita, Phys. Rev. Lett. **103**(26), 266103 (2009)
98. M. Yasutake, Jpn. J. Appl. Phys. **34**, 3403 (1995)
99. C. Sommerhalter, T. Glatzel, T. Matthes, A. Jäger-Waldau, M. Lux-Steiner, Appl. Surf. Sci. **157**, 263 (2000)
100. S.A. Burke, J.M. LeDue, Y. Miyahara, J.M. Topple, S. Fostner, P. Grütter, Nanotechnology **20**(26), 264012 (2009)
101. S. Kawai, T. Glatzel, S. Koch, B. Such, A. Baratoff, E. Meyer, Phys. Rev. Lett. **103**(22), 220801 (2009)
102. S. Kawai, T. Glatzel, S. Koch, B. Such, A. Baratoff, E. Meyer, Phys. Rev. B **81**, 085420 (2010)
103. H. Diesinger, D. Deresmes, J.P. Nys, T. Melin, Ultramicroscopy **108**, 773 (2008)

Index

S. Sadewasser and T. Glatzel (eds.), *Kelvin Probe Force Microscopy*, Springer Series in Surface Sciences 48, DOI 10.1007/978-3-642-22566-6,